Characterisation of the stellar populations in the outer parts of spiral galaxies

Tomás Ruiz Lara
Depto. Física Teórica y del Cosmos
Universidad de Granada
Programa oficial de doctorado en
Física y Ciencias del Espacio

A thesis submitted for the degree of
Doctor in Physics
Supervised and directed by:
Dr. Isabel Pérez Martín and Dr. Estrella Florido Navío
February 2016

Editor: Universidad de Granada. Tesis Doctorales
Autor: Tomás Ruiz Lara
ISBN: 978-84-9125-868-1
URI: http://hdl.handle.net/10481/43696

Thesis title: *"Characterisation of the stellar populations in the outer parts of spiral galaxies"*

Date of the PhD Exam: 25^{th} February 2016

PhD Supervisors: Dr. Isabel Pérez Martín
Dr. Estrella Florido Navío

Examining commitee:

President:	Dr. Reynier Peletier
Secretary:	Dr. Almudena Zurita
Vocals:	Dr. Stéphane Courteau
	Dr. Javier Gorgas
	Dr. Simon Verley
External referees:	Dr. Peter Erwin
	Dr. Esther Mármol-Queraltó

Part of this work has been published in international refereed journals such as *Astronomy & Astrophysics* and *Monthly Notices of the Royal Astronomical Society*:

- *"Recovering star formation histories: Integrated-light analyses vs stellar colour-magnitude diagrams"* by T. Ruiz-Lara, I. Pérez, C. Gallart, D. Alloin, M. Monelli, M. Koleva, E. Pompei, M. Beasley, P. Sánchez-Blázquez, E. Florido, A. Aparicio, E. Fleurence, E. Hardy, S. Hidalgo, and D. Raimann. Published in *Astronomy & Astrophysics*, Volume 583, id.A60, 23 pp. Year: 2015. DOI: 10.1051/0004-6361/201526752.

- *"No direct coupling between bending of galaxy disc stellar age and light profiles"* by T. Ruiz-Lara, I. Pérez, E. Florido, P. Sánchez-Blázquez, J. Méndez-Abreu, M. Lyubenova, J. Falcón-Barroso, L. Sánchez-Menguiano, S. F. Sánchez, L. Galbany, R. García-Benito, R. M. González Delgado, B. Husemann, C. Kehrig, Ángel R. López-Sánchez, R. A. Marino, D. Mast, P. Papaderos, G. van de Ven, C.J. Walcher, S. Zibetti, and the CALIFA team. Published in *Monthly Notices of the Royal Astronomical Society: Letters*, Volume 456, Issue 1, p.L35-L39. Year: 2016. DOI: 10.1093/mnrasl/slv174.

- *"The imprint of satellite accretion on the chemical and dynamical properties of disc galaxies"* by T. Ruiz-Lara, C. G. Few, B. K. Gibson, I. Pérez, E. Florido, I. Minchev, and P. Sánchez-Blázquez. Accepted for publication in *Astronomy & Astrophysics*. arXiv ID: 1512.00625. DOI: 10.1051/0004-6361/201526470.

El doctorando Tomás Ruiz Lara y las directoras de la tesis Dra. Isabel Pérez Martín y Dra. Estrella Florido Navío, garantizamos, al firmar esta tesis doctoral, que el trabajo ha sido realizado por el doctorando bajo la dirección de las directoras de la tesis y hasta donde nuestro conocimiento alcanza, en la realización del trabajo, se han respetado los derechos de otros autores a ser citados, cuando se han utilizado sus resultados o publicaciones.

Granada, 26 de enero de 2016

El doctorando:

Tomás Ruiz Lara

Las directoras:

Dra. Isabel Pérez Martín

Dra. Estrella Florido Navío

A mi familia,
a Marta y Alberto,
a LAURA.
∞

Acknowledgements

Hay quien lleva meses bromeando con la longitud de esta sección de agradecimientos, hay hasta quien piensa que la sección de agradecimientos puede vencer en cuanto a longitud a la propia tesis. Yo creo que exageran, pero ya veremos cuando termine qué sucede. Lo que tengo claro es que: i) *"Es de bien nacidos ser agradecidos"* y ii) NADA de esto habría sido posible sin la ayuda, generalmente desinteresada, de tantos y tantos que me han ayudado a lo largo de estos años. Por desgracia no pueden firmar todos ellos este humilde manuscrito, pero al menos sus nombres quedarán escritos para siempre en estas páginas... GRACIAS, GRACIAS y, siempre, GRACIAS.

Por supuesto debo de empezar por las dos personas que durante más de cinco años (se dice pronto) han estado aguantándome y, sobre todo, formándome. Estas dos personas son, evidentemente, mis "directoras de tesis", Isa y Estrella, Estrella e Isa. Y digo "directoras de tesis" entre comillas porque ellas no han sido solo "directoras de tesis", han sido mucho más que eso. Han sido educadoras, han sido formadoras, han sido compañeras de trabajo, han sido apoyos en los momentos difíciles, han sido fuentes de información, han sido fuentes de tareas a realizar, han sido (y lo son) ejemplos a seguir... pero lo más importante, han sido (y serán) amigas y, casi me atravería a decir, han sido casi como mis segundas madres. Anteponiendo mi bien ante todo, no solo desde el punto de vista profesional, sino también personal. Estando a mi disposición en todo momento y dándomelo todo y más. Una tesis no es algo que se haga en 3 meses, desde junio de 2010 que asistí a mi primera reunión científica con ellas ha llovido bastante. Yo he cambiado, y en parte ellas me han modelado para ser una persona mucho mejor de la que era. Trabajar todo este tiempo en este ambiente me ha hecho amar (aunque también odiar en momentos) lo que hago y, especialmente amar la astronomía. Por esto, y por mucho más que no soy capaz de expresar con palabras... GRACIAS.

Y como no solo de trabajo vive el hombre, debo de dar un "gracias" muy especial también a mi familia, a todos ellos, claro está, pero particularmente a algunas personas muy especiales. A mis padres, Tomás y Antonia, por hacerme como soy, con mis defectos y mis cualidades, mis caprichos y locuras, mis creencias e inquietudes, mi forma de pensar y de ver la vida... por hacerme creer que siempre un mundo mejor es posible y que la gente es, por

naturaleza, buena, y es que mucho bueno he encontrado a lo largo de estos años. Por tener siempre palabras de apoyo y confianza hacia mí, por hacerme siempre creer que se puede aunque no sé hasta qué punto he cumplido con sus expectativas. A mi hermana, Mariani, que siempre me ha apoyado y confiado en mí, en las buenas y en las malas, incluso cuando dejaba de ser yo, ahí estaba ella, sin cambiar, con una sonrisa en la boca y con un gesto cómplice de tranquilidad. A su marido, mi cuñado, Beni, por esas horas y horas en coche haciendo el caminito Granada-Úbeda, Úbeda-Granada, por mostrarme en su día que una carrera en astrofísica era posible y por tantas noches de sufrimientos y alegrías que nuestro "Madrid" nos ha dado a lo largo de estos años. A mis tíos, Leo y Paqui, que me dejaban su conexión a Internet desde antes de terminar la carrera para buscar informaciones varias o para hacer algún trabajo, por esas tardes de piscina, por apoyarme antes de ir a Australia y por atreverse a montar en el coche conmigo, pero sobre todo, por estar ahí y siempre tener palabras de apoyo hacia mí. Al resto de tíos (Luci, Luis, Pepe, Manola, Esteban y Josefina) y a mis primos (Pepa, José Luis, María del Mar, Juan, Marisa y Mariani) por preguntar siempre por qué lugar del mundo andaba y por preocuparse de mí. Pero en especial, a las dos criaturas que nacieron cuando estudiaba la carrera y que me han visto evolucionar a lo largo de estos 5 años y yo evolucionar a ellos. A aquellos que tantas veces han dicho: *"Joer, Tete, otra vez estudiando"*. A los únicos que creían que esto era estudiar en lugar de trabajar, aunque realmente eran los únicos que sabían la verdad, porque la vida es estudiar, un continuo aprendizaje del que espero ellos cojan lo poco bueno que hay en mí, y desprecien lo mucho malo que tengo. A ellos que tanto me han echado de menos durante mis largos y lejanos viajes, a ellos que tanto me han apoyado a su manera y que tanto me han permitido desconectar del desarrollo de esta tesis, a ellos que sin saberlo me ayudaban constantemente, a ellos que se han convertido en mi estrella binaria preferida... gracias. Tal vez cuando leáis esto no sepáis muy bien de lo que se trata, pero espero que con el tiempo lo entendáis y acabéis escribiendo algo parecido sobre mí algún día... significará que algo habré hecho bien en esta vida. Por esto, y por mucho más que sigo sin ser capaz de expresar con palabras... GRACIAS.

A los miembros de la Asociación Astronómica Quarks de Úbeda, que siempre han creído en mí, y que siempre han estado orgullosos de mí, aunque sigo sin entender por qué. Ellos son los que deben de estar orgullosos de ellos mismos, de lo que hacen y de cómo lo hacen. Aún recuerdo esa primera observación en "El Paso", allá por finales de agosto de 2003, en plena oposición favorable de Marte, cuando un joven de 16 años se acercaba a ellos para que le enseñaran el Universo que hay sobre nosotros, pero sobre todo, la grandeza humana que nos rodea. A Pedro, por ese primer trabajo de investigación basado en variables de tipo Cefeida en M3, más que un profesor, un maestro, más que un maestro, un amigo, más que un amigo, casi un padre... Pedro, NO cambies nunca, tan importante para la ciencia es investigar como

hacer nacer en jóvenes ese amor por la ciencia y la investigación. Ojalá sea yo capaz algún día de hacer algo así y de la forma que solo tú sabes hacerlo. Sabes que en buena parte estoy escribiendo esto ahora por ti, y no es un reproche, es un gracias. A Alfonso, por esas presentaciones en las charlas... Según tú llevo ya unos años como doctor, ¿verdad? Por esas subidas a la Fresnedilla, por esa preocupación constante por cómo iba mi investigación y mi vida en general, por esos "Tomás, come que estás enclavijao". A Antonio, por esa pedazo de foto de contraportada mostrando la grandeza del cielo de la Fresnedilla. A Cristóbal, Juan Antonio, Javier, Esteban, Blas... A Juan de Dios (D.E.P), por tantas tardes que me llamaba para cargar el telescopio e ir a observar a algún terreno cercano. Por esto, y por mucho más que no soy capaz de expresar con palabras... GRACIAS.

A mis amigos de toda la vida, a todos aquellos que tantas veces me han dicho "¡Deja de estudiar y de trabajar y vente y emborráchate que es lo que te hace falta!". A aquellos que siempre han estado y estarán allá donde yo esté, aunque la distancia sea larga. Aquellos con los que tanto he reído y tanto he vivido. ¡GRANDE MANADA! A Manuel, Marcos, Miguel, Alfonso, Chema, Agustín, Andrés, Antonia, Dani (Bellón), Samuel, Moya, Ana, Dani (Miras), Pamela, Loren, Tato, *Ugo*, Ismael, Villa, Jesús, Ana Villacañas... y tantos otros que seguro no he olvidado, pero se me ha pasado mencionar. Pero también a las nuevas *adquisiciones*. A Rubén y Elena por compartir los altibajos correspondientes a los últimos meses de tesis. A Adrián, Simon y Pablo por esas risas que tan necesarias eran a la hora de comer. A todos los que habéis pasado por el despacho (Israel, Simón, Pablo y Laura) y que de paso habéis dejado una huella imborrable en mi memoria y mi corazón. A esos compañeros de fútbol por unas tardes inolvidables (Alberto, Salva, Alba, Alejandro, Paloma, Razvan, Álvaro, Ignacio, etc.). Por esto, y por mucho más que no soy (ni seré) capaz de expresar con palabras... GRACIAS.

A todos los miembros del Departamento de Física Teórica y del Cosmos, en especial al grupo de Astrofísica Galáctica. Trabajar rodeado de gente que constantemente están dispuestos a ayudar es todo un placer. A Eduardo, Almu, Jorge, Ute, Mónica, Israel, Ana, Bea y Adri. Y un gracias especial a Simon, el gurú de Python y de Linux que tan dispuesto está SIEMPRE a ayudar a quien lo necesite. Ojalá haya muchas más personas como tú en este mundo. Incluso cuando no se te pide ayuda parece que tienes un don especial para detectar personas en apuros y siempre tienes un huequito (huecazo en muchas ocasiones) para ayudar a cualquiera, pero sobre todo a los que estamos empezando que somos los que más lo necesitamos. Gracias por modelarme y por enseñarme la senda de cómo debe de ser un buen compañero de trabajo... y un buen amigo. Por esto, y por mucho más que no soy capaz de expresar con palabras... GRACIAS.

However, I cannot finish this acknowledgements section without having some special words to all of you who have helped directly in the development of the content of this thesis. I would like to thank all the collaborators and

co-authors of the papers part of this PhD. Special thanks to Gareth, Jairo, Carme, Danielle, Patricia, Raúl, Marja, Jesús, Sebastián, Adri, Esther... who have taught me more than they think they have. I would like to thank Brad and Sebastián for hosting me in Preston and Mexico City during some of the most exciting months I have ever had and for treating me as part of their own family. Special thanks to Lisa, Ken, and Ángel for unveiling to me one of the most amazing and incredible countries I will ever be, Australia. And my more sincere gratitude to Jesús, Patricia, and Carme who have "fostered" me as their own students to help me develop some of the most important parts in this thesis. For all the above said, and much much more that I am not able to express with words... THANKS.

In addition, I would like to thank the anonymous referees of my three published papers for useful comments and suggestions that, unintentionally, have improved this thesis. During the development of this work I have made used of python (`http://www.python.org`), Matplotlib (Hunter 2007), a suite of open-source python modules that provides a framework for creating scientific plots, and Astropy, a community-developed core Python package for Astronomy (Astropy Collaboration et al. 2013). Finally, as without money almost nothing in this life can be done, I would like to acknowledge here all the grants and fellowships that have made this thesis posible. This thesis has been partly supported by the Spanish Ministry of Science and Innovation (MICINN) under grants AYA2011-24728 and AYA2014-53506-P and by the Junta de Andalucía (FQM-108). Specially, I would like to thank the support given by the Spanish Ministerio de Educación, Cultura y Deporte by means of the FPU fellowship (year 2010). Part of this research has been part of the CALIFA collaboration, and thus, it is based on observations collected at the Centro Astronómico Hispano Alemán (CAHA) at Calar Alto, operated jointly by the Max-Planck Institut für Astronomie and the Instituto de Astrofísica de Andalucía (CSIC). For all the above said, and much more that I am not able to express with words... THANKS.

Pero sobre todo, esta tesis es gracias a TI. A la persona que me ha enseñado a ser yo de nuevo incluso sin conocerme antes de que dejara de serlo. A la persona que me ha enseñado a valorarme y a luchar por lo que creo. A la persona que me ha hecho volver a creer en un mundo de fantasía e ilusión, en un mundo en el que la verdad, la bondad y la dulzura ganan a la mentira, la maldad y la amargura. A la persona que ha conseguido que piense en mí y que trate de ser feliz por encima de todas las cosas. A la persona que me ha enseñado que no solo se puede llorar de tristeza, sino también de alegría y de agradecimiento, de empatía y de amor. A la persona que me ha dado más que nadie en este mundo ha sido capaz de darme (y todo en tan poco tiempo). A la persona que ha sido capaz de anteponer NUESTRA felicidad a la suya, NUESTRO bienestar al suyo, un futuro JUNTOS a un futuro separados... A la persona que tanto me ha ayudado desde el principio en el trabajo, dejándome sus códigos, discutiendo papers,

hablando de ciencia... A la persona que tanto me ha hecho desconectar del trabajo para conectar con más fuerza aún. A la persona con la que tanto me he reído hablando, viendo una película, una serie o leyendo. A la persona con la que sé que seré feliz durante el resto de mi vida, porque con ella he aprendido el verdadero sentido de vivir. A la persona con la que he disfrutado de las más inolvidables observaciones astronómicas, porque las estrellas del firmamento brillan con más luz y parecen más bonitas al contagiarse de su brillo y su belleza. A la persona que aún mereciéndose algo mucho mejor que yo, ha preferido conformarse conmigo haciéndome la persona más feliz en el Universo (y creedme, soy consciente de la inmensidad de este). A la persona que ha revisado todas y cada una de las palabras de esta tesis antes de que la leyera cualquier otra persona. A la persona que tantas horas ha dedicado a una contraportada perfecta. A la persona que me ha dado ese plus de energía que necesitaba para terminar esta tesis, sin ella no sabría cómo habría terminado. A la única persona que forma parte de todas y cada una de las categorías en las que he dividido esta sección. Mi compañera de despacho, mi colaboradora científica, mi compañera de observaciones, mi compañera de viajes, mi amiga, mi familia... una parte muy importante de mí. A la persona que ha conseguido hacerme sentir INFINITO. A la persona que ha conseguido que no desee nada más en esta vida, que no pida nada extra al futuro, porque soy consciente que con ella lo tengo TODO. Lau, por esto, y por mucho más que soy consciente NUNCA seré capaz de expresar ni con palabras, ni con gestos, ni con acciones, ni de ninguna forma humana porque tú te mereces y te merecerás siempre algo mejor... GRACIAS, GRACIAS, GRACIAS, GRACIAS...

Y así termino esta sección que, efectivamente, y como ya vaticinaban las personas que bien me conocen ha quedado bastante larga. Pero no me importa, porque es una sección importante, ya que sin esta sección, nada de lo que viene a continuación tendría sentido alguno... ¡GRACIAS!

"You don't write because you want to say something; you write because you've got something to say."
— F. Scott Fitzgerald

"Somewhere, something incredible is waiting to be known."
— Carl Sagan

"The most outstanding fact about the Universe is the knowledge that the atoms that comprise life on Earth, the atoms that make up the human body, are traceable to a crucial moment when light elements were transformed into heavy elements in stellar cores under extreme temperatures and pressures. These stars were unstable in their latter years, they collapsed and then exploded scattering the enriched gas across the Galaxy, gas made of hydrogen, carbon, nitrogen, oxygen, and all the fundamental ingredients for life itself. These ingredients became part of gas clouds that condensed, collapsed and formed the next generation of solar systems, stars with orbiting planets. Those planets now have the ingredients for life itself. So, when I look up at the night sky, I know that we are part of this Universe and we are in this Universe, but perhaps more important than both of those facts, is that the Universe is in us. Many people feel small because they are small and the Universe is big, but I feel big because my atoms came from those stars and we are participants on this Universe just by being alive."
— Neil deGrasse Tyson

Contents

Summary

Galaxies, the *building blocks* of the Universe, are gravitationally linked systems made up of baryonic (stars, gas, and dust) and dark matter. How they form and evolve is one of the most studied, yet not understood, topics in modern astrophysics. To unveil their formation and evolution, the analysis of the stars populating these systems has been proven a powerful tool as the different stages in the evolution of a galaxy are imprinted in its stellar content. In particular, this analysis up to the outer parts of the galaxies is essential. As in these faint regions gravity is lower and the dynamical timescales longer, fossil records from the time of galaxy assembly and formation are retained.

In this thesis we use high-quality, spectroscopic (CALIFA) and photometric (SDSS) data along with cosmological simulations (`RaDES`) to characterise the stellar content in spiral galaxies, paying special attention to their outer regions. We define a sample of 88 disc galaxies from the CALIFA survey, for which we study their light distribution and obtain their stellar age and metallicity radial profiles.

The classification of their Surface Brightness (SB) profiles in types I, II, and III is made on a two-dimensional basis applying the GASP2D code to the SDSS science frames. We obtain that different decomposition methods arise different SB classifications but we stick to this more realistic 2D approach. The stellar content of the analysed galaxies is obtained by applying a set of *full-spectrum fitting* codes (`pPXF`, `GANDALF`, and `STECKMAP`) to the CALIFA data. This method successfully replicates the stellar content recovered from more reliable, resolved stellar populations analysis in a case example, i.e. a region in the Large Magellanic Cloud bar.

The outer parts of the CALIFA galaxies reveal "U-shape" light-weighted age profiles for type I and II galaxies, suggesting that age and SB profiles are not directly coupled and thus, different mechanisms shape both properties. This age upturn disappears when we compute mass-weighted quantities, pointing to an important role in creating such age profile of the most recent star formation. This outer ageing is not found in all the analysed galaxies. Although this can be interpreted as a lack of universality, it can be a consequence of the limited radial coverage of the CALIFA data. Stellar radial migration has been regarded as a mechanism affecting the SB and

other stellar population parameter profiles. The study of the inner stellar content discloses no differences between galaxies displaying the diverse outer SB profiles, setting limits on the importance of radial migration. Based on these results we cannot conclude whether migration is the main factor shaping the SB profiles or not. However, we can claim that the fraction of the migrated stellar mass is not significant enough as to affect the inner galaxy stellar content.

In this thesis we also assess the effect of the cosmological assembly history on the chemical and dynamical properties of the discs of the `RaDES` spiral galaxies up to their outskirts. We find that assembly histories can be divided into three phases according to the number of satellites surrounding the host discs. A merger dominated phase is followed by a quieter one before a "secular" epoch settles the discs. The stars born during the third phase and found in the most external regions of the simulated discs display inverted Age-Metallicity Relation as a consequence of the joint effect of radial motions and star formation in satellites temporarily located in these outer parts. In addition, "U-shape" age profiles are found in all the cases even if radial motions are not taken into account, suggesting that the outer age upturn could be a universal feature.

The study carried out throughout this thesis suggests that the outer parts of spiral galaxies seem to display an age upturn as a frequent feature (supported by observations and simulations). This upturn is neither linked to a particular SB profile nor the result of an unique mechanism such as radial migration. This shape seems to be a consequence of inside-out growth of the disc, radial motions of disc stars (inwards and outwards), accretion of old stars from satellites, and the presence of an early *in situ* star formation along the entire disc of the galaxy. The fact that this outer ageing disappears in the mass-weighted age profiles suggests the importance of recent star formation in shaping these features. Although we cannot rule out radial migration as the main driver shaping the SB profiles, according to our findings it does not seem to redistribute a large amount of disc stellar mass as the inner gradients of stellar properties for different galaxies do not seem to differ.

Resumen

Las galaxias, consideradas como los *ladrillos* del Universo, son sistemas ligados gravitatoriamente formados fundamentalmente por materia bariónica (estrellas, gas y polvo) y materia oscura. Cómo se forman y evolucionan es uno de los temas más estudiados, y aún sin entender, de la astrofísica moderna. Para desvelar las incógnitas sobre la formación y evolución de las galaxias, podemos considerar como una poderosa herramienta el análisis de las estrellas que pueblan estos sistemas ya que las diversas fases que atraviesa una galaxia durante su evolución quedan reflejadas en su contenido estelar. En particular, dicho análisis incluyendo las partes más externas de las galaxias es esencial. Debido a que en estas zonas poco brillantes la gravedad es más baja y las escalas de tiempo dinámicas más largas, su estudio nos revela información sobre las épocas más tempranas en la evolución de las galaxias.

En esta tesis usamos datos espectroscópicos (CALIFA) y fotométricos (SDSS) de alta calidad combinados con simulaciones cosmológicas (`RaDES`) con el fin de caracterizar el contenido estelar de las galaxias de tipo espiral, prestando especial atención a sus partes más externas. Para ello, definimos una muestra de 88 galaxias de disco observadas dentro del proyecto CALIFA para las cuáles estudiamos su distribución de luz y obtenemos sus perfiles radiales de edad y metalicidad estelares.

La clasificación de los perfiles de brillo superficial en tipos I, II y III se lleva a cabo empleando un código de análisis en dos dimensiones llamado GASP2D. Aunque encontramos que diversos métodos de descomposición arrojan diferentes resultados en la clasificación, preferimos utilizar este método (más realista) basado en un análisis bidimensional. El contenido estelar de las galaxias analizadas se obtiene mediante un conjunto de códigos (`pPXF`, `GANDALF` y `STECKMAP`) que ajustan el espectro obtenido a partir de los datos de CALIFA usando un amplio rango espectral. Este método ha resultado eficaz reproduciendo el contenido estelar obtenido a partir de métodos más fidedignos basados en el análisis de poblaciones resueltas para un caso concreto, una región en la barra de la Gran Nube de Magallanes.

Las partes externas de las galaxias de CALIFA revelan una forma en "U" en los perfiles de edad pesados por luz para galaxias de tipos I y II, indicando que los perfiles de edad y luz no están acoplados y, por lo tanto, el origen de su forma debe estar relacionado con mecanismos diferentes. Esta subida en el perfil de edad de las partes externas desaparece cuando analizamos las cantidades pesadas por masa, sugiriendo que la formación estelar más reciente debe jugar un papel importante definiendo dichos perfiles de edad. Sin embargo, esta forma en "U" no se observa en todas las galaxias analizadas. Aunque esto podría entenderse como una falta de universalidad, puede ser simplemente una consecuencia de la limitada cobertura radial de los datos de CALIFA. Por otra parte, la migración radial ha sido propuesta como un mecanismo que afecta tanto a los perfiles de brillo superficial como a los

de otras propiedades estelares. El estudio llevado a cabo en esta tesis del contenido estelar en las partes internas no nos muestra diferencia alguna entre galaxias con distintos perfiles de luz, constriñendo la importancia de dicho mecanismo. En base a estos resultados, no podemos concluir si la migración es el principal factor que da forma a los perfiles de brillo superficial o no. Sin embargo, sí podemos afirmar que la fracción de masa estelar que migra no debe de ser lo suficientemente significativa como para afectar al contenido estelar de las zonas internas de las galaxias analizadas.

En esta tesis también abordamos el efecto de la historia de ensamblaje cosmológico en propiedades químicas y dinámicas de los discos hasta sus partes más externas para una serie de galaxias espirales simuladas (`RaDES`). Encontramos que dicho ensamblaje se puede dividir en tres fases en base al número de satélites que rodean los discos principales. Una fase dominada por satélites fusionándose con el disco "anfitrión" es seguida de otra más tranquila hasta que una tercera fase "secular" relaja y estabiliza el disco. Las estrellas formadas durante esta tercera fase, y que se encuentran en las partes más externas de estas galaxias simuladas, muestran tendencias inversas en la relación edad-metalicidad como consecuencia de migración radial junto con una formación estelar en satélites que orbitan en torno al disco principal y que se encuentran temporalmente en estas zonas externas. Además, encontramos perfiles de edad con forma en "U" en todos los casos incluso si no tenemos en cuenta la migración radial, lo que sugiere que la existencia de población de mayor edad en las partes externas podría ser un rasgo universal de las galaxias espirales.

El estudio llevado a cabo a lo largo de esta tesis nos lleva a pensar que las partes externas de las galaxias espirales podrían mostrar un envejecimiento como una característica frecuente (en base a observaciones y simulaciones). Esta mayor edad en la parte externa ni tiene relación con un tipo de perfil de luz concreto ni es el resultado de un único mecanismo como puede ser la migración radial. La forma en "U" observada en los perfiles de edad parece producirse como consecuencia de la acción conjunta de diversos mecanismos: crecimiento del disco de dentro hacia afuera, movimientos radiales de las estrellas del disco (hacia adentro y hacia afuera), acreción de estrellas viejas provenientes de satélites y la presencia de una formación estelar temprana a lo largo de todo el disco de las galaxias. El hecho de que esta forma en "U" desaparezca si pesamos por masa nos sugiere que la formación estelar reciente juega un papel clave dando forma a estos perfiles. Aunque no podemos descartar que la migración radial sea el principal mecanismo dando forma a los perfiles de luz, los resultados presentados en esta tesis nos sugieren que la migración radial no afecta a una gran cantidad de la masa estelar total, ya que los gradientes de propiedades estelares internos no parecen diferir de unas galaxias a otras.

Chapter 1

Introduction

"Begin at the beginning and go on until you come to the end; then stop."
— Lewis Carroll, Alice in Wonderland

Contents

Astronomy is an observational science, we do not have any laboratories at our disposition to test hypotheses. The analysis of the light coming from the objects composing the Cosmos is the only way we have to understand it. However, after years of observations, failures, and achievements, the knowledge that we nowadays have about our Universe is unimaginable.

The biased vision we have of the Universe from our point of view is very misleading. Everything seems to be orbiting around us as if this Universe was created for our entertainment. Apparently, there are no logical hints to think of our planet Earth as a tiny planet among billions and billions of them. But this is the truth: nothing (except the Moon) is orbiting around us and we are living in a humble world, orbiting a modest star (the Sun), embedded in a normal-size galaxy (the Milky Way). However, the more sophisticated the instruments (telescopes, maths, computers, etc.) to study the Universe are, the better our knowledge about nature around us is. This thesis is nothing but another small step in the humble attempt of understanding a small part of the knowledge that our Universe is hiding, nothing but a modest effort towards the understanding of how galaxies form and evolve.

1.1 A brief galactic overview

A clear, starry summer night surprises us with a nebulous band crossing the sky from North to South. This hazy path in the sky was known since the ancient Greece and was named *galaktos*, meaning *Milky Way*, our Galaxy. However, it was not until 1610 that the Italian astronomer Galileo Galilei turned his rudimentary telescope towards this part of the sky and realised that this misty cloud in the sky, extending all around the celestial sphere, was composed by thousands of dim stars. Our Galaxy was a system made up of stars and we were part of it. However, the thirst for knowledge of astronomers raised more and more questions regarding its size, shape, and nature in general. We are at the dawn of *Galactic Astronomy*.

Thomas Wright and Immanuel Kant, taking into account Galileo's and later observations of our Milky Way, described our Galaxy as a discy, stellar system with our Sun immersed in it. However, Kant went further suggesting the existence of more systems of the same nature as our own Galaxy located at great distances from us, the so-called *island universes*. This idea was considered for more than a century a philosophical speculation more than a real scientific hypothesis. Nonetheless, the discovery of spiral structure in some nebular objects (*spiral nebulae*) such as the arms in M51 (see Fig. 1.1) observed by William Parsons in 1845, triggered new speculations supporting Kant's ideas.

Apart from these speculations little was known regarding the real structure of our Galaxy by the end of the eighteenth century. The first scientific

approximation to that problem was made by the English astronomer William Herschel in 1785. Herschel, using star counting on 683 regions well scattered along the night sky, created the first map of our Galaxy. He thought that the largest stellar density should be found towards the centre of the system, but his counting gave almost the same number of stars regardless the sky direction under analysis. This implied that we were located at (or very close to) the centre of the Milky Way. Later on, during the twentieth century, Jacobus Kapteyn reached similar conclusions using a slightly more refined counting method.

The problem was that both, Herschel and Kapteyn, were limited to study just the solar neighbourhood because of the interstellar dust absorption. It turned out that our Galaxy was not only composed by stars, other components such as gas and dust (material from which stars are born) were also present and interacted with the starlight. This was not discovered until 1930 when Robert J. Trumpler noticed that some open stellar clusters (groups of hundreds of young stars) within our Milky Way were fainter than they should be according to their distance. Therefore, there had to be a medium obscuring the light coming from the stars. The space among the stars populating the Milky Way (the interstellar space) was not empty but filled with dust and gas. Little by little, astronomers were bringing to light more and more characteristics of our Galactic system.

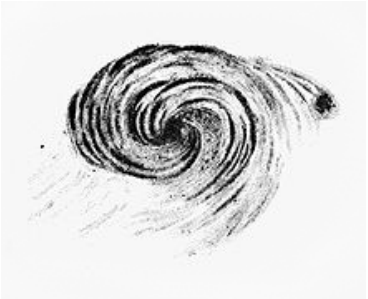

Figure 1.1: Drawing of the Whirlpool Galaxy (M51) by William Parsons, 3^{rd} Earl of Rosse, in 1845 from his 72-inch telescope, colloquially known of as the *Leviathan of Parsonstown*.

Harlow Shapley published a series of papers ($1915 - 1919$) probing an alternative Milky Way structure. According to those works, we were displaced from the centre of the Milky Way to a place located far from it. Shapley, in order to avoid the dust effect, determined the position of 93 globular clusters (groups of thousands of old stars) within our Milky Way realising that they followed a spherical distribution with the centre located at around 50 000 light-years from us. Nowadays, we know that this measure was mistaken by a factor of 2; however, he was able to provide a closer view to the real structure of our Galaxy.

All the observable objects (including the *spiral nebulae*) were located within our Milky Way according to Shapley's ideas. His new view of our Milky Way suggested that our Galaxy was largest than thought. However, a group of astronomers lead by H. D. Curtis disagreed with Shapley's ideas. Curtis and collaborators believed in Kant's ideas and his *island universes* and they thought that our Milky Way was just one galactic system among a great number of them with similar properties. Both positions were sup-

ported by observational facts that were confronted in 1920 at the National Academy of Sciences meeting in the so-called the astronomy's *great debate*. It was not a real debate; in such meeting both astronomers had thirty-minute talks to present and defend their hypothesis. Although there was not a real *winner*, Curtis' line of reasoning caught the attention of more astronomers. In addition, some new observations supporting the *island universes* theory were about to be made, changing the view of the Universe forever.

Figure 1.2: First pages of the original manuscritpt *The Realm of the Nebulae* by Edwin Hubble.

Edwin Hubble, American astronomer working at the Mount Wilson Observatory, discovered in 1923 the presence of Cepheid variables in M31. Analysing the temporal light variations in those stars, he was able to determine the distance to M31, probing that, by far, it was located beyond our Milky Way boundaries and its size was comparable to our own Galaxy. This discovery supported Curtis' ideas and probed the existence of the *island universes*, other galaxies (with small g) as our own. In the subsequent years, Hubble thoroughly studied the distribution and nature of these objects, and all his achievements and discoveries were reflected in his book *The Realm of the Nebulae* (see Fig. 1.2).

The Realm of the Nebulae is considered one of the most important books in galactic astronomy from a historical point of view. In this book, Hubble published the famous *Hubble's law*, the first observational evidence in favour of an expanding Universe in which every galaxy was moving away from us at a receding speed proportional to its distance. In addition, in this book appeared the first galactic classification, which was based on the morphology of these systems.

Therefore, it was not until the 1930s and after an exciting chain of events that the concept of galaxy was established. Nowadays, we consider that a galaxy is a gravitationally linked system formed by stars, gas, dust, cosmic rays, magnetic fields, and dark matter. They are considered as the *building blocks* of our Universe, which is made up of billions and billions of these systems. Taking into account the wide variety of shapes, sizes, and physical properties found in galaxies, it is almost impossible to create a proper galactic classification. Properties such as light distributions, stellar population and gas characteristics, kinematics, etc. are highly dependant on the individual analysed systems. However, for historical reasons and following with the scheme sketched by Hubble (see Fig. 1.3), we can roughly divide

galaxies into three main groups (not taking into account irregular systems):

Elliptical galaxies, E These galactic systems are mainly formed by old stars, with little amounts of gas and dust that greatly minimise the star formation in these galaxies. Although some rotation can be found in some of these objects, stellar velocities mainly follow a random distribution. As a consequence, the shape of these galaxies resembles that of an ellipsoid and its light-distribution is well fitted by a Sérsic profile (Sérsic 1968).

Spiral galaxies, S Spiral galaxies are considered one of the most beautiful and interesting objects found in nature. They are mainly formed by two components: the bulge and the disc. The disc is a flat, rotating structure formed by stars, gas, and dust. It can be divided into two different components: the thin (mainly formed by young stars characterised by a small disc scale-heights) and the thick (formed by older stars spread over a thicker region of space) discs. Its most notable features are the so-called spiral arms (where star formation takes place). Some disc galaxies also exhibit other components such as bars or rings. The disc light distribution follows an exponential decline. The other main component forming these galaxies is the bulge. The bulge is a spheroid-like component made up of old stars. It can be defined as a deviation from the exponential profile in the centre of a galaxy. A typical spiral galaxy as our own has a mass of around 10^{11} solar masses spread over a disc of around 30 kpc in diameter. 10 % of this visible mass is made by gas and around 1 % is dust.

Lenticular galaxies, S0 These objects present some elliptical and spiral characteristics. They are formed by a rotating disc with no spiral structure surrounded by a big ellipsoidal system. Important amounts of dust and gas are found in these systems and thus, we can find a considerably high star formation in lenticular galaxies.

Today, we have a broader understanding on galaxies, however, it is still far from being satisfactory as many questions still remain unsolved. How were these systems formed? How do they evolve? If we were able to, we would like to take different snapshots as a galaxy is evolving to understand its formation and evolution. Unfortunately, this is not possible. The astronomical time-scales are not comparable to human lifetimes, and thus, it is impossible to even observe small changes in external galaxies (let alone significant ones). However, we do can play archeologists, analyse fossil records left by past events, and try to reconstruct the history of the galaxies. Here is where the analysis of the stellar populations plays its role. Around 90 % of the baryonic matter in a galaxy is made up of stars. Every stage in the

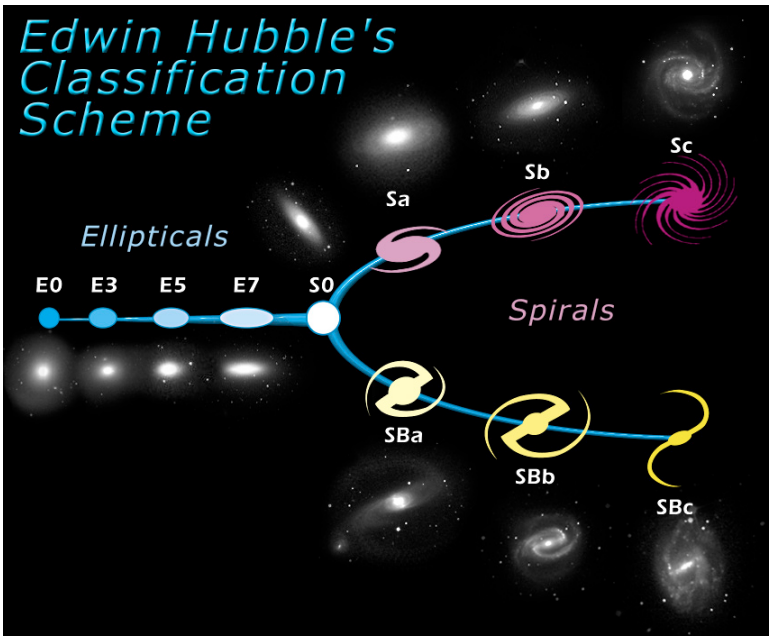

Figure 1.3: Hubble's morphological classification scheme of galaxies, also known as *Hubble's tuning fork*. Image taken from Wikipedia.

evolution of a galaxy, every violent or mild event, is imprinted in the stellar content. Therefore, the study and analysis of the stellar populations in galactic systems can offer us valuable information about how galaxies have formed and evolved.

1.2 Stellar populations

An unexpected blackout in Los Angeles in 1944 allowed Walter Baade to analyse the stellar content in external galaxies in a way nobody had done before. He was able to resolve individual stars in some nearby galactic systems using the 100-inch Mount Wilson telescope. Based on those observations he realised that the dominant stars in elliptical galaxies and the bulges of spiral galaxies were different to those found in the discs and spiral arms of spiral galaxies. Consistently, Baade classified for the first time stars into two main populations, population I and population II. Stars of population I are young, luminous, blue stars located in the discs (especially distributed along the spiral arms) of late type galaxies (dust-and-gas-rich environment); while stars of population II are old and red stars located in the halo and the spheroid component of spiral galaxies and in elliptical galaxies (dust-and-gas-free environment). This simple classification was nothing but the start of the concept of *stellar population*.

Other important studies have contributed to the development on the

knowledge and characterisation of the stellar content in galaxies was greatly improved. In particular, Ejnar Hertszprung and Henry Norris Russell (1913) noticed independently that when stars were arranged in a colour versus luminosity diagram, they were not randomly distributed but located along well-defined paths (see Fig. 1.4). This kind of representation was called Hertszprung-Russell (HR) diagram or, as it is commonly known, Colour Magnitude Diagram (CMD), following its modern form (colour versus absolute magnitude). Later, it was seen that such paths in the CMD were not a coincidence, but intimately related to key astrophysical concepts such as mass or stellar evolution (mainly determined by the stellar mass), and that the colour could be interpreted as the surface temperature of the stars. The analysis of a deep CMD and the advances on the knowledge of stellar evolution allowed astronomers to better understand the light coming from the stars populating galactic systems.

Stars are born from the collapse of molecular clouds forming the Interstellar Medium (ISM). During their lifetime, the high temperatures reached in their cores produce the ignition of nuclear fusion reactions (such as the *pp-chain* or the CNO cycle), allowing stars to create new elements (metals) from basic ones (Hydrogen and Helium). As a star dies in a cataclysmic event, the new-formed elements are expelled to the ISM and the chemical composition of the surroundings is modified enhancing the metallicity of the gas and dust clouds present in a galaxy. The next generation of stars will be the result of the collapse of such enriched clouds and its chemical composition will retain information about previous generations. Such chemical composition, as well as the age of the star, is reflected in its Spectral Energy Distribution (SED). Thus, what we observe in galaxies is the accumulated history of generations and generations of stars. The properties of the stars currently located in a galaxy reflect the different episodes of star formation and the ISM enrichment processes undergone. Therefore, deriving the current stellar composition in galaxies we can trace back the history of how stars have been formed over the entire evolution of the galaxy, i.e. we can obtain its Star Formation History (SFH).

The study of the SFHs of galaxies is an essential element in understanding their past evolution. The success on extracting the stellar population information in stellar systems is one of the most outstanding breakthroughs in the history of the observational astronomy. This analysis is based on the development of a series of key elements: i) an Initial Mass Function (IMF) that provides information about the number of stars of different masses that is formed during a star forming burst (e.g. Salpeter 1955; Vazdekis et al. 1996; Kroupa 2001; Weidner et al. 2013b,a; Peacock et al. 2014); ii) a robust theory of stellar evolution with information on how stars of different masses evolve by means of model isochrones and evolutionary tracks (e.g. Girardi et al. 2000a; Pietrinferni et al. 2004; Bressan et al. 2012; Pietrinferni et al. 2013); iii) a complete set of observational (spectral and photometric)

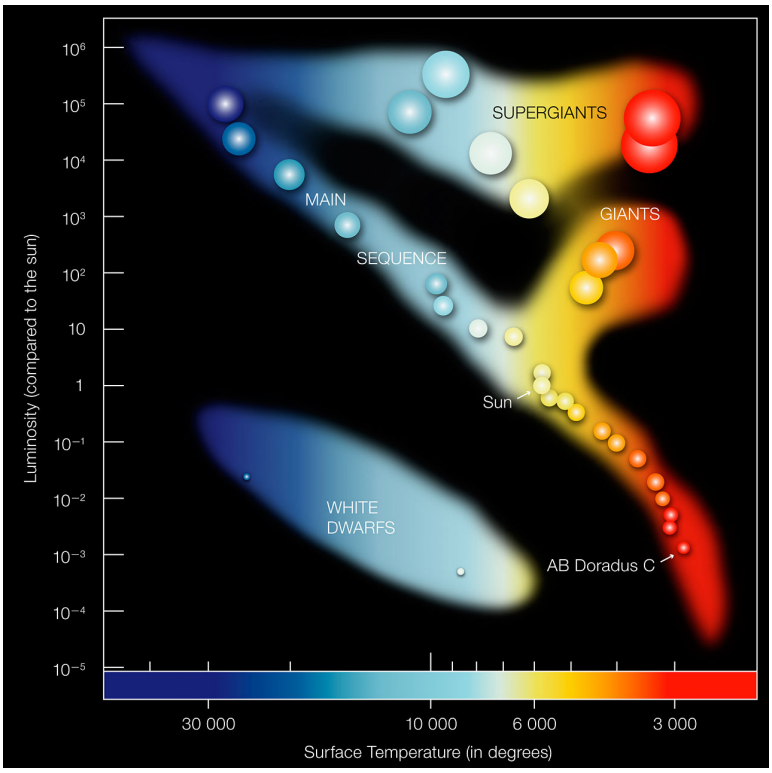

Figure 1.4: Colour-Magnitude Diagrams (CMDs) can be interpreted as a representation of stellar luminosities as a function of the surface temperature of the stars (also known as Hertzsprung-Russell diagram). Stars at different evolutionary stages and with different masses occupy different locations in this diagram. These diagrams are one of the most important tools to study the stellar content and trace stellar evolution. Credit: European Southern Observatory (ESO).

libraries to know how evolved stars emit light (stellar templates hereafter, e.g. Prugniel & Soubiran 2001; Le Borgne et al. 2003; Valdes et al. 2004; Sánchez-Blázquez et al. 2006b; Prugniel et al. 2007); and iv) inversion codes to compare models with observations to obtain the stellar properties (e.g. Heavens et al. 2000; Reichardt et al. 2001; Tojeiro et al. 2007; Cid Fernandes et al. 2005; Ocvirk et al. 2006b,a; Koleva et al. 2009).

One of the main obstacles on the recovery of the stellar content is the known age-metallicity degeneracy (Peletier 2013). The ageing of the stars or an increase in their metal content produce a similar effect on the light that stars emit. However, different ways have been proposed to deal with such a problem.

Deep CMDs (see Fig. 1.4) reaching the oldest Main-Sequence Turnoff (oMSTO) are generally regarded as the most direct and reliable observables that can be used to obtain a detailed SFH of a galaxy (Gallart et al. 2005). At magnitudes brighter[1] than the oMSTO, stars along the Main Sequence (MS) are distributed in a sequence of age: short lived, young, massive stars are the bluest and brightest, and less massive and therefore stars with longer lifetimes are located at the faintest and reddest part of the bright MS. While there remains some age-metallicity degeneracy in the positions of the stars on the MS, it is significantly less than that seen in other stellar evolutionary phases such as the Red Giant Branch (RGB) or the horizontal branch. In such phases, the position of the stars are mainly determined by metallicity and there is very little age sensitivity. By combining the information of the position of the stars in the MS of a CMD reaching the oMSTO with the number of them across it, it is possible to minimise the remaining age-metallicity degeneracy and obtain accurate, detailed, and reliable SFHs, including information from the early times of the galaxy's history (e.g. Gallart et al. 1999; Dolphin 2002; Cole et al. 2007; Noël et al. 2009; Monelli et al. 2010a,c; Hidalgo et al. 2011; de Boer et al. 2012; Meschin et al. 2014; Skillman et al. 2014). However, this kind of analysis has been limited to a few dozen nearby systems, those within a distance of $\sim$ 1–2 Mpc (see McConnachie et al. 2005, for an updated census of the Local Group, and the distance of its members to the Milky Way). The wide variety of morphologies and characteristics found in galaxies forces us to study systems at larger distances where the analysis of individual stars is unfeasible. In these systems, because of the limited spatial resolution, we need to derive the stellar content using colours or spectral information coming from integrated stellar populations (e.g. de Jong 1996; MacArthur et al. 2004; Pérez & Sánchez-Blázquez 2011; Sánchez-Blázquez et al. 2011, among many others).

In order to characterise the composite stellar content of unresolved galax-

[1] Below the oMSTO there is basically no age information, but the luminosity function of the low Main Sequence (MS) can be used to obtain information on the IMF of low mass stars (e.g. Kalirai et al. 2013).

ies, and in particular of galaxies at high redshift, significant effort has been made since the early 1980s to interpret integrated stellar populations (e.g. Pickles 1985; Bica 1988). Broadband colours were first used to distinguish between old/young, metal poor/rich stellar populations (Searle et al. 1973; Tinsley & Gunn 1976; Peletier & Balcells 1996). However, this type of analysis is affected by the known age-metallicity degeneracy and the effect of dust (e.g. Worthey 1994; Ganda et al. 2009). Spectroscopic analysis can help to minimise that degeneracy. The very first spectroscopic approach was developed by de Vaucouleurs & de Vaucouleurs (1959), later followed by Spinrad (1962) and Alloin et al. (1971). Stellar spectra are characterised by a series of absorption features whose intensity (line strength) is linked to the physical properties of these systems. The use of line equivalent widths or line–strength indices, taking into account their dependence on metallicity and age, became popular in the 1980s and 1990s (e.g. Rose 1984; Faber et al. 1985; Bica & Alloin 1986a,b; Bica 1988; Gorgas et al. 1993; Worthey 1994; Bica et al. 1994; Vazdekis et al. 1996; Worthey & Ottaviani 1997; Kauffmann et al. 2003). Indices have been used to obtain Single Stellar Population (SSP) equivalent values (age and metallicity) or even to derive the whole SFH shape (e.g. Proctor et al. 2000). The use of indices has been relatively successful in the characterisation of stellar populations in *simple* systems such as globular clusters or elliptical galaxies (e.g. Peletier et al. 2007; Kuntschner et al. 2010); however, these studies i) are still hampered by the age-metallicity degeneracy hindering the derivation of a reliable SFH, ii) are biased towards the youngest stellar populations that contribute much to the light while involving a small mass fraction, iii) make use of a limited part of the observed spectra, and iv) are quite limited when replicating the whole shape of the SFH. Combinations of different indices allow us to better constrain the stellar information, but this approach is still affected by the above limitations. Other approaches must be used to study the actual shape of the SFH in galaxies with complex stellar compositions.

With the goal of increasing the spectral coverage (and thereby maximizing the information used from the observed spectra) and of being able to reproduce the SFH of complex systems, SED fitting codes have been developed such as `MOPED` (Heavens et al. 2000; Reichardt et al. 2001), `VESPA` (Tojeiro et al. 2007), or `STARLIGHT` (Cid Fernandes et al. 2005). In this approach the overall shape of the observed spectrum is fitted through a combination of stellar population models. These codes are sensitive to problems in the data such as flux calibration or extinction errors because they also take into account the continuum in the fit. At the same time, the first so-called full spectrum fitting codes (e.g. Ocvirk et al. 2006b,a; Koleva et al. 2009, STECKMAP and ULySS) became available. These techniques avoid problems in the flux calibration and extinction in the spectra by fitting a polynomial to the shape of the continuum. Both SED and full spectrum fitting codes are better at reducing the impact of the age-metallicity degen-

eracy than line-strength indices analysis as they maximise the information used from the observed spectrum (Koleva et al. 2008; Sánchez-Blázquez et al. 2011; Beasley et al. 2015). Along with this evolution in the fitting codes, there has been huge progress in other key elements to study the stellar content in galaxies such as the modelling of stellar populations (e.g. Bruzual & Charlot 2003; Lee & Worthey 2005; Schiavon 2007; Conroy et al. 2009; Vazdekis et al. 2010) partly as a result of the improvement of stellar libraries (e.g. Prugniel & Soubiran 2001; Le Borgne et al. 2003; Valdes et al. 2004; Sánchez-Blázquez et al. 2006b; Prugniel et al. 2007), isochrones and evolutionary tracks (e.g. Girardi et al. 2000a; Pietrinferni et al. 2004; Bressan et al. 2012; Pietrinferni et al. 2013), and studies on the IMF (Salpeter 1955; Vazdekis et al. 1996; Kroupa 2001; Weidner et al. 2013b,a; Peacock et al. 2014).

Different studies have tested the various SED and full spectrum fitting codes using artificial spectra (e.g. Cid Fernandes et al. 2005; Ocvirk et al. 2006a; Sánchez-Blázquez et al. 2011; Koleva et al. 2011). In particular, Koleva et al. (2011) test `STARLIGHT`, `STECKMAP`, and `ULySS` with 48 mock spectra with different known SFHs. A general result of these studies is that the final success in the recovery of the stellar population content lies in the quality of the spectrum: the better the Signal to Noise ratio (S/N) and the resolution of the observed spectra, the more reliable the stellar population determination will be.

However, the observation of spectra in external systems with the required quality as to obtain reliable stellar population information was limited to elliptical galaxies or to the inner parts of spiral galaxies (MacArthur et al. 2009; Pérez et al. 2009; Sánchez-Blázquez et al. 2011). The emergence of Integral Field Spectroscopy (IFS) makes possible a reliable analysis of the stellar content even in the outer parts of disc galaxies due to the adopted binning schemes to obtain spectra with higher S/N (e.g. Cappellari & Copin 2003).

1.3 The galactic outskirts

In the recent years, the analysis of the outer parts of spiral galaxies is gaining in importance. The presence of stars in the outskirts of spiral galaxies, where the gas density is well below the threshold required for an efficient star formation ($\sim$ 10 $M_{\odot}/pc^2$), is still not understood. In addition, the light distribution of these galaxies in their outer parts display significant differences among them, and their causes remain under study. However, the study of these faint regions is essential to comprehend how spiral galaxies have evolved to their present stage. Because of the low gravity and the consequent long dynamical time-scales, the galactic outskirts retain information from the earliest epochs in the history of the galaxies. Therefore, figuring

out the mechanisms that have moved the stars to their present location or created them *in situ* through the analysis of the stellar content in these outer parts is fundamental to get a comprehensive picture of disc galaxy formation.

Pioneering studies on the light distribution of spiral galaxies found that light from galactic discs followed an exponential decline with radius (e.g. Patterson 1940; de Vaucouleurs 1958; Freeman 1970). However, deeper and higher-quality images allow us to reach further out finding that some galaxies display other types of light distribution profiles that deviate from this simple behaviour (van der Kruit 1979; Florido et al. 2001; de Grijs et al. 2001; Kregel et al. 2002; Erwin et al. 2005; Pohlen & Trujillo 2006; Florido et al. 2006; Erwin et al. 2008; Gutiérrez et al. 2011). Based on this variety of SB shapes, different galaxy classifications have been proposed (e.g. Pohlen & Trujillo 2006; Florido et al. 2006). One of the most extended among the community is the one presented in Pohlen & Trujillo (2006). However, although it has six different galaxy types, for the sake of simplicity and taking into account that sometimes galaxy light distribution can be very irregular, in this thesis we prefer to stick to its simple version based on three different types. In this way, some galaxies exhibit the typical pure exponential profile up to large galactocentric distances (type I, Bland-Hawthorn et al. 2005), while some other systems show a lack (type II) or an excess (type III) of light in their outer parts. These *broken* profiles can be described as two distinct exponential declines (displaying different disc scale-lengths) with the break radius (R_{break}) marking the boundary between the inner and the outer disc (see Fig. 1.5). Observational works suggest that typical disc scale-length values range from 1.0 and 6.0 kpc and *breaks* are generally located at around $2.0 - 5.0$ inner disc scale-lengths (e.g. Pohlen & Trujillo 2006; Erwin et al. 2008; Gutiérrez et al. 2011; Muñoz-Mateos et al. 2013; Laine et al. 2014). In addition, these *broken* features seem to be long-lived structures as they have been also observed in the early Universe ($z \sim 1$, Pérez 2004). Recent studies claim that the break radius increases with time (Trujillo & Pohlen 2005; Azzollini et al. 2008). The wide variety of Surface Brightness (SB) profiles reported suggests that its study may be an essential element unveiling the processes involved in the formation and evolution of disc galaxies.

On the other hand, other features have been observed in the light distribution of the outer parts of spiral galaxies, the *truncations* (van der Kruit 1979; Florido et al. 2001, 2006). These characteristics, in contrast to *breaks*, can be defined as a sharp but gradual decline in the light distribution (Florido et al. 2007), which does not follow a double exponential. In Martín-Navarro et al. (2012), the authors suggest that *breaks* and *truncations* are different properties. According to this study, *breaks* are changes in the slope of the exponential light distribution, while *truncations* are sharper light declines located further out and observed preferentially in edge-on systems because of the low SB values of these regions.

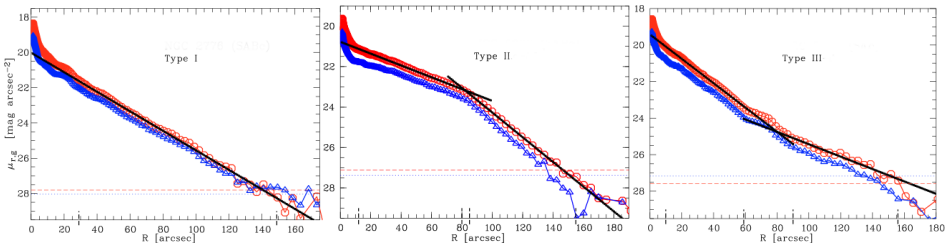

Figure 1.5: Example of the three different type of behaviours found in the SB profiles of spiral galaxies: pure exponential profile (type I, left), down-bending profile (type II, middle) and up-bending profile (type III, right). Images from Pohlen & Trujillo (2006).

Different scenarios have been proposed for the origin of these downbending outer light profiles. van der Kruit (1987) proposed that, in absence of radial redistribution of material in the disc, a collapsing gaseous sphere results on an double-exponential disc with the break corresponding to the maximum in the angular momentum of the baryonic matter. Breaks have also been linked to star formation thresholds (Kennicutt 1989; Schaye 2004). In this scenario, the lack of light in the outer parts of type II galaxies is linked to the impossibility of forming stars where the gas density is below the critical value for star formation. However, the existence of an exponential decline beyond the break radius or the existence of ultraviolet outer discs suggesting recent star formation in these outer parts (Gil de Paz et al. 2005, 2007; Thilker et al. 2007) make this scenario unlikely. Elmegreen & Hunter (2006) found that breaks result naturally from multi-component star formation taking into account gravitational instabilities, spiral wave shocks, stellar compression, and turbulence compression. A more complex scenario in which both elements (angular momentum conservation and a star formation threshold) are combined was also proposed to explain the existence of breaks (van den Bosch 2001). However, a conclusive explanation is still missing.

Another likely scenario to explain the observed light profiles is based on the assumption that stars do not necessarily remain at their birth location. Recently, some theoretical works have found that substantial amounts of stars migrate towards inner and, especially, outer positions (e.g. Battaner et al. 2002; Sellwood & Binney 2002; Debattista et al. 2006; Roškar et al. 2008a; Martínez-Serrano et al. 2009; Sánchez-Blázquez et al. 2009; Minchev & Famaey 2010; Minchev et al. 2012b,a). The reason for such radial migration has been investigated by a good number of works. Sellwood & Binney (2002) proposed that stars close to the corotation resonance of transient spirals experience large changes in their radial positions. In addition, a nonlinear coupling of non-axisymmetric structures such as the bar and the spiral structure lead to stronger migrations to those caused by the single presence of transient spirals (Minchev & Famaey 2010; Minchev et al. 2012b,a; Roškar

et al. 2012).

This stellar radial migration might have an effect on the outer parts of spiral galaxies, in particular in the light distribution and the age profile. In Roškar et al. (2008a), using N-body and Smooth Particle Hydrodynamics (SPH) simulations of an isolated and idealised disc, the authors obtained age profiles with a characteristic "U-shape" (i.e. an age radial decline followed by an upturn) for their type II simulated disc. They suggest that the resulting broken surface mass density profile and the age upturn are attributed to the interplay between a radial star formation cutoff and radial redistribution of stars induced by transient spiral arms. However, apart from these idealised discs, more complex simulations such as those run in a cosmological context are needed to assess the effect of the environment and satellite accretion in shaping these outer discs (Younger et al. 2007; Bird et al. 2012). Sánchez-Blázquez et al. (2009), using fully-cosmological hydrodynamical simulations, also found such an age profile in their simulations, but proposed the combination of two different processes to explain it: i) a radial change in the slope of the star formation profile linked to a drop in the gas density (due to a warp) as the main cause and ii) radial migration of stars towards larger radii. However, it is important to note that such "U-shaped" age was found even in the absence of radial migration. In both works, the analysed discs exhibit a type II light distribution with the break located almost at the position where younger stars are found according to the stellar age profile.

Recently, Herpich et al. (2015a,b) investigated the role of the halo spin parameter (λ) in shaping the outer SB profiles analysing a set of controlled simulations of isolated galaxies. They find a clear transition from type III systems displaying low spin parameters to type II galaxies showing higher values with type I discs having intermediate values ($\lambda \sim 0.035$). In particular, they suggest that orbital resonances with a central bar can produce stellar migration shaping outer discs leading to upbending SB profiles. In Younger et al. (2007), the authors claim that minor mergers in galactic discs can also cause type III SB profiles due to two main effects: i) the accumulation of mass in the inner parts induced by the mergers leading to the contraction of the inner disc density profile; and ii) the transfer of angular momentum outwards producing an expansion of the outer disc. However, there are still not theoretical predictions on the stellar content in the outer parts of type I and III galaxies and further theoretical work is needed.

Although there is no clear consensus on the causes of radial migration or a definite explanation for the simulated SB and age profiles, all these works point towards an important amount of stars migrating from the inner regions to the outer parts. In particular, Sánchez-Blázquez et al. (2009) found that 57 % of the stars currently located in the outer parts of their cosmologically-simulated disc came from the inner region, with mean values of the traversed radial distance of ~ 3.4 kpc. These radial motions are mainly caused by over-

heating in their analysed discs. Other works have also analysed the amount of stellar particles populating the outer parts and coming from the inner regions: Roškar et al. (2008b) found that the percentage of stellar particles populating the outer parts migrated from the inner parts due to secular processes is up to $\sim$ 85 % with the average change in radius being 3.7 kpc, while heating in the Martínez-Serrano et al. (2009) simulations suggested a percentage as high as 64 % – 78 %. In Roškar et al. (2012), they analyse in detail the origin of the radial migration observed in their idealised and isolated discs obtaining that nearly 50 % of the stars populating their solar neighbourhood ($7 < \mathrm{R[kpc]} < 9$) came from the inner disc with some of them experiencing radial changes as high as 7 kpc (although it is not the norm).

This radial redistribution of material must affect, not only the outer parts ("U-shape" age profiles), but the overall stellar population distribution, especially if this radial distribution affects to a high number of stars. In particular, in Sánchez-Blázquez et al. (2009), where the broken profiles are caused by the combination of a radial change in the star formation rate linked to a warp and radial migration, the authors speculate that the different observed SB profiles might be explained by different combinations of both processes. If one ignored the effect of the warp, one would expect a smooth change in the star formation rate per area unit leading to a pure exponential profile. Depending on how intense radial migration is, we could change from galaxies displaying a type I surface density profile to galaxies displaying a type III profile. Thus, different radial migration efficiencies might produce different SB profiles. If this scenario proposed by Sánchez-Blázquez et al. (2009) is correct, then galaxies displaying different SB distributions must present differences in the outer stellar content (and also in the inner one). Therefore, the analysis of the stellar populations from the inner regions up to the outer discs of spiral galaxies is essential to better understand the role of radial migration and the general assembly of spiral galaxies and to refine and constrain galaxy formation models.

Some observational works have studied the stellar content in these outer regions. Bakos et al. (2008) stacked 85 $g - r$ colour profiles from Pohlen & Trujillo (2006) distinguishing between type I, II, and III galaxies. They found a clear reddening in the outer parts of their type II galaxies while type I and type III galaxies showed a flattening or a slight blue upturn. This outer reddening has been also found regardless their light distribution in Roediger et al. (2012). Bakos et al. (2008) claim that this feature starts at the break radius in the case of the type II galaxies, while Roediger et al. (2012) do not find any correlation between the position of the onset of the reddening and the location of the break. In addition, other recent studies have also focused on the stellar populations in the outer parts of galactic systems based on photometric data. Zhang et al. (2012) analysed 34 dwarf irregular galaxies finding hints of old stellar populations over the entire disc

from their SED modelling. Similar results have been found by Zheng et al. (2015) analysing SED modelling of 698 galaxies from the Pan-STARRS1 Medium Deep Survey images.

To minimise the age-metallicity degeneracy that affects photometry-based analysis, the study of integrated (based on spectroscopic data) and resolved (based on deep CMDs) stellar populations is needed. A recent (Bernard et al. 2015) study has carefully analysed the stellar content in the outer parts of M31 by means of 14 resolved fields by reconstructing precise CMDs from data collected at the Hubble Space Telescope (HST). They find that the outermost fields show that a significant fraction of their mass had already formed by z $\sim$ 1, while fields a bit closer to the centre are on average younger. These are hints for the presence of an "U-shape" age profile in M31 caused by a complicated galaxy evolution due to mergers, as suggested by the authors. Other works have also analysed individual stars in very nearby systems (M31 and M33) finding evidences for the existence of an old outer disc (e.g. Bernard et al. 2012; Radburn-Smith et al. 2012). However, the use of this kind of analysis limits these studies to nearby systems. The development of spectroscopic techniques have allowed astronomers to extend the study of the outer stellar content to a larger variety of systems. Nonetheless, as already mentioned above, obtaining high quality spectra to analyse the stellar content in the outermost regions of external galaxies is not straightforward. Due to observational limitations and the high S/N required for our purposes, previous works on the stellar populations in spiral galaxies based on spectroscopy were mainly limited to the inner discs (e.g. MacArthur et al. 2009; Sánchez-Blázquez et al. 2011). Here is where IFS data come into play. The 2D coverage of IFS data allows an accurate stellar content recovery up to the outer regions due to the different spatial binning schemes to obtain high S/N spectra. Yoachim et al. (2012), using this kind of data from the Mitchell spectrograph (formerly VIRUS-P, Hill et al. 2008), examined the radial stellar content of 12 spiral galaxies integrating over elliptical apertures. They were able to reach the outer parts for 6 type II discs but just three of them displayed the predicted "U-shape" age profile (light-weighted values). This "U-shape" implies the presence of old stellar populations in these outer parts regardless of the physical interpretation for such shape.

Despite all this effort, the details of the build-up of the outer parts of spiral galaxies remain unclear and many questions are still unanswered. Are light and age profiles coupled? Are "U-shape" age profiles a universal feature? Is the minimum in age always located at the position where the light breaks? Does radial migration really have an important effect on shaping the outskirts of spiral galaxies? The key to unveil this riddle might lie on the analysis of the stellar populations. However, previous works studying the stellar content on discs are based on highly-degenerated photometric data,

focused on nearby systems, study a low number of galaxies, or are limited to their inner parts. A more detailed and extended study of the outskirts of spiral galaxies linking observations and simulations is essential in this attempt to understand how galaxies form and evolve.

In this thesis we try to shed some light on the different mechanisms and processes building the outer parts of spiral galaxies. For that purpose, we make use of two very well differentiated techniques for the study of the formation and evolution of galaxies: observations and simulations. We characterise the stellar content up to the outer parts of a sample of *real* spiral galaxies by analysing IFS data from the Calar Alto Legacy Integral Field Area (CALIFA) survey (Sánchez et al. 2012a). We employ a novel methodology based on full spectrum fitting techniques to obtain reliable stellar age and metallicity profiles as well as radially-resolved stellar age distribution for the sample of galaxies under analysis in this thesis. We also analyse their light distribution by applying a 2D light decomposition to Sloan Digital Sky Survey (SDSS) images with the aim of investigating a possible link between stellar population and light profiles (York et al. 2000). In addition, we also analyse a set of cosmological simulations called Ramses Disc Environment Study (RaDES) and presented in Few et al. (2012) to assess the influence of the cosmological assembly history on the stellar content of the outer parts of spiral galaxies.

The outline of this thesis is as follows. In Chapter 2 we describe the data used along this thesis (CALIFA and SDSS), the sample of galaxies, and the details and results of a 2D light decomposition to the SDSS photometric data. Chapter 3 is devoted to the methodology applied to obtain stellar content from spectroscopic data; we describe and carefully test such methodology in order to assess the validity of our findings. The main results regarding the stellar populations up to the outer discs on the CALIFA galaxies are presented in Chapter 4. The analysis of the `RaDES` simulations and how satellite accretion affects those discs is explained in Chapter 5. After that, the main conclusions and ideas for future work are outlined.

Chapter 2

Sample selection and characterisation of the observational data

"Space is big. You just won't believe how vastly, hugely, mind-bogglingly big it is. I mean, you may think it's a long way down the road to the chemist's, but that's just peanuts to space."
— Douglas Adams, The Hitchhiker's Guide to the Galaxy

Contents

It is undeniable that the success of any scientific research comes from the impact and reliability of the obtained results on the belonging field of study. However, to reach such results, there is a long and complex process that cannot (and should not) be forgotten or undervalued. This process starts with the definition of the sample to be analysed and the choice of an adequate dataset suited to obtain the expected results. Both aspects are of vital importance to provide validity to the results and are required for the success of any developed work.

The study conducted in this thesis is not an exception. Indeed, the analysis of the stellar populations up to large galactocentric distances presents the difficulty of obtaining reliable information from these faint regions. Therefore, the sample of galaxies under study and the data from which the stellar content is drawn, together with the set of codes and tools used to analyse them (see Chapter 3), are fundamental pillars on the development of the present work.

In this chapter, we define and characterise the main properties of the sample of galaxies on which this study is based (Sect. 2.1). In Sect. 2.2, we describe the CALIFA data used for the stellar population properties recovery as well as examine the accuracy of the sky subtraction, a crucial step to achieve our goal. In this chapter we also present a two-dimensional characterisation of the light distribution of the sample of galaxies that allows us to obtain their main morphological components and the corresponding structural parameters along with radial colour profiles (see Sect. 2.3).

2.1 Sample selection

The study that composes this thesis has been carried out on the basis of a sub-set of 88 galaxies from the CALIFA (Sánchez et al. 2012a) survey sample which comprises more than 600 galaxies in the Local Universe ($0.005 < z < 0.03$, Walcher et al. 2014). To define this sample of galaxies we apply the following criteria based on parameters from the Hyperleda[1] catalogue (Paturel et al. 2003):

i) they must be spiral galaxies ($0 \leq T \leq 8$, according to the numerical code for the revised morphological type by de Vaucouleurs et al. 1991);

ii) with low to intermediate inclinations ($0° \leq i \leq 75°$);

iii) small enough to fit most of the galaxy within the field of view of the Potsdam Multi-Aperture Spectrograph (PMAS) in its PMAS fiber Package (PPak) configuration ($d_{25} < 94.8''$, where d_{25} is the length of the projected semi-major axis of a galaxy at the isophotal level 25 mag/arcsec^2 in the B-band);

iv) we have visually rejected galaxies showing signs of interaction.

[1] We acknowledge the usage of the HyperLeda database (`http://leda.univ-lyon1.fr`).

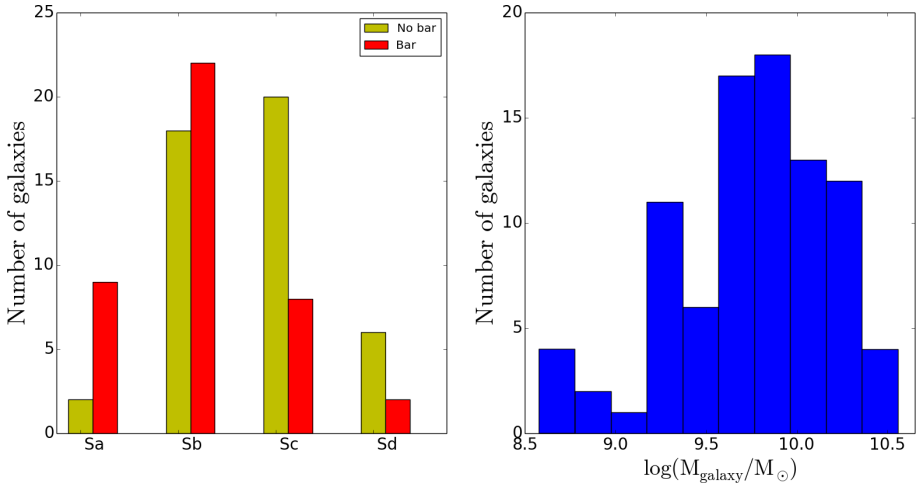

Figure 2.1: Characterisation of the analysed sample of galaxies. Left hand panel: distribution of morphological types of the sample distinguishing between barred and unbarred galaxies. Right hand panel: distribution of stellar masses in the analysed sample of galaxies.

The morphology distribution of the sample of galaxies is shown in the left-hand panel of Fig. 2.1. Although we have spiral galaxies of all morphological types (Sa to Sd), there is a lack of earlier (Sa) and later (Sd) types. This distribution is a consequence of the selection criteria of the original mother sample classification (the CALIFA sample). In this figure we also distinguish between barred (41 galaxies, 46.6 % of this sample) and unbarred (47 galaxies, 53.4 %) galaxies as classified after performing a 2D analysis of their light distribution (see Sect. 2.3). The morphology distribution of barred and unbarred galaxies also follows the CALIFA mother sample behaviour (see Walcher et al. 2014). The right-hand panel of Fig. 2.1 represents the stellar mass distribution of the CALIFA galaxies under analysis in this work. This distribution also adopts the CALIFA sample distribution with the exception of the early types and more massive galaxies that are excluded in this thesis. Figure 2.2 shows the distribution of the galaxy sample in a colour $(u - z)$ magnitude (M_z) diagram. As can be seen in that figure this galaxy sample is representative of the CALIFA mother sample distribution and thus, it is unaffected by any mass bias (according to Walcher et al. 2014). In Table A.1 (see Appendix A) we show some general information of the galaxies under study (right ascention, declination, morphological type, stellar mass, d_{25}, redshift, and distance).

2.2 Spectroscopic data, CALIFA

IFS instruments gather spectra over a two-dimensional field of view solving the issues of classical long-slit spectroscopy (restricted to one dimension) and

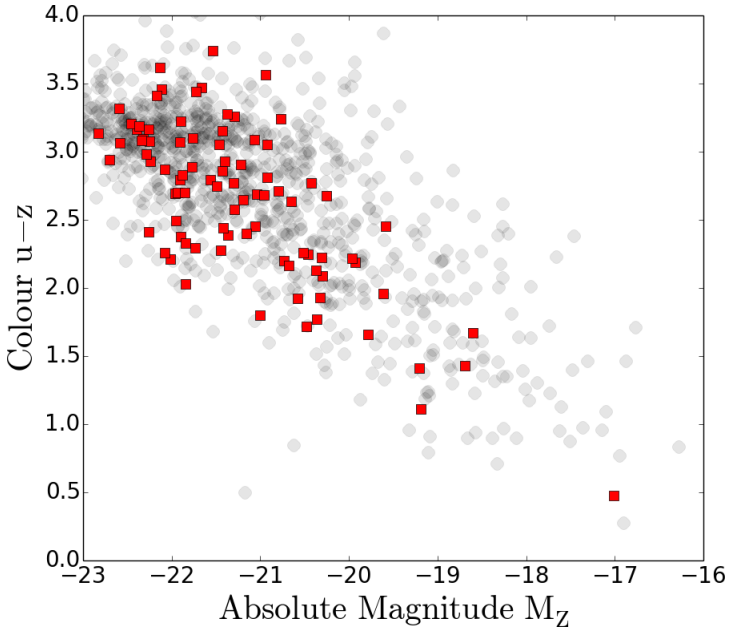

Figure 2.2: Distribution of the sample of galaxies in the $(u-z)-M_z$ colour magnitude diagram. Red squares represent individual galaxies in the present work sample, whereas grey circles represent the whole CALIFA mother sample.

allowing the extraction of high S/N spectra even in low surface brightness regions if the appropriate spatial binning is adopted. These instruments mainly consist of two parts: the spectrograph and the Integral Field Unit (IFU). The spectrograph is the optical device devoted to splitting the light into the different wavelengths. The IFU divides the 2D spatial plane in order to obtain different spectra from different spatial positions along the observed field of view. This division can be achieved by means of a lenslet array, fibres, or image-slicers. Each of the units in which the IFU divides the observed field is called *spaxel*[2].

The advent of recent IFS surveys such as CALIFA (Sánchez et al. 2012a), PINGS (Rosales-Ortega et al. 2010), Disk Mass (Bershady et al. 2010), SAMI (Croom et al. 2012), VENGA (Blanc et al. 2013), or MANGA (Law & MaNGA Team 2014) can be considered one of the most important steps towards the understanding of the two-dimensional distribution of the stellar and gas properties in spiral galaxies. The large amount of data collected by those surveys allows the statistical characterisation of these systems and the survey collaborative effort facilitates the handling of such vast quantity of data. For this thesis we make use of the IFS data from the CALIFA survey (Sánchez et al. 2012a) to analyse the stellar content up to the outer parts of spiral galaxies.

[2]See `http://ifs.wikidot.com/` for further information about IFS.

CALIFA collected data at the 3.5 m telescope at Calar Alto using the PMAS spectrograph employing the PPak wide-field IFU (Roth et al. 2005; Kelz et al. 2006). This project provides high quality spectra over a wide, hexagonal field of view of $72'' \times 64''$ (331 science fibres with a fibre size of $2.7''$, see Fig. 2.3) of ~ 600 galaxies in the local Universe ($0.005 < z < 0.03$). These 600 galaxies were randomly observed (depending on visibility and observing dates) from a diameter-selected sample comprising 939 galaxies (Walcher et al. 2014). The data from 200 of these galaxies is publicly available through two data releases[3] (Husemann et al. 2013; García-Benito et al. 2015) and the data for the entire sample will be released by April 2016. Two different observing set-ups have been adopted to maximise the scientific impact of the survey, one at high resolution (V1200) and the other at a lower resolution (V500). This survey allows the study of gas ionisation mechanisms, the analysis of gas abundances, the recovery of stellar population properties, or the measurement of galaxy kinematics in gas and stars. The wavelength range of the V500 (V1200) data is $3745 - 7300$ Å ($3400 - 4750$ Å) with a spectral resolution, measured as the Full Width at Half Maximum (FWHM) of 6.0 Å (V500) and 2.7 Å (V1200). The CALIFA observational strategy acquires data at three different positions (pointings) to obtain a 100 % coverage of the entire field of view with a final exposure time of 2700 s for the V500 data (5400 s for the V1200 setup). To verify the high quality of these data and the good performance of the data reduction pipeline we encourage the reader to carefully check the papers where the two previous data releases are described (Husemann et al. 2013; García-Benito et al. 2015).

In this thesis, we use the CALIFA COMBO cubes from the last stable version of the pipeline (version 1.5, García-Benito et al. 2015), i.e. a combination of the V500 and the V1200 (degraded to the V500 resolution) datacubes avoiding the vignetting of the data in the blue and red end of some fibres for the V500 data (for further information see Sánchez et al. 2012a). Although the V500 and V1200 data are publicly available, the COMBO cubes are just for internal use and thus, not released yet. This dataset displays high-quality spectra along the entire field of view in the wavelength range from 3700 Å to 7500 Å.

2.2.1 CALIFA sky subtraction

As we are focused on studying the outer parts of galaxy discs, where the SB is comparable with the brightness of the night sky, a careful sky subtraction to the spectroscopic data is essential to be able to extract reliable information from those regions.

The PMAS spectrograph has an additional set of 36 fibres dedicated

[3]The data are accessible from the CALIFA webpage, `http://califa.caha.es/`.

to sample the sky background and are distributed in six bundles at a radial distance from the centre of $\sim 95''$ (see Fig. 2.3). To deal with the sky subtraction, the automated CALIFA reduction pipeline (in its 1.5 version) calculates a single sky spectrum (let's call it *global sky spectrum*) to be subtracted to all the 331 science fibres. This global sky spectrum is computed as the mean of the 30 faintest sky fibres, which robustly rejects a whole sky bundle that could be contaminated by some additional light and thus, not representative of the sky. One *global sky spectrum* is obtained for each pointing and then subtracted to all the fibres in that particular pointing before combining the three of them to create the final datacube.

As part of the CALIFA collaboration we tried to improve, or at least check, the accuracy of this simple recipe for the sky subtraction . We apply an alternative and more sophisticated procedure for the sky subtraction involving the simultaneous fit of stellar and sky templates to match the observed spectra. First of all, we consider that what we observe is a combination of the light coming from the stars populating the target galaxy, some gaseous emission lines (that will be avoided by masking them), and the emission of the Earth's atmosphere. Then, we obtain a representative spectrum of the entire galaxy by integrating a region at an intermediate distance from the centre. This representative spectrum is fitted by a combination of model stellar templates (accounting for the stellar contribution) and sky templates (accounting for the sky emission). This spectrum is selected from fibres located in a ring in the inner disc of the galaxy where the light intrinsic to the galaxy dominates. We avoid the inner regions because the spectra from those fibres are clearly dominated by the galaxy light and thus, a good estimation of the sky light is hampered. In addition, we also avoid the outer regions as those fibres are more sky dominated and it can lead to errors in the derived stellar contribution. We use the observed sky spectra as sky templates and thus, we can obtain a more sophisticated *global sky spectrum* from the observed data than the one obtained by the CALIFA automated pipeline. However, this *global sky spectrum* might not be representative of the sky

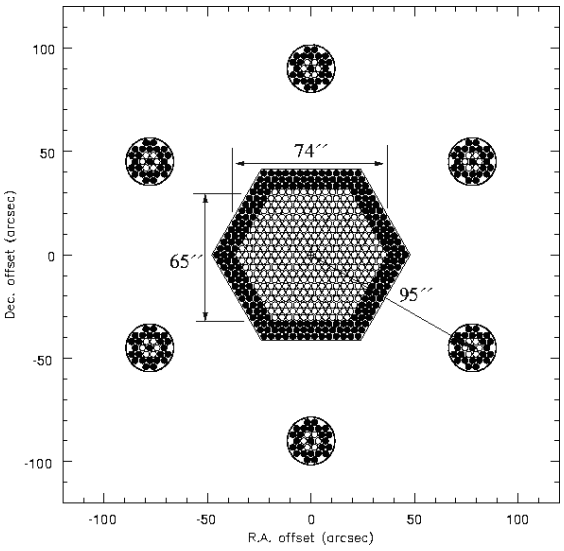

Figure 2.3: Fibre layout and dimensions of the PMAS spectrograph in its PPak configuration. From Kelz et al. (2006).

in the entire field of view as small fluctuations are expected, therefore we apply again the same procedure in a fibre-per-fibre basis. This time we use this *global sky spectrum* as the only sky template, and we allow the fit to determine the multiplicative factor (weight) to be applied to this *global sky spectrum* to account for the more representative sky spectrum in each fibre.

With such procedure in mind we take advantage of the ability of the "penalised pixel fitting" (pPXF) code (Cappellari & Emsellem 2004; Cappellari et al. 2011) to simultaneously fit sky and stellar templates to optimise the calculation of the global sky spectrum. Although `pPXF` is commonly used to analyse the stellar kinematics, we modify the code to make it suitable for our purposes. We analyse the spectra from the 36 sky fibres from each of the pointings and discard the six brightest fibres to ensure that we eliminate cases that are clearly not dominated by the sky. The remaining 30 sky fibres are used as sky templates for `pPXF`. We choose as input galaxy spectra to fit with this code a representative galaxy spectrum at intermediate galactocentric distances as explained above. After masking emission lines to avoid nebular contamination we run `pPXF`, obtaining the best stellar combination and the best sky combination. This procedure therefore provides the combination of the 30 faintest sky fibres that best matches the observed data (not just the mean spectrum). To refine this method, we run `pPXF` again on a fibre-per-fibre basis using as sky templates only the best combination found in the previous step. This latest step allows us to obtain a multiplicative factor to be applied to this best sky solution in each of the fibres including the sky-dominated outer fibres. The resulting sky weights are rather constant over the field of view of the instrument with a scatter of ~ 4 % (see Fig. 2.4).

This method was applied to a set of objects in the sample of the first CALIFA data release (Husemann et al. 2013). We then compared the sky-subtracted spectra before cube reconstruction using both sky subtraction schemes, i.e. the implemented in the CALIFA pipeline and the one outlined above. This comparison was made by calculating the S/N in the continuum to the sky subtracted fibres following both approaches. We consider that an improvement in the sky subtraction will produce an improvement in the continuum S/N. For some fibres, the method described above improves the sky subtraction with an average difference in the S/N of 3.7 ± 2.8 %. However, this statement is not valid for all the fibres analysed. In some cases this alternative sky subtraction worsened the outcomes, with S/N as low as 5 times lower than the S/N using the v1.5 reduction pipeline sky subtraction, as a consequence of the low quality of those spectra hampering a reliable fit.

The above described exercise allows us to conclude that the simple recipe implemented in the v1.5 reduction pipeline for dealing with the sky subtraction is accurate and hard to improve, simultaneously, over the entire field of view. The larger improvement that we obtain with this complex, alternative

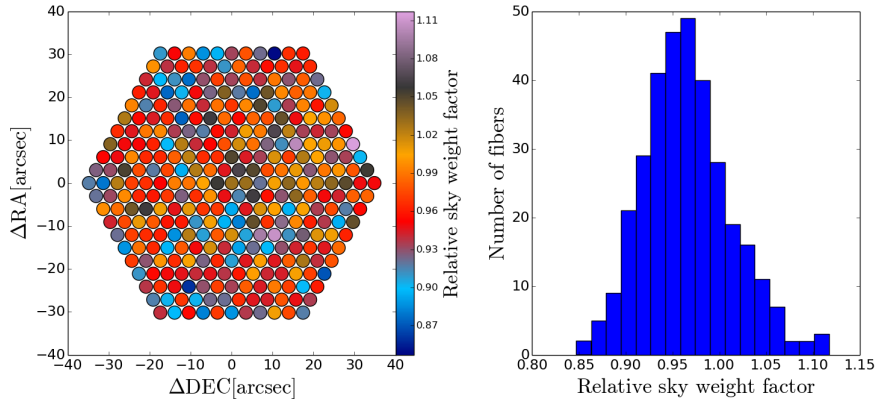

Figure 2.4: Left panel: 2D distribution of the sky weight factors of the *global sky spectrum* (second calculation) as inferred with pPXF across the PPak field for the second pointing of UGC 03944 (V1200). Right panel: distribution of those sky weight factors for that particular pointing.

sky subtraction is of ~ 4 % in the S/N, providing an estimation of the errors produced in this step. In addition, although the *ideal* sky spectrum to be removed to the different fibres may slightly change (see Fig. 2.4), this variation is small enough as to claim that the subtraction of a single spectrum over the entire field of view is sufficient. We must note that the strongest residual from the sky occurs in the Hg I λ4358, Hg I λ5461, O I λ5577, Na I D (around 5890 Å), O I λ6300, and O I λ6364 emission lines as well as at the telluric B band absorption. All these regions are avoided when the CALIFA spectra are analysed (see Sect. 3.1 and Fig. 3.3).

2.3 Photometric data, SDSS

SDSS is one of the most ambitious and fruitful ongoing projects in astronomy. This survey is collected photometric and spectroscopic data at a dedicated 2.5m telescope located at Apache Point Observatory in Southern New Mexico. The goal of this project is to observe one quarter of the entire sky providing the community with an unprecedented view of the Universe. A good number of recent works are based on their photometric or spectroscopic data as well as on other by-products such as imaging catalogues (e.g. magnitudes, astrometry) or redshifts. In this thesis we use the data provided by the SDSS collaboration to characterise the light distribution and the colour profiles of the galaxy sample.

As in the case of the spectroscopic data, the sky subtraction in the photometric images is an essential step to analyse the light distribution up to the outer parts. Different SDSS data releases have different ways of dealing with this sky subtraction. While some of them provide fully-calibrated, sky-

subtracted data frames (such as the tenth data release, DR10, Ahn et al. 2014), others are not sky-subtracted (as the seventh data release, DR7, Abazajian et al. 2009). The fact that the DR7 data are not sky-subtracted allows us to test the use of alternative sky subtraction procedures. Here we assess the quality of the DR10 automated sky subtraction by comparing it with an alternative procedure to perform such task in the not-sky-subtracted DR7 data. This exercise allowed us to decide which approach should be followed for a proper light distribution characterisation up to the outer discs.

With such purpose we analyse the fully-calibrated g, r, and i band images from the SDSS DR7 with a spatial coverage of $\sim 13.51 \times 9.83$ arcmin^2, an exposure time of ~ 53.9 s, and a pixel size of 0.396 arcsec. SDSS DR7 provides aside a measurement of the sky level as the median value of every pixel after a sigma-clipping is applied. Although valid for other purposes, to study the fainter parts of spiral galaxies this estimation has been proven insufficient (Pohlen & Trujillo 2006). Thus, we apply the alternative sky subtraction procedure proposed in Pohlen & Trujillo (2006) to the DR7 SDSS data. We automatically mask every frame using the code Source Extractor (SExtractor) presented in Bertin & Arnouts (1996) as well as visually-inspect and manually-mask small features that `SExtractor` might have missed. We apply the `ellipse IRAF`[4] task to the masked DR7 frames with ellipses of fixed ellipticity and position angle to match the disc outermost isophotes (from the 2D light distribution analysis, see Sect. 2.3.1) reaching as far from the galaxy as possible (see Fig. 2.5). We compute the sky level by averaging the counts value in a region where the galaxy and other distant sources have no influence, i.e. the radial count profile is flat (vertical dashed green lines in Fig. 2.5). The value calculated in this way is subtracted to the science frame.

The flux calibration of the SDSS DR7 frames is described in the SDSS DR7 webpage[5]. Basically, the SB value (μ) is obtained by applying:

$$\mu_{\rm j} = -2.5 \times \log[({\rm f}/{\rm f}_0)_{\rm j}], \tag{2.1}$$

where

$$({\rm f}/{\rm f}_0)_{\rm j} = \frac{({\rm counts}_{\rm j} - 1000)}{53.9 * 0.396^2} \times 10^{0.4*({\rm aa}_{\rm j}+{\rm kk}_{\rm j}*{\rm airmass}_{\rm j})} \tag{2.2}$$

and the parameters $\rm aa_j$, $\rm kk_j$, and $\rm airmass_j$ are characteristics of the observations for the filter j (g, r, and i) and can be found in the SDSS DR7 explorer webpage[6].

As previously stated, other SDSS data releases offer sky subtracted, fully calibrated frames. To test if the sky subtraction procedure followed here im-

[4] `IRAF` is distributed by the National Optical Astronomy Observatory, which is operated by the Association of Universities for Research in Astronomy (AURA) under cooperative agreement with the National Science Foundation.

[5] `http://www.sdss2.org/dr7/algorithms/fluxcal.html`

[6] `http://skyserver.sdss.org/dr7/en/tools/explore/obj.asp`

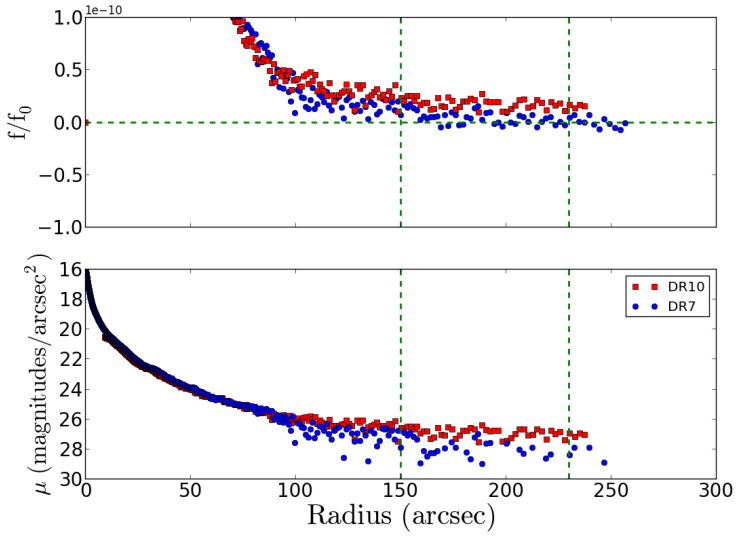

Figure 2.5: Radial distribution of f/f_0 and surface brightness profiles for SDSS i-band using DR7 and DR10 after sky subtraction is applied for the galaxy NGC0001. Note the improvement of ~ 60 % in the sky level comparing the alternative sky subtraction scheme presented in this section with the one implemented in the DR10. Dashed, vertical green lines indicate the radial range used for the calculation of the sky value.

proves those applied to later SDSS data releases, we compare it to the fully-calibrated, sky-subtracted DR10 data (g, r, and i filters). As different flux calibration schemes are adopted for each data release, for a fair comparison we have decided to compare the f/f_0 quantity[7].

In Fig. 2.5 we compare the SB profiles and the f/f_0 i-band profiles of NGC 0001 using both approaches, i.e. DR7 with the here-explained alternative sky subtraction scheme and DR10 with the automatise procedure performed by the SDSS DR10 pipeline. In the case of the i-band we improve such determination by a factor of 60.0 %[8] (the largest improvement). For the g-band and r-band, this factor is still large enough to be considered a substantial improvement, 54.1 % and 53.8 %, respectively.

Therefore, for the characterisation of the light distribution in the sample of galaxies under study in this thesis, we use the fully-calibrated SDSS DR7 g, r, and i images with the above explained alternative sky subtraction procedure.

[7]See `https://www.sdss3.org/dr10/algorithms/magnitudes.php` for a complete explanation on how such quantity is computed in SDSS DR10.

[8]Computed as $(f_{10} - f_7)/f_{10}$, where f_{10} and f_7 are the mean value of the f/f_0 curve between the two green, dashed, vertical lines in Fig. 2.5 for the tenth and the seventh data releases, respectively.

2.3.1 2D light distribution

In order to investigate possible relations between the stellar content of the galaxies under analysis with the different SB profiles that they exhibit, we need to analyse their light distribution. A 2D analysis of the light distribution is a closer approach to the real light distribution than azimuthally-averaged 1D approaches followed by previous works (e.g. Pohlen & Trujillo 2006; Erwin et al. 2008; Gutiérrez et al. 2011).

We use the GAlaxy Surface Photometry 2 Dimensional Decomposition (GASP2D) code (Méndez-Abreu et al. 2008, 2014) to provide with a 2-D decomposition of the SB of the sample of galaxies from the fully-calibrated, sky-subtracted g, r, and i band images from the SDSS DR7 (previously discussed). For completeness, we briefly outline the main characteristics of this code. GASP2D iteratively fits a model with different morphological components of the SB distribution to the pixels of the galaxy image by means of a non-linear least-squares minimisation based on a robust Levenberg-Marquardt method (Moré et al. 1980) using the MPFIT algorithm (Markwardt 2009). It weights every pixel in the image according to the variance of its photon counts taking into account the detector readout noise. It deals with seeing effects by convolving the model image with a circular Moffat (Trujillo et al. 2001) Point Spread Function (PSF) with the FWHM measured directly from stars in the galaxy image.

This way, GASP2D provides us with the set of structural parameters of these components that better fits the observed light distribution, such as the ellipticity (e), the position angle (PA), the bar length (a_{bar}), break radius (R_{break}), inner disc scale-length (h_{in}), outer disc scale-length (h_{out}), etc.

We adopt a Sérsic law (Sérsic 1968) to describe the light intensity of the bulge component

$$I_{bulge}(r) = I_e 10^{-b_n\left[(\frac{r}{r_e})^{1/n}-1\right]}, \tag{2.3}$$

where r is the radius measured in the Cartesian coordinates describing the reference system of the bulge in the plane of the sky. r_e, I_e, and n are the effective radius, the intensity at r_e, and the Sérsic index, respectively, and $b_n = 0.868\ n - 0.142$ (Caon et al. 1993).

We assume that the disc follows a classical exponential decline (Freeman 1970):

$$I_{disc}(r) = I_0\, e^{-(\frac{r}{h_{in}})}, \tag{2.4}$$

where r is the radius measured in the Cartesian coordinates describing the reference system of the disc. I_0 and h_{in} are the central surface brightness and scale-length of the disc, respectively.

To account for the different behaviours that some galaxies exhibit in their outer parts (broken profiles) we adopted the following functional pa-

rameterisation of the disc component

$$I_{disc}(r) = I_0 \left[e^{\frac{-r}{h_{in}}} \theta + e^{\frac{-R_{break}\,(h_{out}-h_{in})}{h_{out}\,h_{in}}} e^{\frac{-r}{h_{out}}} (1-\theta) \right], \qquad (2.5)$$

where

$$\begin{cases} \theta = 0 & \text{if} \quad r > R_{break} \\ \theta = 1 & \text{if} \quad r < R_{break} \end{cases}$$

and r is the radius measured in the Cartesian coordinates describing the reference system of the disc. I_0, h_{in}, h_{out}, and R_{break} are the central intensity, inner scale-length, outer scale-length, and break radius of the disc, respectively.

For barred galaxies, we adopt for the bar component the projected surface density of a three-dimensional Ferrers ellipsoid (Ferrers 1877; Aguerri et al. 2009) whose intensity vary with radius as:

$$I_{bar}(r) = I_{0,bar} \left[1 - (\frac{r}{a_{bar}})^2 \right]^{n_{bar}+0.5}, \qquad r < a_{bar}; \qquad (2.6)$$

where r is the radius measured in the Cartesian coordinates describing the reference system of the bar and using generalised ellipses (Athanassoula et al. 1990). $I_{0,bar}$, a_{bar} and n_{bar} represent the central bar intensity, length and shape parameters of the bar, respectively. To avoid the high degeneracy degree that n_{bar} introduces during the fit, we keep it fixed to a value of 2 (see also Laurikainen et al. 2005)

As an example of the GASP2D performance, Fig. 2.6 shows the 2D decomposition of bulge and double disc components for IC 1199. Left hand column displays three panels with the observed SDSS r-band image (top), the 2D model (middle), and the residuals (model – observed, bottom). Right hand column shows the SB (top), ellipticity (e, middle), and position angle (PA, bottom) profiles. In those panels black dots and shaded areas represent the observed values and the errors computed as one sigma of the distribution of values within the ellipse. The solid green line is the output from the `ellipse IRAF` task applied to the model image. In both cases (black dots and green solid line) `ellipse` fits the azimuthally-averaged galaxy isophotal light distribution of the model and SDSS science frames by means of ellipses of variable e and PA. The top right-hand panel also illustrates the fit for the bulge (dashed blue line) and the double disc (dotted red line) components. Dotted-dashed vertical lines and the dotted-dashed ellipse in top-left panel delimit the inner region (affected by the bulge) and the disc-dominated region ($R_{lim,in}$, see Sect. 2.3.2 for details). The break radius (R_{break}) is indicated by dashed vertical lines and a dashed ellipse in the observed image. Despite the difficulties of fitting complex systems dominated by spiral structure or H II regions using smooth components, the agreement between

observed and reconstructed profiles is reasonably good. On average for the entire sample, the SB residuals oscillate between ± 0.45 mag/arcsec^2, with the bulk of pixels showing residuals within ± 0.15 mag/arcsec^2. The disc structural parameters for the entire sample of galaxies is given in Table A.2 in the Appendix A.

Table 2.1 and Fig. 2.7 summarise the information from the 2D light decomposition outlined before. We find that type I (42.0 %) and II (52.3 %) SB profiles are the most frequent ones in the analysed galaxies with only 5 galaxies (5.7 %) displaying an upbending profile (Sb and Sc unbarred galaxies). Type II galaxies exhibit the most extended inner discs (h_{in} = 7.0 ± 1.6 kpc), followed by type I (4.5 ± 0.9 kpc) and type III (2.1 ± 0.4 kpc) discs. The breaks are located at much larger galactocentric distances for type II than for type III galaxies (13.1 ± 2.3 vs. 6.2 ± 0.9 kpc), although in terms of h_{in} this trend is reversed (2.1 ± 0.3 vs. 3.1 ± 0.3 h_{in}). Although we have tried to find correlations with morphology of the different structural parameters (h_{in}, R_{break}, and R_{break}/h_{in}), no correlations are found.

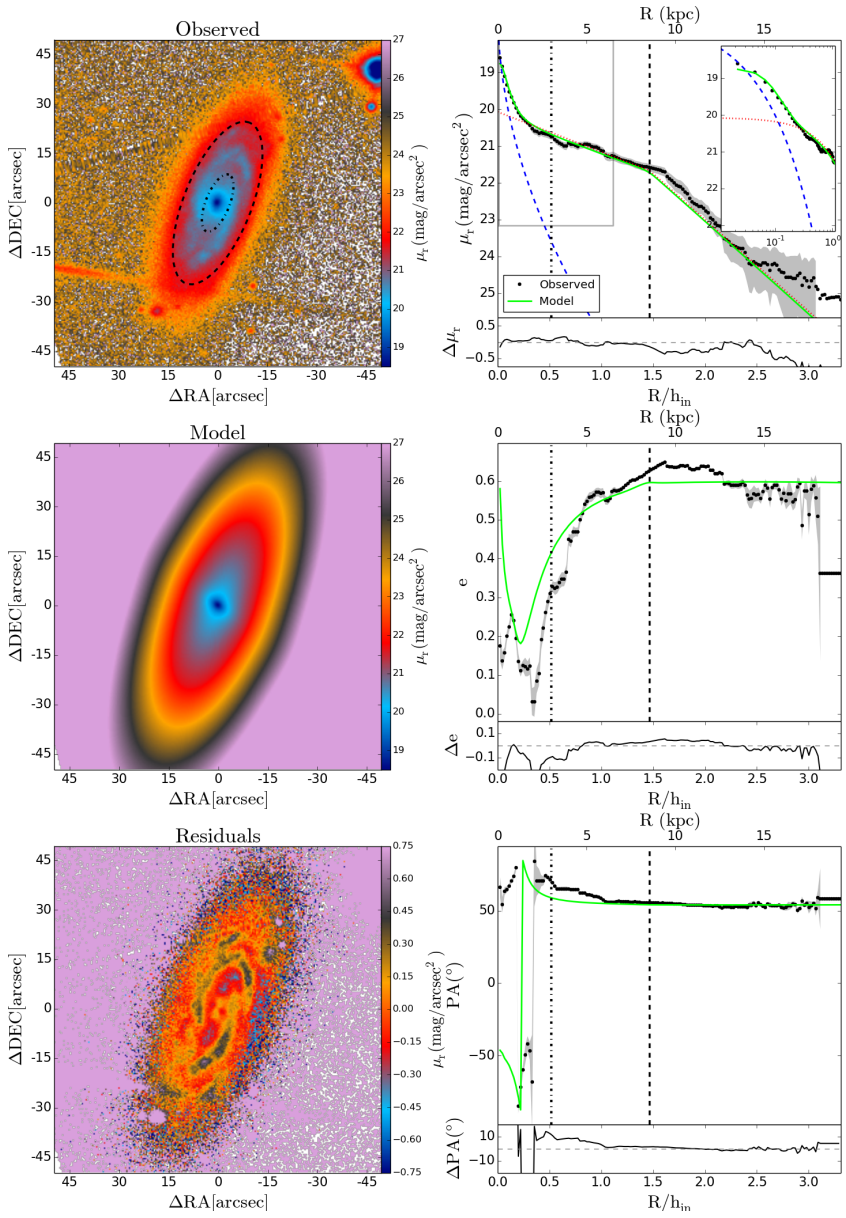

Figure 2.6: GASP2D decomposition for IC1199 in SDSS r-band with two components: a bulge and a double disc. Left column shows the observed image (top), the fitted model (middle), and the residuals (model – observed, bottom). The north is up in all images. Right pannels illustrate the SB (top), ellipticity (e, middle), and position angle (PA, bottom) profiles. Points represent the observed magnitude; shadow areas account for the errors, computed as the one sigma of the distribution of values within the ellipse; red dotted line is the double disc model; blue dashed line follows the bulge light distribution; green line is the output of the `ellipse IRAF` task applied to the model; the inset in top right panel is focused on the inner part with a logarithmic radial scale. All right-hand panel plots show an auxiliary plot in the lower part with the residuals of the fit. Dotted-dashed vertical lines and the dotted-dashed ellipse delimit the bulge-dominated region. Dashed vertical lines and the dashed ellipse are at the break radius.

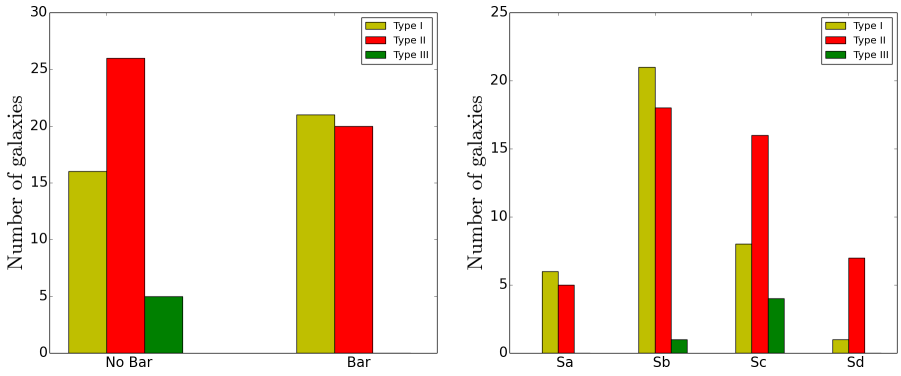

Figure 2.7: Characterisation of the sample of galaxies according to their SB profiles. Left: number of galaxies with different SB profiles distinguishing between the presence or not of a bar. Right: number of galaxies with different SB profiles according to their morphological type.

	N	h_{in} (kpc)	R_{break} (kpc)	R_{break}/h_{in}		N	h_{in} (kpc)	R_{break} (kpc)	R_{break}/h_{in}
Type I	37 (42.0 %)	4.5 ± 0.9	–	–	Sa	6 (6.8)	4.1 ± 0.6	–	–
					Sb	21 (23.9)	4.4 ± 0.8	–	–
					Sc	8 (10.7)	4.2 ± 0.7	–	–
					Sd	1 (1.3)	7.0 ± 1.2	–	–
Type II	46 (52.3 %)	7.02 ± 1.59	13.1 ± 2.3	2.1 ± 0.3	Sa	5 (5.7)	9.1 ± 2.4	11.7 ± 1.2	1.6 ± 0.4
					Sb	18 (20.5)	8.0 ± 1.5	13.7 ± 2.1	1.8 ± 0.3
					Sc	16 (18.2)	5.3 ± 1.0	12.7 ± 2.7	2.5 ± 0.4
					Sd	7 (7.9)	7.0 ± 1.2	13.6 ± 2.3	2.0 ± 0.3
Type III	5 (5.7 %)	2.1 ± 0.4	6.2 ± 0.9	3.1 ± 0.3	Sa	–	–	–	–
					Sb	1 (1.1)	2.7 ± 1.5	8.6 ± 1.6	3.2 ± 0.8
					Sc	4 (4.6)	1.9 ± 0.4	5.6 ± 0.8	3.1 ± 0.4
					Sd	–	–	–	–

Table 2.1: Surface brightness profile parameters for the analysed sample of galaxies from the 2D decomposition using GASP2D (see Sect. 2.3.1 for further details).

For the sake of completeness, we compare our results with other works focused on the 1D light distribution of the outer discs using visible light, i.e. Pohlen & Trujillo (2006, hereafter PT06), Erwin et al. (2008, hereafter E08), and Gutiérrez et al. (2011, hereafter G11). This comparison is summarised in Table 2.2. We must highlight the different selection criteria adopted to define each sample. PT06 was focused on analysing the light distribution for late type galaxies (98 galaxies with $2.99 < T < 8.49$), while E08 and G11 were focused on S0-Sb galaxies (66 barred and 47 unbarred galaxies, respectively).

The comparison among the works (including the one presented here) shows some differences. Especially striking is the discrepancy in the frequency of profile types obtained by these studies. While this work, PT06, and E08 suggest that galaxies mostly display downbending profiles, upbending SB distributions are most frequently found in G11. However, we find a lack of type III galaxies with the 2D decomposition method outlined before. The values for the inner disc scale-lengths are in relative agreement, with type II galaxies having larger values than type I and III galaxies. PT06, E08, and G11 find that the break radius is located around the same position for type II and III galaxies (in physical units) and thus, the different values found for the R_{break}/h_{in} for different SB types are mainly due to the differences in the inner disc scale-lengths. However, according to the 2D decomposition the type II breaks are located at larger galactocentric radii than type III breaks.

Before drawing any conclusions, we must bear in mind the great discrepancies among the compared works: i) PT06, E08, and G11 follow a 1D analysis of the light distribution while this analysis makes use of a 2D decomposition; in addition, ii) different galaxy samples are analysed in each work; if the samples under analysis are not similar (masses, morphology, etc.) then, the results should not be comparable.

		This work (2D) (1)	This work (1D) (2)	PT06 (3)	E08 (4)	G11 (5)
Type I	%	42.0	22.7	11	27	28
	h_{in}(kpc)	4.5 ± 0.9	4.3 ± 0.5	2.8 ± 0.8	2.9 ± 0.7	6.0 ± 2.7
	R_{break} (kpc)	–	–	–	–	–
	R_{break}/h_{in}	–	–	–	–	–
Type II	%	52.3	56.8	66	42	21
	h_{in}(kpc)	7.0 ± 1.6	5.6 ± 1.1	3.8 ± 1.2 / 6.9 ± 2.3	6.1 ± 2.5	4.5 ± 1.8
	R_{break} (kpc)	13.1 ± 2.3	13.2 ± 2.5	9.2 ± 2.4 / 9.5 ± 3.3	7.7 ± 1.9	7.9 ± 2.4
	R_{break}/h_{in}	2.1 ± 0.3	2.5 ± 0.5	2.5 ± 0.6 / 1.7 ± 0.4	2.1 ± 0.8	2.1 ± 0.4
Type III	%	5.7	20.5	33	24	51
	h_{in}(kpc)	2.1 ± 0.4	3.0 ± 0.6	1.9 ± 0.6	1.9 ± 0.4	2.3 ± 0.5
	R_{break} (kpc)	6.2 ± 0.9	12.8 ± 2.9	9.3 ± 3.3	8.2 ± 1.7	9.4 ± 2.2
	R_{break}/h_{in}	3.1 ± 0.3	4.3 ± 0.5	4.9 ± 0.6	4.4 ± 0.4	4.2 ± 0.6

Table 2.2: Comparison between the surface brightness profile parameters presented here and other works. (1) Results applying a 2D decomposition using GASP2D (see Sect. 2.3.1 for further details) to the sample of galaxies analysed in this thesis; (2) results applying a more classical 1D approch (see text for details) to the sample of galaxies; (3) results from PT06, for type II galaxies the parameters are divided into classical truncations and breaks associated with the Outer Lindblad Resonance (II-CT/II-o.OLR); (4) results from E08; and (5) results from G11.

We check to what extend the decomposition method affects the global parameters for type I, II, and III galaxies by applying a 1D analysis to the same sample of galaxies. To perform such exercise we have analysed the 1D SB distributions computed applying `ellipse` to the SDSS frames (see Sect. 2.3.2 for further information). We fit these 1D SB profiles with a classical exponential decline (Freeman 1970) in the case of type I galaxies:

$$I_{disc}(r) = I_0\, e^{-(\frac{r}{h_{in}})}, \tag{2.7}$$

where $I_{disc}(r)$ is the disc intensity as a function of the radius (r), I_0 is the central intensity, and h_{in} is the scale-length of the disc. For type II and III galaxies we use the function defined in E08 (equations 5 and 6):

$$I_{disc}(r) = S\, I_0\, e^{-r/h_{in}} \left[1 + e^{\alpha(r-R_{break})}\right]^{\frac{1}{\alpha}\left(\frac{1}{h_{in}}-\frac{1}{h_{out}}\right)}, \tag{2.8}$$

where h_{out} is the outer scale-length of the disc, R_{break} is the position of the break, α is a parametrisation of the sharpness of the break, and S is a scaling factor in the form:

$$S = \left(1 + e^{-\alpha R_{break}}\right)^{\frac{1}{\alpha}\left(\frac{1}{h_{in}}-\frac{1}{h_{out}}\right)}. \tag{2.9}$$

The results of this 1D analysis of the light distribution are shown in column (2) of Table 2.2. Some differences still remain in the profile type percentages. However, in this case the frequency of profile types is closer to that presented in the works where a similar 1D approach was followed. The values for the inner disc scale-lengths are fairly similar, but the larger differences are found for the break position in type III galaxies. The mean radius at which the break is found for these type III galaxies with the 1D approach (12.8 $\pm$ 2.9 kpc) is much further out than in the case of the 2D analysis (6.2 $\pm$ 0.9 kpc). On the other hand, the values of all the parameters (h_{in} and R_{break}) from this 1D analysis are in general agreement with the parameters presented in the other works with small differences attributed to the different samples under study.

In summary, the differences among the compared works are mainly due to two aspects. On one hand, the different decomposition methods used (1D vs 2D) must play an important role in the derived structural parameters; however, a 2D analysis of the light distribution is a more realistic procedure, and thus, we decide to follow this approach. On the other hand, the different selection criteria to define each sample and thus, the different morphologies under consideration, might arise different results. It is clear that larger statistical samples are needed to properly assess the variety of SB profiles in nature.

2.3.2 Colour profiles

SDSS data are also used to compute the $g-r$, $g-i$, and $r-i$ colour profiles for this sample of galaxies by running `ellipse` to the g, r, and i science frames. We fix the e and PA of the successive ellipses matching those of the outer disc (according to the GASP2D analysis). The 1D light profiles in the three filters are calibrated as explained in the SDSS DR7 webpage[9] and subtracted accordingly to obtain the three colour profiles. The errors in the colour profiles are quadratically propagated from the errors in the SB profiles of the bands involved (e.g. g and r bands in the case of the $g-r$ colour) computed as one sigma of the distribution of values (see Sect. 2.3.1).

We compute linear fits to these colour profiles to quantify and describe their general trends. We restrain the fit to the disc region, avoiding the inner or bulge-dominated part. Considering that the bulge region is where the observed light distribution deviates from the disc exponential profile, we define the inner limit ($R_{lim,in}$) as:

$$\mu_{disc}(r) - \mu_{obs}(r) > 0.2\,mag/arcsec^2 \qquad \forall\, r < R_{lim,in}; \tag{2.10}$$

where r is the galactocentric radius, μ_{disc} is the functional shape of the disc light distribution found by GASP2D, and μ_{obs} is the observed SB profile (black points in top-left panel of Fig. 2.6).

For a fair comparison between colour and stellar parameters profile gradients (see Chapter 4), we have decided to apply an outer limit ($R_{lim,out}$) for the colour linear fits as the one defined from the stellar age and metallicity profiles (see Sect. 3.1.3). We compute the inner gradients taking into account colour values from $R_{lim,in}$ to $R_{lim,out}$ for type I galaxies and from $R_{lim,in}$ to R_{break} for type II and III galaxies. In these later cases, we also compute the outer gradient from R_{break} to $R_{lim,out}$ for those galaxies reaching beyond the break radius. We must highlight that we are able to compute high-quality colour profiles beyond $R_{lim,out}$. However, we stick the outer limit to $R_{lim,out}$ for a fair comparison with the stellar parameters gradients (see Sect. 3.1.3). In Fig. 2.8, we show the colour profiles and the results of the linear fits for IC 1199 as an example. The performed linear fits are error-weighted and take into account the observational errors of the radial points to derive the parameters of the fit, such as the gradient and its error. All the values for the colour inner gradientes can be found in Appendix A, Table A.5.

[9] `http://www.sdss2.org/dr7/algorithms/fluxcal.html`

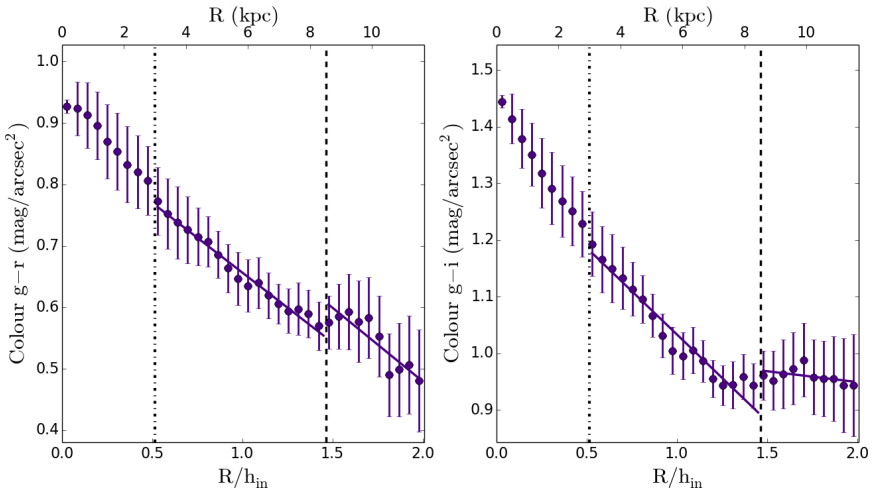

Figure 2.8: $g-r$ and $g-i$ colour profiles for IC 1199 as an example. The colour profiles are represented by means of purple circles. The dotted-dashed vertical line delimits the bulge-dominated region ($R_{lim,in}$), while the dashed vertical is located at the break radius (R_{break}).

Chapter 3

Stellar populations from integrated spectra: methodology and reliability tests

"On the way to the impossible, we might find something eminently doable."
— Brian Cox

"It's kind of fun to do the impossible."
— Walt Disney

Contents

The purpose of astronomical data analysis is the physical characterisation of the properties of the celestial sources under study. However, this is far from a straightforward task. Not only we need to handle great amounts of data in complex formats, but we also need to rely on years of development of physical theories and computational codes helping us to decipher what the Universe is telling us.

In this thesis, we aim to understand the mass assembly processes on spiral galaxies via the analysis of the properties of the stars populating their outer regions. In particular, we study how the mean stellar age and metallicity vary along the galactocentric distance and the radial variation of the proportion of young versus old stars (stellar age distribution) in external galactic systems. In other words, we want to analyse the integrated light coming from millions of stars of different ages, chemical compositions, and physical origins up to large galactocentric distances to invert the problem and obtain the distribution of stars whose outcome would look like the observed light. As the reader may have noticed, this is not an easy duty and thus, the procedure to obtain this information is critical to decide whether we should rely on that information or not.

In this chapter we carefully explain the methodology that we use to obtain, from sets of thousands of spectra, the radial stellar content of the galaxies comprising the sample of galaxies under analysis (see Sect. 3.1). This procedure is briefly described in Ruiz-Lara et al. (2016) and in Ruiz-Lara et al. (in prep). In addition, we show some of the tests we have performed to check the reliability of the results coming from this methodology (see Sect. 3.2). In particular, we show the first comparison between the SFH recovered from a high quality CMD and integrated spectrum of a complex systems as the bar of the Large Magellanic Cloud (LMC), work published in Ruiz-Lara et al. (2015b).

3.1 Methodology

In this section, we will explain the main steps taken to obtain the stellar content from integrated spectra based on full-spectrum fitting techniques. Before carrying out any analysis, and as a preliminary step in this methodology, we need to mask the CALIFA datacubes to avoid foreground and background stars, as well as bad or low S/N spaxels. With such purpose, we use the spatial masks provided by the CALIFA collaboration. They are based on masks created using `SExtractor` (see Sect. 2.3) to the SDSS r-band images. The World Coordinate Systems (WCS) information available in the headers is used to reproject the SDSS masks to the scale, orientation, and pixel size of the CALIFA cubes. Further masking is applied to those spaxels flagged by the CALIFA reduction pipeline as bad quality spaxels. The main steps for the extraction of the stellar information from the CALIFA data

are explained below.

3.1.1 Stellar kinematics (pPXF)

We plan to integrate over elliptical apertures the CALIFA datacubes to obtain the radial stellar content on the sample of galaxies (see Sects. 3.1.2 and 3.1.3). However, the differences in the stellar kinematics between spaxels at the same galactocentric distance can have an important effect. An elliptical binning scheme artificially broaden the binned spectra as we are adding spectra with differences in the Line-of-Sight Velocity Distribution (LOSVD) as high as $\sim$ 400 km s^{-1} (typical spiral galaxy rotation curve can have an amplitude of $\sim \pm$ 200 km s^{-1}). Therefore, we need to correct the CALIFA datacubes to avoid it. We apply a stellar kinematics pipeline specifically designed for dealing with CALIFA data (Falcón-Barroso et al. in prep). This method has been applied to the totality of the observed CALIFA sample by the stellar kinematics team withing CALIFA and has been tested and used in different projects (e.g. Barrera-Ballesteros et al. 2014; García-Lorenzo et al. 2015; Barrera-Ballesteros et al. 2015). This pipeline makes use of the `pPXF` code (Cappellari & Emsellem 2004; Cappellari et al. 2011). Although in literature the computation of the LOSVD has been done in different ways, we use `pPXF` as this is a more sophisticated approach and it uses a penalised fitting procedure with more statistical significance. This code uses a maximum-likelihood approach to match the observed spectrum with a combination of stellar templates, once they have been convolved with a LOSVD. The LOSVD used by `pPXF` can be described via the Gauss-Hermite parametrisation, allowing the measurement of the velocity, the velocity dispersion and higher order Gauss-Hermite moments up to the h3 and h4 (Gerhard 1993; van der Marel & Franx 1993). To derive the velocity and velocity dispersion maps we analyse individual spectra coming from an adaptive Voronoi method following the Cappellari & Copin (2003) algorithm with a goal continuum S/N of 20 and considering just spaxels with a minimum S/N of 3 (measured again in the continuum). We use a subset of the INDOUSv2 library (Valdes et al. 2004) as stellar templates. Typical errors in the velocity determination are of the order of 5 to 20 km s^{-1} (for inner to outer spaxels). Before running `pPXF` we mask some spectral regions in order to avoid emission lines, residual sky lines (see Sect. 2.2.1), and low-quality pixels.

According to this information, we shift all the individual spectra of the datacube to the rest-frame and convolve them to a common velocity dispersion of FWHM = 8.4 Å, especially suited for low-intermediate mass spiral galaxies (Vazdekis et al. 2010). Therefore, for our purposes, this is just an intermediate step to obtain kinematics corrected datacubes. A deep study of the stellar kinematics for all the CALIFA galaxies (including the ones in this sample) will be presented in Falcón-Barroso et al. (in prep).

3.1.2 Emission line removal (GANDALF)

Once the datacube is shifted to the restframe and convolved to a common FWHM, we integrate over elliptical apertures to obtain radial stellar age and metallicity profiles. The ellipticity and position angle of the ellipses are fixed, matching the outer disc isophotes (see section 2.3.1). The centre is also fixed and obtained performing a 2D gaussian fit of the centre of the reconstructed image from the CALIFA datacube. However, the width of the successive elliptical rings is not fixed in order to have spectra with at least a S/N of 20 (per Å) in the continuum. We follow this elliptical binning scheme to collect high-quality spectra up to the outermost regions of the galaxies analysed in this thesis (see Yoachim et al. 2010, 2012) and the goal S/N of 20 has been set to be able to obtain reliable stellar information.

When studying integrated stellar populations it is important to take into account any contributions from the underlying ionised gas that can blur stellar information. Gaseous emission and stellar absorption features are sometimes located at the same wavelength, with the former filling the later and disabling the extraction of stellar information from these spectral regions. A way to deal with this emission is by masking those features, however an emission line removal is a more refined procedure as it allows the usage of those regions. For this purpose we make use of a code called Gas AND Absorption Line Fitting (GANDALF) described in detail in Sarzi et al. (2006); Falcón-Barroso et al. (2006). This code is able to simultaneously recover the stellar and ionised gas kinematics (with the aid of pPXF), and the stellar and the ionised gas content. GANDALF treats emission lines as additional gaussian templates to add to the best combination of stellar templates (accounting for the stellar continuum). For correcting the continuum shape, GANDALF applies a multiplicative correction to the continuum shape of the stellar model and observed spectra using a Legendre polynomial fitting. The degree of the polynomial used is 4. We use this code in an iterative way. We run GANDALF for the first time just to obtain information of the more common emission lines (namely, Hβ, [O III] λ5007, Hα, [N II] λ6583, and [S II] doublet). In the second iteration we fit all the emission lines in the observed wavelength range as additional gaussians using the kinematics of the stronger lines computed in the previous step. We use an optimal subset of the Vazdekis et al. (2010) models (hereafter, V10) with a Kroupa Universal IMF. These models are based on the Medium resolution INT Library of Empirical Spectra (MILES) library[1] (Sánchez-Blázquez et al. 2006b; Cenarro et al. 2007) as observed stellar templates and computed using the solar-scaled isochrones of Girardi et al. (2000b). In this step we use the entire spectral coverage of the data with the exceptions of pixels flagged by the CALIFA reduction pipeline as bad pixels and regions affected by sky residuals (see Sect. 2.2.1). The shape and position of the emission lines computed in this way are sub-

[1]The models are publicly available at http://miles.iac.es.

tracted to the observed spectrum (with contribution from stars and gas) to obtain a *pure-absorption* stellar spectrum (see Fig. 3.3).

In Fig. 3.1 we show an example of a GANDALF fit. The recovery of the shape of the observed spectrum by adding the contributions that GANDALF finds for the stellar and gaseous contribution to the observed spectrum is highlighted by the small residuals found (lower panel of Fig. 3.1). The good performance of this code, although extensively tested in the literature (e.g. Sarzi et al. 2006; Falcón-Barroso et al. 2006; Oh et al. 2011; Singh et al. 2013), is analysed in Sect. 3.2.2.

3.1.3 Stellar parameters extraction (STECKMAP)

The integrated light coming from external galaxies contains information from the stars. This information is hidden in the continuum as well as in some absorption features. The comparison of this observed light with theoretical- or empirical-based models allows the extraction of stellar parameters. As outlined in Chapter 1, this can be done in different ways ranging from the analysis of colours, line strength indices, or full spectrum fitting among many other techniques. In this thesis we recover the stellar content shaping all the above described *absorption-pure* spectra using the STEllar Content and Kinematics via Maximum A Posteriori likelihood (STECKMAP)[2] code (Ocvirk et al. 2006a,b). We prefer STECKMAP above other codes and approaches because no *a priori* assumptions are made and it provides smooth and continuous SFH solutions via its regularisation. Although STECKMAP has been broadly used and tested (Koleva et al. 2008; Sánchez-Blázquez et al. 2011), in Sect. 3.2 we further evaluate the validity of the stellar information derived from STECKMAP.

STECKMAP is aimed at simultaneously recovering the stellar content and stellar kinematics using a Bayesian method via a maximum *a posteriori* algorithm. It is based in the minimisation of a penalised χ^2 while no *a priori* shape of the solution is assumed (i.e. it is a non-parametric program). The definition of the penalised χ^2 function to minimise is:

$$\mathrm{Q}_\mu = \chi^2(\mathrm{s}(\mathrm{x},\mathrm{Z},\mathrm{g})) + \mathrm{P}_\mu(\mathrm{x},\mathrm{Z},\mathrm{g}), \tag{3.1}$$

where s is the modelled spectrum which depends on the stellar content (age distribution, x; and metallicity distribution, Z) and the stellar kinematics (broadening function, g). The solution from STECKMAP consists on three different solutions, the Stellar Age Distribution (SAD), the Age-Metallicity relation (AMR), and the LOSVD. Those solutions with smooth SAD, AMR, and LOSVD are favoured while solutions with strong variations (those that are thought to be non-physical) are penalised by means of the penalisation

[2] STECKMAP can be downloaded at http://astro.u-strasbg.fr/~ocvirk/.

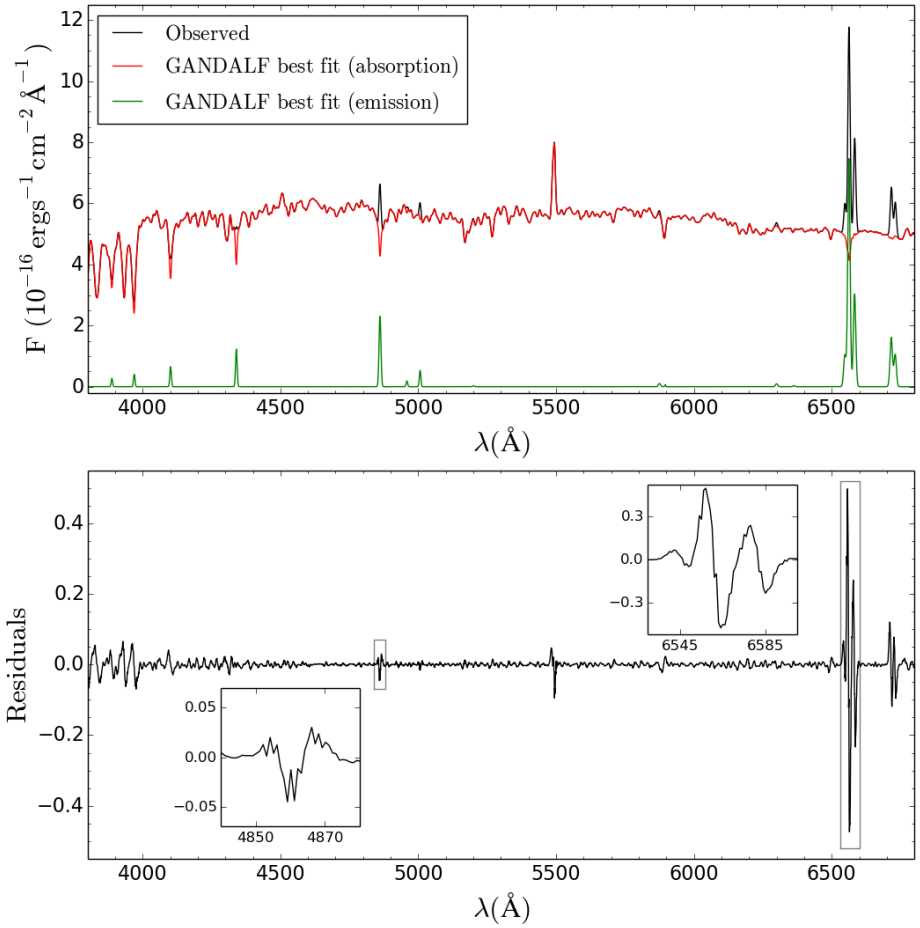

Figure 3.1: Example of a **GANDALF** fit to a typical CALIFA spectrum. We show the spectrum of IC 1199 at 24 arcsecs (1.34 h_{in}). Upper panel: **GANDALF** fit; the red line is the best combination of stellar templates and the green line is the recovered emission lines to better fit the observed spectrum (black solid line). Lower panel: residuals (in flux units, i.e. 10^{-16} erg s^{-1} cm^{-2} Å^{-1}) of the **GANDALF** fit with two insets in the region of Hβ and Hα. In this panel we are showing the outcome of subtracting to the best combination of stellar and emission line templates the observed spectrum.

function (P_μ in equation 3.1). This penalisation function is defined as

$$\mathrm{P}_\mu(\mathrm{x},\mathrm{Z},\mathrm{g}) = \mu_\mathrm{x}\mathrm{P}(\mathrm{x}) + \mu_\mathrm{Z}\mathrm{P}(\mathrm{Z}) + \mu_\mathrm{v}\mathrm{P}(\mathrm{g}). \tag{3.2}$$

The different smoothing parameters (μ_x, μ_Z, and μ_v) allow the user to choose the smoothness for the different solutions (SAD, AMR, and LOSVD). The smoothness is completely accomplished by means of the function P. This function gives higher penalisation values to strongly oscillated functions while lower values to smooth solutions. The interpretation of these values is as follows: higher values for the smoothing parameters as input parameters implies more smoothed solutions are preferred. The function P also can adopt different shapes (for further information see Ocvirk et al. 2006b,a). In addition, `STECKMAP` uses a polynomial to deal with the shape of the continuum, thus, avoiding flux calibration and extinction errors. Those errors might be important and they might dominate the χ^2 values and hence determine the fit (Koleva et al. 2008).

Before applying `STECKMAP` we investigate which combination of input parameters better fits the CALIFA spectroscopic data. According to those tests, we decide to use a square laplacian smoothing kernel for the shape of the function P for the SAD and AMR solutions, with values $\mu_\mathrm{x} = 0.01$ and $\mu_\mathrm{Z} = 100$, respectively. For further information about these parameters and the choice of them we encourage the reader to check previous works (Ocvirk et al. 2006a,b; Ocvirk 2010; Sánchez-Blázquez et al. 2014) and Sect. 3.2.1.2 of this thesis. As we study the LOSVD with especially devoted codes (see Sect. 3.1.1), we do not allow `STECKMAP` to fit the kinematics. Thus, we fix the kinematics to a velocity dispersion of 8.4 Å and rest frame to avoid the velocity dispersion-metallicity degeneracy reported in Sánchez-Blázquez et al. (2011). In this step we use the entire set of the V10 models (previously described) with ages ranging from 63 Myr to 17.8 Gyr (30 bins equally log-spaced) and metallicities from -2.32 to $+0.2$ ($[M/H]$). We perform the fit on the wavelength range from 3800.0 Å to 6800.0 Å. This range allows us to maximise the information coming from the stellar populations avoiding the bluest (displaying spectral issues in some galaxies) and reddest (with not so valuable stellar information) parts of the spectrum. This wavelength range is masked accordingly to avoid bad quality pixels and regions affected by an imperfect sky subtraction (see Sect. 2.2.1). As we are analysing *absorption pure* spectra (after running `GANDALF`), we do not mask spectral regions affected by gaseous emission lines. To match the continuum shape with the polynomial according to the `STECKMAP` standard fit, we use 30 control points.

To compute the age and metallicity profiles, light-weighted (L-W) and mass-weighted (M-W), we average the AMR and the SAD in logarithmic scale, as extensively done in the literature (e.g. Sánchez-Blázquez et al. 2011; Cid Fernandes et al. 2013; Sánchez-Blázquez et al. 2014):

$$< \log(\mathrm{Age[yr]}) >_{\mathrm{M-W}} = \frac{\sum_\mathrm{i} \mathrm{mass(i)} \times \log(\mathrm{Age_i})}{\sum_\mathrm{i} \mathrm{mass(i)}}, \tag{3.3}$$

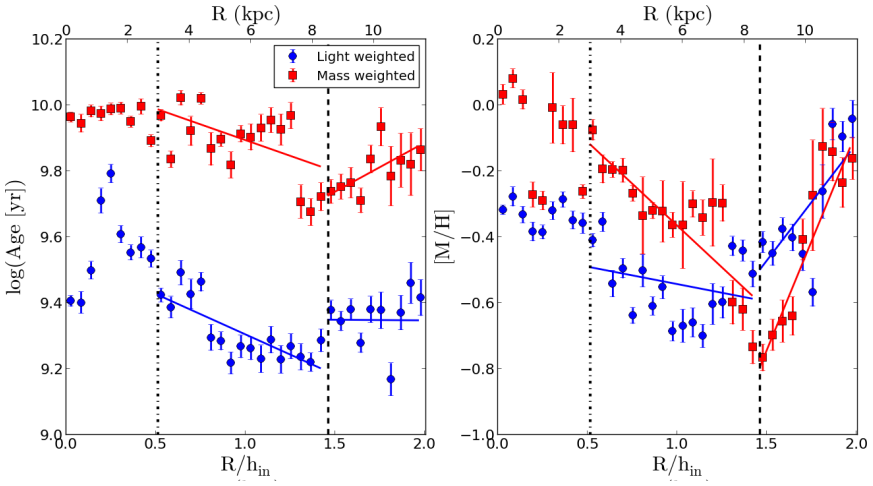

Figure 3.2: Stellar age (left) and metallicity (right) profiles for IC 1199 as an example. Blue circles represent L-W stellar age or metallicity. Red squares symbolise M-W stellar age or metallicity. The dotted-dashed vertical line delimits the bulge-dominated region ($R_{lim,in}$), while the dashed vertical is located at the break radius (R_{break}). Solid lines represent the linear fits computed to the age and metallicity (L-W and M-W) profiles

$$< \log(\mathrm{Age[yr]}) >_{\mathrm{L-W}} = \frac{\sum_i \mathrm{flux(i)} \times \log(\mathrm{Age_i})}{\sum_i \mathrm{flux(i)}}, \tag{3.4}$$

$$< [\mathrm{M/H}] >_{\mathrm{M-W}} = \frac{\sum_i \mathrm{mass(i)} \times \log(\mathrm{Z_i/Z_\odot})}{\sum_i \mathrm{mass(i)}}, \tag{3.5}$$

$$< [\mathrm{M/H}] >_{\mathrm{L-W}} = \frac{\sum_i \mathrm{flux(i)} \times \log(\mathrm{Z_i/Z_\odot})}{\sum_i \mathrm{flux(i)}}, \tag{3.6}$$

where $Z_\odot$ is the solar metallicity (0.02), mass(i) and flux(i) are the mass and the flux of the i^{th} stellar population with age, Age_i and metallicity, Z_i. Errors in all of the above defined quantities are computed by means of 25 Monte Carlo (MC) simulations: once that `STECKMAP` determines the best combination of stellar populations to fit the observed spectrum (best model), we add some noise to that *best model* spectrum and run `STECKMAP` again to the noisy *best model*. This test is done 25 times in every observed spectrum and the standard deviation of the recovered age and metallicity in those tests is considered as the error in each magnitude. Although other works usually perform up to 250 MC realisations (Sánchez-Blázquez et al. 2014), we have tested that the computed errors with this limited number of simulations are compatible to those computed using a larger number.

Once we have derived the age and metallicity radial distributions, we compute linear fits in a similar way as we explained for the colour profiles (see Sect. 2.3.2). We use the same definition of $R_{lim,in}$ as outlined there and the definition of $R_{lim,out}$ is imposed by the quality of the CALIFA spectroscopic data or the performance of this method. Thus, $R_{lim,out}$ is given by the last

radial spectrum with a S/N > 20 or by the last radial spectrum from which reliable stellar population results are drawn. We must highlight that in a small number of cases (corresponding to the outermost regions), although the computed S/N is higher than 20, a visual inspection of the `GANDALF` or `STECKMAP` fits suggests that they are not good enough (bad emission line removal, deficient continuum shape reconstruction, etc.) and thus, non-reliable stellar population results are obtained. The information from these spectra is discarded. For type I galaxies we compute a single (inner) gradient from $R_{lim,in}$ to $R_{lim,out}$ while for type II and III galaxies two gradients are computed, one from $R_{lim,in}$ to R_{break} (inner) and the other one from R_{break} to $R_{lim,out}$ (outer). In this case, again, the performed linear fits are error-weighted, taking into account the errors of the age and metallicity values to derive the gradients and their errors. Figure 3.2 shows an example of the typical age and metallicity profiles that we obtain with the CALIFA data.

Figure 3.3 shows an example of a typical spectrum analysed with this methodology. The kinematics correction applied to the CALIFA datacubes and the elliptical integration allow us to obtain high quality spectra even in the outer parts of the galaxies analysed in this thesis. In this particular case, we are showing a spectrum (solid black line) at an intermediate-to-large galactocentric distance from IC 1199 (24 arcsecs, 1.34 h_{in}). We must note the high quality of the spectrum (S/N = 41.3 per pixel in the continuum), as can be seen in some features such as the D4000 break, emission lines (Hβ, [O III], [N II], Hα, [S II], etc.), and absorption details (Ca II, Mg I, etc.). We can observe some remainings of the CALIFA sky subtraction in the O I sky line at 5577 Å, region that is masked (shaded areas) and thus, not considered in the `STECKMAP` fit. The solid red line shows the `STECKMAP` fit to the emission-free spectrum (from `GANDALF`). The inset is focused on the region where Hβ and Mg I absorption features are located. This figure allows us to have an idea, not only of the good quality of the CALIFA data, but also of the good performance of this method fitting observed spectra to obtain stellar population information. However, this method has to be further tested (see Sect. 3.2).

Different uncertainties in the spatial elliptical binning can considerably affect the final results. We have extensively tested the effect of an inaccurate determination of the ellipse parameters (centre, ellipticity, and position angle) in the final age and metallicity profiles. An inaccuracy of 2 pixels in the x and y position might produce an average change in the reconstructed mean log(age) values of around 13 % and 14 % in the metallicity values ([M/H]). Although this might change considerably the final profiles, we do not need to concern about it as the centre determination has an accuracy better than 1 pixel. The determination of the external ellipticity and position angle is a more subtle issue as their values can change considerably

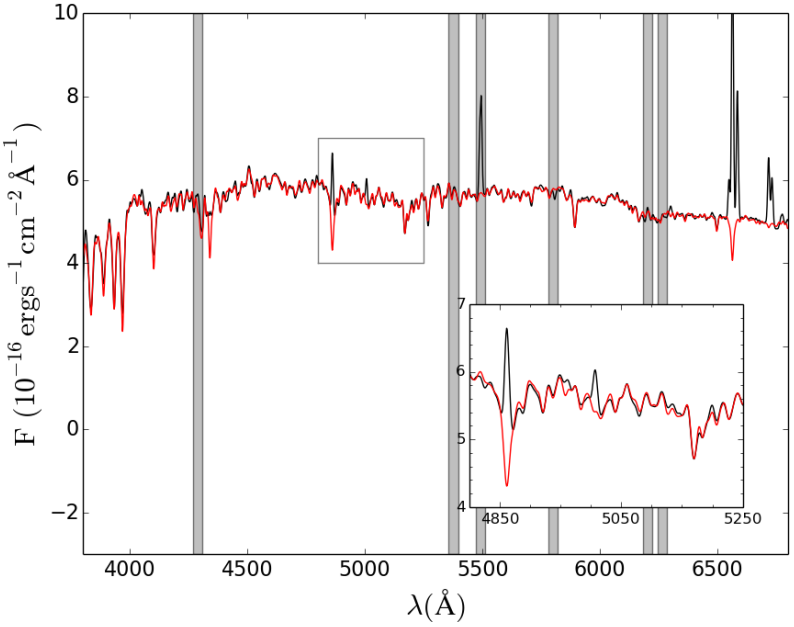

Figure 3.3: Example of a typical CALIFA spectrum analysed with this method. In particular, this is the spectrum of IC 1199 at 24 arcsecs (1.34 h_{in}). Solid black line represents the observed, rest-framed spectrum. Solid red line is the `STECKMAP` best fit to the observed spectrum after removing the gaseous emission lines with `GANDALF`. The shaded regions of the spectrum are the masked regions (not considered in the fit). The inset is focused on the Hβ-Mg I spectral region ($4800 - 5250$ Å). See text for further details.

depending on the isophotal analysis or the definition of *outer* disc. However, an indetermination of 50 % in the ellipticity and position angle affects in less than 14 % and 17 % the mean age and metallicity values, respectively. These sources of errors are well accounted by the error bar determination followed in this thesis ($\sim$ 30 %).

3.2 Testing the methodology

As this is a new developed methodology to analyse the stellar content in spiral galaxies, we need to demonstrate that the obtained results are reliable within reasonable uncertainties and thus, we can rely on what we are claiming. With such purpose in mind we have done two different kinds of tests:

i) we compare the (in principle) more reliable CMD results to those obtained applying this methodology to extract stellar information from high quality integrated spectra. This exercise should reveal where it fails and where it succeeds, and thus provides information about the spectral ranges and features that are more likely to improve this approach. The analysis

of the CMD was performed by the group led by Dr. Carme Gallart in the Instituto de Astrofísica de Canarias (IAC) independently to the analysis of the integrated spectrum. For completeness, we explain the method carried out by Gallart's group to obtain the SFH of the analysed region from the resolved stellar population information in Sect. 3.2.1.2. This comparative work has been published in Ruiz-Lara et al. (2015b) and is explained in Sect. 3.2.1;

ii) we apply the above outlined method to mock spectra created from known stellar compositions and CALIFA-like quality. The comparison of our results with the input stellar content will allow us to further address the reliability of this method (see Sect. 3.2.2).

3.2.1 Integrated vs. resolved stellar populations: The LMC case example

The kind of test we propose here is not straightforward. Not only CMDs containing stars as faint as those on the oMSTO need to be studied, but also high resolution and high S/N integrated spectra must be obtained, which is difficult because of the often low surface brightness of nearby resolved systems. Although previous studies have tried to do something similar in star clusters (e.g. Gibson et al. 1999; Beasley et al. 2002; de Grijs & Anders 2006; Santos et al. 2006; González Delgado & Cid Fernandes 2010; Barber et al. 2014) and in dwarf galaxies (e.g. Makarova et al. 2010; García-Benito & Pérez-Montero 2012), it is necessary to improve those tests by analysing more complex systems (i.e. systems with complex SFH) with available data of individual stars down to the oMSTO in the CMD.

We have performed such a test using one of the few fully resolved bright galaxies where this test can be carried out, the LMC. In particular, we study a region of the LMC bar as a guinea pig for which we can compare complex SFHs derived through integrated-light synthesis techniques and through the CMD of the resolved stellar population. We emphasise the fact that, for this test, the SFH in the LMC bar region was derived from the CMD without knowing the results from the integrated spectrum analysis and vice versa, making this a blind test in order to avoid any possible bias towards a common solution by adjusting the fitting parameters.

Throughout this section we will consider that the SFH is composed of three main functions: one is the Star Formation Rate (SFR) as a function of time, SFR (t); the second is the chemical enrichment history (AMR); and the third is the IMF.

We show the LMC bar SFH derived after applying this method to its integrated spectrum (using EFOSC2) and we compare it to the CMD results from HST data. Although this method makes use of `STECKMAP` to derive the stellar parameters from spectroscopic data, we will also compare the results obtained using other spectral fitting codes such as Université de Lyon

Spectroscopic analysis Software (ULySS) presented in Koleva et al. (2009) and STARLIGHT (Cid Fernandes et al. 2005) for completeness. As previously mentioned, STECKMAP gives a higher probability to smooth solutions (by means of a penalised χ^2 fitting algorithm; see Ocvirk et al. 2006b,a, for further information). The smoothness implemented in STECKMAP makes the comparison with the CMD results easier.

3.2.1.1 Observations and data reduction

To proceed with the comparison between integrated and resolved stellar population approaches in the case of a complex stellar population, we selected a field in the LMC bar (see Fig. 3.4). The centre of the LMC bar is bright enough to obtain a high quality integrated-light spectrum with high S/N, which we did from observations at the 3.6 m ESO telescope on La Silla using EFOSC2 (Alloin et al. 2002). It is also sufficiently close and resolved for a CMD reaching the oMSTO to be secured with the HST. Such a CMD has been already published by Smecker-Hane et al. (2002) and various SFHs have been derived by different groups, and published in Skillman & Gallart (2002). We present a newly derived SFH with more sophisticated analysis techniques here.

When the spectroscopic observations were obtained (15 years ago) the only HST field available with sufficient surface brightness to carry out this project was the field observed with the Wide Field and Planetary Camera 2 (WFPC2). Unfortunately, the poor dynamic range of the camera limits the observations of the brightest stars. However, we can overcome this limitation with the methodology used to analyse the data (see Sect. 3.2.1.2).

Resolved stellar populations

The photometry and artificial star tests necessary to reconstruct the SFH of the LMC bar region were obtained from the HST Local Group Stellar Photometry Archive (Holtzman et al. 2006), maintained by J. Holtzmann[3]. In particular, we downloaded the data of two WFPC2 pointings, namely the u4b112 and u4b115 fields, located at the centre of the LMC bar (see Fig. 3.4) and originally observed within the GO programme 7382 (Principal investigator T. Smecker-Hane). Table 3.1 details the observing log, including the position of the two fields, the integration time in both the $F555W$ and $F814W$ filters, and the date of the observations.

The (M_{F814W}, M_{F555W} – M_{F814W}) CMD is presented in Fig. 3.5. The photometry reaches down to $M_{F814W} \sim 6$, well below the oMSTO. A prominent bright MS is visible up to $M_{F814W} \sim -1$, indicating that star formation continued until very recent epochs in this region. The RGB, comprising stars

[3] http://astronomy.nmsu.edu/holtz/archival/html/lg.html

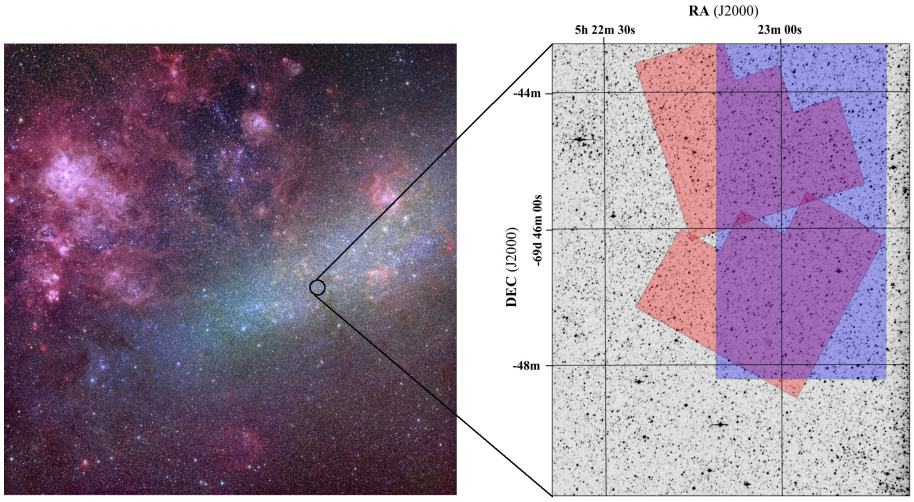

Figure 3.4: Left panel: image of the LMC bar and its surroundings (Credit: John Gleason). The location in the centre of the bar of the field studied in this section is indicated. Right panel: positions of the two WFPC2 fields (red shaded areas), and the 2.5×5 area covered by sweeping the slit in the east-west direction (blue shaded area), superimposed on a VIMOS B-band image.

Field	R.A. (h m s)	Dec. (^{o} $'$ $''$)	Exp. Time – $F555W$ (s)	Exp. Time – $F814W$ (s)	Date
u4b112	05 22 57	−69 46 53	4×500	2×300+2×700	1997 Nov 27
u4b115	05 22 55	−69 42 51	4×500	2×300+2×700	1999 Jan 05

Table 3.1: Observing log of the WFPC2/HST photometric data.

older than $\sim$ 1 Gyr, is also highly populated up to $M_{F814W} \sim -2$. Finally, we also highlight the presence of a prominent red clump of centrally He-burning stars ($M_{F814W} \sim -0.5$), while the old horizontal branch is barely populated. We have indicated four regions in the figure that will be discussed in Sect. 3.2.1.2.

The lack of stars brighter than $M_{F814W} \sim -1$ and $M_{F814W} \sim -2$, along the MS and the RGB, respectively, is likely due to saturation. Visual inspection of the brightest sources in the field confirms that a number of bright stars ($\sim$ 200) are saturated in both filters. The region of the CMD affected by saturation will not be used in the SFH derivation. At the metallicity of the youngest LMC stars, the saturation magnitude of F814W ~ -1 on the MS corresponds to the turnoff of a $\sim$ 0.3 Gyr stellar population. The bright massive stars younger than this age do not appear in the CMD, and this implies that we are not using all the possible information to derive the SFH for these ages. However, because lower mass stars of the same ages are present at fainter magnitudes, the SFH can be still obtained from them, under the assumption of a given IMF.

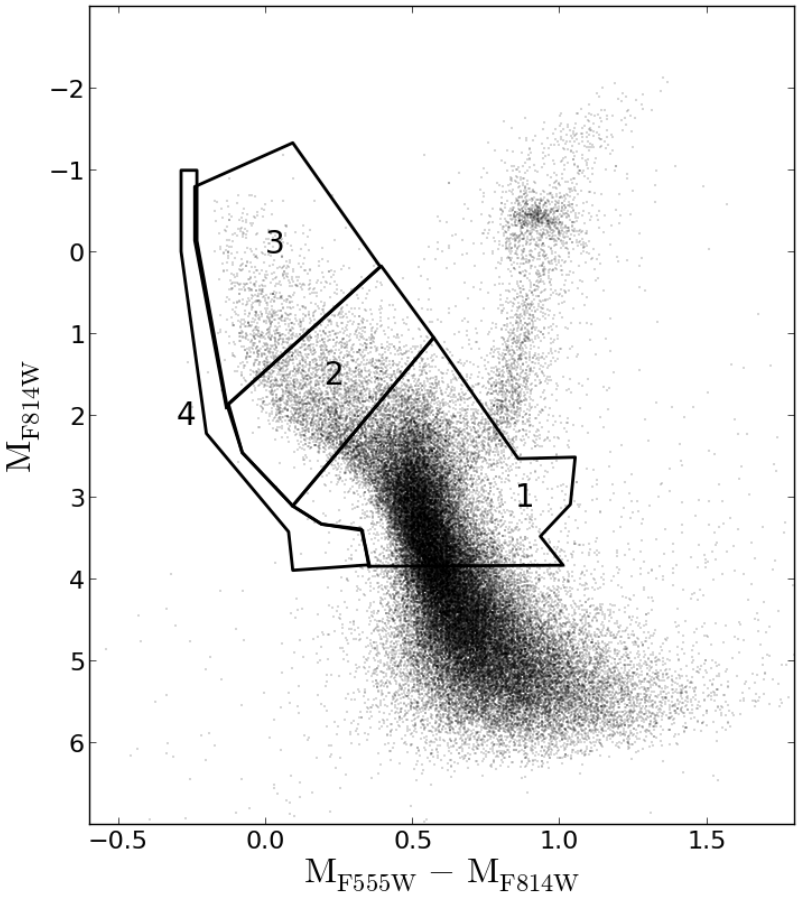

Figure 3.5: M_{F814W} vs M_{F555W} – M_{F814W} CMD based on WFPC2 data. The four polygons show the regions used to derive the SFH using the IAC-star/MinnIAC/IAC-pop suite of routines (see text for details).

Integrated spectrum

Integrated-light spectra of the LMC bar and a sky field were collected at the 3.6 m ESO telescope on La Silla, using EFOSC2 (Buzzoni et al. 1984), on 18-20 December 2000. The J2000 right ascention of the observed target field is 05h 23m 17s while the declination is $-69°45'42''$. We use a north-south $5'$ long and $1.5''$ wide slit, which is swept along the east-west direction; this allows us to cover a full area of $2.5'$ by $5'$, which approximately matches the WFPC2 pointings (see Fig. 3.4). Four different grisms are used, spanning in total the wavelength range $3500 - 8745$ Å (see Fig. 3.6). We smooth the spectra from the four grisms to a common final dispersion of 1.9 ± 0.1 Å/pix (see Fig. 3.6). A mean exposure time of 5400 s divided into three separate exposures is adopted for each grism, both for the target field and also for the sky field. The sky-field spectrum is taken 6° north of the target-field position. The sky position is chosen as a compromise between the sky field being relatively close and thus representative of the foreground Milky Way contamination and sky light present in the LMC bar field, and to mimimise the contribution from LMC light. We note, however, that with a galactocentric radius of at least 16° (Majewski et al. 2009; Saha et al. 2010), even at 6° from its centre, the LMC still presents a highly populated CMD, with many intermediate-age stars (Gallart et al. 2008; Saha et al. 2010).

The 2D spectra corresponding to the four grisms for both the target and the sky fields are reduced through standard techniques, using `MIDAS` and `IRAF` packages. A full 2D wavelength calibration is built up to correct for geometrical distortions. The spectra were flux calibrated using the spectrophotometric standard EG 21 and LTT 4816; the error in flux calibration is estimated to be around 10 %. After this step, the 1D spectra of the four grisms were matched together and the quality of the match controlled through the overlapping wavelength regions. The reduction of this EFOSC2 integrated spectrum was performed by the group led by Dr. Danielle Alloin.

To check whether small number statistics in the sampling of minority stellar populations in the target field (such as the insertion of a few young stars dominating the final spectrum but with little mass contribution) could lead to significant fluctuations in the SFH, we perform the following test. From the integrated-light, spatially resolved 2D spectra, we extract two series of integrated-light 1D spectra, one for the target field and one for the sky field, with extraction windows of $5'$ and of $2.5'$. We end up with four 1D spectra over the $3500 - 8745$ Å range (FWHM $\sim$ 10 Å), two corresponding to the integrated light in the LMC bar field over spatial areas of respectively $2.5' \times 5'$ (field 1) and $2.5' \times 2.5'$ (field 2, included in field 1) and the other two corresponding to the integrated light in the sky field with the same extraction windows. At face value, the sky-subtracted spectra of the target field through the two different extraction windows exhibit very similar

characteristics. In terms of the shape of their spectra, we scale the field 2 spectrum to match the higher flux level of field 1 spectrum. The average difference of both spectra relative to the field 1 spectrum, over the whole spectral range, is 1.6 % (i.e. the two scaled spectra are almost identical). We then derive the SFH of both spectra (field 1 spectrum and the scaled, field 2 spectrum) using `STECKMAP`. The residuals between both recovered SFR(t) are within the computed error values (see Sect. 3.1.3 for further information). This analysis indicates that we are properly sampling the stellar content in the analysed fields in spite of the very small fraction of the galaxy's light present in them. Therefore, we decided to analyse in detail the composite stellar population corresponding to the spectrum covering the $2.5' \times 5'$ area ($40\,\mathrm{pc} \times 80\,\mathrm{pc}$), which has a better S/N ratio as a consequence of the wider range of spatial coverage of an area with intrinsically the same stellar content. The corresponding final sky-subtracted spectrum is shown in Fig. 3.6. The final S/N ratio of this spectrum is ~ 36.3 (per Å).

3.2.1.2 Determination of the star formation history

We obtain the SFH using the data described in Sect. 3.2.1.1, following carefully developed and well-tested methodologies to study the stellar content via CMD (Aparicio & Gallart 2004; Monelli et al. 2010c) and spectroscopic analysis (see Sect. 3.1.3 and Sánchez-Blázquez et al. 2011, 2014; Seidel et al. 2015; Ruiz-Lara et al. 2016). This study is meant to be a blind test to compare the two approaches. Thus, all the results obtained and described in this section are analysed and studied independently (without knowing the results from the other approach) in order to avoid any possible bias to a common solution.

CMD analysis

The SFH from the CMD was obtained using the IAC-star/MinnIAC/IAC-pop (Aparicio & Gallart 2004; Aparicio & Hidalgo 2009; Hidalgo et al. 2011; Monelli et al. 2010c) suite of routines by the group led by Dr. Carme Gallart. For completeness, in this section we outline the main steps of their analysis. This SFH derivation is based on the comparison, through a χ^2 minimisation, of the distribution of stars in the observed and in a model CMD. The model CMD is obtained from a synthetic CMD computed with IAC-star, after simulation of the observational errors. For the calculation of the synthetic CMD, which contains $9{\times}10^6$ stars, we assume a constant star formation rate at all ages between 0 and 13.5 Gyr, and flat metallicity distribution between Z = 0.0002 and 0.02. For consistency with the analysis of the integrated spectrum, we used the Padova stellar evolution library (Girardi et al. 2000b; Marigo et al. 2008). Finally, we assume a Kroupa IMF (Kroupa 2001) and a binary fraction of 40 % (Monelli et al. 2010c). The

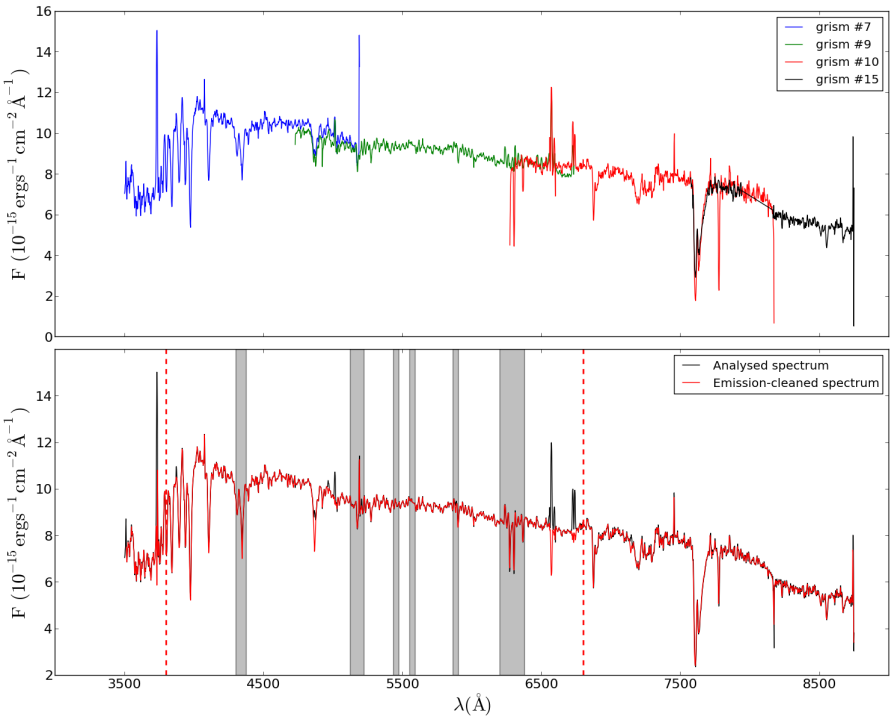

Figure 3.6: Composite spectrum of the LMC bar field used in the integrated stellar population analysis. Top row: the spectrum is divided according to the four different grisms used: blue for grism # 7 (3500 − 5185 Å), green for grism # 9 (4725 − 6730 Å), red for grism # 10 (6275 − 8160 Å), and black for grism # 15 (7565 − 8745). For each grism the corresponding sky spectrum, i.e. the spectrum taken in the sky field, has been subtracted. Only the LMC bar contribution is shown here. Bottom row: fully reduced composite spectrum of the LMC bar (black) and fully reduced, emission-cleaned composite spectrum (red). For the stellar content analysis we use the wavelength range from 3800 to 6800 Å (dashed vertical red lines; see text for details). The shaded regions of the spectrum are the masked regions (not considered in the fit).

observational errors are simulated using the information from the artificial stars tests. These allow for the inclusion of the completeness of the photometry, and more importantly, how the photometric errors displace a star from its original position in the CMD. The model CMD is divided into simple stellar populations by adopting a basic set of age and metallicity bins, whose limits are age (Gyr) = [0, 0.25, 0.5, 1.0, 1.5 to 13.5 in steps of 1 Gyr] and Z = [0.0002, 0.0006, 0.001 to 0.01 in steps of 0.001, 0.015, 0.02]. We adopt a distance modulus $(m - M)_0 = 18.5$ mag and reddening E(B – V) = 0.1 mag to shift the observed CMD to the absolute magnitude plane.

Following previous investigations of other dwarf galaxies (Hidalgo et al. 2009; Monelli et al. 2010c,b; Hidalgo et al. 2011; Meschin et al. 2014), the SFH is derived using only the MS and Subgiant Branch (SGB) regions, avoiding the regions where the completeness is less than ~ 50 %. Figure 3.5 presents the CMD with the regions adopted for SFH derivation (called bundles) highlighted. The star counts are performed in each bundle by dividing it into boxes of different sizes. The finest sampling was used in bundle 1 (0.01 mag and 0.2 mag for the colour and magnitude, respectively) and bundle 2 (0.02, 0.1). Bundle 3 was sampled in (0.2,0.5) boxes and bundle 4 was used as a single box. This strategy takes into account that i) the physics of MS stars is best understood, and ii) the largest number of stars in the CMD are located in the lower MS. Of the 69 209 observed stars, 27 556 are counted in the four bundles.

To take into account possible errors in the distance, reddening, and photometric or model calibration, a number of different solutions are derived introducing small shifts in colour and magnitude, in a grid of 25 positions within $\pm$ 0.06 mag and $\pm$ 0.15 mag in colour and magnitude, respectively. In order to minimise the effect of the sampling choice, in each position of the grid 24 solutions are calculated varying the assumed age and metallicity bins of the simple stellar populations, and moving the boxes inside the bundles. In each position of the grid, the 24 solutions are averaged and the corresponding $\overline{\chi^2}$ is calculated as the average of the χ^2 of the solutions. The minimum value of $\overline{\chi^2}$ ($\overline{\chi^2_{\rm min}}$) indicates the position in the grid where the best solution is obtained, which turns out to be $\Delta[(M_{F555W} - M_{F814W}), \Delta(M_{F814W})] = [0.03, 0]$.

Figure 3.7 shows the SFH derived from this analysis. This figure displays the SFR (t) and Z (t) projections of the SFH, as the average of the 24 individual solutions calculated at the position of the grid where $\overline{\chi^2_{\rm min}}$ was obtained (Hidalgo et al. 2011). We should note here that the averaging of the 24 solutions has the effect of smoothing the final SFH. Error intervals are calculated from the dispersion of these 24 solutions. This provides errors equal to or in excess of the so-called several solutions criterion which was shown by Aparicio & Hidalgo (2009) to produce reliable estimates of total internal errors. Figure 3.7 shows that the SFR (t) is relatively smooth over

the whole time interval, with a slight change at around 4.5 Gyr ago and increased SFR (t) at later times. This is reminiscent of the period of low star formation activity followed by a later increase found by other studies in LMC regions located at larger galactocentric distances (e.g. Meschin et al. 2014, and references therein). The intermediate-age SFR (t) in the LMC bar, however, seems to differ substantially from that of the disc at different galactocentric distances, in which the two main periods of star formation, separated by an epoch of lower star formation activity, are barely seen in the bar and are replaced by a much flatter SFR (t). The SFR (t) between 3.5 and 0.25 Gyr obtained here is rather flat followed by a decrease for stars younger than 0.25 Gyr. The AMR is similar to the one reported in previous studies (e.g. Olszewski et al. 1991; Dirsch et al. 2000; Grocholski et al. 2006), showing an exponential decline from $Z \sim 0.0175$ at young ages to $Z \sim 0.0004$ at old ages. The metallicity dispersion in the AMR is found to increase towards younger ages.

Integrated spectrum analysis

We apply the methodology outlined in Sect. 3.1 to the integrated spectrum of the LMC bar to obtain its SFR (t) and AMR. Despite the differences between the IFS CALIFA data and the spectrum analysed for the LMC case (2D coverage vs. single spectrum), we extract the stellar content from both data sets following the basic steps explained before. However, because of the spectral differences on the EFOSC2 and CALIFA data (wavelength range, resolution, S/N, etc.), the `STECKMAP` input parameters have to be accordingly chosen for this particular case. We take advantage of the good quality of this spectrum to investigate the robustness of this method by assessing the effect of the choice of input parameters on the SFH reconstruction.

We explore the entire input parameter space in 24 different tests to choose the best combination for the `STECKMAP` run (see Sect. 3.2.1.2). Table 3.2 summarises the main input parameters for each test and the corresponding rms. We can divide these tests into three main blocks: i) in the first block we check the effect of using different stellar models, the age range used during the fit, and the simultaneous recovery of the stellar kinematics (tests 1 to 8); ii) based on the previous block and our experience (Sánchez-Blázquez et al. 2011, 2014; Seidel et al. 2015; Ruiz-Lara et al. 2016), in this second block we use the V10 models (age-range: 0.063×10^9 to 17.8×10^9 yr) and fix the stellar kinematics (tests 9 to 16) while exploring the smoothing parameters (μ_x and μ_Z) with values ranging from 10^{-15} to 10^{15}; and finally, iii) in this third block (tests 17 to 24) we use the same ingredients as in the second block but we limit the age range to 13.5×10^9 yr (to match the CMD analysis age range). In all the tests we use a square Laplacian smoothing kernel for the shape of the penalisation function, P.

Test	Models	Age range (yr)	Kinematics	μ_x	μ_Z	μ_v (**)	rms
(1)	(2)	(3)	(4)	(5)	(6)	(7)	(8)
1	V10	$[0.063\times10^9, 17.8\times10^9]$	FIX	10^{-2}	10^2	–	0.1215
2	V10 + GD05	$[0.001\times10^9, 17.8\times10^9]$	FIX	10^{-2}	10^2	–	0.1298
3	V10	$[0.063\times10^9, 13.5\times10^9]$	FIX	10^{-2}	10^2	–	0.1216
4	V10 + GD05	$[0.001\times10^9, 13.5\times10^9]$	FIX	10^{-2}	10^2	–	0.1298
6	V10 + GD05	$[0.001\times10^9, 17.8\times10^9]$	FIT	10^{-2}	10^2	10^{-2}	0.1764
7	V10	$[0.063\times10^9, 13.5\times10^9]$	FIT	10^{-2}	10^2	10^{-2}	0.1768
8	V10 + GD05	$[0.001\times10^9, 13.5\times10^9]$	FIT	10^{-2}	10^2	10^{-2}	0.1766
9	V10	$[0.063\times10^9, 17.8\times10^9]$	FIX	10^2	10^2	–	0.1218
10	V10	$[0.063\times10^9, 17.8\times10^9]$	FIX	10^{-2}	10^{-2}	–	0.1217
11	V10	$[0.063\times10^9, 17.8\times10^9]$	FIX	10^{-6}	10^5	–	0.1224
12	V10	$[0.063\times10^9, 17.8\times10^9]$	FIX	10^{-8}	10^{-8}	–	0.1217
13	V10	$[0.063\times10^9, 17.8\times10^9]$	FIX	10^4	10^5	–	0.1223
14	V10	$[0.063\times10^9, 17.8\times10^9]$	FIX	10^{15}	10^{14}	–	0.1224
15	V10	$[0.063\times10^9, 17.8\times10^9]$	FIX	10^{-15}	10^{-14}	–	0.1217
16	V10	$[0.063\times10^9, 17.8\times10^9]$	FIX	10^{-2}	10^6	–	0.1227
17	V10	$[0.063\times10^9, 13.5\times10^9]$	FIX	10^2	10^2	–	0.1218
18	V10	$[0.063\times10^9, 13.5\times10^9]$	FIX	10^{-2}	10^{-2}	–	0.1218
19	V10	$[0.063\times10^9, 13.5\times10^9]$	FIX	10^{-6}	10^5	–	0.1226
20	V10	$[0.063\times10^9, 13.5\times10^9]$	FIX	10^{-8}	10^{-8}	–	0.1218
21	V10	$[0.063\times10^9, 13.5\times10^9]$	FIX	10^4	10^5	–	0.1224
22	V10	$[0.063\times10^9, 13.5\times10^9]$	FIX	10^{15}	10^{14}	–	0.1249
23	V10	$[0.063\times10^9, 13.5\times10^9]$	FIX	10^{-15}	10^{-14}	–	0.1218
24 (*)	V10	$[0.063\times10^9, 13.5\times10^9]$	FIX	10^{-2}	10^6	–	0.1225

Table 3.2: Set of characteristics and parameters used in the different tests to examine the robustness of the `STECKMAP` solutions. Column 1 is the number of the test. Column 2 shows the models used in each test, i.e. Vazdekis et al. (2010) (V10) or Vazdekis et al. (2010)+González Delgado et al. (2005) (V10+GD05). Column 3 gives the age range. In Col. 4 we highlight the fact of fitting or fixing the kinematics. μ_x stands for *smoothing parameter for the stellar age distribution*, μ_Z stands for *smoothing parameter for the age-Z relation*, and μ_v stands for *smoothing parameter for the line-of-sight velocity distribution*. The last column gives the quality of each of the tests by means of its residuals rms computed as the mean values of the absolute differences between the data and the fit. (*) Test chosen to be compared with the CMD results (see text for details). (**) As we are fixing the stellar kinematics and thus not fitting it, this parameter is not applicable in some cases.

A visual inspection of the fits and the quantitative value of their rms ($\sim$ 0.12 with little dispersion, see Table 3.2) for all the tests, lead us to conclude that there is no easy way to choose the combination of input parameters that best suits the analysed data. In terms of the reconstructed SFR(t) and AMR shapes, all of the tests show very similar results (compatible within errors), except for tests 5, 6, 7, and 8 (see Appendix C), which show the largest discrepancies (also in terms of their rms). These tests share the property that we fit simultaneously the stellar kinematics, which considerably hampers the correct SFH reconstruction. This behaviour highlights the overall stability of the `STECKMAP` solutions, since as the general shape (if not the precise details) of the solutions is quite similar among tests.

As there is no clear set of input parameters to favour over the others, we decide to use the following reasonable set of input parameters: i) we fix the stellar kinematics to the values found with `pPXF` following Sánchez-Blázquez et al. (2011); ii) we match the age range used in the CMD analysis using SSP model templates with ages from 0.063×10^9 to 13.5×10^9 yr; and iii) we focus on the results using V10 models. In Figure 3.8 we show a comparison between the commonly used V10 models, V10 with the extension towards younger stellar populations from González Delgado et al. (2005, hereafter GD05), and the Bruzual & Charlot (2003, hereafter BC03) models. We find small differences in the SFR(t) between the models. Larger differences are found in the recovered AMR, with discrepancies within the errors. In particular, the inclusion of the GD05 models (based on theoretical stellar libraries) with ages younger than 63 Myr might affect the SFH recovery depending on the real amount of young stars present in the observed field. If we do not include these models, in principle, the contribution of these stars would be included in older bins modifying the recovered SFH shape. Further investigation is needed to understand whether the impacts on the solutions make sense or not.

Bearing this in mind, we show test 24 as an example of the recovered SFH. We use this test just for illustration purposes, but most of the considered tests could have been used without modifying the main conclusions. We can see in Fig. 3.7 that the LMC bar displays an almost constant SFR (t) from its formation until $\sim$ 4 Gyr ago according to the analysis of the integrated spectrum. Afterwards, a progressive increase in the SFR (t) is found with a peak at $\sim$ 1 Gyr ago followed by a drop in the SFR (t) to the present day. The AMR exhibits an exponential increase with old stellar populations showing the lowest metallicity ($[M/H] \sim -0.6$) and young stars the highest metallicities ($[M/H] \sim 0.2$). We note that this exponential behaviour in the AMR shape is mainly caused by our particular choice of smoothing parameters (μ_Z is 10^6 for test 24). The only difference in tests 17 to 24 is the choice of values of the smoothing parameters. As expected (see Appendix C), high values of μ_x give smooth SFR(t) shapes (tests 17, 21, and 22) and high values of μ_Z give smooth AMR shapes, (tests 17, 19, 21, 22, and 24) while

low smoothing parameter values (μ_x and μ_Z) give highly oscillating results. In order to easily compare this data with the rest of the solutions, we plot a shaded region corresponding to the average of all the solutions using V10 models and ages ranging from 0.063 to 13.5 Gyr. As can be seen, our chosen test is within that shaded region showing again the robustness of the STECKMAP results.

3.2.1.3 Comparison between CMD and integrated spectrum analysis

In the previous section (Sect. 3.2.1.2) we derive the SFHs in a region of the LMC bar using two different techniques. In the first one we use the resolved stars in a deep CMD and compare them to theoretical CMDs based on theoretical isochrones. In the second one we apply a methodology for extracting stellar population information from spectroscopic data based on full spectrum fitting techniques (see Sect. 3.1). These analyses are performed independently in a blind test. The comparison between the SFH from both approaches will then allow us to test how well modern spectral fitting techniques recover the characteristics of a complex stellar population.

Star formation rate, SFR (t)

The upper panel of Fig. 3.7 shows the normalised SFR (t) in the LMC bar region obtained using CMD and STECKMAP typical analyses, as discussed in Sect. 3.2.1.2. The normalisation of the SFR (t) is performed in such a way that the sum of the areas of the different rectangles (SFR $[M_{\odot/yr}] \times \Delta t$) is 1 (upper panel). The overall shape of SFR (t) is qualitatively similar in both derivations, with an almost continuous star formation since the earliest epochs until 4 Gyr ago, when small differences between the SFH obtained from both approaches appear. The CMD analysis reveals a rather flat SFR (t) between $\sim$0.25 and $\sim$3.5 Gyr with a clear drop in the star formation during the last 0.25 Gyr. The STECKMAP analysis shows a SFR (t) that can be described as a Gaussian skewed towards older ages with the peak around 1 Gyr. Although the youngest populations are better sampled in the case of the integrated analysis than in the case of the resolved analysis, the decline of SFR (t) at ages younger than 0.25 Gyr is consistent in both cases. The lower panel of Fig. 3.7 shows the cumulative mass fraction as a function of time obtained following both approaches. Small differences can be noted between the curves representing the mass build-up of this region of the galaxy. They are, however, consistent within the error bars and so are not significant.

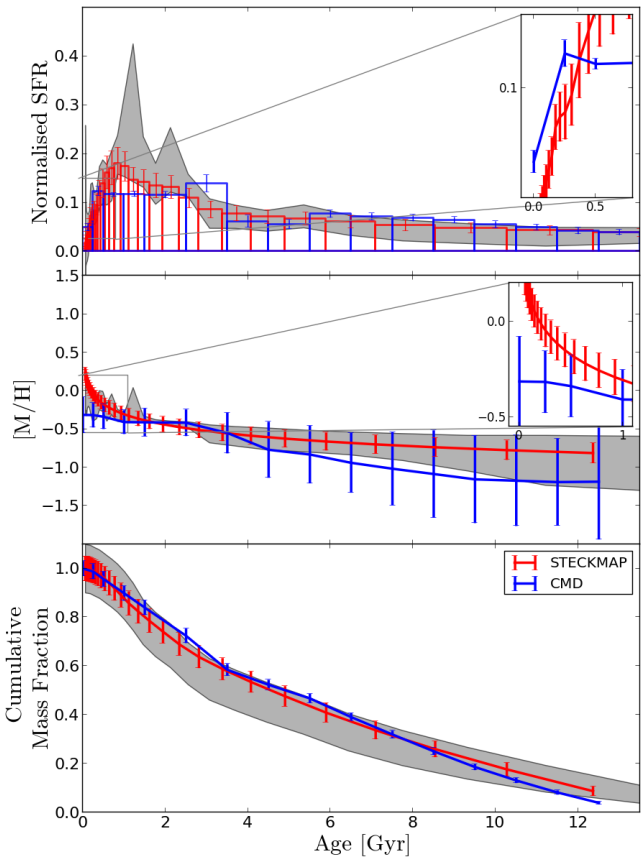

Figure 3.7: Comparison between the LMC bar SFH from the CMD and the integrated spectrum using `STECKMAP` (test 24). The three panels show, from top to bottom, the normalised SFR(t), the AMR, and the cumulative mass fraction with a zoom at young ages for the normalised SFR(t) and the AMR. We plot the envelope of the histograms in the main plots in the insets. In order to make a fair comparison a normalisation is needed. We normalise the SFR (t) in such a way that the sum of the areas of the different rectangles (SFR $[M_{\odot/yr}] \times \Delta t$) is 1 (upper panel). The AMR plot shows the average metallicity at every age bin. Error bars are 1σ of the resulting distribution of solutions from a series of 25 MC simulations in the case of STECKMAP and 600 different solutions by applying small shifts in the CMD for the CMD analysis (see text for details). The shaded regions correspond to the mean values and standard deviations of all the solutions using the V10 models and ages ranging from 0.063 to 13.5 Gyr (tests 3, 7, 17, 18, 19, 20, 21, 22, 23, and 24).

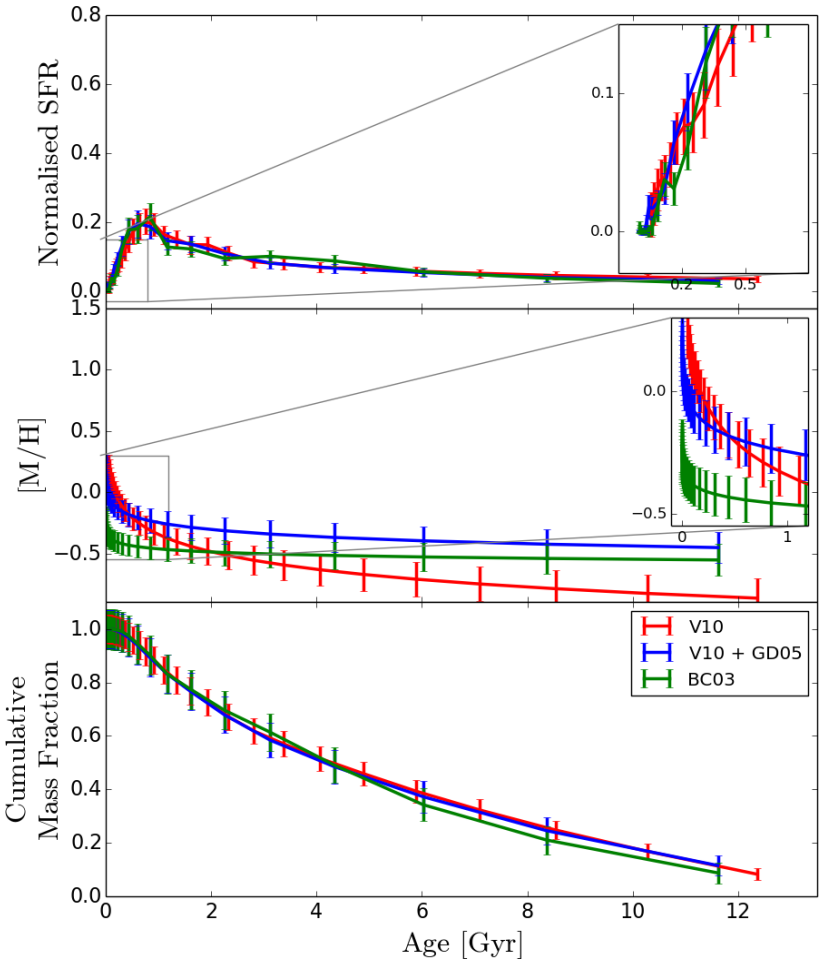

Figure 3.8: Comparison of the different SFHs from `STECKMAP`, paying special attention to the choice of models (V10, V10 + GD05, or BC03). A zoom at the younger ages for the SFR (t) and the AMR is applied. The rest of `STECKMAP` input parameters as in test 24 (see Table 3.2). See caption of Fig. 3.7 for a complete explanation.

Age-metallicity relation

In Fig. 3.7 (middle panel) we show the AMRs from the CMD and the STECKMAP study with a zoom at young ages. The overall shape and the metallicity range are consistent. Even though larger metallicities are systematically found in the STECKMAP analysis, they are consistent within the error bars for most of the time interval, except the last $\simeq 0.25$ Gyr. In the spectrum solution, there is an upturn from $\sim$1.5 Gyr to now, which is not found in the CMD analysis, where the metallicity remains constant and always below the STECKMAP values. We find the main similarities in the age range between $\sim$1.5 and $\sim$3.5 Gyr. At ages older than $\sim$3.5 Gyr the AMR from the integrated spectrum shows a very shallow negative gradient while the AMR from the analysis of the CMD shows a steeper negative gradient and lower metallicities. A plausible explanation might be found in the choice of the smoothing parameters. The best test uses a smoothness parameter in the AMR of 10^6, thus, very smooth solutions for the AMR shape, like the one found, are preferred. If we compare this solution (Fig. 3.7) with other solutions using different smoothing parameters (see Sect. 3.2.1.2 and Appendix C), we can see that this young, metal-rich component disappears for those tests with a low value of the AMR smoothness parameter. Thus, the main differences regarding the AMR shape (outlined above) might be an artefact from the high smoothing parameter imposed on the AMR. In fact, tests 17, 18, 20, and 23 (tests with a lower μ_Z) all show quite similar AMR shapes when compared to the CMD results. This is also true of the SFR(t) shapes.

3.2.1.4 Results from other available codes

For the sake of completeness, we also use other available full spectrum and SED fitting codes (see Chapter 1). This extension of this test allows us to compare this method with other alternatives to extract the stellar content from spectroscopic data. However, as this is not meant to be an exhaustive comparison between all the available codes, here we analyse the results from two of the codes more widely used (ULySS, STARLIGHT, and an analysis based on integrated cluster spectra for historical reasons). The input parameters for these tests are as similar to the STECKMAP input parameters as possible.

ULySS

ULySS[4] (Koleva et al. 2009) is a full spectrum fitting code that uses Levenberg-Marquardt minimisation (from Markwardt 2009) to fit a linear combination of non-linear parameters. It parametrises the inverse problem

[4] ULySS can be downloaded at http://ulyss.univ-lyon1.fr.

as

$$\mathrm{F_{Obs}}(\lambda) = \mathrm{P_n}(\lambda) \times \left(\mathrm{LOSVD}(\mathrm{v_{sys}}, \sigma, \mathrm{h3}, \mathrm{h4}) \otimes \sum_{\mathrm{i=0}}^{\mathrm{i=m}} \mathrm{W_i\, Cmp_i}(\mathrm{a_1}, \mathrm{a_2}, \lambda) \right), \quad (3.7)$$

where $\mathrm{F_{Obs}}(\lambda)$ is the observed flux at every value of the wavelength (λ); P_n is the multiplicative polynomial with n being its degree; LOSVD is the stellar line-of-sight velocity distribution that depends on kinematics parameters such as the systemic velocity ($\mathrm{v_{sys}}$), velocity dispersion (σ), and higher momenta (h3, h4); $\mathrm{Cmp_i}$ are the different components or SSPs dependent on age ($\mathrm{a_1}$) and metallicity ($\mathrm{a_2}$) with different weights (W_i) computed during the fit.

We carry out different tests with different input parameters using `ULySS`. In a first approach, the model is computed as a subset of $i = 15$ SSPs broadened by a LOSVD from a subset of the V10 models (as for the `STECKMAP` analysis). While the ages of the SSPs are fixed between 63 Myr and 13.5 Gyr (equally log-spaced) the metallicities are left free and they could vary between the limits of the models (-2.3 and 0.2 dex, the subset of models comprises 105 different SSPs). We use the emission-cleaned spectrum obtained in Sect. 3.2.1.2 and fixed the stellar kinematics. We refer to this test as *SSP* as we use SSPs as spectral templates. The best fit SFR (t) and AMR are shown in Fig. 3.9. The overall shape of the SFR (t) is qualitatively similar to the `STECKMAP` and CMD reconstructions, although showing sporadic bursts of star formation, which is expected as we are using a combination of SSPs. `ULySS` is not able to replicate the AMR at ages younger than $\sim$0.5 Gyr; the metallicities recovered are lower than those inferred from the CMD and the `STECKMAP` approaches. However, at intermediate and old ages (older than 0.25 Gyr) `ULySS` AMR results are in fair agreement with the CMD and STECKMAP values.

Although the SSP approach is widely used when recovering the stellar content from integrated spectra, we also employ a more complex set of spectral templates, more similar to the ones used in the CMD analysis. We make use of the IAC `MILES` webtools[5] to create spectral templates via user defined SFHs. We use 35 spectra of populations with constant SFR (t) between $0.063 - 0.178$, $0.178 - 0.501$, $0.501 - 1.413$, $1.413 - 3.981$, and $3.981 - 13.49$ Gyr (equally log-spaced in intervals of 0.45 dex) and fixed metallicities ranging from -2.32 to 0.22 dex [M/H]. These spectral templates may be a better representation of the continuous mode of star formation expected in real galaxies than discrete SSPs. We name these new spectral templates *complex* Stellar Populations (SSP). Thus, we use these $i = 35$ complex SPs ($\mathrm{Cmp_i}$) following the same approach outlined above (input spectrum, wavelength range, fixed stellar kinematics, etc). We refer to this

[5] `http://miles.iac.es/pages/webtools/get-spectra-for-a-sfh.php`

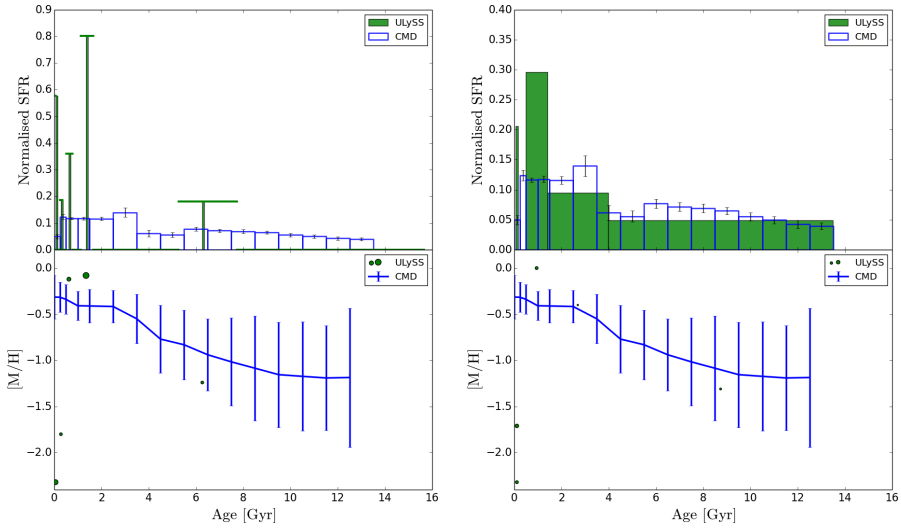

Figure 3.9: Comparison between the SFH (top panels) and the AMR (bottom panels) from the ULySS analysis using two different approaches for the spectral templates. Left panels: we use the V10 models younger than 13.5 Gyr (*SSP* test). Right panels: we use as spectral templates a set of 35 spectra generated from a constant SFR (t) and single metallicity (see text for details). **NOTES:** SFH: we note that the representation of the SFH is different for left panels to the representation in the case of STECKMAP (see Fig. 3.7). In this case we use SSPs with no smoothing applied and thus, vertical lines are chosen to show the mass contribution of the different SSPs instead of a bar plot. However, for a fair comparison, a similar normalisation has been applied. Horizontal lines represent the Δt used in this case (computed based on stellar population models used). For further information see Fig. 3.7. AMR: the representation of the AMR is also different for left-side panels. Green points represent the age and metallicity of the different single stellar populations with a non-zero weight in the fit. The point size is proportional to the weight.

test as *constant SFR*. The results are shown in Fig. 3.9. The use of complex SPs considerably improves the recovery of the shape of the SFR (t). The main discrepancies are found at ages younger than 0.5 Gyr, with an absence of populations with ages between $0.178 - 0.501$ Gyr and an excess contribution in the youngest bin ($0.063 - 0.178$ Gyr). The AMR shape is similar to the one we obtain using SSPs, with the youngest ages showing metallicities that are too low.

STARLIGHT

We have also used STARLIGHT (Cid Fernandes et al. 2005)[6] to obtain the SFH from the observed integrated spectrum. STARLIGHT is a SED fitting code that tries to match the observed spectrum (continuum and spectral features) by means of a combination of stellar models. It also fits the reddening and stellar kinematics simultaneously.

[6] STARLIGHT can be downloaded at http://astro.ufsc.br/starlight/.

The details of how STARLIGHT works are given in Cid Fernandes et al. (2004) and Cid Fernandes et al. (2005). STARLIGHT mainly requires as input an observed spectrum, a configuration file, a mask file, a set of $N_\star$ base spectra (templates), and a reddening law. Essentially, the code then tries to obtain the SFH, reddening, and stellar kinematics by the minimisation of a χ^2,

$$\chi^2 = \sum_\lambda \Big[(\mathrm{O}_\lambda - \mathrm{M}_\lambda)\mathrm{w}_\lambda\Big]^2, \tag{3.8}$$

where O_λ is the observed flux, M_λ is the modelled flux, and w_λ is the weight (0 for masked regions) at the wavelength λ. STARLIGHT normalises the observed spectrum and the spectral templates at a given wavelength (with the unit being the flux at such given wavelength); in this case we use the window between 5590 and 5680 Å for the observed spectrum normalisation, and the flux at 5635 Å for the template normalisation. The expression that this code uses for the modelled spectrum is

$$\mathrm{M}_\lambda = \mathrm{M}_{\lambda 0}\Big[\sum_{\mathrm{j}=1}^{\mathrm{N}_\star} \mathrm{x_j b_{j,\lambda} r_\lambda}\Big] \otimes \mathrm{G}(\mathrm{v}_\star, \sigma_\star), \tag{3.9}$$

where $\mathrm{M}_{\lambda 0}$ is the synthetic flux at the normalisation wavelength; M_λ is the modelled flux at λ; x_j is the weight of the j^{th} element of the set of base spectra; and $\mathrm{b}_{j,\lambda} r_\lambda$ is the normalised reddened-spectrum for this j^{th} component, where $r_\lambda = 10^{-0.4(A_\lambda - A_{\lambda 0})}$ is the extinction term. This first part of the expression accounting for the stellar content and the reddening is convolved ($\otimes$) by the LOSVD of the stellar component ($\mathrm{G}(v_\star, \sigma_\star)$). We maee use of the LMC reddening law provided by the STARLIGHT package and presented in Gordon et al. (2003).

We analyse the LMC bar integrated spectrum following a recipe similar to the one discussed in Sect. 3.2.1.2; this test is called *SSP* as it will be based on SSPs as spectral templates. We use the same set of models[7] (V10 up to 13.5 Gyr) as in previous cases, remove the emission line contribution using GANDALF, fix the stellar kinematics to the pPXF values, and run STARLIGHT to match every spectral feature in the wavelength range from 3800 to 6800 Å. We mask transition regions between grisms and sky features, but not the emission lines as they have meaningful information after applying GANDALF. We find that the results from STARLIGHT show some important differences when compared to the CMD and STECKMAP results (see Fig. 3.10). The

[7] In the case of STARLIGHT, as well as for STECKMAP, we use the entire set of models, [ages (Gyr)] × [M/H] = [0.0631, 0.0708, 0.0794, 0.0891, 0.1000, 0.1122, 0.1259, 0.1413, 0.1585, 0.1778, 0.1995, 0.2239, 0.2512, 0.2818, 0.3162, 0.3548, 0.3981, 0.4467, 0.5012, 0.5623, 0.6310, 0.7079, 0.7943, 0.8913, 1.0000, 1.1220, 1.2589, 1.4125, 1.5849, 1.7783, 1.9953, 2.2387, 2.5119, 2.8184, 3.1623, 3.5481, 3.9811, 4.4668, 5.0119, 5.6234, 6.3096, 7.0795, 7.9433, 8.9125, 10.0000, 11.2202, 12.5893, 14.12] × [−2.32, −1.71, −1.31, −0.71, −0.4, 0.0, 0.22].

recovered SFR (t) shows some episodic bumps of star formation younger than 2 Gyr and a predominant old stellar population (older than 10 Gyr), while an intermediate population between 2 and 10 Gyr is not found. The main discrepancies regarding the AMR are found at ages younger than 0.5 Gyr. As in the case of `ULySS`, the discontinuity in the recovered SFR (t) is a direct consequence of the use of SSPs as spectral templates.

These discrepancies encourage us to carry out a set of 36 tests modifying different input parameters and procedures to check the reliability of the results: i) we test the effect of changing the set of model templates and the age range; ii) to reduce the degrees of freedom in the fit we also inspect the effect of imposing an a priori AMR from Carrera et al. (2008), using a carefully selected set of spectral templates from the different models; iii) considering that `STARLIGHT` also fits the continuum shape of the spectrum, we also try to obtain stellar content with this code avoiding the emission line removal step with `GANDALF`, masking the emission lines instead in order to test if the discrepancies are caused by a bad emission line subtraction; and iv) we also allow `STARLIGHT` to fix or fit the stellar kinematics.

We obtain a wide variety of solutions from these different tests. Two clear bumps are found in the SFR (t) shape using the V10 and V10 + GD05 models, with contributions from young and old populations (younger than 2 Gyr and older than 8 Gyr) and a lack of an intermediate component. However, the use of the BC03 models results in a more spread out or smoother SFR (t) with contributions at all ages. Imposing an observed AMR strongly restricts the number of templates used, and gives poor fits. Fixing the kinematics gives slightly better results than fitting it. Using `GANDALF` or masking the emission lines plays a minor role in the recovery of the stellar content.

In addition, as we do with `ULySS` (see Sect. 3.2.1.4), we perform a further test where we used complex SPs, rather than SSPs, as spectral templates (see Sect. 3.2.1.4). We name this test *constant SFR* as previously done with `ULySS`. The results of this test are shown in Fig. 3.10. Using complex SPs we are able to obtain a closer approximation to the CMD results regarding the SFR (t) shape. However, we find a lack of stars with ages ranging from $0.501 - 1.413$ Gyr and an excess of stars in the youngest age bin ($0.063 - 0.178$ Gyr). The obtained AMR is very similar to the one recovered using SSPs as spectral templates (again, similar to the `ULySS` results), displaying the same issues at the youngest ages.

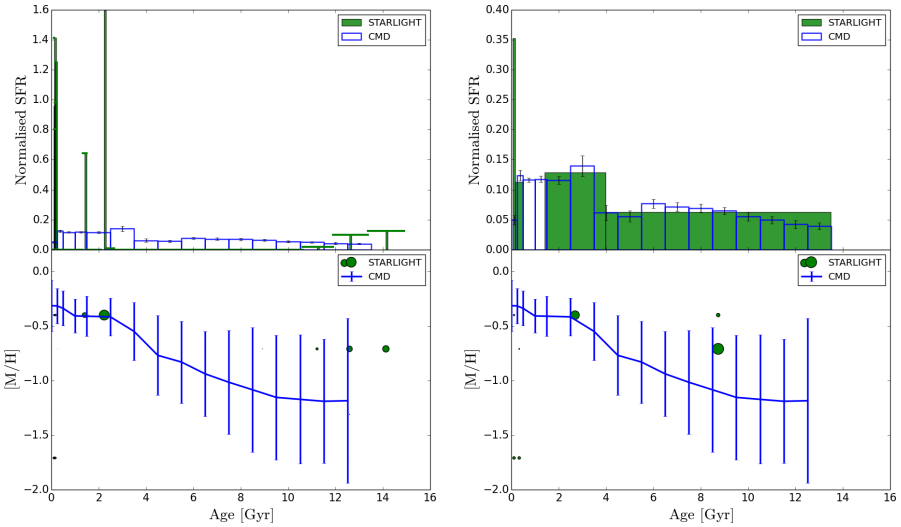

Figure 3.10: Comparison between the SFH (top panels) and the AMR (bottom panels) from the `STARLIGHT` analysis using two different approaches for the spectral templates. Left panels: we use the V10 models younger than 13.5 Gyr (*SSP* test). Right panels: we use as spectral templates a set of 35 spectra generated from a constant SFR (t) and single metallicity (see text for details). **NOTES:** SFH: we note that the representation of the SFH is different for left panels to the representation in the case of `STECKMAP` (see Fig. 3.7). In this case we use SSPs with no smoothing applied and thus, vertical lines are chosen to show the mass contribution of the different SSPs instead of a bar plot. However, for a fair comparison, a similar normalisation has been applied. Horizontal lines represent the Δt used in this case (computed based on stellar population models used). For further information see Fig. 3.7. AMR: the representation of the AMR is also different for left-side panels. Green points represent the age and metallicity of the different single stellar populations with a non-zero weight in the fit. The point size is proportional to the weight.

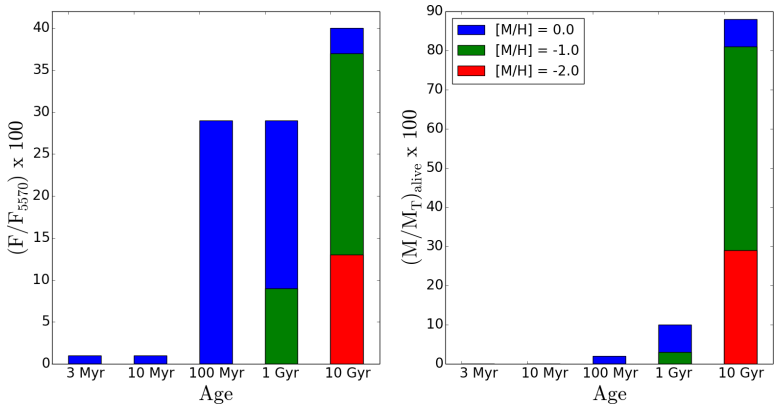

Figure 3.11: Synthesis results using the Bica analysis. Left-hand panel, flux fraction of the different base elements. Right-hand panel, mass alive fraction of the different base elements.

Analysis using a base of integrated cluster spectra (Bica method)

To historically link previous methods to study the stellar content in galaxies with modern SED and full spectrum fitting techniques, we analyse the data via a spectral population synthesis technique originally developed by Bica (1988), and later updated by Schmitt et al. (1996). This part of the comparison was done by the group led by Danielle Alloin. This method aims at reproducing the observed equivalent widths (Ws) and the continuum ratios (Cs) using the integrated-light spectra of an ensemble of star clusters with different ages and metallicities (e.g. Bica & Alloin 1986a,b, 1987; Bica et al. 1988, 1994). The W and C values from the cluster base are built in a grid parametrised by the age and the metallicity, and extrapolated in the case of high metallicities unreachable through observations. In the current analysis, we use eight components to map the age-metallicity plane, with the constraint that their metallicities be solar and subsolar. Indeed, in a low mass galaxy such as the LMC, we do not expect to find stellar components with metallicity above solar (Pagel & Tautvaisiene 1998). The base elements used in the analysis are listed in Table 3.3. The results are shown in Fig. 3.11.

From the population analysis above it is clear that the 1 Gyr and 100 Myr components are almost as important in flux as the 10 Gyr component (see Fig. 3.11, left-hand panel). It is also important to compute how much they represent in terms of mass fractions. For such purposes we employ a flux-mass transformation method (Bica et al. 1988). This method uses different ratios of mass to V-light (M/L_V) related to each age component. It also takes into account metallicity effects among old star clusters. We show in Fig. 3.11 (right-hand panel) the mass distributions for each component. We

3 Myr	10 Myr	100 Myr	1 Gyr	10 Gyr	[M/H]
8	7	6	4	1	0.0
			5	2	−1.0
				3	−2.0

Table 3.3: Base elements in the age × metallicity plane for the Bica (1988) analysis. $E(B\text{-}V)_i = 0.0$. The different base elements are identified by numbers running from 1 to 8.

Range (Gyr)	M_{alive} (%)
$5 - 14$	88
$0.5 - 5$	10
< 0.5	2

Table 3.4: Results for the Bica (1988) analysis. M_{alive} represents the percentage in mass that is still present as stars.

can see that the 1 Gyr and 100 Myr components are less than 10 % and 5 % in mass, respectively.

We can interpret those results as star formation along three different age ranges (less than 0.5 Gyr, $0.5 - 5$ Gyr, and $5 - 14$ Gyr; see Table 3.4). If we consider that the mass at every age range was formed uniformly and we compute a *pseudo-SFR* dividing the mass alive percentage by the age width for each population, which leads us to recent star formation of 4.4 Gyr^{-1}, followed by a drop (2.2 Gyr^{-1}) with a higher *pseudo-SFR* at older ages. These results differ from the STECKMAP and CMD results, essentially because of a lack of time resolution at old ages (see Table 3.5).

3.2.1.5 Discussion

The LMC bar is an appropriate astronomical object to perform a comparison between the SFH obtained for a composite stellar population by means of the information from its resolved stars and from its integrated light. The reason is twofold: i) we can obtain a CMD reaching the oMSTO using HST data, and ii) its high surface brightness allows us to observe a high quality integrated spectrum. By analysing the CMD and integrated spectrum of the LMC bar we derive and compare its SFHs. In this test we mainly focused on the comparison between CMD analysis and full spectrum fitting analysis using `STECKMAP` (Ocvirk et al. 2006b,a). In principle, the stellar populations of the LMC bar represent a challenging case for inversion codes analysing integrated stellar spectra because of its complex nature and rich stellar di-

versity. However, the agreement in the SFR(t) and the AMR between the CMD and the integrated spectrum analysis strongly supports the use of state-of-the-art full spectrum fitting codes in deriving the SFH of complex stellar systems. These blind tests show that the results of both approaches are consistent when trying to recover the SFH of the same object. However, during the analysis we identify several issues that should be further studied.

The most striking difference between the STECKMAP and the CMD results appears in the derived AMRs. Both AMRs show a metallicity monotonically increasing with time, but the AMR derived from the CMD starts at lower metallicities ($\simeq -1.2$ dex) and does not reach solar metallicity at young ages. The AMR obtained with STECKMAP starts at [M/H] $\simeq -0.75$ dex at old ages, remains quite flat for most of the time range, and increases steeply in the last $\simeq 2$ Gyr, reaching metallicity slightly over solar at the present time. The overall SFR (t) shape also displays some differences for populations younger than 4.0 Gyr. The SFR (t) is almost flat between $\sim$0.25 and $\sim$3.5 Gyr from the CMD analysis, whereas from the `STECKMAP` analysis we see a skewed Gaussian towards older ages with the peak at $\sim$ 1 Gyr. There are several possible explanations for these differences in SFH obtained from the two methods:

a) the CMD analysis produces precise results when it reaches below the oMSTO (as in this case). The methodology described in Sect. 3.2.1.2 (CMD case) has been extensively tested by recovering SFHs using mock CMDs with known stellar content (e.g. Aparicio & Hidalgo 2009; Monelli et al. 2010a,c; Hidalgo et al. 2011). However, these analyses are not error-free. Differences in the solutions are found owing to slight changes in the analysis method (e.g. way of dealing with errors, bundle definition, minimisation algorithm). Also, tests with mock stellar populations reveal that an age-dependent smoothing of the SFH features is produced, with age resolution worsening at old ages, owing to the limitations in the age resolution intrinsic to the method (see e.g. figure 8 in Hidalgo et al. 2011). Having a large number of stars in the CMD is important for a reliable solution, and we cannot exclude the possibility that the shape of the SFR (t) at young ages is not well recovered because of the small data set. This may be aggravated by the fact that the brightest, youngest stars in the MS are saturated, and therefore do not appear in the CMD. Even though the SFR (t) at the corresponding ages may still be recovered from lower mass stars, which are fainter on the MS, some information is obviously lost. Thus, further investigation using a CMD taken over a larger area, and covering the whole magnitude range would be of interest;

b) there could be a lack of young stars in the field where the integrated spectrum was observed. This might produce a deficit of flux coming from the youngest populations, and therefore might result in the failure of `STECKMAP` to reproduce the AMR at such young ages. However, we note that `STECKMAP`, `STARLIGHT`, and `ULySS` all find some contribution at very young ages (see Fig.

3.7). In addition, a visual inspection of the observed spectrum shows some helium absorption lines (He Iλ3819 and He Iλ4922), which are signatures of the presence of young, hot stars. Therefore, it does not seem that a deficit of signal from young stars is the cause of the differences in the metallicity inferred for the very young population;

c) the AMR shape is especially affected by the smoothing penalty function in the AMR (μ_Z). In particular, the shape of the recovered AMR using STECKMAP (see Fig. 3.7) is very smoothed as a consequence of imposing a large smoothing parameter ($\mu_Z = 10^6$). The discrepancies between this AMR and that from the CMD analysis in the younger and older edges of the used age range could be due to the effect of this parameter. In fact, tests with μ_Z above 10^2 currently present supersolar stars and primordial metallicities greater than [M/H]$= -1.0$. Other tests with different smoothing parameters for the AMR (see Appendix C) are better able to reproduce the AMR shape derived in the CMD analysis while still providing a good fit for the SFR(t);

d) as shown in Sect. 3.2.1.2, different input parameters give similar SFH results and very accurate fits (see Appendix C and Table 3.2) when STECKMAP is applied to a high quality spectrum. The overall shape of the recovered SFH is reasonably consistent for the different tests although slight differences do arise between them. Therefore, we conclude that the shape of the recovered SFH from high quality spectra is accurately reproduced regardless of the input parameters.

Despite these small discrepancies, the similarities between the CMD and the STECKMAP results are very reassuring. The manner in which STECKMAP deals with the intrinsically ill-posed inversion problem (regularisation through a penalised χ^2) has proven to be very powerful. The smoothed solutions from STECKMAP make sense physically; star formation in galaxies is a complex mechanism, and a consequence of continuous galaxy evolution. In STARLIGHT and ULySS no such smoothing is implemented, and thus, the use of SSPs as spectral templates naturally leads to a SFR (t) characterised by discrete bursts of star formation. Although the use of SSPs as a base for reconstructing the SFH of galaxies is a good first approximation, these SSPs are idealised realisations of bursts of star formation that are not necessarily expected in nature. The inclusion of some kind of smoothing techniques in these codes might eliminate these discontinuities.

Since the exact determination of the shape of the SFR (t) is difficult in STARLIGHT and ULySS if SSPs are employed, we use a set of spectral templates computed assuming populations with a range of ages (complex SPs). Although the shape of the AMR is very similar irrespective of whether we use SSPs or complex SPs, the shape of the SFR (t) obtained using this second approach is closer to the CMD and STECKMAP SFR (t) shapes. The use of complex SPs seems in some sense to mimic the effect of imposing a smoothing on the solution (see Figs. 3.9 and 3.10) and it is preferred to the

Approach	Young (%)	Intermediate (%)	Old (%)
CMD	4.3	49.0	46.7
`STECKMAP`	4.2	49.4	46.4
`ULySS` *SSP*	3.9	51.4	44.7
`ULySS` *const. SFR*	2.4	51.3	46.3
`STARLIGHT` *SSP*	9.0	54.9	36.1
`STARLIGHT` *const. SFR*	7.7	33.1	59.2
Bica	2.0	10.0	88.0

Table 3.5: Percentages of the total stellar mass in three different stellar subpopulations: young (younger than 0.5 Gyr), intermediate (older than 0.5 Gyr and younger than 5.0 Gyr), and old (older than 5.0 Gyr). In the cases of `ULySS` and `STARLIGHT` we show the results from the SSP and the mock spectral template approaches. We include the Bica analysis for historical comparison.

use of SSPs as it allows us to obtain some intermediate contribution that otherwise is impossible to detect. This suggests that these kinds of spectral templates may be better in order to study the stellar content of external complex systems (e.g. galaxies, not just star clusters).

We also evaluate whether, although they do not always produce consistent SFR(t) shapes, the different methods are able to reproduce the relative contribution in mass of young, intermediate, and old components (the age intervals for this test are defined to match the Bica analysis; see Sect. 3.2.1.4). Table 3.5 shows the contributions to the total stellar mass for different age ranges, as inferred using all the analysed approaches. The outcomes from the CMD, `STECKMAP`, `STARLIGHT`, and `ULySS` (*SSP* and *complex SSP* tests) display roughly similar percentages of stars in each age range, although slightly larger discrepancies are found in the `STARLIGHT` analysis.

A common issue in the `ULySS` and `STARLIGHT` results is the excess of young stars (see Figs. 3.9 and 3.10). As discussed in Sect. 3.2.1.1, some bright stars (F814W ~ -1) are saturated, and thus, are not taken into account in the SFH recovery from the CMD. This saturation magnitude roughly corresponds to the MS turnoff of a ~ 0.3 Gyr old population. However, we consider in this calculation other stars with the same age that are not saturated (lower mass and, therefore, fainter stars), so we can still recover the information at the youngest ages. As this saturation affects the brightest (and youngest) stars which might be dominating in the light integrated spectrum, the excess of young stars found with `ULySS` and `STARLIGHT` may be a consequence of this limitation. We note that this issue is somehow observed in the `STECKMAP` results with low smoothing parameters. This should be further investigated via the comparison with other Local Group galaxies using a similar analysis to this test.

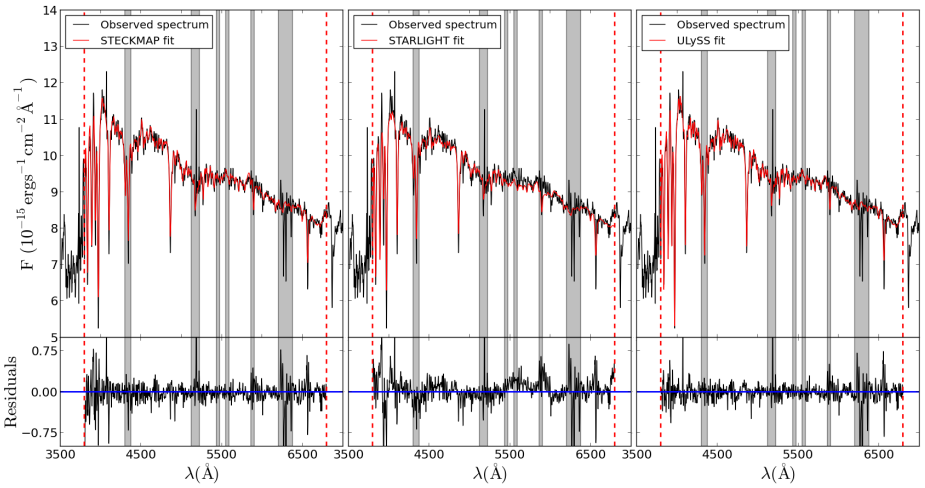

Figure 3.12: Top panels: comparison between the observed spectrum and the fit from STECKMAP (left), STARLIGHT (middle), and ULySS (right). For STARLIGHT and ULySS we use the *constant SFR* approach. Black: fully reduced, emission-cleaned composite spectrum of the LMC bar. Red: fit from the different codes. Bottom panels: residuals of those fits computed as observed – best model. For the stellar content analysis we use the wavelength range from 3800 to 6800 Å (dashed vertical red lines; see text for details). The shaded regions of the spectrum are the masked regions (not considered in the fits). The residuals are in units of 10^{-15} erg^{-1} cm^{-2} Å^{-1}.

In Fig. 3.12 we analyse each spectral fit (STECKMAP, ULySS, and STARLIGHT) in order to assess where the observed discrepancies discussed above (SFH and age percentages) may come from. At first glance the three codes seem to properly fit the observed spectrum. The *rms* of the residuals is 0.12 for the STECKMAP fit, 0.21 for the STARLIGHT fit and 0.18 for the ULySS fit (in the cases of the *SSP* and *constant SFR* tests for ULySS and STARLIGHT). A careful inspection shows that STECKMAP and ULySS are able to better reproduce some individual spectral features than STARLIGHT as a consequence of the polynomial fitting. Figure 3.13 shows a more detailed comparison between the STECKMAP and STARLIGHT best models (*constant SFR*), i.e. the spectrum corresponding to the recovered stellar content. We note some important differences in the shape of the continuum (wave-like features in the residual plot) as well as differences in some specific absorption features. Among the features with larger discrepancies we can highlight Hϵ, Hβ, the Ca II doublet (3933, 3969 Å), the magnesium feature at 5175 Å (Mg I), and the sodium absorption line (Na I λ5892). Every stellar feature is deeper in the STECKMAP best model than in the case of the STARLIGHT fit except for the sodium feature. These differences considerably affect the recovered stellar content.

Although the techniques for the analysis of unresolved stellar populations give good results when compared to the CMD reconstruction, based on this

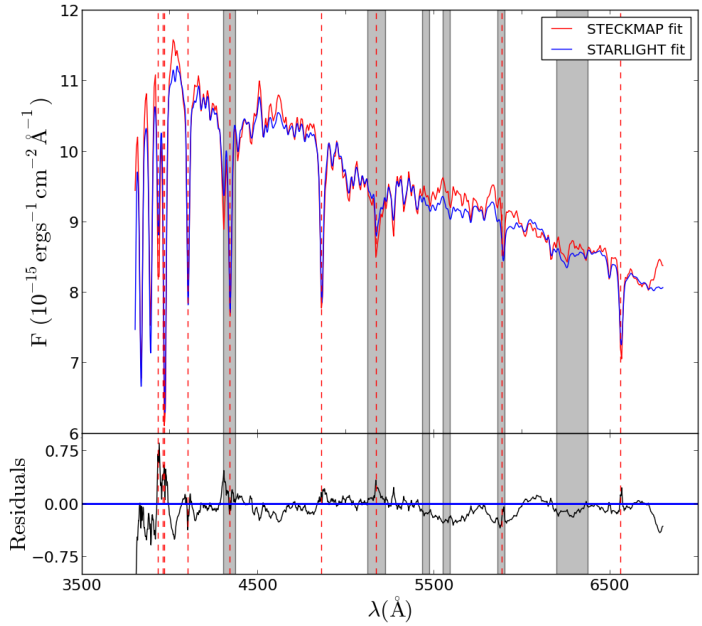

Figure 3.13: Comparison between the `STECKMAP` and `STARLIGHT` (using spectral templates mimicking constant SFR) best models. Top panel: the `STECKMAP` best model is plotted in red. The `STARLIGHT` best model is plotted in blue. Bottom panel: differences of both best models (`STECKMAP` – `STARLIGHT`). The shaded regions of the spectrum are the masked regions (not considered in the fits). Vertical, dashed red lines are located at the wavelengths of the main stellar absorption features. The residuals are in units of 10^{-15} erg^{-1} cm^{-2} Å^{-1}.

test we find that there is still room for improvement. For example, a wider range of spectral coverage might help to overcome the issues at young ages and to better constrain the recovered SFH. Few empirical stellar libraries are available in the ultraviolet (150 to 333 nm) and near-infrared (up to 2 microns) and thus, theoretical SSPs limited to the optical range are used (e.g. Riffel et al. 2009; Storchi-Bergmann et al. 2012; Martins et al. 2010, 2013). In addition, we find that a successful way of overcoming the ill-conditioned problem of the reconstruction of the stellar content from an observed spectrum is by imposing smoothed solutions (which have more physical meaning), or by using spectral templates composed of complex SPs. We suggest that this could be a basis for improvement in the next generation stellar population synthesis codes from integrated spectra.

3.2.2 Analysis of mock spectra

Our method has been proven successful in reproducing the stellar content derived from the analysis of resolved stellar populations (see Sect. 3.2.1). Such resolved analysis, based on the study of CMDs, is not feasible for external galaxies as we cannot detect individual stars in them, and the only way to obtain information about their stellar content is by means of integrated spectra. The previously described test encourages us to claim that we can rely on this procedure to extract reliable stellar information in those systems. In this thesis, we are interested in analysing the stellar content in external galaxies from the IFS CALIFA data. Although CALIFA is revealing an unprecedented view of galaxies, the quality of the CALIFA spectra is not as high as in the previously analysed LMC spectrum. Therefore, we need to further test this method by applying it to spectra with CALIFA-like quality.

We make use of the `MILES` IAC webtools[8] to create a series of mock spectra (43) with different SFHs. This tool, provided by the `MILES` team, allows us to obtain spectra and line-strength predictions based on the V10 models for a given SFH. Among the different parametrisations that the shape of the SFH might present, this tool offers the following different possibilities:

Truncated (trunc): using a constant value of the SFR between the starting age (t_0) and the age of truncation (t_{trunc}), zero elsewhere.

Exponential (exp): consisting on an exponential decline in the shape of the SFH with a power-law rising at early times in the form:

$$SFR(t) = \left[\frac{t_0 - t}{t_0}\right]^n \times e^{(t_0 - t)/\tau}, \tag{3.10}$$

where t represents the time, t_0 is the age at which star formation starts, n is the index of the power law, and τ is the time scale of the formation.

[8] `http://miles.iac.es/pages/webtools/get-spectra-for-a-sfh.php`

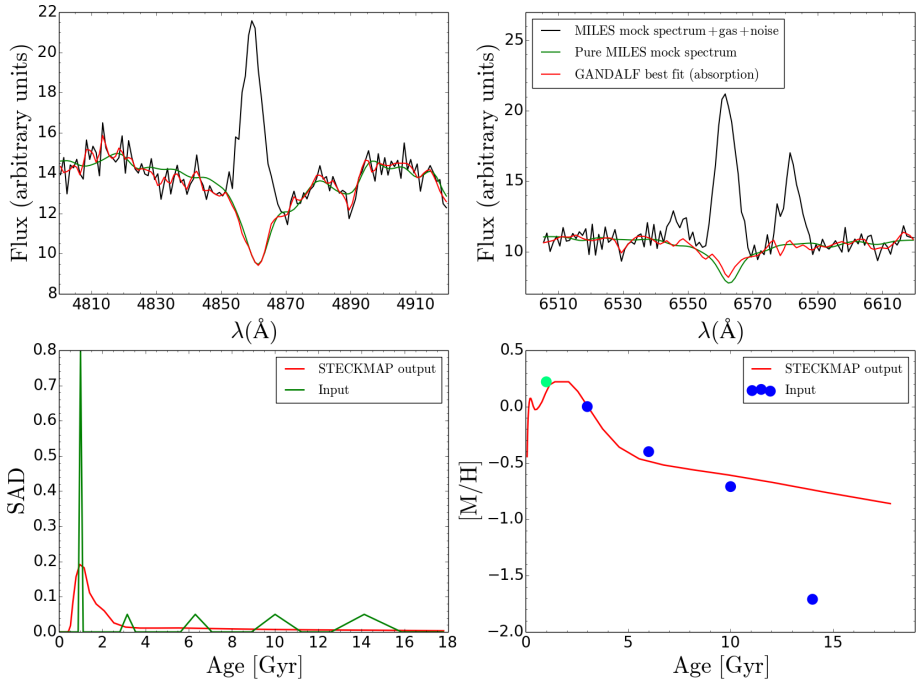

Figure 3.14: GANDALF and STECKMAP performance tests. We show test number 14 (see Table 3.6) as an example. Upper row: plots showing the emission line removal from GANDALF in the Hβ (left) and Hα (right) regions. The black line is the input spectrum, i.e. a combination of noise, the mock spectrum, and some gaussians replicating emission lines. The green line is the model mock spectrum (no gas, no noise, pure absorption spectrum). The red line is the GANDALF output after subtracting the computed emission lines. Bottom row: plots showing the stellar content recovery by STECKMAP. Left: stellar age distribution. Green line represents the real stellar content used to create the mock spectrum. Red line in the reconstructed SAD. Right: age-metallicity relation. The points represent the positions in the Age-[M/H] plane of each stellar population. The cyan point shows the higher fraction of young stars (80 %, M-W fraction) in contrast to the rest of the points (contributing just 5 %, M-W). The red line shows the AMR recovered by STECKMAP.

Multiple SSP bursts (Npop): consisting on a number of bursts with different mass fractions of a given age and metallicity (up to 5).

Exponential + multiple SSP bursts (expB): a combination of the two previous parametrisations.

User defined SFH : the MILES IAC webtools also allow users to implement SFHs with different and more complex shapes.

We have manipulated these mock spectra (see Tables 3.6 and 3.7) adding some Gaussian noise to mimic the typical S/N ($\sim$ 40 per pixel in the continuum) of the CALIFA spectra and some fake emission lines to mimick the Hβ, Hα, and [N II] gas emission. We apply GANDALF and STECKMAP to these

mock spectra in order to check the performance of the method devolped in this thesis removing emission lines and determining the stellar content from integrated spectra with known inputs. We apply both codes following the recipe described in Sect. 3.1. In Fig. 3.14 we show the outcome of one of these tests as an example. In this particular case we analyse the mock spectrum following a star formation history composed by 5 star formation bursts at 1.0, 3.0, 6.31, 10.0, and 14.13 Gyr with a negative AMR (test number 14, see Table 3.6). The younger stellar population accounts for the 80 % of the mass while each of the other star forming bursts contributes with 5 % to the total light.

Test	SFH Type	t_0 (Gyr)	τ (Gyr)	n	[M/H] (dex)
1	exp	12.0	−3.0	0.0	−1.31
2	exp	12.0	3.0	0.0	−1.31
3	exp	12.0	3.0	1.0	−1.31
4	exp	3.0	12.0	1.0	−1.31
5	exp	17.0	3.0	0.0	−2.32
6	exp	12.0	3.0	0.0	0.22
7	exp	5.0	3.0	0.0	0.00
8	exp	0.1	1.0	0.0	0.00

Test	SFH Type	t_0 (Gyr)	t_{trunc} (Gyr)	[M/H] (dex)
9	trunc	10.0	2.0	0.22
10	trunc	10.0	2.0	0.00
11	trunc	10.0	2.0	−1.71
12	trunc	5.0	3.0	−2.32

	Burst 1			Burst 2			Burst 3			Burst 4			Burst 5		
Test	Mass fraction	Age (Gyr)	[M/H] (dex)	Mass fraction	Age (Gyr)	[M/H] (dex)	Mass fraction	Age (Gyr)	[M/H] (dex)	Mass fraction	Age (Gyr)	[M/H] (dex)	Mass fraction	Age (Gyr)	[M/H] (dex)
13	0.2	1.0	0.22	0.20	3.0	0.00	0.20	6.0	−0.40	0.20	10.0	−0.71	0.20	14.0	−1.71
14	0.8	1.0	0.22	0.05	3.0	0.00	0.05	6.0	−0.40	0.05	10.0	−0.71	0.05	14.0	−1.71
15	0.8	1.0	0.22	0.05	3.0	0.22	0.05	6.0	0.22	0.05	10.0	0.22	0.05	14.0	0.22
16	0.8	1.0	−1.31	0.05	3.0	−1.31	0.05	6.0	−1.31	0.05	10.0	−1.31	0.05	14.0	−1.31

	Burst 1			Burst 2		
Test	Mass fraction	Age (Gyr)	[M/H] (dex)	Mass fraction	Age (Gyr)	[M/H] (dex)
17	0.8	1.0	0.22	0.05	3.0	0.0
18	0.8	1.0	−2.32	0.05	3.0	0.0

						Burst 1			Burst 2			Burst 3		
Test	SFH Type	t_0 (Gyr)	τ (Gyr)	n	[M/H] (dex)	Mass fraction	Age (Gyr)	[M/H] (dex)	Mass fraction	Age (Gyr)	[M/H] (dex)	Mass fraction	Age (Gyr)	[M/H] (dex)
19	expB	17.0	3.0	0.00	−2.32	0.10	1.0	0.00	0.10	5.0	−0.40	0.10	8.0	−0.71
20	expB	17.0	3.0	0.00	−2.32	0.05	1.0	0.00	0.05	5.0	−0.40	0.05	8.0	−0.71
21	expB	17.0	3.0	0.00	0.22	0.10	1.0	0.00	0.10	5.0	−0.40	0.10	8.0	−0.71
22	expB	17.0	3.0	0.00	−1.40	0.05	1.0	0.00	0.05	5.0	−0.40	0.05	8.0	−0.71
23	expB	3.0	0.0	0.00	0.22	0.05	1.0	0.00	0.05	5.0	−0.40	0.05	8.0	−0.71
24	expB	3.0	1.0	0.00	0.00	0.05	1.0	0.00	0.05	5.0	−0.40	0.05	8.0	−0.71
25	expB	3.0	0.5	−0.40	0.00	0.05	1.0	0.22	0.05	5.0	−0.40	0.05	8.0	−0.71

Table 3.6: Set of parameters defining the SFH for the analysed mock spectra (I).

	Burst 1			Burst 2			Burst 3		
Test	**Mass fraction**	**Age (Gyr)**	**[M/H] (dex)**	**Mass fraction**	**Age (Gyr)**	**[M/H] (dex)**	**Mass fraction**	**Age (Gyr)**	**[M/H] (dex)**
26	0.34	0.5	0.0	0.33	7.0	−0.4	0.33	13.0	−1.71
27	0.01	0.5	0.0	0.30	7.0	−0.4	0.69	13.0	−1.71
28	0.15	0.5	0.0	0.25	7.0	−0.4	0.60	13.0	−1.71
29	0.34	0.5	0.0	0.33	4.0	−0.4	0.33	13.0	−1.71
30	0.01	0.5	0.0	0.30	4.0	−0.4	0.69	13.0	−1.71
31	0.15	0.5	0.0	0.25	4.0	−0.4	0.60	13.0	−1.71
32	0.70	0.5	0.0	0.15	7.0	−0.4	0.15	13.0	−1.71
33	0.80	0.5	0.0	0.10	4.0	−0.4	0.10	13.0	−1.71
34	0.05	0.5	0.0	0.05	7.0	−0.4	0.90	14.0	−1.71
35	0.45	0.5	0.0	0.10	4.0	−0.4	0.45	14.0	−1.71

Test	**SFH Type**	$\mathbf{t_0}$ **(Gyr)**	$\mathbf{t_{trunc}}$ **(Gyr)**	**[M/H] (dex)**
36	trunc	17.8	0.63	0.00
37	trunc	17.8	0.63	0.22
38	trunc	17.8	0.63	−0.71

Test	**SFH Type**	$\mathbf{t_0}$ **(Gyr)**	τ **(Gyr)**	n	**[M/H] (dex)**
39	exp	17.8	2.0	0.0	−1.31
40	exp	17.8	2.0	0.0	−0.40
41	exp	17.8	5.0	0.0	−1.31
42	exp	17.8	10.0	0.0	−0.40
43	exp	17.8	13.0	0.0	−0.40

Table 3.7: Set of parameters defining the SFH for the analysed mock spectra (II).

We can quantify the GANDALF performance (see Fig. 3.14) by analysing the relative error of the spectrum recovered by GANDALF in the absorption lines. Such relative error is of about 4 ± 2 % for the Hα absorption feature and 2 ± 2 % for Hβ (as an average considering all the tests). With this test we demonstrate the good performance of this code, whic extensively tested and used in other works (e.g. Sarzi et al. 2006; Falcón-Barroso et al. 2006; Oh et al. 2011; Singh et al. 2013). An example of the GANDALF performance in a real case was shown in Fig. 3.1.

STECKMAP has also been widely tested and gives very accurate results reproducing SFHs of mock spectra and galactic objects (e.g. Koleva et al. 2008; Sánchez-Blázquez et al. 2011; Ruiz-Lara et al. 2015b). However, to evaluate the good performance of STECKMAP in similar data to the ones we are using in this thesis, we apply it to the emission cleaned spectra from the above described GANDALF tests. We analyse the STECKMAP output in two different ways. First of all, we compute average age and metallicity values from the SAD and AMR recovered by this code. Second of all, we estimate the contribution to the total mass of different subpopulations according to their age. We consider three subpopulations: young (0 to 1.5 Gyr); intermediate (1.5 to 10.0 Gyr); and old (10.0 to 17.8 Gyr). The results of all of these tests are shown in Figs. 3.14 and 3.15 and Tables 3.8 and 3.9.

In particular, in Fig. 3.14 we show the result of one of these tests as an example. The relative error in the determination of mean ages and metallicities according to MC simulations on these tests is below 30 %. This value is in agreement with the errors that we are computing using the CALIFA data (see Sect. 3.1.3). In the example that we are showing in Fig. 3.14, the theoretical mean L-W age is 1.20 Gyr (2.48 Gyr, M-W value) and the metallicity is 0.035 ([M/H]) while the computed L-W values are 1.58 ± 0.52 Gyr and 0.18 ± 0.05 dex (2.58 ± 1.37 and 0.12 ± 0.07 dex, M-W quantities). The theoretical age values are within the error range of the values computed using STECKMAP after removing the emission line contribution (GANDALF) while the recovery of the metallicity values is more difficult. Regarding the recovery of the contribution to the total mass from different stellar subpopulations we can conclude that, in this particular case, the trend is recovered (more contribution from the youngest ages) but we find an excess of contribution of intermediate stars. In the case of the young component the mass fraction input was 0.8 while we recover 0.53 ± 0.07. For the intermediate component the input was 0.1 and STECKMAP recovered 0.43 ± 0.04, while more similar results were found for the oldest component, 0.1 versus the 0.04 ± 0.03 that we obtained. An example of a STECKMAP fit in a real case was shown in Fig. 3.3.

Test	Age (Gyr), L-W		Age (Gyr), M-W		[M/H], L-W		[M/H], M-W	
	IAC	STECKMAP	IAC	STECKMAP	IAC	STECKMAP	IAC	STECKMAP
1	0.90	1.67 ± 0.42	3.03	6.18 ± 1.25	−1.31	−0.80 ± 0.17	−1.31	−1.14 ± 0.10
2	7.99	8.11 ± 0.60	10.30	10.53 ± 0.59	−1.31	−1.15 ± 0.15	−1.31	−1.26 ± 0.06
3	4.06	5.42 ± 0.69	7.33	8.88 ± 1.01	−1.31	−1.01 ± 0.14	−1.31	−1.24 ± 0.06
4	0.53	1.22 ± 0.46	1.14	4.11 ± 2.10	−1.31	−0.81 ± 0.16	−1.31	−1.07 ± 0.12
5	13.95	6.65 ± 0.62	15.58	10.91 ± 0.49	−2.32	−1.26 ± 0.15	−2.32	−1.28 ± 0.09
6	7.99	7.81 ± 0.53	10.30	10.83 ± 0.48	0.22	0.20 ± 0.02	0.22	0.22 ± 0.04
7	1.89	3.84 ± 1.41	3.37	10.01 ± 3.14	0.00	−0.007 ± 0.10	0.00	0.05 ± 0.17
8	0.08	0.09 ± 0.08	0.08	0.12 ± 2.19	0.00	0.03 ± 0.10	0.00	0.04 ± 0.12
9	5.04	6.52 ± 0.57	6.23	8.58 ± 0.56	0.22	0.19 ± 0.03	0.22	0.16 ± 0.05
10	5.04	7.43 ± 0.77	6.23	9.35 ± 0.89	0.00	0.05 ± 0.05	0.00	−0.04 ± 0.05
11	5.04	7.18 ± 0.58	6.23	10.73 ± 0.60	−1.71	−1.26 ± 0.08	−1.71	−1.31 ± 0.06
12	4.03	5.70 ± 0.47	4.14	10.99 ± 0.38	−2.32	−1.31 ± 0.11	−2.32	−1.31 ± 0.07
13	3.04	3.27 ± 0.94	6.92	6.24 ± 1.98	−0.52	0.09 ± 0.06	−0.52	−0.06 ± 0.12
14	1.20	1.58 ± 0.52	2.48	2.58 ± 1.37	0.04	0.18 ± 0.03	0.04	0.12 ± 0.07
15	1.20	1.68 ± 0.58	2.48	2.88 ± 1.61	0.22	0.18 ± 0.04	0.22	0.12 ± 0.07
16	1.20	2.49 ± 0.26	2.48	6.57 ± 0.64	−1.31	−0.45 ± 0.20	−1.31	−0.83 ± 0.13
17	1.04	1.76 ± 0.33	1.13	3.25 ± 1.02	0.21	0.18 ± 0.04	0.21	0.10 ± 0.06
18	1.04	0.85 ± 0.26	1.13	3.15 ± 1.65	−2.18	−0.44 ± 0.14	−2.18	−0.70 ± 0.13
19	5.49	6.80 ± 0.86	12.38	10.24 ± 0.73	−2.26	−0.71 ± 0.21	−2.26	−0.97 ± 0.16
20	7.91	7.45 ± 0.44	14.03	11.02 ± 0.29	−2.29	−1.26 ± 0.14	−2.29	−1.29 ± 0.06
21	5.49	3.81 ± 1.04	12.38	7.65 ± 2.28	0.20	0.09 ± 0.09	0.20	0.07 ± 0.12
22	7.91	9.09 ± 1.70	14.03	12.44 ± 1.76	−1.39	−0.51 ± 0.17	−1.39	−0.84 ± 0.13
23	5.49	4.81 ± 0.63	12.38	10.28 ± 1.24	0.21	0.10 ± 0.03	0.21	0.10 ± 0.05

continues on next page

continues from previous page

	Age (Gyr), L-W		Age (Gyr), M-W		[M/H], L-W		[M/H], M-W	
Test	IAC	STECKMAP	IAC	STECKMAP	IAC	STECKMAP	IAC	STECKMAP
24	1.86	3.04 ± 1.39	2.78	7.10 ± 4.04	−0.005	0.01 ± 0.08	−0.005	−0.06 ± 0.17
25	2.86	7.61 ± 1.95	3.30	11.61 ± 2.75	−0.004	−0.06 ± 0.07	−0.004	−0.08 ± 0.12
26	1.33	0.93 ± 0.49	6.66	3.14 ± 3.11	−0.70	−0.005 ± 0.21	−0.70	−0.14 ± 0.20
27	8.54	9.71 ± 2.17	10.82	12.33 ± 2.29	−1.30	−1.03 ± 0.23	−1.30	−1.13 ± 0.22
28	2.62	3.07 ± 0.94	9.40	7.97 ± 2.68	−1.13	−0.15 ± 0.18	−1.13	−0.57 ± 0.49
29	1.27	0.73 ± 0.82	5.64	1.20 ± 4.46	−0.70	−0.17 ± 0.31	−0.70	−0.20 ± 0.23
30	6.66	8.04 ± 2.35	9.89	11.00 ± 2.72	−1.30	−0.84 ± 0.25	−1.30	−1.03 ± 0.27
31	2.44	2.90 ± 1.29	8.62	7.50 ± 3.18	−1.13	−0.20 ± 0.27	−1.13	−0.59 ± 0.43
32	0.70	0.48 ± 0.26	3.30	1.11 ± 1.84	−0.32	0.17 ± 0.10	−0.32	0.12 ± 0.14
33	0.61	0.50 ± 0.19	2.06	0.79 ± 1.35	−0.21	0.08 ± 0.11	−0.21	0.02 ± 0.15
34	5.86	4.61 ± 1.08	13.09	9.66 ± 1.96	−1.56	−0.99 ± 0.44	−1.56	−1.24 ± 0.17
35	1.05	0.68 ± 0.29	6.98	2.02 ± 1.75	−0.81	−0.06 ± 0.19	−0.81	−0.09 ± 0.21
36	5.28	6.22 ± 2.03	9.70	10.15 ± 2.92	0.00	0.04 ± 0.11	0.00	−0.02 ± 0.12
37	5.28	6.16 ± 0.78	9.70	10.35 ± 0.84	0.22	0.18 ± 0.06	0.22	0.22 ± 0.08
38	5.28	4.69 ± 2.73	9.70	8.45 ± 4.70	−0.71	−0.67 ± 0.34	−0.71	−0.52 ± 0.20
39	16.08	10.37 ± 1.64	16.54	12.15 ± 1.45	−0.40	−1.23 ± 0.10	−0.40	−1.27 ± 0.09
40	16.08	14.34 ± 2.73	16.54	14.94 ± 2.17	−1.31	−0.32 ± 0.11	−1.31	−0.34 ± 0.08
41	9.77	8.56 ± 1.15	14.02	11.47 ± 0.77	−1.31	−1.27 ± 0.19	−1.31	−1.30 ± 0.08
42	5.92	6.51 ± 2.93	12.04	11.11 ± 3.96	−0.40	−0.39 ± 0.26	−0.40	−0.26 ± 0.20
43	5.17	6.86 ± 2.79	11.48	12.06 ± 3.90	−0.40	−0.31 ± 0.22	−0.40	−0.41 ± 0.16

Table 3.8: Theoretical versus recovered mean stellar ages and metallicities after applying GANDALF and STECKMAP to the mock spectra generated with the MILES IAC webtools.

Test	Young		Intermediate		Old	
	IAC	STECKMAP	IAC	STECKMAP	IAC	STECKMAP
1	0.37	0.230 ± 0.04	0.593	0.48 ± 0.02	0.037	0.23 ± 0.03
2	0.009	0.01 ± 0.01	0.275	0.52 ± 0.03	0.716	0.47 ± 0.03
3	0.044	0.05 ± 0.01	0.661	0.60 ± 0.04	0.295	0.35 ± 0.04
4	0.689	0.44 ± 0.06	0.311	0.44 ± 0.05	0.000	0.12 ± 0.06
5	0.002	0.01 ± 0.01	0.048	0.49 ± 0.02	0.950	0.50 ± 0.02
6	0.009	0.01 ± 0.01	0.275	0.49 ± 0.02	0.716	0.50 ± 0.02
7	0.136	0.10 ± 0.03	0.864	0.42 ± 0.12	0.000	0.49 ± 0.13
8	1.00	0.99 ± 0.09	0.00	0.01 ± 0.05	0.000	0.01 ± 0.06
9	0.00	0.003 ± 0.01	0.868	0.70 ± 0.03	0.132	0.30 ± 0.03
10	0.00	0.007 ± 0.01	0.868	0.60 ± 0.04	0.132	0.40 ± 0.04
11	0.00	0.01 ± 0.01	0.868	0.50 ± 0.03	0.132	0.49 ± 0.03
12	0.00	0.02 ± 0.01	1.00	0.46 ± 0.01	0.000	0.52 ± 0.02
13	0.20	0.21 ± 0.04	0.40	0.58 ± 0.05	0.400	0.21 ± 0.06
14	0.80	0.53 ± 0.07	0.10	0.43 ± 0.04	0.100	0.04 ± 0.03
15	0.80	0.46 ± 0.05	0.10	0.50 ± 0.03	0.100	0.04 ± 0.03
16	0.80	0.26 ± 0.02	0.10	0.49 ± 0.01	0.100	0.25 ± 0.02
17	0.941	0.48 ± 0.04	0.059	0.46 ± 0.04	0.000	0.07 ± 0.03
18	0.941	0.55 ± 0.08	0.059	0.36 ± 0.05	0.000	0.09 ± 0.04
19	0.101	0.05 ± 0.01	0.226	0.49 ± 0.03	0.673	0.46 ± 0.03
20	0.051	0.01 ± 0.01	0.131	0.49 ± 0.01	0.817	0.50 ± 0.01
21	0.101	0.13 ± 0.03	0.226	0.60 ± 0.05	0.673	0.27 ± 0.06
22	0.051	0.05 ± 0.01	0.131	0.30 ± 0.07	0.817	0.65 ± 0.07
23	0.101	0.10 ± 0.01	0.226	0.40 ± 0.05	0.673	0.49 ± 0.06

continues on next page

continues from previous page

	Young		Intermediate		Old	
Test	IAC	STECKMAP	IAC	STECKMAP	IAC	STECKMAP
24	0.156	0.17 ± 0.05	0.844	0.57 ± 0.14	0.000	0.27 ± 0.16
25	0.054	0.04 ± 0.01	0.946	0.34 ± 0.12	0.000	0.62 ± 0.13
26	0.34	0.68 ± 0.15	0.33	0.22 ± 0.09	0.330	0.11 ± 0.08
27	0.01	0.009 ± 0.01	0.30	0.35 ± 0.11	0.690	0.64 ± 0.11
28	0.15	0.21 ± 0.06	0.25	0.45 ± 0.09	0.600	0.34 ± 0.10
29	0.34	0.86 ± 0.19	0.33	0.13 ± 0.14	0.330	0.01 ± 0.13
30	0.01	0.02 ± 0.01	0.30	0.46 ± 0.12	0.690	0.52 ± 0.12
31	0.15	0.23 ± 0.10	0.25	0.47 ± 0.08	0.600	0.31 ± 0.10
32	0.70	0.88 ± 0.10	0.15	0.11 ± 0.07	0.150	0.01 ± 0.04
33	0.80	0.92 ± 0.09	0.10	0.08 ± 0.06	0.100	0.01 ± 0.03
34	0.05	0.08 ± 0.02	0.05	0.49 ± 0.07	0.900	0.43 ± 0.08
35	0.45	0.89 ± 0.12	0.10	0.03 ± 0.09	0.450	0.08 ± 0.04
36	0.049	0.04 ± 0.01	0.436	0.52 ± 0.14	0.515	0.44 ± 0.14
37	0.049	0.03 ± 0.01	0.436	0.51 ± 0.03	0.515	0.47 ± 0.04
38	0.049	0.05 ± 0.02	0.436	0.58 ± 0.20	0.515	0.37 ± 0.20
39	0.00	0.002 ± 0.01	0.012	0.38 ± 0.07	0.988	0.62 ± 0.07
40	0.00	0.00 ± 0.01	0.012	0.13 ± 0.10	0.988	0.87 ± 0.10
41	0.009	0.01 ± 0.01	0.136	0.43 ± 0.03	0.855	0.56 ± 0.03
42	0.03	0.03 ± 0.01	0.262	0.43 ± 0.17	0.708	0.55 ± 0.17
43	0.04	0.04 ± 0.03	0.298	0.31 ± 0.16	0.664	0.65 ± 0.17

Table 3.9: Theoretical versus recovered percentages of young (0 to 1.5 Gyr), intermediate (1.5 to 10.0 Gyr), and old (10.0 to 17.8 Gyr) components after applying GANDALF and STECKMAP to the mock spectra generated with the MILES IAC webtools. The values are normalised to a total mass of 1.

Before drawing general conclusions from these tests we must note that we use spectra mimicking the stellar emission coming from SFHs with very different parametric shapes (see Tables 3.6 and 3.7), i.e. idealised SFHs. Although we have tried to make them more realistic by adding some emission lines and noise (to match the CALIFA quality), these spectra are still far from what we observe in nature. Therefore, the recovery of the stellar content from such idealised spectra is very difficult using present stellar population recovery codes as they are optimised to deal with real data (Cid Fernandes, private communication). Bearing that in mind, in Fig. 3.15 we represent the recovered age and metallicity values as a function of the theoretical ones for all the tests. In most of the cases the L-W age values are reasonably well recovered, with the real values mostly within the error bars of the computed quantities. Mass-weighted age values are more difficult to obtain but the trend of larger ages for older spectra is found. Even more difficult is the recovery of the exact metallicity values. However, although finding exact values seems to be hampered, we are able to extract the tendency, for spectra from metal-poor stellar content we obtain lower metallicities (see Table 3.8 and Fig. 3.15).

We went a step further and we also checked the recovery of the mass fraction for different subpopulations (see Table 3.9). In some cases, the agreement between the computed fractions and the theoretical input is astonishing (see tests 3, 8, or 27, as examples). However, some other cases display very large differences (tests 16 or 35). However, these are extreme cases, the general tendency is an overall good agreement with discrepancies that are larger than the error bars in some cases.

Another important aspect to be checked and that substantially affects works studying the stellar content in galaxies is the age-metallicity degeneracy. Sánchez-Blázquez et al. (2011) proved that this degeneracy is highly minimised when using `STECKMAP` rather than line strength indices. The positive correlations found in Fig. 3.15 further demonstrate that this degeneracy is minimised with this method. However, we should warn the reader that, although we have extensively tested this method against such degeneracy, some effects might still remain.

3.3 Concluding remarks

In this section we have explained the processing of the CALIFA data to recover the stellar content of the analysed sample of galaxies. In addition, we have extensively tested this procedure in two well differentiated ways:

1. First (see Sect. 3.2.1), we have studied the SFH and the AMR of the LMC bar using two distinct approaches to analyse the stellar content in galaxies: resolved and integrated stellar populations. We compare the results from the reconstruction of an observed CMD reaching the

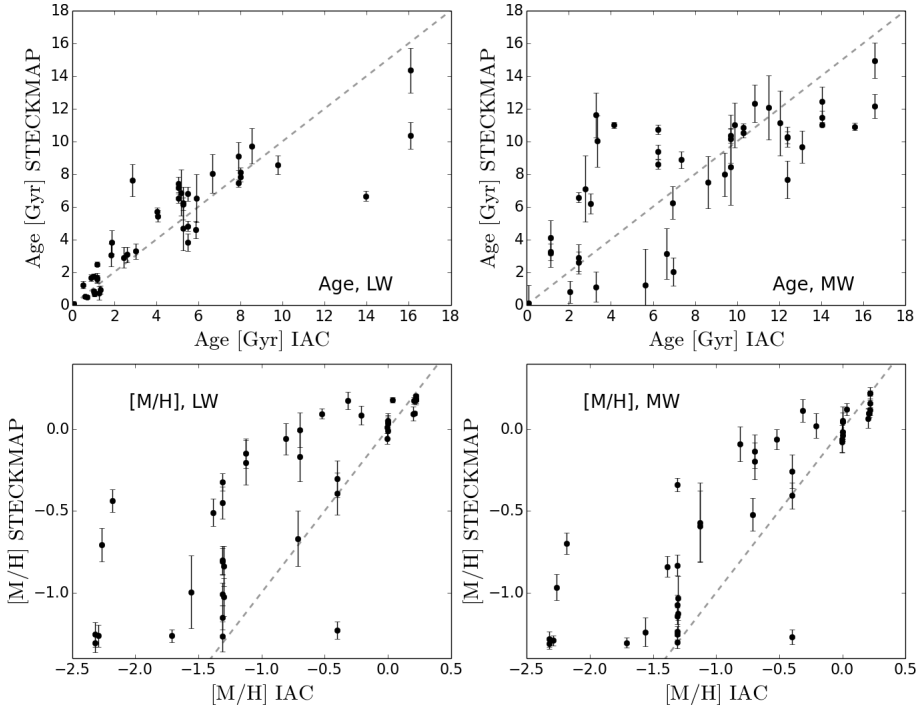

Figure 3.15: Age and metallicity recovery after applying `GANDALF` and `STECKMAP` to the spectra generated with the IAC `MILES` webtools. Top panels: a representation of the recovered L-W (left panel) and M-W (right panel) age as a function of the theoretical age from parametric SFHs. Bottom panels: a representation of the recovered L-W (left panel) and M-W (right panel) [M/H] as a function of the theoretical [M/H] from parametric SFHs. The dashed grey lines represent the one-to-one relation.

oMSTO, obtained from WFPC2 data from the HST, with the results from the spectral fitting of an integrated spectrum taken at the 3.6 m ESO telescope on La Silla, using EFOSC2. Owing to the relatively high surface brightness of the LMC bar and its close proximity, the chosen field is a unique one in which both an accurate, deep CMD and a high quality spectrum can be obtained. We have applied state-of-the-art models, stellar libraries, isochrones, and codes following each approach in order to derive the SFR (t) and AMR of this bar field. Although focused on `STECKMAP` as the main ingredient of the here described and tested procedure, other codes (`ULySS`, and `STARLIGHT`) have been also used to recover the stellar content from the integrated spectrum and the results compared to the CMD analysis. The analysis of the integrated spectrum using each code has been performed in a consistent manner, and in an effort to avoid any biases in the solutions the CMD analysis was performed independently from the spectral analysis.

The best agreement between the integrated spectrum analysis and the CMD analysis was found using `STECKMAP`, the only full spectrum fitting code that we tested with a penalisation implemented. `STECKMAP` produces SFR (t) and AMR in good agreement with those obtained from the CMD. This code minimises the impact of the age-metallicity degeneracy and has the advantage of preferring smooth solutions to recover complex SFHs by means of a penalised χ^2. All the spectral fitting codes used in this study are normally used with SSPs as spectral templates. `ULySS` and `STARLIGHT` do not use any penalisation and, as a consequence, solutions dominated by episodic bursts are derived if SSPs are used as spectral templates. `ULySS` is able to reproduce the overall shape of the SFR (t) but with bursts of star formation. However, this code is not able to reproduce the AMR, especially at young ages. `STARLIGHT` is able to approximately reproduce the AMR (except at the youngest ages), but has problems with the shape of SFR (t), especially at intermediate ages where no equivalent contribution in the CMD is found. We have been able to improve these results (both with `ULySS` and `STARLIGHT`) by using a set of complex spectral templates constructed adopting a constant SFR (t) in bins of log-spaced ages instead of SSPs. This suggests that complex SP templates, rather than simple SP spectral templates should be preferred when analysing the stellar content of composite stellar systems.

This is the first time that the results of these two different approaches for studying stellar populations in galaxies have been compared for an object with a complex SFH, and for which a CMD reaching the oMSTO could be obtained. Such studies are of crucial importance in order to test recent advances in the field, especially in the analysis of

the integrated stellar populations. Important ongoing and upcoming projects such as CALIFA (Sánchez et al. 2012a), SAMI (Croom et al. 2012), or MANGA (Law & MaNGA Team 2014) will make use of these techniques to study the formation and evolution of galaxies.

2. Second (see Sect. 3.2.2), we have obtained mean ages and metallicities, as well as mass fractions for three different stellar subpopulations, studying mock spectra with a known SFH matching the quality of the CALIFA spectra. The values for the mean ages are well recovered (especially the L-W ones). However, we cannot reconstruct the exact values for the metallicities but, at least, we were able to recover the general trend, i.e. lower metallicities are found for those spectra created from low metallicity stars than for high metallicity stars. The recovery of the stellar subpopulation fractions is a more difficult task, especially considering that we are analysing idealised spectra, but our results are quite reassuring obtaining good agreement between the theoretical input and the recovered values.

   We should also highlight that the stellar population models that we use in this method (V10) include ages ranging from 0.063 to 17.8 Gyr, i.e. stars older than the Universe. The agreement between the recovered and theoretical age values in this set of tests is partly based on the fact that both stellar templates and mock spectra, are based on stars with the `MILES` age range. However, if we plan to apply this method to real data, where the maximum permitted stellar age is $\sim$ 13.5 Gyr (the age of the Universe), we should consider that this might have an impact in the exact age values that this method gives.

   Therefore, we conclude that the mean age and metallicity values derived with the method developed in this thesis can be different to the real values. However, based on these tests, we can guarantee that relative differences, and thus, radial tendencies (if we analyse spectra at different radii, as we do in this thesis) can be recovered. Therefore, we can claim that this method is appropriate for the objective of this thesis as we are mainly focused on stellar age and metallicity radial profiles on the sample of galaxies under analysis.

Chapter 4

Stellar content in disc galaxies

"Scientific theory is never regarded as certain; it's continually confronted with testing, asking if it can explain what we can see in nature. That work is never finished. There are always some things left that haven't yet been explained. That's true of physics as well as biology... This work goes on and on – it's not a weakness of the theory. I don't regard it as a weakness of my own work that it hasn't explained everything in elementary particle physics."
— Steven Weinberg

Contents

The interpretation of processed data is the last stage in the course of any scientific study aiming to understand nature. In our field of study, astrophysicists observe the Universe around them, manipulate data collected at large telescopes, and infer the physical properties characterising the objects under study. All those physical properties are the main pieces of a complex puzzle. The task of astrophysicists is to match all those pieces together and interpret the results to reach to the comprehension of the original problem; how nature works.

In the previous chapters we have explained how we obtain the radial stellar content as well as colour profiles for the spiral galaxies studied in this thesis. This is the first time that reliable stellar population information up to the outer parts of a large sample of disc galaxies is gathered relating them with SB profiles. All this information needs to be interpreted with the aim of shedding some light into the topic of the building-up of the outskirts of spiral galaxies. In this chapter we collect all this information and try to infer constraints to theoretical models seeking a plausible scenario for the formation of the outer parts of disc galaxies.

4.1 “U-shape” age profiles

In the recent years the analysis of the stellar content in the outer parts of spiral galaxies has gained in importance (see Chapter 1 and references therein). Theoreticians have developed elaborated models up to the disc outskirts including processes affecting these outermost regions such as radial migration or satellite bombardment. Observers push telescopes and instruments to their limits to obtain high quality information from these faint regions. However, there is still much to understand in this topic. For instance, although there is a tendency to claim that galaxies displaying downbending light distributions also present “U-shape” age profiles or a radial colour outer reddening (e.g. Bakos et al. 2008; Roškar et al. 2008b), to date, there are no clear observational evidences of a correlation between SB and other stellar parameters such as age (e.g. Yoachim et al. 2012). In this section we focus on the behaviour of the observed age profiles in the outer parts of the sample of galaxies under study to relate such behaviour with the different observed SB profiles.

First of all, we must define *outer parts*. We use the break radius as the transition point between the inner and the outer disc. Thus, we consider that we are analysing the outskirts of the analysed galaxies if we have stellar population information beyond around three disc scale-lengths (for type I galaxies) and beyond their break radius (for type II and III galaxies). For type I galaxies we have decided to use this limit ($\sim 3\ h_{in}$) as breaks for type II and III galaxies seem to be located around such galactocentric distances. However, this analysis is not always possible. Observational constraints

such as the limited field of view or low S/N in the outer parts hamper the reliable stellar populations recovery up to the outer regions, leaving us with a sample of 68 galaxies (out of the 88 analysed systems) for which this study is feasible. Those galaxies are marked in Table A.2 with a star.

Therefore, in this section we study the radial age distribution up to the outer parts of this subset of 68 spiral galaxies and relate these profiles to their SB distributions. From this reduced sample, only four of the analysed galaxies display a type III SB profile (not showing any signs of age upturn). As a consequence, we can only achieve statistical results for type I and II galaxies.

We find that 29 galaxies ($\sim$ 43 %) out of the 68 comprising the analysed sample show clear "U-shapes" in the L-W age profile regardless of their SB distribution (11 type I and 18 type II galaxies, see Fig. 4.1). For these galaxies we show the position of the minimum in age (R_{min}/h_{in}) in Table A.2 (see Appendix A). Such "U-shape" disappears for all cases for the M-W age values, displaying a flatter and almost constant distribution along the whole disc. The differences between L-W and M-W age tendencies suggest that recent star formation is an important driver in shaping the L-W age profile. The mean M-W age value, averaged over the entire disc (avoiding the inner region, $R_{lim,in}$), is 10.6 $\pm$ 0.6 Gyr. This flatness of the M-W age profile has been previously found in previous works (MacArthur et al. 2009; Sánchez-Blázquez et al. 2014; González Delgado et al. 2015). In particular, in González Delgado et al. (2015) the authors find a correlation with morphological types: early-type galaxy discs tend to be older than late-type ones. In Fig. 4.2 we show the values of the average M-W age for the galaxies for which we obtain reliable stellar information up to the outer parts as a function of morphological type (T parameter). As it is shown in that figure, we do not find any correlation with morphology as found in González Delgado et al. (2015). The 39 galaxies with no "U-shape" L-W age profiles present different behaviours with no clear pattern (see Appendix B). Figure 4.1 shows the L-W (blue circles) and M-W (red squares) age profiles for a type I galaxy (NGC0551) and a type II (NGC4711) along with their 1D light distributions from the analysis of the SDSS data (grey continuous lines and right-hand axis, see Sect. 2.3). In these two examples we can clearly distinguish the "U-shape" L-W age profile and the flattening displayed in the M-W case with no distinction in the SB profile type.

This is the first time that "U-shaped" age profiles are found indistinctly in type I and II galaxies from spectroscopic data. To date, such profiles had been found (observationally and theoretically) just in type II galaxies (Roškar et al. 2008b; Bakos et al. 2008; Sánchez-Blázquez et al. 2009; Yoachim et al. 2012). As part of this thesis, we also analyse cosmological simulations of Milky Way like galaxies finding that this age upturn is more common than expected (see Chapter 5 and Appendix D). An important result from this observational analysis to constraint galaxy formation models

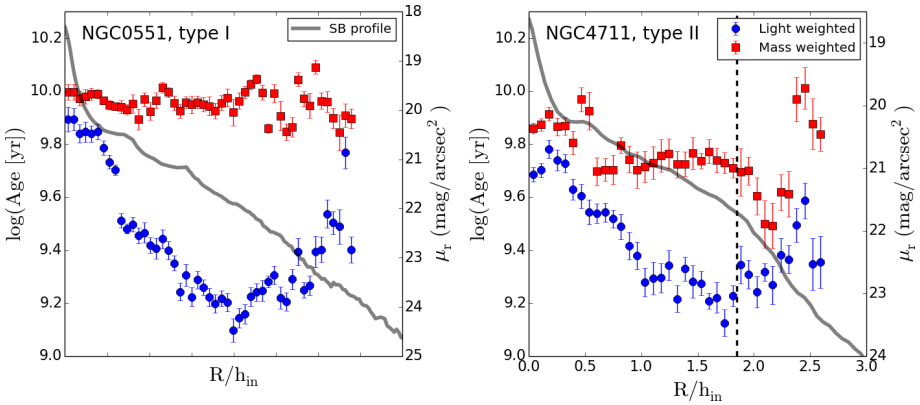

Figure 4.1: Stellar ge radial profile in logarithmic scale and surface brightness profile (SDSS r-band) for NGC 0551 (left panel, type I) and NGC 4711 (right panel, type II). Red (blue) squares (points) indicate mass-weighted (light-weighted) values. The black dashed line is located at the break radius. Grey continuous lines corresponds to the SB profiles (see right y-axis).

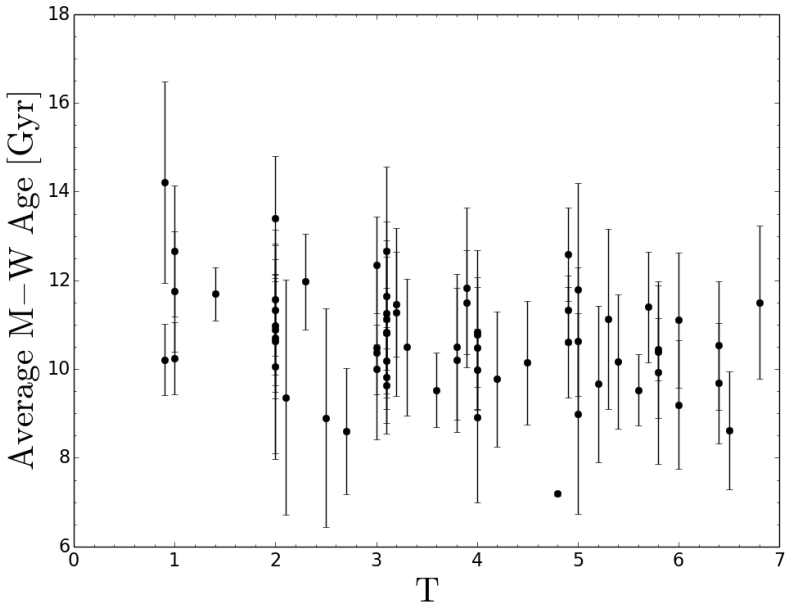

Figure 4.2: Mean disc M-W age as a function of morphological type for the galaxies for which reliable stellar content has been derived up to the outer parts. Black dots represent the different galaxies. Errors are calculated as the standard deviation of the radial M-W age values taking into account the errors in each point.

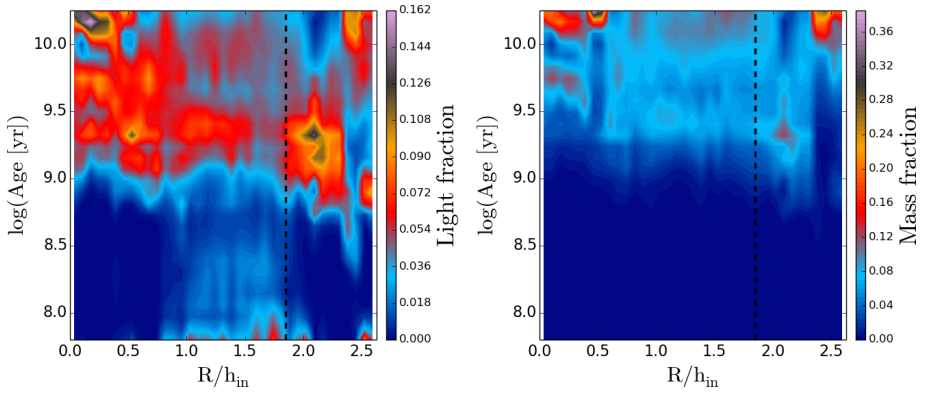

Figure 4.3: Radial stellar age distribution for NGC 4711: left panel, luminosity-weighted; right panel, mass-weighted. The black dashed line is located at the break radius. See text for further information.

is the fact that not all the analysed galaxies display an "U-shape" in the age profile (although it can be an observational artifact due to the limited field of view of the instrument) and it appears in both type I and II. These findings allow us to conclude that the mechanisms responsible for the presence of a break in the SB distribution are not coupled to those shaping the stellar age profile. Thus, this work seems to mitigate the statement that breaks are necessarily linked to changes in the stellar population age. In other words, older outer discs do not necessarily lead to type II SB profiles. This observational fact can be used to further constraint numerical simulations. Other aspects must be responsible for the observed SB profiles such as star formation thresholds (Kennicutt 1989), magnetic fields influence (Battaner et al. 2002), radial redistribution of material caused by non-axisymmetric instabilities (e.g. Debattista et al. 2006), multicomponent star formation prescriptions (Elmegreen & Hunter 2006) or the host halo's initial angular momentum (Herpich et al. 2015a,b). We must highlight though, that the lack of universality of "U-shaped" age profiles might be a consequence of the limited field of view. The age upturn might be present in all galaxies but located at larger galactocentric distances and thus, not observed in this work. To check this likely possibility similar studies must be carried out ensuring reliable analysis of the stellar content in the outermost regions.

It is also important to note that the "U-shape" age profiles shown in simulations are M-W quantities. However, the observed M-W profiles show no sign of "U-shape" at all, suggesting that star formation in simulations has been higher at later times than in real galaxies. We have also tested the existence of any correlation between the "U-shape" occurrence with other properties such as morphology, galaxy mass, and bar presence. Although we do not find any pattern among these properties, we should highlight that we suffer from low number statistics and this point should be further

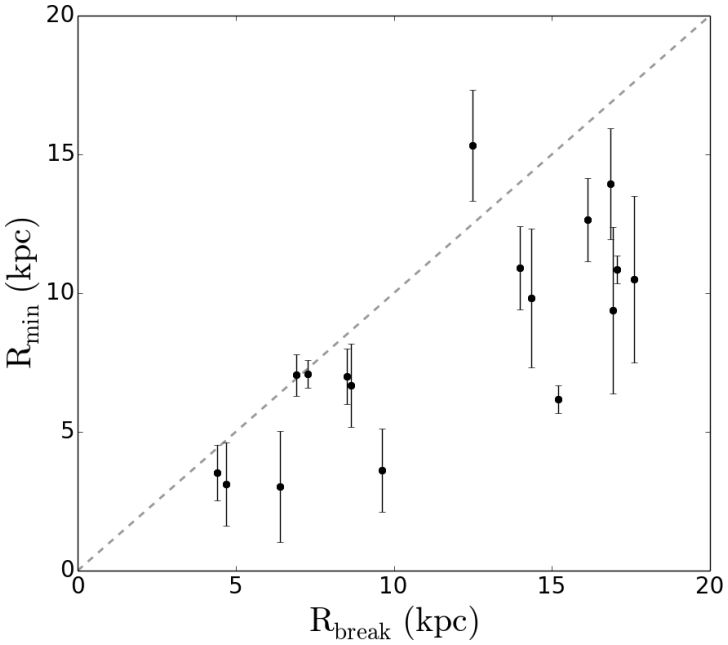

Figure 4.4: Location of the minimum in age (R_{min}) as a function of the break radius (R_{break}) for the galaxies displaying “U-shape” age profiles. The dashed grey line represents the one-to-one relation.

investigated with a larger number of galaxies.

The location of the minimum in age with respect to the position where discs bend is another interesting point to discuss. In most of the cases, the observed minimum age is located prior to the break radius, with the exceptions of NGC 6478 with the minimum in age located after the break and MCG-01-10-015 and NGC 4711 with the minimum in age located at the position of the break (see Fig. 4.4). In the literature there is no clear consensus about a possible link between the location of the break in the light distribution and the minimum in age, neither from observations nor from theoretical works. While some works point towards younger stars (bluer colours if they are based on photometric data) located exactly at the break radius (Roškar et al. 2008b; Bakos et al. 2008; Marino et al. 2016) others claim that such minimum age is found prior to it (Sánchez-Blázquez et al. 2009; Yoachim et al. 2012) or with no relation at all (Roediger et al. 2012). The results presented in this section suggest that the minimum in the age profile does not seem to match the position of the break.

In Sect. 2.3.2, we made use of the 1D SDSS SB profiles to compute the colour profiles of the studied sample of galaxies. Now, we perform a one-to-one comparison of the shape of the age and colour profiles computed in this thesis paying special attention to the “U-shape” occurrence. We find that the existence of “U-shaped” age profiles do not necessarily imply the

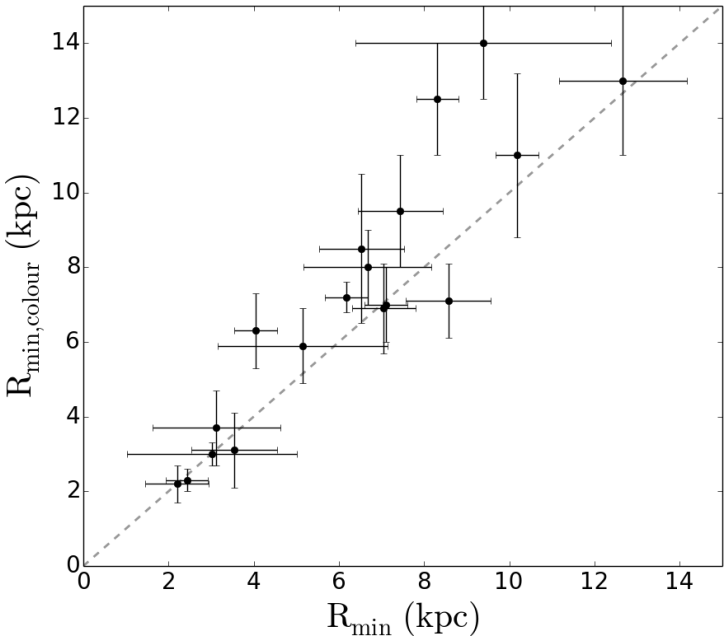

Figure 4.5: Location of the minimum in the colour profiles ($R_{min,colour}$, mean $R_{min,colour}$ value considering the colour profiles for which a "U-shape" is identified; i.e. $g-r$, $g-i$, and/or $r-i$) as a function of the location of the minimum in age (R_{min}) for the galaxies displaying both "U-shape" age and colour profiles. The dashed grey line represents the one-to-one relation.

same behaviour for the colour profiles. Some galaxies (IC1683, NGC0873, NGC5267, UGC02099, and UGC12653) exhibit a reddening in the outer parts even when the age profile does not display such outer ageing. In the cases of galaxies displaying "U-shaped" age profiles, 31 % of them also show a reddening in all analysed colour profiles ($g-r$, $g-i$, and $r-i$), while for 38 % of them this outer reddening is not detected. For the rest of "U-shaped" galaxies (31 %), this outer reddening is just observable in the $g-i$ and $r-i$ colour profiles, i.e. in those colours where the reddest SDSS filter is considered (i SDSS band). In Fig. 4.5 we compare the position of the minimum in age (R_{min}) with the mean location of the minimum in any of the analysed colour profiles ($g-r$, $g-i$, and/or $r-i$, $R_{min,colour}$) for those galaxies displaying both "U-shape" age and colour profiles. The $R_{min,colour}/h_{in}$ values can be found in Table A.2 (see Appendix A). The found relation is close to the one-to-one, with the minimum in the colour profiles generally located at larger galactocentric distances than the minimum in the L-W age profile. In addition, the scatter in the points tends to be larger if these features are located further out.

Apart from radial profiles of averaged quantities (age and metallicity), the stellar content analysis carried out in this thesis also provides spatially-resolved stellar age distributions (see Appendix B). Figure 4.3 shows the

L-W and M-W versions of such spatially-resolved stellar age distributions for NGC 4711. In this representation we encode with a colour bar the light (left) or mass (right) fraction of stellar populations of different ages (y-axis) located at different galactocentric distances (x-axis). Violet colours denote populations with higher contribution to the total radial light or mass while blue colours indicate lower contributions. We normalise these distributions in such way that the sum of all the light or mass fractions at a given radial distance is 1. As we have to take into account that stars do not remain at their birth locations but might undergo radial inwards and outwards incursions, these stellar age distributions cannot be interpreted as SFHs. However, its analysis might give us important insights on how galaxies have been built. L-W stellar age distributions are more sensitive to young stellar populations, and thus, they can help us to understand how recent star formation proceeded; M-W quantities are more sensitive to the mass-dominating old components and thus, they can provide with more general information as well as information about star formation at earlier epochs.

The observed L-W radial stellar age distributions (see example in left-hand panel of Fig. 4.3 and Appendix B) for the 68 galaxies show clear evidences suggesting that star formation in them have been quenched inside-out (i.e. inner regions mainly dominated by old stars, with young stars becoming more important as we move outwards), in agreement with previous CALIFA works on the stellar mass growth (Pérez et al. 2013), stellar populations radial profiles (González Delgado et al. 2014; Sánchez-Blázquez et al. 2014; González Delgado et al. 2015) and gas abundance gradients (Sánchez et al. 2012b, 2014; Sánchez-Menguiano et al. 2016). Apart from that, an outermost old stellar component appears again for those galaxies presenting "U-shape". On the other hand, the M-W radial stellar age distributions (see example in right-hand panel of Fig. 4.3) do not show any population younger than 2 Gyr with the bulk of stars being $\sim$ 10 Gyr old suggesting that an old underlying disc is present along the entire disc of all the analysed galaxies.

This work supports recent observations finding old outer discs (e.g. Bernard et al. 2012, 2015; Radburn-Smith et al. 2012), pointing towards an early star formation along the entire disc followed by an inside-out quenching of the star formation as the cause of the age upturn. However, we cannot rule out other scenarios considering the effects of other mechanisms (radial migration, different star formation recipes, satellite accretion, etc.) shaping different SB profiles after the age profile is built.

4.2 Stellar population inner gradients

At this point the reader may have noticed that the analysis of the stellar populations in the outer parts of spiral galaxies is an essential element to

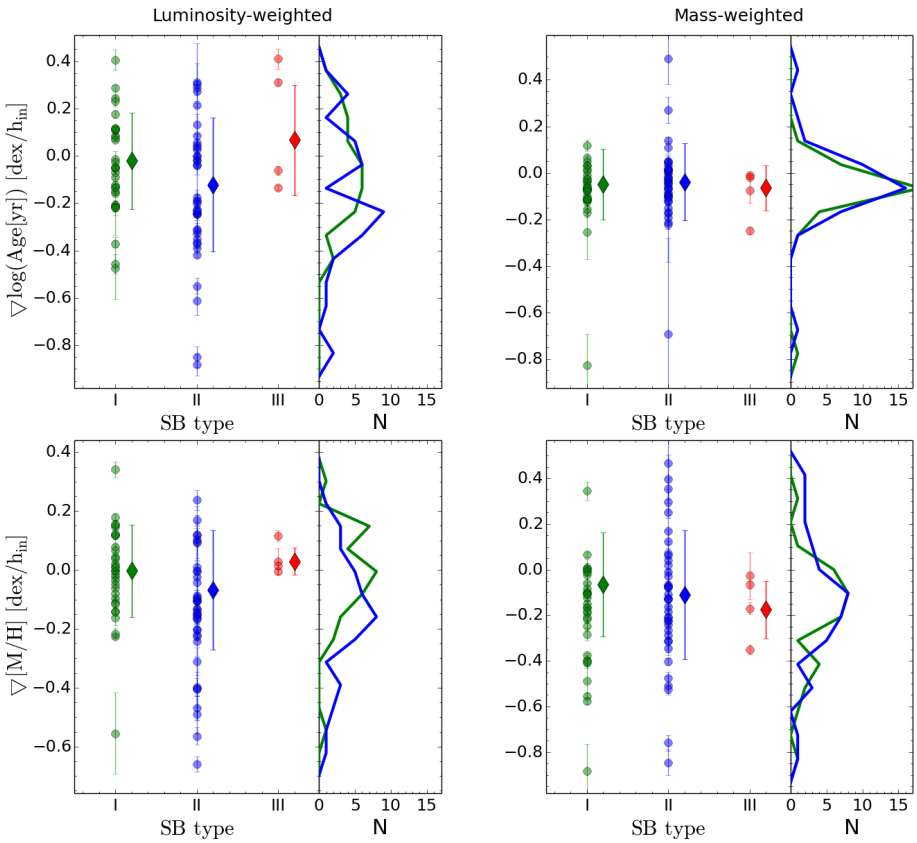

Figure 4.6: Distribution of the inner gradients of the log(age[yr]) and [M/H] profiles as a function of the surface brightness profiles of the galaxies. We also show the histograms for each distribution colour coded according to the SB type: type I (green), type II (blue), and type III (red). Top-left: L-W age; top-right: M-W age; bottom-left: L-W [M/H]; bottom-right: M-W [M/H]. Dots represent the observational values while diamonds indicate the error-weighted average values and their dispersions, we have applied a x-shift to the average values for clarity purposes.

decipher the formation of the galactic outskirts. However, such analysis is not straightforward and it is highly hampered by different aspects as commented in the previous section (instrumental field of view, low SB of these regions, etc.). In particular, we could analyse the outermost regions for around the 77 % of the sample of galaxies (68 out of the 88 analysed galaxies). The analysis of the stellar content in the inner regions is a more accessible task and it might also give us valuable information about the processes building the outskirts of spiral galaxies.

We know from previous works that stellar radial migration do exist in spiral galaxies. Recent galaxy simulations claim that stars do not remain at their birth location but radially migrate due to the effects of different possible processes, such as the spiral structure interacting with the central bar (Minchev & Famaey 2010; Minchev et al. 2011, 2012b), transient spiral arms (Sellwood & Binney 2002; Roškar et al. 2008b,a), magnetic fields (Battaner et al. 2002), or satellite accretion (Younger et al. 2007; Quillen et al. 2009; Bird et al. 2012). In fact, a good number of theoretical works have also tried to quantify how important this migration is (see Chapter 1 and references therein); however, migration still remains a matter of debate.

In addition, some works have tried to assess to what extent radial migration is important in shaping the SB profiles and other stellar population properties. In Roškar et al. (2008b), the authors claim that a radial star formation cutoff and a radial redistribution of stars would result on the observed type II profiles and an age upturn. Sánchez-Blázquez et al. (2009), analysing cosmological simulations studied the effect of suppressing radial migration in the shape of the age and surface mass density profiles in their warped simulated disc. They found that the absence of radial motions changes the surface mass density profiles from type I to type II (see figure 16 of that paper). In addition, the authors speculate that different combinations between radial changes in the star formation slope (linked to differences in the gas volume density due to a warp) and different radial migration efficiencies might explain the presence of type I, II, and III profiles. A smooth radial change in the star formation would lead to type I galaxies, while differences in the radial migration efficiency would lead to type II (low efficiency) or type III (high efficiency) systems. Nevertheless, the real role of radial migration still remains a mystery.

However, regardless of how important radial migration is or if different radial migration efficiencies shape different SB types, what is clear is that, if radial redistribution of material is important, it must have an effect in the stellar content of the inner and the outer regions, and thus, galaxies displaying different degrees of radial migration efficiency should display differences in their inner stellar content. Therefore, the analysis of the inner stellar age and metallicity gradients segregating in the different SB profile types can help us to shed light into the role of radial migration in the shaping of the stellar parameter and the light distribution profiles.

	SB profile		
	Type I	Type II	Type III
L-W age	-0.02 ± 0.20	-0.12 ± 0.28	0.07 ± 0.23
L-W metallicity	-0.00 ± 0.16	-0.07 ± 0.20	0.03 ± 0.05
M-W age	-0.05 ± 0.15	-0.04 ± 0.16	-0.06 ± 0.10
M-W metallicity	-0.06 ± 0.23	-0.11 ± 0.28	-0.18 ± 0.13

Table 4.1: Error-weighted average and dispersion values of the inner gradients for the stellar age and metallicity (see text for details). Units are in dex/h_{in}.

To test such hypothesis, Fig. 4.6 shows the distribution of the inner gradients of the log(age[yr]) and [M/H] profiles (L-W and M-W) according to the SB profiles of the galaxies under analysis (see Tables A.3 and A.4 in Appendix A). This analysis has been conducted using a subset of 76 galaxies from the original sample of 88 galaxies as there are several factors hampering the computation of the inner gradients (see Sect. 3.1.3 about the calculation of these gradients): i) the avoided central region is larger than the radial coverage with the CALIFA data (ESO540-G003, NGC1211, NGC6186, NGC7738, UGC02403, UGC05396, UGC10796, and UGC11740); ii) we have less than 4 data points to perform the linear fit within the chosen radial range (NGC5888, NGC6394, and UGC01659), i.e. the region between the end of the avoided central region and the onset of the outer region (R_{break}) or the limit of the valid data ($R_{lim,out}$) or iii) problems with the CALIFA data (UGC00139). All this information is detailed for each particular galaxy in Tables A.3 and A.4 in Appendix A. Fig. 4.6 shows very similar gradient distributions (age and metallicity, L-W and M-W), especially for type I and II galaxies. We must highlight that, despite the low number of type III galaxies, the inner gradient distribution for these galaxies seem to be also drawn from the same distribution as type I and II galaxies. The actual values for the error-weighted average gradients and their dispersions are shown in Table 4.1.

The similar average values and the large dispersions suggest that there are no differences in the inner gradients between type I, II, and III galaxies. To quantify such statement, we make use of two different statistical tests used to check if these distributions are drawn from the same one, the Kolmogorov-Smirnov (KS) and the Anderson-Darling (AD) tests. These tests are used to compare two samples and provide estimations on how different these two distributions are by means of a parameter called *p-value*. If this statistical parameter is below a significance level (generally ~ 0.05) then, we can reject the *null hypothesis*, i.e. we can conclude that the two samples are drawn from different distributions. KS tests seem to indicate that the observed distributions are basically identical, with high p-values (~ 0.4 on average among tests). However, this test is suited for samples with larger

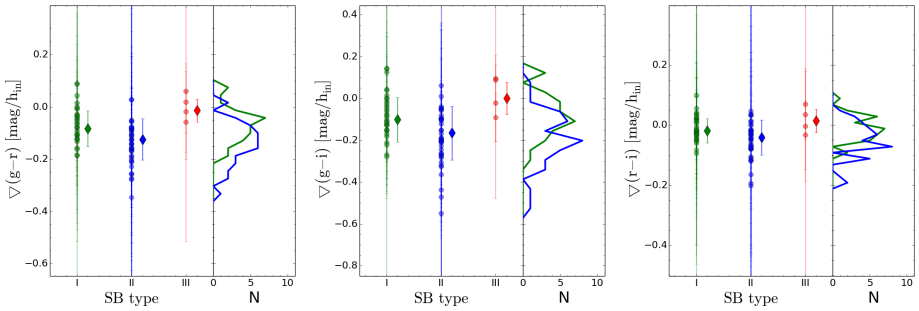

Figure 4.7: Distribution of the inner $g-r$ (left), $g-i$ (middle), and $r-i$ (right) colour gradients as a function of the surface brightness profiles of the galaxies. We also show the histograms for each distribution colour coded according to the SB type: type I (green), type II (blue), and type III (red). Dots represent the observational values while diamonds indicate the error-weighted average values and their dispersions, we have applied a x-shift to the average values for clarity purposes.

statistics. We also use the AD test, better suited for small samples like the studied here, arising similar results, i.e. the samples are drawn from the same distribution. Although this statistical test shows that some distributions (such as the inner gradients of the light-weighted metallicity for type I and II) might be different (p-value of 0.04), the p-value is still close to the significance level in those cases. Therefore, to be able to claim differences among distributions (if present) a larger sample needs to be studied.

Our hypothesis states that if migration is capable of redistributing a sufficient mass fraction as to affect the observed inner stellar content, and different radial migration efficiencies affect the shaping of the outer light distributions, galaxies with different SB profiles should display differences in their inner stellar age and metallicity gradients. Because we do not find any difference in the inner stellar age and metallicity gradients for the different SB profiles it implies that if radial migration is the main driver for the shaping of the outer SB profiles, the percentage of mass moved to the outer parts must represent a small fraction of the total disc stellar mass. However, it could also imply that there are more processes involved in the formation of the outer parts than migration, in agreement to what found in Sect. 4.1.

In any case, these observational results help us to constraint future theoretical works studying the origin of the outskirts of spiral galaxies. We can conclude that regardless of the role of radial migration in shaping the observed SB profiles, it does not transport a substantial amount of stellar mass.

4.2.1 Inner colour gradients

Historically, several works studied the stellar populations in external systems by means of colours (e.g. Peletier 1989; de Jong 1996; Peletier & Balcells 1996; Jansen et al. 2000; Bell & de Jong 2000; MacArthur et al. 2004; Muñoz-

	SB profile		
	Type I	Type II	Type III
$g-r$	-0.08 ± 0.07	-0.12 ± 0.08	-0.02 ± 0.04
$g-i$	-0.10 ± 0.10	-0.17 ± 0.13	0.00 ± 0.08
$r-i$	-0.02 ± 0.04	-0.04 ± 0.06	0.01 ± 0.04

Table 4.2: Error-weighted average and dispersion values of the inner gradients for the $g-r$, $g-i$, and $r-i$ colour profiles (see text for details). Units are in mag/h_{in}.

Mateos et al. 2009, among many others), obtaining that the outer parts of disc galaxies tend to be bluer. In these works colours are interpreted as a proxy for the stellar age. Although we know that drawing stellar population information from colours is highly degenerated (Ganda et al. 2009), we have also studied the colour inner gradient distribution for type I, II, and III galaxies for the sake of completeness. The larger field of view of the SDSS data allows us to reach further out for the colour profile recontruction than for the stellar content (see Sect. 2.3.2). However, for a fair comparison, we have decided to restrict the colour gradient fit to the stellar populations outer limit ($R_{lim,out}$, see Sect. 3.1.3). Figure 4.7 shows the distribution of the inner gradients for the $g-r$, $g-i$, and $r-i$ colour profiles (numerical values can be found in Table A.5 in Appendix A). The error-weighted mean values of the inner gradient distribution for the $g-r$, $g-i$, and $r-i$ colour profiles are given in Table 4.2. Although these averaged values and their errors suggest that the three distributions are very similar, a visual inspection hints some small differences. To test if those differences are significant or not we use again the KS and AD statistical tests. Relatively low p-values are found using the KS test when comparing the colour inner gradient distributions for type I, II, and III galaxies (lower than 0.04 in all cases), suggesting that both samples could be drawn from different distributions. On the other hand, AD tests (better suited for small samples of galaxies) seems to point towards colour gradients for type I and II galaxies being drawn from different distributions (p-values as small as 0.005). Then, we can conclude that the colour profile inner gradient distributions for type I, II, and III galaxies seem to be more different than in the case of the stellar populations (see Sect. 4.2). However, larger samples of galaxies need to be studied to draw stronger conclusions. The question that arises now is whether colours can be really used as a good proxy for the stellar age or not.

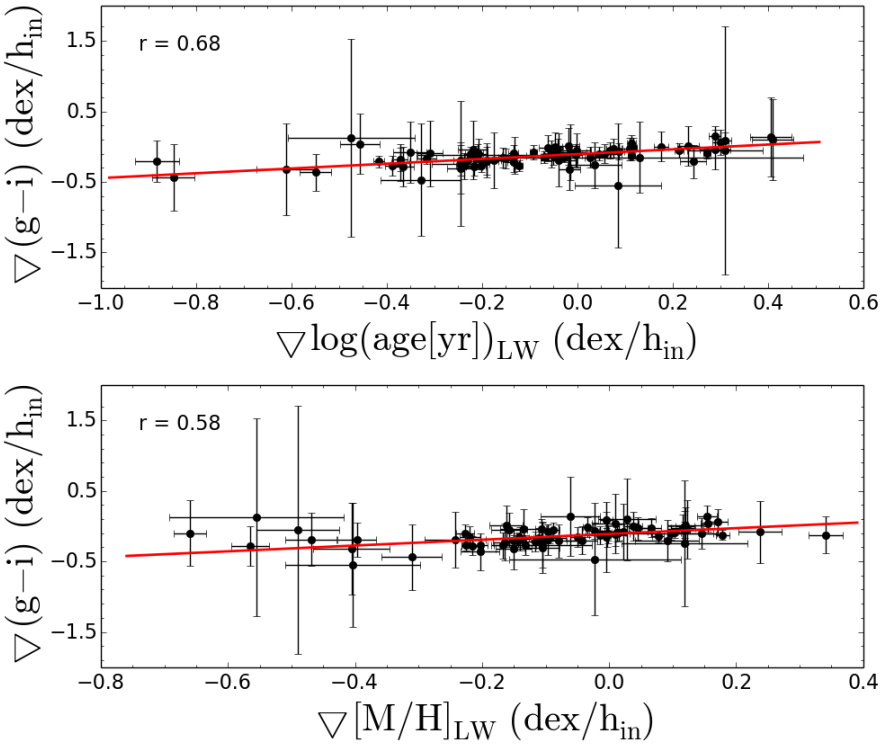

Figure 4.8: $g-i$ colour inner gradients as a function of the light-weighted age (top) and metallicity (bottom) inner gradients for the analysed sample of galaxies. The red solid line represents a linear fit to the cloud of points. Note that we can outline a positive trend between both magnitudes with the highest values of the light-weighted age inner gradients displaying also the highest $g-i$ colour inner gradient values. The correlation coefficients in both cases are 0.68 (age) and 0.58 (metallicity).

4.3 Colour trends as a proxy for stellar age and metallicity

We know that, although the age-metallicity degeneracy is present in the study of the stellar populations based on both colours and spectroscopic data, it is highly minimised when using the second kind of data (Sánchez-Blázquez et al. 2011). As part of this thesis we have computed colour profiles from SDSS (see Sect. 2.3.2) and stellar age and metallicity profiles from spectroscopic data (see Sect. 3.1.3) up to large galactocentric radius. This allows us to compare both sets of profiles to assess the validity of analysing colour profiles as a proxy for stellar populations. The analysis is now performed on a galaxy-by-galaxy base, in contrast to the general and statistical trends analysed in Sect. 4.2.

The number of works confronting colour information with stellar ages and metallicities or line-strength indices is very limited, and basically concentrated on general properties of the galaxies. In Ferguson (1994), the author compared line strength indices and global colours (colour–line-strength diagrams) for dwarf elliptical galaxies, not obtaining conclusive results. den Brok et al. (2011) went a step further in this comparison and tried to relate colour and line index profiles rather than just global values of these properties. They used deep, high-spatial-resolution images from the Advanced Camera for Surveys (ACS) mounted at the HST to obtain high-quality colour gradients and compared them with literature Mgb gradients (Mehlert et al. 2003; Sánchez-Blázquez et al. 2006a; Kuntschner et al. 2010), finding consistent results within large error bars. In this section we go a step further and we try to connect colour profile gradients with stellar age and metallicity gradients obtained from state of the art full spectrum fitting techniques.

In Fig. 4.8 we represent the position of each of the galaxies according to its $g - i$ colour inner gradient and the L-W age and metallicity inner gradients (computed in Sects. 2.3.2 and 3.1.3). In order to check if there is any correlation between both magnitudes we perform an error-weighted linear fit to the cloud of points. We obtain that the error-weighted correlation coefficient (r) is 0.68 in the case of the L-W age and 0.58 for the L-W metallicity. Apart from this relation, we have analysed the correlations of the L-W stellar parameters with other colours ($g - r$ and $r - i$), finding r values ranging from 0.49 to 0.70 (see Table 4.3) and similar results, i.e. the colours seem to better correlate with the stellar age than with the metallicity. Although it is not a 1:1 correlation, at least we can conclude that the steeper the inner gradient in L-W quantities is, the steeper the colour profile tends to be. We have also studied the connection between colour and M-W quantity trends. A similar representation as the one shown in Fig. 4.8 of colour gradients as a function of M-W stellar parameters gradients gives a

r **coefficients** (colour vs. stellar parameters inner gradient linear fits)			
	$g-r$	$g-i$	$r-i$
L-W age	0.63	0.70	0.70
L-W metallicity	0.60	0.58	0.49
M-W age	0.16	0.18	0.19
M-W metallicity	0.28	0.28	0.24

Table 4.3: Values of the correlation coefficients (r) when performing a linear fit to the colour vs. stellar parameter inner gradients for the entire sample of galaxies (see Fig. 4.8).

cloud of points with null correlation ($r < 0.3$, see Table 4.3). These results are in agreement with what expected, i.e. L-W quantities are more similar to colour profiles as both are dominated by the youngest stellar populations in the galaxy, while M-W quantities account for the effect of the oldest stars, contributing more to the total galaxy mass.

Although we find a correlation between L-W stellar parameter and colour inner gradients we cannot conclude that colour profiles can be used as a valid estimation of the general trend for stellar age and metallicity. The main problem affecting colours to use them as a proxy for stellar properties is how to quantify the age and metallicity contribution to a change in the colours. In fact, in the objects analysed in this work, colour trends seem to be mainly driven by age as this quantity correlates better than metallicity. However, although this fact can be interpreted as a consequence of the age-metallicity degeneracy we need to analyse a larger sample of galaxies to draw further conclusions.

To investigate if further correlations with other galactic quantities might exist, we have made similar figures to Fig. 4.8 but segregating the sample of galaxies in bins of stellar mass[1], absolute magnitude, and morphology,

[1]We compute galaxy masses following this recipe:
We use the transformation equations presented in Jester et al. (2005) from SDSS magnitudes to the Jonhson system:

$$\mathrm{V} = \mathrm{petroMag_g} - 0.59 \times (\mathrm{petroMag_g} - \mathrm{petroMag_r}) + 0.09, \tag{4.1}$$

$$\mathrm{B} - \mathrm{V} = 0.98 \times (\mathrm{petroMag_g} - \mathrm{petroMag_r}) + 0.12, \tag{4.2}$$

where $\mathrm{petroMag}_j$ is the integrated petrosian magnitude computed by the SDSS team in the filter j, B is the B-band absolute magnitude and V is the V-band absolute magnitude of the analysed galaxy. For the mass calculation we use the equations presented in Bell & de Jong (2001):

$$\mathrm{L_{gal}} = \mathrm{L_\odot} \times 10^{(\mathrm{V_\odot} - \mathrm{V} - 5 \times \log(\mathrm{des/deg}))/2.5}, \tag{4.3}$$

$$\mathrm{M} = 10^{1.404 \times (\mathrm{B-V}) - 0.734} \times \mathrm{L_{gal}}/\mathrm{M_\odot}, \tag{4.4}$$

where $\mathrm{L_{gal}}$ is the total luminosity of the galaxy, $\mathrm{L_\odot}$ is the total luminosity of the Sun, $\mathrm{V_\odot}$ is the V-band absolute magnitude of the Sun (-26.78), $\mathrm{M_\odot}$ is the Sun mass (1.9891×10^{33} g), "des" is the Earth-Sun distance (4.85×10^{-12} Mpc), "deg" is the Earth-galaxy comoving distance (see Table A.1), and M is the galaxy mass.

with the same number of galaxies in each bin. We have performed error-weighted linear fits to each of these representations of colour versus stellar parameter inner gradients (as previously done) for different subsamples of galaxies (according to the previously mentioned bins). This test allows us to analyse the recovered values of r as a function of the different galactic magnitudes under study. We find no correlation between r and the absolute magnitude or morphological type. However, we do obtain some correlation between r and the galaxy mass.

Figure 4.9 shows an example of this correlation with mass. This figure displays the r values for the $g-r$ versus stellar parameter inner gradients (L-W age in the upper panel and L-W [M/H] in the lower panel) linear fits considering galaxies in different mass bins as a function of the galaxy mass. We can see that, for low mass galaxies, the inner gradients of the $g-r$ colour profile display a tighter correlation with the stellar age and metallicity inner gradients than for high mass galaxies. However, as in the previous case, the correlation is stronger in the case of the age than for the metallicity. This statement is also true considering other colours such as $g-i$ and $r-i$ (see Table 4.4).

Therefore, we can conclude that the obtained correlation between the colour and the L-W stellar parameter profile inner gradients (see Fig. 4.8) is mainly driven by low mass galaxies. To explain the existence of this correlation for low mass galaxies, in Fig. 4.10 we represent the light fraction of stars younger than 150 Myr (from the stellar age distributions computed in Sect. 3.1.3) as a function of the stellar galaxy mass. The general behaviour reflects a larger fraction of young stars for low mass galaxies than for high mass galaxies. This suggests that low mass galaxies display a more efficient star formation in the last $\sim$ 150 Myr. Thus, the correlation found for low mass galaxies between the colour and the stellar age and metallicity (L-W) gradients can be interpreted as a consequence of low mass galaxies being the ones for which recently formed stars strongly dominate in light, i.e. consequence of low mass galaxies being the ones with the most recent star formation. However, this correlation, although existent for L-W quantities, is not strong enough (and just applicable to low mass stars) as to claim that colour profiles can be used as a proxy for the stellar age general behaviour.

4.4 Conclusions

In this section we have analysed all the information obtained in previous chapters. We put together radial stellar content information as well as SB distributions and colour profiles looking for correlations providing information about possible galaxy formation fingerprints on the stellar populations. Our main conclusions are:

i) we obtain "U-shape" L-W age profiles in some of the galaxies regardless

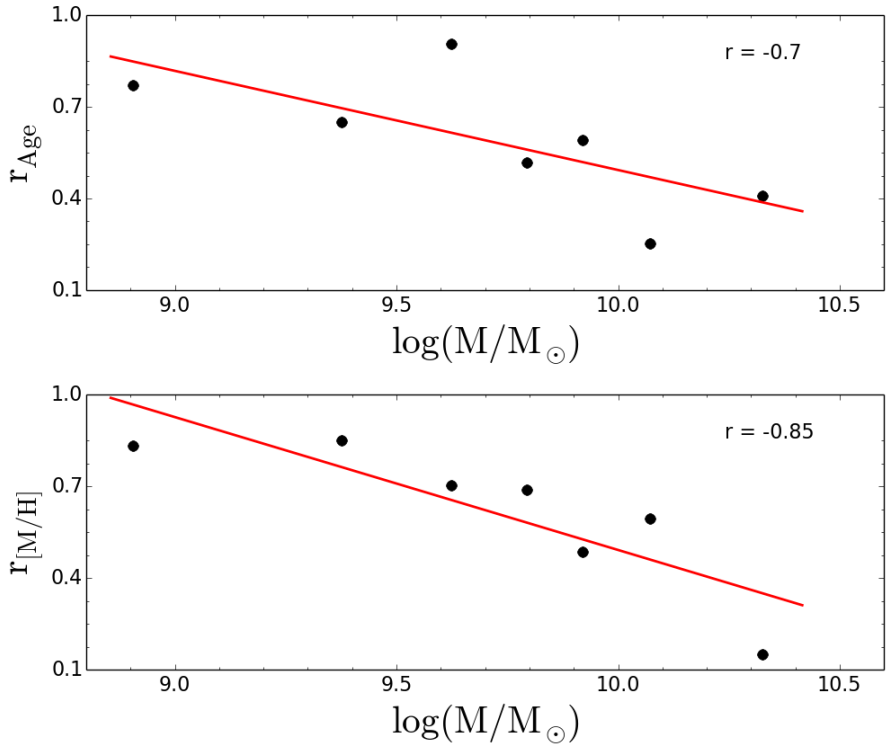

Figure 4.9: Representation of the r value corresponding to the $g-r$ vs. L-W stellar parameters inner gradients linear fit as a function of the galaxy mass. Each point is located at the central position of the mass bin (x-axis) and at the corresponding r value (y-axis) of the linear fit (inner colour gradients vs inner stellar parameter gradients) for galaxies with masses within that mass bin. The red solid line represents the linear fit to the cloud of points. The corresponding value of the correlation coefficient is indicated in each panel. Upper panel: the stellar parameter analysed is the L-W age. Bottom panel: the stellar parameter analysed is the L-W [M/H].

r **coefficients** (r vs. mass linear fits)			
	$g-r$	$g-i$	$r-i$
L-W age	0.70	0.76	0.74
L-W metallicity	0.85	0.67	0.34

Table 4.4: Values of the correlation coefficients (r) when performing a linear fit to the r values vs. galaxy mass (see Fig. 4.9). The r values for such fit (y-axis) are computed from the colour vs. stellar parameter inner gradient linear fits for different subsamples at different mass bins, while the galaxy mass (x-axis) is computed as the central mass value of the interval. See text for details. L-W stands for light-weighted quantities whereas M-W stands for mass-weighted.

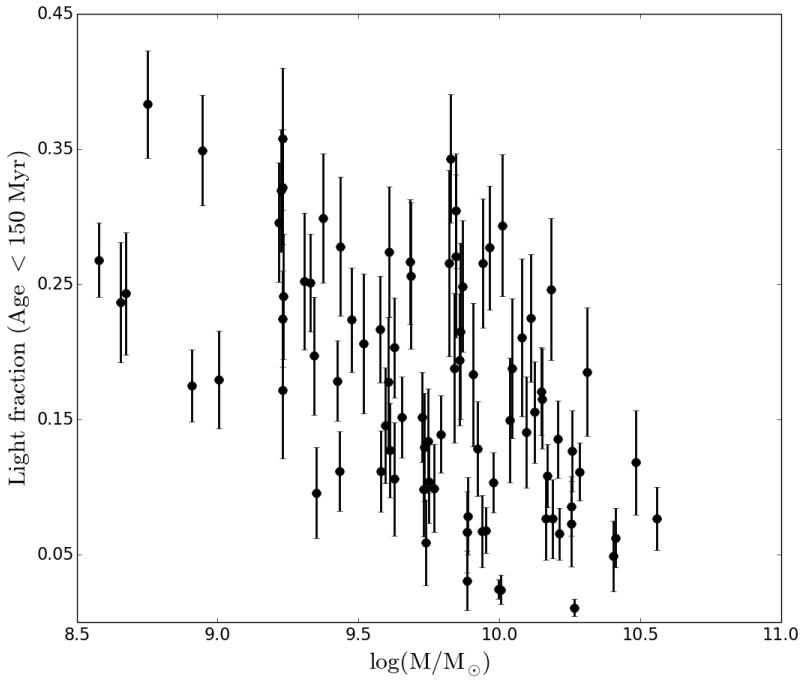

Figure 4.10: Light fraction of stars younger than 150 Myr present in the analysed galaxies as a function of the stellar galaxy mass. Such fraction has been computed from the galaxy stellar age distributions obtained in Sect. 3.1.3.

if their SB distributions display a type I or a type II profile. Such age profile shape disappears if we represent M-W quantities, resulting in flat and old profiles. These findings suggest that: a) mechanisms shaping the SB and stellar age distributions are not coupled, i.e. more processes must be involved in the type II SB profile formation; b) this upturn in age is not a universal feature (appears only in 29 out of 68 galaxies), although this statement might be a consequence of our limited instrument field of view hampering the analysis at larger galactocentric distances; and c) recent star formation is responsible for the "U-shape" in the L-W age profile. A possible explanation for the age upturn compatible with our results is an early build-up of the entire disc followed by an inside-out star formation quenching (see Chapter 5 where we obtain results supporting this scenario from simulations). These results have been presented in Ruiz-Lara et al. (2016);

ii) there are no statistical differences in the behaviour of the stellar age and metallicity profile trends in the inner parts of the analysed galaxies. These results do not allow us to conclude whether radial migration is the main driver shaping the different behaviours of the light distributions in the outer parts or not. However, they set limits for future simulations on the amount of stellar mass affected by migration, i.e. we can conclude that migrated stars do not represent an important fraction of the total disc stellar mass. Nevertheless, more observational and theoretical effort is needed to shed further light into this issue and the differences that we find with a similar analysis of the colour inner gradients need to be further investigated. These results will be presented in Ruiz-Lara et al. (in prep.);

iii) there is a (not strong) correlation between the colour and the L-W stellar age and metallicity inner profile gradients, especially driven by low mass galaxies (showing stronger correlations than high mass galaxies). $M - W$ quantities are not traced by colour profiles. Colours, although somehow related to the stellar content, should not be used as stellar properties tracers. These results will be presented in Ruiz-Lara et al. (in prep.).

Chapter 5

Chemo-dynamical simulations of disc galaxies

"I believe in everything until it's disproved. So I believe in fairies, the myths, dragons. It all exists, even if it's in your mind. Who's to say that dreams and nightmares aren't as real as the here and now?"
— John Lennon

Contents

The accepted scenario of galaxy formation involves an extended process of hierarchical merging of structures until systems settle into the entities we observe today (e.g. White & Rees 1978; Lacey & Cole 1993). During these mergers, satellites are thought to leave a signature of their impact upon the host. Whether these signatures are major, minor, long-, or short-lived, remains an intense topic of debate; however, it is clear that the interplay between such merger/interaction-driven processes and later, internal, secular evolution, all combine to shape the galaxies we see now (e.g. Dressler 1980; Donzelli & Pastoriza 2000; Márquez et al. 2002; Lambas et al. 2003; Kewley et al. 2006; Michel-Dansac et al. 2008).

In this chapter of the thesis, we make use of the `RaDES` cosmological hydrodynamical simulations of Milky Way-mass galaxies presented in Few et al. (2012) to further analyse the effect of such satellite bombardment in galaxy discs. In particular, we study those simulated galaxies to search for signatures of their assembly processes in the age-metallicity-radius relationship. Although the outer parts of the disc represent a small fraction of a galaxy's total mass, the study of the assembly of these outer regions is especially important because these regions are very sensitive to satellite accretion or external mass perturbations and provide a guide to galaxy formation and evolution. These results have been published in Ruiz-Lara et al. (2015a).

While idealised galaxy simulations are important to understand secular processes (e.g. Athanassoula 2005; Debattista et al. 2006; Roškar et al. 2008a, 2012; Athanassoula et al. 2009a,b, 2010), simulations run in a cosmological context allow us to study the environmental effects of evolution, including the impact of satellite-host interactions through to the quiescent, settled, disc phase (e.g. Katz & Gunn 1991; Navarro & Benz 1991; Katz et al. 1992; Navarro & White 1994; Steinmetz & Muller 1995; Steinmetz & Navarro 2002; Abadi et al. 2003). These simulations are a critical tool for understanding the effect of accretion and interactions in the build-up of disc galaxies (e.g. Abadi et al. 2003; Governato et al. 2004; Kazantzidis et al. 2008), especially important in shaping the outer discs (Sánchez-Blázquez et al. 2009).

However, early cosmological simulations failed to replicate late-type massive spiral galaxies because of the so-called *angular momentum problem* (e.g. Steinmetz & Navarro 2002). This problem consists of the over-production of the spheroid component of simulated galaxies due to enhanced star formation at early epochs. Currently, by modifying numerical and physical parameters in the simulations, more realistic galaxies have been reproduced (see Hummels & Bryan 2012, for a study about the effect on the angular momentum of numerical parameters such as SuperNova (SN) feedback, spatial resolution, and star formation efficiency, amongst many others). State-of-the-art numerical simulations have overcome this *angular momentum problem* and are able to reproduce the scaling relations and galaxy properties

found in nature (e.g. Robertson et al. 2004; Governato et al. 2007; Scannapieco et al. 2009; Sánchez-Blázquez et al. 2009; Stinson et al. 2010; Rahimi et al. 2010; Brooks et al. 2011; Brook et al. 2012; Stinson et al. 2012; Calura et al. 2012; Gibson et al. 2013; Obreja et al. 2014; Few et al. 2014, amongst others).

Most of the successful cosmological simulations have been focused on reproducing Milky Way-type galaxies (e.g. House et al. 2011; Macciò et al. 2012; Calura et al. 2012; Gibson et al. 2013; Walker et al. 2014; Marinacci et al. 2014). Our privileged position inside the Milky Way allows us to take high quality spatial and spectroscopic data against which to confront simulations. A number of contemporary observational studies are exploring the solar neighbourhood with unprecedented quality, providing astronomers with a vast amount of information, including `Gaia` (Perryman et al. 2001), `RAVE` (Steinmetz et al. 2006; Zwitter et al. 2008; Siebert et al. 2011; Kordopatis et al. 2013), and `SEGUE` (Yanny et al. 2009). Simulations play a pivotal role in interpreting the physical mechanisms that shape these datasets.

One of the most striking observations that needs a theoretical counterpart to be understood is the AMR in the solar neighbourhood (e.g. Powell 1972; Hearnshaw 1972; Twarog 1980). Stars are born from the collapse of molecular clouds that imprint their chemical composition upon newly formed stars. Those stars undergo nuclear fusion reactions in their cores, thereby, changing their chemical composition (see Chapter 1). According to stellar evolution and galactic chemical evolution models (e.g. Prantzos & Aubert 1995; Fenner & Gibson 2003; Romano et al. 2005), once these stars reach the end of their lives they form new elements and expel part of their mass to the interstellar medium, increasing the latter ISM metal content. As a direct consequence, the subsequent generation of stars is more metal rich than the former[1], resulting in a tightly correlated AMR in which younger stars are more metal rich and older stars are more metal poor. However, studies of the AMR in the solar neighbourhood have found an almost flat AMR for thin disc stars with significant dispersion in metallicity at a given age (e.g. Carlberg et al. 1985; Edvardsson et al. 1993; Feltzing et al. 2001; Nordström et al. 2004; Bergemann et al. 2014), while thick disc stars seem to show a steep AMR (Haywood et al. 2013).

Different theoretical works have been able to reproduce aspects of the observed AMR of the solar neighbourhood, bulge, and nearby dwarf discs, by allowing for stellar radial motions in their models that contaminate the expected relation for stars born in the solar neighbourhood (e.g. Roškar et al. 2008a; Sánchez-Blázquez et al. 2009; Schönrich & Binney 2009; Pilkington et al. 2012b). Radial motions (especially of older stars) can mix stars with different enrichment histories and different chemical composition

[1]Note though that certain star formation and infall rate scenarios can lead, in some cases, to a subsequent decline in metallicity (e.g. Matteucci & Gibson 1995).

(i.e. formed from different molecular clouds at different galaxy evolutionary stages). This effect can lead to flattening and greater dispersion in the AMR. Several authors have tried to explain what stimulates stars to move radially (see Sect. 1.3). Some of the proposed causes are i) the exchange of angular momentum at the corotation resonance of transient spiral arms (e.g. Sellwood & Binney 2002; Roškar et al. 2008b); ii) non-linear coupling between the bar and the spiral waves (e.g. Minchev & Famaey 2010; Minchev et al. 2012b,a); and iii) the influence of satellites (e.g. Younger et al. 2007; Quillen et al. 2009; Bird et al. 2012). These theoretical works have eased the debate about the observed AMR in the solar neighbourhood. However, there are some observational works still claiming that, although some changes to the AMR can be attributed to stellar migration, a large part of the observed scatter is intrinsic to the star formation processes or related to contamination of the solar neighbourhood by stars on apo- and pericentres (Feltzing et al. 2001; Haywood et al. 2013).

Despite the high quality, spatial resolution, and details of the data that we can acquire for stars in the Milky Way, the study of our Galaxy presents a number of significant disadvantages: i) the Milky Way is just one galaxy amongst the myriad different types of galaxies in the Universe; ii) our inside view restricts the observations to the solar neighbourhood because the observable region is obscured by dust, preventing a global view of the Milky Way. To achieve a wider understanding of galaxies in the Universe, we need to study external systems (e.g. MacArthur et al. 2009; Yoachim et al. 2012; Pérez & Sánchez-Blázquez 2011; Sánchez-Blázquez et al. 2011; Peletier et al. 2012; Catinella et al. 2013; Ahn et al. 2014; Sánchez-Blázquez et al. 2014). Those studies provide us with statistical information about integrated properties such as age and metallicity gradients (M-W and L-W), SFHs, light and mass distributions, or AMRs (see Chapters 3 and 4 of this thesis). The new full spectrum fitting techniques used on these unresolved systems have been proved reliable when compared with the analysis of resolved stellar populations (Ruiz-Lara et al. 2015b).[2]

In this chapter of the thesis we exploit the fact that the joint study of observations and realistic simulations can expand our knowledge about galaxy formation and evolution focusing on their outskirts (e.g. Bakos et al. 2008; Sánchez-Blázquez et al. 2009; Martínez-Serrano et al. 2009; Pilkington et al. 2012a; Yoachim et al. 2012). Simulations allow one to isolate the primary impact of satellite merging in different environments, including, for example the formation of thick discs (e.g. Quinn et al. 1993; Brook et al. 2004; Villalobos & Helmi 2008), inflows of external material (e.g. Kereš et al. 2005; Dekel & Birnboim 2006), or radial mixing (e.g. Quillen et al. 2009; Bird et al. 2012). The establishment of testable predictions through simulations

[2]Conversely, comparing resolved stellar populations with only a restricted subset of line indices can prove problematic (e.g. Gibson et al. 1999).

can be a powerful tool in designing future observational campaigns.

In Sect. 5.1, we present the sample of galaxies, the simulations, and their assembly histories. Section 5.2 presents the main observational characteristics of each simulation. The primary results of this particular analysis are shown in Sect. 5.3 where we discuss the impact of the assembly history on both the AMR and spatially-resolved SFH of the disc. The discussion, main conclusions and links with the results found in previous sections are provided in Sect. 5.4.

5.1 Sample of galaxies

In this chapter, we use the `RaDES` (Few et al. 2012) galaxies. The `RaDES` set of galaxies was created to study differences between galaxies in loose group and field environments through cosmological simulations. The `RaDES` galaxies are comprised of 19 galaxies with masses similar to the Milky Way and disc characteristics similar to other observed disc galaxies (Few et al. 2012; Pilkington et al. 2012a). While each system has similar properties in relation to their matter content (total, dark, stellar, baryonic, and gaseous mass), they also show important differences concerning their kinematic heating profiles (see figure 9 of Few et al. 2012), SFHs (see figure A.1 of Few et al. 2012), disc fractions, and assembly histories.

For brevity, here we focus on the analysis of three discs from the `RaDES` sample. These three span the range of assembly histories of the full sample, from intensive to quiescent; our conclusions are robust against the specific choice of systems. For completeness, the primary plots employed for the analysis of our three *canonical* simulations are repeated for all 19 `RaDES` galaxies in Appendix D.

5.1.1 Simulations

The `RaDES` galaxies are simulated with the adaptive mesh refinement code RAMSES (Teyssier 2002). The simulations track dark matter, stars and gas on cosmological scales. The hydrodynamical evolution of gas uses a refining grid such that the resolution of the grid evolves to follow over-densities reaching a peak resolution of 436 pc (16 levels of refinement). The RAMSES code includes gas cooling/heating and a polytropic equation of state is used for dense gas to prevent numerical fragmentation.

Star formation occurs in gas that is more dense than $\rho_0 = 0.1$ n_H cm^{-3} at a rate of $\dot{\rho} = -\rho/t_\star$, where $t_\star = t_0(\rho/\rho_0)^{-1/2}$, with $t_0 = 8$ Gyr. Stellar feedback is delayed by 10^7 years and imparts kinetic energy, mass, and metals to the gas within a two-cell radius sphere. The mass fraction of stellar particles that explode as SN is 10% and each SN provides 10^{51} erg; 10 % of non-metals are converted to metals by each star particle.

The galaxies were simulated with cosmological parameters as follows: $H_0 = 70$ km s^{-1}Mpc^{-1}, $\Omega_m = 0.28$, $\Omega_\Lambda = 0.72$, $\Omega_b = 0.045$, and $\sigma_8 = 0.8$[3]. Two volumes are used with a size of 20 h^{-1} Mpc and 24 h^{-1} Mpc. The mass resolution of dark matter particles is either 5.5×10^6 M$_\odot$ or 9.5×10^6 M$_\odot$ depending on which of two volumes the galaxy is drawn from. Details of the halo selection process and the simulation parameters may be found in Few et al. (2012) and in Sect. 5.1.2, below.

5.1.2 RaDES assembly histories

The assembly histories of the RaDES galaxies have been obtained with a careful study of the merger trees discussed in Few et al. (2012). In short, we use the *adaptahop* algorithm (Aubert et al. 2004) to create a catalogue of haloes and sub-haloes in the simulation at each time step. We are able to identify, not only each halo, but also their progenitors, descendants, sub-haloes, etc. By linking all these catalogues, we can create merger trees for the different haloes following the *most massive substructure method* (Tweed et al. 2009). The analysis of those merger trees shows that all RaDES galaxies display, generally speaking, similar disc assembly histories in terms of phases or stages.

In Fig. 5.1, we plot the distance between the centre of the host galaxy and its satellites for two RaDES galaxies as a function of lookback time (Selene, left panel; Oceanus, right panel). Each point in Fig. 5.1 represents one satellite at a given timestep with the points colour-coded on a logarithmic scale according to the virial mass of the satellite divided by the virial mass of the host halo (M_{sat}/M_{host}). All RaDES galaxies underwent three well-defined assembly phases: 1) an initial phase of merger-dominated evolution lasting $\sim 3.2 \pm 0.4$ Gyr on average, while mergers of systems with similar masses occur, M_{sat}/M_{host} (when the distance to the host galaxy is lower than 5 kpc) ranging from 0.1 (the majority) to 3 (several of them). This first period is followed by 2) a quieter phase where the number of mergers is minimised by a factor of two with respect to the previous stage. During this phase (lasting $\sim 4.4 \pm 2.0$ Gyr) several major satellites with $M_{sat}/M_{host} = 0.01$–0.3, merge with the host galaxy. This phase ends with a last merging event, occurring at different times depending on the galaxy in question. We refer to this stage in the galaxy's evolution as t_{jump} (see Table 5.1), defined as the time at which this last merger dissolves in the host galaxy. Finally, 3) the disc settles and evolves *secularly*, with just minor satellite mergers ($M_{sat}/M_{host} < 0.01$) disturbing the host disc (lasting $\sim 5.5 \pm 2.0$ Gyr).

This last accreted satellite is characterised by a value of M_{sat}/M_{host}

[3]Here, H_0 is the Hubble constant, Ω_m the fraction of total matter, Ω_Λ the fraction of the dark energy, Ω_b the fraction of baryonic matter, and σ_8 the strength of the primordial density fluctuations.

around 0.12 ± 0.09 at the time it enters the virial radius ($(M_{sat}/M_{host})_v$) and $M_{sat}/M_{host} \sim 0.013 \pm 0.006$ (averaged values) when it merges at t_{jump} ($(M_{sat}/M_{host})_t$). All the characteristics of these latest mergers are shown in Table 5.1.

While most of the galaxies exhibit just one merger epoch (Phases 1 and 2) followed by a quiescent phase (Phase 3), some others show two different merging events (two Phase 2 events) with the above outlined characteristics. After the first merger event (t_{jump-a}), Phase 2 does not end, but continues until a second event takes place (t_{jump-b}). Artemis and Oceanus are examples of this behaviour (see right panel of Fig. 5.1).

This figure shows the satellites affecting the discs of Selene and Oceanus as two examples of the above outlined behaviour (one-merging-epoch and two-merging-epoch galaxies, respectively). For resolution/aesthetic purposes, we applied a cut in Fig. 5.1 to remove the more insignificant satellites, i.e. $(M_{sat}/M_{host})_t$ below 0.005. We checked that those satellites not fulfilling this criterion have low masses, and thus, little influence in the disc evolution. For Selene, during the first 3.5 Gyr the evolution is characterised by an unsettled phase dominated by satellite accretion (Phases 1 and 2). The lack of important mergers is the main characteristic during the rest of the simulation, although some low-mass satellites do orbit the host. The last important merger that Selene underwent took place ~ 6.0 Gyr ago (t_{jump}) with $(M_{sat}/M_{host})_v \sim 0.089$ and $(M_{sat}/M_{host})_t \sim 0.013$. In the case of Oceanus (two-merging-epochs), the unsettled phase lasts for almost 6 Gyr, finishing with a satellite with $(M_{sat}/M_{host})_v \sim 0.056$ and $(M_{sat}/M_{host})_t \sim 0.006$ (at $t_{jump-a} \sim 7.5$ Gyr). After that, a 6 Gyr quiescent phase follows with several low-mass satellites remaining isolated from the host disc, followed by another merging episode ~ 1.2 Gyr ago with $(M_{sat}/M_{host})_v \sim 0.050$ and $(M_{sat}/M_{host})_t \sim 0.005$ ($t_{jump-b} \sim 1.2$ Gyr).

In Sects. 5.2 and 5.3, we concentrate on the effect that these assembly histories produce on the `RaDES` galaxies.

5.2 Disc characteristics

In this section we carefully define what we consider disc particles in the `RaDES` simulated galaxies and characterise their main properties such as stellar age and metallicity profiles, age-velocity dispersion relation, and their AMR.

5.2.1 Disc decomposition

One of the classic problems plaguing the simulation of disc galaxies in a cosmological context is the overproduction of stars associated with the spheroid (bulge and/or halo). Significant advances have been made over the past

Name	t_{jump} (Gyr)	$(M_{sat}/M_{host})_v$	$(M_{sat}/M_{host})_t$
(1)	(2)	(3)	(4)
Apollo	**3.5**	**0.112**	**0.013**
Artemis (a)	7.5	0.063	0.010
(b)	1.8	0.126	0.010
Atlas	5.0	0.050	0.013
Ben	6.0	0.223	0.031
Castor	8.0	0.004	0.002
Daphne	2.0	0.100	0.013
Eos	7.5	0.063	0.011
Helios	8.5	0.100	0.010
Hyperion	7.5	0.050	0.010
Krios	4.5	0.063	0.013
Leia	7.5	0.125	0.019
Leto	1.2	0.316	0.018
Luke	2.0	0.125	0.010
Oceanus (a)	**7.5**	**0.056**	**0.006**
(b)	**1.2**	**0.050**	**0.005**
Pollux	5.5	0.281	0.019
Selene	**6.0**	**0.089**	**0.013**
Tethys	6.5	0.250	0.025
Tyndareus	4.0	0.316	0.012
Zeus	4.0	0.039	0.011

Table 5.1: Characteristics of the last accretion episode. (1) Name of the galaxy; (2) time of the last accretion (lookback time); (3) ratio between the mass of the satellite that merges and the host galaxy at the moment the satellite enters the virial radius; (4) ratio between the mass of the satellite that merges and the host galaxy at the moment of the merge (t_{jump}). In the case of Artemis and Oceanus the two events are labelled as *a* and *b* (see text for details). In this chapter we focus on the three `RaDES` galaxies in bold font.

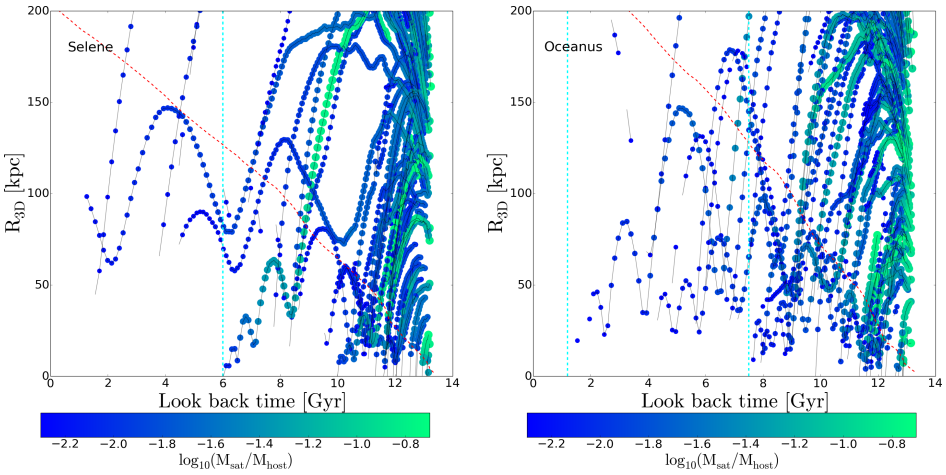

Figure 5.1: Schematic representation of the satellite orbits for Selene (left) and Oceanus (right). On the y-axis we plot the three-dimensional distance (R_{3D}) from the satellite centre to the host galaxy centre. On the x-axis we plot the lookback time (13.5 Gyr being the beginning of the simulation). Each point represents one satellite at a given snapshot with points corresponding to the same satellite at different timesteps linked by a solid grey line. In some cases, the halo tracking between snapshots fails leading to missing connecting lines. We colour-code the points according to $\log_{10}(M_{\rm sat}/M_{\rm host})$ (the size of each point is also proportional to that value) as an indicator of the magnitude of the mergers. We have applied a cut in $\log_{10}(M_{\rm sat}/M_{\rm host})$ to clean the plot of the least massive satellites; satellites with $(M_{\rm sat}/M_{\rm host})$ when they merge with the host galaxy below 0.005 are ruled out in the plots. The dashed red line represents the time evolution of the host galaxy virial radius. Last merger times ($t_{\rm jump}$) are denoted via dashed cyan vertical lines. For Selene (left), the last merger happened 6.0 Gyr ago with $M_{\rm sat}/M_{\rm host} \sim 0.089$ when it enters the virial radius and ~ 0.013 when the merger happens. The merging event finishing the first phase of intense satellite accretion has $(M_{\rm sat}/M_{\rm host}) \sim 0.056$ when the satellite crosses the virial radius and $(M_{\rm sat}/M_{\rm host}) \sim 0.006$ when the satellite merges; in the case of the merging event ending the second phase those values are 0.050 and 0.005, respectively.

decade in ameliorating this problem, although this manifestation of the classical over-cooling and angular momentum catastrophe problems has not yet been fully eliminated. Instead, as is standard practice in the field, we post-process the simulations to mitigate the contamination of the disc by spheroid stars.

To separate the disc from the spheroid component, we apply a kinematic selection criterion based upon the circularity (J_z/J_{circ}[4]) distribution (e.g. Scannapieco et al. 2009; Stinson et al. 2010). We have labelled disc stars as those with circularities ranging from 0.9 to 1.1; in this way, we ensure we are considering particles on circular orbits in the plane of the disc. Although different selection criteria can be found in the literature (e.g. Sánchez-Blázquez et al. 2009; Few et al. 2012; Pilkington et al. 2012a) ending with subtly different sub-sets of *disc* particles, we have checked that our results are robust to the specific selection criteria: while the chosen circularity criterion might appear restrictive, the characteristics of the discs so defined (mass, age, and metallicity profiles, etc.) are consistent with those of observed galaxy discs (see Sect. 5.2.3).

Figure 5.2 shows the spatial distribution of the stellar particles for Selene when the kinematic criterion is applied (right) compared to the distribution when all the particles are represented (left). A careful inspection of the edge-on views allows us to conclude that this criterion properly clean the `RaDES` discs from the spheroid component. The thick disc is not strictly spatially resolved in these simulations and the disc selection is an aggregate thick and thin disc. The face-on view of this particular galaxy highlights some disc characteristics, such as the spiral structure, and we conclude that this strict selection of disc particles allows us to perform our analysis without contamination by halo stars.

To spatially sample each disc's characteristics from the inner to the outer disc, we scaled each one to the radius corresponding to a stellar mass surface density of 10^7 $M_\odot$ kpc^{-2} (hereafter R_7); this normalisation corresponds to the typical break radius in the surface density profile of disc galaxies (e.g. Roškar et al. 2008b; Sánchez-Blázquez et al. 2009), and has been chosen as useful scaling, but does not impact the conclusions whatsoever. We study four radial regions (see Table 5.2), defined as i) inner, this region accounts for the particles in the inner disc scale-length (h_{in}) obtained analysing the SDSS r-band mock images from `SUNRISE` (Jonsson 2006); the images generated by `SUNRISE` can be seen in Few et al. (2012) (see Appendix D for further information); ii) middle disc, this is a h_{in}-width region around $R_7/2$; iii) outer disc, h_{in}-width region around R_7; and iv) outskirts, $3h_{in}$-width region

[4]We calculate J_{circ} as the angular momentum of an object in a circular orbit with a given radius (the radius where the star is located in the final output). J_z is defined as the angular momentum in the z direction. We assume in the calculation of J_z and J_{circ} that the gravitation force at a given radius is given by the mass enclosed by a sphere at that radius.

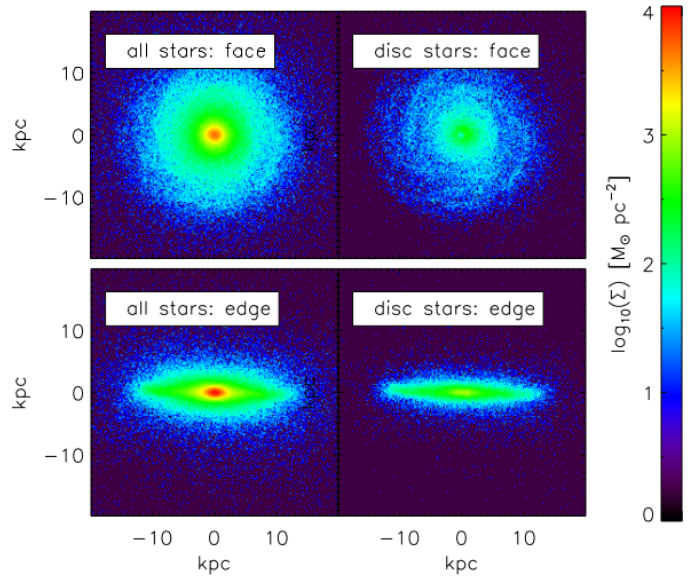

Figure 5.2: Face-on (top panels) and edge-on (bottom panels) surface density maps of Selene considering every particle in the simulation (left panels) or just disc particles (right panels).

around $R_7 + 2 \times h_{in}$. We apply these spatial cuts for every galaxy, avoiding overlap between regions. We followed the same approach for every `RaDES` galaxy, with no assumptions regarding the surface brightness profile of the discs. Again, we tested various ways of radially scaling our discs and the results are not contingent upon this convenient normalisation.

5.2.2 Stellar age and metallicity distribution of disc stars

Different groups have tried to study, both observationally and theoretically, the properties of the stellar populations as a function of radius in spiral galaxies (see Chapters 1 and 4 for references). The comparative study of age and metallicity profiles from simulations and observations can help us to better understand the behaviour of the stellar content in the outer parts of spiral galaxies.

With this purpose, we have studied the age and metallicity distribution of the `RaDES` galaxies' discs by means of one-dimensional profiles. We obtain those profiles by applying a M-W average to all disc particles within 0.5 kpc-wide radial bins. Fig. 5.3 shows the age, metallicity, and velocity dispersion profiles characterising the disc of one such galaxy, Selene. Each of the 19 analysed galaxies show similar profiles regardless their morphology and characteristics: i.e. negative M-W metallicity gradients, and "U-shaped" M-W age profiles. The radius where the minimum in age is reached is roughly located in region 3 for all of them. The outermost parts of every galaxy show an extended, old plateau (older than 10 Gyr, beyond $\sim 6.4\ h_{in}$). The

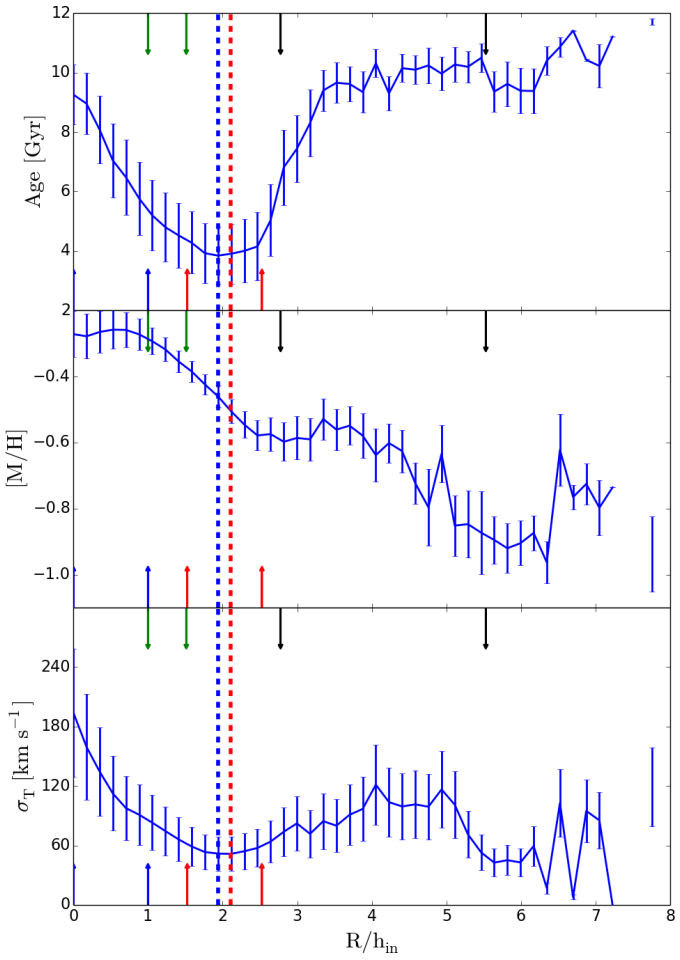

Figure 5.3: Upper panel: Selene stellar disc age profile. Middle panel: Selene stellar disc metallicity profile. Bottom panel: Selene total velocity dispersion profile (disc stars). Red vertical dashed lines are located at the surface brightness break radius. Blue vertical dashed lines are located at the location of the minimum in age. The error bars indicate the standard deviation of the values of every particle within each radial bin. h_{in} is the inner disc scale-length in SDSS r-band mock images from `SUNRISE` (Jonsson 2006). These mock images can be seen in Few et al. (2012). Vertical arrows are located at the beginning and the end of the four regions defined in Table 5.2. Blue, region 1; green, region 2; red, region 3; black, region 4.

Regions	General		Selene		Oceanus	
	Lower limit	Upper limit	Lower limit (kpc)	Upper limit (kpc)	Lower limit (kpc)	Upper limit (kpc)
(1)	(2)	(3)	(4)	(5)	(6)	(7)
1	0.00	h_{in}	0.00	5.67	0.00	8.07
2	$R_7/2 - h_{in}/2$	$R_7/2 + h_{in}/2$	5.67	8.59	8.07	11.09
3	$R_7 - h_{in}/2$	$R_7 + h_{in}/2$	8.67	14.34	11.09	18.14
4	$R_7 + 0.75 \times h_{in}$	$R_7 + 3.5 \times h_{in}$	15.75	31.35	20.15	42.35

Table 5.2: Definition of the four radial regions studied in this analysis. (1) Number of the region; (2) general definition of the lower limit in units of inner disc scale-length (h_{in}, 5.67 and 8.07 kpc for Selene and Oceanus) and the radius corresponding to a stellar mass surface density of 10^7 $M_\odot$ kpc^{-2} (R_7, 11.5 and 14.1 kpc for Selene and Oceanus); (3) general definition of the upper limit in units of h_{in} and R_7; (4) lower limit for Selene (kpc); (5) upper limit for Selene (kpc); (6) lower limit for Oceanus (kpc); (7) upper limit for Oceanus (kpc). The value of h_{in} was obtained analysing the SDSS r-band mock images from `SUNRISE` (Jonsson 2006); those images can be seen in Few et al. (2012). The values of h_{in} for all the simulated discs can be found in Table D.1 summarising the results from the surface brightness analysis. Several of the values in columns (4), (5), (6), and (7) coincide as a consequence of applying the general definition avoiding overlapping between regions.

metallicity profiles show a flattening in the centre, mainly caused by the low metallicity of the older stars populating the inner region of the analysed discs (see Figs. 5.5 and 5.7). These profiles are extensively analysed in Sect. 5.4.1.

In addition to the age and metallicity profiles, we obtained the velocity dispersion profiles (bottom panel of Fig. 5.3) for each of the above-defined `RaDES` discs. They also show a "U-shaped" form. In fact, there is a correlation in the shapes of the age and velocity dispersion profiles, with the minimum of both distributions located roughly at the same radial position. This is related to the age-velocity dispersion relation expected for galactic discs (discussed in the following section) where, in general, younger stars have lower velocity dispersions. As stars age they are heated by the effect of the galaxy dynamics and/or satellites (see Fig. 5.4). This aspect might deepen the "U-shape" age profile as the stars that are being born at the minimum age radius have less time to move away and, on average, make other regions younger. Similar "U-shapes" in the velocity dispersion profiles have been found in the Villalobos & Helmi (2008) simulations, as a consequence of the accretion of a discy satellite with an initial orbital inclination for the satellite with respect to the mid-plane of the host disc of 30° (they obtain similar results using spherical satellites and an orbital inclination of 60°).

5.2.3 Age-velocity dispersion relation

In the solar neighbourhood of the Milky Way, the stellar velocity dispersion increases with the stellar age , however the exact shape/behaviour of the relationship remains a matter of debate (e.g. Wielen 1977; Binney et al. 2000; Seabroke & Gilmore 2007). Nordström et al. (2004) made use of the

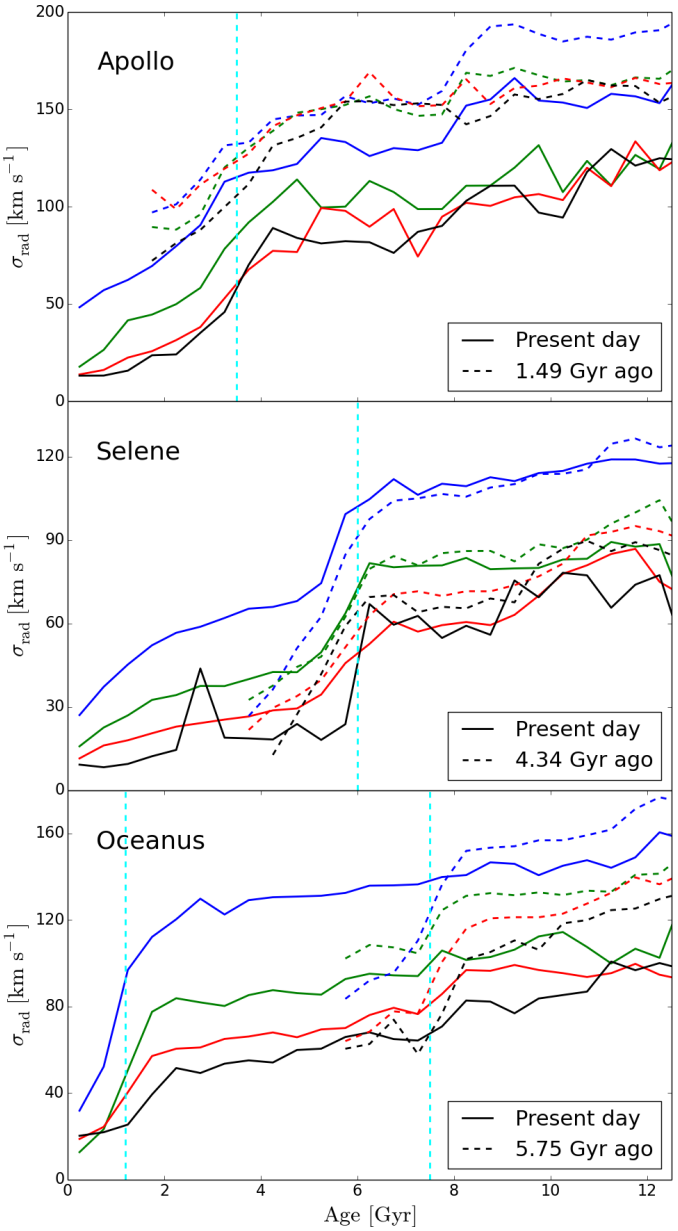

Figure 5.4: Radial velocity dispersion vs. age for Apollo (upper panel), Selene (middle panel), and Oceanus (bottom panel) disc stars, colour-coded according to their radial positions. Blue: region 1: inner region (one disc scale-length width, h_{in} using the SDSS r-band mock images from `SUNRISE` (Jonsson 2006); these mock images can be seen in Few et al. (2012)). Red: region 2: a 1-h_{in} width annulus between the centre and the 10^7 $M_\odot$ kpc^{-2} mass surface density. Green: region 3: a 1-h_{in} width annulus centred at the 10^7 $M_\odot$ kpc^{-2} mass surface density. Black: a 3.5-h_{in} width annulus further out (see text and Table 5.2 for further details). The value of h_{in} is 2.34, 5.67, and 8.07 kpc for Apollo, Selene, and Oceanus respectively. The parameter t_{jump} is denoted with dashed cyan vertical lines (the moment when the last main satellite is accreted). Dashed lines show the AVR at intermediate simulation stages between the formation of the galaxy and the present day to address the effect of the last merger episode in the AVR (1.49 Gyr ago for Apollo, 4.34 for Selene, and 5.75 Gyr for Oceanus).

Geneva–Copenhagen Survey to study the Age-Velocity dispersion Relation (AVR) in the solar neighbourhood. They studied each velocity component separately, finding that power laws can fit the relation found in every direction. They interpreted those results as evidence for a continuous heating of the disc. Conversely, several works have found some saturation in the V and W velocity dispersion components[5] (Soubiran et al. 2008). Aumer & Binney (2009), using *Hipparcos* and GenevaCopenhagen data, were not able to rule out such saturation for stars older than 4 Gyr, combined with an abrupt increase in velocity dispersion for the oldest stars. Martig et al. (2014), based on seven simulated galaxies, proposed that continuous heating takes place to explain the slope of the AVR for stars younger than 8 – 9 Gyr, but also found a step in the AVR for the oldest stellar population, related to an early merger phase. The authors showed that the maximum in σ_z is strongly decreased when age errors of 30 % are implemented, suggesting that observations can easily miss such a *jump* with the current accuracy of age measurements. Although it is hard to distinguish among the different heating agents (e.g. bars, spirals, mergers, and stars born hot at high redshift), Martig et al. showed that radial migration does not heat the disc, in agreement with Minchev et al. (2012b) and Vera-Ciro et al. (2014).

In a comparison of these simulations with both the existing empirical and model AVRs, in order to identify the heating mechanisms underpinning `RaDES`, in Fig. 5.4 we show how the stellar radial velocity dispersion varies as a function of stellar age for three of the `RaDES` galaxies (Apollo, Selene, and Oceanus). We study this relation in the four different regions outlined earlier (Sect. 5.2.1). The behaviour for the individual velocity components (R, ϕ, and z) parallels that of figure 9 of Few et al. (2012). The shape of the AVR is very similar across the four regions suggesting that heating is consistent over the entire disc, albeit, there are qualitative differences in the strength of this heating as a function of radius.

The most remarkable feature we can find in these age-velocity diagrams is the presence of an increase in the velocity dispersion values around a given age ($\sim t_{jump}$), which is a feature that is apparent throughout the entire disc (in the four radial regions). Although for some galaxies this *jump* in the AVR is smooth (as is the case for Apollo), other galaxies show a clear sudden *jump* (e.g. Selene and Oceanus, see Fig. 5.4). Stars older than t_{jump} have a larger velocity dispersion than the stars with ages younger than t_{jump} for all `RaDES` galaxies: this *jump* is clearly linked to their last important merger (happening at t_{jump} with $(M_{sat}/M_{host})_t \sim 0.013$; see Sect. 5.1.2). This *jump* is more evident for the outer parts and fades towards the centre; mergers affect the outer disc more strongly because of its lower surface density.

The dashed lines in Fig. 5.4 represent the AVR at different evolutionary

[5] Usually, the kinematics of Galactic stars is divided into three main components: U is the radial component, W is the vertical component, and V is the tangential one.

stages, which allow us to appreciate how these galaxies have evolved since the last merger. We show the AVR from 1.49 and 4.34 Gyr ago for Apollo and Selene, respectively. We observe that the AVR taken in the present day and just after the mergers have similar shapes across the four regions, i.e. the disc kinematics respond qualitatively the same at all radii. Some differences do exist in how the four regions evolve, however; in the case of Apollo (the galaxy with the smoothest *jump* of the three) the AVR was also smooth 1.49 Gyr ago, yet since that time, regions 2–4 have relaxed more than region 1. For Selene, the AVR 4.34 Gyr ago and the one currently found are similar in that the step in velocity dispersion exists immediately after the merger and persists to the present day. The differences between the AVR at intermediate evolutionary epochs and the AVR displayed at present time suggest that, apart from the effect caused by the mergers, secular evolution following the merger clearly affects the final AVR shape (a similar behaviour is displayed by Oceanus).

In the case of Oceanus, one of the galaxies where two merger episodes can be identified by its assembly history (see Fig. 5.1), we can also distinguish two *jumps* in the AVR. The more recent event presents a more prominent *jump*, while the earlier event is more subtle because it is swamped by the combination effect of the latest merger and secular heating. This swamping of the earlier *jump* might be caused by a differential heating between cold and hot stars minimising the extant *jump*, affecting cold stars more than hot stars. To check this hypothesis, in Fig. 5.4 we show the AVR displayed by Oceanus disc stars 5.75 Gyr ago, i.e. after the first merger event and prior to the second event; while at the end of the simulation, the *jump* at 7.5 Gyr is almost negligible, the AVR at 5.75 Gyr ago shows a more prominent *jump* for stars older than 7.5 Gyr, which is more evident for the inner region. This result favours our idea that the *jump* experienced by stars older than 7.5 Gyr was caused by a merger event 7.5 Gyr ago but has been partially swamped by the last merger and the subsequent secular heating (especially true for region 1).

Major mergers are not the only source of kinematic heating affecting these discs: internal secular evolution processes and other minor mergers can also shape the AVR. These plots do, however, prove that satellite merging is an important heating mechanism affecting the kinematic state of the stars experiencing these events and, therefore, the AVR.

We also find another striking point shown by the AVRs in the values found for the velocity dispersion. Our velocity dispersions are higher than those observed in the solar vicinity (e.g. Holmberg et al. 2009). Old stars show values as high as twice the value for Milky Way, old stars and young stars show those values presented by solar neighbourhood old stars. It is expected that higher velocity dispersions are found within our simulated discs than for the Milky Way as high velocity dispersions are endemic to almost all of the cosmological simulations of disc galaxies (see House et al.

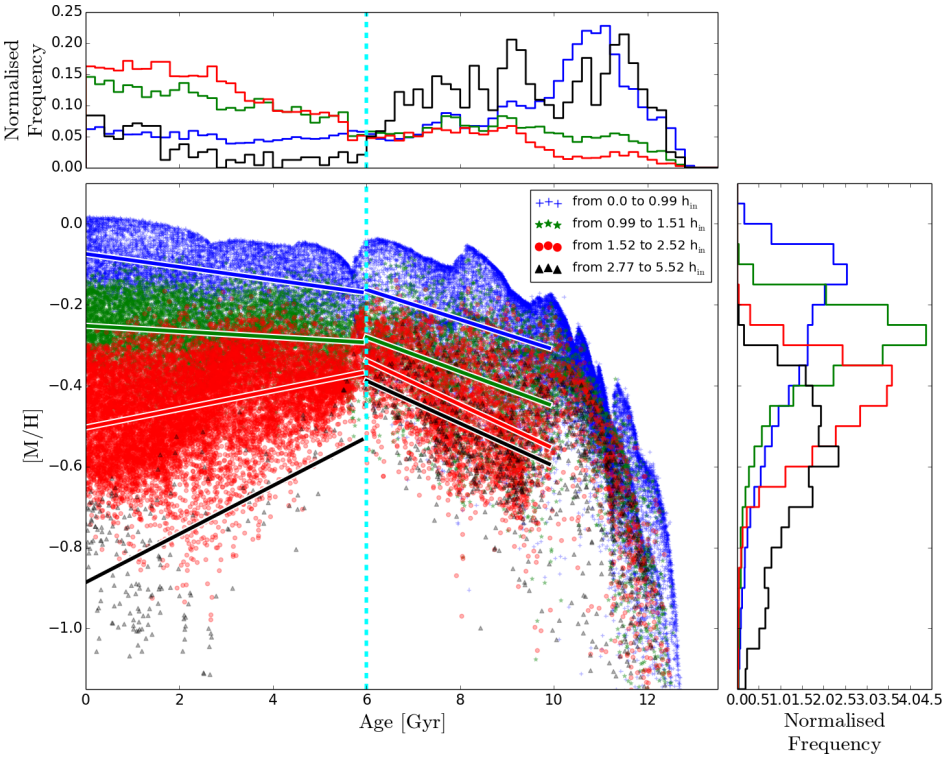

Figure 5.5: Age-metallicity relation for Selene disc stars, colour-coded according to their current radial positions (see text, Table 5.2, and Fig. 5.4 for more information). Blue crosses represent stars currently located in region 1. Green asterisks represent stars currently in region 2. Red dots represent stars currently in region 3. Black triangles represent stars currently in region 4. The two histograms on top of the AMR and on the right represent the age and metallicity distribution function, respectively (colour-coded in the same way). The parameter t_{jump} is denoted by the dashed cyan vertical line. Solid lines correspond to the linear fits performed to the AMR of the stars in the four radial regions for Phase 2 (from t_{jump} until 10 Gyr ago) and Phase 3 (from the present day until t_{jump}).

2011). High velocity dispersions may also be due to contamination of the disc by spheroid stars, however, we have minimised that effect by applying a disc particle criterion. Furthermore, none of the galaxies are a perfect match to the Milky Way, so we do not expect the same behaviour as shown by the Milky Way, which has a different assembly history than the simulated discs underwent.

5.2.4 Age-metallicity relation

We analyse the AMR for the discs of the `RaDES` galaxies. In Figs. 5.5 and 5.7 we show, as two representative examples, the AMR for the Selene and Oceanus disc stars, colour-coded according to their radial location (see Table 5.2 for the definition of the extent of each region). In these figures

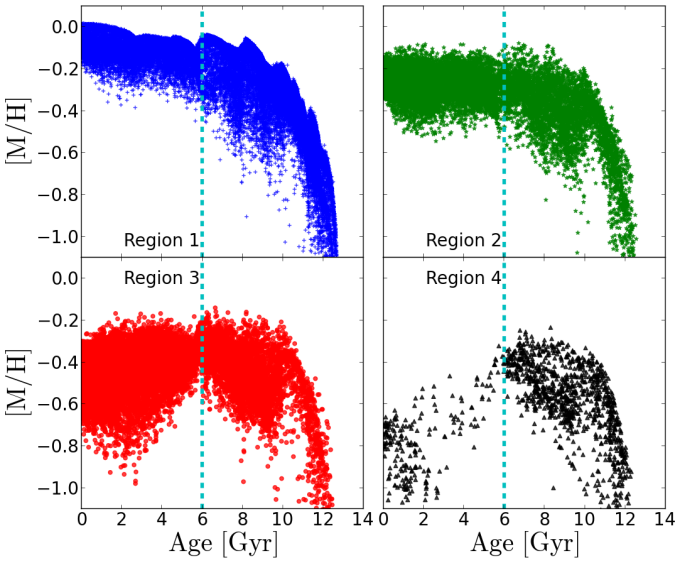

Figure 5.6: Age-metallicity relation for Selene disc stars, equivalent to Fig. 5.5, but split into four different panels; one per region.

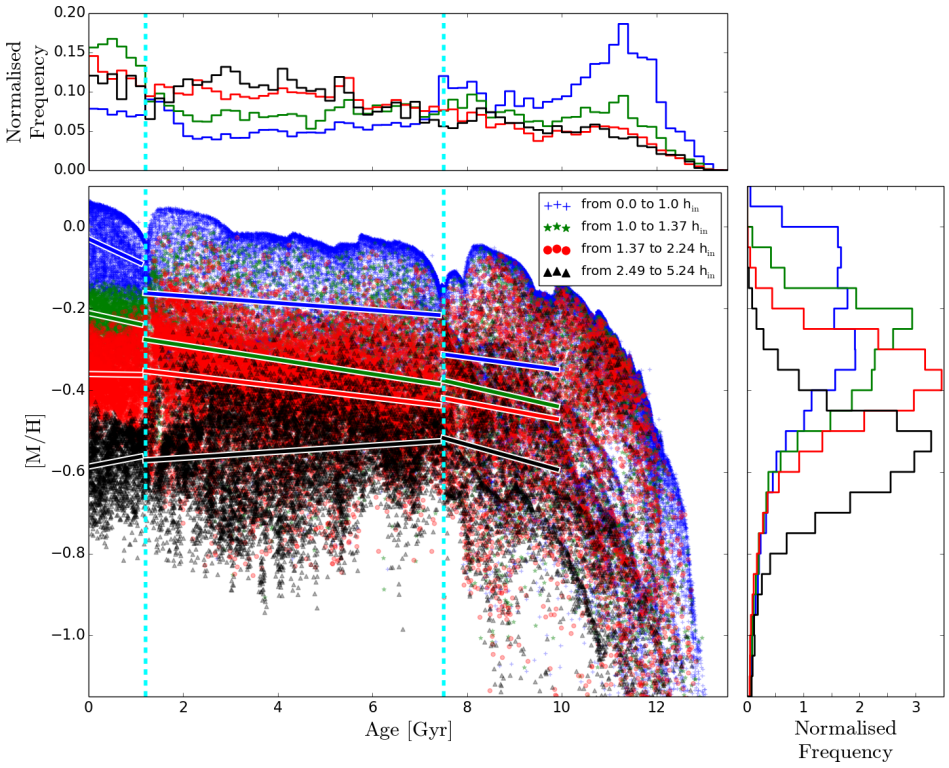

Figure 5.7: Age-metallicity relation for Oceanus disc stars; see Fig. 5.5 for more information. The parameters t_{jump-a} and t_{jump-b} are denoted by the dashed cyan vertical lines.

we also show the age and metallicity distribution functions for each region (top and right-hand panels respectively). We split such figure in 4 different panels corresponding to the 4 radial regions under study (see Fig. 5.6) to properly appreciate the details of Fig. 5.5.

Common to all the analysed galaxies, the chemical properties of the stars show a different behaviour depending on the assembly history stage they were born in. Figure 5.6 clearly shows well-differentiated phases according to the dispersion of the AMR displayed by the stars corresponding to the three-phase assembly history described in Sect. 5.1.2: stars formed during Phase 1 (older than 10 Gyr) show a very tight AMR, while stars born at Phases 2 and 3 display a more spread relation. This tight AMR for old stars is a direct consequence of the origin of old stars, accreted from satellites or formed in the early host galaxy: these environments are spatially small and have comparatively homogeneous metal abundances and enrichment histories. Afterwards, when quiescent phases dominate the mass assembly, the diversity of satellite metallicity increases and the galaxy develops a metallicity gradient that enhances the dispersion of the AMR. The metallicity distribution is also broadened as late-forming satellites with lower metallicities are accreted by the enriched host galaxy. Radial stellar motions also increase the dispersion of each region as stars move from the metal-enhanced centre of the galaxy and the relatively metal-poor outskirts to other regions. These radial motions tend to affect older populations more strongly (as we show in Sect. 5.3.1), yet only broaden the dispersion of the AMR if stars exist with distinct metallicities in other regions of the galaxy. It is for this reason that radial motions broaden the AMR dispersion for a given region for the Phase 2 stars (because a metallicity gradient exists at this time) but does not broaden the AMR dispersion for Phase 1 (when the metallicity is very homogeneous) or Phase 3 stars (when less radial migration has taken place; see Sect. 5.3.1).

In addition, we have carefully analysed other aspects of the AMR such as: i) the metallicity distribution, suggesting different degrees of chemical mixing according to the age-metallicity plots; and ii) the slopes in the AMR, we should note that we compute these slopes in the AMR for Phases 2 and 3, avoiding the more turbulent Phase 1. Below, we expand those features:

i) In Fig. 5.8 we analyse the Metallicity Distribution Function (MDF) for stars in regions 1 to 4, distinguishing between young (younger than t_{jump}, 1 to 2 Gyr) and old (older than t_{jump}, 8 to 9 Gyr) stars (see left panel of Fig. 5.8 for Selene). For every galaxy, the metallicity dispersion is larger in the outer parts than in the inner parts (irrespective of age), ranging from 0.04 vs. 0.10 dex in region 1 to 0.07 vs. 0.13 dex in region 4 for the young vs. old components, respectively (averaged values for all 19 `RaDES` galaxies). This is consistent with Minchev et al. (2014), where the increase in the AMR scatter with radius was related to the expected increase in contamination from migration and heating with radius. The metallicity

dispersion for old stars is also larger than for young stars. If we define the change in the metallicity dispersion between old and young component as $100\times(\sigma_{\rm met,old} - \sigma_{\rm met,young})/\sigma_{\rm met,old}$, its radial evolution is 58.7 % in region 1, 37.9 % in region 2, 26.4 % in region 3, and 21.6 % in region 4, i.e. the differences are minimised at greater radii.

If we do not focus on the radial evolution of the MDF for old or young stars, we can find interesting differences in the discrepancies between old and young populations. Young stars show very different MDFs for the different radial bins, while more similar distributions are shown by old stars in regions 1 to 4. We analysed, the differences between the metallicity distributions of different radial regions for young and old stars (at their current positions), using KS statistical tests, to quantify this a statement. The KS test effectively determines whether two sets of data are drawn from the same statistical distribution and the differences between those distributions. For our purposes, larger KS values when comparing different radial regions would imply a greater degree of chemical mixing. According to these tests, young stars show distinct metallicity distributions between the different radial regions, while old stars in each region show similar metallicity distributions to one another. The average of the KS statistic values for all the galaxies comparing all the possibilities of pair or regions (i.e. 1 – 2, 1 – 3, 1 – 4, 2 – 3, 2 – 4, and 3 – 4) is 0.85 for young stars and 0.45 for old stars. These KS tests allow us to conclude that the degree of chemical mixing is greater for old stars than for young stars.

Figure 5.8 shows the MDF for young and old stars not only at the current position (left panel), but also at their birth location (middle panel) for Selene to properly assess the cause of the different mixing degrees for old and young stars. If the well-mixed MDFs displayed by old stars were due to the merger event, we should observe that old stars, taken at their birth location, exhibit distinct MDFs. However, Fig. 5.8 (left and middle panels for old stars) reveals that while there is some degree of mixing of the MDFs after the formation of the stars, there is no clear separation as found in the younger populations and the majority of the similarity in the MDFs of old stars in different regions is imprinted at birth. This statement is backed by the mean and dispersion values displayed by these distributions. Although slightly lower dispersion values and larger mean metallicity ranges are found for stars at their birth position than at the current position, this is not enough as to suggest that the mixing was imprinted by merger events[6].

To further quantify the importance of mixing induced by accretion (in contrast to mixing imprinted at birth, the right panel of Fig. 5.8 shows the

[6]For Selene, the mean metallicities ([M/H]) for old stars at their current position are −0.23, −0.38, −0.48, and −0.56 from regions 1 to 4, with metallicity dispersion of 0.13, 0.12, 0.12, and 0.11, respectively. However, at their birth location those values change to −0.20, −0.44, −0.58, and −0.31 (mean metallicities) and 0.09, 0.07, 0.07, and 0.16 (metallicity dispersions).

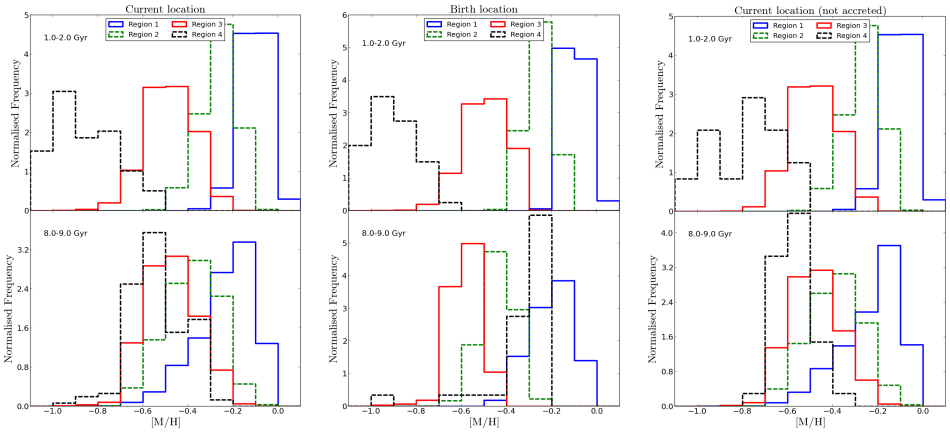

Figure 5.8: Metallicity distribution in the four different radial regions distinguishing between young (1 – 2 Gyr, upper panel) and old stars (8 – 9 Gyr, bottom panel) for Selene (left, current locations; middle, birth locations; right, current location not considering accreted stars). Blue, green, red, and black histograms represent particles in regions 1, 2, 3, and 4, respectively. The distributions are different for the young stars compared to the similar distributions in the case of the old component.

MDF of the Selene stars of star particles at regions 1 to 4 (current position) excluding accreted stars (i.e. $R_{birth} > 20$ kpc and $|z| > 3$ kpc). The mean metallicity values of those MDFs are −0.23, −0.39, −0.48, and −0.56 while their dispersions are 0.13, 0.12, 0.11, and 0.07 for old stars from regions 1 to 4. If we compare these values with those computed for the MDFs for old stars at their current positions (mean metallicities of −0.23, −0.38, −0.48, and −0.56 and dispersions of 0.13, 0.12, 0.12, and 0.11 for regions 1 – 4 respectively) and also compare the MDF shapes, we can conclude that the mixing is particularly important for region 4.

In Fig. 5.9 we show the MDFs of these stars at their current location (top panel) and at their birth location (bottom panel) to determine if the MDFs of Phase 1 stars (10 to 11.5 Gyr old) have changed during the evolution of the galaxy. The time evolution of these old stars is much weaker than for other age ranges because the MDFs of the four regions are mixed so well when the stars are born[7]. The MDFs of regions do change over time but there is no clear trend present in the MDFs taken at birth locations. Taken together with Fig. 5.8 this further demonstrates that the clearly separated MDFs seen in the youngest stars were never present in older populations that form with more homogeneous MDFs.

In summary, the well-mixed MDFs displayed by stars born during Phases 1 and 2 is not directly a result of a single satellite accretion event (although

[7]The displayed metallicity dispersions are 0.13, 0.15, 0.16, and 0.18 (0.12, 0.24, 0.20, and 0.18) from regions 1 to 4 at their current (birth) locations and their mean values are −0.44, −0.51, −0.55, and −0.65 (−0.42, −0.61, −0.58, and −0.57).

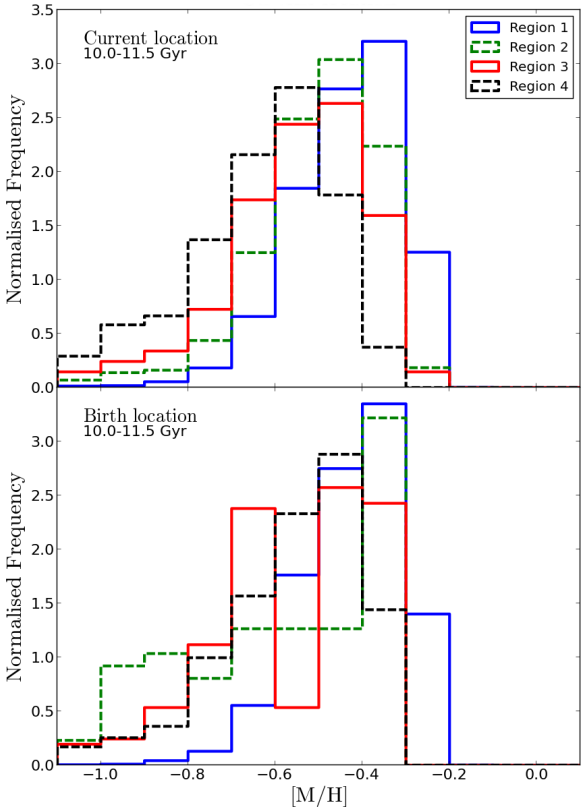

Figure 5.9: Metallicity distribution in the four different radial regions for very old stars (10.0 – 11.5 Gyr) for Selene. Coloured histograms follow the colour code explained in Fig. 5.8.

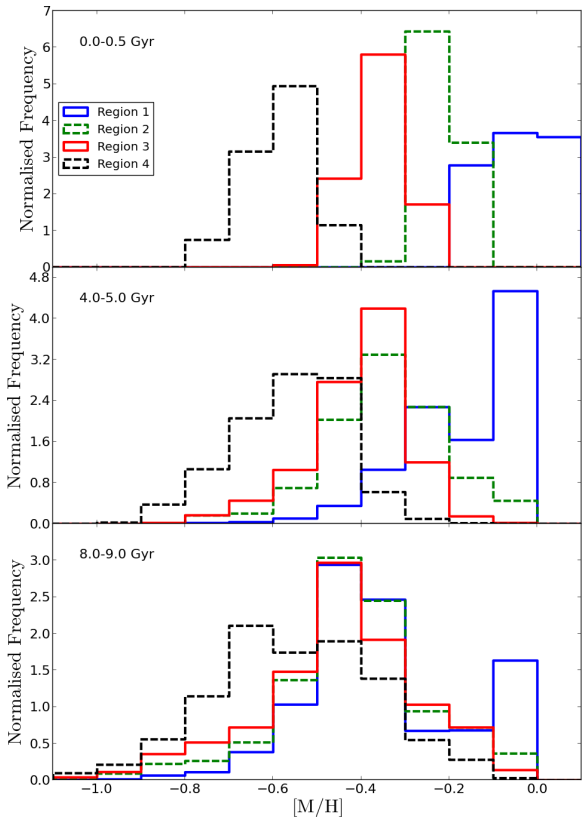

Figure 5.10: Metallicity distribution in the four different radial regions distinguishing between young (0 – 0.5 Gyr, upper panel), intermediate (4 – 5 Gyr, middle panel) and old stars (8 – 9 Gyr, bottom panel) for Oceanus (current locations). Coloured histograms follow the colour code explained in Fig. 5.8. The distributions are different for young stars compared to the similar distributions in the case of the old component. Intermediate-aged stars show an intermediate behaviour.

it also has an effect), but because of the collective activity these phases that homogenises the chemical characteristics of the gas from which stars are born.

ii) The slopes of the AMR for the four regions are always negative for the old stars (for every galaxy with just one t_{jump}). These slopes are computed by means of a linear fit to the points in the AMR in the plane $[M/H]$-Age (thus in units of dex/Gyr). These old-star AMR slopes are roughly similar, as expected from stars born at a more chemically homogeneous time in the assembly history. The relative slope differences $(100\times(\text{slope}_i - \text{slope}_j)/\text{slope}_j$, with i and j ranging from 1 to 4 accounting for all the possibilities) are under 40 % for the entire sample of the `RaDES` galaxies (40 % is reached just for the most extreme cases; the median is around 20 %). When considering the younger part of the AMR (stars younger than t_{jump}), the slopes range from negative (regions 1 and 2) to positive (region 4) in most of the galaxies. Region 3 is the region with the shallowest AMR slope. The average values considering the 19 `RaDES` galaxies are −0.031, −0.027, −0.004, and 0.008 dex/Gyr for regions 1 to 4, respectively. In the particular case of Selene the values are −0.016, −0.007, 0.002, and 0.06 dex/Gyr from region 1 to 4.

The case of Oceanus (as well as Artemis, not shown here) is a special one that deserves to be analysed in further detail. As we have already commented, Oceanus shows two merger episodes during the simulation with similar characteristics to those described in Sect. 5.1.2. Both episodes imprint a *jump* in the AVR (see Sect. 5.2.3; the *jump* at 7.5 Gyr is later erased by the effect of the last merger event) and leave a signature in the AMR. In Fig. 5.7 we can clearly distinguish three main age regions, delimited by $t_{jump-a} \sim 7.5$ and $t_{jump-b} \sim 1.2$ Gyr. Fig. 5.10 shows the metallicity distributions for three different age bins (young, intermediate, and old) for Oceanus. In this case the radial evolution of the MDF is weaker for the older age bins. The young component shows metallicity dispersions of 0.071, 0.036, 0.056, and 0.071 dex (regions 1 to 4). For the intermediate (old) component, we find a radial evolution of 0.132, 0.133, 0.111, and 0.125 dex (0.176, 0.170, 0.182, and 0.188 dex). However, it is still true (even for this two-event galaxy) that the metallicity dispersion is higher for older stars (those with ages in the range 7.5 – 10 Gyr), the metallicity dispersion has intermediate values for intermediate-aged stars, and lower values for young stars. As already outlined in the case of Selene, these well-mixed MDFs displayed by stars born during Phases 1 and 2 are mainly a consequence of gas mixing that is imprinted on the stars at birth. The radial evolution of the slope in the AMR from negative to positive is also found for the youngest stars (−0.054, −0.025, −0.0018, and 0.022 dex/Gyr), while negative AMR slopes are obtained for the intermediate and old components (except for the slope of intermediate-aged stars in region 4 which is consistent with the increasingly positive slope as a function of radius). To assess the degree of chemical

mixing we decided, as described above, to make use of KS tests. We can draw similar conclusions as before, i.e. the youngest component of the AMR has four different metallicity distributions (KS statistic of 0.96), the intermediate component shows a higher degree of mixing (KS statistic of 0.60), and the old component shows the most similar metallicity distributions (KS statistic of 0.24).

The negative-to-positive change (with decreasing age) in the slopes of the AMRs deserves a further explanation. Negative slopes in the AMR are a direct consequence of chemical enrichment due to stellar evolution. Positive slopes are difficult to produce (and indeed are not frequently found in nature) owing to chemical evolution alone, requiring efficient inflows of unenriched gas into the galaxy. Inversion of the AMR is more easily achieved through the dynamical effects of satellite accretion (metal-rich stars that are formed in the core of the satellites while passing through region 4), accretion of metal-poor gas (to form young, metal-poor stars), and radial migration. Further details can be found in Sect. 5.4.

In order to check the influence of the applied kinematic selection criterion for disc/non-disc particles on the AMR, we have repeated this analysis of the AMR for Selene considering four different J_z/J_{circ} ranges (0.5 – 0.7, 0.7 – 0.9, 0.9 – 1.1, and 1.1 – 1.3, see Fig. 5.11). The main results outlined in this section remain true for each of the J_z/J_{circ} selections, albeit with slight differences: there tend to be fewer stars forming post-t_{jump} in the lower J_z/J_{circ} cuts (particularly at larger radii) making the inverted portion of the AMR non-existent. Our disc star criterion ($0.9 < J_z/J_{circ} < 1.1$) strengthens our results as this choice is the most representative of a disc population, though it should be clear from Fig. 5.11 that the inversion is present if stars with J_z/J_{circ} in the range 0.5 – 1.3 were all included.

5.3 Chemo-dynamical imprints of satellite accretion: radial stellar motions

Sections 5.2.3 and 5.2.4 clearly point towards the effect of satellite accretion on observables such as the AVR or the AMR. We can, however, study galaxy properties other than those presently apparent, such as time evolution, stellar motions, and angular momentum. considering the richness of cosmological simulations. A careful inspection of these simulations can help us to understand the mechanisms responsible for the present-day observed properties.

In this section, we further investigate the effect of satellite accretion in the stellar age distribution at different radii (see Sect. 5.3.1) and the signatures that these events leave in the AMR (see Sect. 5.3.2).

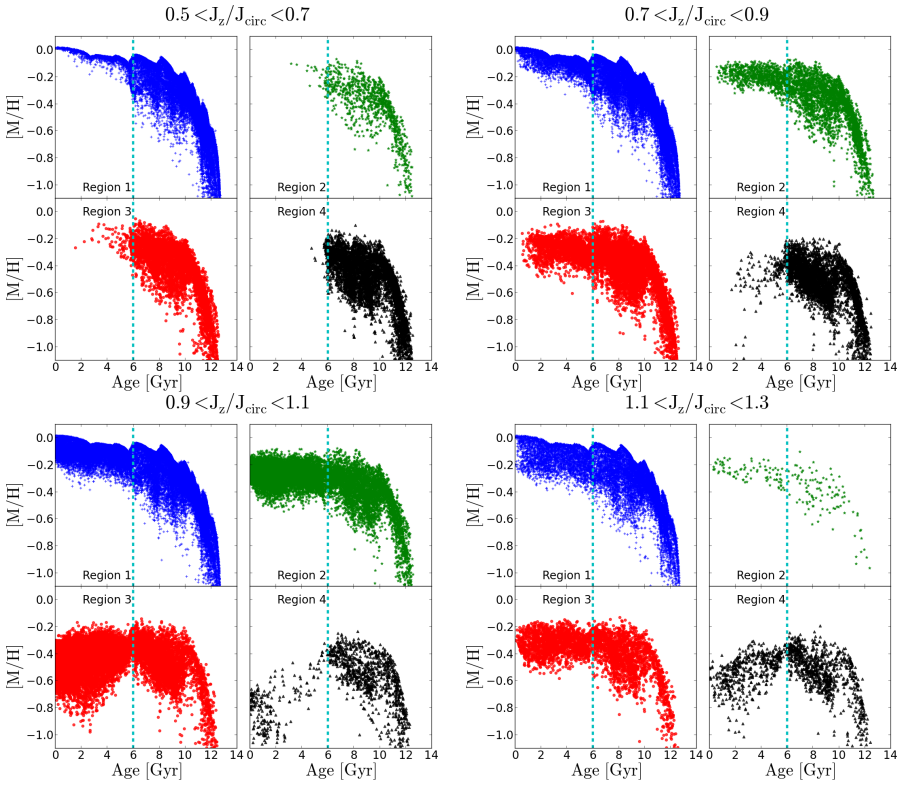

Figure 5.11: Age-metallicity relation for Selene applying different cuts in the J_z/J_{circ} ratio. Upper left, particles with J_z/J_{circ} between 0.5 and 0.7; upper right, particles with J_z/J_{circ} between 0.7 and 0.9; lower left, particles with J_z/J_{circ} between 0.9 and 1.1; lower right particles with J_z/J_{circ} between 1.1 and 1.3

5.3.1 Hints from the stellar age distribution

The study of stellar properties, such as the age or metallicity of stars currently located at specific regions, as well as their original positions, can provide us with keys to understanding galaxy evolution. Fig. 5.12 shows the current SAD (normalised to the mass of the whole galaxy) for Selene's disc stars in the four scaled regions (solid black line). At this stage we add two more regions from the outermost parts corresponding to the old plateau: region 5 at $4.4h_{in}$ – $6.2h_{in}$ and region 6 at $6.2h_{in}$ – $7.9h_{in}$. We separate the components of this current SAD according to i) particles born in each region that have stayed there (*in situ* stars, solid red line); ii) born outwards then moved in (solid green line less than 5.0 kpc, solid cyan line more than 5.0 kpc); and iii) stars born inwards and moved out (solid blue line). In this third case, we also divide them depending on the birth region: iiia) born in region 1 (dotted blue line); iiib) born in region 2 (dotted-dashed blue line); and iiic) born in region 3 (dashed blue line). Our birth radius is very close to the instantaneous radius at the time of the birth of the stars. It is defined as the location of the star in the first snapshot.

As a general trend, radial region 1 is mainly populated by old stars (older than 10 Gyr whose distribution shows a peak at 12 Gyr) that were born and stayed in that region (red line, accounting for $\sim$ 23 % of the mass in region 1), with a non-negligible fraction of stars coming from the outer parts ($\sim$ 20 % of the mass in region 1). The oldest stars (older than 10 Gyr) in radial region 2 were formed inside ($\sim$ 5 % of the mass in region 2) or far outside ($\sim$ 7 % of the mass in region 2), while the majority of the young stars (younger than 4 Gyr) formed *in situ* ($\sim$ 33% of the mass in region 2) with an important contribution of stars also born inside and outside that region ($\sim$ 6 % of the mass in region 2). The same dichotomy is found in regions 3 and 4 where older stars were born inside or much further out while young stars mainly formed there or moved outwards from the inner regions with fewer *in situ* stars, especially for region 4, which is mainly dominated by migrated stars with a small percentage of *in situ* stars ($\sim$ 16 % of the mass in region 4). Studying outwards travellers in region 4, we can see that the older the star is the more it has travelled outwards (from regions 1, 2, or 3). The radial evolution of the red lines reflects a clear inside-out growth of the disc, and we can analyse when star formation starts in each radial region: stars were formed in region 1 since the beginning of the simulation; region 2 started forming stars 10 Gyr ago; region 3, 6 Gyr ago; and region 4, 2 Gyr ago. The vast majority ($\sim$ 92 %) of stars migrating more than 5 kpc (solid cyan lines in Fig. 5.12) are accreted from outside the galaxy, i.e. $R_{birth} > 20$ kpc and $|z_{birth}| > 3$ kpc. The age distribution of these accreted stars is shown in Fig. 5.12 as a dashed cyan line.

Regions 5 and 6 are mainly populated by old stars on circular orbits coming from well outside the host galaxy (cyan lines in Fig. 5.12). Some

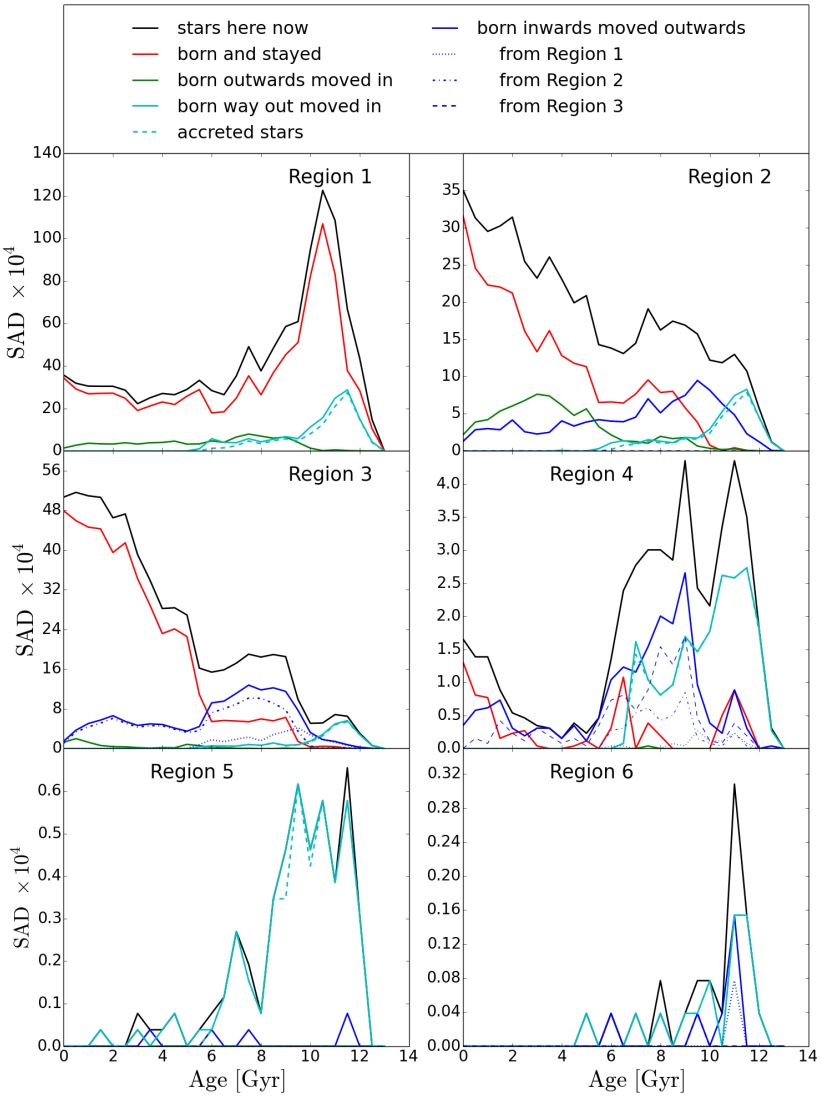

Figure 5.12: Radially resolved, stellar age distribution for the Selene disc normalised to the total stellar mass. The different panels show the stellar age distribution of the stars currently located in regions 1 (upper left), 2 (upper right), 3 (middle left), and 4 (middle right), see Table 5.2 for more information. We added two more regions in the outer most part of the galaxy. Region 5 goes from $4.4h_{in}$ to $6.2h_{in}$ and region 6 goes from $6.2h_{in}$ to $7.9h_{in}$. These two regions have been added to study the causes of the old plateau in the age distribution seen in the outermost disc. Black solid lines represent particles currently in that region; solid red line particles born and stayed there; solid green line particles born outwards and moved in; solid cyan line particles born way out and moved in; dashed cyan line accreted particles (i.e. $R_{birth} > 20$ kpc and $|z| > 3$ kpc); solid blue line particles born inwards and moved outwards currently in that region, this population of stars is divided into three more classes according to their position of origin: dotted blue line particles born in region 1 that end up there; dotted-dashed blue line particles born in region 2 that end up there; and dashed blue line particles born in region 3 that end up there. The definitions of the lines are described in full in the main text.

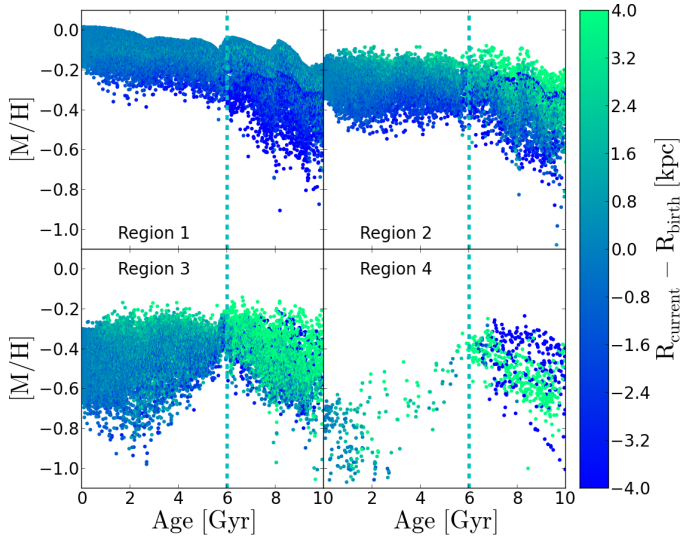

Figure 5.13: Age-metallicity relation for Selene disc particles in four different radial bins (current positions); every point represents a stellar particle colour-coded according to its $R_{current} - R_{birth}$. Distribution of plots as in Fig. 5.12 (regions 1 to 4). Dashed cyan vertical lines are located at t_{jump}. We must highlight that, although the colour-coded range goes from −4 to 4 kpc, we plot all the disc particles in that region, i.e. light green (dark blue) really means $R_{current} - R_{birth} \geq 4.0$ ($R_{current} - R_{birth} \leq -4.0$).

stars from the inner parts are also found, however, the main cause of the old plateau observed in all the `RaDES` galaxy discs is the accretion of old stars from early satellites. This is in contrast to the interpretation by Roškar et al. (2008a), who suggested that the oldest stars in the outskirts have migrated from the inner disc. We find no stars that were born in the outer parts, are still in that region, and meet the applied criterion for disc stars.

5.3.2 Hints from the AMR

In Sect. 5.2.4 we showed the radial evolution of the AMR in the `RaDES` disc galaxies and outlined the first signatures left by satellite accretion in this relation. Here, we study in more detail the AMR and expand the imprints of satellite accretion on the chemistry and dynamics of these galaxies.

Fig. 5.13 shows the same AMR displayed in Fig. 5.5 but this time split into four different sub-panels (one for each radial region) and colour-coded according to the $R_{current} - R_{birth}$ for each particle. We can draw similar conclusions to those outlined in the previous section: region 1 is mainly populated by *in situ* stars at all ages with a significant number of stars that have moved inwards, particularly from the last satellite (cyan line, stars born before t_{jump}; see Fig. 5.12). As we compare the inner with the outer regions, more and more stars appear that are moving outwards (especially amongst older populations) and fewer stars move inwards, except for those

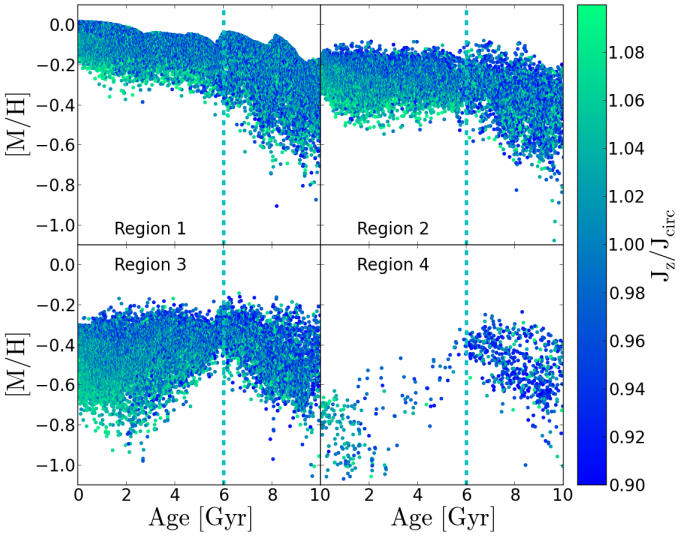

Figure 5.14: Age-metallicity relation for Selene disc particles in four radial bins (current positions), every point represents a stellar particle colour-coded according to its J_z/J_{circ}. Distribution of plots as in Fig. 5.12 (regions 1 to 4). Dashed cyan vertical lines are located at t_{jump}.

stars moving inwards that were born at the furthest distances in satellites (dark blue points in Fig. 5.13). The extreme case is found in region 4 where the majority of particles have been formed at smaller radii, some old stars come from satellites, and just a few have been born *in situ* (stars younger than 2 Gyr, when the inside-out growth of the disc reached region 4). Every old particle now located in regions 3 or 4 is either coming from the inner parts or from satellites (consistent with Fig. 5.12).

The AMR of the last accreted satellite can be discerned from the older and dark blue points in regions 1 and 2 in Fig. 5.13 (for aesthetic reasons we restrict the colour bar range from −4 to 4 kpc, i.e. dark blue points mean $R_{\rm current} - R_{\rm birth} \leq -4.0$). The shape of this AMR mimics that of the host galaxy. There is a correlation between *dips* in the AMR envelope of the host disc stars and of the satellite. We can explain such correlation as the consequence of repeated fly-bys that the satellite has experienced during its approach.

In Pilkington et al. (2012a), we studied the time evolution of one of the `RaDES` galaxy's (Apollo) *instantaneous* or gas-phase metallicity gradient, finding a shallower profile presently than at early simulation stages, i.e. the metallicity gradient of the galaxy is flattening with time. According to that work, we would expect the mean metallicity of each region to be similar for young stars and more different for older stars. However, Fig. 5.5 shows the opposite behaviour, i.e. the difference in the mean metallicity at a given age between two adjacent regions is increasing as we are moving towards

younger ages. However, this neglects the effect of stellar migration which may flatten the metallicity profile. Radial motion causes this effect as stars from the metal-rich centre of the galaxy move to the outskirts. This pushes up the mean metallicity for intermediate-aged stars found at larger radii and inverts the expected trend of the AMR because the youngest stars are born from gas with a metallicity that is lower than the centre had in the past.

A striking segregation can be seen in the metallicity of stars depending upon how they have migrated. Stars that have moved outwards are systematically more metal rich than particles that have stayed in a region or moved inwards (see Fig. 5.13). This is a direct consequence of the negative metallicity gradients and stellar radial motions and consistent with Minchev et al. (2013). In fact, if we infer the metallicity gradients from these plots (~ -0.071 dex/kpc), we obtain similar results to those presented in Few et al. (2012), see table 2 of that paper (~ -0.061 dex/kpc).

Satellite accretion not only produces a mixture in the spatial distribution of stars and an exchange of stars moving inwards/outwards, it also leaves a signature in the dynamics of the stars. In Fig. 5.14 we show the AMR split in four sub-panels, as in Fig. 5.13, but now colour-coding each stellar particle according to its circularity (J_z/J_{circ}). Despite the narrow range of J_z/J_{circ} we are considering as discs particles (0.9 – 1.1) we find another interesting trend. Specifically, in every analysed region there is little or no correlation between the stellar metallicity and J_z/J_{circ} prior to t_{jump}. This might suggest that during the epoch of satellite accretion (Phases 1 and 2 in Sect. 5.1.2), the disc was hot and mixed well, and those stars still preserve that state (as already shown and quantified in Sect. 5.2.4). If we consider the subsequent quiescent phase after satellite accretion, the stars born after t_{jump} display a new segregation with the more metal-rich stars, which tend to be migrating outwards, with the least circular orbits and vice versa.

We should emphasise that Fig. 5.1 shows (by means of t_{jump}, dashed cyan vertical lines) the moment when the last satellite merges with the disc of the host galaxy. After this time the satellites do not dynamically affect the host disc any longer. We can conclude from the above outlined analysis that satellites affect the disc properties in a continuous way until the last one totally merges with the host galaxy (not when it enters the virial radius), after that, our discs evolve mostly quiescently.

5.4 Discussion and conclusions

In this chapter of the thesis we have analysed the stellar content of the `RaDES` galaxies (Few et al. 2012) to study the effect of satellite accretion in shaping the chemo-dynamical properties of their discs. In particular, we concentrate on the characterisation of the assembly history of these galaxies and the influence of this assembly on stellar disc properties such as the age

and metallicity profiles (Sect. 5.2.2); the AVR (see Sect. 5.2.3); the AMR (see Sect. 5.2.4); and other dynamic and kinematic properties (see Sect. 5.3). We study the radial evolution of several of those properties by dividing the RaDES discs into four radial regions (see Table 5.2). In this last section we summarise all the above information as well as link with the observational results found analysing the IFS CALIFA data (see Chapter 4).

The assembly histories of the RaDES galaxies are characterised by three main phases: i) a first merger-dominated phase, when most of the mass of the galaxy is formed via accretion of massive satellites (M_{sat}/M_{host} ranging from 0.1 to 3). ii) During the second phase the host galaxy still suffers several mergers but decreases in number and mass ratio (M_{sat}/M_{host} ranging from 0.01 to 0.3, at a distance smaller than 5 kpc). iii) This second phase is followed by a quiescent period (with some sporadic satellite accretion with $M_{sat}/M_{host} \sim 0.001$) in which the disc has settled. We define t_{jump} as the time boundary between Phases 2 and 3, at which time the last satellite merges with the host galaxy. This latest accretion event is characterised by its satellite having similar characteristics for all the RaDES galaxies ($M_{sat}/M_{host} \sim 0.12 \pm 0.09$ when it enters the virial radius and $M_{sat}/M_{host} \sim 0.013 \pm 0.006$ when the merger happens, averaged values; see Table 5.1). This event marks the end of the active merging period and the beginning of quiescent evolution.

This assembly history leaves an imprint on the chemical and dynamical properties of the stellar discs of the galaxies. The AVR shows a clear *jump* (sudden for some galaxies, smooth for others) at around t_{jump} (see Fig. 5.4). This feature is a direct consequence of the heating produced by the satellite accretion. Those stars that underwent Phases 1 and 2 (older than t_{jump}) are in a hotter state now (high velocity dispersion) than young stars that were born in the quiescent Phase 3. The smoothness of the *jump* depends on the merging time-scale of the latest accretion event and subsequent internal evolution.

These differences in the velocity dispersion between old and young stars lead to differential chemical mixing in these discs. While different radial regions show different AMRs (with very different metallicity distributions) for young stars, Kolmogorov-Smirnov statistical tests show that the metallicity distributions of old stars display similar characteristics at different radii (see Figs. 5.5, 5.7, 5.8, and 5.10). Although the radial redistribution of stars due to satellite accretion and secular activity does take place, we find that the radial distribution of metals in the gas from which old stars were formed was homogeneous during Phases 1 and 2 compared with the Phase 3, and that this is the main cause of the similar MDFs displayed by old stars. Thus, radial redistribution of stars does little to change the MDFs of these older stars that are born with a flat metallicity gradient.

Most of the analysed galaxies show the above outlined assembly scenario leaving the same imprints in the AMR and MDFs. However, two of these

galaxies show two different accretion events after the disc is settled (Artemis and Oceanus; see Figs. 5.4 and 5.7). Similar results and conclusions as the ones outlined before for the rest of galaxies apply to these two cases. The bottom panel of Fig. 5.4 shows how this second event is able to heat the stars of the entire disc, regardless of their ages. The fact that the *jump* in the AVR at 7.5 Gyr is smoother than that at 1.2 Gyr might be a consequence of such heating produced by this latest accretion event (at 1.2 Gyr). To test this hypothesis, we analysed the AVR at 5.75 Gyr ago (dashed lines in the bottom panel of Fig. 5.4). We can observe that the *jump* in velocity dispersion at 7.5 Gyr was more important in the past than it is currently. This confirms the suggestion that the merger event is able to heat the entire disc of the host galaxy, swamping previous *jumps* in the AVR, especially in the inner regions. Thus, old steps in the AVR can be erased by later mergers as heating produced by mergers is more efficient on kinematically cold stars than on hot stars. In the particular case of Oceanus, the latest merger event blurs the *jump* observed at 7.5 Gyr. Our KS tests comparing the radial metallicity distribution of three age bins according to these two merger events also show that old stars display higher mixing degree, while intermediate-aged and young stars show a lower mixing degree (with the youngest stars displaying the lowest mixing, see Fig. 5.10). Although part of the observed mixing might be induced by merging of structures, the greater mixing degree displayed by old stars was imprinted at birth (as for the case of galaxies with just one merger event). The activity in Phases 1 and 2 homogenises the chemical characteristics of the gas along the entire galaxy and, as a consequence, stars formed from this homogenised gas display similar MDFs regardless their location.

Figures 5.5, 5.7, and 5.15 show *dips* in the maximum [M/H] of the central region (region 1) located at t_{jump} as well as at other time steps (to a lesser degree). Those shallower *dips* are related to the galaxy accretion history as they correspond to close encounters between the host galaxy and minor satellites. The *dips* are caused by temporary dilution of the gas in the central region by the merger either bringing metal-poor gas from the halo of the galaxy or simply adding the metal-poor gas from the surroundings of the satellite. In both cases this gas has a lower metallicity than the gas in the centre of the galaxy.

We observe two interesting segregations in the AMR plots (see Figs. 5.13 and 5.14). The innermost regions (regions 1 and 2) of the `RaDES` galaxies show that metal-rich stars have moved outwards, while metal-poorer stars have moved inwards. This behaviour can easily be explained by the observed negative metallicity profile (in fact, their gradients can be inferred from such plots; see Sect. 5.3.2). The outermost parts of the galaxies (regions 3 and 4) show such behaviour for the young stars (younger than t_{jump}), while the old stars populating those regions have migrated from the inner parts or come from satellites, i.e. formed outside of the galaxy itself.

The segregation in circularity (J_z/J_{circ}) deserves a further explanation. Fig. 5.14 shows that old stars display well-mixed values of their circularity regardless of their metallicity (a consequence of the heating mechanisms that they have undergone). However, in the case of the young stars (younger than t_{jump}), the more metal rich the star is, the lower the circularity is. We can explain this by the expectation that stars with higher J_z/J_{circ} and lower metallicities are born outside the studied annulus (as shown by Fig. 5.13). There are two ways in which these stars can appear in an annulus inwards of their birth places: i) their angular momenta decreased (i.e. inwards migration) to the value of the stars born locally, in which case J_z/J_{circ} is close to 1; or ii) they have reached the final annulus on their pericentres, but with angular momenta that is still larger than that appropriate for the annulus under consideration. It is the second case that causes the green outline at the lower metallicity range. Those stars have guiding radii outside the studied region. Similarly, lower angular momentum disc stars (dark-blue points) are accumulated at the upper metallicity edge.

In Sect. 5.2.4, we describe and quantify the main characteristics of the AMR in different radial bins for Selene. Apart from the differences in the chemical mixing between old and young stars, one of the most interesting aspects outlined is the progressive change in slope from regions 1 to 4. A negative slope in the AMR is easily explained by the fact that young stars (in a simple scenario) are born from enriched gas, and thus, are expected to be more metal rich than old stars populating the same region. The presence of radial motions (as those described in Fig. 5.13) combined with a negative metallicity profile can produce a higher dispersion in the AMR and a change in the AMR slope (Roškar et al. 2008a; Sánchez-Blázquez et al. 2009). Extreme radial motions can even cause the inversion that we observe: old stars migrate from the metal-rich centre of the galaxy to the outer parts, and stars from intermediate radii (less metal rich) move inwards. However, if we now recreate Fig. 5.5, this time colour-coding the point according to the region in which the stars were born instead of their present-day position, we still have some inversion (see Fig. 5.15). A careful analysis of the time evolution of the AMR at birth location for region 4 can explain this inverted AMR. Satellites orbiting around the host galaxy are forming stars in their inner parts with metallicities similar to those displayed by the centre of the host galaxy. Before merging with the host galaxy, the satellites pass through region 4 several times (the clusters of black triangles at $\sim$ 6.5 and 8.0 Gyr in the case of the satellite responsible for the t_{jump}) forming stars within region 4, particles that after the merger took place acquire a circular orbit (fulfilling the disc criterion). These particles are metal-rich stars. In addition, we find a low number of particles that are born in region 4 from metal-poor gas accreted from the halo or other satellite haloes with ages between 3.0 and 6.0 Gyr. As a consequence of the metal-poor gas accretion and the low star formation activity, gas in region 4 becomes progressively

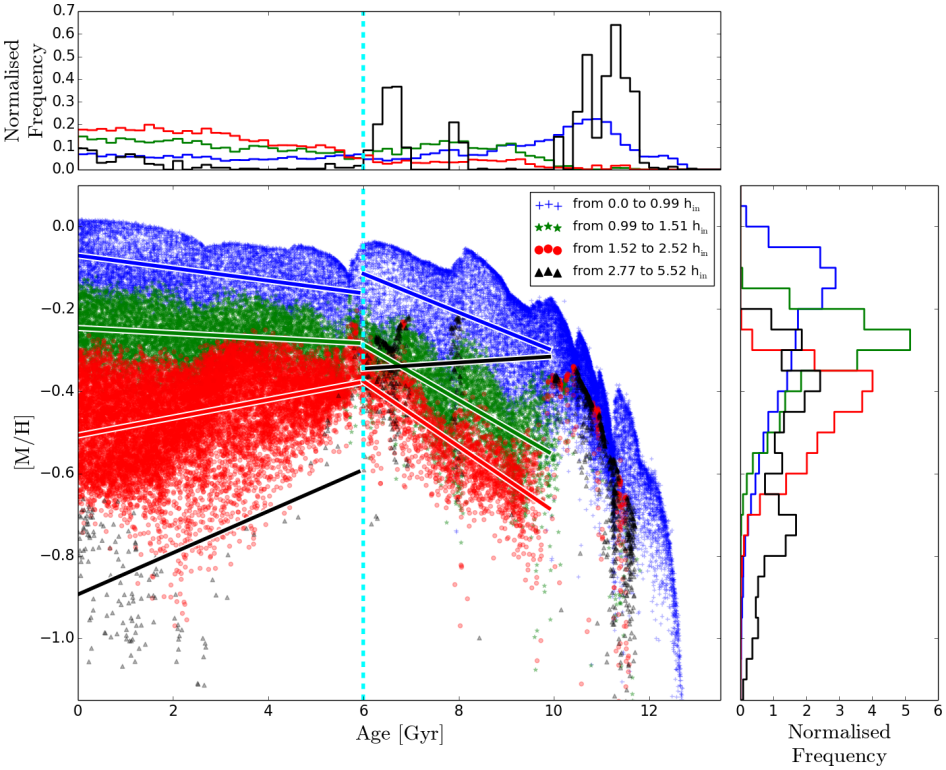

Figure 5.15: Age-metallicity relation for Selene disc stars, colour-coded according to their birth radius. See Fig. 5.5 for further information.

more metal poor. Finally, we find a group of newly born stars (younger than 2.0 Gyr) due to inside-out growth of the disc reaching region 4 (see red line in region 4, Fig. 5.12). Once true disc star formation is established the normal negative gradient to the AMR reappears (the last 2.0 Gyr). This scenario naturally leads to an inverted AMR in region 4 even when radial motions are not considered. The same reasoning can be applied to region 3 (outer parts in general), with the difference that inside-out growth reaches this region much sooner (6 Gyr ago, see Fig. 5.12).

Positive slopes in the AMR of the outer parts of nearby galaxies have already been observed. Bernard et al. (2012) studied the SFH and AMR of two outer fields in M31 and another field in M33 using the data from Barker et al. (2011), both based on HST/ACS CMDs. The SFH and AMR found in both galaxies show enhanced star formation at ~ 2 Gyr and an inverted AMR for stars younger than ~ 3 Gyr, similar to that in the outer parts of Oceanus in this work. They suggest that this star formation enhancement and the inverted AMR is caused by a close encounter between M31 and M33 2 – 3 Gyr ago according to the N-body simulations by McConnachie et al. (2009). In addition, Bernard et al. (2012) find that the analysed outer fields

in M31 and M33 are older than the inner parts, suggesting a "U-shaped" age profile in contrast to the purely negative profile found by Williams et al. (2009) in M33. To compare with our results we must keep in mind that, while they are observing the consequences of a close encounter between two massive spiral galaxies, we are considering the entire assembly history of the `RaDES` galaxies. This work and these observational and theoretical works confirm that satellite merging or galaxy encounters leave a signature in observable quantities, such as the AMR or the age profile, especially in the outer parts.

In Bernard et al. (2015), the team expanded upon their previous analysis in M31 by analysing 14 outer fields located along the disc, the Giant Stellar Stream (GSS) which is caused by satellite accretion, and in regions in between. They are able to confirm the inverted AMR already outlined in Barker et al. (2011) and Bernard et al. (2012) for all the analysed fields. In addition, they deduce that most of the mass in the disc regions was already formed by z $\sim$ 1, while stream-like regions are on average older, as expected since the GSS origin is linked to satellite accretion. Joining the above result with our findings we confirm that satellite merging or galaxy encounters leave a signature in observable quantities such as the AMR or the age profile, especially in the entire outer disc.

In Villalobos & Helmi (2008, 2009), the authors study the effect that 1:5 mass-ratio (at virial radius) satellite mergers have upon the thick disc properties using N-body simulations of a satellite that is accreted by a pre-existing disc galaxy. They find that $\sim$ 2 Gyr after the merger event occurs the properties of the heated discs have settled and stop evolving further (roughly consistent with our findings). They claim that the kinematic impact on their host (thin) discs is almost negligible in the case of the vertical and azimuthal components, while in the case of the radial velocity dispersions they usually increase their value by 5 – 10 km s^{-1} at all radii. We find increases from $\sim$ 50 % in the inner parts to $\sim$ 100 % in the velocity dispersion of the outer parts for Selene (latest satellite with a mass ratio of $\sim$ 1:10). This suggests strong disc flaring, an important aspect of the formation of thick discs in a cosmological context (Minchev et al. 2015). However, although the effect we see in these simulations in the heating of the discs from satellite accretion is greater than in the case of Villalobos & Helmi (2008, 2009), we must take into account that the *jump* in the AVR is a consequence of Phases 1 and 2. While Villalobos & Helmi (2008, 2009) analyse controlled experiments in which one unique satellite merges with a host galaxy, these simulations are embedded in a cosmological context and, thus, this greater heating is not only caused by the latest merging event, but is a consequence of all previous mergers.

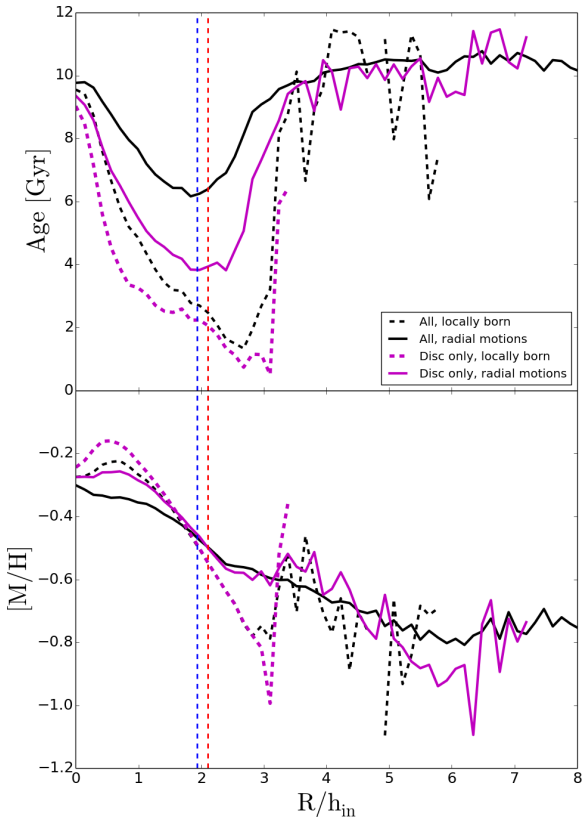

Figure 5.16: Selene age and metallicity profiles for all particles and for disc particles alone, either including or removing radial motions. Solid lines: we allow stars to move radially to compute the age and metallicity profiles. Dashed lines: stars born locally, not allowing radial motions. Black lines: all the particles in the simulation (disc+spheroid). Magenta lines: particles fulfilling the disc criterion. This plot is focused on understanding the effect of radial motions in the age and metallicity profiles. Red (blue) vertical dashed lines are located at the break (minimum age) radius. h_{in} is the inner disc scale-length in SDSS r-band mock images from `SUNRISE` (Jonsson 2006), these mock images can be seen in Few et al. (2012).

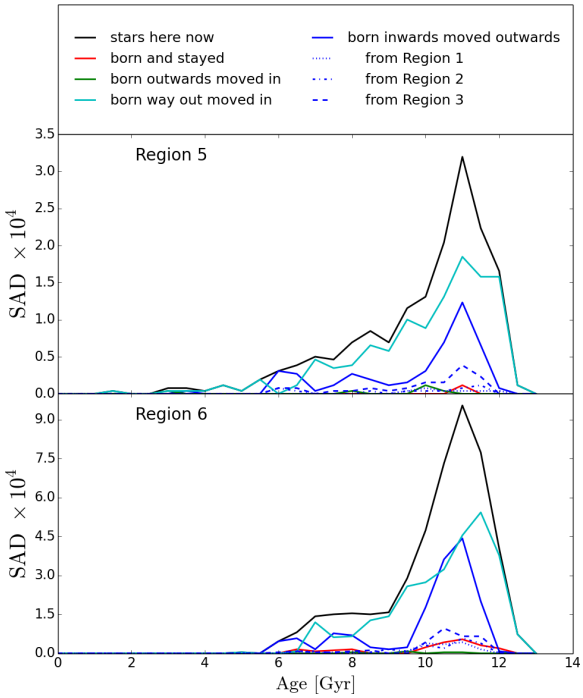

Figure 5.17: Radially resolved, stellar age distribution for Selene, normalised to the total stellar mass. In this plot we study all the particles in the simulation (in Fig. 5.12 we show only disc particles). The upper panel shows the stellar age distribution of the stars currently located in region 5 (from $4.4h_{in}$ to $6.2h_{in}$) while the bottom panel shows stars currently located in region 6 ($6.2h_{in}$ to $7.9h_{in}$). Lines and colours represent the same as in Fig. 5.12. A low number of old, *in situ* stars are responsible for shaping the old outer plateau even in the absence of radial motions if we do not apply the disc criterion.

5.4.1 Revisiting the "U-shape" age profile

Every age profile for the RaDES galaxies exhibits the same behaviour (see Sect. 5.2.2 and Fig. 5.3): a negative profile, followed by an upturn that ends up in an old plateau at large galactocentric radius. Although recent simulations find these "U-shape" profiles in the stellar age distribution of their simulated discs displaying downbending SB profiles (e.g. Roškar et al. 2008b,a; Sánchez-Blázquez et al. 2009; Martínez-Serrano et al. 2009), in this analysis we are able to find such "U-shaped" age profiles regardless their SB (see Appendix D; 2 type I, 8 type II, and 9 type III galaxies). The analysis of the light distribution in the RaDES galaxies has been performed in a 1D basis using some mock images generated with SUNRISE (see Appendix D for further information). As commented in Sect. 2.3.1, the different samples under analysis and the different decomposition method employed can explain the different percentages of SB profiles found here if compared with CALIFA (see Sect. 2.3.1).

Different mechanisms have been proposed to explain "U-shaped" age profiles, but there is still a lack of consensus (see Chapter 1 and Sect. 5.2.2). The findings presented in this chapter, and consistently with the results in Chapter 4, point to three main aspects responsible for shaping the disc age profiles:

a) An inside-out growth of the disc: as discussed in Sect. 5.3.1 and shown by Fig. 5.12 (red lines), RaDES discs display a clear inside-out growth of the disc. This mechanism can account for the inner part (negative gradient) of the age profile.

b) Radial motions (inwards and outwards) of stars belonging to the disc: Figure 5.12 (blue lines) also shows that the regions where the upturn in age appears are dominated by old stars that have move outwards (especially region 4) with the contribution of some young, *in situ* stars.

c) Accreted, old stars from satellites: Phases 1 and 2 populate the analysed discs with old stars coming from the accretion of satellites. Such accretion is also responsible for the "U-shape" in the age profile as part of the old stars in regions 3 and 4 come from satellites (cyan lines in Fig. 5.12). However, these old accreted stars are especially responsible for the old plateau observed at large galactocentric distances (see Fig. 5.3). Regions 5 and 6 are mainly populated by these old accreted stars.

However, although radial motions might play an important role in creating the "U-shaped" age profile (Roškar et al. 2008b,a), they are not necessarily needed to build up such a profile according to some simulations (Sánchez-Blázquez et al. 2009; Halle et al. 2015). In Fig. 5.16 we analyse the effect that radial motions and the disc-particle criterion (based on J_z/J_{circ}) imprint in the shape of the age and metallicity profiles.

Radial motions have their greatest effect on the age minimum, i.e. a younger minimum in the age profile is found when suppressing radial mo-

tions. This is because the minimum age is in a prime location to be migrated to (it can easily receive stars from larger and smaller radii) and because migrating stars tend to be older. However, "U-shaped" age profiles are found whether we allow stars to migrate or not, i.e. radial motions affect the shape of the age profile but are not in fact the origin of the "U-shape".

To explain why the "U-shaped" age profile is still recovered after suppressing radial motions we need to analyse the stellar content in the outer parts of the RaDES simulated galaxies (regions 4, 5, and 6, see Fig. 5.12). Region 4 shows some *in situ* star formation around 6, 7, and 11 Gyr ago, this star formation can easily explain the upturn in the age profile. However, the old plateau disappears if we suppress radial motions for disc stars (while still visible if we analyse all the particles, see Fig. 5.16). This old plateau disappears for disc particles because of the lack of *in situ* disc stars at large radii. However, if we study the entire sample of stellar particles (spheroid and disc component), we can find that an old, non-disc population exists in this outermost regions of the RaDES galaxies, suggesting early star formation in these outer parts (see Fig. 5.17).

In recent years, there is a growing body of work claiming that the formation of the outer disc of the Milky Way may have begun as early as 10 Gyr ago (e.g. see discussions in Haywood et al. 2013; Snaith et al. 2014; Halle et al. 2015). This suggests that, apart from radial migration, other mechanisms might be in place while shaping these outer regions. In particular, Nidever et al. (2014), analysing APOGEE data (Majewski et al. 2010), find a complex Milky Way formation from a well-mixed and turbulent interstellar medium with different SFHs for inner and outer discs. In addition, more studies are finding upturns in the age profiles in the outer parts of, not only spiral galaxies, but also dwarfs (Hidalgo et al. 2013).

These findings are in agreement to what obtained from the analysis of the CALIFA data. In Sect. 4.1 we find that "U-shaped" age profiles are more common than expected, not only restricted to type II galaxies, but also present in type I. Although we do not find that all those analysed galaxies display such behaviour, we can conclude that the mechanisms shaping the SB and age profiles are not coupled. In this chapter we detect hints suggesting that all spiral display an age upturn in their outermost regions. The lack of universality of this "U-shape" from the observed galaxies might be just an observational effect caused by the CALIFA limited field of view. In Sect. 4.2 we further check the role of radial motions on shaping the SB and age profiles concluding that radial migration cannot be the main responsible of the light distribution observed profiles or, at least, that the redistribution of material is not significant.

The decoupling in the causes of the light and age distributions in spiral galaxies together with the fact that radial migration cannot be the most important mechanism shaping both distributions support the above proposed scenario. The findings presented in this thesis support an scenario where

the outer parts are built by a combination of an inside-out growth of the disc, radial motions (inwards and outwards) of disc stars, accreted stars from satellites, and an early star formation along the entire disc.

Both radial motions and the application of less restrictive disc-particle criteria have a flattening effect on the metallicity profiles. The reason for this is straightforward; particles that move radially inwards by the greatest distances are old, metal-poor stars that strongly affect the regions where the average metallicity is higher (lowering the average metallicity). In addition, particles moving outwards were formed in high-metallicity gas and move towards regions dominated by low-metallicity stars, thus, this outwards motion increases the mean stellar metallicity in the outer parts. The impact of relaxing our disc-particle criterion has the same effect. Relaxing the criteria allows more spheroid particles to be considered in the analysis, in particular particles that are characterised as old and metal poor, and thus reduces the mean metallicity in the metal-rich regions more strongly while making little difference to the metal-poor regions. In the case of Selene, the metallicity gradient evolves from -0.20, -0.19, -0.13, and -0.12 dex/h_{in} from locally born disc stars, all locally born stars, disc stars with radial motions, and all stars with radial motions, respectively.

The assembly history of disc galaxies leaves important fingerprints in their chemical and dynamical properties. Based on this assembly history, we have been able to explain previously observed features, such as the dispersion in the AMR, inverted AMR gradients, and "U-shaped" age profiles. Satellites mainly affect the host disc when they completely merge with it, although some star formation and gas dilution can be observed during the different satellite fly-bys. These fingerprints should be easily observed in present and upcoming spectroscopic surveys such as `Gaia` (Perryman et al. 2001), `RAVE` (Steinmetz et al. 2006; Zwitter et al. 2008; Siebert et al. 2011; Kordopatis et al. 2013), `SEGUE` (Yanny et al. 2009), `APOGEE` (Majewski et al. 2010), or `4MOST` (de Jong et al. 2012) helping us to understand the physics shaping the present-day observable properties of the Milky Way.

Conclusions and future work

"You know nothing, Jon Snow."
— George R.R. Martin, A Song of Ice and Fire

"All we have to decide is what to do with the time that is given us."
— J.R.R. Tolkien, The Fellowship of the Ring

In this thesis we have tried to contribute to the general understanding on how spiral galaxies form and evolve through the analysis of the stellar content up to their outer parts. The importance of analysing these outer regions rely on the fact that they display very long dynamical time-scales compared with the more turbulent inner regions, and thus, they retain fossil records from the time of galaxy assembly and formation. Recent developments in instrumentation and analysis techniques have made possible to carry out an observational study of these outer regions, something that was not feasible with classical tools. This study is crucial for testing and constraining galaxy formation and evolution models.

We have made use of CALIFA IFS and SDSS photometric data for a sample of 88 spiral galaxies to characterise their light distribution and their stellar content up to their outermost regions. In addition, we have analysed the `RaDES` set of fully-cosmological simulated galaxies to study the effects of the cosmological assembly history on the chemical and dynamical properties of their discs up to the outskirts. Every single step has turned out to be a laborious task that has allowed us to contribute to the complex attempt of studying and understanding how galaxies work.

1. We have analysed the light distribution of the studied sample of galaxies using a 2D approach (GASP2D). We have obtained the structural components (bulge, bar, disc, broken disc, etc) that better suit the SDSS science frames in three filters independently (g, r, and i). In addition, we compare these results with other works published in the literature, finding some important discrepancies in the frequency of

profile types and in the recovered structural parameters. Although some of them can be attributed to the different criteria defining the analysed samples, others might be due to the different decomposition methods used. For this reason, we also apply an alternative 1D decomposition to the sample of galaxies analysed in this thesis. We obtain different results with both approaches, suggesting that the study of the SB profiles is biased by the decomposition method used.

As future work, we plan to carry out an exhaustive analysis of the light distribution on a larger sample of galaxies. We intend to perform such study following different decomposition methods, able to detect broken exponentials, by fitting 1D SB profiles (e.g. Pohlen & Trujillo 2006; Erwin et al. 2008; Gutiérrez et al. 2011) and 2D photometric data (e.g. Méndez-Abreu et al. 2008, 2014; Erwin 2015). With this analysis we aim to assess why the recovered light distribution parameters are contingent upon the use of different decomposition methods.

2. We have followed a strategy based on full spectrum fitting codes (`pPXF`, `GANDALF`, and `STECKMAP`) applied to the CALIFA IFS data. This methodology allows us to obtain reliable information of the stellar content of external galaxies, where the analysis of resolved stellar populations is not feasible. We evaluate the reliability of this method by comparing SFHs from integrated spectra to those obtained from deep CMDs of resolved stars in a region in the Large Magellanic Cloud bar. The similarities found in the recovered SAD and AMR following both approaches (average differences ~ 4.1 %) support the use of full spectrum fitting techniques and give reliability to the obtained results.

   In the future, we plan to expand this analysis to a sample of Local Group dwarf galaxies bracketing a range of properties. This will allow us to identify the impact that different factors (such as different SFHs, fractions of young vs old stars, the existence of a blue horizontal branch or blue straggler stars) may have on the results. Not only will this comparison identify where full spectrum fitting techniques may fail and where they succeed, but it will also provide information on the spectral ranges and features that are more likely to improve these techniques. Understanding the limits of the reliability of SFHs obtained from integrated spectra provides an important basis for the understanding of galaxies at low and high redshift.

3. We observe "U-shape" L-W age profiles indistinctly for galaxies displaying type I and II SB profiles. Based on these results we can claim that the different behaviours showed by the light distributions in the outer parts of spiral galaxies are not due to a change in the age of the stars populating those regions. In other words, different mechanisms have to be responsible for the shape of the SB and the stellar age

distributions. Although we do not observe "U-shape" age profiles in all the analysed galaxies, we cannot discard that it is a consequence of the limited field of view, with the mentioned age upturn appearing beyond the analysed regions. In addition, this feature disappears if we obtain M-W profiles, displaying flat trends of ~ 10 Gyr suggesting that recent star formation plays an important role in shaping the observed "U-shape" L-W age profiles. These results are in agreement with a scenario in which an early star formation builds up an old, extended disc; and afterwards, subsequent star formation is quenched inside-out while radial migration progressively smoothens the observed age profile.

The analysis of the inner stellar content, also carried out in this thesis, allows us to put constraints on the role of radial migration for future theoretical works. We find that there are no differences in the inner gradients of stellar properties for galaxies with different SB types. With this result we cannot conclude whether radial migration is the main mechanism or it is just one of many mechanisms shaping the different SB profiles. However, we can claim that the amount of stars displaced from their birth locations is not a significant fraction of the total stellar mass.

The comparison between the inner radial trends of the L-W stellar properties and colours suggests the existence of a weak correlation between them. However, this correlation is mainly driven by low massive galaxies as the recent star formation dominates in light in these systems. M-W quantities are not traced at all by colours.

The flexibility of the employed method to extract stellar information from integrated spectra allows an easy extension to other IFS datasets such as SAMI (Croom et al. 2012) or MANGA (Law & MaNGA Team 2014) to enlarge the number of galaxies under analysis. This will ensure obtaining statistically significant results. In addition, it can be applied to data with higher spatial resolution such as MUSE (Bacon et al. 2010) allowing a 2D characterisation of the galaxies without precedent.

4. In this thesis we also analyse the `RaDES` set of simulated galaxies. `RaDES` comprises 19 Milky Way-like systems with a wide variety of properties such as kinematic heating profiles, SFHs, disc fractions, or SB profiles. Despite these different characteristics, some important similarities are displayed by all of them.

   According to the analysis of the `RaDES` galaxies, assembly histories in spiral galaxies leave important fingerprints in their discs. At earlier times, satellite accretion is the main mechanism causing the growth of the disc and this intense bombardment leaves its signature in observ-

ables such as the AMR, AVR, or the SAD. In particular, this period ends with a last merging event (at time t_{jump}) marking the onset of important radial differences in those observables.

Inverted AMR trends in the outer parts of discs, for stars younger than t_{jump}, are found as a consequence of the combined effect of radial motions and star formation in satellites temporarily located in these outer parts. "U-shaped" stellar age profiles change to an old plateau ($\sim$ 10 Gyr) in the outer discs for the entire `RaDES` sample. This shape is a consequence of the inside-out growth of the disc, radial motions of disc stars (inwards and outwards), and the accretion of old stars from satellites. We see comparable age profiles even when ignoring the influence of stellar migration due to the presence of an early *in situ* star formation in the outer regions of the galaxy.

As future work, we plan to analyse radial motion efficiencies in this set of simulations for galaxies displaying different SB profiles. This will allow us to theoretically assess the main conclusions outlined in chapter 4 about the role of radial migration in shaping SB profiles and the amount of stellar mass displaced from their birth locations.

Conclusiones y trabajo futuro

"No sabes nada, Jon Nieve."
— George R.R. Martin, Canción de Hielo y Fuego

"Todo lo que tenemos que decidir es qué hacer con el tiempo que se nos ha dado."
— J.R.R. Tolkien, La Comunidad del Anillo

En esta tesis hemos tratado de contribuir a la comprensión general sobre cómo las galaxias espirales se forman y evolucionan mediante el estudio de su contenido estelar analizando estos sistemas hasta sus partes más externas. La importancia de analizar estas regiones exteriores recae en el hecho de que presentan escalas de tiempo dinámicas muy grandes en comparación con las turbulentas regiones internas y, como consecuencia, conservan información sobre la formación y ensamblaje de las galaxias. Recientes avances en instrumentación y técnicas de análisis han permitido el estudio observacional hasta estas partes externas de estos sistemas, algo que no era posible con las herramientas clásicas. Este estudio es crucial para testear y constreñir modelos de formación y evolución galáctica.

A lo largo de esta tesis hemos hecho uso de los datos de espectroscopía de campo integral proporcionados por el proyecto CALIFA y de datos fotométricos de Sloan (SDSS) para un muestra de 88 galaxias espirales con el fin de caracterizar su distribución de luz y su contenido estelar hasta las partes más externas. Además, hemos analizado un conjunto de galaxias simuladas en un marco cosmológico (`RaDES`) para estudiar los efectos de su ensamblaje en las propiedades químicas y dinámicas de sus discos hasta sus límites exteriores. Todos y cada uno de los pasos dados han resultado ser una dura labor que nos ha permitido contribuir al difícil proceso de estudiar y entender cómo funcionan las galaxias.

1. Hemos analizado la distribución en dos dimensiones de la luz prove-

niente de las galaxias estudiadas haciendo uso del código GASP2D. De esta forma hemos obtenido las componentes estructurales (bulbo, barra, disco, doble disco, etc) que mejor se ajustan a los datos fotométricos analizados en tres filtros de manera independiente (g, r e i). Además comparamos dichos resultados con otros trabajos publicados en la literatura encontrando algunas diferencias importantes en los porcentajes de galaxias con distintos tipos de perfil de brillo superficial y en los parámetros estructurales que recuperamos. Aunque algunas de las diferencias pueden ser debidas a los diferentes criterios utilizados para definir las muestras de galaxias analizadas, otras podrían ser debidas a los diferentes métodos de descomposición empleados. Por esta razón, nosotros también llevamos a cabo una descomposición alternativa en una dimensión sobre la muestra de galaxias analizada en esta tesis. Dicha comparativa arroja diferentes resultados con ambos métodos, sugiriendo que el estudio de los perfiles de brillo superficial está sesgado por el método de descomposición utilizado.

Como trabajo futuro, tenemos planeado llevar a cabo un análisis exhaustivo de la distribución de luz en una muestra de galaxias más grande. Nuestra intención es hacer dicho estudio empleando diversos métodos de descomposición que sean capaces de detectar discos con dobles exponenciales en perfiles en una dimensión (como en Pohlen & Trujillo 2006; Erwin et al. 2008; Gutiérrez et al. 2011) y en datos fotométricos en dos dimensiones (Méndez-Abreu et al. 2008, 2014; Erwin 2015). Con este análisis pretendemos abordar las causas que provocan que los parámetros que caracterizan las distribuciones de luz observadas dependan del método de descomposición utilizado.

2. Hemos seguido una estrategia basada en códigos capaces de maximizar el rango de longitud de onda utilizado de los espectros observados de CALIFA (`pPXF`, `GANDALF`, and `STECKMAP`). Esta metodología nos permite obtener información del contenido estelar en galaxias externas, donde el análisis de poblaciones estelares resueltas no es posible. Evaluamos la credibilidad de este método para derivar historias de formación estelar a partir de datos espectroscópicos comparando la información obtenida a partir de espectros integrados con aquella utilizando diagramas de color-magnitud de estrellas resueltas en una región de la barra de la Gran Nube de Magallanes. La concordancia encontrada en las distribuciones de edad estelar y la relación edad-metalicidad siguiendo ambas metodologías (diferencias del orden del 4.1 %) respalda el uso del método desarrollado durante esta tesis dando fiabilidad a los resultados obtenidos.

   En un futuro, tenemos pensado expandir este análisis a una muestra de galaxias enanas del Grupo Local cubriendo un amplio rango

de propiedades. Esto nos permitirá identificar el impacto que diversos factores (como diferentes historias de formación estelar, diferentes fracciones de población joven y vieja o la existencia de estrellas en la rama horizontal azul) pueden tener en los resultados. Esta comparación nos permitirá identificar las limitaciones de estas técnicas espectroscópicas así como los rangos y características espectrales en los que centrarnos para la mejora de las mismas. Comprender hasta qué punto podemos creernos las historias de formación estelar obtenidas a partir de espectros integrados es básico para llegar a un entendimiento general sobre la física de las galaxias.

3. Observamos forma en "U" en los perfiles de edad pesados por luz para galaxias que muestran distintos perfiles de brillo superficial (tipos I y II). En base a estos resultados podemos afirmar que los distintos comportamientos de la distribución de luz en las partes externas de las galaxias espirales no se deben a un cambio en la edad de las estrellas que pueblan dichas regiones. En otras palabras, los mecanismos responsables para la formación de las distribuciones de edad estelar y de luz deben ser diferentes. Aunque no observamos dicha forma en "U" en todas las galaxias analizadas, tampoco podemos descartar que sea simplemente consecuencia del campo de visión de CALIFA y que por lo tanto, el envejecimiento exterior se encuentre más allá de la región analizada. Además, esta forma en "U" desaparece si analizamos perfiles pesados por masa, mostrándonos entonces un aplanamiento en torno a unos 10 Giga-años de edad. Esto sugiere que la formación estelar reciente debe jugar un papel fundamental a la hora de producir la observada forma en "U" en los perfiles de edad cuando pesamos por luz. Estos resultados son compatibles con un escenario en el que una formación estelar temprana crea un disco viejo y extendido; tras lo cual, la formación estelar se va apagando de dentro hacia afuera mientras que la migración radial suaviza progresivamente el perfil de edad observado.

   El análisis del contenido estelar interno, también llevado a cabo en esta tesis, nos permite poner límites al papel que juega la migración radial para futuros trabajos teóricos. Encontramos que no hay diferencias en los gradientes internos de propiedades estelares para galaxias de distintos tipos de brillo superficial. En base a este resultado, no podemos concluir si la migración radial es el principal mecanismo o simplemente uno de tantos mecanismos que dan forma a las distribuciones de luz de las galaxias. Sin embargo, sí podemos afirmar que la cantidad de estrellas desplazadas de sus posiciones de nacimiento no es significativa comparada con la masa estelar total del sistema.

   La comparación entre los gradientes radiales internos de las propie-

dades estelares pesadas por luz y los colores sugiere la existencia de una correlación débil entre ambos. Sin embargo, esta correlación es fundamentalmente debido a las galaxias de más baja masa, ya que en ellas la formación estelar más reciente domina en luz. Por otro lado, las propiedades estelares obtenidas pesando por masa no pueden ser trazadas de ninguna manera por medio de colores.

La flexibilidad del método empleado para obtener información de las estrellas a partir de datos espectroscópicos nos permite extenderlo a otros proyectos de espectroscopía de campo integral como SAMI (Croom et al. 2012) o MANGA (Law & MaNGA Team 2014) para aumentar el número de galaxias analizadas. Esto nos asegurará la obtención de resultados con significancia estadística. Además, esta metodología puede ser aplicada a datos con una mayor resolución espacial como los obtenidos con el instrumento MUSE (Bacon et al. 2010), permitiéndonos una caracterización en dos dimensiones de las galaxias espirales sin precedente.

4. Como se ha mencionado anteriormente, en esta tesis también llevamos a cabo un análisis basado en un conjunto de galaxias simuladas (`RaDES`). `RaDES` está compuesto por 19 sistemas de masas comparables a la de la Vía Láctea con una variedad importante de propiedades como perfiles de calentamiento cinemático, historias de formación estelar, tamaño del disco o perfiles de brillo superficial. A pesar de estas características tan diferentes, todas ellas muestran una serie de peculiaridades comunes.

   Según el análisis de las galaxias de `RaDES`, el ensamblaje cosmológico de las galaxias espirales deja huellas importantes en sus discos. En las primeras épocas de la evolución, la acreción de satélites es el principal mecanismo que hace que los discos crezcan y este intenso bombardeo además deja una clara señal en observables como la relación edad-metalicidad, la relación edad-dispersión de velocidades o la distribución de edad estelar. En particular, este período termina con un último evento (en el momento denominado t_{jump}) que marca el comienzo de una serie de importantes diferencias radiales en dichos observables.

   Tendencias inversas en la relación edad-metalicidad en los discos externos, para estrellas más jóvenes que t_{jump}, se encuentran como consecuencia del efecto combinado de migración radial y formación estelar en satélites temporalmente localizados en dichas regiones externas. En todas las galaxias de `RaDES` podemos observar perfiles de edad en forma en "U" que presentan un aplanamiento en la edad ($\sim$ 10 Gyr) en las partes más externas. Esta forma es consecuencia del crecimiento de dentro hacia afuera del disco, de movimientos radiales de estrellas

del disco (hacia adentro y hacia afuera) y de la acreción de estrellas viejas provenientes de satélites. Estos perfiles en forma en "U" son detectables incluso si no tenemos en cuenta la influencia de la migración estelar, debido a la presencia de una formación estelar temprana en las partes externas de las galaxias.

Como trabajo futuro, analizaremos en detalle la eficiencia de dichos movimientos radiales en este conjunto de simulaciones para galaxias con diferentes tipos de brillo superficial. Esto nos permitirá abordar teóricamente las principales conclusiones a las que llegamos en el capítulo 4 sobre el papel de la migración radial a la hora de dar forma a los perfiles de brillo superficial y sobre la cantidad de masa estelar que realmente es desplazadada de sus posiciones de nacimiento.

Final words

As stated in the introduction, this thesis was nothing but a small step in the humble attempt of understanding part of the knowledge that our Universe is hiding. Whether I have accomplish such optimistic goal or not is for you to decide. What I know is that I have given the best of myself. What I know is that I have learnt as much as I could. What I know is that a better version of the guy who started this project five years ago is writing these lines now. But, with no doubt, the best of all this period is not the life experiences I have collected, or the knowledge I have found... The best of this thesis is the people I have met.

Everything is this life has an end, and this thesis is not an exception. Dear reader, with this last sentence I say farewell. This is the end of a project. A project that has lasted for more than five years or, in other words, more than 350 pages. But a new one is knocking on the door. A new period to return to the Universe all the good that it has given me over these years.

∞

Appendices

Appendix A

Sample characterisation tables (CALIFA)

In this appendix we summarise the main properties of the CALIFA galaxies analysed in this thesis in five different tables. These tables include general information (see Table A.1) as well as information obtained in Sects. 2 and 3 of this thesis (see Tables from A.2 to A.5). The explanation to each of these tables is as follows:

Table A.1 Sample characterisation I: general properties
(1) Name of the galaxy; (2)-(3) right ascention and declination (J2000); (4) morphological type; (5) $\log(M_{galaxy}/M_{\odot})$; (6)-(7) d_{25} (in arcsec and kpc); (8) redshift; (9) comoving distance. Columns (1)-(4) and (6)-(8) are taken from the hyperleda database (Makarov et al. 2014). Column (5) is computed according to the recipe outlined in Sect. 4.3. Column (9) is computed from column (8) with the WMAP9 cosmology (Hinshaw et al. 2013).

Table A.2 Sample characterisation II: surface brightness, stellar age, and colour distribution parameters
(1) Name of the galaxy; (2) surface Brightness type; (3)-(4) inner disc scale-length (h_{in}, in arcsec and kpc); (5)-(6) outer disc scale-length (h_{in}, in arcsec and kpc); (7) break radius in units of h_{in} (R_{break}/h_{in}); (8) mean ellipticity of the outermost isophotes; (9) mean position angle of the outermost isophotes; (10) radius at which the minimum in age is found, normalised to h_{in} (R_{min}/h_{in}); (11) radius at which the minimum in colour is found, normalised to h_{in} ($R_{min,colour}/h_{in}$, where $R_{min,colour}$ is the mean value between the colour profiles for which a "U-shape" is identified; i.e. $g-r$, $g-i$, and/or $r-i$). Columns (2) to (9) are the results from the 2D light distribution decomposition using GASP2D (see Sect. 2.3.1). Tenth column comes from the analysis of the stellar content from the CALIFA data (see Sect. 4.1). Eleventh column comes from the analysis of the SDSS colour profiles (see Sect. 2.3.2). The galaxies for which we can analyse the stellar content in the outer parts (beyond around three disc scale-lengths for type I galaxies and beyond the break radius for type II and III galaxies) are marked with

a star in the first column.

In tables A.3, A.4, and A.5, along with the name of the galaxy (first column), a number is found reporting problems with the linear fits to the stellar parameters profiles:

[1] No gradients are computed because the avoided central region is larger than the CALIFA radial coverage.

[2] No outer gradients are computed as R_{break} is greater than the CALIFA radial coverage.

[3] No outer gradients are computed as we have less than 4 valid data points in the radial profiles.

[4] No inner gradients are computed as we have less than 4 valid data points in the radial profiles between the end of the avoided central region and the onset of the outer region (R_{break} or the limit of the valid data, etc.).

[5] No gradients are computed due to issues with the analysed CALIFA data. We do not have valid data points in the radial profiles beyond the avoided central region.

Table A.3 Sample characterisation III: stellar age gradients
(1) Name of the galaxy; (2)-(3) slope of the linear fit to the luminosity-weighted stellar log(Age) profile in the inner parts (dex/h_{in} and dex/kpc); (4)-(5) slope of the linear fit to the luminosity-weighted stellar log(Age) profile in the outer parts (dex/h_{in} and dex/kpc); (6)-(7) slope of the linear fit to the mass-weighted stellar log(Age) profile in the inner parts (dex/h_{in} and dex/kpc); (8)-(9) slope of the linear fit to the mass-weighted stellar log(Age) profile in the outer parts (dex/h_{in} and dex/kpc). This table is the result of applying the methodology outlined in Sect. 3.1 to the analysed sample of CALIFA galaxies.

Table A.4 Sample characterisation IV: stellar metallicity gradients
(1) Name of the galaxy; (2)-(3) slope of the linear fit to the luminosity-weighted stellar [M/H] profile in the inner parts (dex/h_{in} and dex/kpc); (4)-(5) slope of the linear fit to the luminosity-weighted stellar [M/H] profile in the outer parts (dex/h_{in} and dex/kpc); (6)-(7) slope of the linear fit to the mass-weighted stellar [M/H] profile in the inner parts (dex/h_{in} and dex/kpc); (8)-(9) slope of the linear fit to the mass-weighted stellar [M/H] profile in the outer parts (dex/h_{in} and dex/kpc). This table is the result of applying the methodology outlined in Sect. 3.1 to the analysed sample of CALIFA galaxies.

Table A.5 Sample characterisation V: colour inner gradients
(1) Name of the galaxy; (2)-(3) slope of the linear fit to the $g - r$ profile in the inner parts (dex/h_{in} and dex/kpc); (4)-(5) slope of the linear fit to the $g - i$ profile in the inner parts (dex/h_{in} and dex/kpc); (6)-(7) slope of the linear fit to the $r - i$ profile in the inner parts (dex/h_{in} and dex/kpc). This table is the result of the light distribution analysis presented in Sect. 2.3 to the analysed sample of CALIFA galaxies.

Table A.1 Sample characterisation I: general properties

Name	R.A. (h m s)	Dec. (^{o} $'$ $''$)	Morph. type	$\log(M_{galaxy})$ ($M_\odot$)	d_{25} ($''$)	d_{25} (kpc)	z	Distance (Mpc)
(1)	(2)	(3)	(4)	(5)	(6)	(7)	(8)	(9)
ESO540-G003	00 35 39.49	−20 07 31.37	SABb	9.43	87.73	20.17	0.01111	47.95
IC0159	01 46 25.05	−08 38 11.83	SBb	9.23	81.12	21.79	0.01301	56.13
IC0776	12 19 03.11	+08 51 22.15	SBd	8.65	67.17	11.35	0.00814	35.15
IC1199	16 10 34.34	+10 02 25.32	Sbc	9.79	71.47	23.23	0.01580	68.10
IC1256	17 23 47.28	+26 29 11.47	Sb	9.75	76.59	25.05	0.01590	68.54
IC1683	01 22 38.92	+34 26 13.65	Sc	9.95	78.91	26.26	0.01619	69.75
IC5309	23 19 11.64	+08 06 34.04	Sb	9.47	77.12	22.27	0.01401	60.39
MCG-01-10-015	03 38 39.16	−05 20 50.45	Scd	9.34	87.13	24.73	0.01377	59.36
NGC0001	00 07 15.86	+27 42 29.09	Sb	10.08	94.01	29.31	0.01515	65.29
NGC0234	00 43 32.39	+14 20 33.24	SABc	10.01	94.44	28.92	0.01487	64.10
NGC0237	00 43 27.84	−00 07 29.74	SABc	9.68	78.19	22.38	0.01388	59.86
NGC0477	01 21 20.48	+40 29 17.33	SABc	9.87	93.14	37.31	0.01956	84.24
NGC0496	01 23 11.59	+33 31 45.38	Sbc	9.85	53.48	21.95	0.02005	86.35
NGC0551	01 27 40.63	+37 10 58.73	SBbc	10.15	89.16	31.76	0.01735	74.76
NGC0716	01 52 59.68	+12 42 30.50	Sb	10.04	79.10	24.94	0.01532	66.04
NGC0768	01 58 40.93	+00 31 45.16	SBbc	9.96	93.57	44.51	0.02334	100.41
NGC0873	02 16 32.37	−11 20 54.52	Sc	9.86	88.75	24.51	0.01339	57.72
NGC1093	02 48 16.13	+34 25 11.35	SABa	9.92	69.69	25.31	0.01770	76.25
NGC1094	02 47 27.83	−00 17 06.47	SABa	10.11	79.46	34.85	0.02147	92.40
NGC1211	03 06 52.42	−00 47 40.17	S0a	10.00	89.57	19.92	0.01075	46.37

continues on next page

continues from previous page

Name	R.A. (h m s)	Dec. (^{o} $'$ $''$)	Morph. type	log(M_{galaxy}) ($M_\odot$)	d_{25} ($''$)	d_{25} (kpc)	z	Distance (Mpc)
(1)	(2)	(3)	(4)	(5)	(6)	(7)	(8)	(9)
NGC1659	04 46 29.94	−04 47 19.87	Sbc	9.82	89.98	28.22	0.01523	65.67
NGC1677	04 50 52.08	−04 53 33.56	Sbc	8.91	89.98	17.22	0.00923	39.85
NGC2449	07 47 20.29	+26 55 48.70	Sab	10.17	86.13	28.92	0.01634	70.40
NGC2486	07 57 56.48	+25 09 39.12	Sa	9.89	89.16	28.40	0.01548	66.72
NGC2540	08 12 46.44	+26 21 42.39	Sc	9.85	74.50	31.90	0.02095	90.18
NGC2572	08 21 24.62	+19 08 51.99	Sa	10.25	72.97	39.39	0.02658	114.30
NGC3815	11 41 39.29	+24 48 01.79	Sab	9.59	86.33	22.09	0.01239	53.42
NGC3994	11 57 36.86	+32 16 39.43	Sc	9.61	50.95	10.87	0.01030	44.46
NGC4470	12 29 37.77	+07 49 27.12	Sa	9.23	76.94	12.57	0.00787	33.96
NGC4644	12 42 42.66	+55 08 43.89	SBb	9.75	90.81	30.71	0.01645	70.91
NGC4711	12 48 45.86	+35 19 57.72	SBb	9.61	72.30	20.27	0.01359	58.61
NGC4961	13 05 47.56	+27 44 02.89	SBc	8.95	66.86	11.86	0.00855	36.90
NGC5267	13 40 39.96	+38 47 38.71	SBb	10.25	92.08	37.25	0.01976	85.10
NGC5376	13 55 16.05	+59 30 23.80	SABa	9.58	88.95	12.87	0.00696	30.05
NGC5633	14 27 28.38	+46 08 47.67	Sb	9.42	65.34	10.53	0.00776	33.49
NGC5657	14 30 43.59	+29 10 50.95	SBb	9.61	29.39	7.93	0.01308	56.41
NGC5682	14 34 44.97	+48 40 12.83	SBb	8.58	38.74	6.10	0.00758	32.71
NGC5732	14 40 38.95	+38 38 16.16	Sbc	9.23	73.82	19.16	0.01257	54.22
NGC5888	15 13 07.37	+41 15 52.67	SBbc	10.56	79.83	47.00	0.02908	124.97
NGC5947	15 30 36.00	+42 43 01.00	SBbc	9.90	70.01	28.17	0.01965	84.62
NGC5971	15 35 36.90	+56 27 42.07	Sa	9.35	75.19	17.53	0.01127	48.62
NGC6155	16 26 08.33	+48 22 00.46	Sc	9.33	79.64	13.35	0.00807	34.84
NGC6186	16 34 25.48	+21 32 27.26	Sa	9.77	94.22	19.18	0.00983	42.41
NGC6394	17 30 21.42	+59 38 23.62	Sc	10.21	25.95	14.94	0.02842	122.16
NGC6478	17 48 37.73	+51 09 13.68	Sc	10.13	86.93	40.20	0.02267	97.56

continues on next page

continues from previous page

Name	R.A. (h m s)	Dec. (^{o} $'$ $''$)	Morph. type	log(M_{galaxy}) ($M_\odot$)	d_{25} ($''$)	d_{25} (kpc)	z	Distance (Mpc)
(1)	(2)	(3)	(4)	(5)	(6)	(7)	(8)	(9)
NGC6497	17 51 17.96	+59 28 15.15	Sb	9.65	87.13	18.93	0.01050	45.29
NGC6978	20 52 35.43	−05 42 40.04	Sb	10.28	90.60	36.97	0.01994	85.85
NGC7047	21 16 27.64	−00 49 35.37	Sb	10.15	80.20	31.76	0.01933	83.26
NGC7311	22 34 06.79	+05 34 13.16	Sab	10.48	88.34	27.36	0.01504	64.83
NGC7321	22 36 28.02	+21 37 18.35	Sbc	10.31	84.75	41.03	0.02376	102.24
NGC7466	23 02 03.46	+27 03 09.34	Sb	10.10	92.50	47.16	0.02506	107.79
NGC7489	23 07 32.69	+22 59 53.12	Sc	9.83	72.97	31.03	0.02079	89.53
NGC7536	23 14 13.18	+13 25 34.95	SBbc	9.74	95.31	30.72	0.01567	67.53
NGC7563	23 15 55.92	+13 11 46.04	Sa	10.27	91.87	27.16	0.01435	61.86
NGC7738	23 44 02.05	+00 30 59.83	Sb	10.41	71.15	33.16	0.02285	98.32
NGC7819	00 04 24.50	+31 28 19.22	Sb	9.68	86.33	29.58	0.01668	71.86
UGC00005	00 03 05.64	−01 54 49.80	Sbc	10.18	83.59	41.43	0.02434	104.71
UGC00036	00 05 13.88	+06 46 19.30	Sa	10.26	88.75	38.02	0.02096	90.23
UGC00139	00 14 31.86	−00 44 15.20	SABc	9.22	94.01	25.55	0.01317	56.80
UGC01368	01 54 13.13	+07 53 01.14	Sab	10.16	80.20	43.59	0.02677	115.11
UGC01659	02 09 56.90	+16 01 57.30	SBc	10.04	83.78	46.54	0.02738	117.71
UGC01918	02 27 32.47	+25 40 07.55	SBab	9.88	91.44	31.86	0.01696	73.09
UGC02099	02 37 12.98	+21 34 03.30	S0a	10.40	70.49	39.25	0.02745	117.99
UGC02403	02 55 57.25	+00 41 33.37	SBa	9.88	82.06	23.19	0.01370	59.09
UGC02405	02 55 57.57	+06 29 41.21	Sc	9.86	81.31	42.47	0.02569	110.50
UGC02443	02 58 21.50	−02 02 30.76	Sc	9.00	78.37	13.65	0.00839	36.21
UGC02690	03 20 42.94	−01 06 31.09	SBbc	9.52	81.50	34.93	0.02097	90.26
UGC03253	05 19 41.88	+84 03 09.43	Sb	9.73	82.44	23.40	0.01377	59.36
UGC03944	07 38 36.50	+37 38 00.63	Sc	9.23	41.51	11.16	0.01302	56.17
UGC04145	07 59 40.11	+15 23 12.52	Sa	9.98	87.13	27.81	0.01551	66.85

continues on next page

continues from previous page

Name	R.A. (h m s)	Dec. (^{o} $'$ $''$)	Morph. type	log(M_{galaxy}) ($M_\odot$)	d_{25} ($''$)	d_{25} (kpc)	z	Distance (Mpc)
(1)	(2)	(3)	(4)	(5)	(6)	(7)	(8)	(9)
UGC04195	08 05 06.90	+66 46 58.92	SBb	9.84	92.29	31.19	0.01644	70.85
UGC05108	09 35 26.28	+29 48 45.43	SBab	10.21	65.64	36.11	0.02711	116.57
UGC05359	09 58 51.64	+19 12 53.91	SABb	9.94	93.36	53.53	0.02830	121.62
UGC05396	10 01 40.48	+10 45 23.13	Sc	9.57	87.93	32.62	0.01809	77.91
UGC07012	12 02 03.14	+29 50 52.73	SBc	8.75	64.89	13.73	0.01022	44.08
UGC07145	12 09 50.98	+38 13 07.05	Sc	9.73	82.82	37.46	0.02216	95.37
UGC08004	12 51 37.96	+31 21 09.94	SABc	9.37	66.09	27.94	0.02067	88.99
UGC09067	14 10 45.45	+15 12 33.85	Sab	9.94	48.77	25.93	0.02617	112.54
UGC09476	14 41 32.02	+44 30 45.97	SABc	9.43	90.19	20.36	0.01091	47.08
UGC09542	14 49 01.18	+42 27 50.13	Scd	9.63	86.13	32.32	0.01830	78.82
UGC10796	17 16 47.72	+61 55 12.42	Sb	8.67	78.19	16.56	0.01023	44.13
UGC10811	17 18 43.72	+58 08 06.42	Sb	10.19	72.14	42.49	0.02909	125.02
UGC11262	18 30 35.69	+42 41 33.70	Sc	9.22	82.06	31.33	0.01862	80.22
UGC11740	21 26 14.35	+09 47 52.45	Sbc	9.73	70.49	30.98	0.02151	92.60
UGC12185	22 47 25.06	+31 22 24.67	SBab	10.00	83.78	37.93	0.02218	95.46
UGC12224	22 52 38.36	+06 05 37.04	Sc	9.63	89.57	21.78	0.01176	50.75
UGC12653	23 32 29.96	+14 49 00.62	Sc	9.23	88.54	24.50	0.01341	57.84
UGC12816	23 51 50.68	+03 04 57.90	SABc	9.31	53.48	19.51	0.01778	76.61

Table A.1: Sample characterisation I: general properties.

Table A.2 Sample characterisation II: surface brightness and stellar age distribution parameters

Name	SB profile	h_{in} ($''$)	h_{in} (kpc)	h_{out} ($''$)	h_{out} (kpc)	R_{break}/h_{in}	e	PA (^{o})	R_{min}/h_{in}	$R_{min,colour}/h_{in}$
(1)	(2)	(3)	(4)	(5)	(6)	(7)	(8)	(9)	(10)	(11)
ESO540-G003	I	14.76	3.39	–	–	–	0.55	115.13	–	–
IC0159*	I	12.16	3.27	–	–	–	0.31	57.98	1.58	1.80
IC0776	II	28.84	4.87	8.85	1.50	1.53	0.47	178.78	–	–
IC1199*	II	17.94	5.83	7.82	2.54	1.46	0.61	111.58	1.20	–
IC1256*	I	10.98	3.59	–	–	–	0.38	176.87	–	–
IC1683*	I	14.69	4.89	–	–	–	0.42	76.51	–	1.53
IC5309*	I	12.76	3.68	–	–	–	0.50	63.69	–	–
MCG-01-10-015*	II	21.12	5.99	9.62	2.73	1.15	0.72	14.93	1.18	1.15
NGC0001*	I	13.83	4.31	–	–	–	0.35	178.01	–	–
NGC0234*	II	18.17	5.56	10.15	3.11	1.55	0.13	19.05	1.20	1.44
NGC0237*	I	9.45	2.70	–	–	–	0.40	92.67	1.50	2.33
NGC0477*	I	16.83	6.74	–	–	–	0.38	132.00	–	–
NGC0496*	II	13.49	5.54	6.50	2.67	3.10	0.44	56.27	–	–
NGC0551*	I	14.30	5.09	–	–	–	0.57	133.50	2.00	2.16
NGC0716*	I	11.66	3.68	–	–	–	0.57	25.83	–	–
NGC0768*	II	13.79	6.56	5.55	2.64	3.12	0.60	64.34	–	–
NGC0873*	I	10.02	2.77	–	–	–	0.15	129.17	–	2.06
NGC1093*	I	12.56	4.56	–	–	–	0.34	173.84	–	–
NGC1094*	III	6.19	2.72	12.63	5.54	3.17	0.32	176.90	–	–
NGC1211	II	23.15	5.15	7.92	1.76	2.94	0.18	128.17	–	–

continues on next page

continues from previous page

Name	SB profile	h_{in} ($''$)	h_{in} (kpc)	h_{out} ($''$)	h_{out} (kpc)	R_{break}/h_{in}	e	PA (^{o})	R_{min}/h_{in}	$R_{min,colour}/h_{in}$
(1)	(2)	(3)	(4)	(5)	(6)	(7)	(8)	(9)	(10)	(11)
NGC1659⋆	I	11.75	3.69	–	–	–	0.36	40.41	–	–
NGC1677⋆	III	6.62	1.27	10.80	2.07	2.91	0.70	131.79	–	–
NGC2449⋆	I	13.39	4.50	–	–	–	0.63	137.40	1.45	1.89
NGC2486	II	26.86	8.56	9.27	2.95	1.31	0.41	177.64	–	–
NGC2540⋆	II	12.51	5.36	5.16	2.21	2.79	0.38	143.61	–	–
NGC2572⋆	I	8.87	4.79	–	–	–	0.58	132.74	1.80	–
NGC3815⋆	I	11.08	2.83	–	–	–	0.59	21.03	2.60	–
NGC3994⋆	III	5.97	1.27	14.89	3.18	4.30	0.55	80.30	–	–
NGC4470⋆	I	10.80	1.76	–	–	–	0.32	88.28	1.25	1.25
NGC4644⋆	I	10.27	3.47	–	–	–	0.66	41.58	–	–
NGC4711⋆	II	14.07	3.94	8.51	2.39	1.85	0.53	48.19	1.80	1.78
NGC4961⋆	II	14.53	2.58	9.46	1.68	2.39	0.32	170.20	–	–
NGC5267⋆	II	24.07	9.74	6.80	2.75	1.45	0.61	37.54	–	1.23
NGC5376⋆	II	20.40	2.95	11.69	1.69	1.50	0.43	25.36	1.20	1.05
NGC5633⋆	I	8.88	1.43	–	–	–	0.33	76.51	1.70	1.61
NGC5657⋆	I	14.65	3.96	–	–	–	0.61	99.82	–	–
NGC5682⋆	I	16.33	2.57	–	–	–	0.70	146.19	–	–
NGC5732⋆	II	9.93	2.58	5.79	1.50	3.75	0.43	50.30	1.40	–
NGC5888⋆	II	16.55	9.74	7.72	4.55	1.66	0.41	117.08	1.30	1.33
NGC5947⋆	II	14.03	5.65	4.96	2.00	2.25	0.18	28.46	–	–
NGC5971	II	18.13	4.23	5.91	1.38	2.26	0.64	138.18	–	–
NGC6155⋆	II	11.65	1.95	7.28	1.22	3.28	0.30	123.50	1.55	1.54
NGC6186	II	40.04	8.15	9.05	1.84	0.93	0.15	27.35	–	–
NGC6394⋆	II	12.47	7.18	7.50	4.32	2.82	0.59	51.83	–	–
NGC6478⋆	II	20.68	9.57	11.90	5.50	1.31	0.63	58.81	1.60	–

continues on next page

continues from previous page

Name	SB profile	h_{in} ($''$)	h_{in} (kpc)	h_{out} ($''$)	h_{out} (kpc)	R_{break}/h_{in}	e	PA (^{o})	R_{min}/h_{in}	$R_{min,colour}/h_{in}$
(1)	(2)	(3)	(4)	(5)	(6)	(7)	(8)	(9)	(10)	(11)
NGC6497⋆	II	20.33	4.42	6.84	1.49	1.78	0.53	-20.47	1.40	1.63
NGC6978⋆	I	14.05	5.73	–	–	–	0.63	142.61	1.45	2.18
NGC7047	II	17.26	6.83	9.02	3.57	1.46	0.51	163.33	–	–
NGC7311⋆	I	11.74	3.63	–	–	–	0.48	77.62	2.05	2.62
NGC7321⋆	I	11.35	5.50	–	–	–	0.45	78.95	2.20	–
NGC7466⋆	II	14.87	7.58	6.41	3.27	2.71	0.61	65.06	–	–
NGC7489⋆	I	12.87	5.47	–	–	–	0.44	105.93	–	–
NGC7536	II	26.94	8.68	9.76	3.15	0.95	0.59	34.22	–	–
NGC7563⋆	II	62.15	18.38	7.77	2.30	0.68	0.50	118.66	–	–
NGC7738	I	17.39	8.11	–	–	–	0.29	19.82	–	–
NGC7819⋆	II	22.47	7.70	12.74	4.37	1.69	0.43	0.04	–	–
UGC00005⋆	II	12.62	6.25	7.92	3.93	2.71	0.49	40.97	1.50	2.24
UGC00036⋆	I	9.53	4.08	–	–	–	0.55	72.11	2.10	1.74
UGC00139	III	12.00	3.26	17.43	4.74	2.49	0.58	11.05	–	–
UGC01368⋆	II	11.82	6.42	9.41	5.12	2.18	0.73	37.70	1.70	–
UGC01659⋆	II	22.83	12.68	8.25	4.58	1.33	0.60	52.27	1.10	–
UGC01918	II	17.96	6.26	9.62	3.35	1.95	0.57	152.24	–	–
UGC02099	I	18.44	10.27	–	–	–	0.64	133.15	–	0.78
UGC02403	I	18.53	5.24	–	–	–	0.62	122.58	–	–
UGC02405	II	13.70	7.15	4.95	2.59	3.55	0.66	103.77	–	–
UGC02443⋆	II	21.10	3.67	7.99	1.39	1.28	0.51	108.18	0.85	1.01
UGC02690	II	11.25	4.82	5.99	2.57	3.33	0.58	119.03	–	–
UGC03253⋆	I	12.60	3.58	–	–	–	0.41	13.29	–	–
UGC03944⋆	I	11.77	3.16	–	–	–	0.49	147.50	–	–
UGC04145⋆	I	15.37	4.91	–	–	–	0.51	137.89	–	–

continues on next page

continues from previous page

Name	SB profile	h_{in} ($''$)	h_{in} (kpc)	h_{out} ($''$)	h_{out} (kpc)	R_{break}/h_{in}	e	PA (^{o})	R_{min}/h_{in}	$R_{min,colour}/h_{in}$
(1)	(2)	(3)	(4)	(5)	(6)	(7)	(8)	(9)	(10)	(11)
UGC04195⋆	II	21.00	7.10	7.72	2.61	1.71	0.43	76.85	–	–
UGC05108⋆	II	28.42	15.64	10.97	6.03	1.16	0.63	129.61	–	–
UGC05359⋆	I	11.32	6.49	–	–	–	0.65	174.68	–	–
UGC05396⋆	II	17.18	6.38	7.13	2.65	2.67	0.66	113.95	1.70	–
UGC07012⋆	III	8.30	1.76	13.62	2.88	2.84	0.45	75.75	–	–
UGC07145⋆	II	14.03	6.35	5.94	2.69	2.71	0.64	117.66	–	–
UGC08004⋆	II	16.07	6.79	7.13	3.01	2.93	0.64	83.61	–	–
UGC09067⋆	I	8.67	4.61	–	–	–	0.54	76.10	–	–
UGC09476⋆	II	17.50	3.95	6.69	1.51	2.46	0.35	146.76	–	–
UGC09542⋆	II	14.56	5.46	9.86	3.70	2.63	0.74	57.42	1.80	–
UGC10796	I	37.37	7.91	–	–	–	0.46	168.31	–	–
UGC10811⋆	II	20.43	12.03	9.31	5.48	1.13	0.66	0.43	–	–
UGC11262	II	17.52	6.69	9.63	3.68	1.81	0.64	42.65	–	–
UGC11740	I	13.62	5.99	–	–	–	0.67	151.06	–	–
UGC12185⋆	II	27.26	12.34	7.89	3.57	1.43	0.54	115.44	0.85	–
UGC12224	I	18.98	4.62	–	–	–	0.15	53.87	–	–
UGC12653⋆	II	16.98	4.70	9.65	2.67	2.51	0.71	169.12	–	1.28
UGC12816	II	21.16	7.72	8.05	2.94	1.81	0.49	130.20	–	–

Table A.2: Sample characterisation II: surface brightness, stellar age, and colour distribution parameters.

Table A.3 Sample characterisation III: stellar age gradients

Name	$\nabla \log(Age)_{\mathrm{L,in}}$		$\nabla \log(Age)_{\mathrm{L,out}}$		$\nabla \log(Age)_{\mathrm{M,in}}$		$\nabla \log(Age)_{\mathrm{M,out}}$	
	(dex/h_{in})	(dex/kpc)	(dex/h_{in})	(dex/kpc)	(dex/h_{in})	(dex/kpc)	(dex/h_{in})	(dex/kpc)
(1)	(2)	(3)	(4)	(5)	(6)	(7)	(8)	(9)
ESO540-G003[1]	–	–	–	–	–	–	–	–
IC0159	0.11 ± 0.01	0.039 ± 0.005	–	–	-0.037 ± 0.009	-0.013 ± 0.003	–	–
IC0776[2]	-0.88 ± 0.05	-0.114 ± 0.006	–	–	-0.09 ± 0.03	-0.012 ± 0.004	–	–
IC1199	-0.25 ± 0.03	-0.081 ± 0.009	0.00 ± 0.08	0.00 ± 0.03	-0.19 ± 0.03	-0.063 ± 0.009	0.30 ± 0.11	0.10 ± 0.04
IC1256	-0.069 ± 0.009	-0.019 ± 0.002	–	–	-0.03 ± 0.01	-0.007 ± 0.004	–	–
IC1683	-0.47 ± 0.13	-0.10 ± 0.03	–	–	-0.26 ± 0.12	-0.05 ± 0.02	–	–
IC5309	-0.05 ± 0.02	-0.013 ± 0.004	–	–	-0.10 ± 0.01	-0.024 ± 0.003	–	–
MCG-01-10-015	-0.55 ± 0.03	-0.090 ± 0.005	0.14 ± 0.04	0.024 ± 0.007	-0.03 ± 0.02	-0.005 ± 0.003	-0.20 ± 0.05	-0.033 ± 0.009
NGC0001	-0.21 ± 0.02	-0.053 ± 0.005	–	–	-0.04 ± 0.02	-0.010 ± 0.005	–	–
NGC0234	-0.15 ± 0.02	-0.026 ± 0.003	0.84 ± 0.10	0.15 ± 0.02	-0.11 ± 0.01	-0.020 ± 0.002	0.16 ± 0.16	0.03 ± 0.03
NGC0237	0.09 ± 0.01	0.030 ± 0.004	–	–	-0.069 ± 0.010	-0.024 ± 0.003	–	–
NGC0477	-0.37 ± 0.01	-0.077 ± 0.003	–	–	-0.12 ± 0.01	-0.024 ± 0.002	–	–
NGC0496[2]	0.214 ± 0.009	0.040 ± 0.002	–	–	-0.041 ± 0.006	-0.008 ± 0.001	–	–
NGC0551	0.28 ± 0.03	0.047 ± 0.006	–	–	0.09 ± 0.03	0.015 ± 0.005	–	–
NGC0716	0.24 ± 0.03	0.058 ± 0.007	–	–	0.03 ± 0.02	0.007 ± 0.005	–	–
NGC0768[2]	0.06 ± 0.01	0.013 ± 0.003	–	–	-0.03 ± 0.01	-0.007 ± 0.002	–	–
NGC0873	0.113 ± 0.008	0.024 ± 0.002	–	–	-0.111 ± 0.010	-0.023 ± 0.002	–	–
NGC1093	-0.12 ± 0.02	-0.036 ± 0.007	–	–	-0.27 ± 0.02	-0.079 ± 0.007	–	–
NGC1094	-0.06 ± 0.02	-0.028 ± 0.008	-0.04 ± 0.02	-0.02 ± 0.01	-0.25 ± 0.02	-0.111 ± 0.007	0.10 ± 0.02	0.04 ± 0.01
NGC1211[1]	–	–	–	–	–	–	–	–
NGC1659	-0.05 ± 0.01	-0.019 ± 0.005	–	–	-0.12 ± 0.01	-0.045 ± 0.005	–	–
NGC1677	0.41 ± 0.04	0.20 ± 0.02	0.03 ± 0.02	0.01 ± 0.01	-0.08 ± 0.05	-0.04 ± 0.02	0.00 ± 0.02	0.00 ± 0.01
NGC2449	0.118 ± 0.008	0.046 ± 0.003	–	–	0.006 ± 0.006	0.002 ± 0.002	–	–
NGC2486[2]	-0.85 ± 0.04	-0.094 ± 0.005	–	–	-0.18 ± 0.03	-0.019 ± 0.004	–	–
NGC2540[3]	-0.02 ± 0.02	-0.005 ± 0.006	–	–	-0.06 ± 0.02	-0.015 ± 0.005	–	–
NGC2572	0.23 ± 0.02	0.061 ± 0.006	–	–	0.12 ± 0.02	0.031 ± 0.006	–	–
NGC3815	0.10 ± 0.01	0.017 ± 0.002	–	–	-0.065 ± 0.008	-0.011 ± 0.001	–	–
NGC3994	0.27 ± 0.01	0.175 ± 0.007	-0.09 ± 0.04	-0.06 ± 0.02	0.024 ± 0.008	0.016 ± 0.005	-0.03 ± 0.03	-0.02 ± 0.02
NGC4470	0.29 ± 0.01	0.125 ± 0.005	–	–	0.03 ± 0.01	0.014 ± 0.004	–	–
NGC4644	-0.208 ± 0.010	-0.124 ± 0.006	–	–	-0.070 ± 0.010	-0.042 ± 0.006	–	–
NGC4711	-0.39 ± 0.02	-0.082 ± 0.003	0.25 ± 0.07	0.05 ± 0.01	-0.10 ± 0.01	-0.021 ± 0.003	-0.20 ± 0.07	-0.04 ± 0.01
NGC4961[3]	-0.35 ± 0.03	-0.086 ± 0.008	–	–	-0.15 ± 0.02	-0.037 ± 0.006	–	–
NGC5267	-0.01 ± 0.03	-0.002 ± 0.006	-0.14 ± 0.09	-0.03 ± 0.02	0.17 ± 0.02	0.041 ± 0.004	-0.44 ± 0.08	-0.10 ± 0.02
NGC5376	-0.36 ± 0.03	-0.044 ± 0.003	0.11 ± 0.05	0.013 ± 0.006	-0.07 ± 0.01	-0.009 ± 0.002	-0.14 ± 0.05	-0.017 ± 0.006
NGC5633	0.113 ± 0.009	0.088 ± 0.007	–	–	-0.052 ± 0.008	-0.041 ± 0.006	–	–
NGC5657	-0.156 ± 0.010	-0.066 ± 0.004	–	–	-0.075 ± 0.008	-0.032 ± 0.003	–	–

continues on next page

continues from previous page

Name	∇ log$(Age)_{\rm L,in}$		∇ log$(Age)_{\rm L,out}$		∇ log$(Age)_{\rm M,in}$		∇ log$(Age)_{\rm M,out}$	
	(dex/h$_{\rm in}$)	(dex/kpc)	(dex/h$_{\rm in}$)	(dex/kpc)	(dex/h$_{\rm in}$)	(dex/kpc)	(dex/h$_{\rm in}$)	(dex/kpc)
(1)	(2)	(3)	(4)	(5)	(6)	(7)	(8)	(9)
NGC5682	0.18 ± 0.01	0.040 ± 0.003	–	–	-0.024 ± 0.008	-0.005 ± 0.002	–	–
NGC5732[2]	0.272 ± 0.008	0.174 ± 0.005	–	–	0.010 ± 0.004	0.007 ± 0.002	–	–
NGC5888[4]	–	–	0.15 ± 0.05	0.04 ± 0.01	–	–	-0.29 ± 0.06	-0.07 ± 0.01
NGC5947	-0.17 ± 0.03	-0.021 ± 0.004	0.72 ± 1.02	0.09 ± 0.12	-0.17 ± 0.03	-0.020 ± 0.004	1.00 ± 0.90	0.12 ± 0.11
NGC5971[2]	-0.19 ± 0.03	-0.026 ± 0.004	–	–	-0.22 ± 0.02	-0.030 ± 0.003	–	–
NGC6155[2]	0.23 ± 0.01	0.085 ± 0.006	–	–	-0.09 ± 0.01	-0.032 ± 0.004	–	–
NGC6186[1]	–	–	–	–	–	–	–	–
NGC6394[4]	–	–	–	–	–	–	–	–
NGC6478	-0.37 ± 0.02	-0.031 ± 0.002	0.07 ± 0.02	0.005 ± 0.002	0.00 ± 0.02	0.000 ± 0.002	0.02 ± 0.02	0.002 ± 0.002
NGC6497	0.13 ± 0.34	0.01 ± 0.04	2.13 ± 1.23	0.23 ± 0.13	-0.69 ± 0.41	-0.07 ± 0.04	4.89 ± 1.15	0.52 ± 0.12
NGC6978	0.073 ± 0.008	0.024 ± 0.002	–	–	-0.073 ± 0.006	-0.024 ± 0.002	–	–
NGC7047[2]	-0.04 ± 0.04	-0.006 ± 0.005	–	–	0.11 ± 0.03	0.015 ± 0.004	–	–
NGC7311	-0.092 ± 0.008	-0.020 ± 0.002	–	–	0.065 ± 0.007	0.014 ± 0.001	–	–
NGC7321	0.78 ± 0.14	0.22 ± 0.04	–	–	0.30 ± 0.21	0.09 ± 0.06	–	–
NGC7466[2]	0.00 ± 0.01	0.000 ± 0.002	–	–	0.01 ± 0.01	0.001 ± 0.002	–	–
NGC7489	-0.122 ± 0.007	-0.019 ± 0.001	–	–	-0.063 ± 0.005	-0.010 ± 0.001	–	–
NGC7536	-0.33 ± 0.08	-0.029 ± 0.007	0.51 ± 0.26	0.04 ± 0.02	-0.21 ± 0.17	-0.02 ± 0.01	-1.18 ± 1.05	-0.10 ± 0.09
NGC7563	0.31 ± 0.08	0.016 ± 0.004	-2.04 ± 0.56	-0.10 ± 0.03	0.27 ± 0.06	0.014 ± 0.003	-1.26 ± 0.36	-0.06 ± 0.02
NGC7738[1]	–	–	–	–	–	–	–	–
NGC7819	-0.02 ± 0.02	-0.002 ± 0.002	-0.65 ± 0.33	-0.06 ± 0.03	0.05 ± 0.02	0.005 ± 0.002	0.03 ± 0.15	0.00 ± 0.01
UGC00005	0.03 ± 0.01	0.006 ± 0.003	1.13 ± 0.26	0.26 ± 0.06	0.04 ± 0.01	0.010 ± 0.003	-0.13 ± 0.28	-0.03 ± 0.06
UGC00036	-0.05 ± 0.02	-0.010 ± 0.003	–	–	0.02 ± 0.01	0.004 ± 0.003	–	–
UGC00139[5]	–	–	–	–	–	–	–	–
UGC01368	0.00 ± 0.03	0.000 ± 0.009	0.35 ± 0.11	0.11 ± 0.03	0.05 ± 0.03	0.016 ± 0.008	-0.24 ± 0.07	-0.08 ± 0.02
UGC01659[4]	–	–	1.06 ± 0.14	0.09 ± 0.01	–	–	-0.59 ± 0.14	-0.05 ± 0.01
UGC01918[2]	0.29 ± 0.03	0.029 ± 0.003	–	–	0.03 ± 0.03	0.003 ± 0.003	–	–
UGC02099	-0.46 ± 0.04	-0.071 ± 0.006	–	–	-0.16 ± 0.03	-0.024 ± 0.004	–	–
UGC02403[1]	–	–	–	–	–	–	–	–
UGC02405[2]	-0.32 ± 0.02	-0.082 ± 0.005	–	–	-0.05 ± 0.02	-0.013 ± 0.004	–	–
UGC02443	-0.19 ± 0.02	-0.017 ± 0.002	0.56 ± 0.15	0.05 ± 0.01	-0.07 ± 0.02	-0.006 ± 0.002	0.31 ± 0.14	0.03 ± 0.01
UGC02690[2]	0.05 ± 0.05	0.02 ± 0.02	–	–	0.00 ± 0.03	0.00 ± 0.01	–	–
UGC03253	-0.02 ± 0.04	-0.003 ± 0.007	–	–	-0.12 ± 0.03	-0.023 ± 0.005	–	–
UGC03944	-0.15 ± 0.02	-0.045 ± 0.005	–	–	-0.06 ± 0.01	-0.019 ± 0.003	–	–
UGC04145	-0.22 ± 0.03	-0.053 ± 0.008	–	–	-0.08 ± 0.03	-0.019 ± 0.006	–	–
UGC04195	-0.25 ± 0.06	-0.037 ± 0.009	-0.73 ± 0.54	-0.11 ± 0.08	-0.11 ± 0.07	-0.02 ± 0.01	-0.27 ± 0.77	-0.04 ± 0.11
UGC05108	1.47 ± 0.38	0.15 ± 0.04	-9.770 ± 4.006	-1.02 ± 0.42	4.70 ± 0.39	0.49 ± 0.04	-6.72 ± 4.21	-0.70 ± 0.44
UGC05359	-0.13 ± 0.01	-0.021 ± 0.002	–	–	-0.11 ± 0.01	-0.018 ± 0.002	–	–
UGC05396[1]	–	–	–	–	–	–	–	–
UGC07012	-0.13 ± 0.01	-0.044 ± 0.003	-0.38 ± 0.11	-0.12 ± 0.04	-0.018 ± 0.009	-0.006 ± 0.003	-0.06 ± 0.06	-0.02 ± 0.02
UGC07145[2]	-0.232 ± 0.009	-0.078 ± 0.003	–	–	-0.020 ± 0.008	-0.007 ± 0.003	–	–
UGC08004[2]	-0.42 ± 0.01	-0.057 ± 0.002	–	2.18 ± 2.18	-0.121 ± 0.007	-0.017 ± 0.001	–	–
UGC09067	-0.027 ± 0.008	-0.007 ± 0.002	–	–	-0.011 ± 0.005	-0.003 ± 0.001	–	–

continues on next page

continues from previous page

Name	$\nabla \log(Age)_{\mathrm{L,in}}$		$\nabla \log(Age)_{\mathrm{L,out}}$		$\nabla \log(Age)_{\mathrm{M,in}}$		$\nabla \log(Age)_{\mathrm{M,out}}$	
	(dex/$\mathrm{h_{in}}$)	(dex/kpc)	(dex/$\mathrm{h_{in}}$)	(dex/kpc)	(dex/$\mathrm{h_{in}}$)	(dex/kpc)	(dex/$\mathrm{h_{in}}$)	(dex/kpc)
(1)	(2)	(3)	(4)	(5)	(6)	(7)	(8)	(9)
UGC09476[3]	-0.233 ± 0.008	-0.025 ± 0.001	-0.07 ± 0.45	-0.01 ± 0.05	-0.142 ± 0.008	-0.015 ± 0.001	0.39 ± 0.59	0.04 ± 0.06
UGC09542[3]	-0.201 ± 0.009	-0.061 ± 0.003	0.86 ± 0.65	0.26 ± 0.20	0.016 ± 0.007	0.005 ± 0.002	0.60 ± 0.44	0.18 ± 0.13
UGC10796[1]	–	–	–	–	–	–	–	–
UGC10811	-0.32 ± 0.07	-0.07 ± 0.02	-0.22 ± 0.12	-0.05 ± 0.03	0.15 ± 0.06	0.04 ± 0.01	-0.64 ± 0.10	-0.15 ± 0.02
UGC11262	-0.24 ± 0.02	-0.023 ± 0.002	0.76 ± 0.75	0.07 ± 0.07	-0.10 ± 0.01	-0.010 ± 0.001	-0.26 ± 0.57	-0.03 ± 0.06
UGC11740[1]	–	–	–	–	–	–	–	–
UGC12185[2]	0.14 ± 0.06	0.012 ± 0.005	–	–	0.54 ± 0.11	0.045 ± 0.009	–	–
UGC12224	-0.22 ± 0.02	-0.025 ± 0.002	–	–	-0.11 ± 0.01	-0.013 ± 0.001	–	–
UGC12653	-0.041 ± 0.010	-0.010 ± 0.002	0.06 ± 0.15	0.01 ± 0.04	-0.066 ± 0.007	-0.016 ± 0.002	-0.06 ± 0.10	-0.01 ± 0.02
UGC12816[2]	0.04 ± 0.06	0.006 ± 0.010	–	–	-0.04 ± 0.04	-0.007 ± 0.006	–	–

Table A.3: Sample characterisation III: stellar age gradients.

Table A.4 Sample characterisation IV: stellar metallicity gradients

Name	∇ [M/H]$_{L,in}$		∇ [M/H]$_{L,out}$		∇ [M/H]$_{M,in}$		∇ [M/H]$_{M,out}$	
	(dex/h$_{in}$)	(dex/kpc)	(dex/h$_{in}$)	(dex/kpc)	(dex/h$_{in}$)	(dex/kpc)	(dex/h$_{in}$)	(dex/kpc)
(1)	(2)	(3)	(4)	(5)	(6)	(7)	(8)	(9)
ESO540-G003[1]	–	–	–	–	–	–	–	–
IC0159	0.05 ± 0.01	0.016 ± 0.005	–	–	-0.10 ± 0.02	-0.037 ± 0.006	–	–
IC0776[2]	0.09 ± 0.05	0.012 ± 0.007	–	–	0.12 ± 0.05	0.016 ± 0.007	–	–
IC1199	-0.11 ± 0.03	-0.035 ± 0.009	0.71 ± 0.08	0.23 ± 0.03	-0.51 ± 0.04	-0.17 ± 0.01	1.32 ± 0.12	0.44 ± 0.04
IC1256	0.077 ± 0.009	0.022 ± 0.003	–	–	0.07 ± 0.01	0.018 ± 0.004	–	–
IC1683	-0.55 ± 0.14	-0.12 ± 0.03	–	–	-0.88 ± 0.12	-0.18 ± 0.02	–	–
IC5309	0.00 ± 0.02	-0.001 ± 0.005	–	–	-0.19 ± 0.04	-0.044 ± 0.009	–	–
MCG-01-10-015	-0.20 ± 0.03	-0.033 ± 0.005	0.07 ± 0.05	0.011 ± 0.009	0.06 ± 0.06	0.01 ± 0.01	-0.30 ± 0.09	-0.05 ± 0.01
NGC0001	0.15 ± 0.02	0.037 ± 0.006	–	–	-0.06 ± 0.03	-0.015 ± 0.008	–	–
NGC0234	-0.09 ± 0.02	-0.016 ± 0.003	0.00 ± 0.16	0.00 ± 0.03	-0.22 ± 0.03	-0.038 ± 0.005	-0.56 ± 0.19	-0.10 ± 0.03
NGC0237	-0.02 ± 0.01	-0.008 ± 0.005	–	–	-0.25 ± 0.02	-0.085 ± 0.008	–	–
NGC0477	-0.14 ± 0.02	-0.029 ± 0.004	–	–	-0.40 ± 0.02	-0.083 ± 0.005	–	–
NGC0496[2]	-0.088 ± 0.009	-0.016 ± 0.002	–	–	-0.40 ± 0.02	-0.074 ± 0.003	–	–
NGC0551	-0.09 ± 0.04	-0.015 ± 0.006	–	–	-0.23 ± 0.04	-0.039 ± 0.008	–	–
NGC0716	-0.08 ± 0.03	-0.019 ± 0.007	–	–	-0.10 ± 0.04	-0.02 ± 0.01	–	–
NGC0768[2]	-0.23 ± 0.01	-0.052 ± 0.003	–	–	-0.52 ± 0.02	-0.121 ± 0.004	–	–
NGC0873	0.18 ± 0.01	0.037 ± 0.002	–	–	-0.11 ± 0.02	-0.022 ± 0.004	–	–
NGC1093	0.28 ± 0.03	0.082 ± 0.009	–	–	-0.36 ± 0.04	-0.11 ± 0.01	–	–
NGC1094	0.12 ± 0.02	0.052 ± 0.008	-0.26 ± 0.03	-0.11 ± 0.01	-0.35 ± 0.02	-0.156 ± 0.010	-0.20 ± 0.03	-0.09 ± 0.01
NGC1211[1]	–	–	–	–	–	–	–	–
NGC1659	-0.01 ± 0.02	-0.006 ± 0.006	–	–	-0.28 ± 0.03	-0.11 ± 0.01	–	–
NGC1677	0.03 ± 0.05	0.01 ± 0.02	0.01 ± 0.03	0.00 ± 0.01	-0.03 ± 0.10	-0.01 ± 0.05	-0.03 ± 0.03	-0.01 ± 0.01
NGC2449	-0.034 ± 0.008	-0.013 ± 0.003	–	–	-0.16 ± 0.01	-0.064 ± 0.004	–	–
NGC2486[2]	-0.31 ± 0.05	-0.034 ± 0.005	–	–	0.17 ± 0.06	0.019 ± 0.006	–	–
NGC2540[3]	0.12 ± 0.03	0.030 ± 0.007	–	–	0.30 ± 0.06	0.07 ± 0.01	–	–
NGC2572	-0.16 ± 0.03	-0.043 ± 0.007	–	–	-0.41 ± 0.03	-0.107 ± 0.007	–	–
NGC3815	-0.03 ± 0.01	-0.005 ± 0.002	–	–	-0.34 ± 0.03	-0.057 ± 0.005	–	–
NGC3994	0.01 ± 0.01	0.009 ± 0.008	0.34 ± 0.04	0.22 ± 0.03	-0.12 ± 0.02	-0.08 ± 0.01	0.86 ± 0.05	0.57 ± 0.03
NGC4470	0.15 ± 0.02	0.067 ± 0.007	–	–	0.00 ± 0.03	0.00 ± 0.01	–	–
NGC4644	0.01 ± 0.01	0.007 ± 0.007	–	–	-0.01 ± 0.02	-0.005 ± 0.009	–	–
NGC4711	-0.13 ± 0.02	-0.028 ± 0.004	0.23 ± 0.09	0.05 ± 0.02	0.02 ± 0.02	0.004 ± 0.004	-1.01 $\pm$ 0.10	-0.21 ± 0.02
NGC4961[3]	0.24 ± 0.03	0.058 ± 0.008	–	–	0.35 ± 0.05	0.09 ± 0.01	–	–
NGC5267	-0.81 ± 0.03	-0.189 ± 0.006	0.66 ± 0.10	0.15 ± 0.02	-0.13 ± 0.03	-0.031 ± 0.007	-0.31 ± 0.13	-0.07 ± 0.03
NGC5376	-0.12 ± 0.02	-0.014 ± 0.002	0.40 ± 0.05	0.048 ± 0.006	0.08 ± 0.02	0.009 ± 0.002	-0.32 ± 0.07	-0.038 ± 0.008
NGC5633	0.15 ± 0.01	0.121 ± 0.008	–	–	-0.12 ± 0.02	-0.10 ± 0.01	–	–
NGC5657	-0.05 ± 0.01	-0.021 ± 0.005	–	–	-0.18 ± 0.02	-0.077 ± 0.008	–	–

continues on next page

continues from previous page

Name	∇ [M/H]$_{L,in}$		∇ [M/H]$_{L,out}$		∇ [M/H]$_{M,in}$		∇ [M/H]$_{M,out}$	
	(dex/h$_{in}$)	(dex/kpc)	(dex/h$_{in}$)	(dex/kpc)	(dex/h$_{in}$)	(dex/kpc)	(dex/h$_{in}$)	(dex/kpc)
(1)	(2)	(3)	(4)	(5)	(6)	(7)	(8)	(9)
NGC5682	0.12 ± 0.01	0.027 ± 0.003	–	–	0.01 ± 0.01	0.002 ± 0.002	–	–
NGC5732[2]	0.103 ± 0.010	0.066 ± 0.006	–	–	0.04 ± 0.01	0.026 ± 0.009	–	–
NGC5888[4]	–	–	0.56 ± 0.06	0.13 ± 0.01	–	–	-0.04 ± 0.06	-0.01 ± 0.01
NGC5947	-0.24 ± 0.05	-0.029 ± 0.006	-2.34 ± 2.21	-0.28 ± 0.27	-0.85 ± 0.06	-0.102 ± 0.007	0.60 ± 1.49	0.07 ± 0.18
NGC5971[2]	-0.40 ± 0.03	-0.054 ± 0.004	–	–	-0.76 ± 0.03	-0.104 ± 0.005	–	–
NGC6155[2]	0.16 ± 0.02	0.060 ± 0.006	–	–	-0.09 ± 0.02	-0.034 ± 0.007	–	–
NGC6186[1]	–	–	–	–	–	–	–	–
NGC6394[4]	–	–	–	–	–	–	–	–
NGC6478	-0.56 ± 0.03	-0.047 ± 0.002	0.17 ± 0.03	0.015 ± 0.003	-0.16 ± 0.03	-0.014 ± 0.002	0.05 ± 0.04	0.004 ± 0.003
NGC6497	-0.004 ± 0.001	0.00 ± 0.00	-0.003 ± 0.002	0.000 ± 0.000	-0.011 ± 0.001	-0.001 ± 0.000	-0.008 ± 0.004	-0.001 ± 0.000
NGC6978	0.126 ± 0.008	0.041 ± 0.003	–	–	-0.119 ± 0.010	-0.039 ± 0.003	–	–
NGC7047[2]	-0.47 ± 0.04	-0.067 ± 0.006	–	–	-0.31 ± 0.05	-0.044 ± 0.007	–	–
NGC7311	-0.097 ± 0.008	-0.021 ± 0.002	–	–	0.004 ± 0.010	0.001 ± 0.002	–	–
NGC7321	-0.001 ± 0.000	0.00 ± 0.00	–	–	-0.007 ± 0.000	-0.002 ± 0.000	–	–
NGC7466[2]	0.01 ± 0.02	0.001 ± 0.002	–	–	0.07 ± 0.02	0.010 ± 0.003	–	–
NGC7489	-0.225 ± 0.007	-0.034 ± 0.001	–	–	-0.55 ± 0.01	-0.084 ± 0.002	–	–
NGC7536	-0.02 ± 0.14	0.00 ± 0.01	0.99 ± 0.57	0.09 ± 0.05	0.47 ± 0.21	0.04 ± 0.02	-0.53 ± 1.16	-0.05 ± 0.10
NGC7563	-0.49 ± 0.06	-0.024 ± 0.003	0.89 ± 0.43	0.04 ± 0.02	-0.29 ± 0.06	-0.014 ± 0.003	0.64 ± 0.42	0.03 ± 0.02
NGC7738[1]	–	–	–	–	–	–	–	–
NGC7819	-0.15 ± 0.03	-0.014 ± 0.003	-0.42 ± 0.47	-0.04 ± 0.04	-0.24 ± 0.03	-0.023 ± 0.002	0.43 ± 0.37	0.04 ± 0.04
UGC00005	-0.22 ± 0.02	-0.051 ± 0.004	0.35 ± 0.38	0.08 ± 0.09	-0.23 ± 0.02	-0.053 ± 0.005	-1.31 ± 0.48	-0.30 ± 0.11
UGC00036	0.04 ± 0.01	0.008 ± 0.003	–	–	-0.15 ± 0.02	-0.032 ± 0.004	–	–
UGC00139[5]	–	–	–	–	–	–	–	–
UGC01368	-0.16 ± 0.03	-0.049 ± 0.009	0.10 ± 0.13	0.03 ± 0.04	-0.07 ± 0.05	-0.02 ± 0.02	-0.29 ± 0.14	-0.09 ± 0.04
UGC01659[4]	–	–	0.40 ± 0.18	0.03 ± 0.01	–	–	-2.39 ± 0.29	-0.19 ± 0.02
UGC01918[2]	-0.14 ± 0.04	-0.014 ± 0.004	–	–	-0.07 ± 0.06	-0.007 ± 0.006	–	–
UGC02099	0.01 ± 0.04	0.001 ± 0.006	–	–	0.34 ± 0.04	0.054 ± 0.006	–	–
UGC02403[1]	–	–	–	–	–	–	–	–
UGC02405[2]	-0.09 ± 0.03	-0.024 ± 0.007	–	–	-0.35 ± 0.03	-0.089 ± 0.008	–	–
UGC02443	-0.04 ± 0.02	-0.004 ± 0.002	1.07 ± 0.21	0.10 ± 0.02	-0.08 ± 0.03	-0.007 ± 0.003	0.62 ± 0.21	0.06 ± 0.02
UGC02690[2]	0.10 ± 0.07	0.05 ± 0.03	–	–	-0.11 ± 0.05	-0.06 ± 0.03	–	–
UGC03253	0.02 ± 0.04	0.004 ± 0.007	–	–	-0.02 ± 0.07	0.00 ± 0.01	–	–
UGC03944	-0.11 ± 0.02	-0.033 ± 0.005	–	–	-0.21 ± 0.03	-0.062 ± 0.008	–	–
UGC04145	0.12 ± 0.03	0.030 ± 0.008	–	–	-0.11 ± 0.03	-0.026 ± 0.007	–	–
UGC04195	0.12 ± 0.10	0.02 ± 0.01	-0.57 ± 1.04	-0.08 ± 0.16	0.40 ± 0.11	0.06 ± 0.02	-0.54 ± 1.15	-0.08 ± 0.17
UGC05108	-0.007 ± 0.001	0.00 ± 0.00	-0.014 ± 0.007	-0.001 ± 0.001	0.003 ± 0.001	0.000 ± 0.000	-0.02 ± 0.02	-0.002 ± 0.002
UGC05359	-0.12 ± 0.02	-0.019 ± 0.002	–	–	-0.58 ± 0.02	-0.092 ± 0.003	–	–
UGC05396[1]	–	–	–	–	–	–	–	–
UGC07012	0.02 ± 0.01	0.005 ± 0.004	0.16 ± 0.10	0.05 ± 0.03	-0.07 ± 0.02	-0.021 ± 0.005	0.04 ± 0.12	0.01 ± 0.04
UGC07145[2]	-0.143 ± 0.010	-0.048 ± 0.003	–	–	-0.08 ± 0.01	-0.027 ± 0.004	–	–
UGC08004[2]	-0.15 ± 0.01	-0.021 ± 0.002	–	–	-0.32 ± 0.02	-0.043 ± 0.003	–	–
UGC09067	-0.142 ± 0.008	-0.039 ± 0.002	–	–	-0.38 ± 0.01	-0.103 ± 0.003	–	–

continues on next page

continues from previous page

Name	∇ [M/H]$_{L,in}$		∇ [M/H]$_{L,out}$		∇ [M/H]$_{M,in}$		∇ [M/H]$_{M,out}$	
	(dex/h$_{in}$)	(dex/kpc)	(dex/h$_{in}$)	(dex/kpc)	(dex/h$_{in}$)	(dex/kpc)	(dex/h$_{in}$)	(dex/kpc)
(1)	(2)	(3)	(4)	(5)	(6)	(7)	(8)	(9)
UGC09476[3]	-0.008 ± 0.010	-0.001 ± 0.001	0.02 ± 0.83	0.00 ± 0.09	-0.05 ± 0.01	-0.005 ± 0.001	-0.72 ± 0.80	-0.08 ± 0.09
UGC09542[3]	-0.20 ± 0.01	-0.062 ± 0.003	-1.07 ± 0.73	-0.32 ± 0.22	-0.18 ± 0.01	-0.056 ± 0.003	-0.28 ± 0.58	-0.09 ± 0.18
UGC10796[1]	–	–	–	–	–	–	–	–
UGC10811	-0.82 ± 0.06	-0.19 ± 0.01	0.59 ± 0.13	0.14 ± 0.03	-0.04 ± 0.09	-0.01 ± 0.02	-1.26 ± 0.20	-0.29 ± 0.05
UGC11262	-0.17 ± 0.02	-0.016 ± 0.002	-0.58 ± 0.79	-0.06 ± 0.08	-0.48 ± 0.03	-0.046 ± 0.003	-2.65 ± 1.66	-0.26 ± 0.16
UGC11740[1]	–	–	–	–	–	–	–	–
UGC12185[2]	-0.74 ± 0.08	-0.062 ± 0.006	–	–	-0.48 ± 0.12	-0.04 ± 0.01	–	–
UGC12224	-0.22 ± 0.02	-0.025 ± 0.002	–	–	-0.40 ± 0.02	-0.047 ± 0.002	–	–
UGC12653	-0.107 ± 0.009	-0.026 ± 0.002	0.15 ± 0.14	0.04 ± 0.03	-0.26 ± 0.01	-0.064 ± 0.003	0.15 ± 0.15	0.04 ± 0.04
UGC12816[2]	-0.10 ± 0.08	-0.02 ± 0.01	–	–	-0.21 ± 0.10	-0.04 ± 0.02	–	–

Table A.4: Sample characterisation IV: stellar metallicity gradients.

Table A.5 Sample characterisation V: $g-r$, $g-i$, and $r-i$ colour inner gradients

Name	$\bigtriangledown\ (g-r)_{\rm in}$		$\bigtriangledown (g-i)_{\rm in}$		$\bigtriangledown (r-i)_{\rm in}$	
	(dex/$h_{\rm in}$)	(dex/kpc)	(dex/$h_{\rm in}$)	(dex/kpc)	(dex/$h_{\rm in}$)	(dex/kpc)
(1)	(2)	(3)	(4)	(5)	(6)	(7)
ESO540-G003[1]	–	–	–	–	–	–
IC0159	-0.03 ± 0.16	-0.01 ± 0.05	-0.03 ± 0.16	-0.01 ± 0.05	-0.01 ± 0.16	0.00 ± 0.05
IC0776[2]	-0.09 ± 0.29	-0.02 ± 0.06	-0.21 ± 0.29	-0.04 ± 0.06	-0.12 ± 0.29	-0.02 ± 0.06
IC1199	-0.23 ± 0.36	-0.04 ± 0.06	-0.31 ± 0.36	-0.05 ± 0.06	-0.08 ± 0.36	-0.01 ± 0.06
IC1256	-0.11 ± 0.08	-0.03 ± 0.02	-0.15 ± 0.08	-0.04 ± 0.02	-0.04 ± 0.08	-0.01 ± 0.02
IC1683	0.09 ± 1.40	0.02 ± 0.29	0.13 ± 1.40	0.03 ± 0.29	0.04 ± 1.40	0.01 ± 0.29
IC5309	-0.09 ± 0.19	-0.02 ± 0.05	-0.11 ± 0.19	-0.03 ± 0.05	-0.02 ± 0.19	-0.01 ± 0.05
MCG-01-10-015	-0.26 ± 0.26	-0.04 ± 0.04	-0.36 ± 0.26	-0.06 ± 0.04	-0.11 ± 0.26	-0.02 ± 0.04
NGC0001	-0.08 ± 0.22	-0.02 ± 0.05	-0.11 ± 0.22	-0.02 ± 0.05	-0.03 ± 0.22	-0.01 ± 0.05
NGC0234	-0.14 ± 0.22	-0.03 ± 0.04	-0.20 ± 0.22	-0.04 ± 0.04	-0.05 ± 0.22	-0.01 ± 0.04
NGC0237	-0.08 ± 0.12	-0.03 ± 0.04	-0.06 ± 0.12	-0.02 ± 0.04	0.01 ± 0.12	0.00 ± 0.04
NGC0477	-0.13 ± 0.17	-0.02 ± 0.02	-0.18 ± 0.17	-0.03 ± 0.02	-0.05 ± 0.17	-0.01 ± 0.02
NGC0496[2]	-0.06 ± 0.10	-0.01 ± 0.02	-0.05 ± 0.10	-0.01 ± 0.02	0.00 ± 0.10	0.00 ± 0.02
NGC0551	0.04 ± 0.56	0.01 ± 0.11	0.14 ± 0.56	0.03 ± 0.11	0.10 ± 0.56	0.02 ± 0.11
NGC0716	-0.16 ± 0.24	-0.04 ± 0.06	-0.21 ± 0.24	-0.06 ± 0.06	-0.05 ± 0.24	-0.01 ± 0.06
NGC0768[2]	-0.11 ± 0.13	-0.02 ± 0.02	-0.10 ± 0.13	-0.02 ± 0.02	0.01 ± 0.13	0.00 ± 0.02
NGC0873	-0.11 ± 0.07	-0.04 ± 0.03	-0.12 ± 0.07	-0.05 ± 0.03	-0.02 ± 0.07	-0.01 ± 0.03
NGC1093	-0.08 ± 0.26	-0.02 ± 0.06	-0.13 ± 0.26	-0.03 ± 0.06	-0.05 ± 0.26	-0.01 ± 0.06
NGC1094	-0.02 ± 0.18	-0.01 ± 0.07	-0.02 ± 0.18	-0.01 ± 0.07	0.00 ± 0.18	0.00 ± 0.07
NGC1211[1]	–	–	–	–	–	–

continues on next page

continues from previous page

Name	$\bigtriangledown\ (g-r)_{\rm in}$		$\bigtriangledown (g-i)_{\rm in}$		$\bigtriangledown (r-i)_{\rm in}$	
	(dex/$h_{\rm in}$)	(dex/kpc)	(dex/$h_{\rm in}$)	(dex/kpc)	(dex/$h_{\rm in}$)	(dex/kpc)
(1)	(2)	(3)	(4)	(5)	(6)	(7)
NGC1659	-0.11 ± 0.13	-0.03 ± 0.03	-0.13 ± 0.13	-0.03 ± 0.03	-0.02 ± 0.13	-0.01 ± 0.03
NGC1677	0.06 ± 0.57	0.05 ± 0.45	0.09 ± 0.57	0.07 ± 0.45	0.03 ± 0.57	0.03 ± 0.45
NGC2449	-0.04 ± 0.14	-0.01 ± 0.03	-0.01 ± 0.14	0.00 ± 0.03	0.02 ± 0.14	0.00 ± 0.03
NGC2486[2]	-0.27 ± 0.47	-0.03 ± 0.05	-0.44 ± 0.47	-0.05 ± 0.05	-0.16 ± 0.47	-0.02 ± 0.05
NGC2540[3]	0.03 ± 0.26	0.01 ± 0.05	0.01 ± 0.26	0.00 ± 0.05	-0.02 ± 0.26	0.00 ± 0.05
NGC2572	-0.01 ± 0.28	0.00 ± 0.06	0.01 ± 0.28	0.00 ± 0.06	0.02 ± 0.28	0.00 ± 0.06
NGC3815	-0.04 ± 0.13	-0.02 ± 0.05	-0.02 ± 0.13	-0.01 ± 0.05	0.02 ± 0.13	0.01 ± 0.05
NGC3994	0.02 ± 0.12	0.01 ± 0.09	0.09 ± 0.12	0.07 ± 0.09	0.07 ± 0.12	0.05 ± 0.09
NGC4470	0.09 ± 0.15	0.05 ± 0.09	0.14 ± 0.15	0.08 ± 0.09	0.06 ± 0.15	0.03 ± 0.09
NGC4644	-0.06 ± 0.13	-0.02 ± 0.04	-0.09 ± 0.13	-0.03 ± 0.04	-0.03 ± 0.13	-0.01 ± 0.04
NGC4711	-0.19 ± 0.14	-0.05 ± 0.04	-0.27 ± 0.14	-0.07 ± 0.04	-0.08 ± 0.14	-0.02 ± 0.04
NGC4961[3]	-0.05 ± 0.44	-0.02 ± 0.17	-0.08 ± 0.44	-0.03 ± 0.17	-0.03 ± 0.44	-0.01 ± 0.17
NGC5267	-0.11 ± 0.46	-0.01 ± 0.05	-0.10 ± 0.46	-0.01 ± 0.05	0.01 ± 0.46	0.00 ± 0.05
NGC5376	-0.16 ± 0.26	-0.05 ± 0.09	-0.23 ± 0.26	-0.08 ± 0.09	-0.07 ± 0.26	-0.02 ± 0.09
NGC5633	0.00 ± 0.12	0.00 ± 0.08	0.04 ± 0.12	0.03 ± 0.08	0.04 ± 0.12	0.03 ± 0.08
NGC5657	-0.12 ± 0.14	-0.03 ± 0.04	-0.15 ± 0.14	-0.04 ± 0.04	-0.03 ± 0.14	-0.01 ± 0.04
NGC5682	-0.03 ± 0.21	-0.01 ± 0.08	0.00 ± 0.21	0.00 ± 0.08	0.03 ± 0.21	0.01 ± 0.08
NGC5732[2]	-0.08 ± 0.07	-0.03 ± 0.03	-0.09 ± 0.07	-0.04 ± 0.03	-0.01 ± 0.07	-0.01 ± 0.03
NGC5888[4]	–	–	–	–	–	–
NGC5947	-0.17 ± 0.39	-0.03 ± 0.07	-0.20 ± 0.39	-0.03 ± 0.07	-0.03 ± 0.39	-0.01 ± 0.07
NGC5971[2]	-0.17 ± 0.24	-0.04 ± 0.06	-0.19 ± 0.24	-0.05 ± 0.06	-0.02 ± 0.24	0.00 ± 0.06
NGC6155[2]	0.03 ± 0.18	0.01 ± 0.09	0.06 ± 0.18	0.03 ± 0.09	0.03 ± 0.18	0.02 ± 0.09
NGC6186[1]	–	–	–	–	–	–
NGC6394[4]	–	–	–	–	–	–
NGC6478	-0.16 ± 0.28	-0.02 ± 0.03	-0.28 ± 0.28	-0.03 ± 0.03	-0.12 ± 0.28	-0.01 ± 0.03

continues on next page

continues from previous page

Name	$\bigtriangledown\ (g-r)_{\rm in}$		$\bigtriangledown(g-i)_{\rm in}$		$\bigtriangledown(r-i)_{\rm in}$	
	(dex/$h_{\rm in}$)	(dex/kpc)	(dex/$h_{\rm in}$)	(dex/kpc)	(dex/$h_{\rm in}$)	(dex/kpc)
(1)	(2)	(3)	(4)	(5)	(6)	(7)
NGC6497	-0.12 ± 0.50	-0.03 ± 0.11	-0.15 ± 0.50	-0.03 ± 0.11	-0.03 ± 0.50	-0.01 ± 0.11
NGC6978	-0.04 ± 0.11	-0.01 ± 0.02	-0.05 ± 0.11	-0.01 ± 0.02	-0.02 ± 0.11	0.00 ± 0.02
NGC7047[2]	-0.14 ± 0.38	-0.02 ± 0.06	-0.19 ± 0.38	-0.03 ± 0.06	-0.05 ± 0.38	-0.01 ± 0.06
NGC7311	-0.06 ± 0.10	-0.02 ± 0.03	-0.08 ± 0.10	-0.02 ± 0.03	-0.01 ± 0.10	0.00 ± 0.03
NGC7321	-0.10 ± 0.13	-0.02 ± 0.02	-0.12 ± 0.13	-0.02 ± 0.02	-0.02 ± 0.13	0.00 ± 0.02
NGC7466[2]	-0.10 ± 0.16	-0.01 ± 0.02	-0.12 ± 0.16	-0.02 ± 0.02	-0.02 ± 0.16	0.00 ± 0.02
NGC7489	-0.19 ± 0.08	-0.03 ± 0.01	-0.27 ± 0.08	-0.05 ± 0.01	-0.08 ± 0.08	-0.02 ± 0.01
NGC7536	-0.28 ± 0.80	-0.03 ± 0.09	-0.47 ± 0.80	-0.05 ± 0.09	-0.19 ± 0.80	-0.02 ± 0.09
NGC7563	-0.08 ± 1.76	0.00 ± 0.10	-0.05 ± 1.76	0.00 ± 0.10	0.03 ± 1.76	0.00 ± 0.10
NGC7738[1]	–	–	–	–	–	–
NGC7819	-0.21 ± 0.28	-0.03 ± 0.04	-0.33 ± 0.28	-0.04 ± 0.04	-0.12 ± 0.28	-0.02 ± 0.04
UGC00005	-0.11 ± 0.14	-0.02 ± 0.02	-0.15 ± 0.14	-0.02 ± 0.02	-0.05 ± 0.14	-0.01 ± 0.02
UGC00036	-0.01 ± 0.20	0.00 ± 0.05	0.00 ± 0.20	0.00 ± 0.05	0.01 ± 0.20	0.00 ± 0.05
UGC00139[5]	-0.17 ± 0.19	-0.05 ± 0.06	-0.23 ± 0.19	-0.07 ± 0.06	-0.06 ± 0.19	-0.02 ± 0.06
UGC01368	-0.06 ± 0.24	-0.01 ± 0.04	-0.06 ± 0.24	-0.01 ± 0.04	0.00 ± 0.24	0.00 ± 0.04
UGC01659[4]	–	–	–	–	–	–
UGC01918[2]	-0.09 ± 0.28	-0.01 ± 0.05	-0.04 ± 0.28	-0.01 ± 0.05	0.05 ± 0.28	0.01 ± 0.05
UGC02099	0.01 ± 0.42	0.00 ± 0.04	0.04 ± 0.42	0.00 ± 0.04	0.03 ± 0.42	0.00 ± 0.04
UGC02403[1]	–	–	–	–	–	–
UGC02405[2]	-0.13 ± 0.08	-0.02 ± 0.01	-0.17 ± 0.08	-0.02 ± 0.01	-0.04 ± 0.08	-0.01 ± 0.01
UGC02443	-0.12 ± 0.20	-0.03 ± 0.05	-0.20 ± 0.20	-0.06 ± 0.05	-0.08 ± 0.20	-0.02 ± 0.05
UGC02690[2]	-0.08 ± 0.09	-0.02 ± 0.02	-0.10 ± 0.09	-0.02 ± 0.02	-0.02 ± 0.09	0.00 ± 0.02
UGC03253	-0.05 ± 0.40	-0.01 ± 0.11	-0.08 ± 0.40	-0.02 ± 0.11	-0.03 ± 0.40	-0.01 ± 0.11
UGC03944	-0.13 ± 0.14	-0.04 ± 0.04	-0.17 ± 0.14	-0.05 ± 0.04	-0.04 ± 0.14	-0.01 ± 0.04
UGC04145	-0.05 ± 0.41	-0.01 ± 0.08	-0.04 ± 0.41	-0.01 ± 0.08	0.01 ± 0.41	0.00 ± 0.08

continues on next page

continues from previous page

Name	$\bigtriangledown\ (g-r)_{\rm in}$		$\bigtriangledown(g-i)_{\rm in}$		$\bigtriangledown(r-i)_{\rm in}$	
	(dex/$h_{\rm in}$)	(dex/kpc)	(dex/$h_{\rm in}$)	(dex/kpc)	(dex/$h_{\rm in}$)	(dex/kpc)
(1)	(2)	(3)	(4)	(5)	(6)	(7)
UGC04195	-0.21 ± 0.89	-0.03 ± 0.12	-0.24 ± 0.89	-0.03 ± 0.12	-0.03 ± 0.89	0.00 ± 0.12
UGC05108	-0.28 ± 0.33	-0.02 ± 0.02	-0.29 ± 0.33	-0.02 ± 0.02	-0.01 ± 0.33	0.00 ± 0.02
UGC05359	-0.16 ± 0.14	-0.02 ± 0.02	-0.22 ± 0.14	-0.03 ± 0.02	-0.06 ± 0.14	-0.01 ± 0.02
UGC05396[1]	–	–	–	–	–	–
UGC07012	-0.06 ± 0.12	-0.03 ± 0.07	-0.09 ± 0.12	-0.05 ± 0.07	-0.03 ± 0.12	-0.02 ± 0.07
UGC07145[2]	-0.16 ± 0.10	-0.02 ± 0.02	-0.20 ± 0.10	-0.03 ± 0.02	-0.04 ± 0.10	-0.01 ± 0.02
UGC08004[2]	-0.14 ± 0.08	-0.02 ± 0.01	-0.21 ± 0.08	-0.03 ± 0.01	-0.07 ± 0.08	-0.01 ± 0.01
UGC09067	-0.12 ± 0.06	-0.03 ± 0.01	-0.15 ± 0.06	-0.03 ± 0.01	-0.03 ± 0.06	-0.01 ± 0.01
UGC09476[3]	-0.08 ± 0.10	-0.02 ± 0.03	-0.10 ± 0.10	-0.03 ± 0.03	-0.02 ± 0.10	-0.01 ± 0.03
UGC09542[3]	-0.19 ± 0.09	-0.03 ± 0.02	-0.27 ± 0.09	-0.05 ± 0.02	-0.08 ± 0.09	-0.01 ± 0.02
UGC10796[1]	–	–	–	–	–	–
UGC10811	-0.26 ± 0.65	-0.02 ± 0.05	-0.32 ± 0.65	-0.03 ± 0.05	-0.07 ± 0.65	-0.01 ± 0.05
UGC11262	-0.20 ± 0.18	-0.03 ± 0.03	-0.28 ± 0.18	-0.04 ± 0.03	-0.07 ± 0.18	-0.01 ± 0.03
UGC11740[1]	–	–	–	–	–	–
UGC12185[2]	-0.35 ± 0.88	-0.03 ± 0.07	-0.55 ± 0.88	-0.04 ± 0.07	-0.20 ± 0.88	-0.02 ± 0.07
UGC12224	-0.18 ± 0.13	-0.04 ± 0.03	-0.28 ± 0.13	-0.06 ± 0.03	-0.09 ± 0.13	-0.02 ± 0.03
UGC12653	-0.08 ± 0.14	-0.02 ± 0.03	-0.04 ± 0.14	-0.01 ± 0.03	0.04 ± 0.14	0.01 ± 0.03
UGC12816[2]	-0.16 ± 0.32	-0.02 ± 0.04	-0.26 ± 0.32	-0.03 ± 0.04	-0.11 ± 0.32	-0.01 ± 0.04

Table A.5: Sample characterisation V: $g-r$, $g-i$, and $r-i$ colour inner gradients.

Appendix B

Sample summary plots (CALIFA)

In this appendix we include a graphic summary of the main properties of the CALIFA galaxies analysed in this thesis. For each galaxy we present this information in a plot divided into eight panels displaying its morphological decomposition and colour profiles as well as its stellar content (following the method outlined in Sects. 2 and 3).

General information: radial distances (bottom x-axis) are normalised (except for the left-hand panel of the first row) to the inner disc scale-length (h_{in}). The dotted-dashed black vertical lines are located at the inner limit for the linear regresion of the stellar parameters (avoiding the bulge/bar region) and the dashed black vertical lines are located at the break radius (R_{break}).

First row (left): r-band SDSS image, the dotted-dashed black ellipse is located at the inner limit for the linear regresion of the stellar parameters (avoiding the bulge/bar region) and the dashed black ellipse is located at the break radius. North is up in this panel.

First row (right): SDSS r-band surface brightness profile (black dots) and its errors (grey area) as well as the model surface brightness profile (solid green line) with a zoom in the inner parts in logarithmic scale. An auxiliary panel at the bottom shows the residuals between the model and the observed light distribution. The different components are also represented in that panel: Bulge (dashed blue line); disc or double disc (dotted red line); bar (solid dark green line).

Second row (left): $g - r$ colour profile; linear fits to the inner and outer $g - r$ colour profiles are denoted by solid purple lines if possible.

Second row (right): $g - i$ colour profile; linear fits to the inner and outer $g - i$ colour profiles are denoted by solid purple lines if possible.

Third row (left): age radial profile in logarithmic scale (log(Age[yr])); blue points indicate mass-weighted quantities while red squares indicate

mass-weighted values. Linear fits (is computed) to the inner and outer age profiles are denoted by solid lines (red, mass-weighted; blue, light-weighted).

Third row (right): [M/H] radial profile; blue points indicate light-weighted values while red squares indicate mass-weighted ones. Linear fits to the inner and outer age profiles are denoted by solid lines (red, mass-weighted; blue, light-weighted).

Fourth row: radial luminosity-weighted (left) and mass-weighted (right) stellar age distributions; in this representation we encode with a colour bar the light (left) or mass (right) fraction of stellar populations of different ages (y-axis) located at different galactocentric distances (x-axis). Violet colours denote populations with higher contribution to the total radial light or mass while blue colours indicate lower contributions. We normalise these distributions in such way that the sum of all the light or mass fractions at a given radial distance is 1.

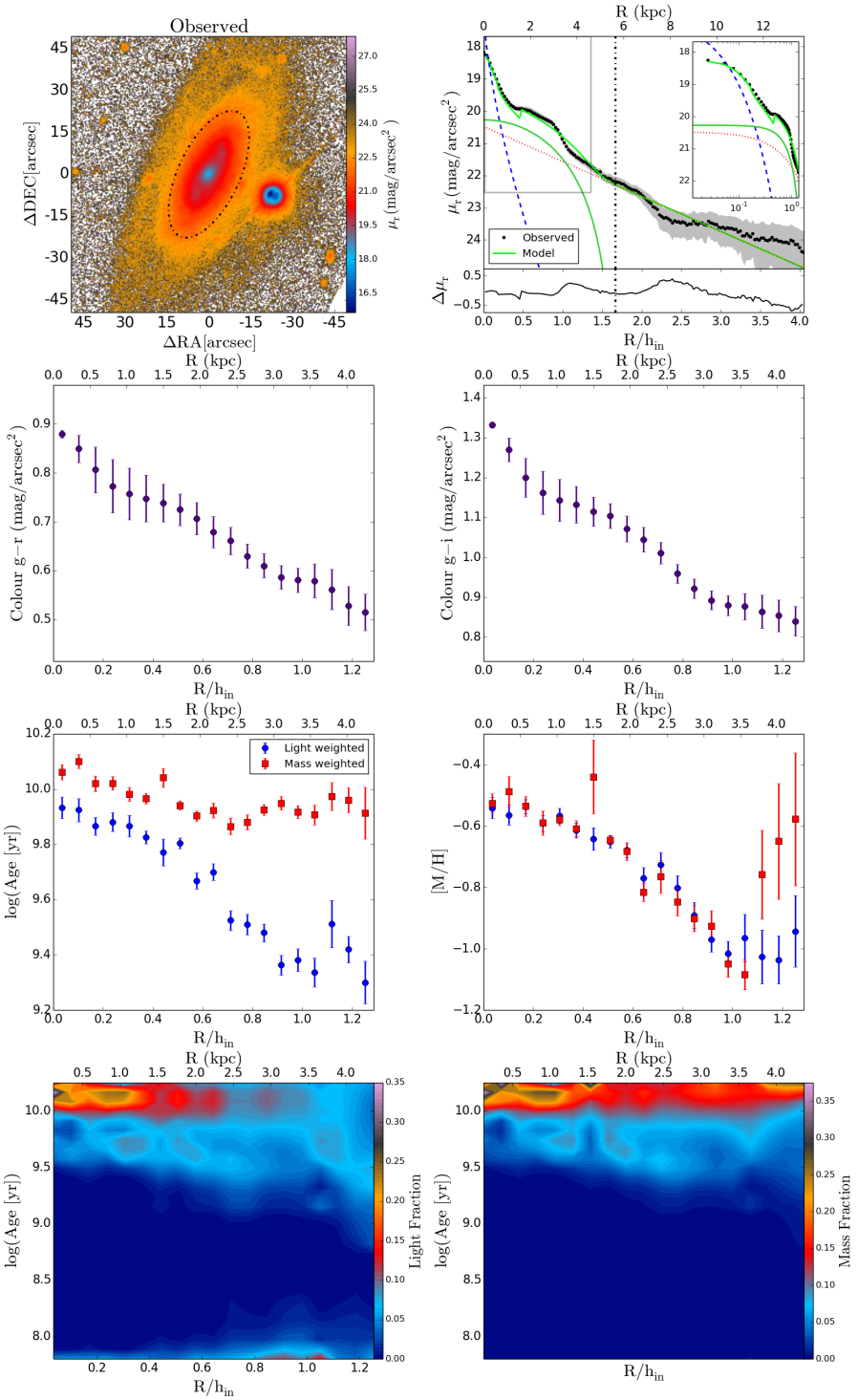

Figure B.1: ESO540-G003.

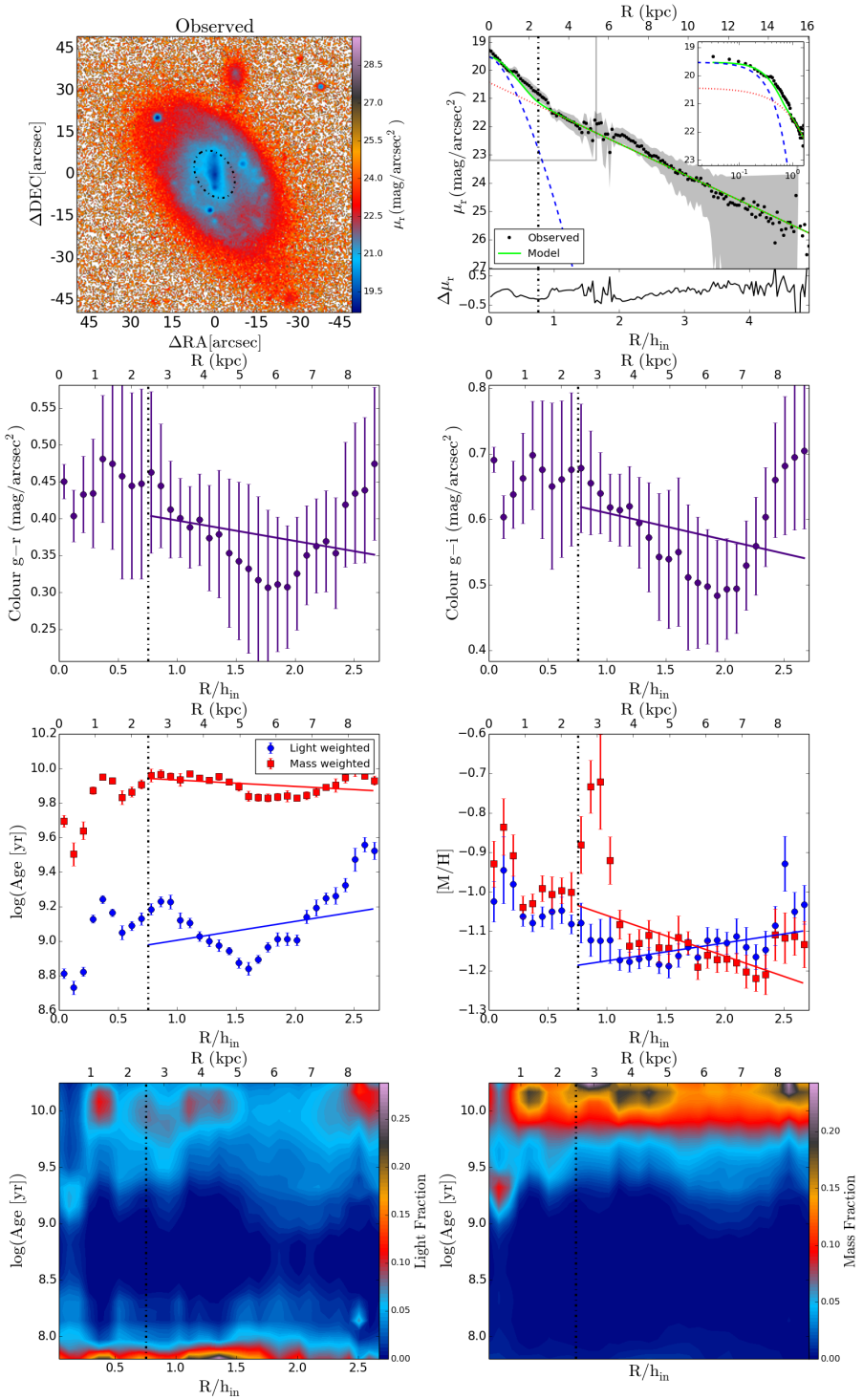

Figure B.2: IC0159.

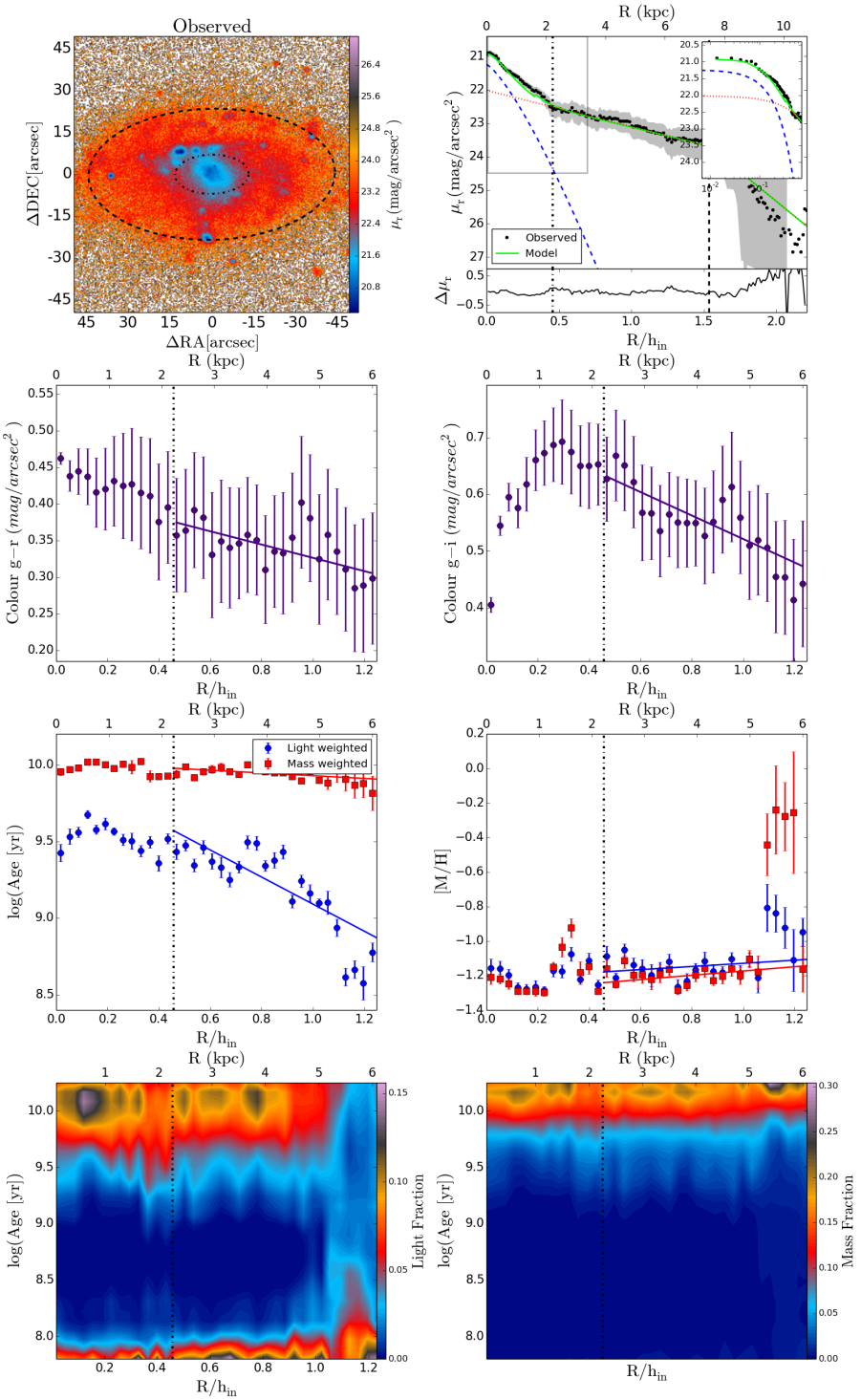

Figure B.3: IC0776.

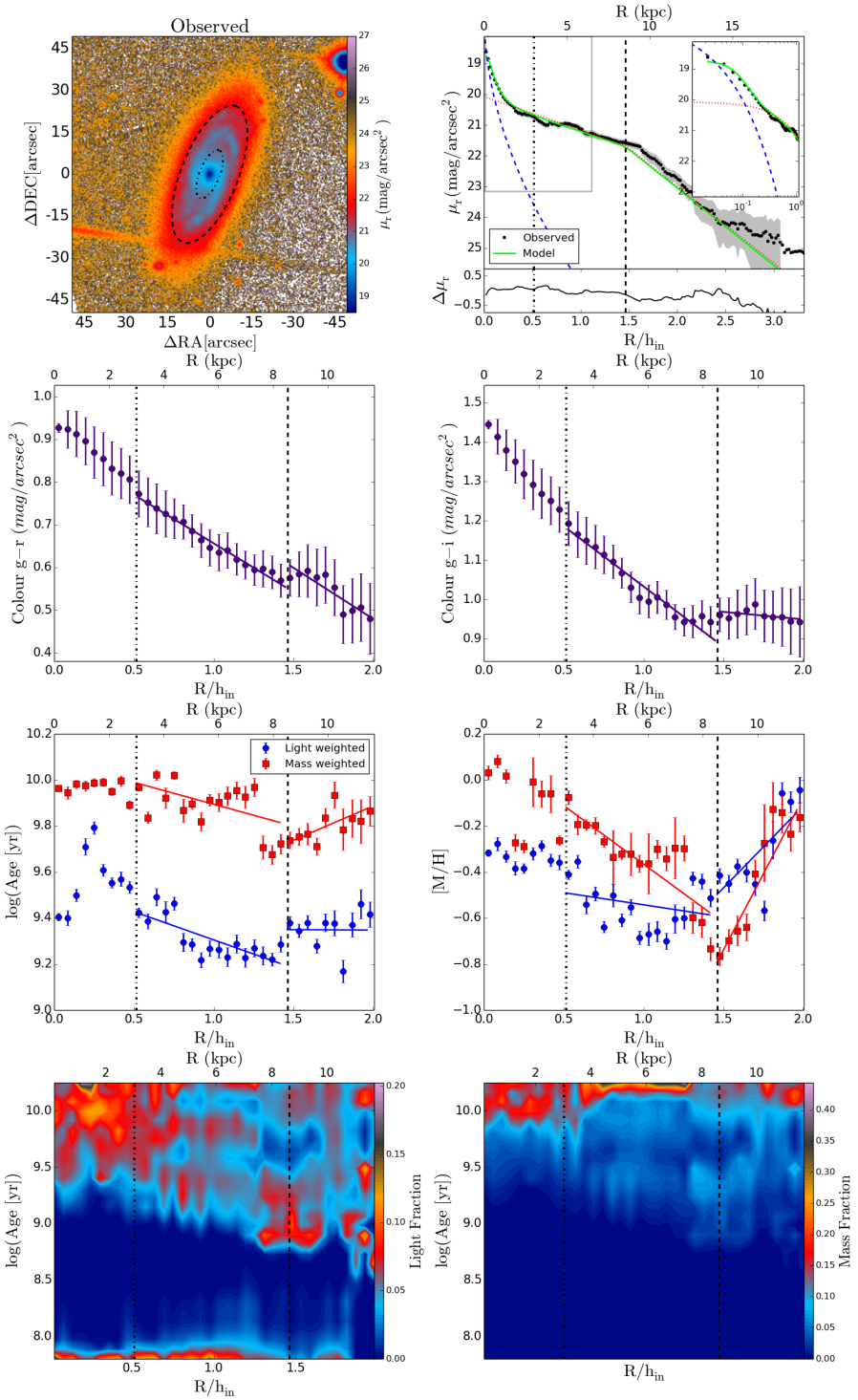

Figure B.4: IC1199.

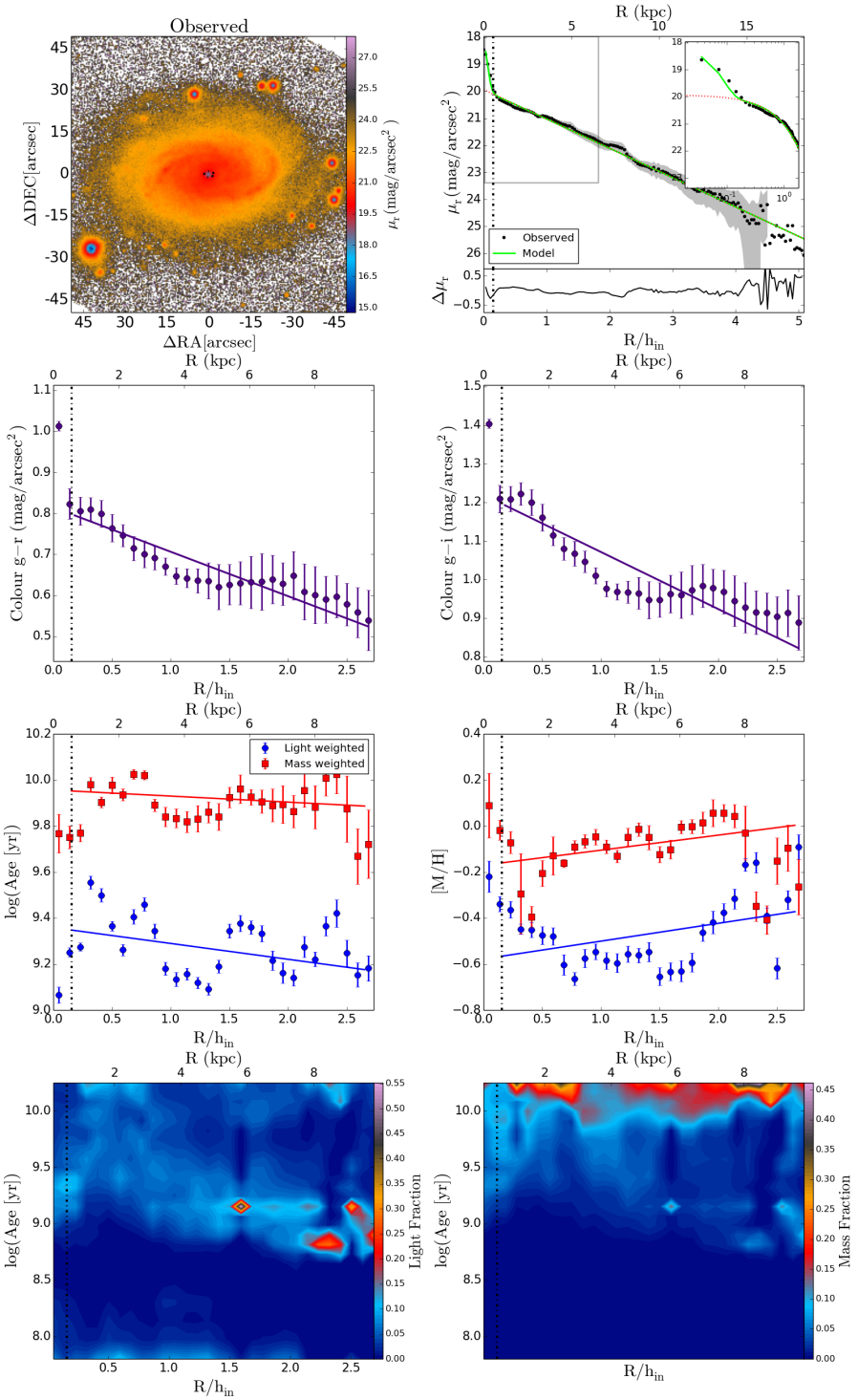

Figure B.5: IC1256.

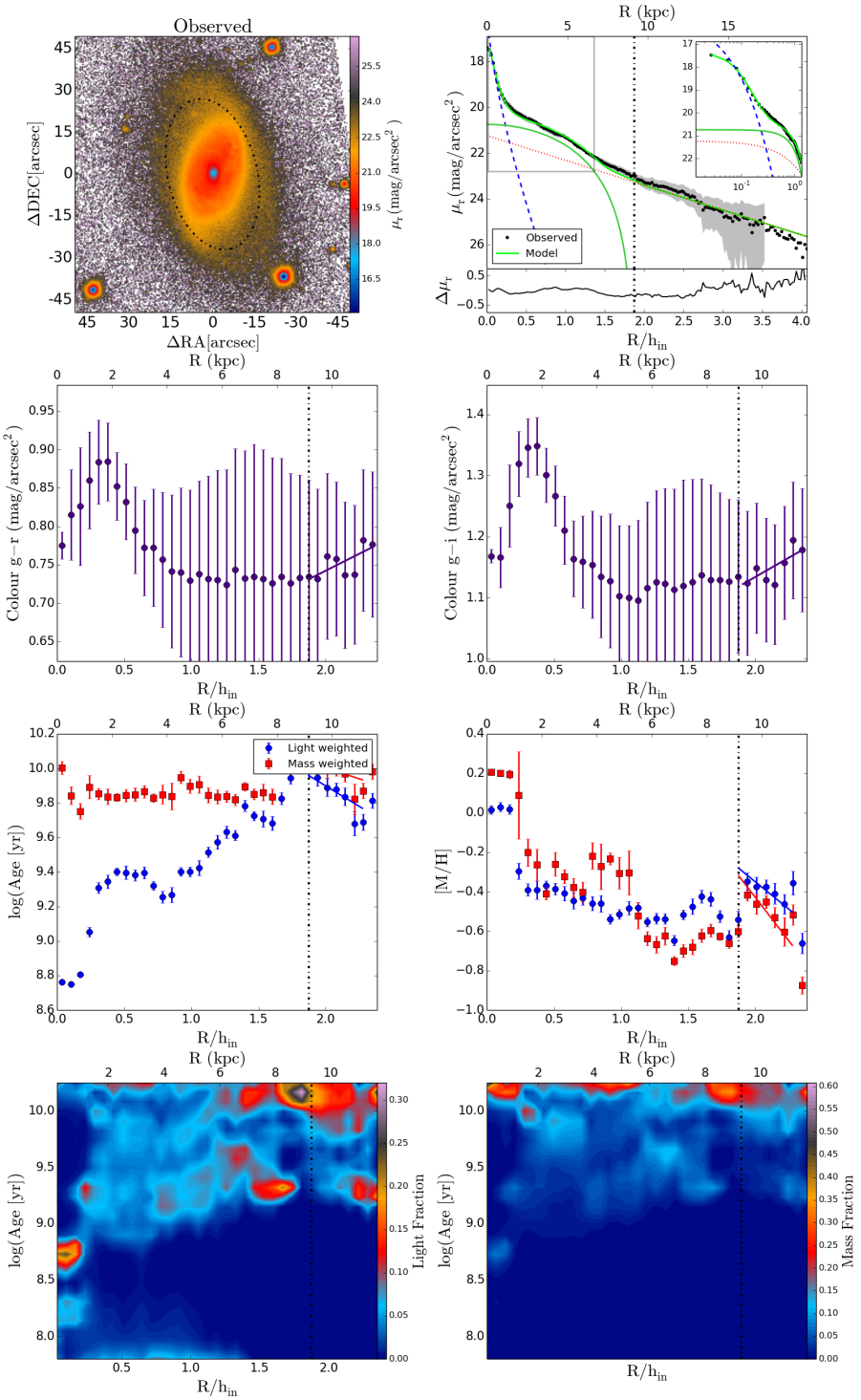

Figure B.6: IC1683.

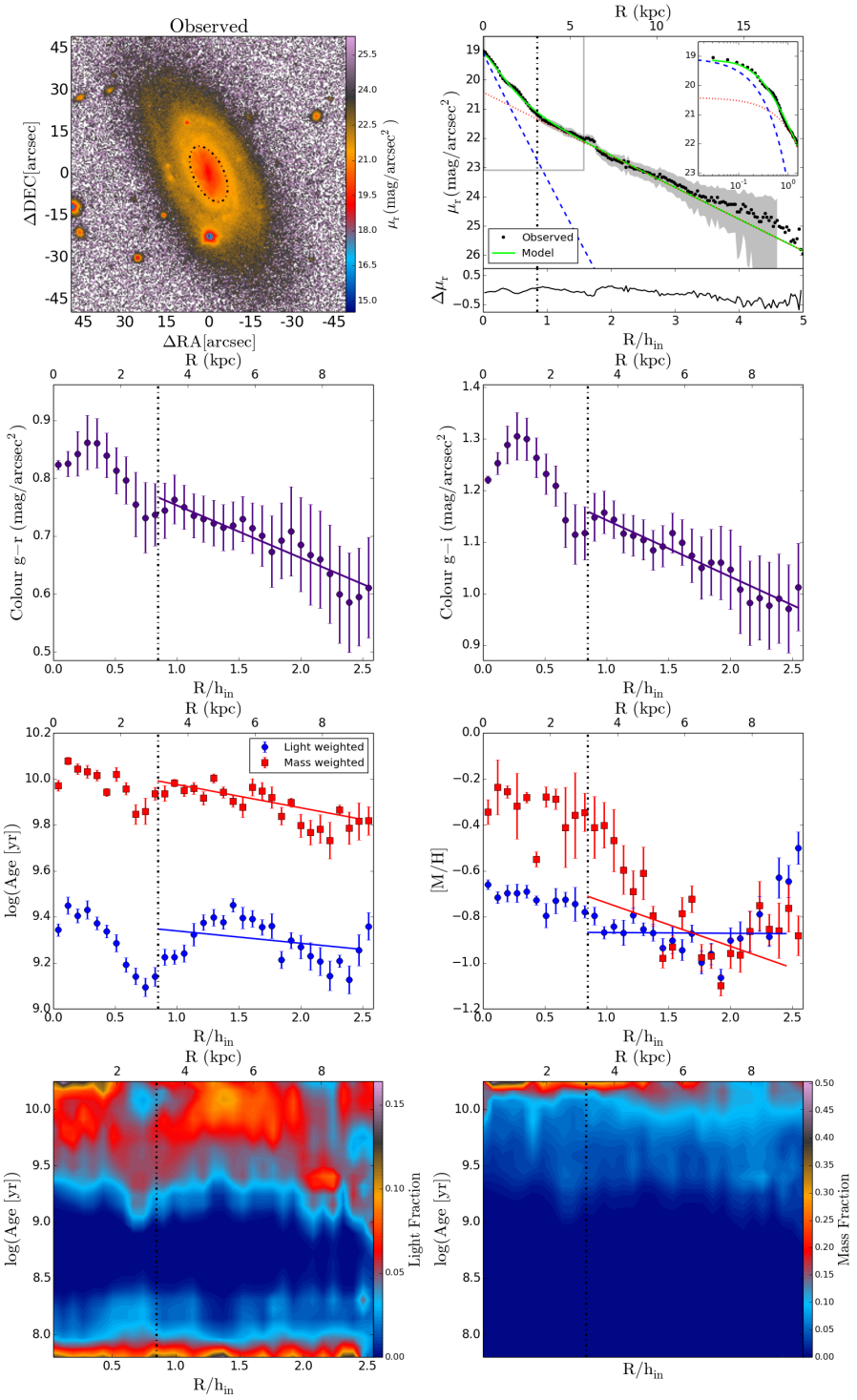

Figure B.7: IC5309.

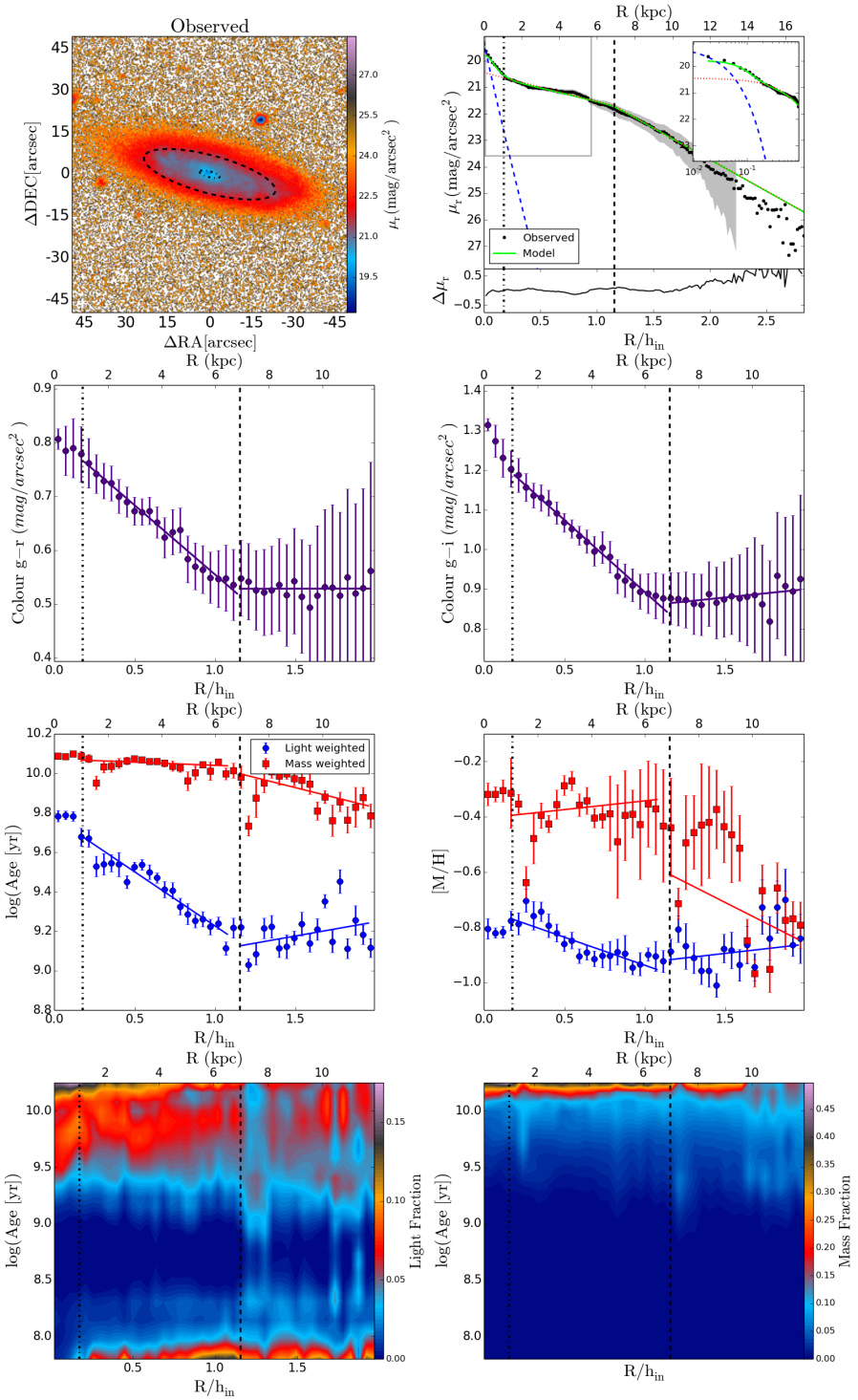

Figure B.8: MCG-01-10-015.

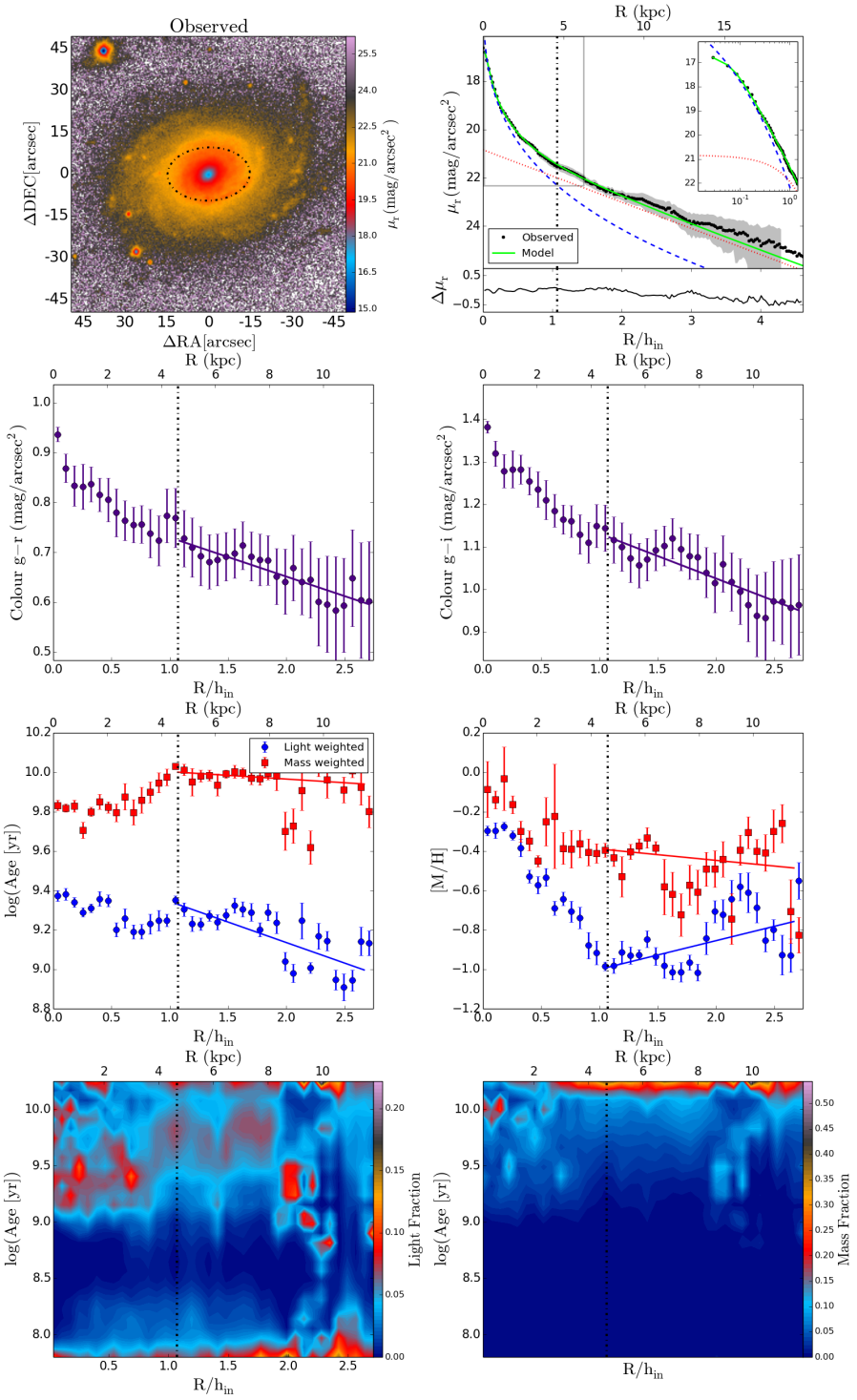

Figure B.9: NGC0001.

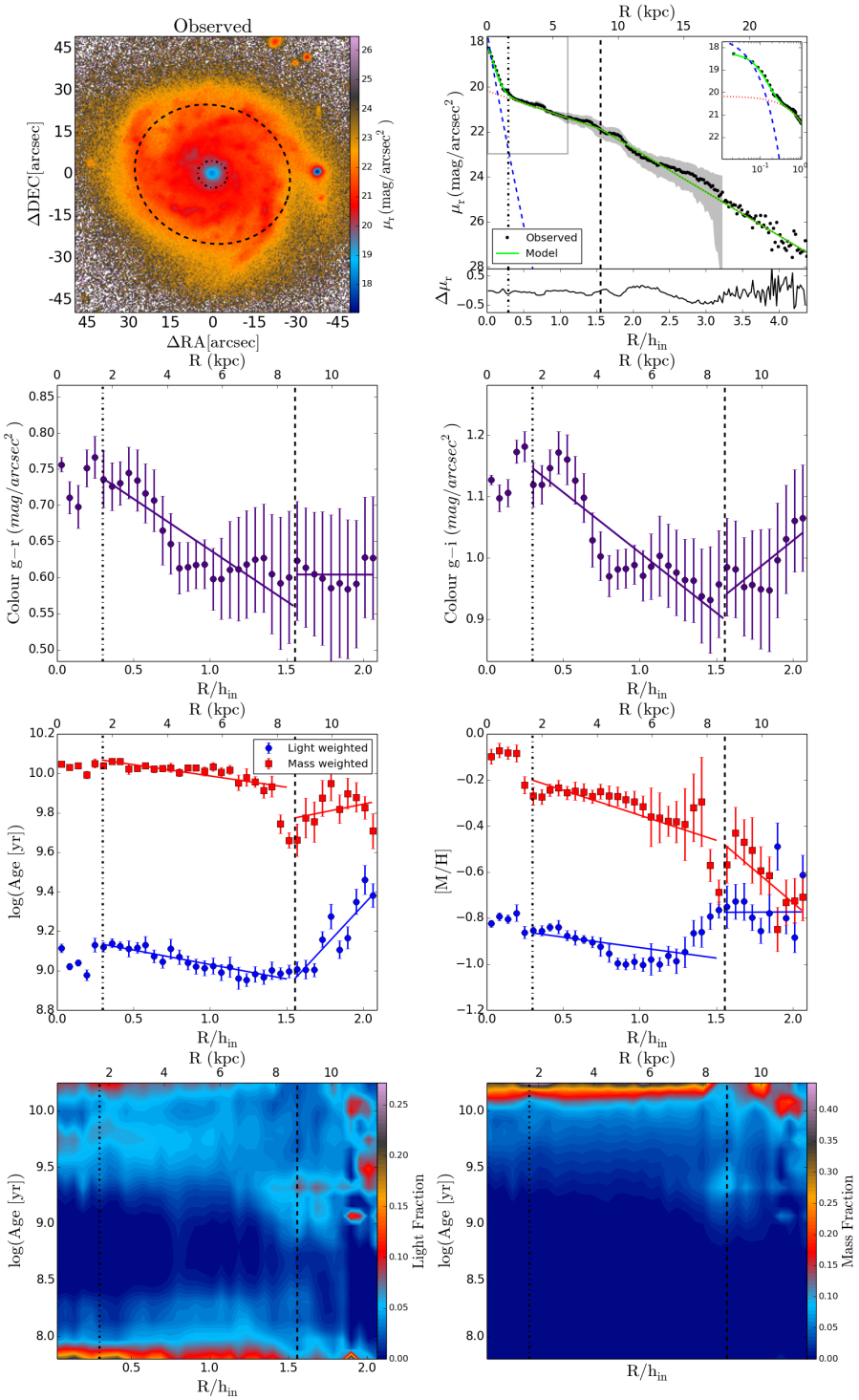

Figure B.10: NGC0234.

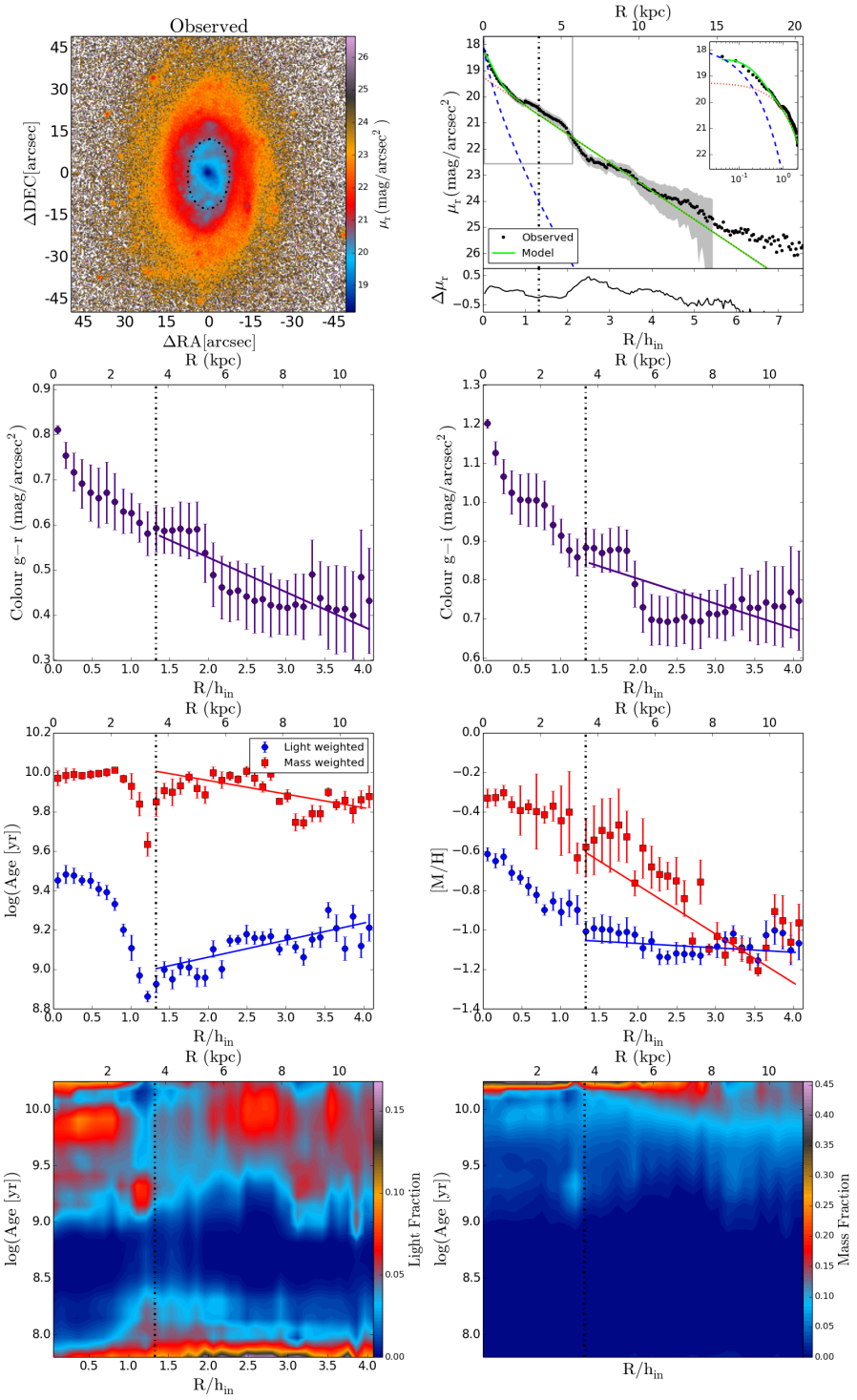

Figure B.11: NGC0237.

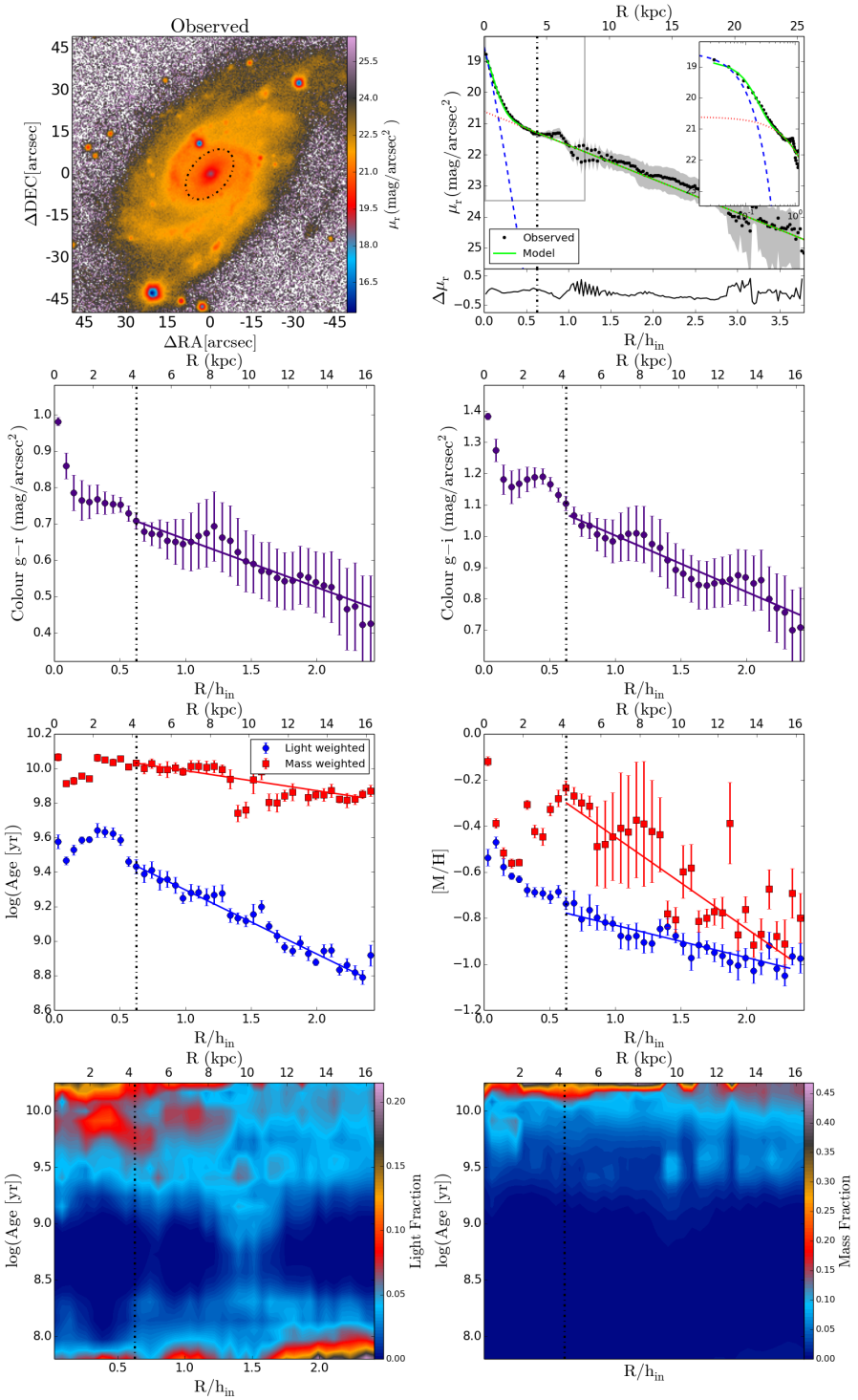

Figure B.12: NGC0477.

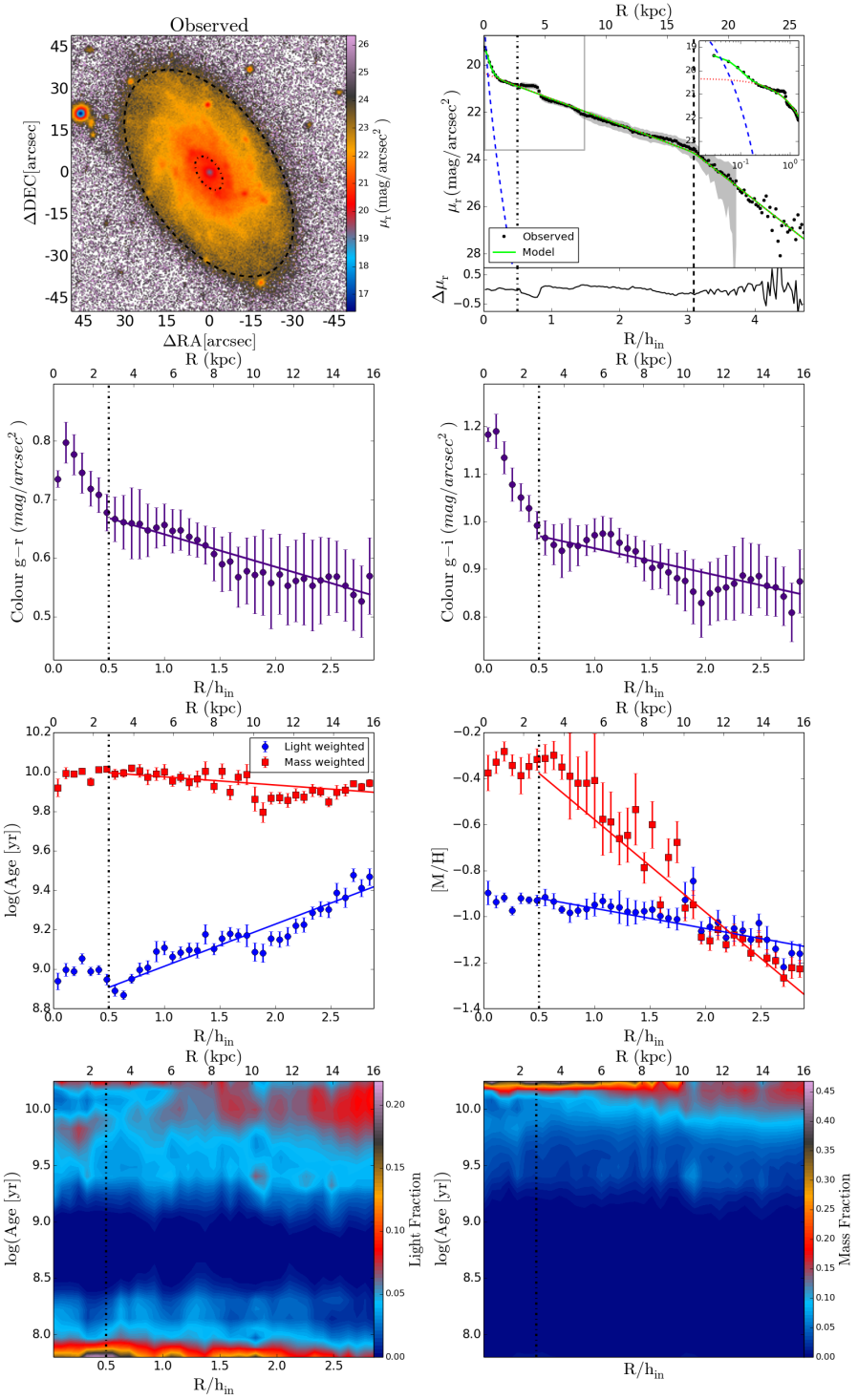

Figure B.13: NGC0496.

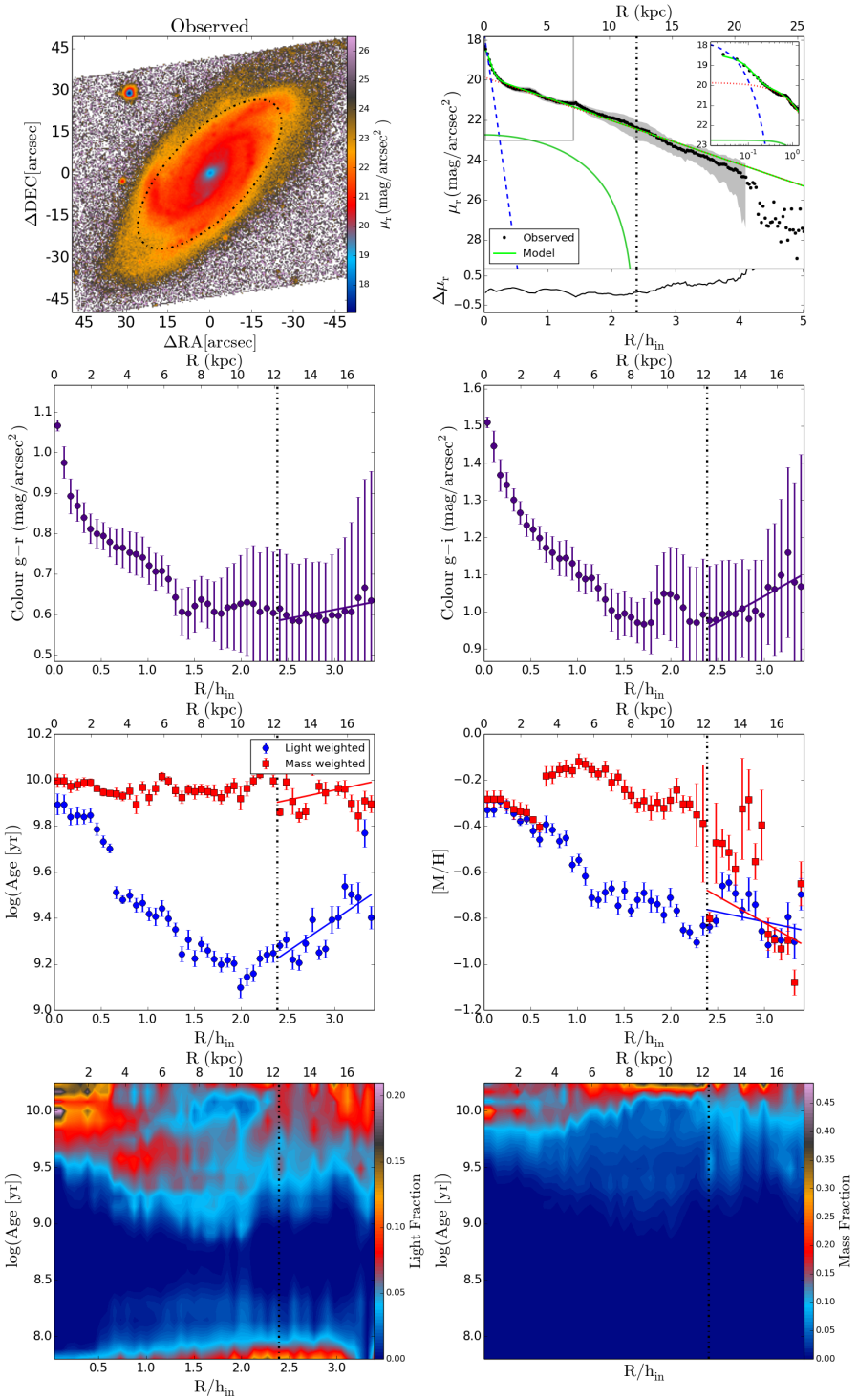

Figure B.14: NGC0551.

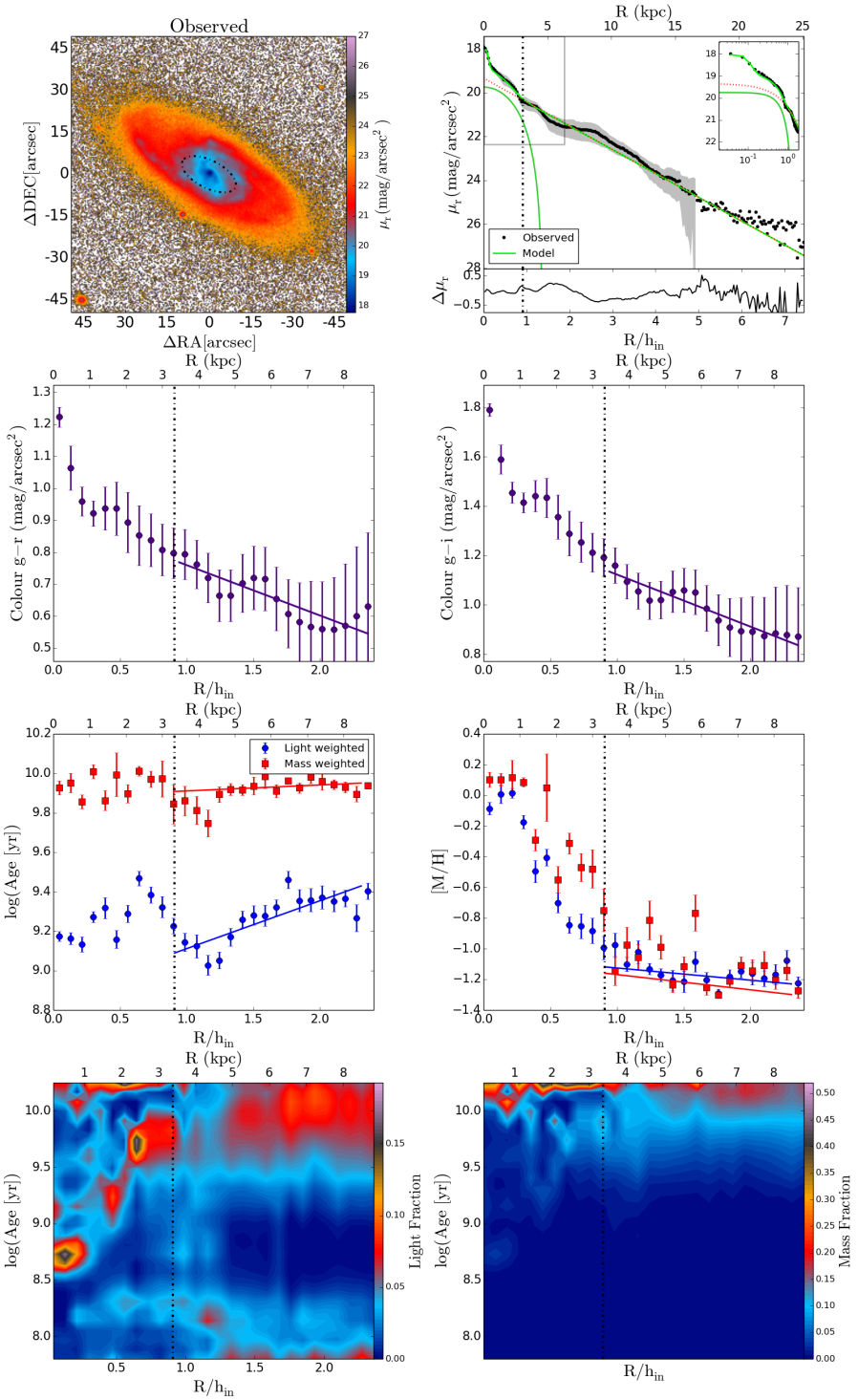

Figure B.15: NGC0716.

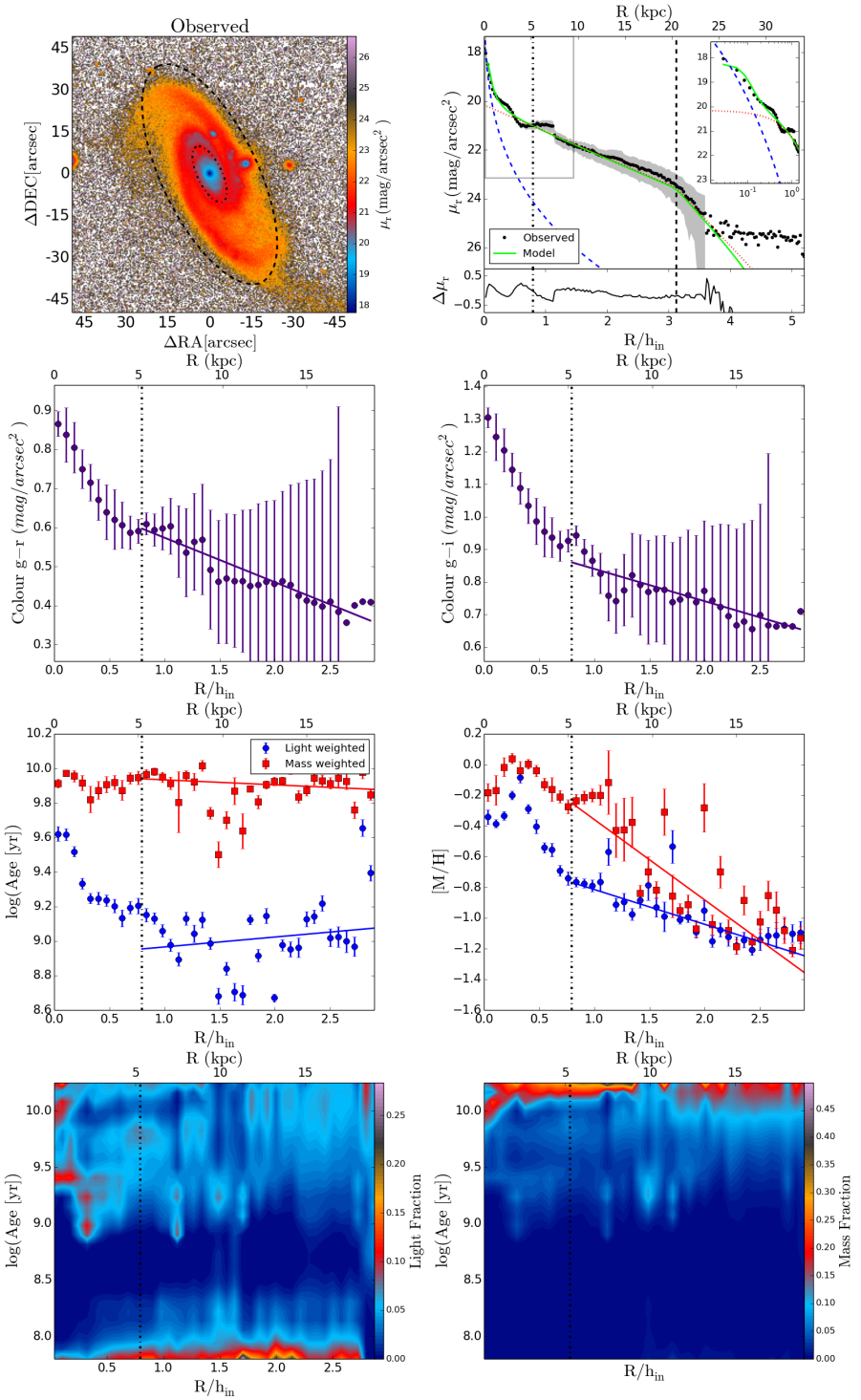

Figure B.16: NGC0768.

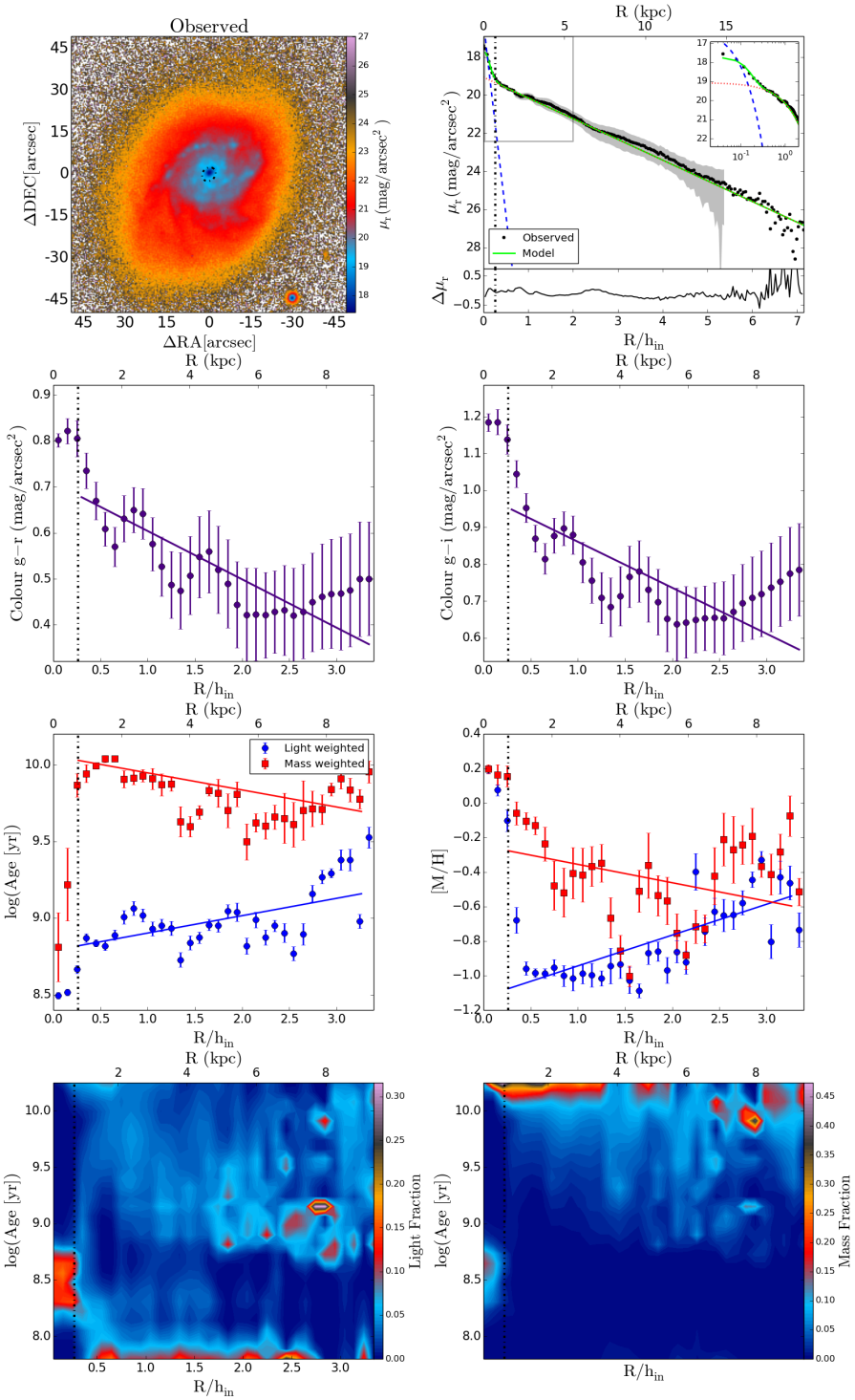

Figure B.17: NGC0873.

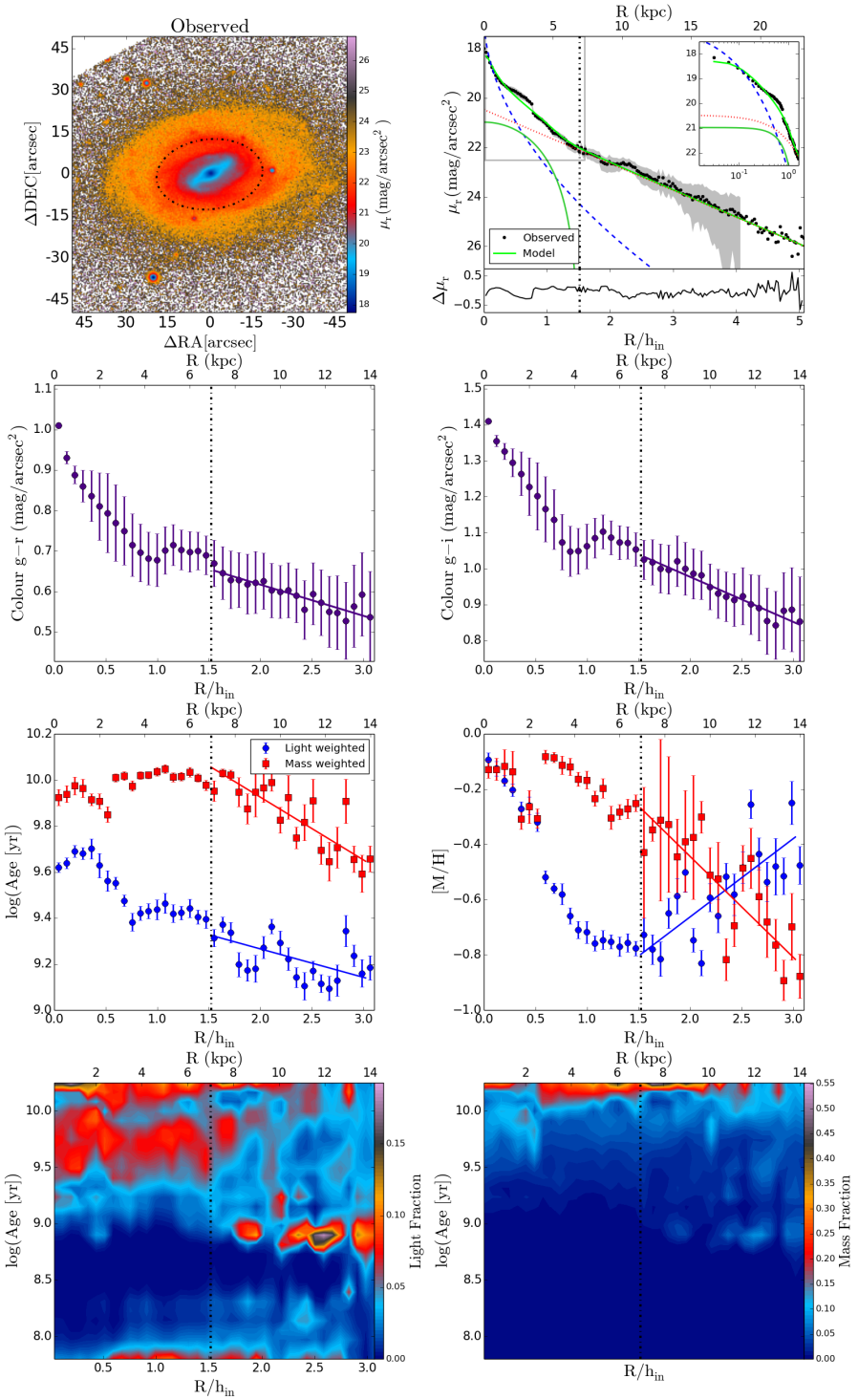

Figure B.18: NGC1093.

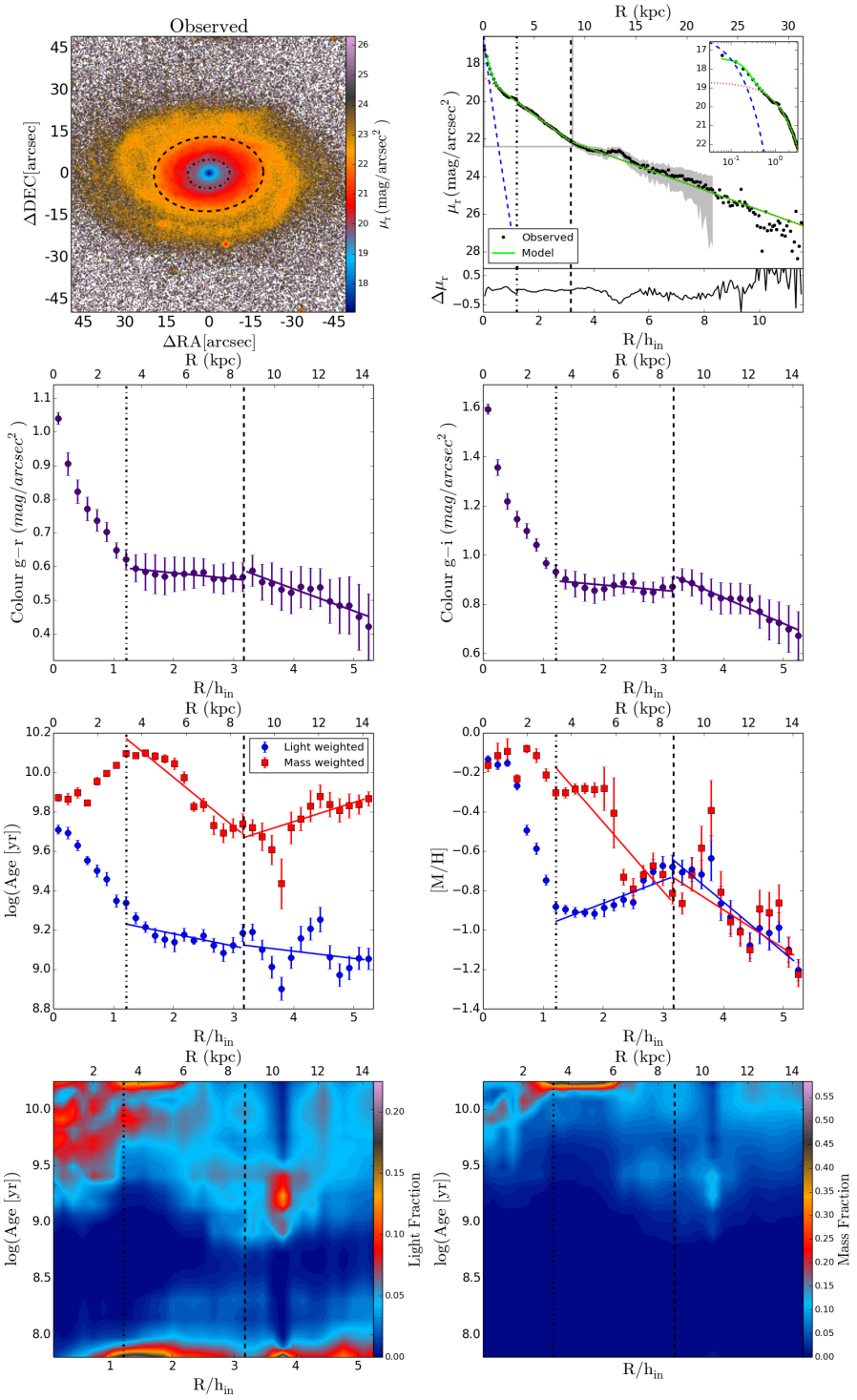

Figure B.19: NGC1094.

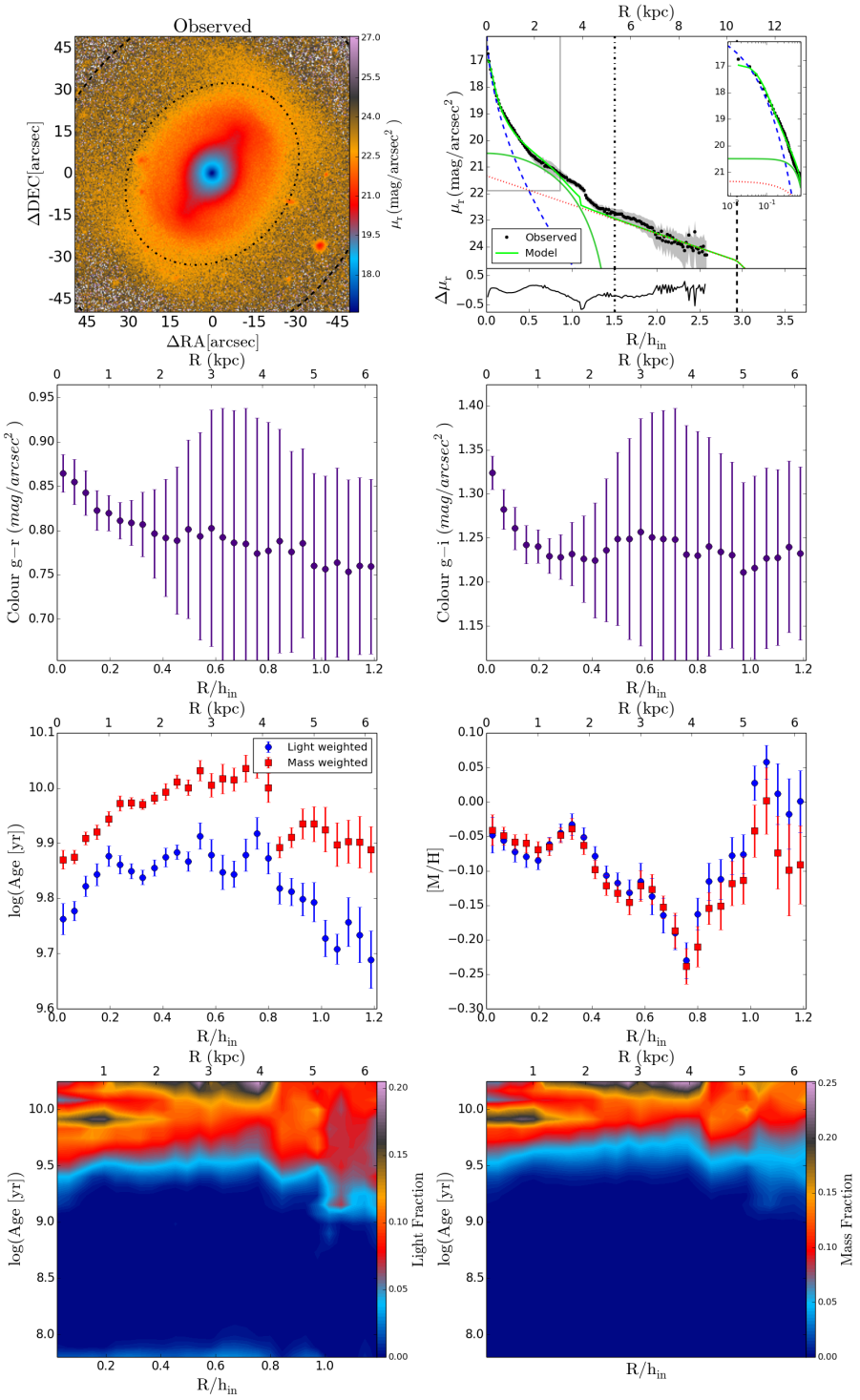

Figure B.20: NGC1211.

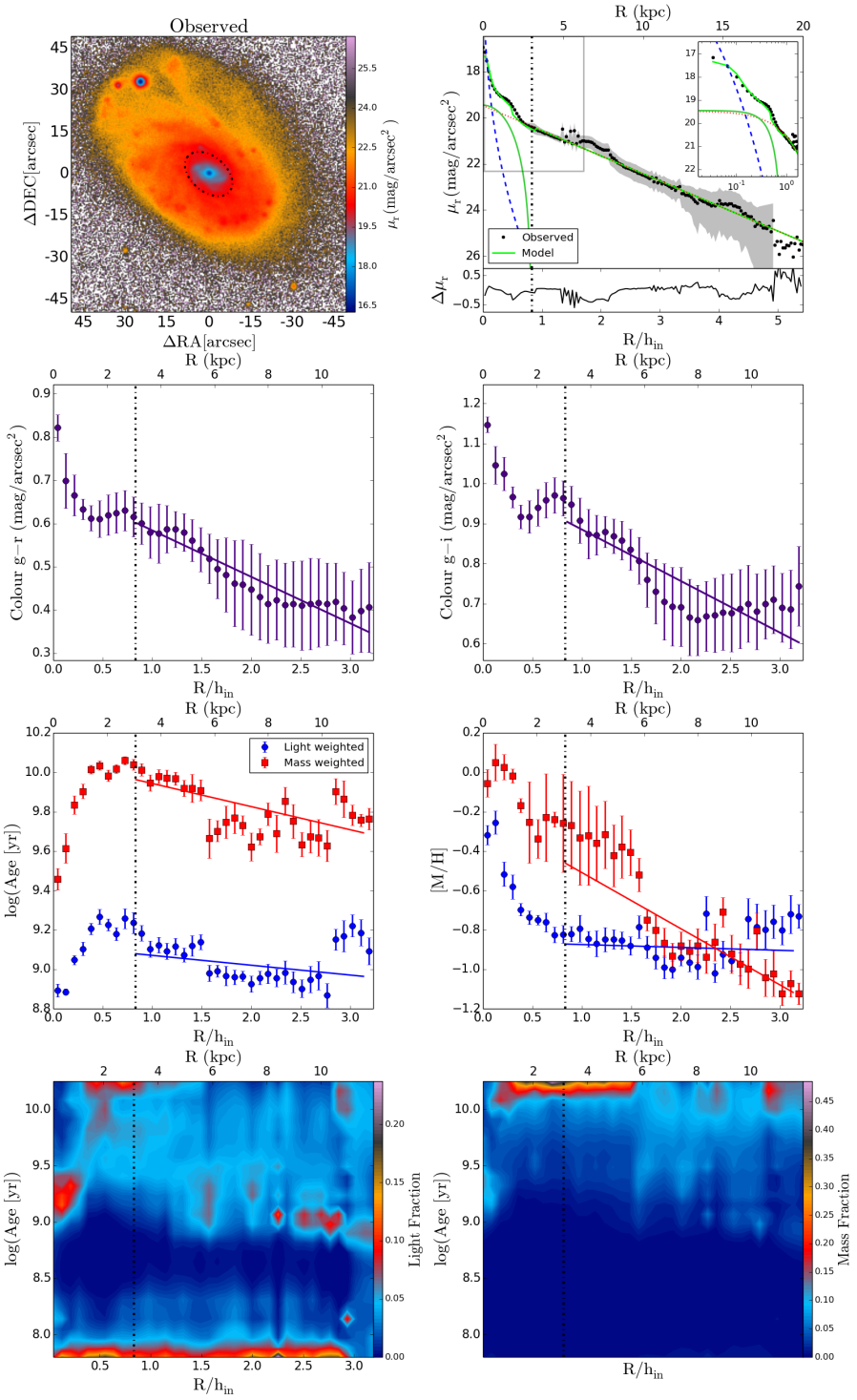

Figure B.21: NGC1659.

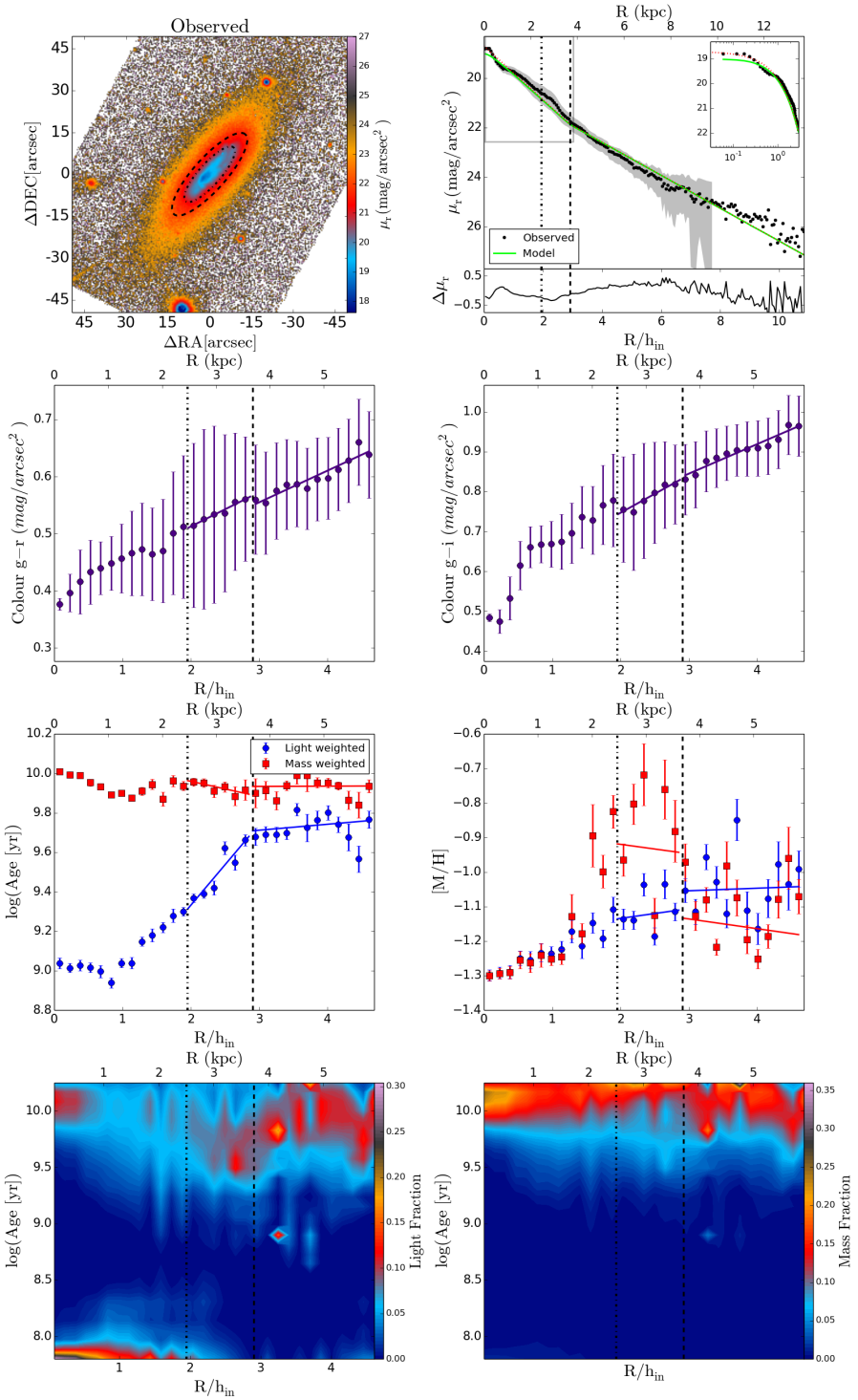

Figure B.22: NGC1677.

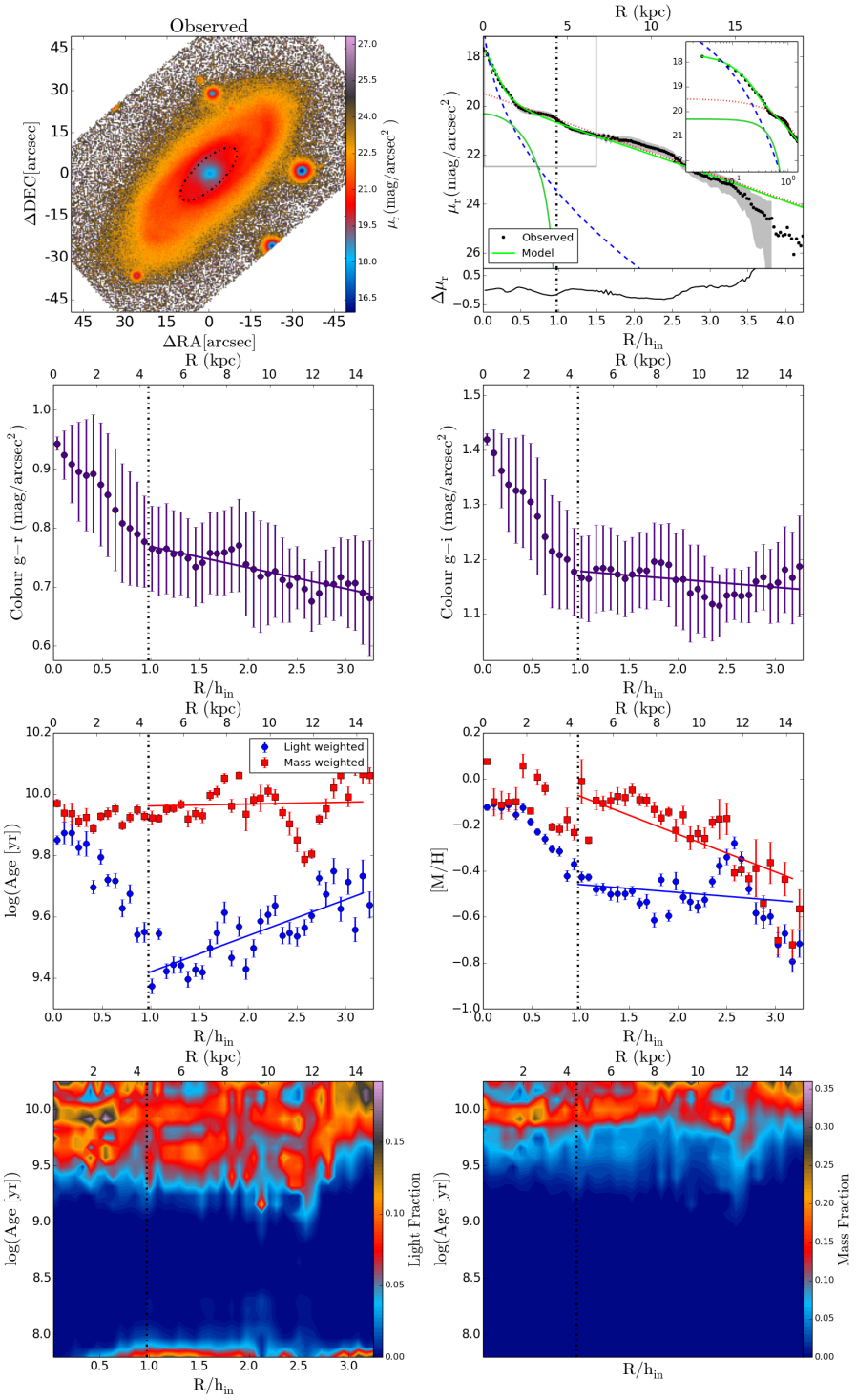

Figure B.23: NGC2449.

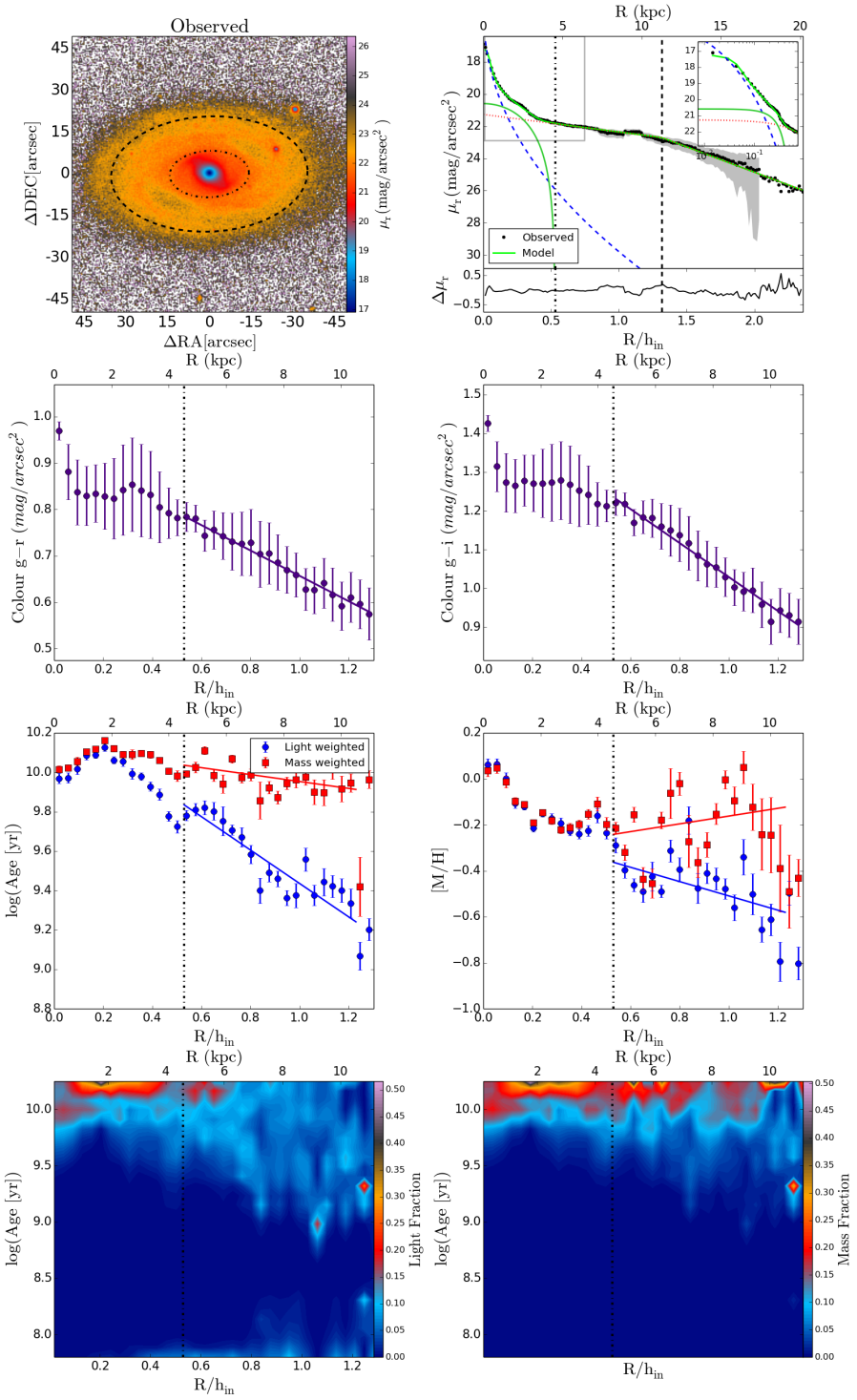

Figure B.24: NGC2486.

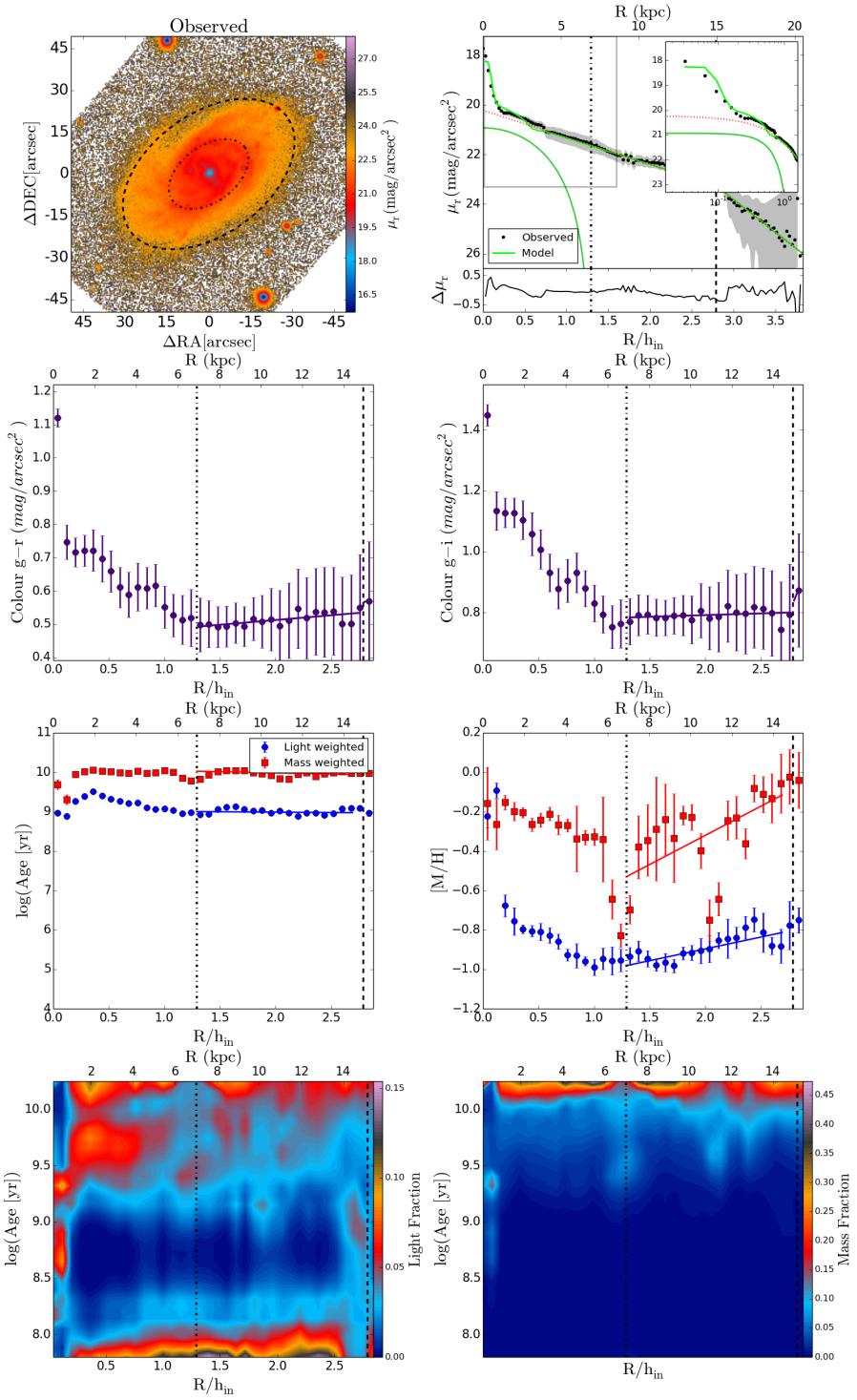

Figure B.25: NGC2540.

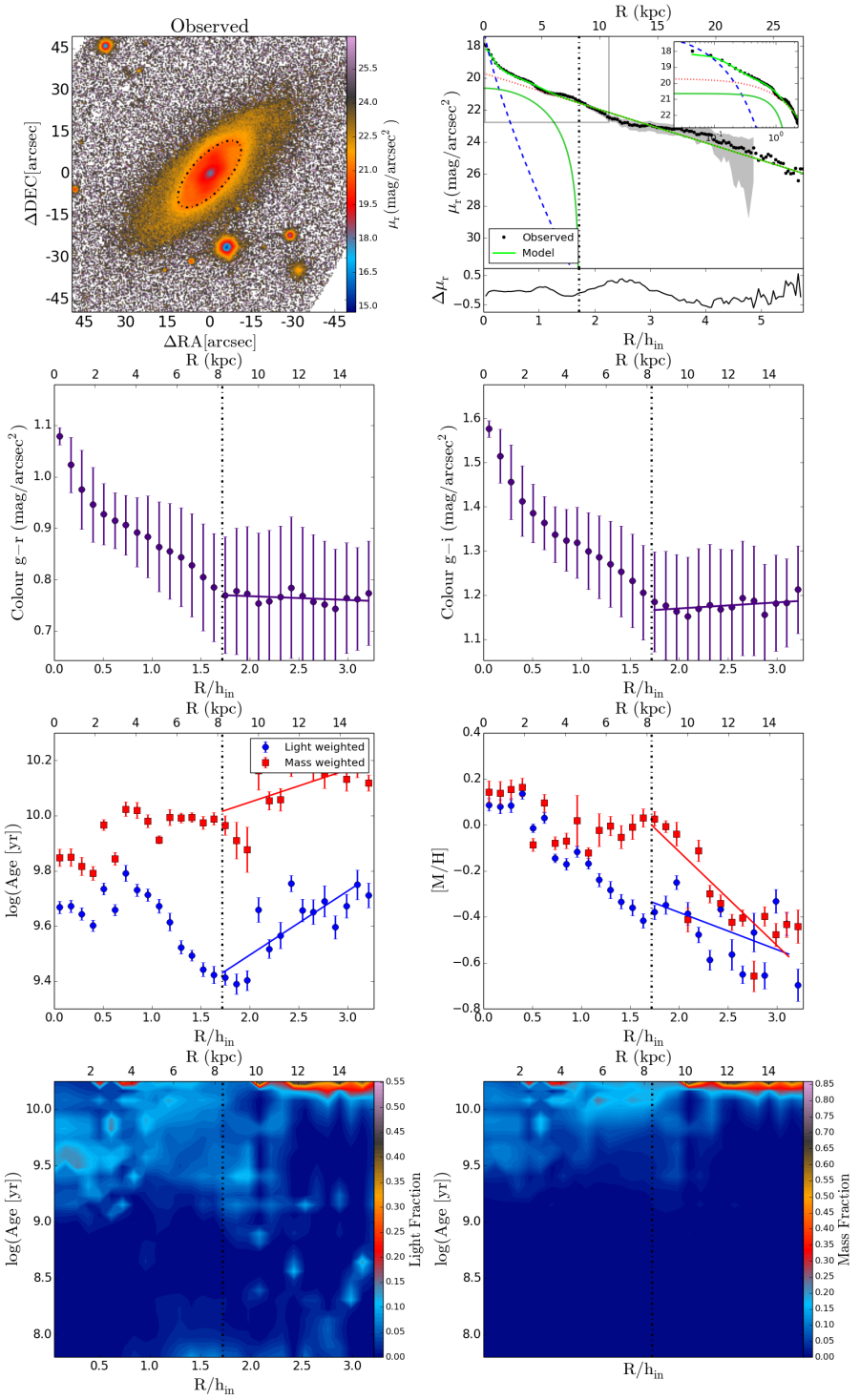

Figure B.26: NGC2572.

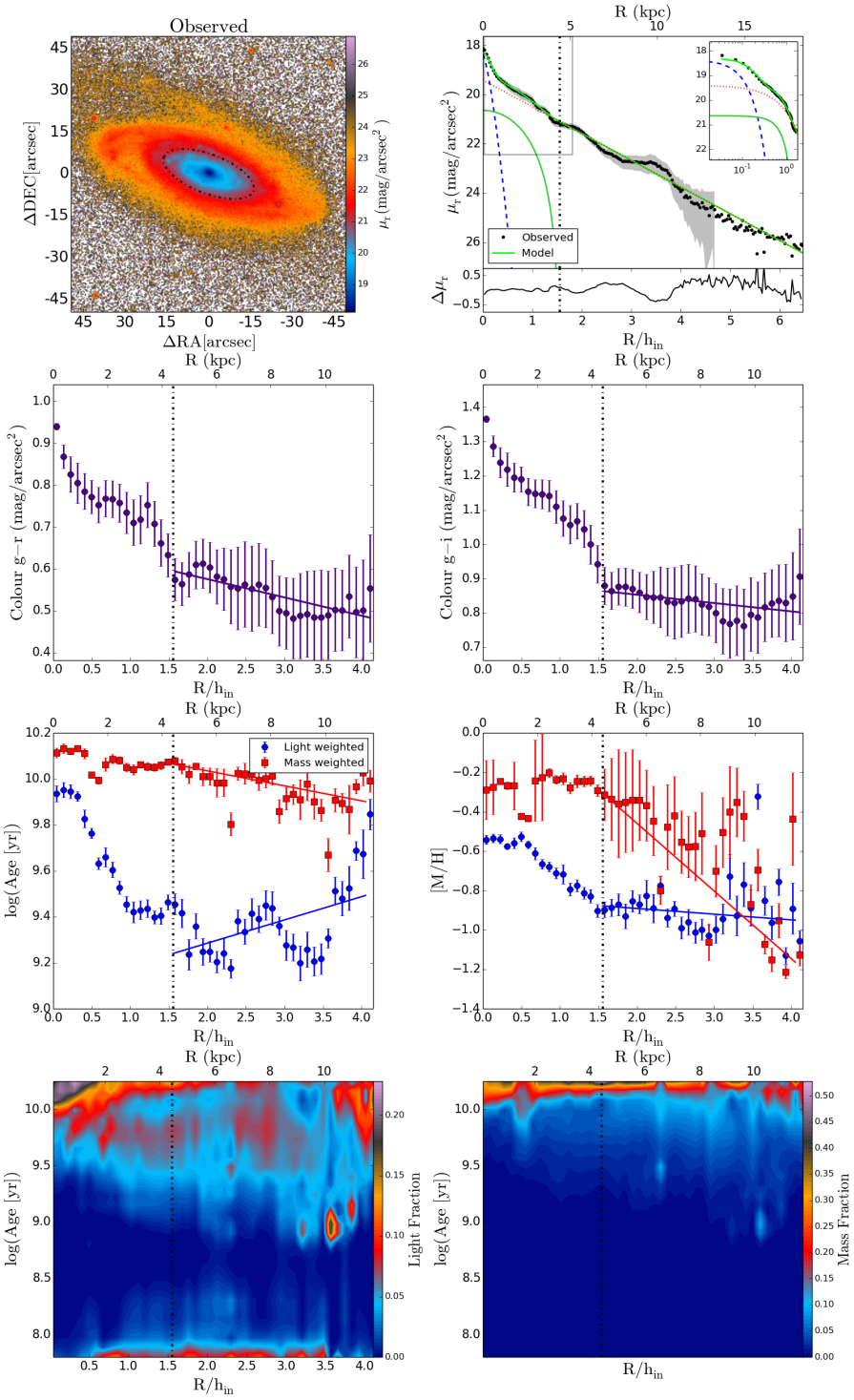

Figure B.27: NGC3815.

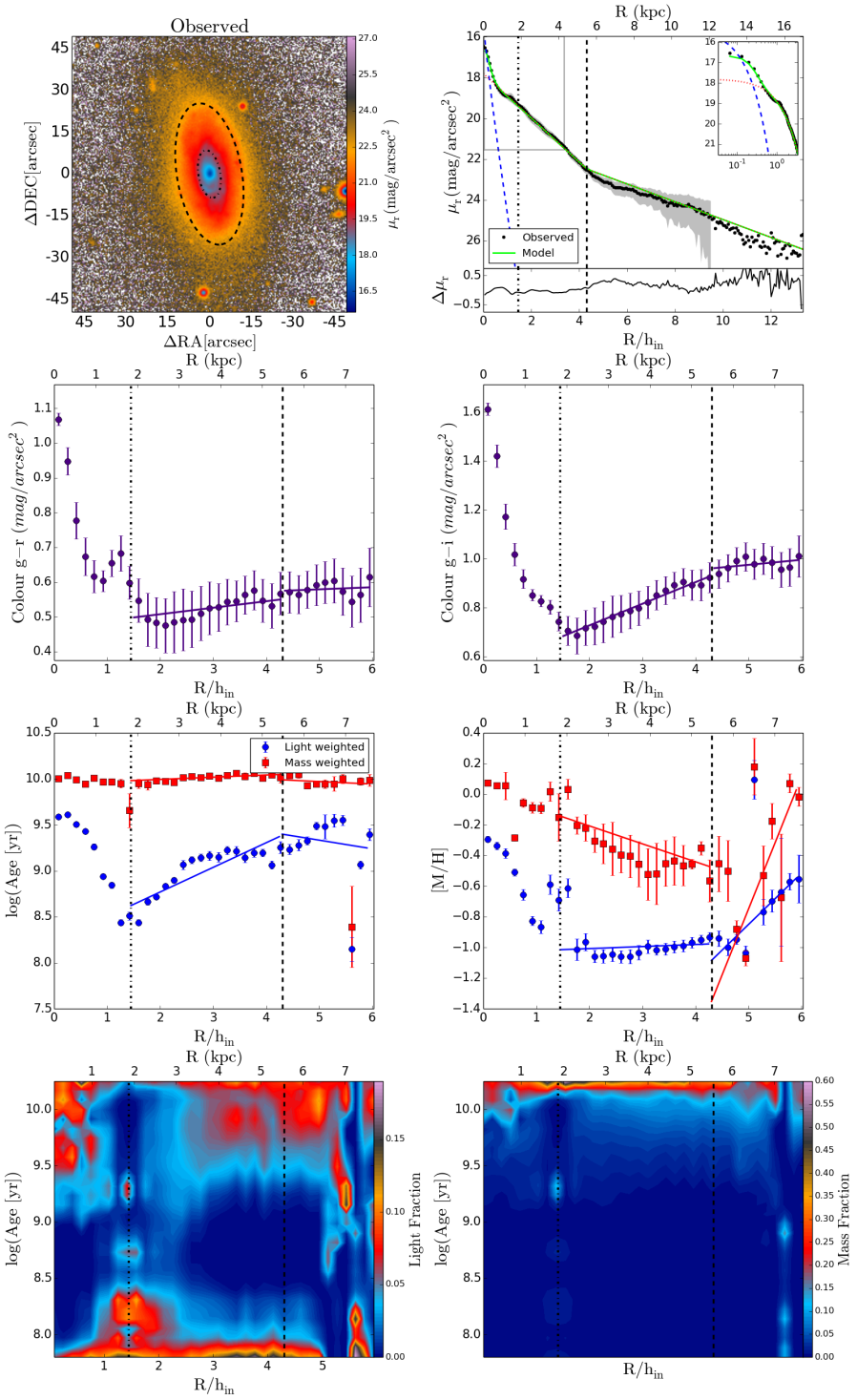

Figure B.28: NGC3994.

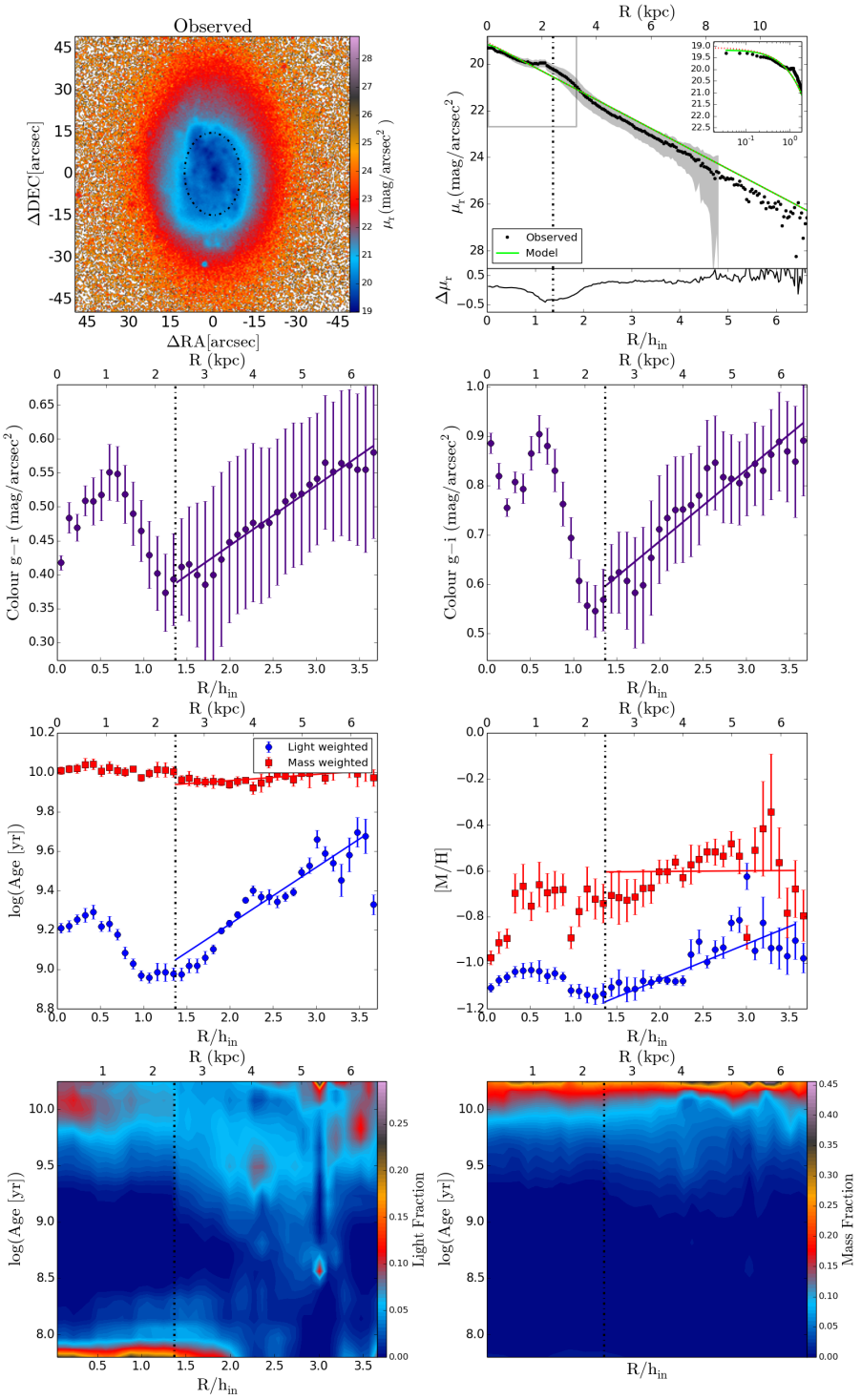

Figure B.29: NGC4470.

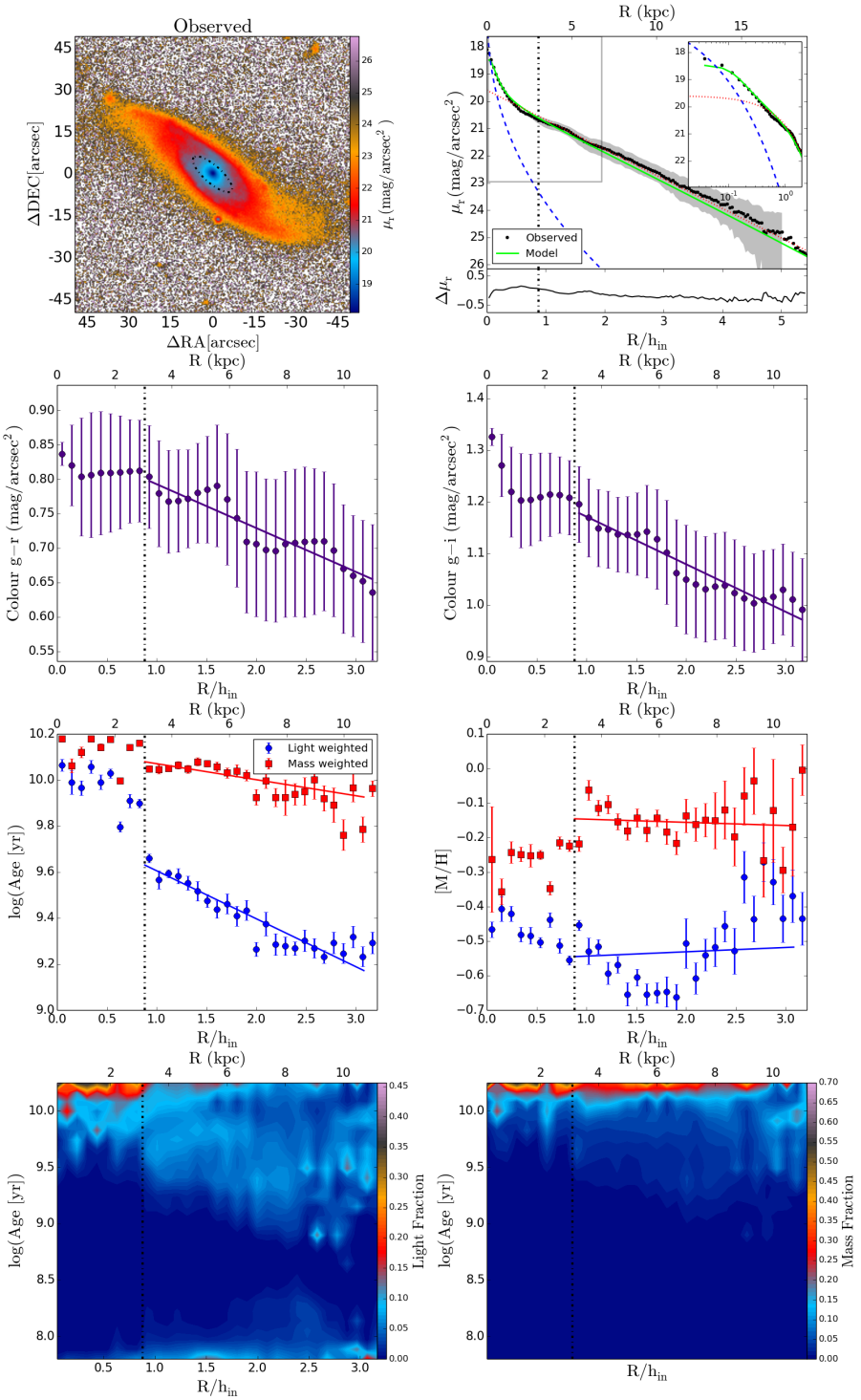

Figure B.30: NGC4644.

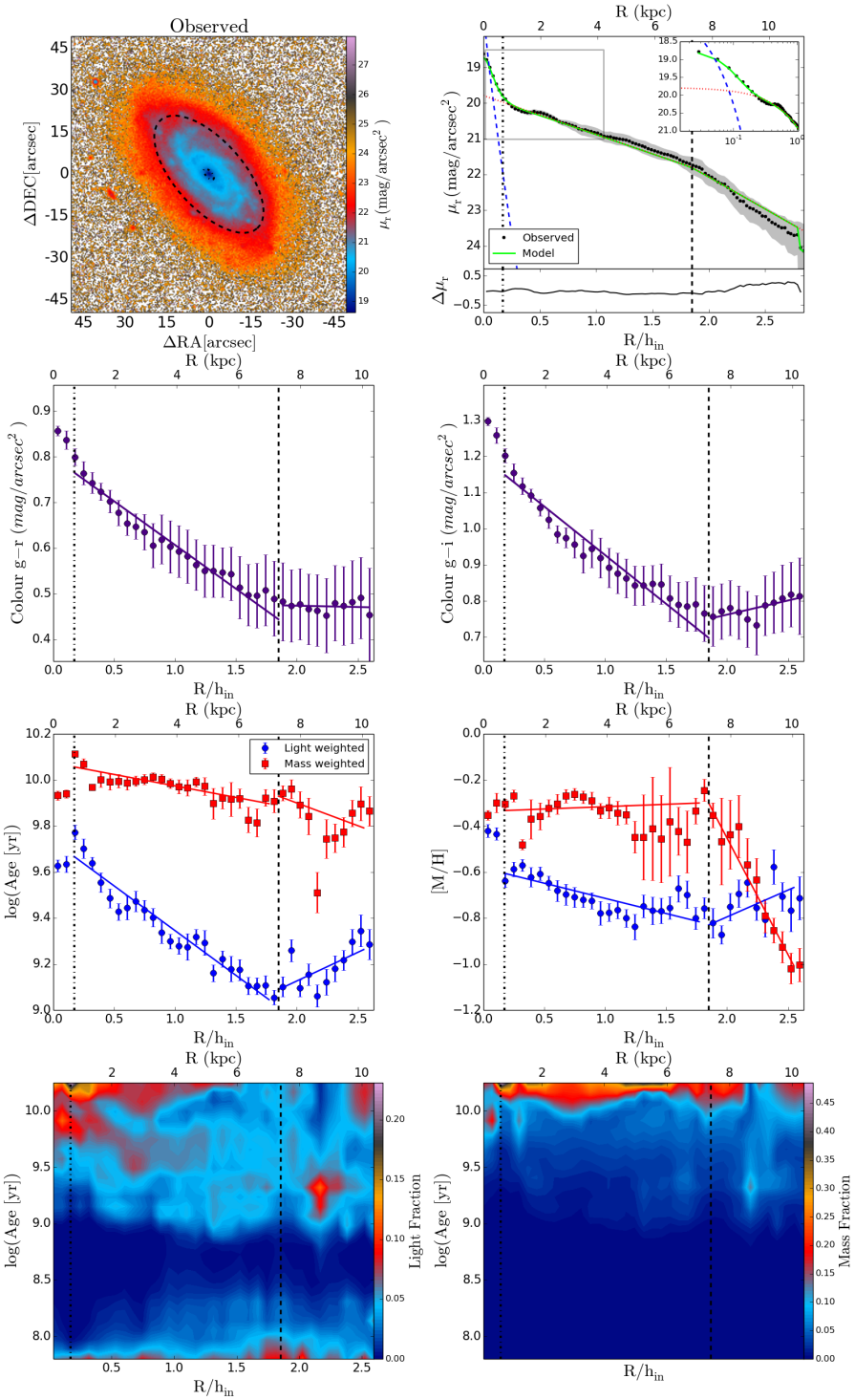

Figure B.31: NGC4711.

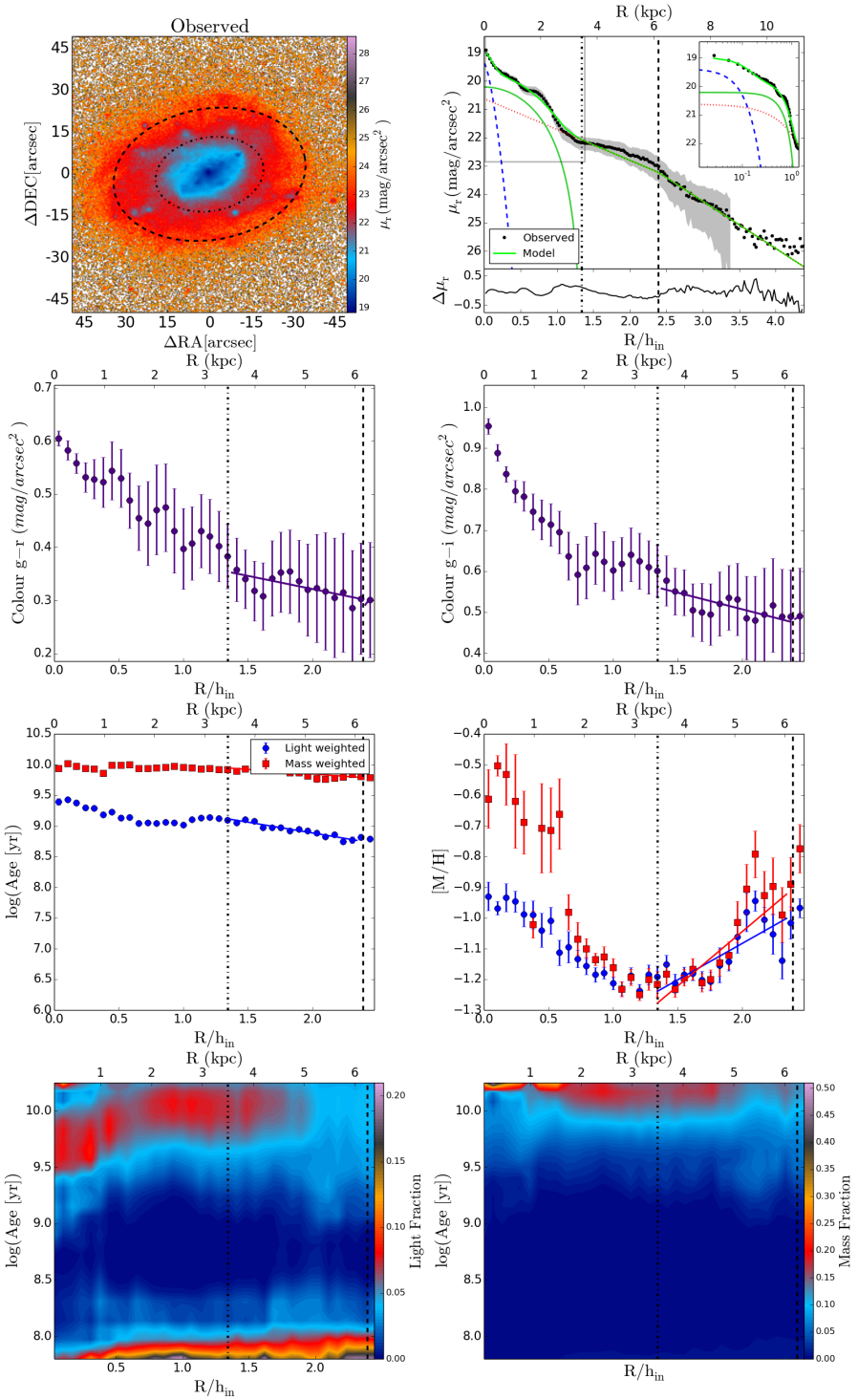

Figure B.32: NGC4961.

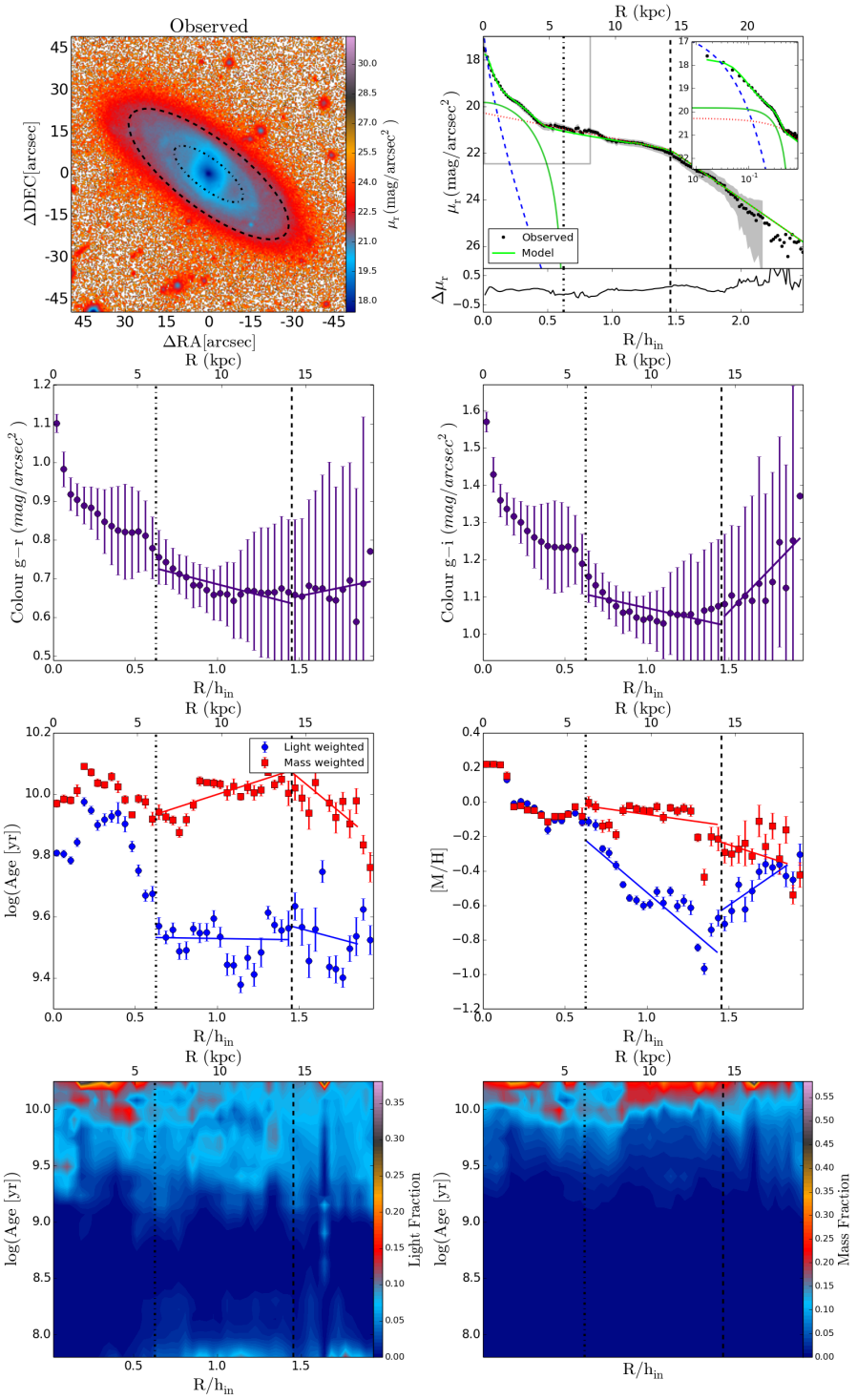

Figure B.33: NGC5267.

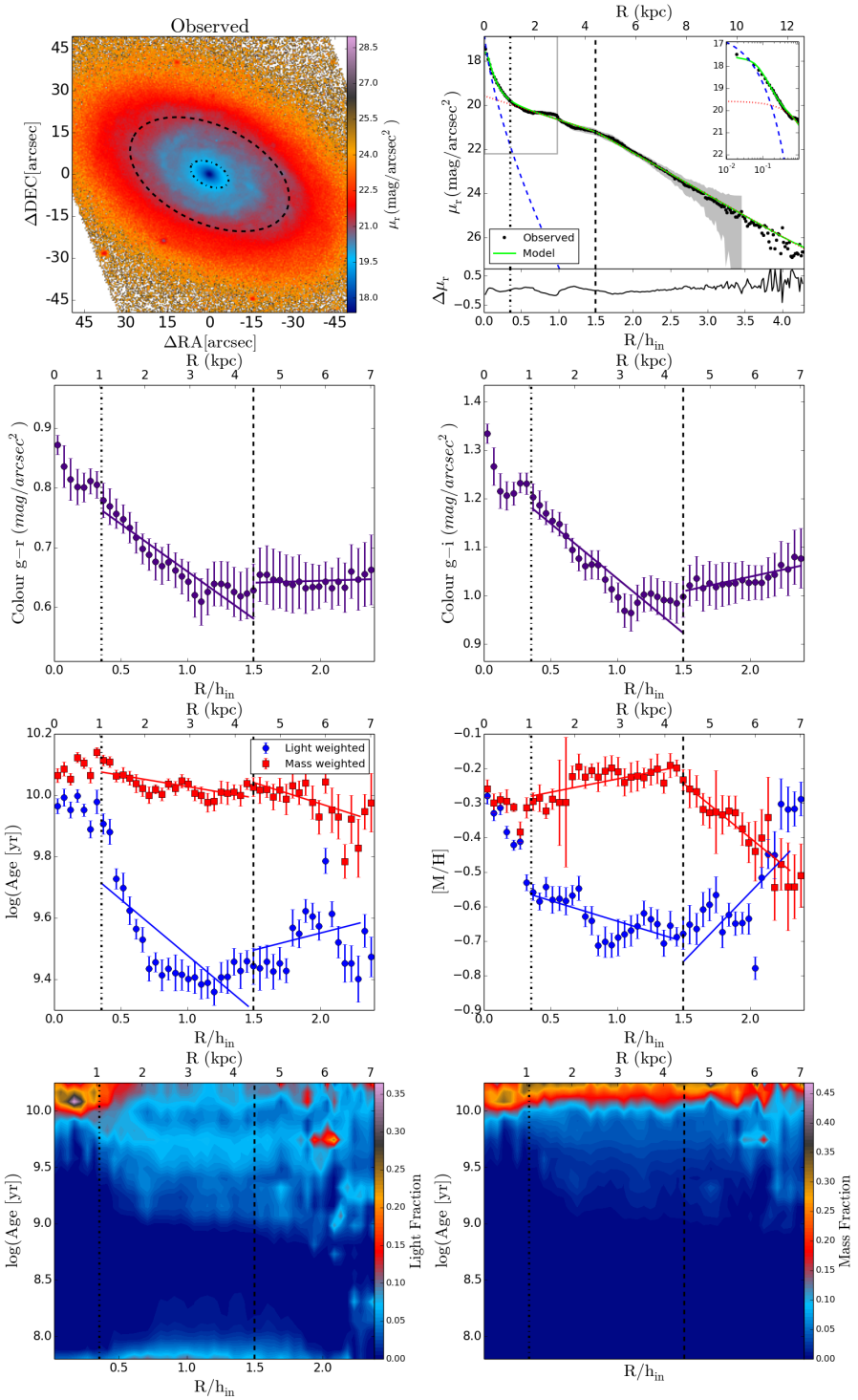

Figure B.34: NGC5376.

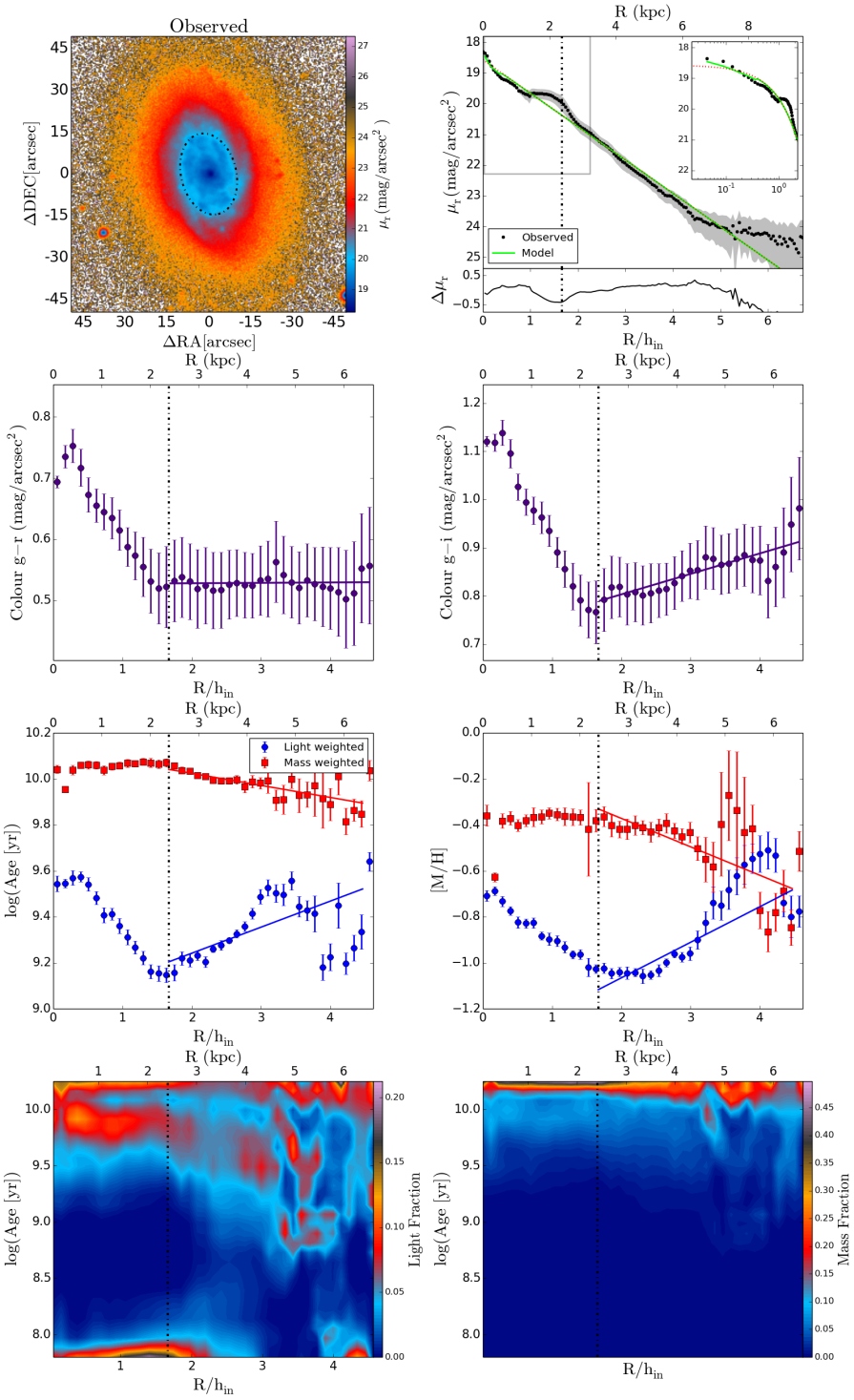

Figure B.35: NGC5633.

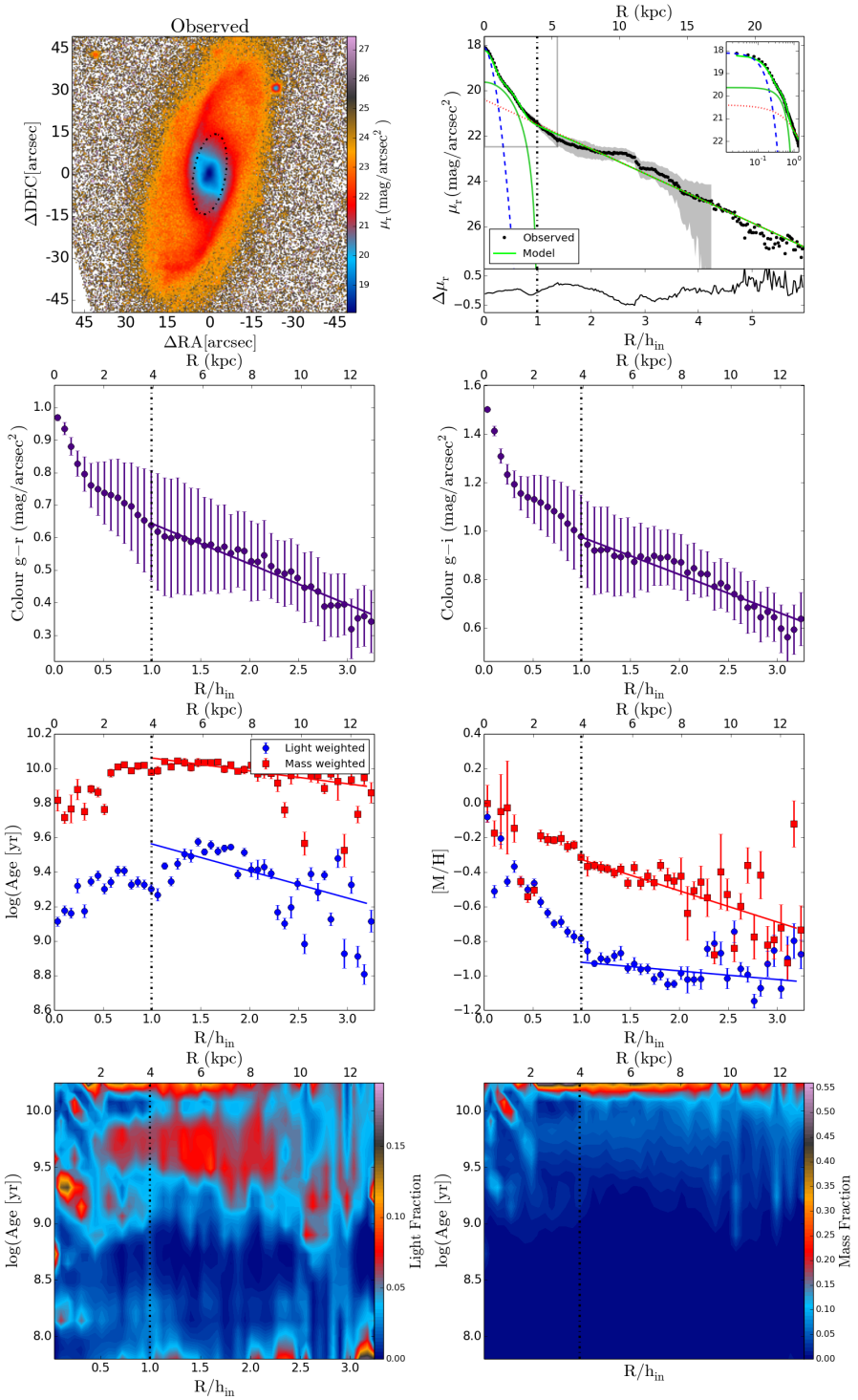

Figure B.36: NGC5657.

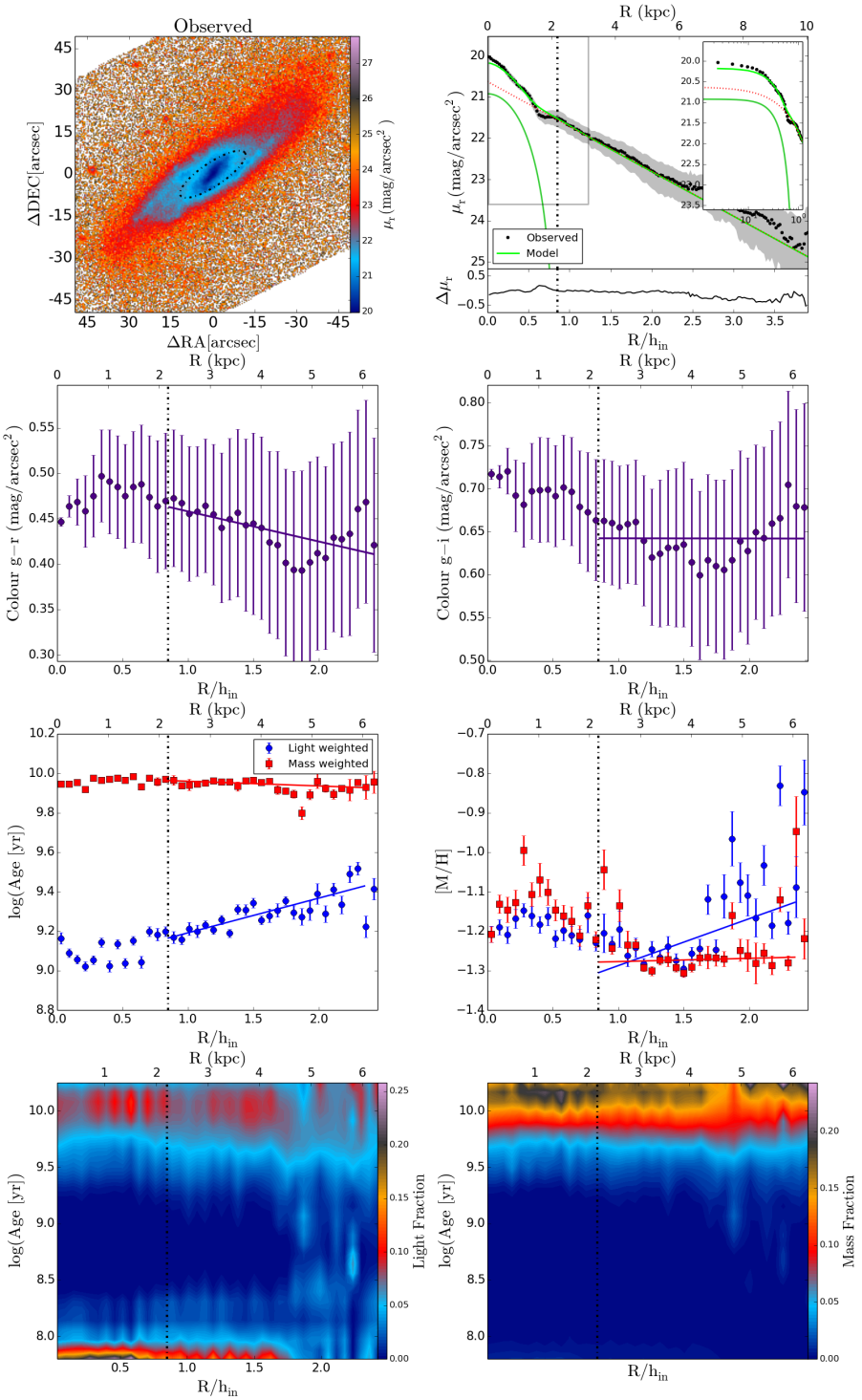

Figure B.37: NGC5682.

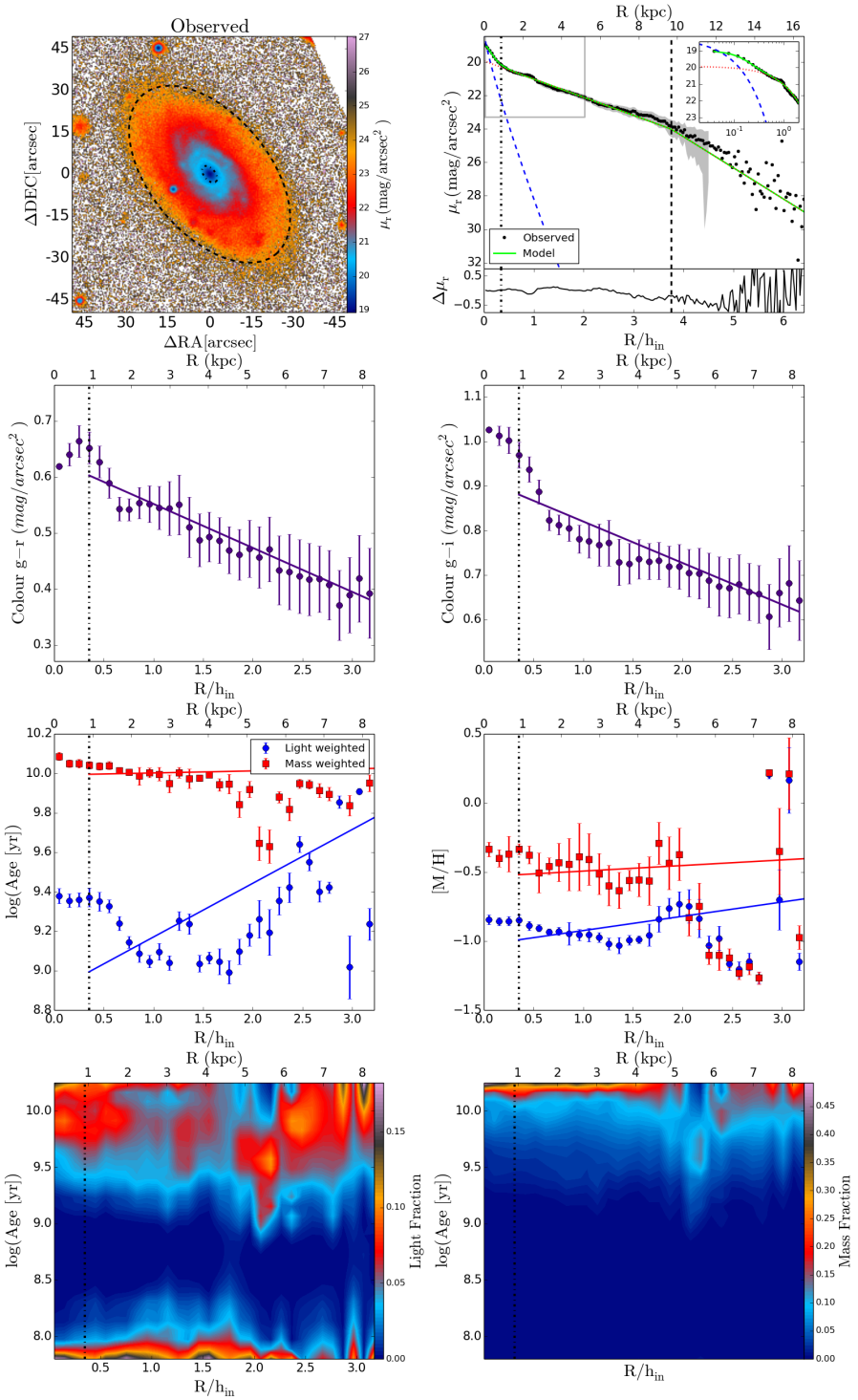

Figure B.38: NGC5732.

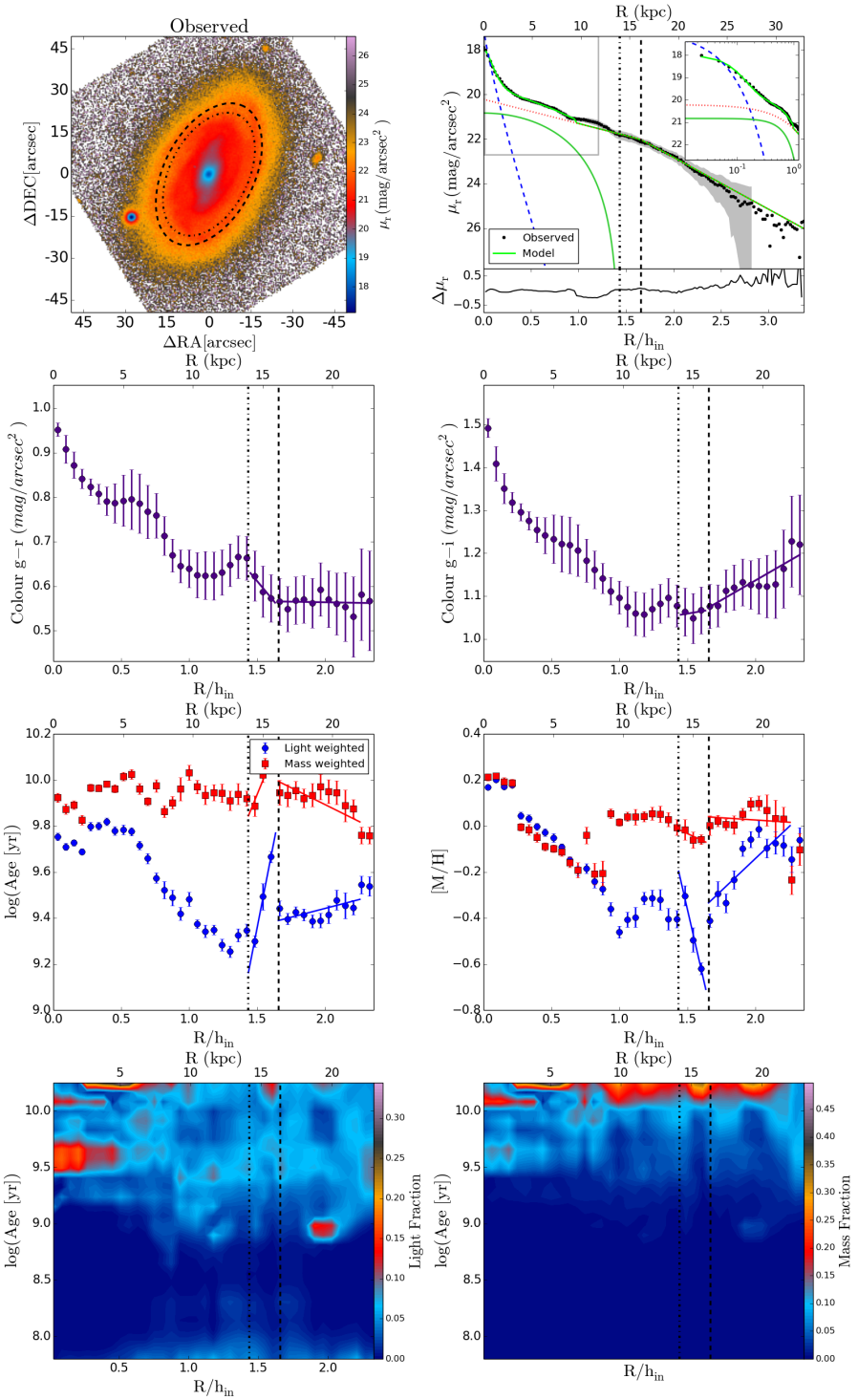

Figure B.39: NGC5888.

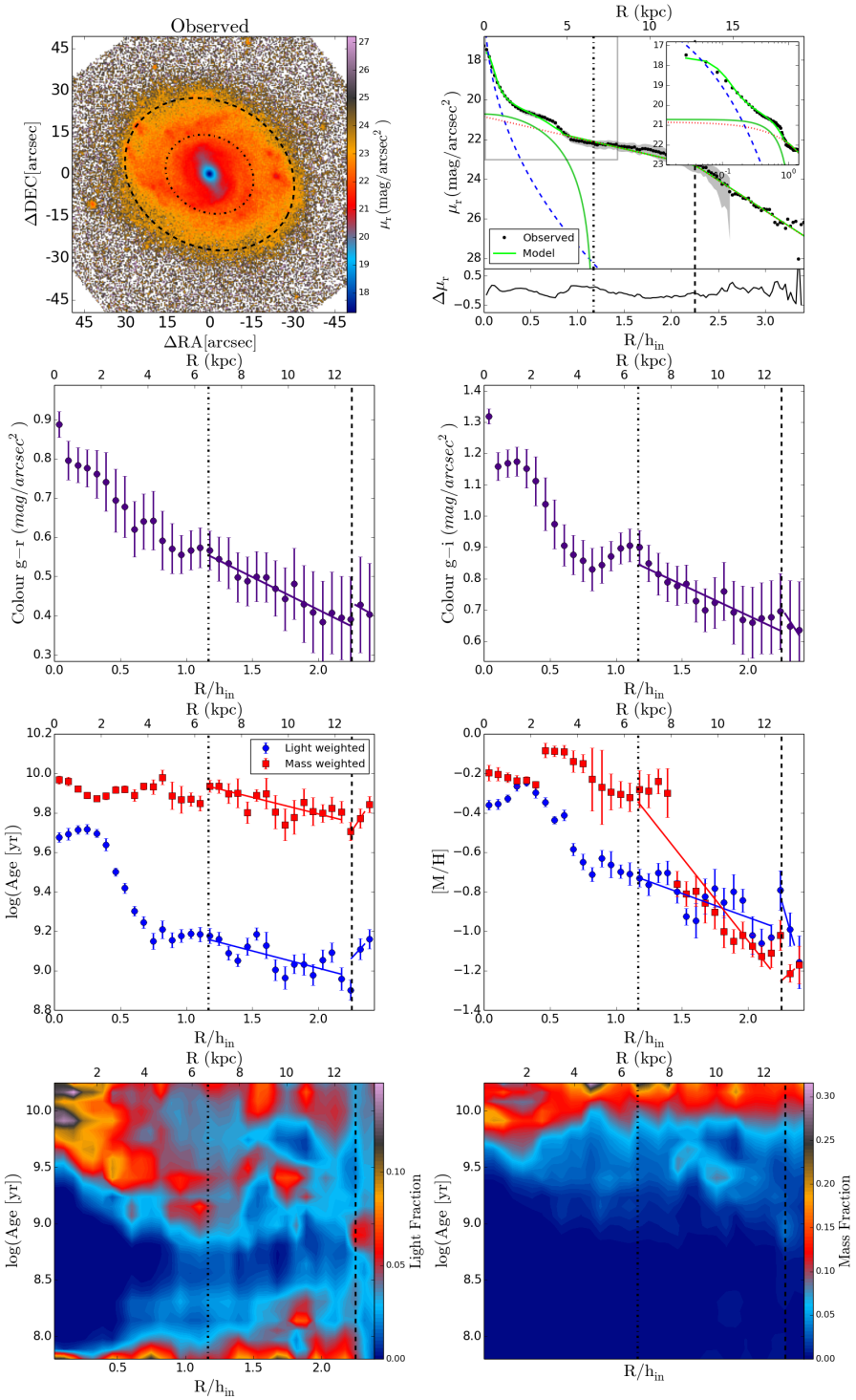

Figure B.40: NGC5947.

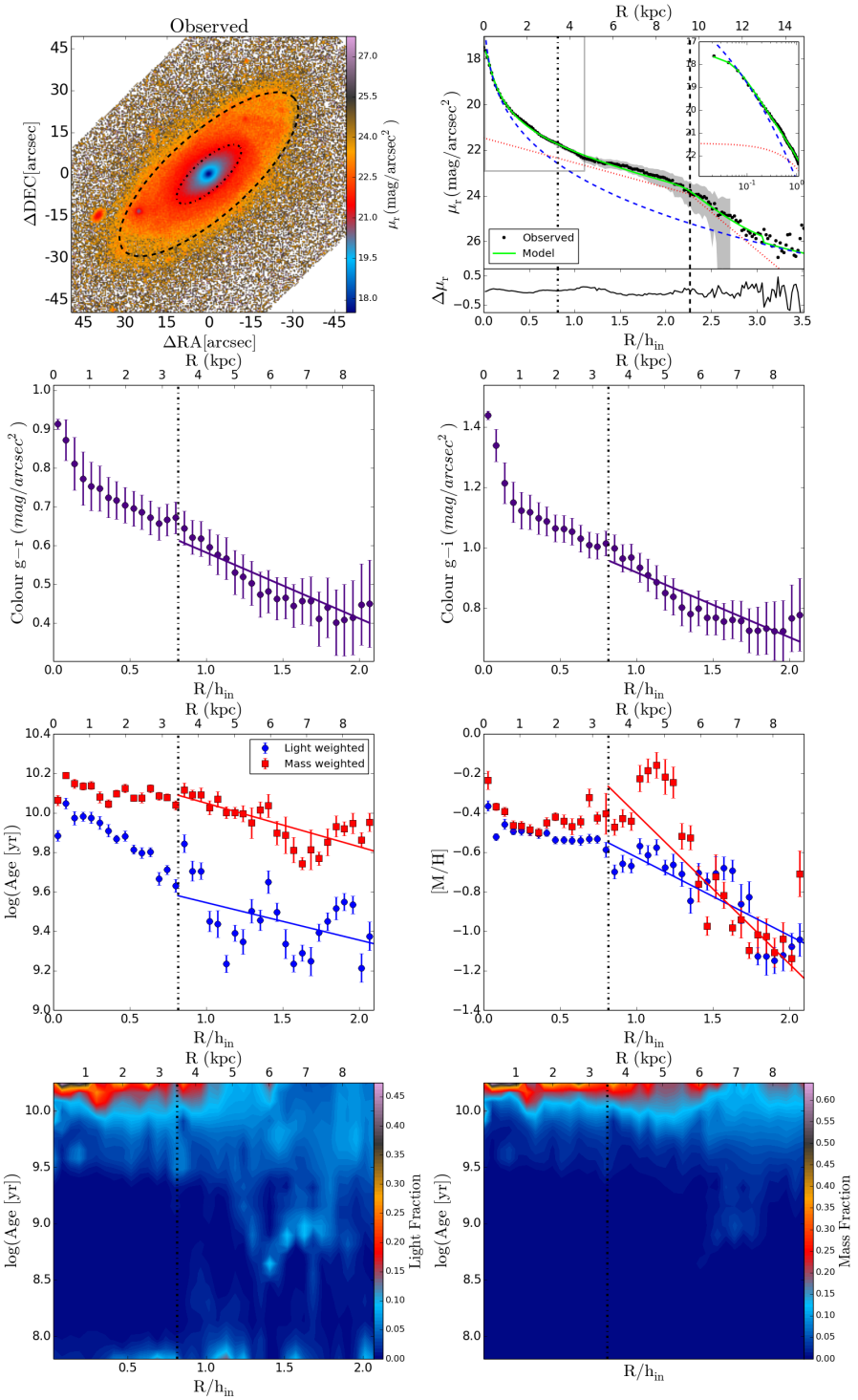

Figure B.41: NGC5971.

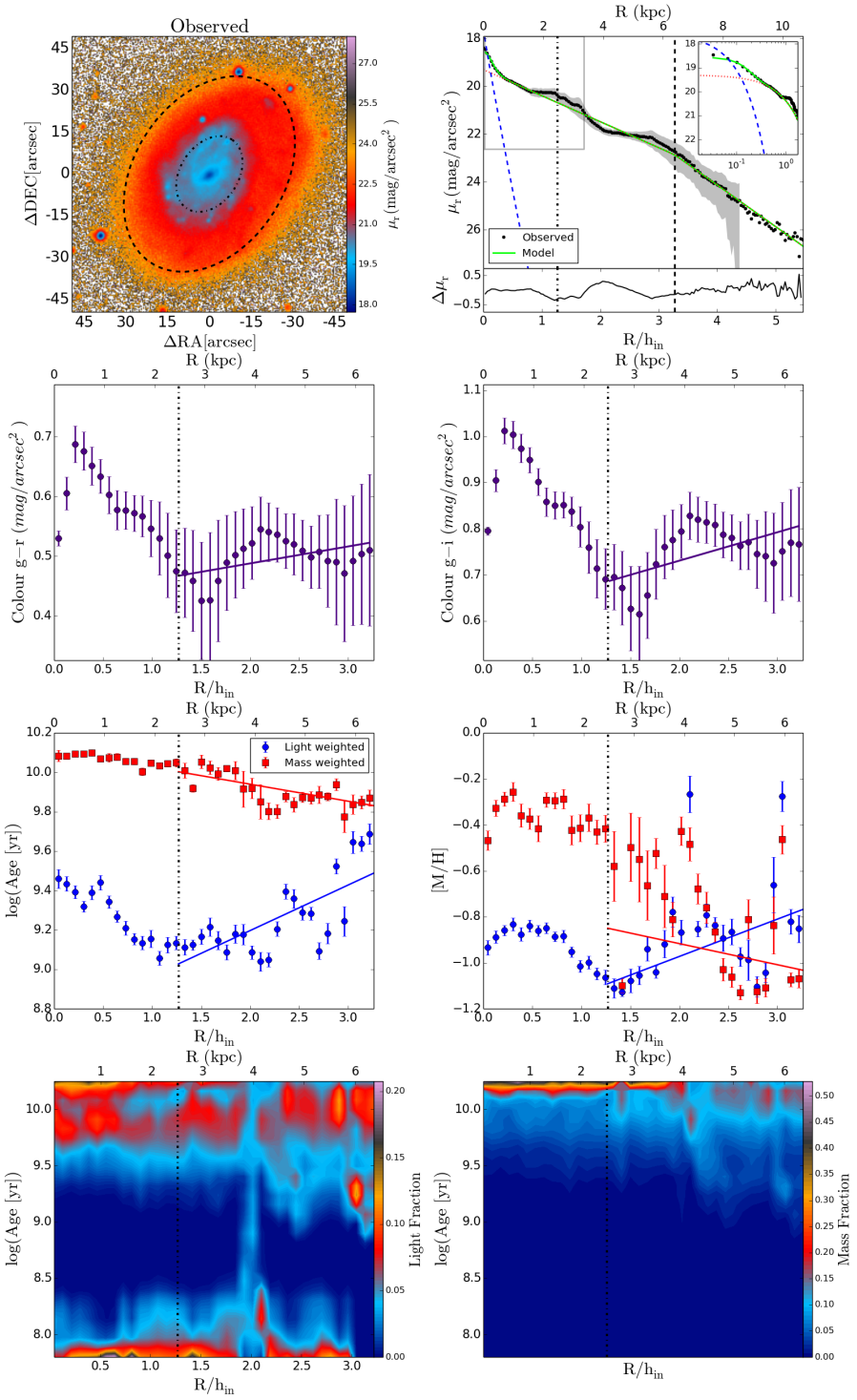

Figure B.42: NGC6155.

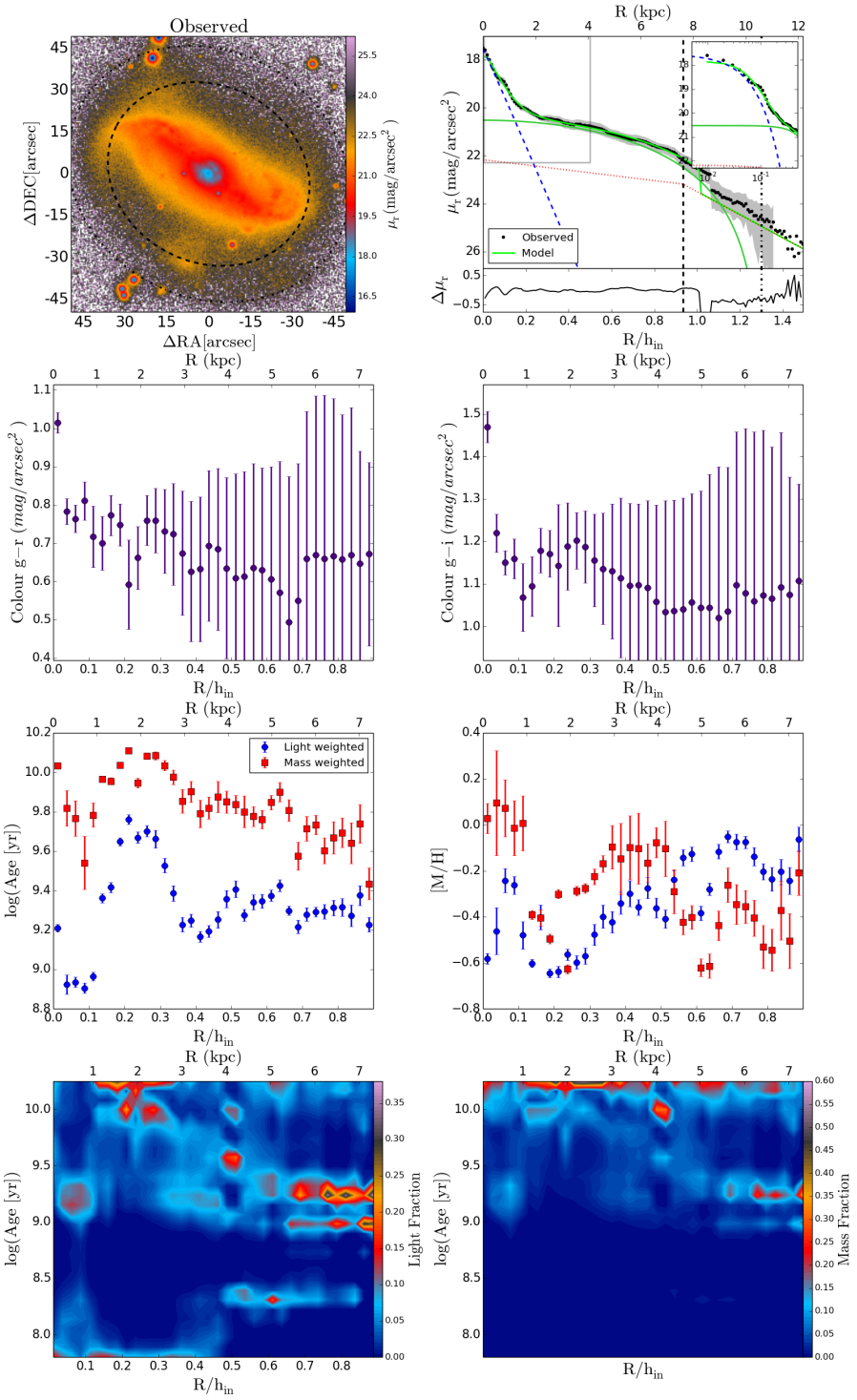

Figure B.43: NGC6186.

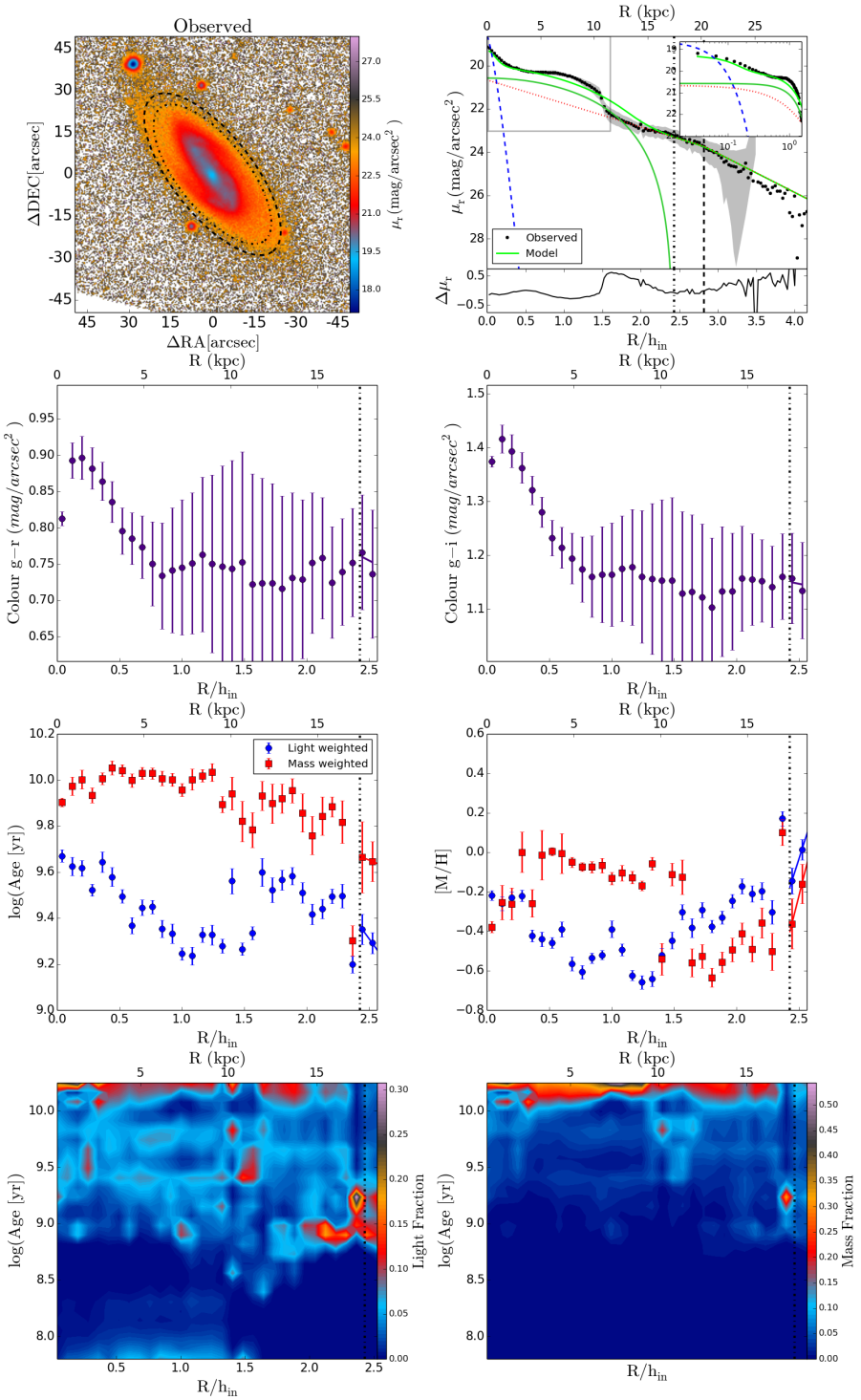

Figure B.44: NGC6394.

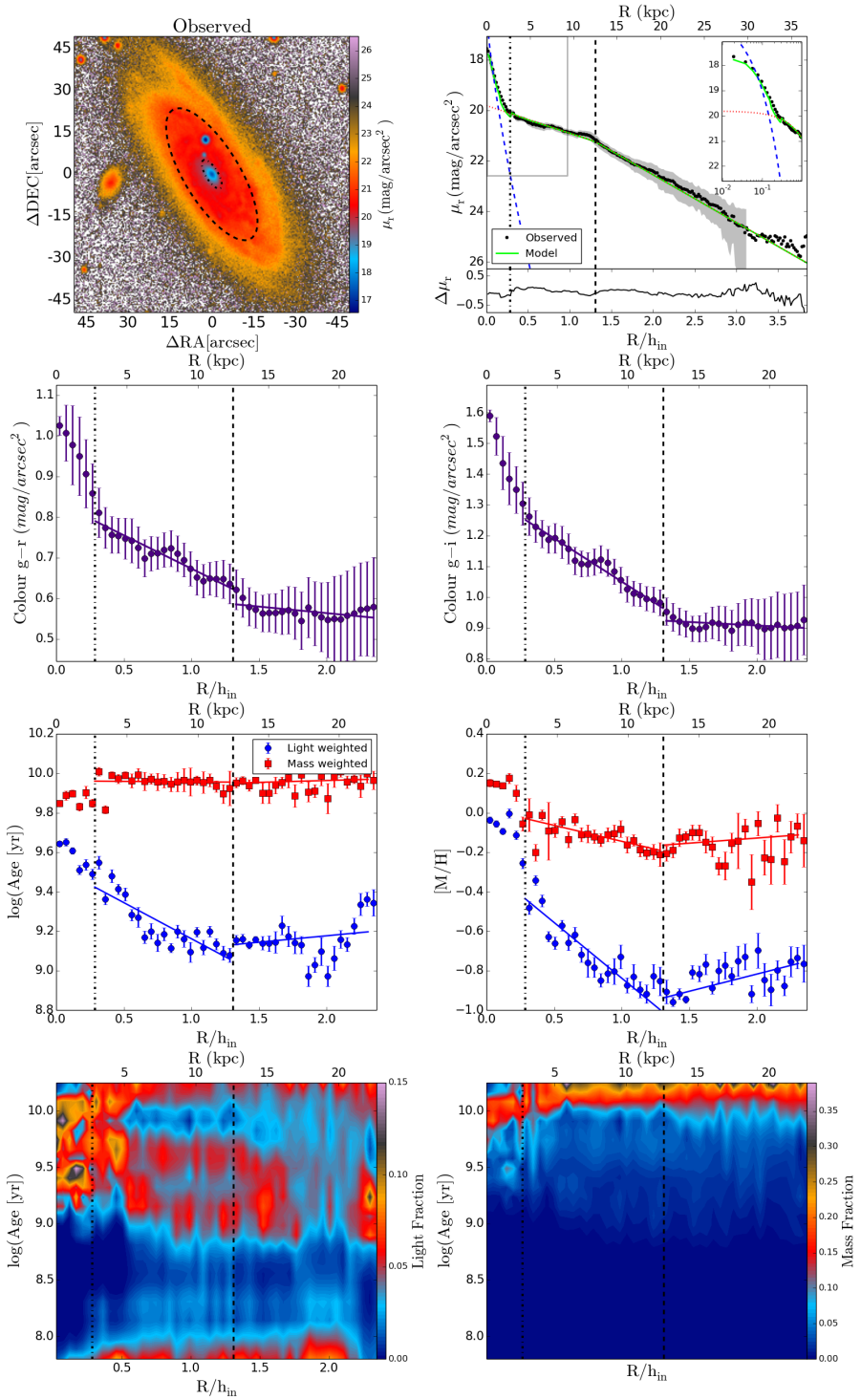

Figure B.45: NGC6478.

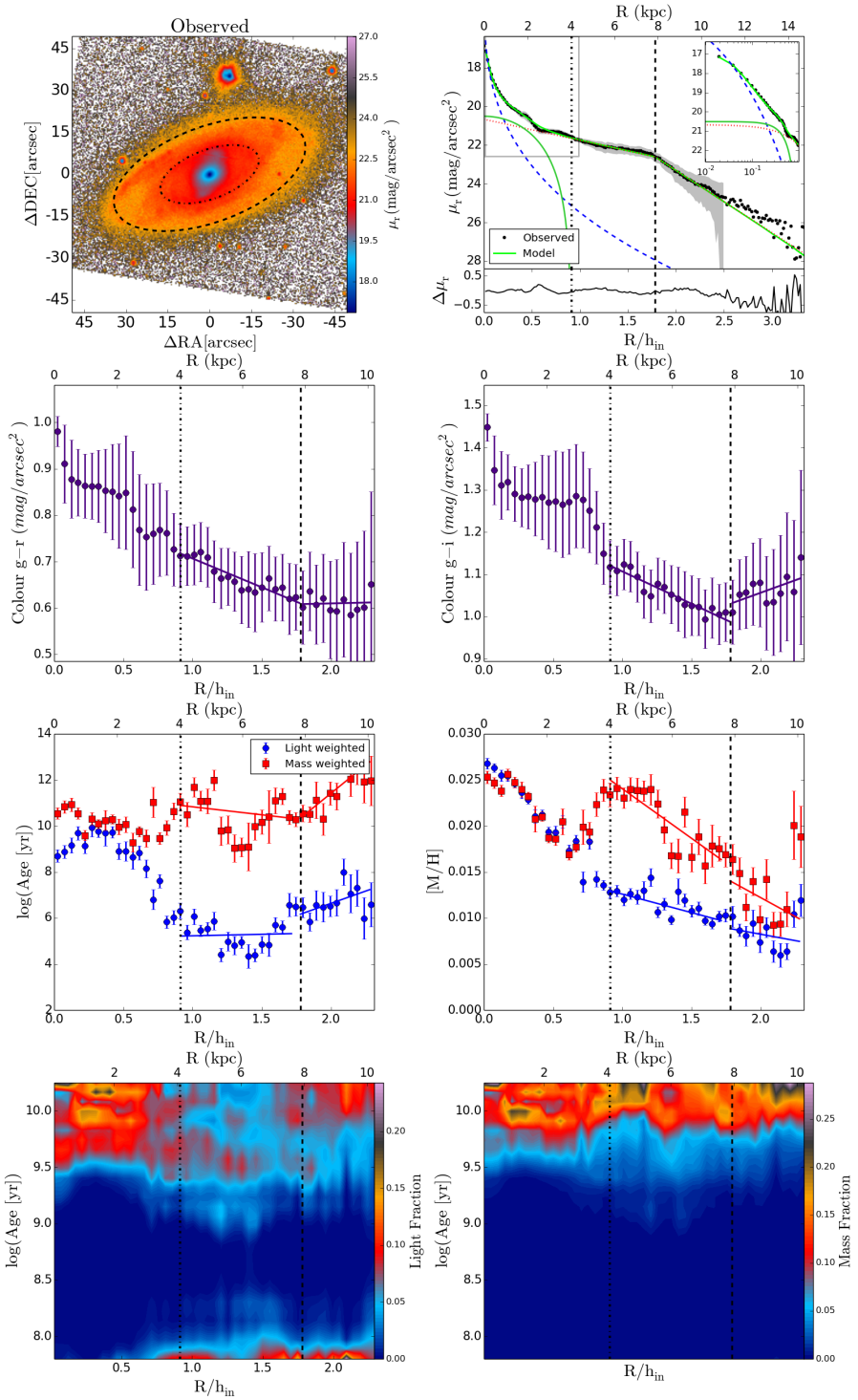

Figure B.46: NGC6497.

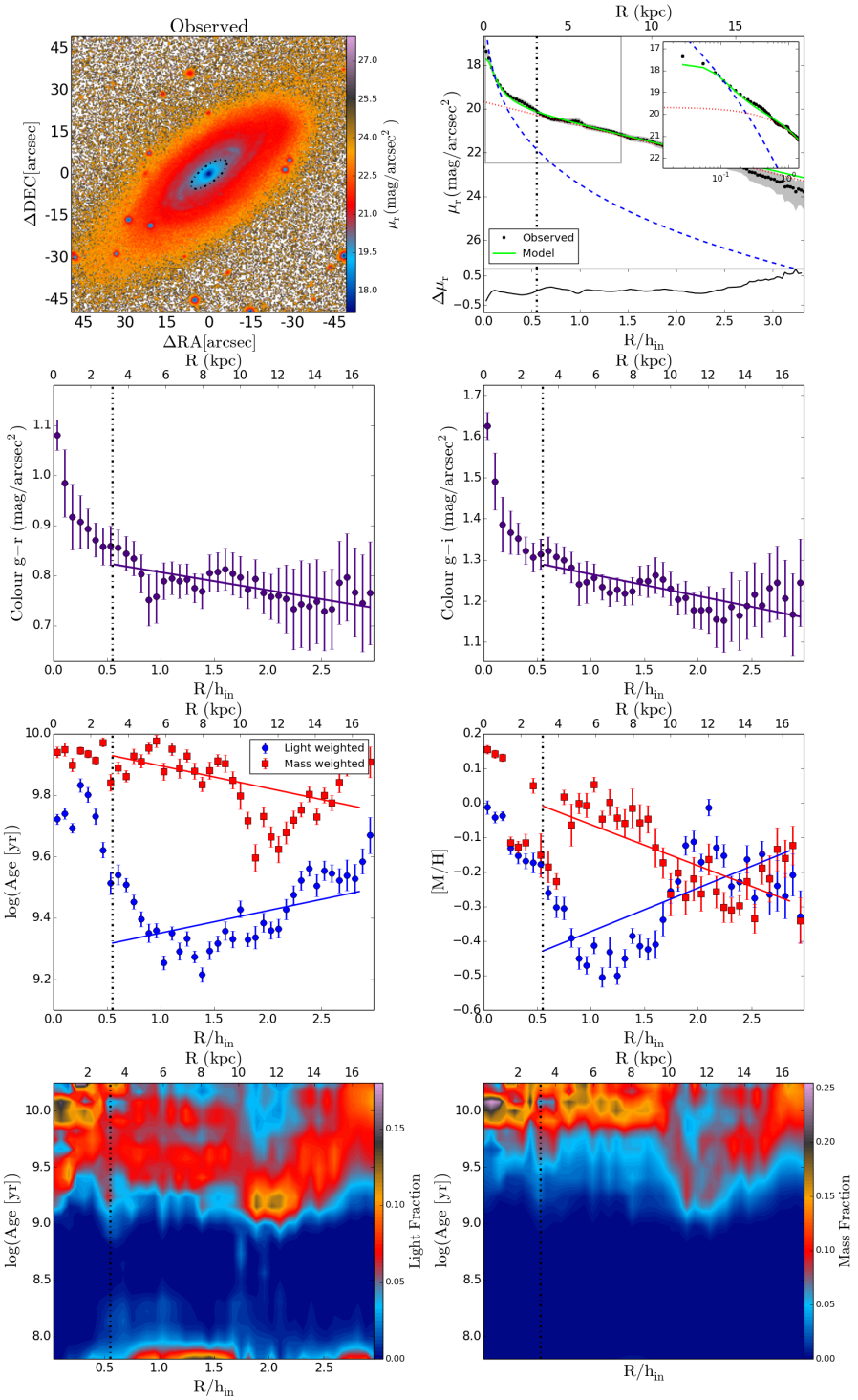

Figure B.47: NGC6978.

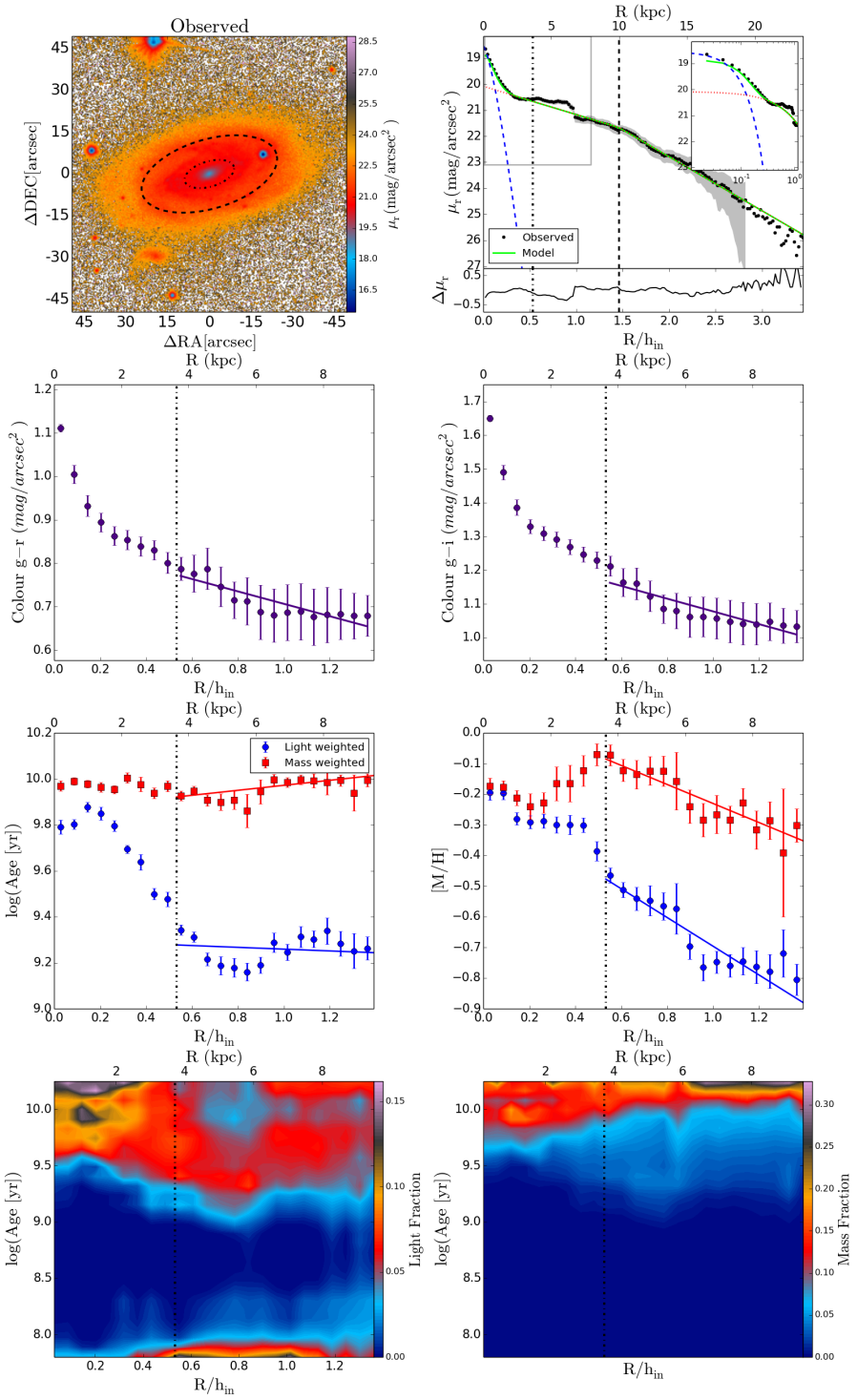

Figure B.48: NGC7047.

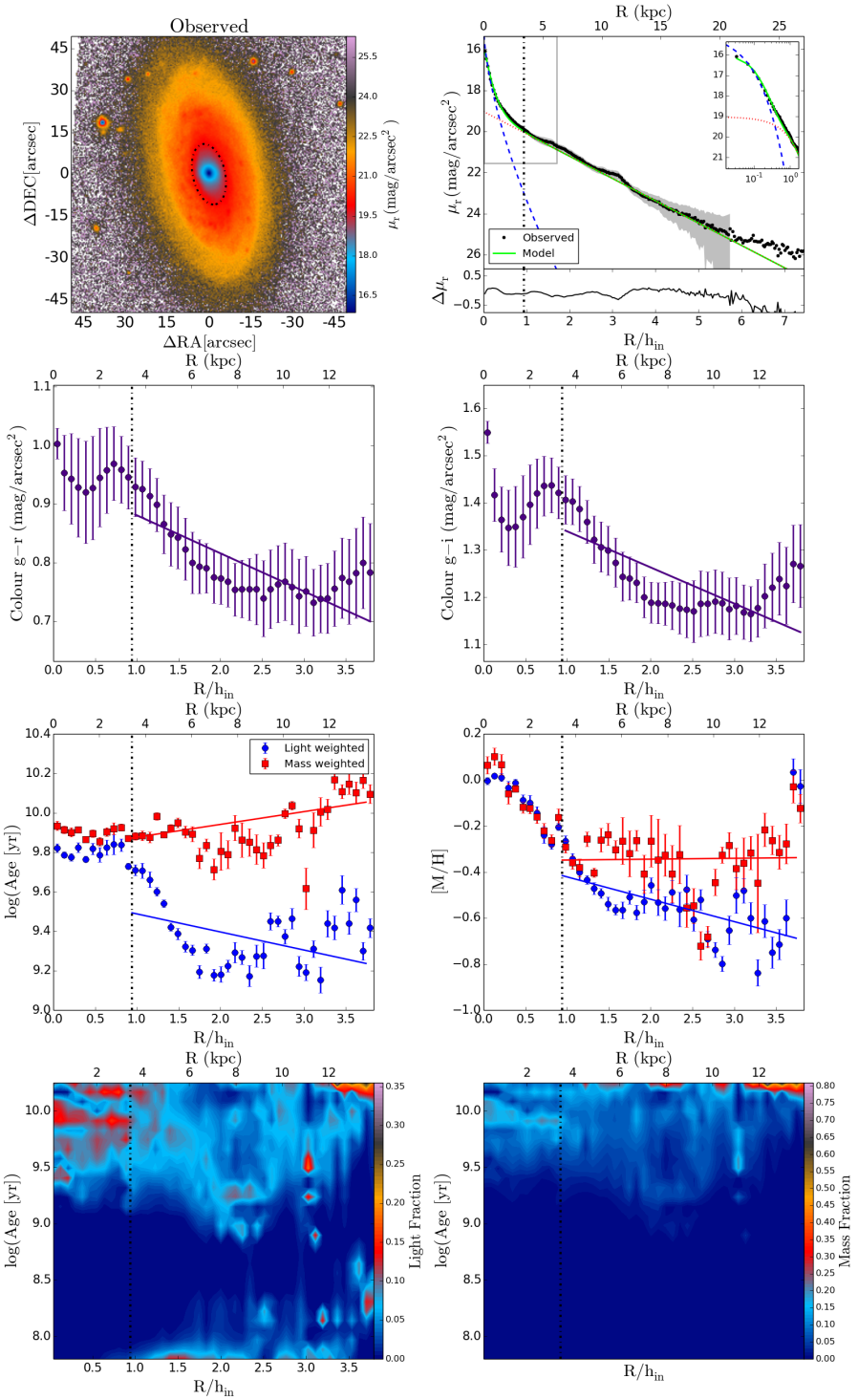

Figure B.49: NGC7311.

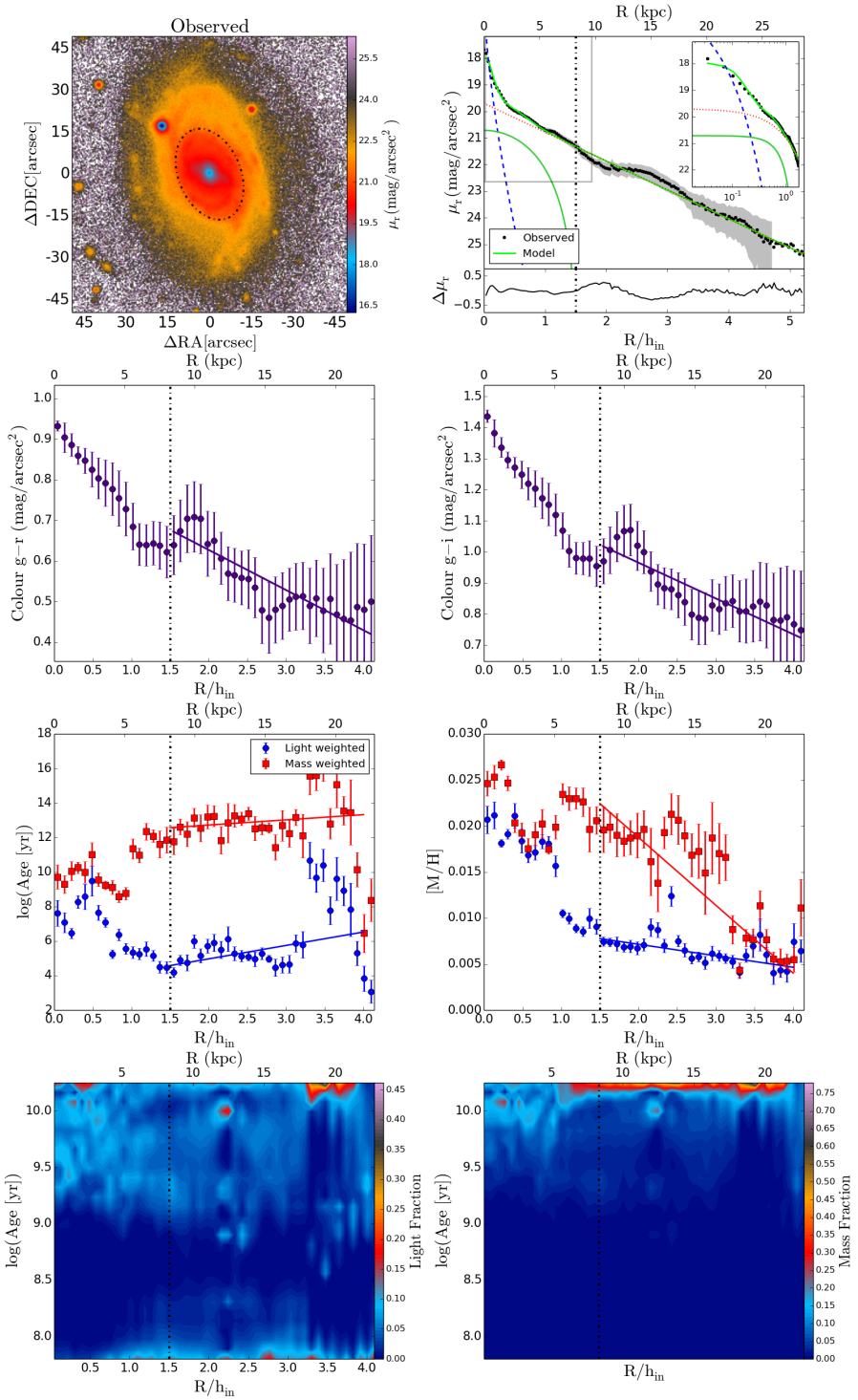

Figure B.50: NGC7321.

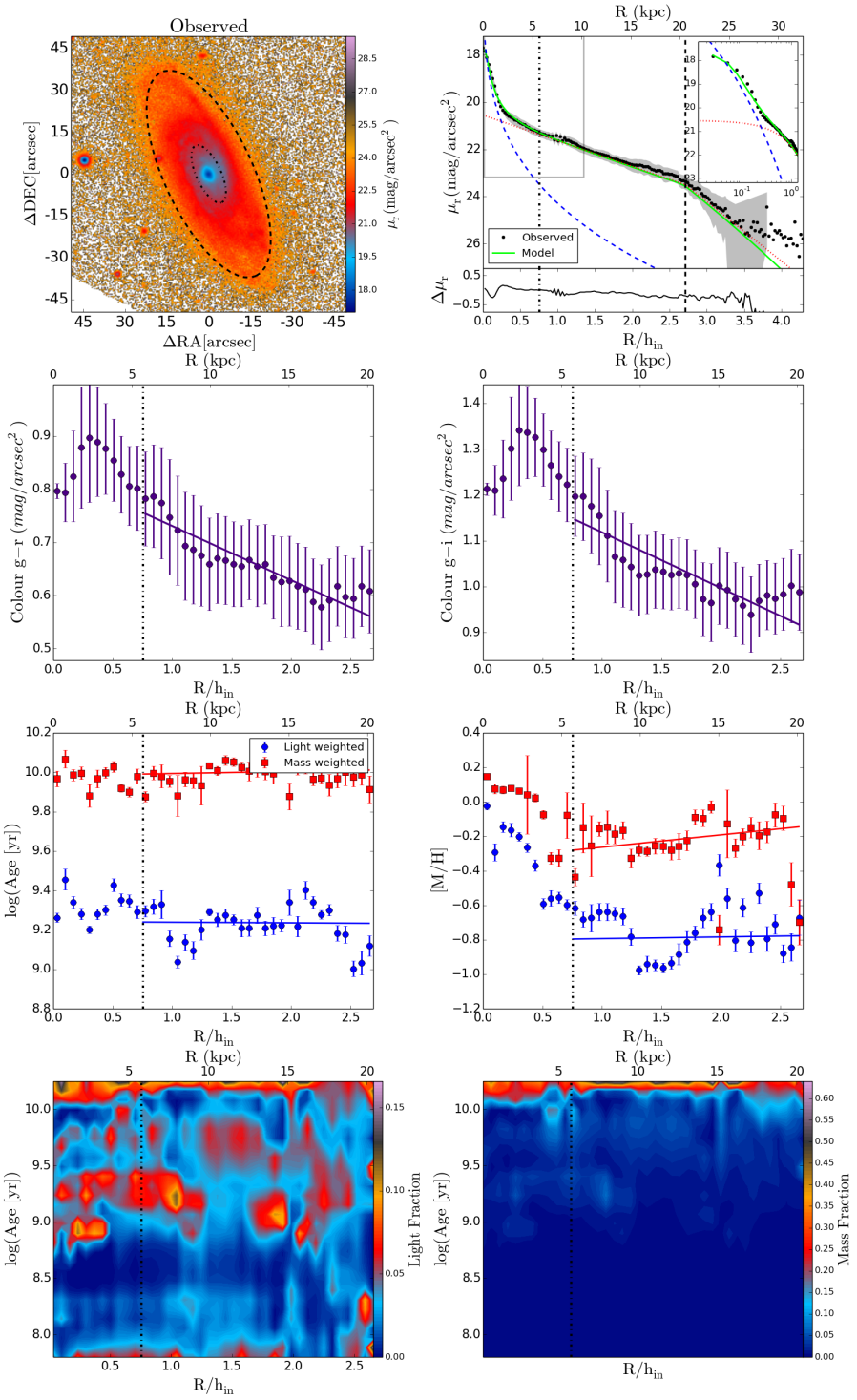

Figure B.51: NGC7466.

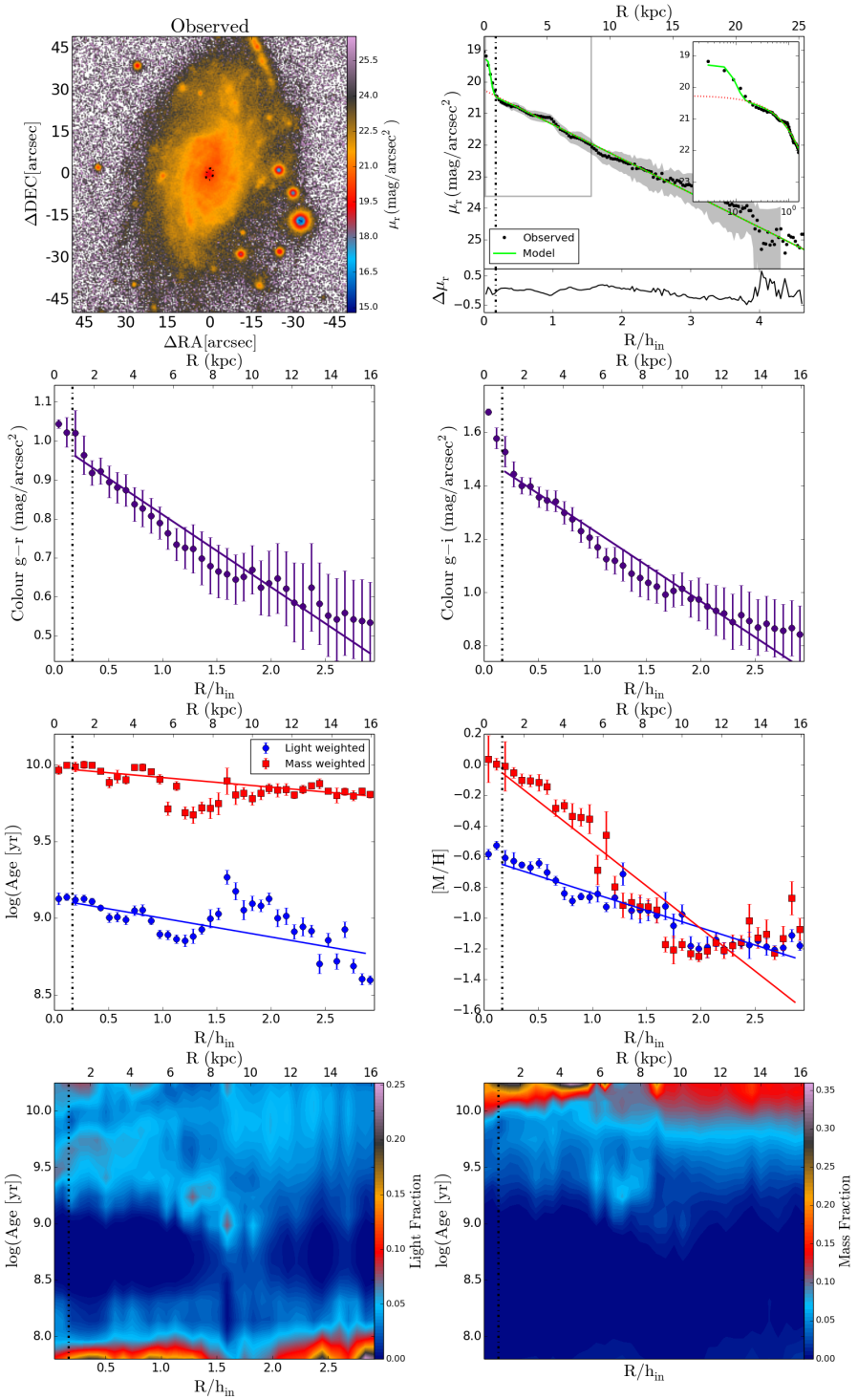

Figure B.52: NGC7489.

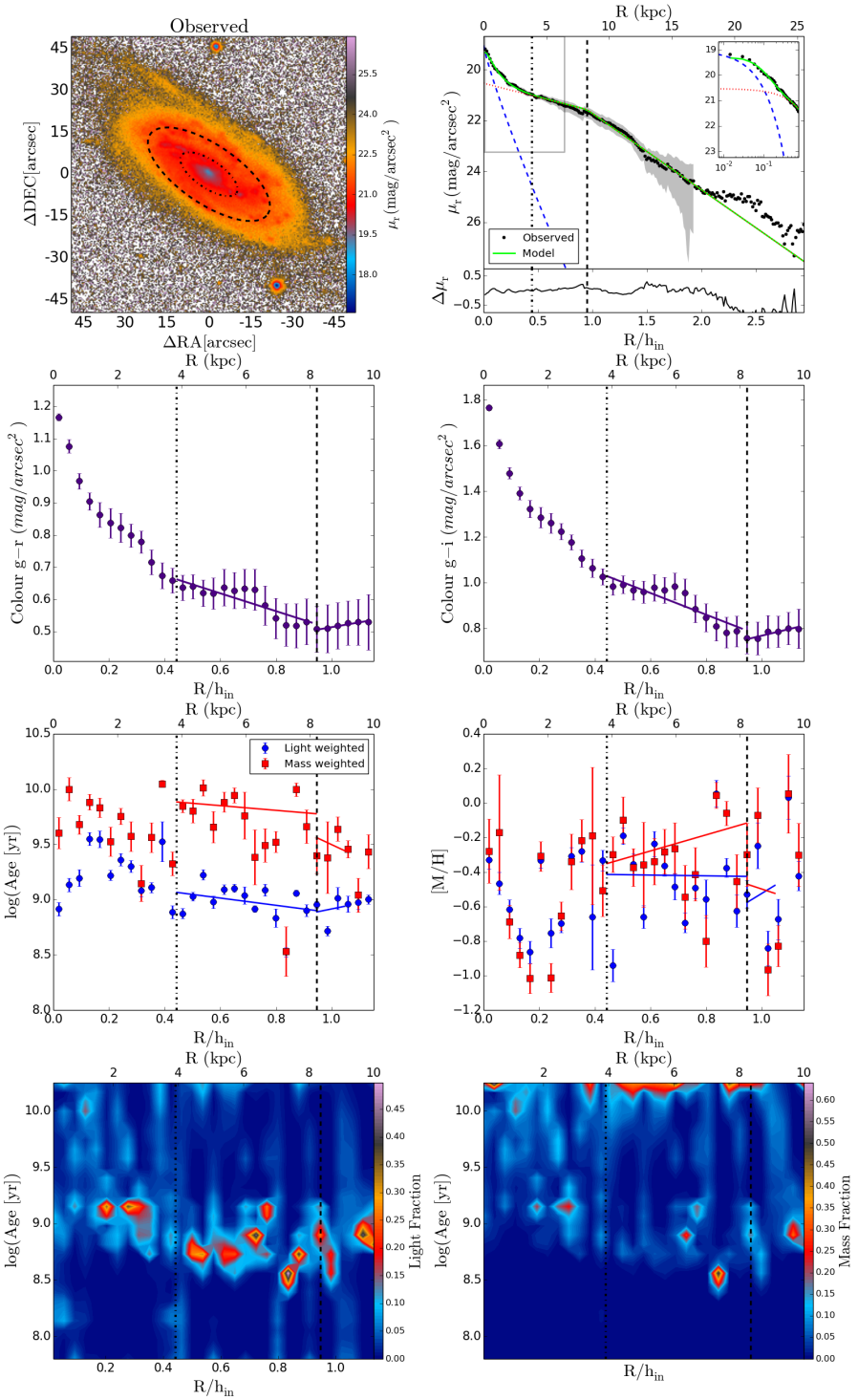

Figure B.53: NGC7536.

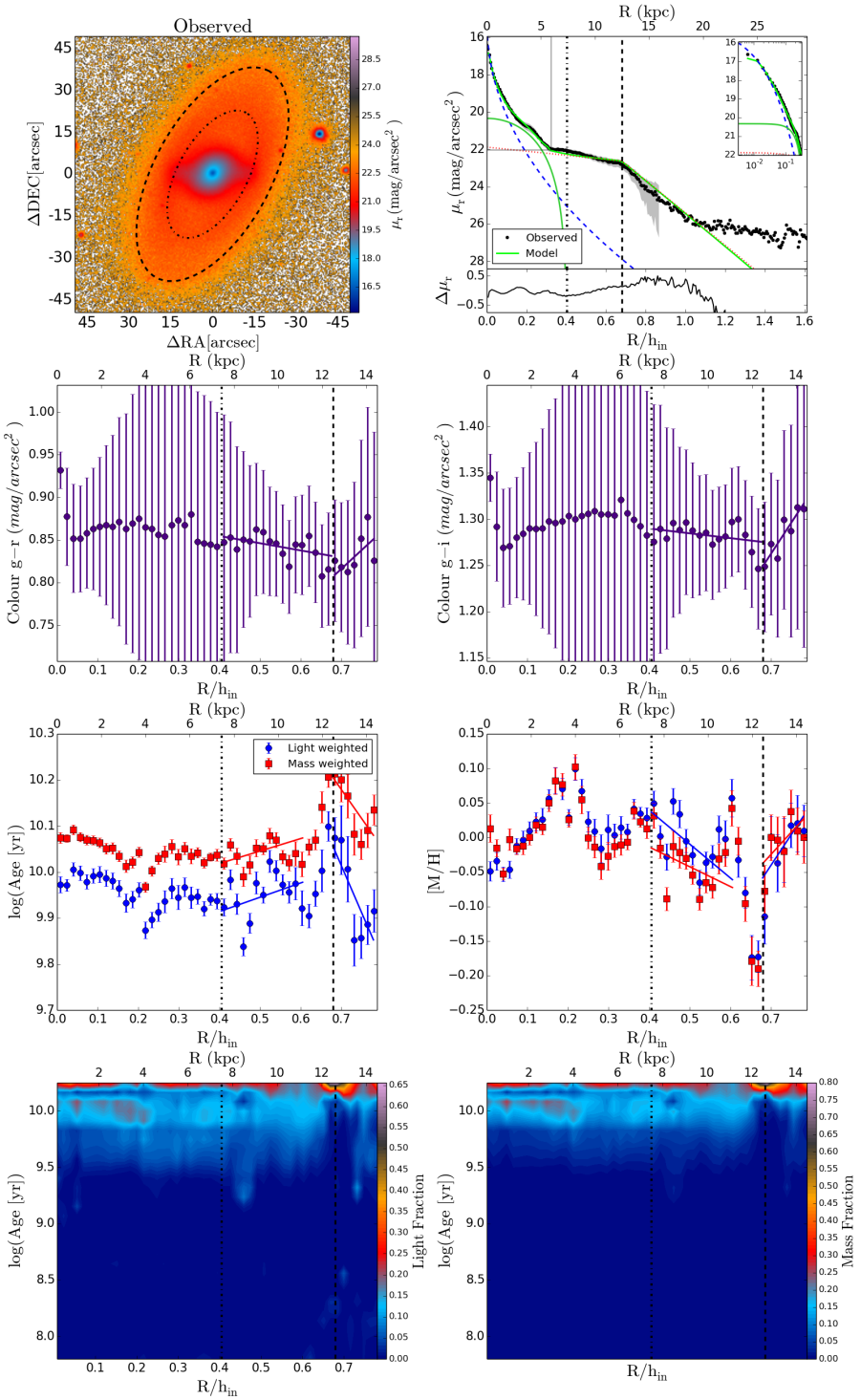

Figure B.54: NGC7563.

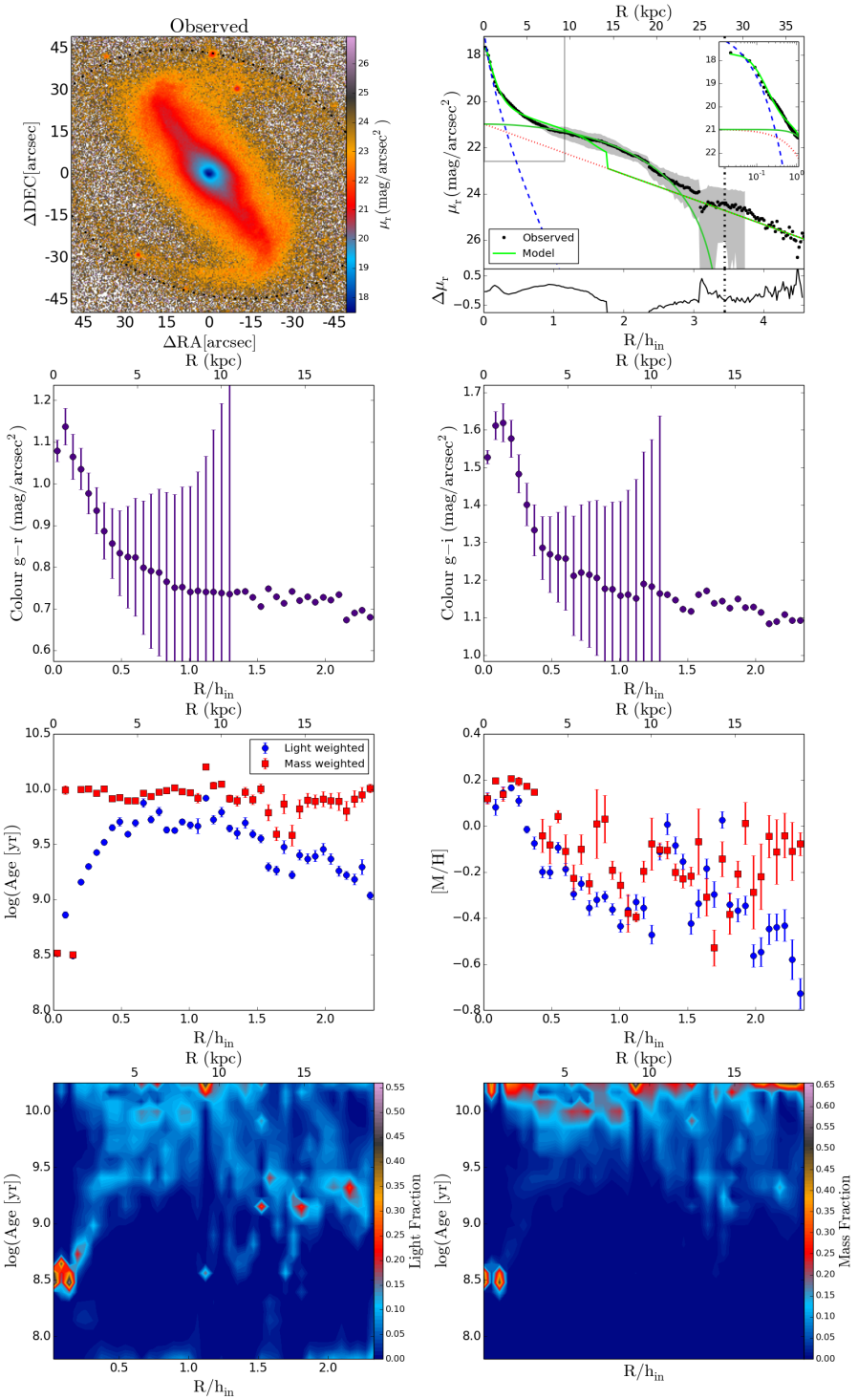

Figure B.55: NGC7738.

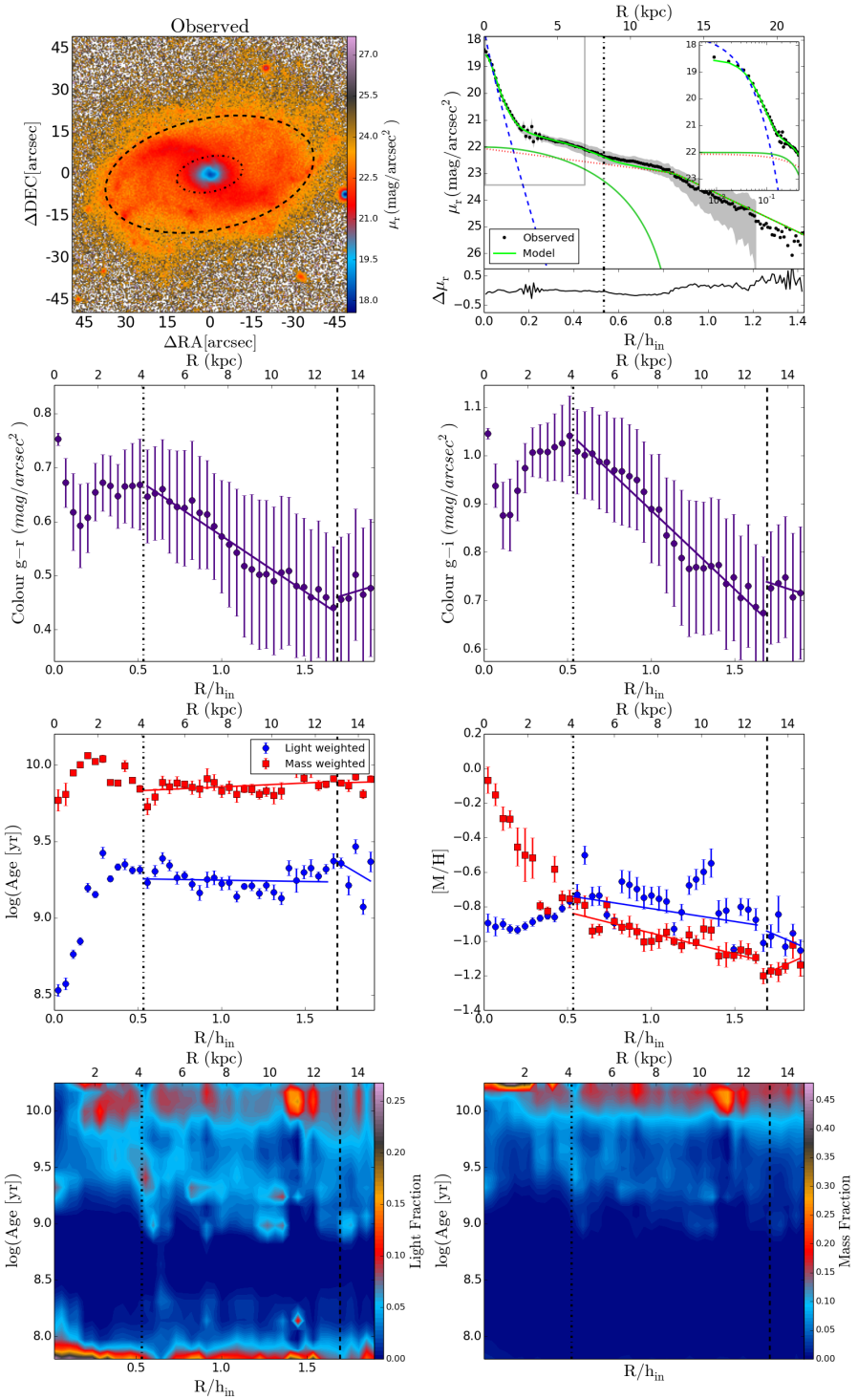

Figure B.56: NGC7819.

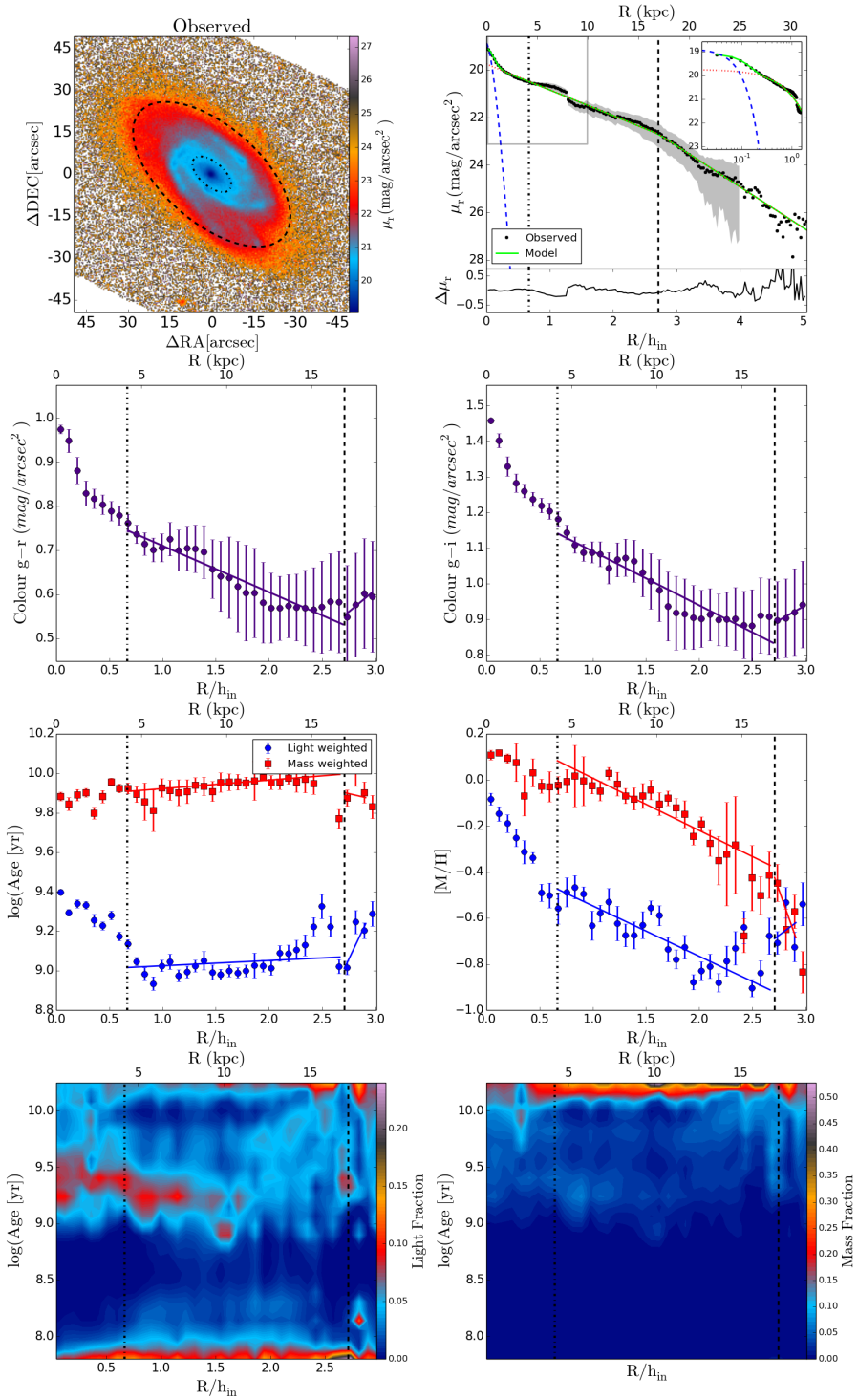

Figure B.57: UGC00005.

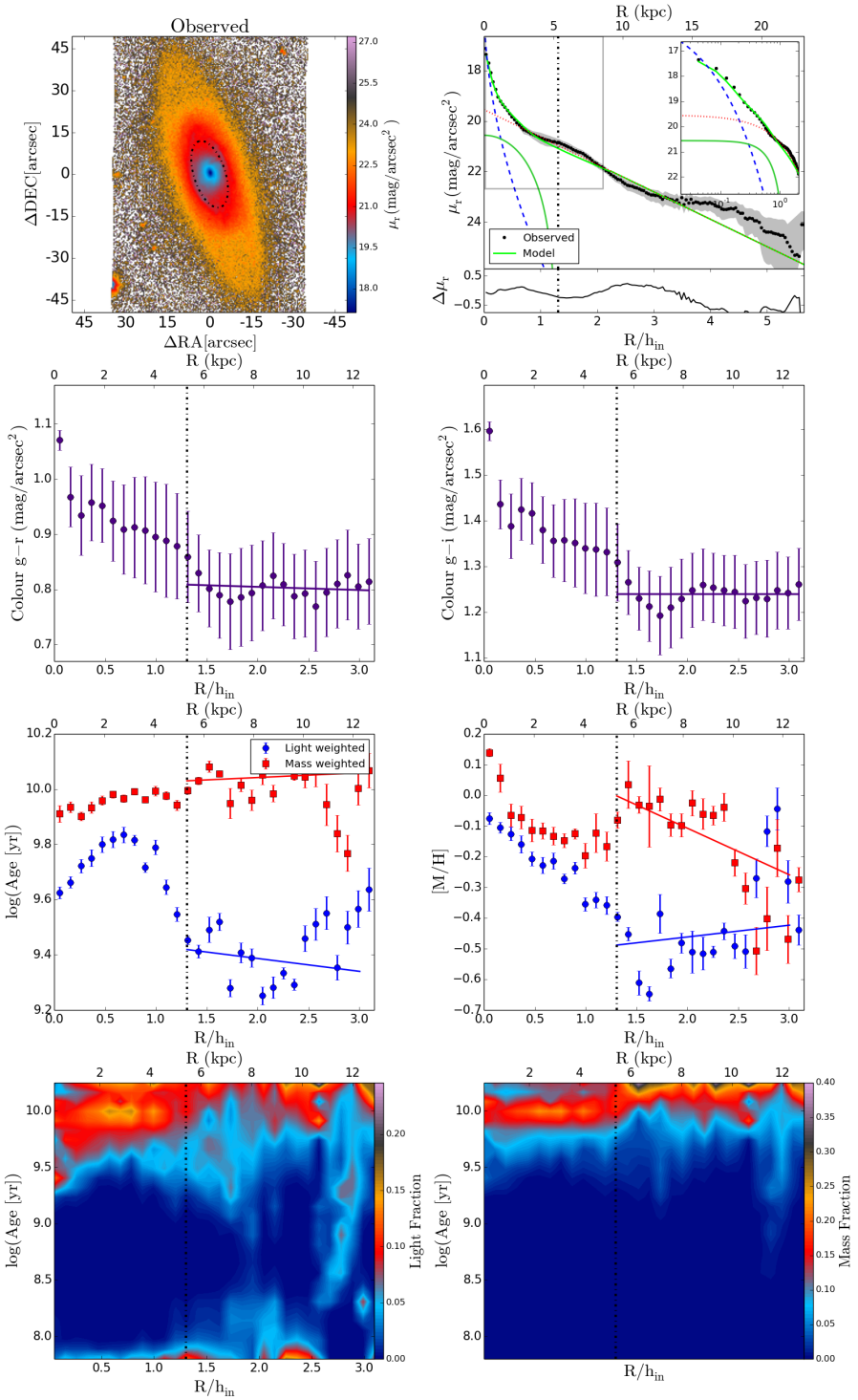

Figure B.58: UGC00036.

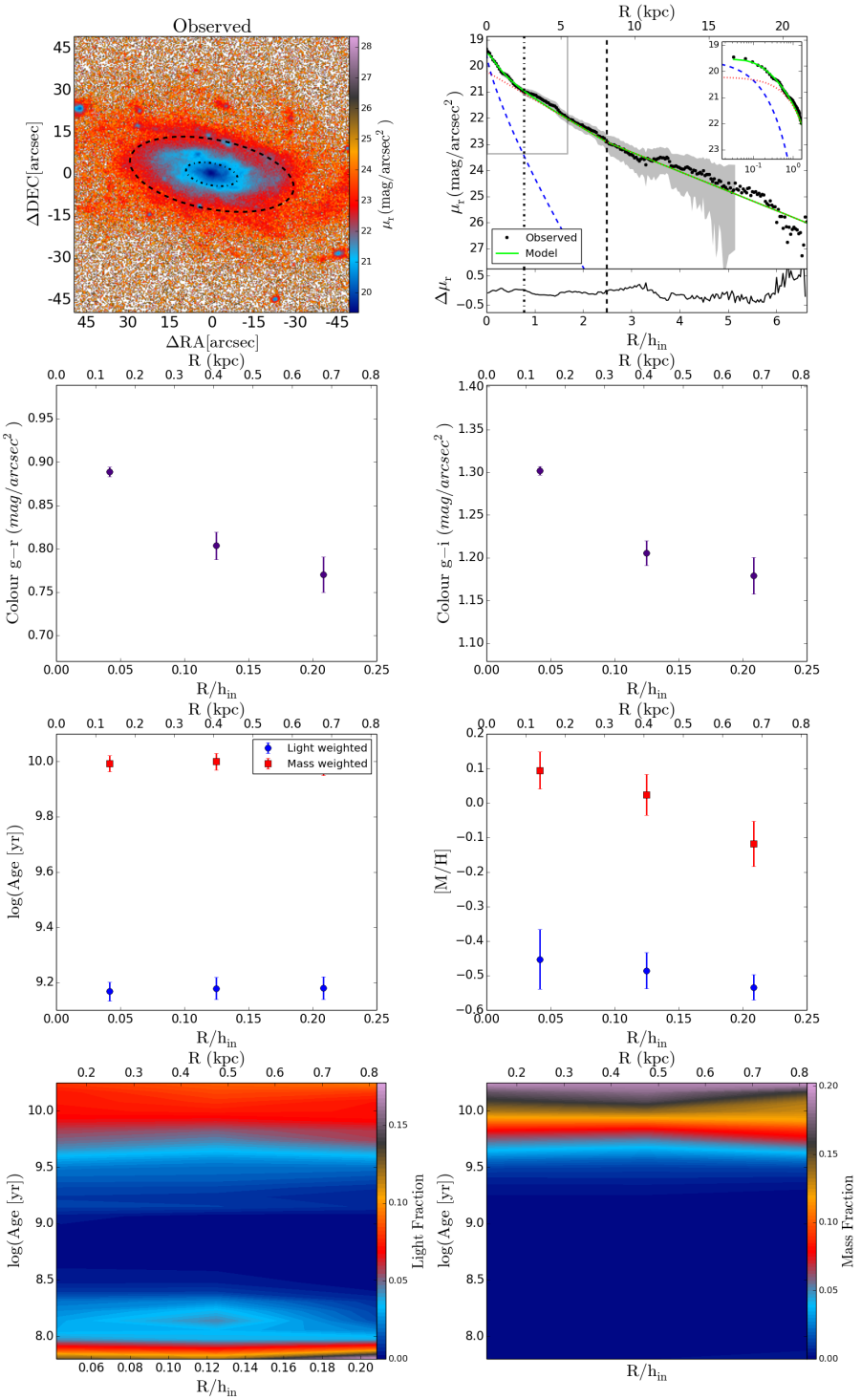

Figure B.59: UGC00139.

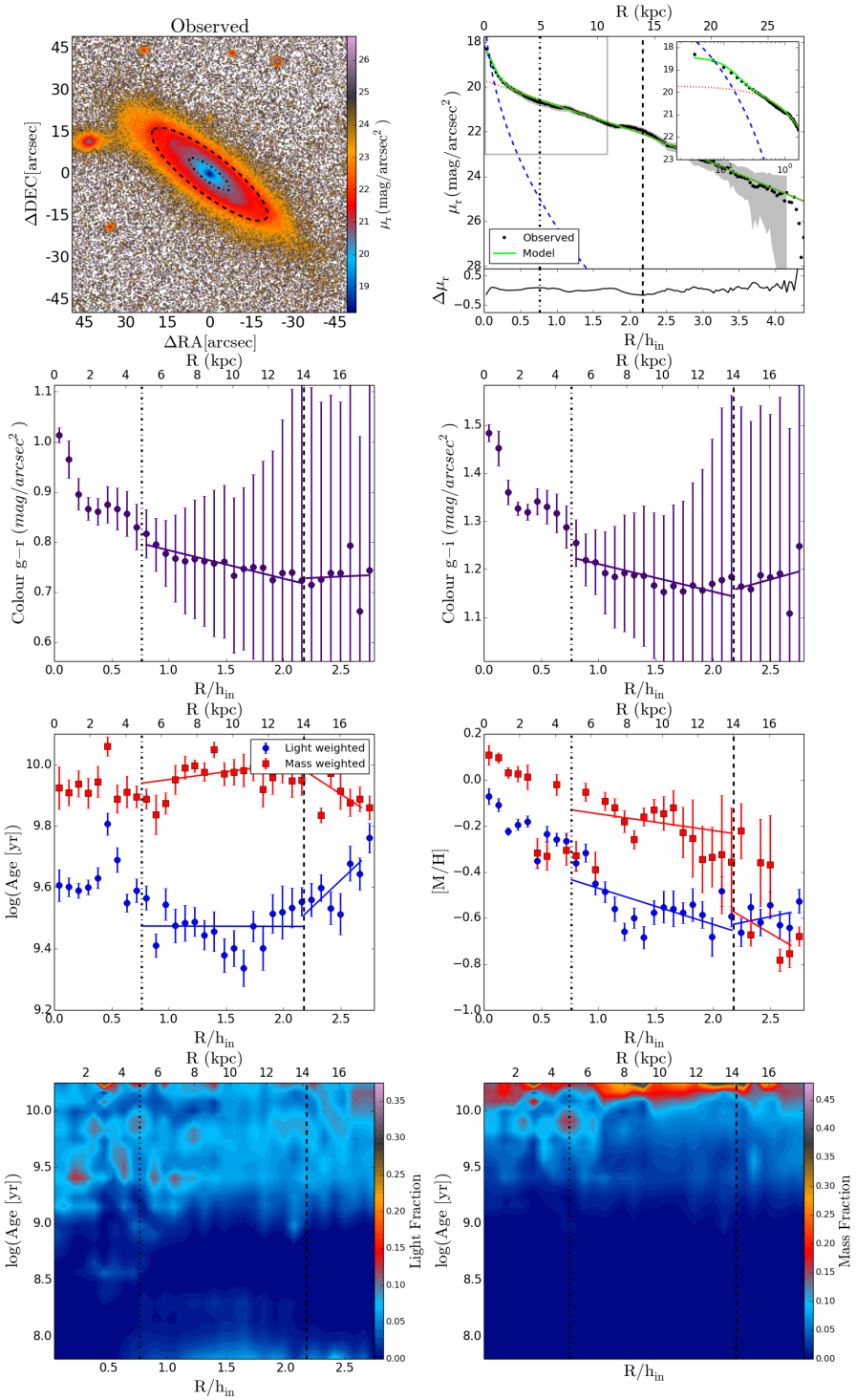

Figure B.60: UGC01368.

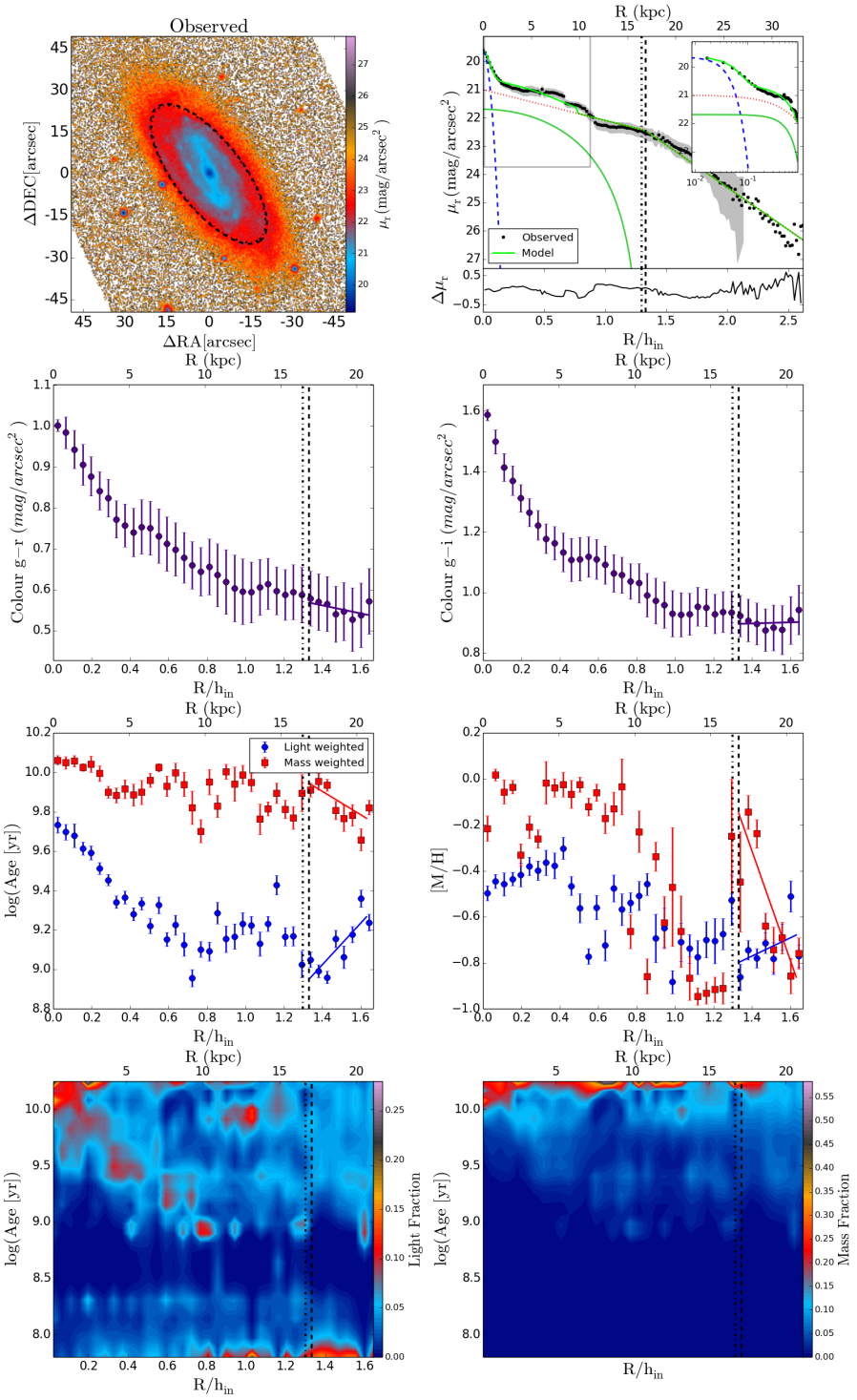

Figure B.61: UGC01659.

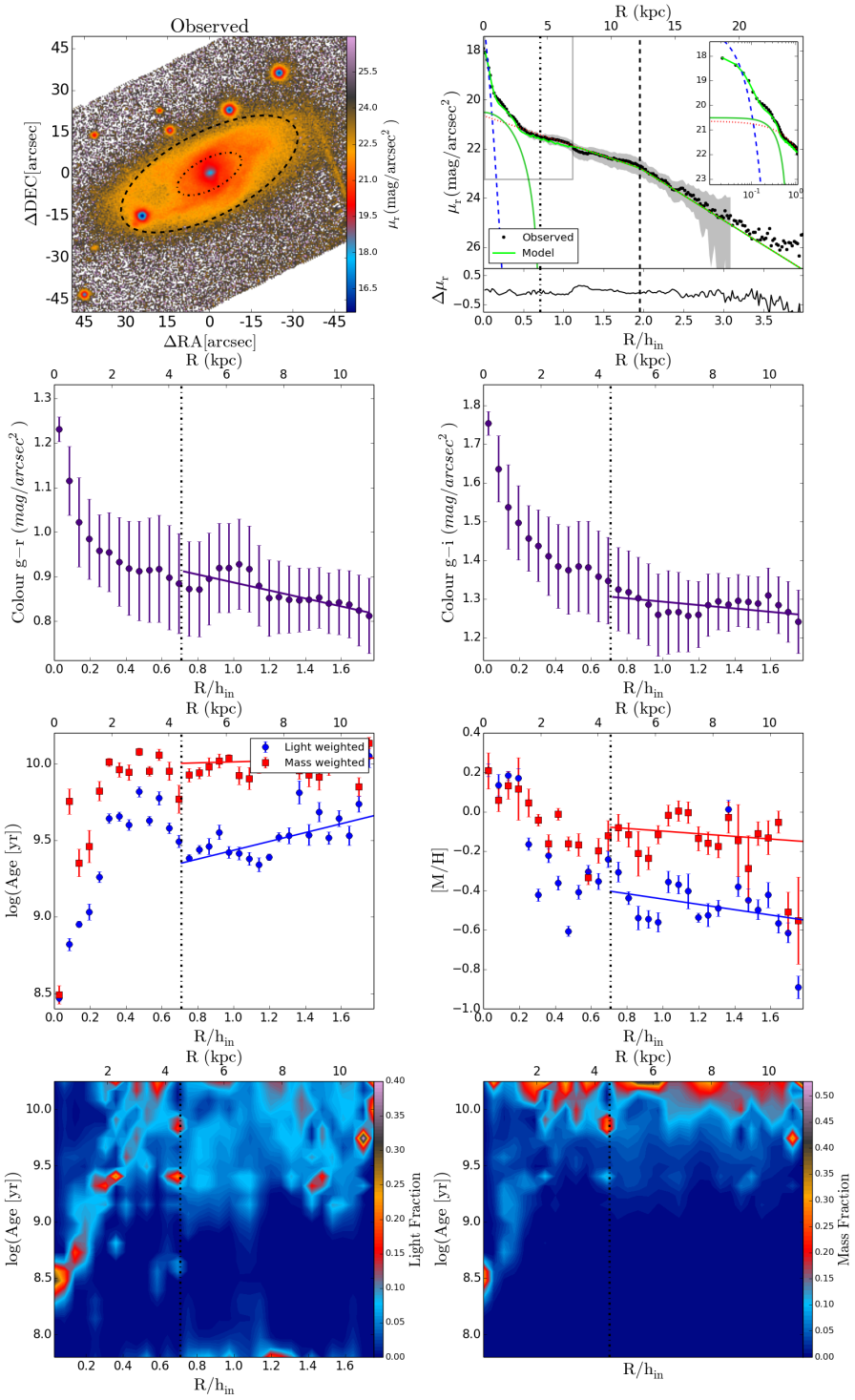

Figure B.62: UGC01918.

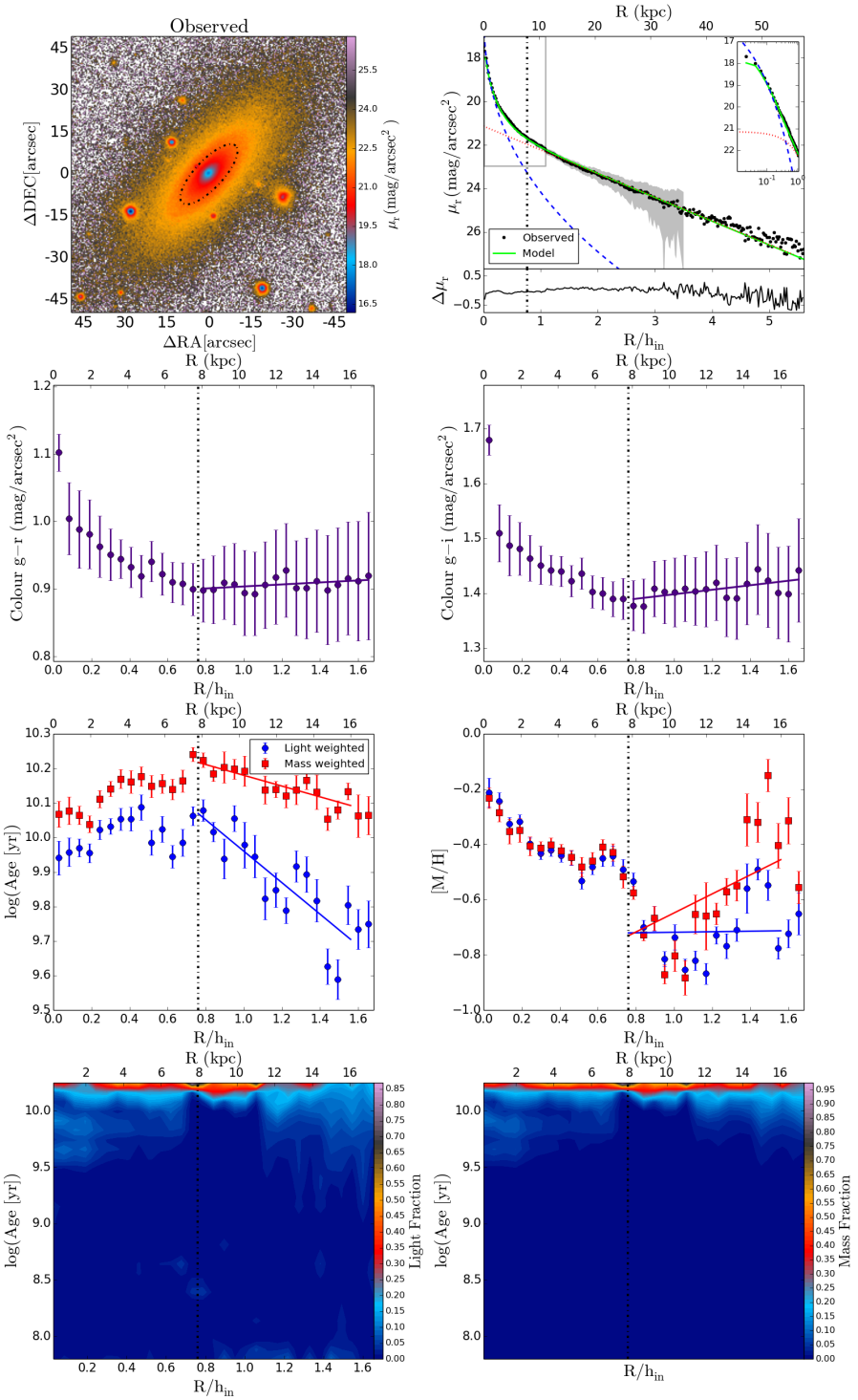

Figure B.63: UGC02099.

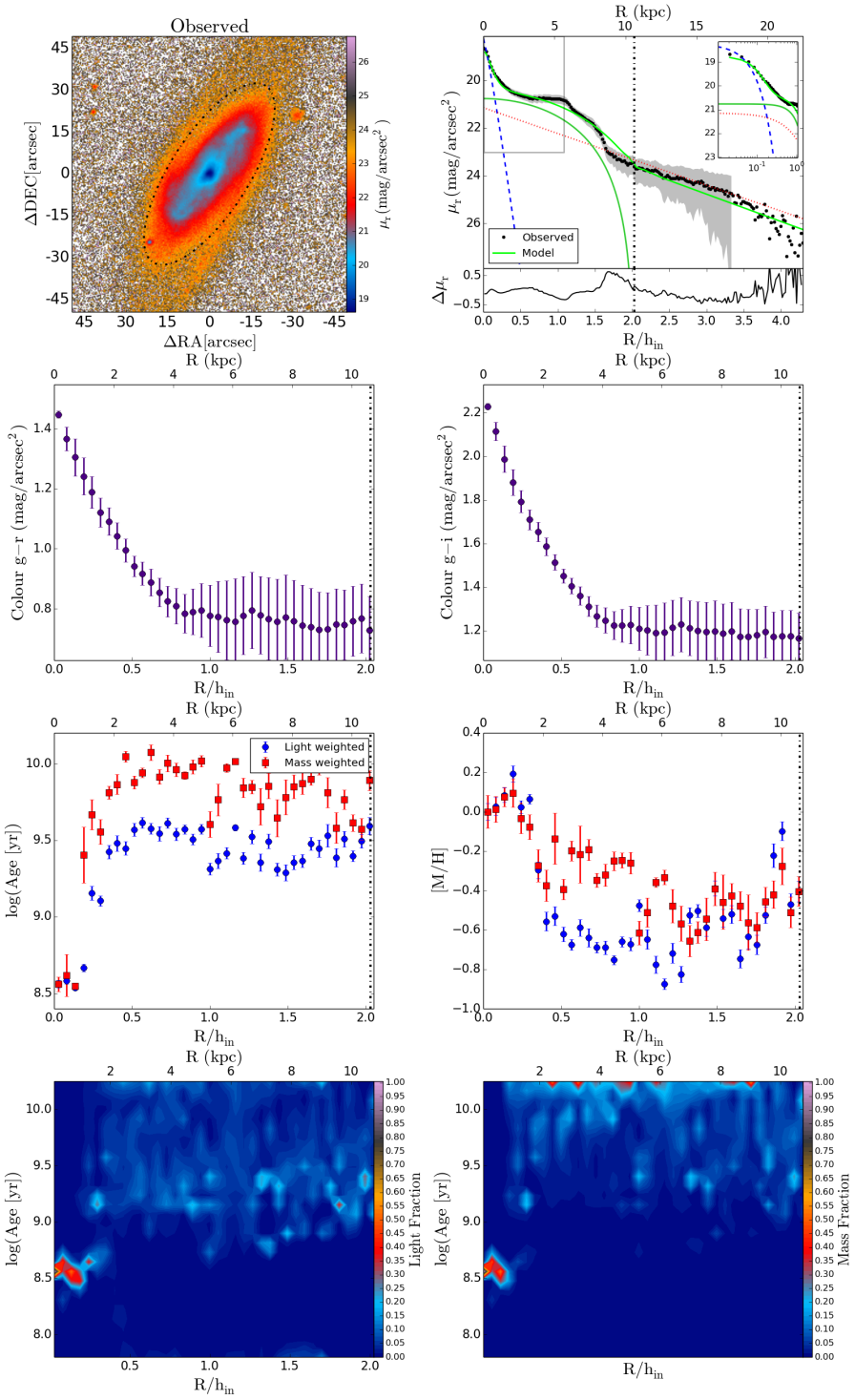

Figure B.64: UGC02403.

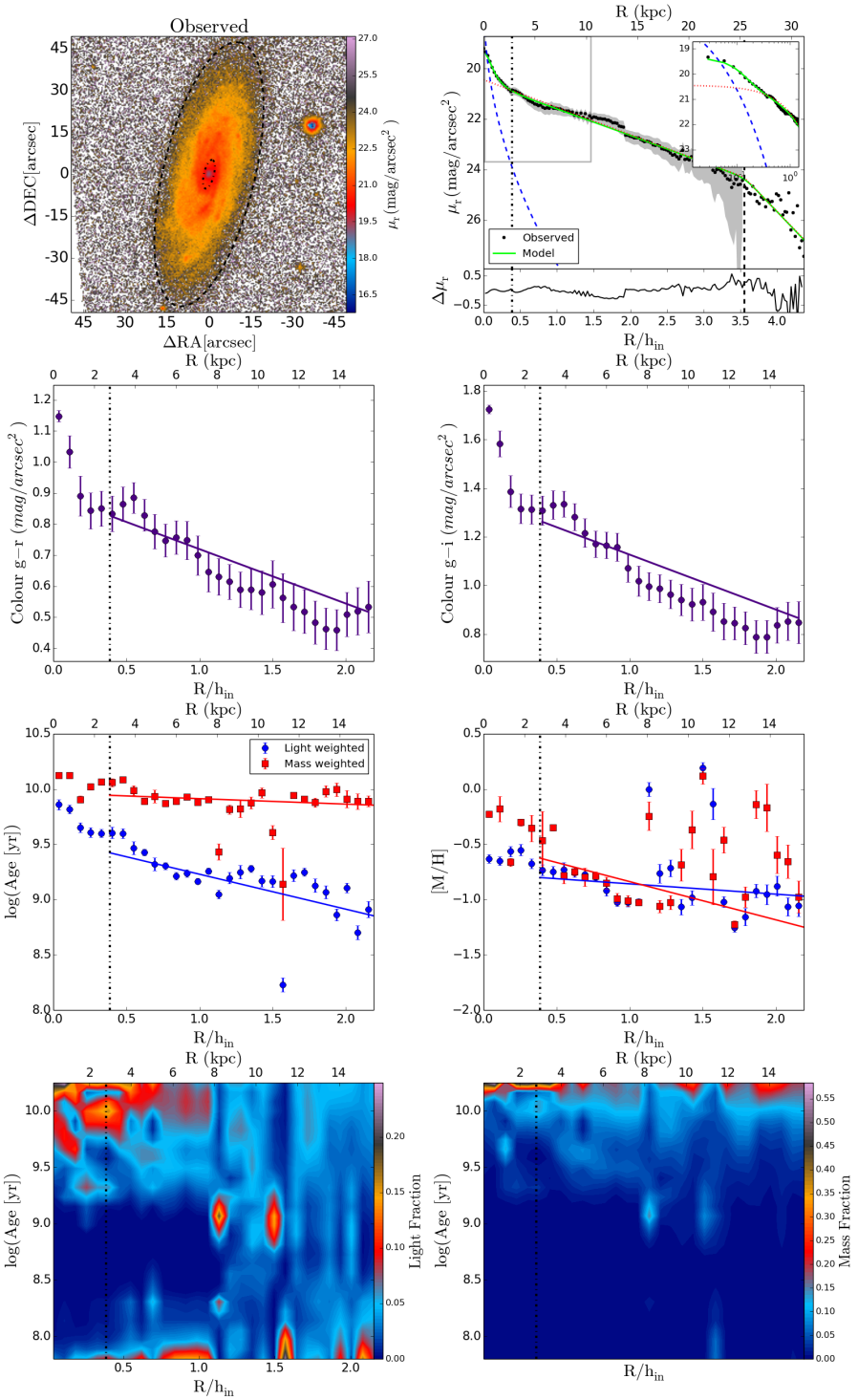

Figure B.65: UGC02405.

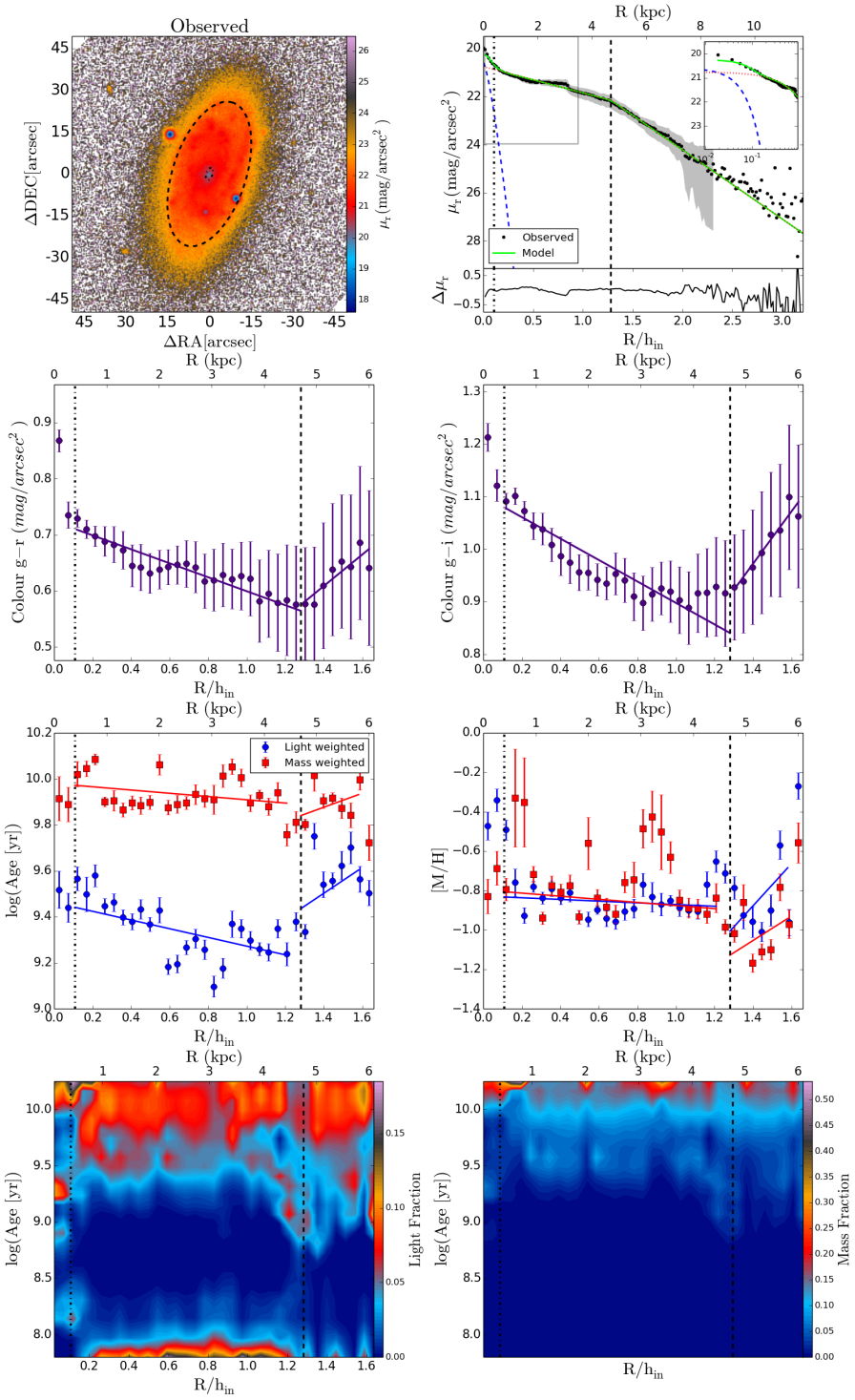

Figure B.66: UGC02443.

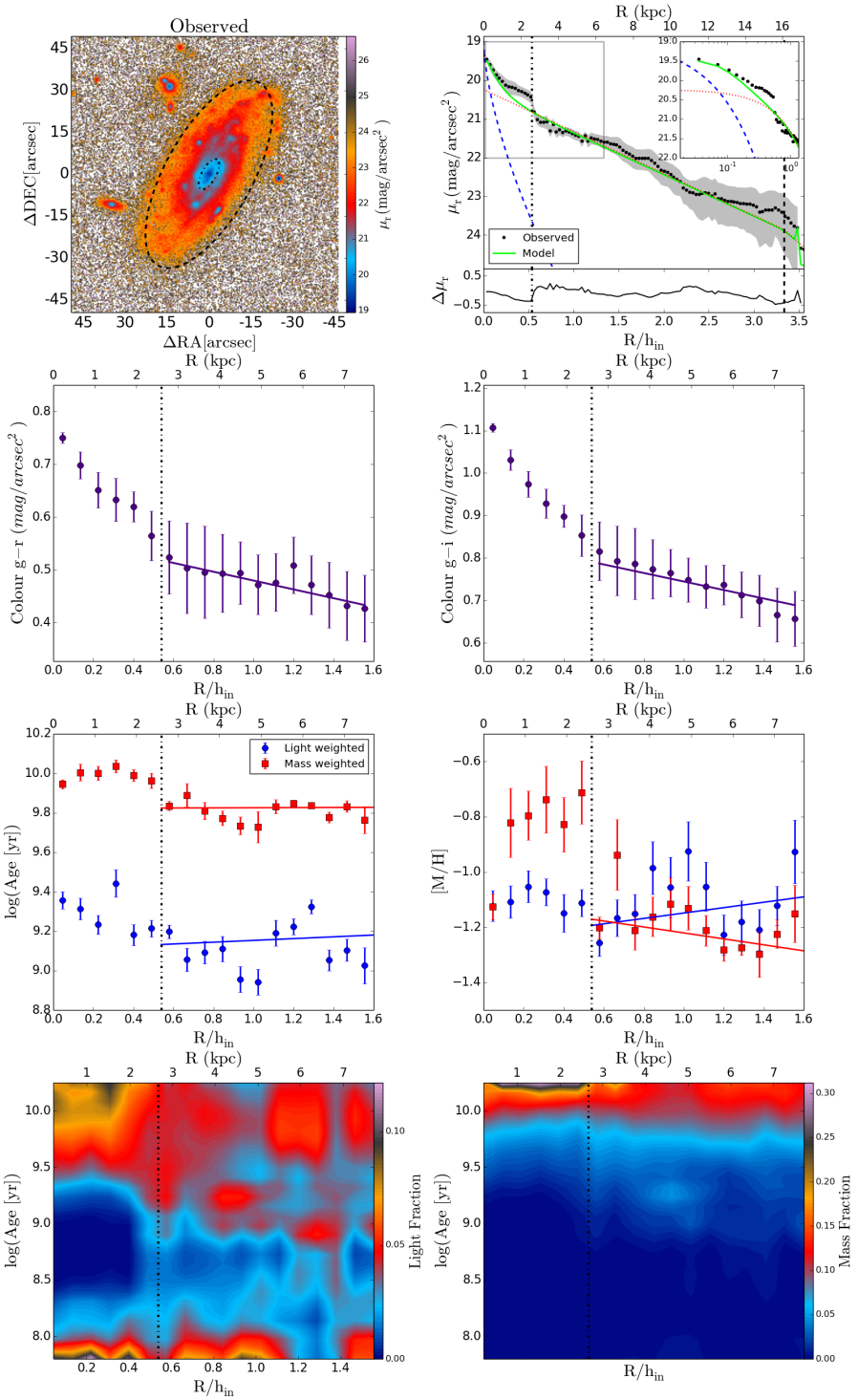

Figure B.67: UGC02690.

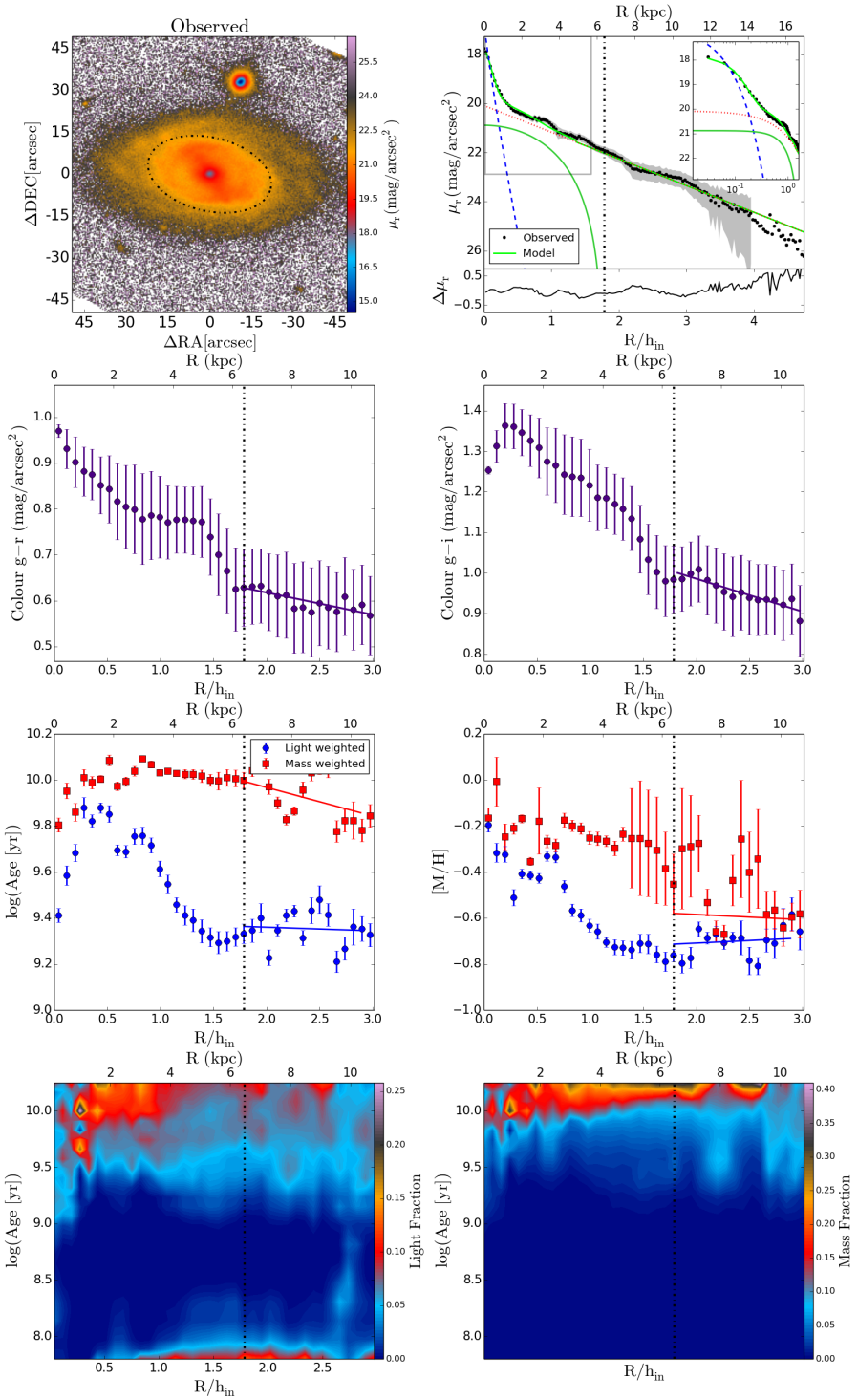

Figure B.68: UGC03253.

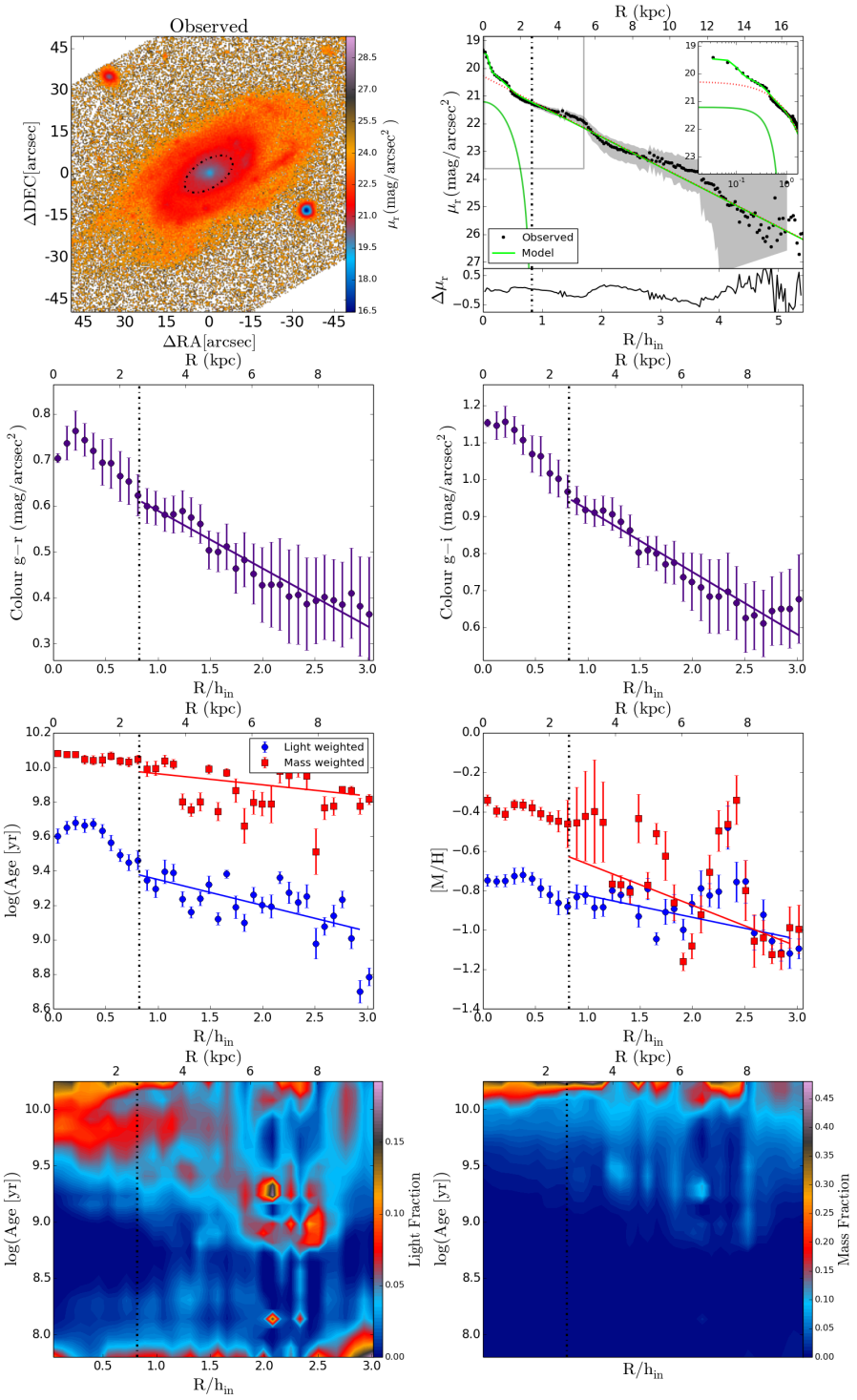

Figure B.69: UGC03944.

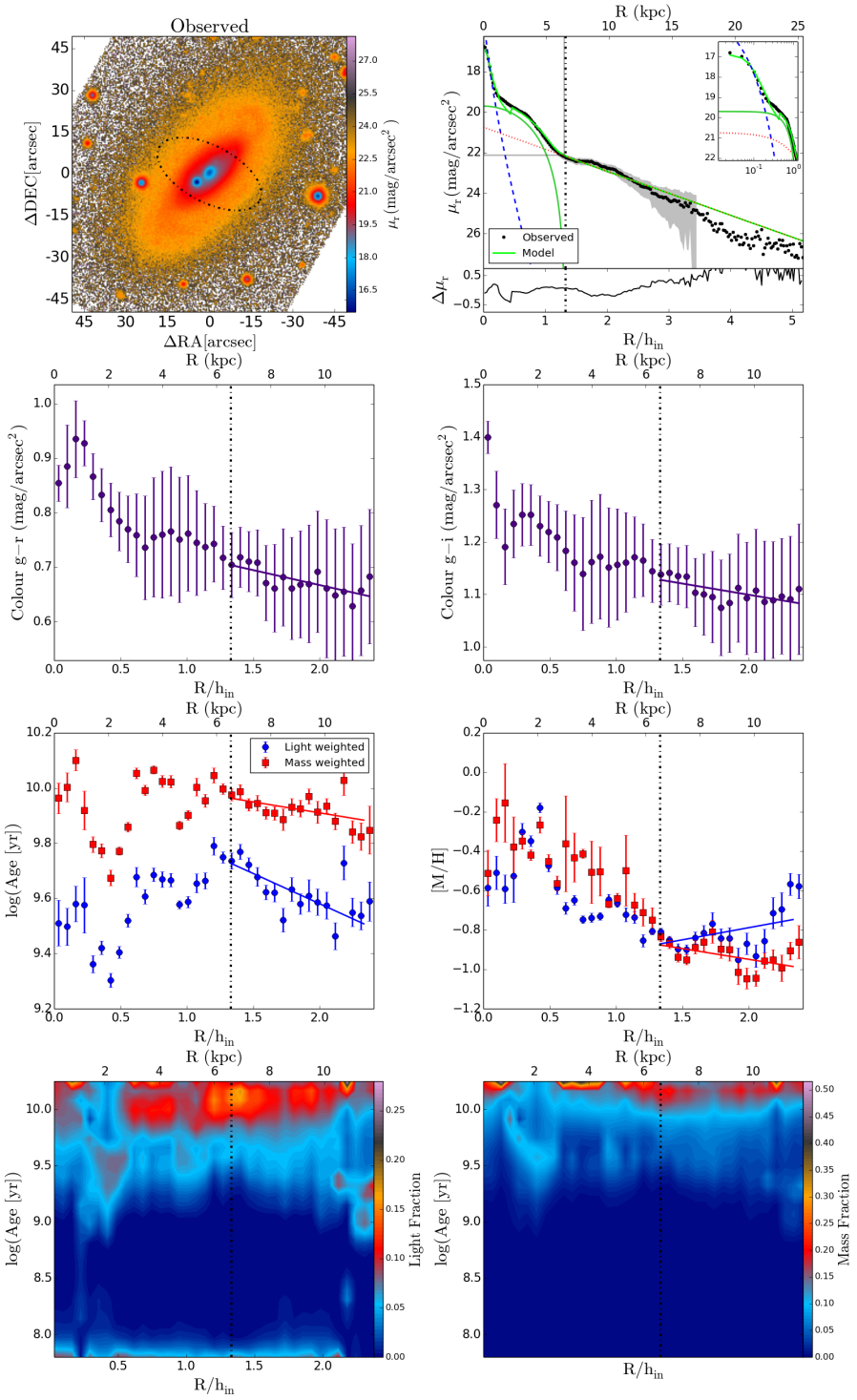

Figure B.70: UGC04145.

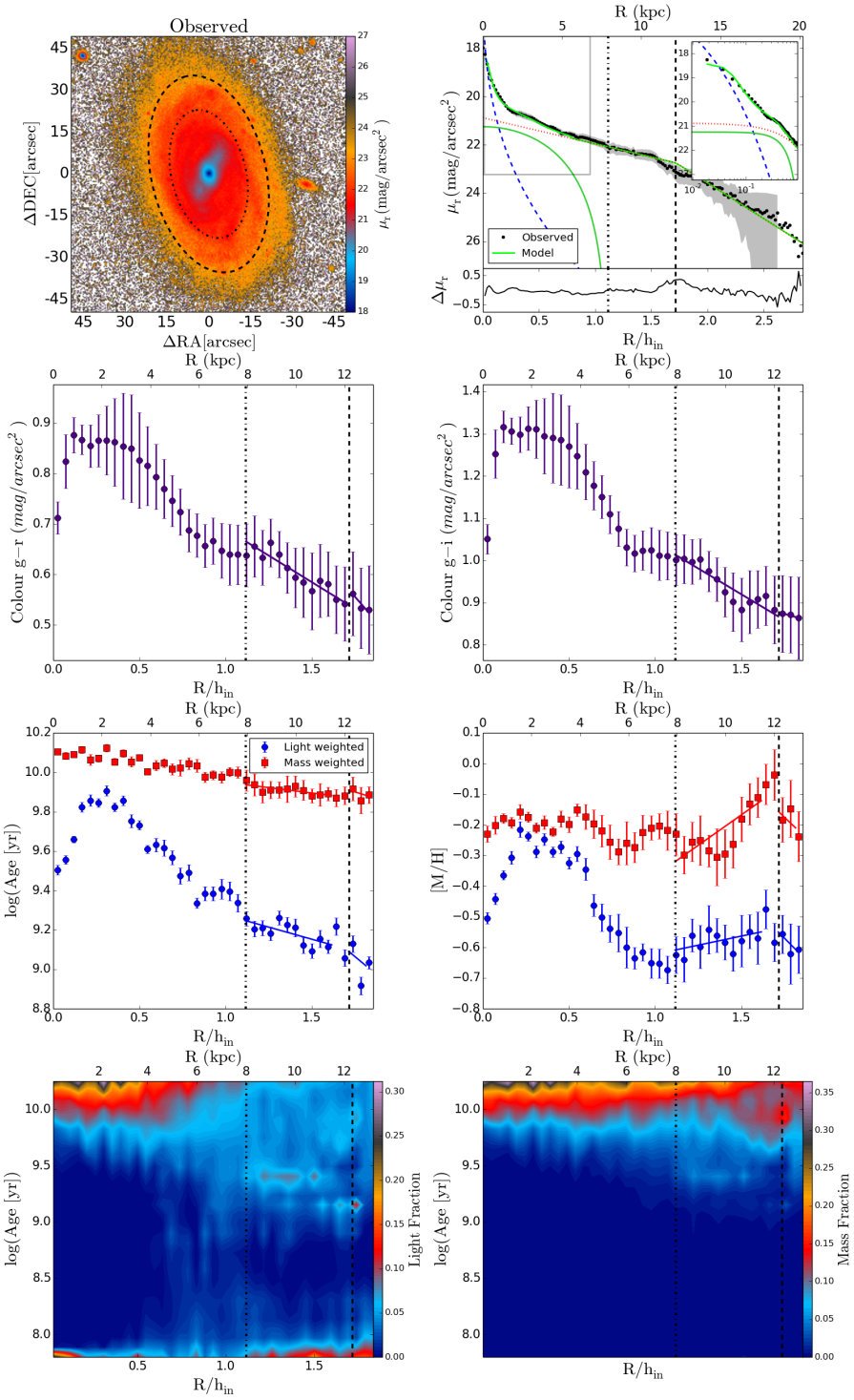

Figure B.71: UGC04195.

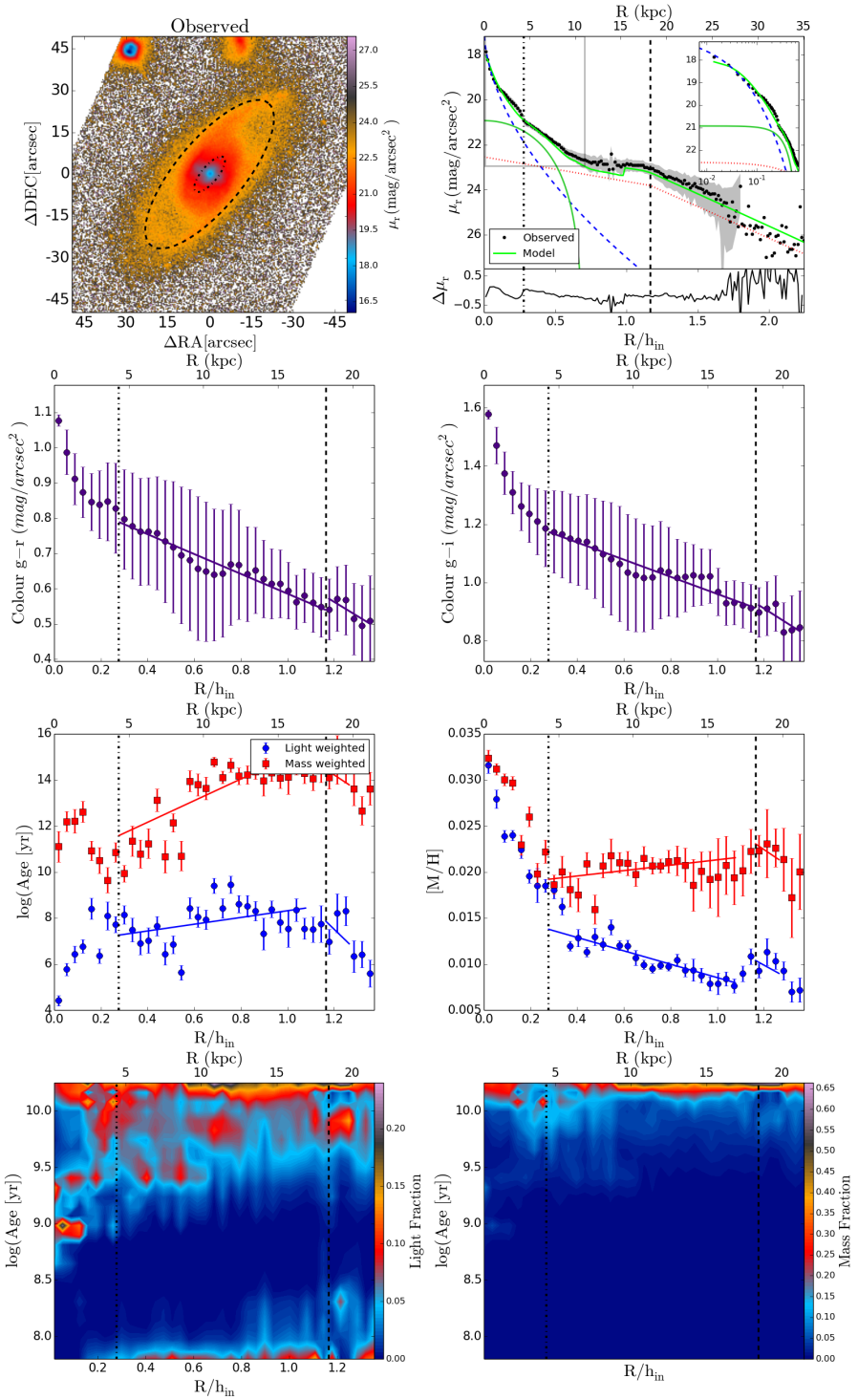

Figure B.72: UGC05108.

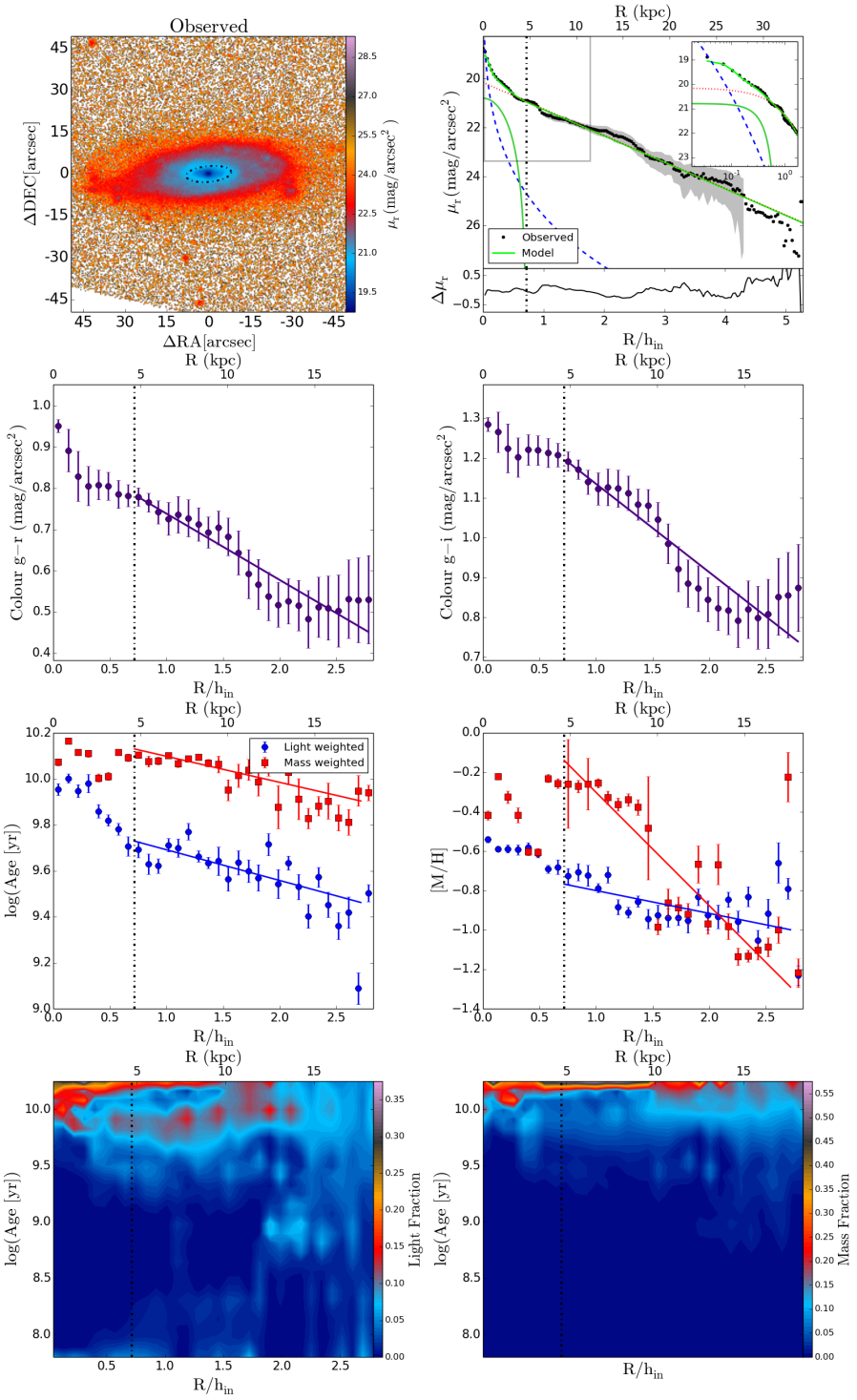

Figure B.73: UGC05359.

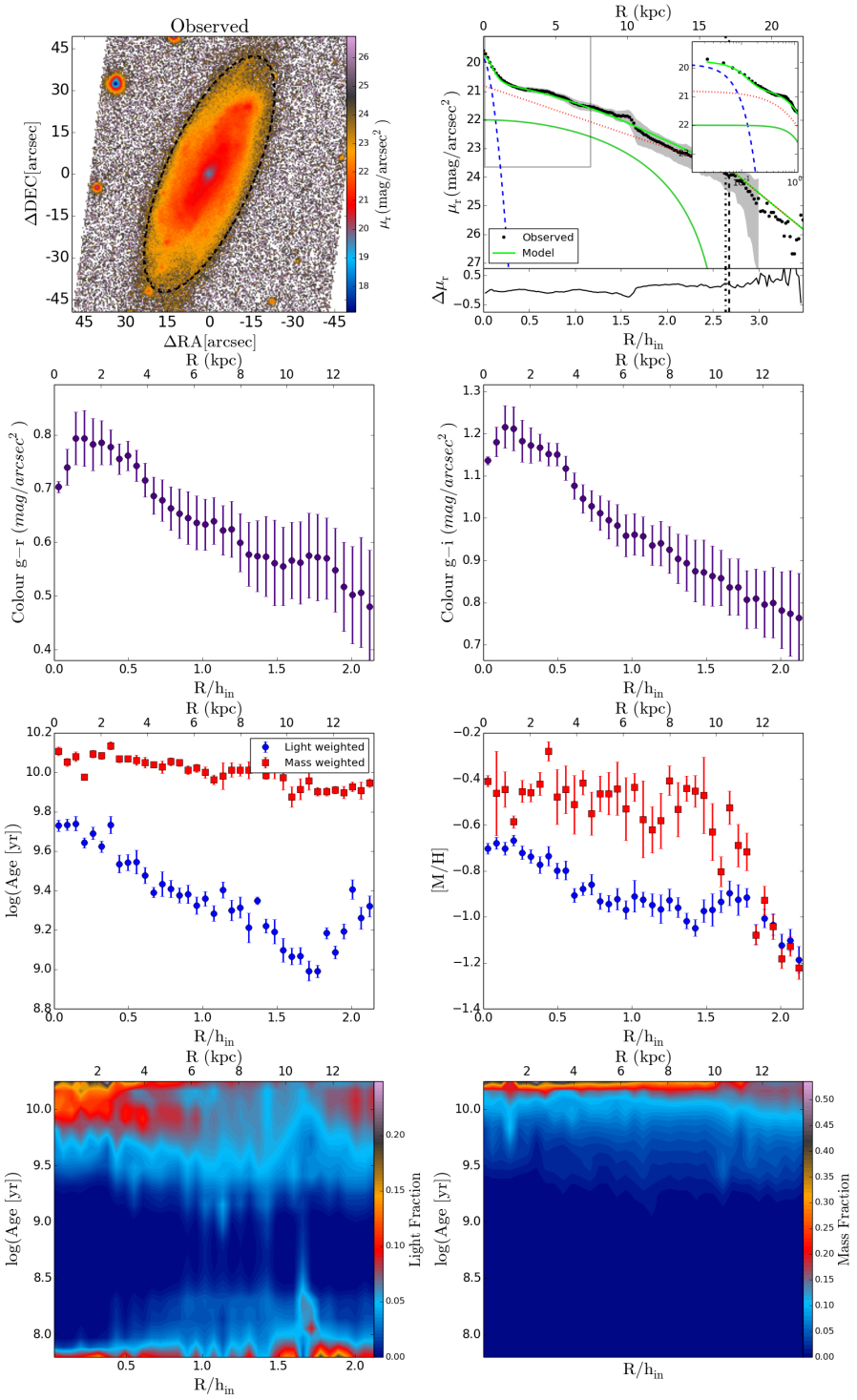

Figure B.74: UGC05396.

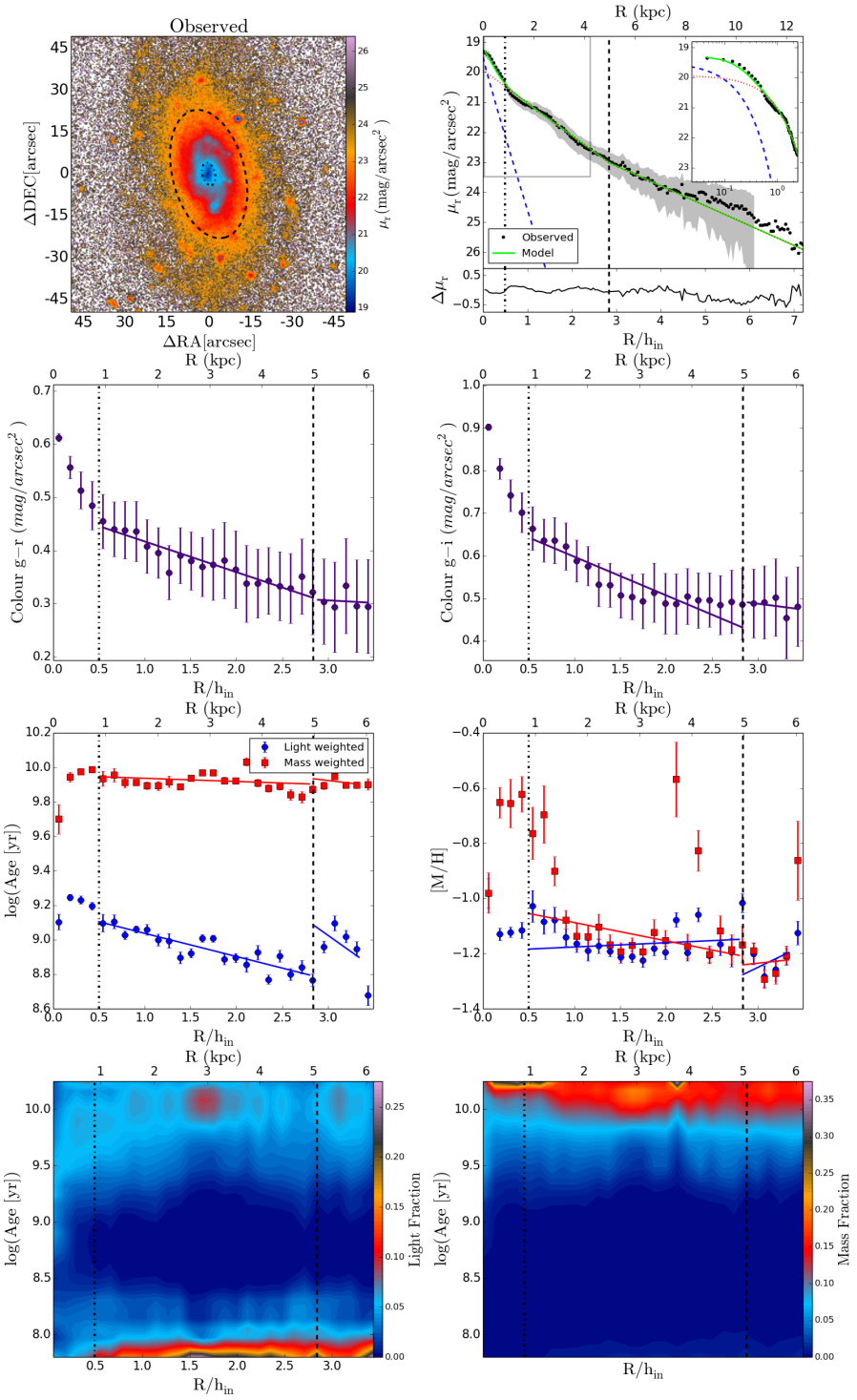

Figure B.75: UGC07012.

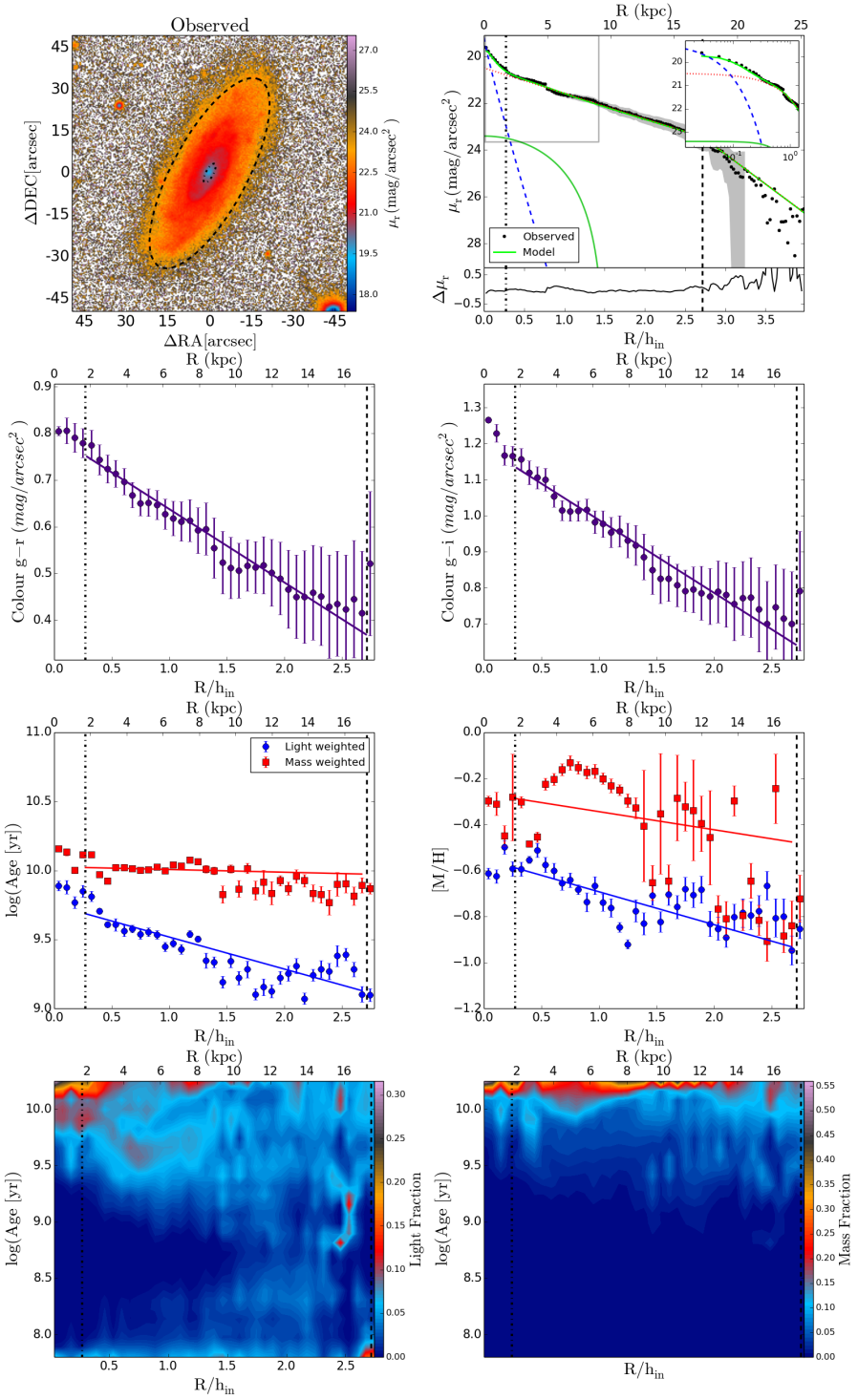

Figure B.76: UGC07145.

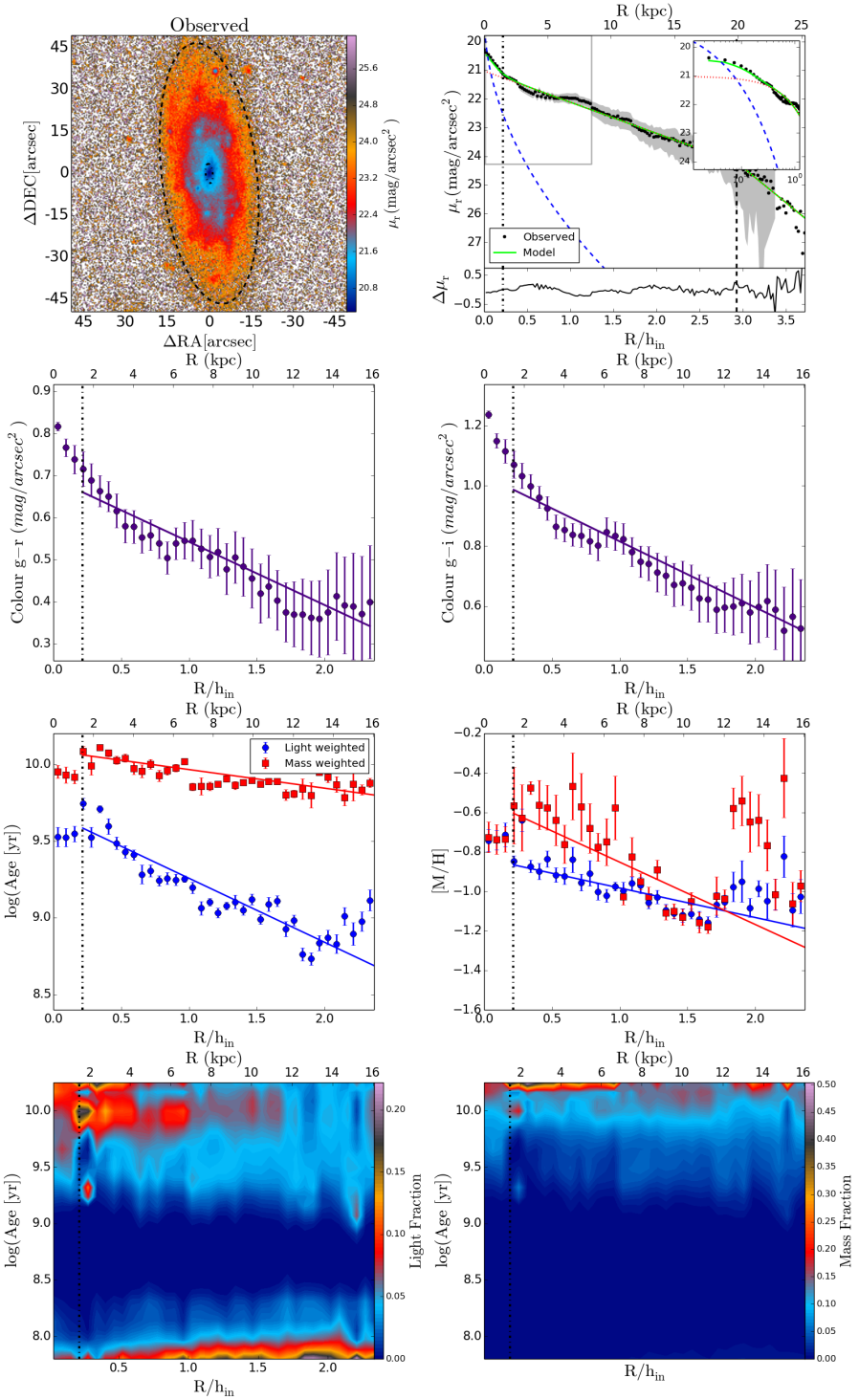

Figure B.77: UGC08004.

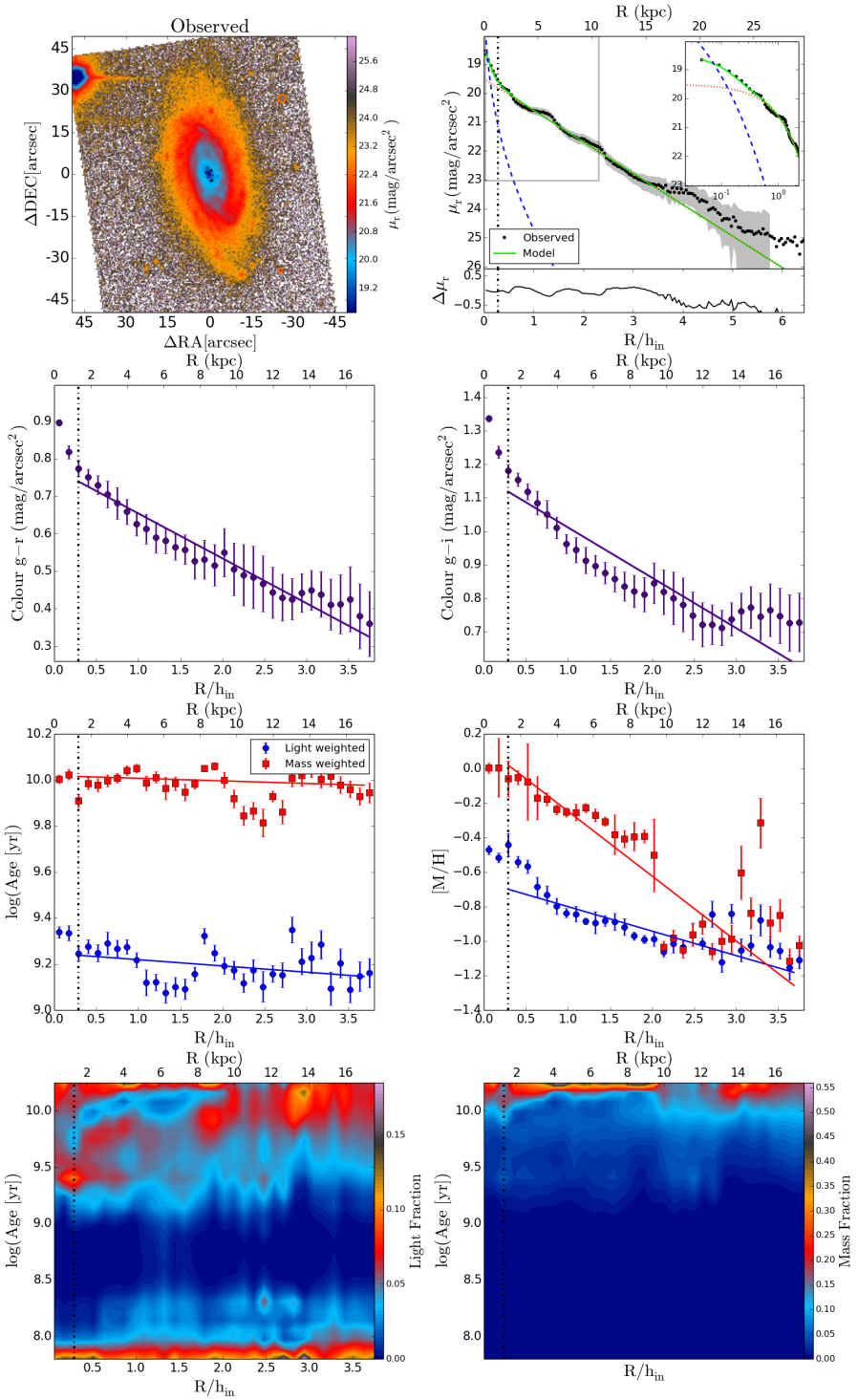

Figure B.78: UGC09067.

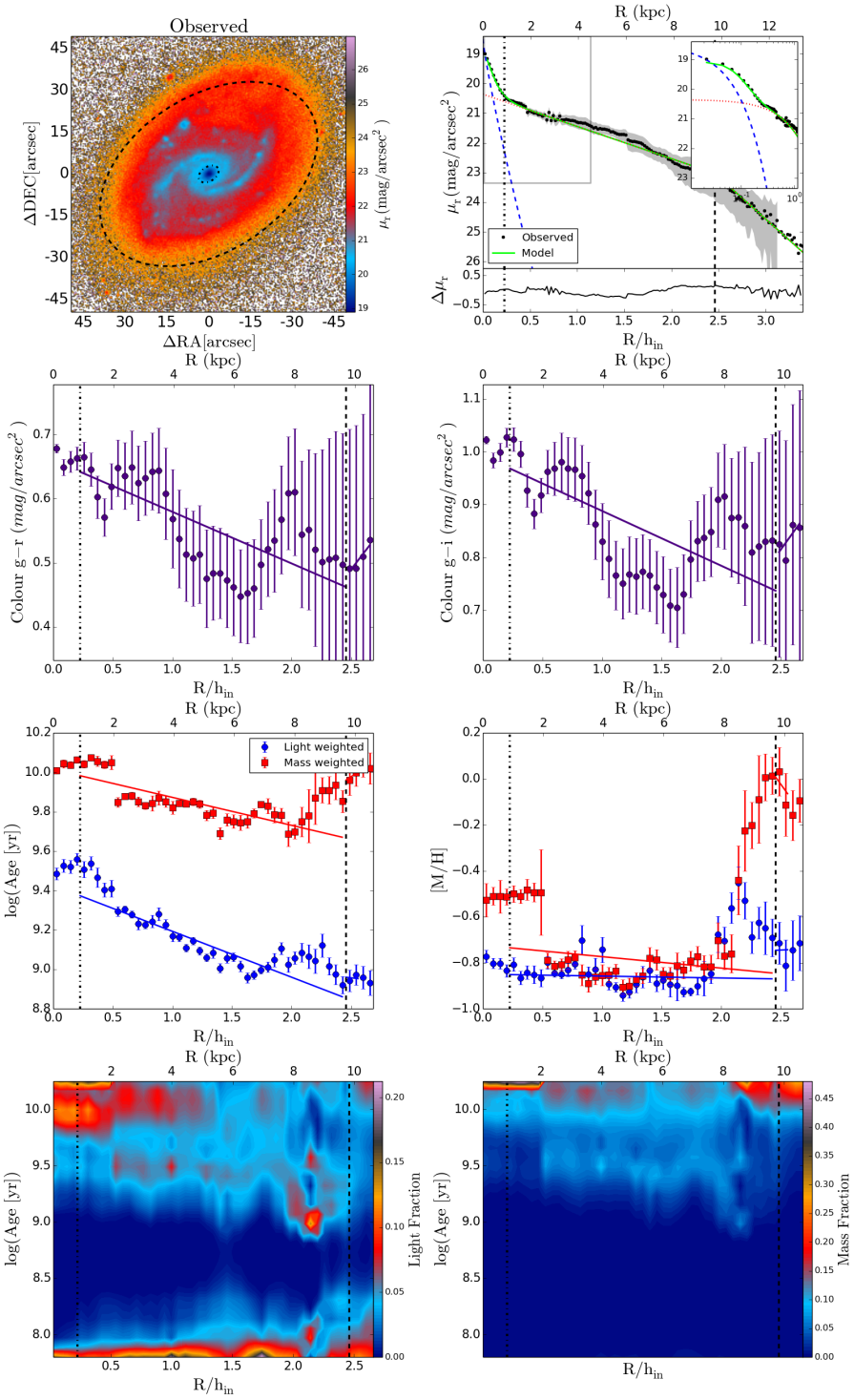

Figure B.79: UGC09476.

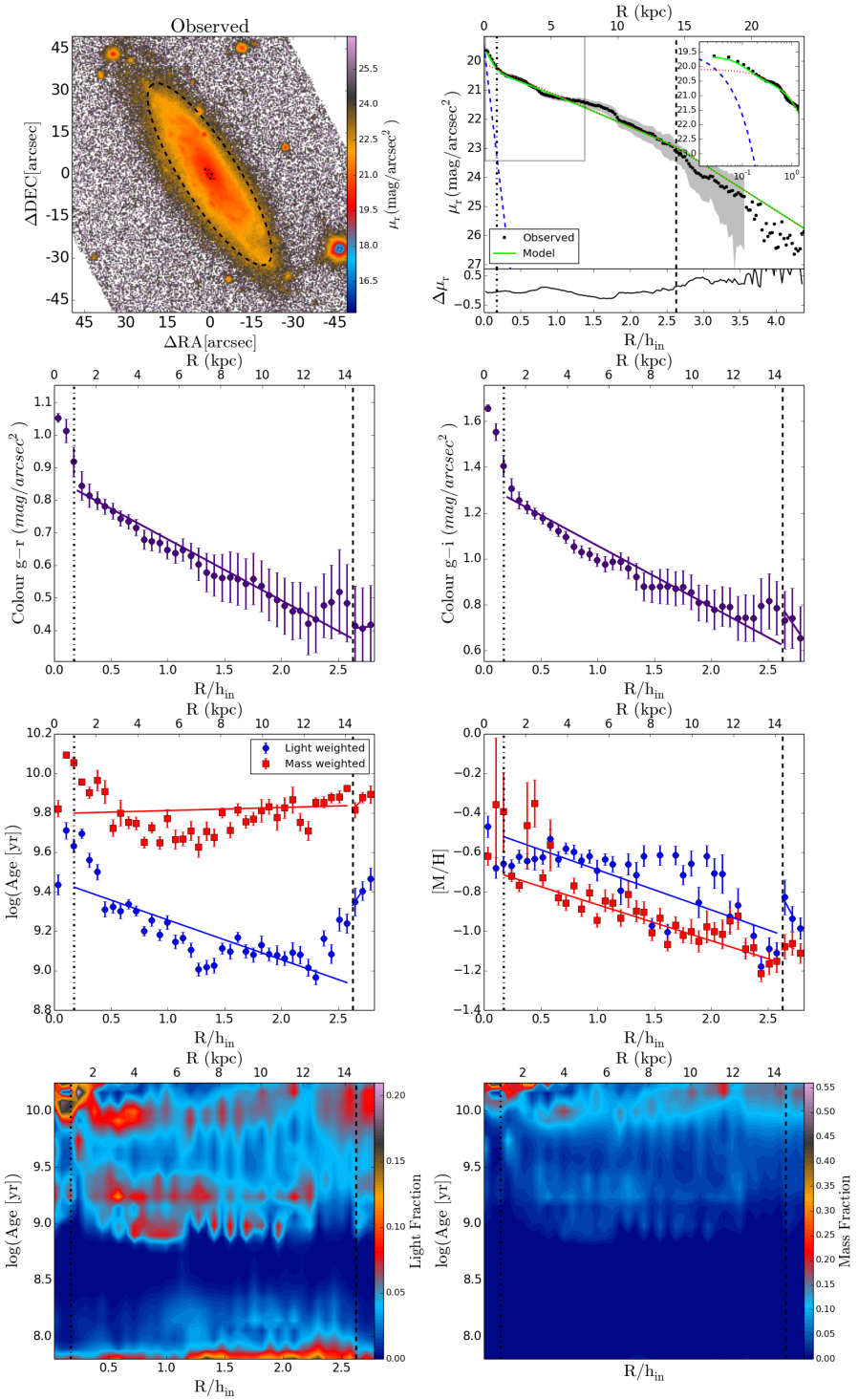

Figure B.80: UGC09542.

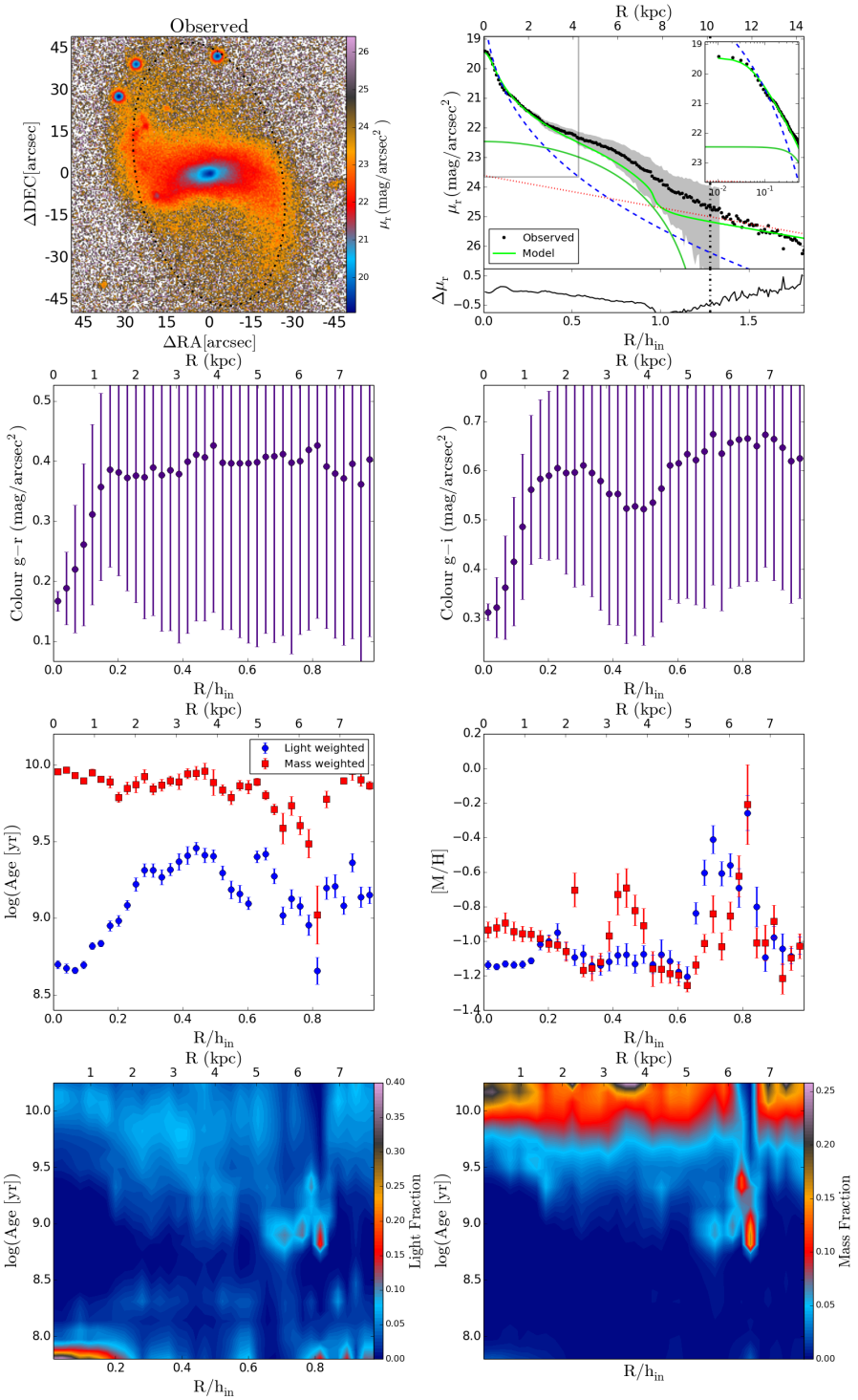

Figure B.81: UGC10796.

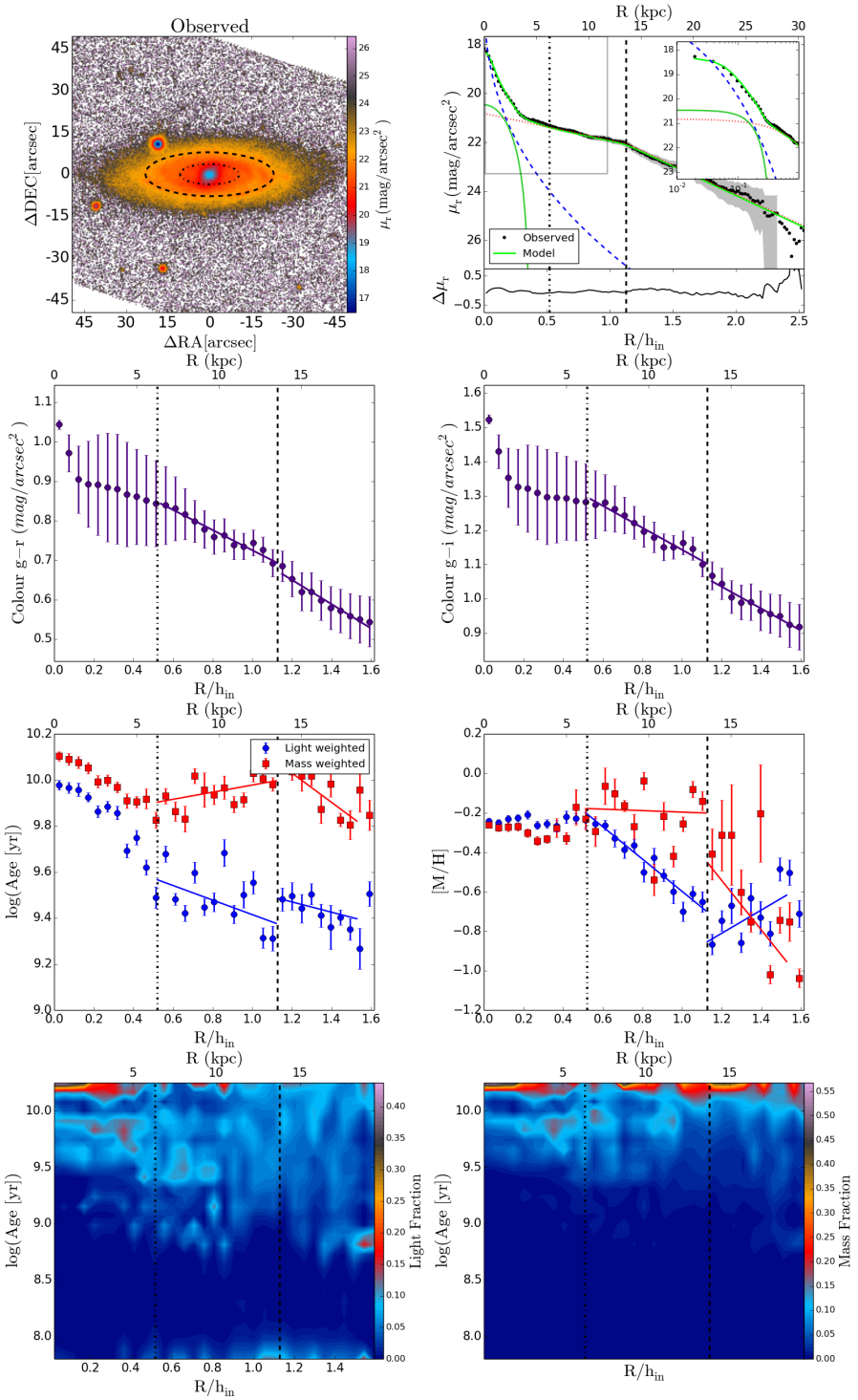

Figure B.82: UGC10811.

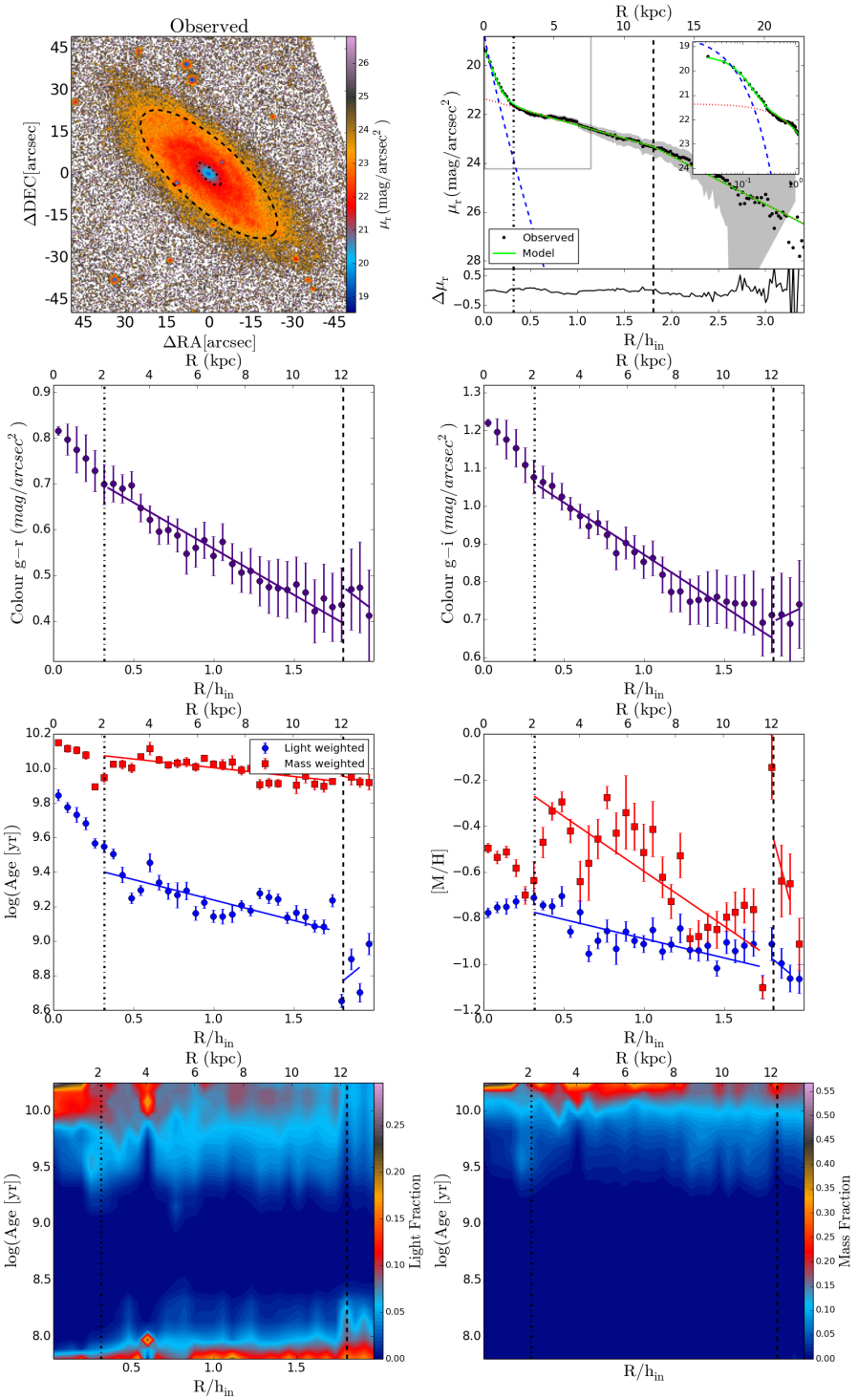

Figure B.83: UGC11262.

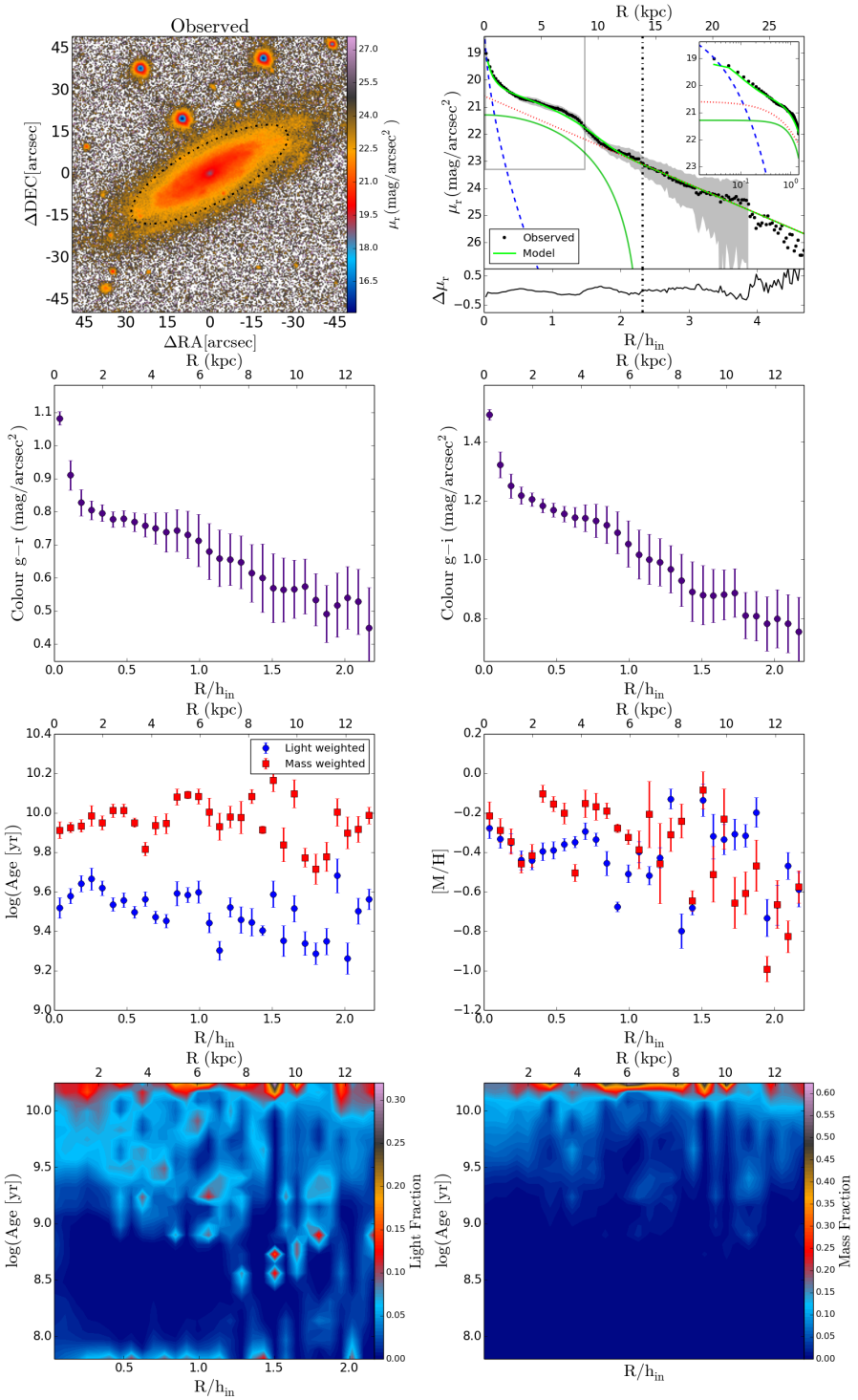

Figure B.84: UGC11740.

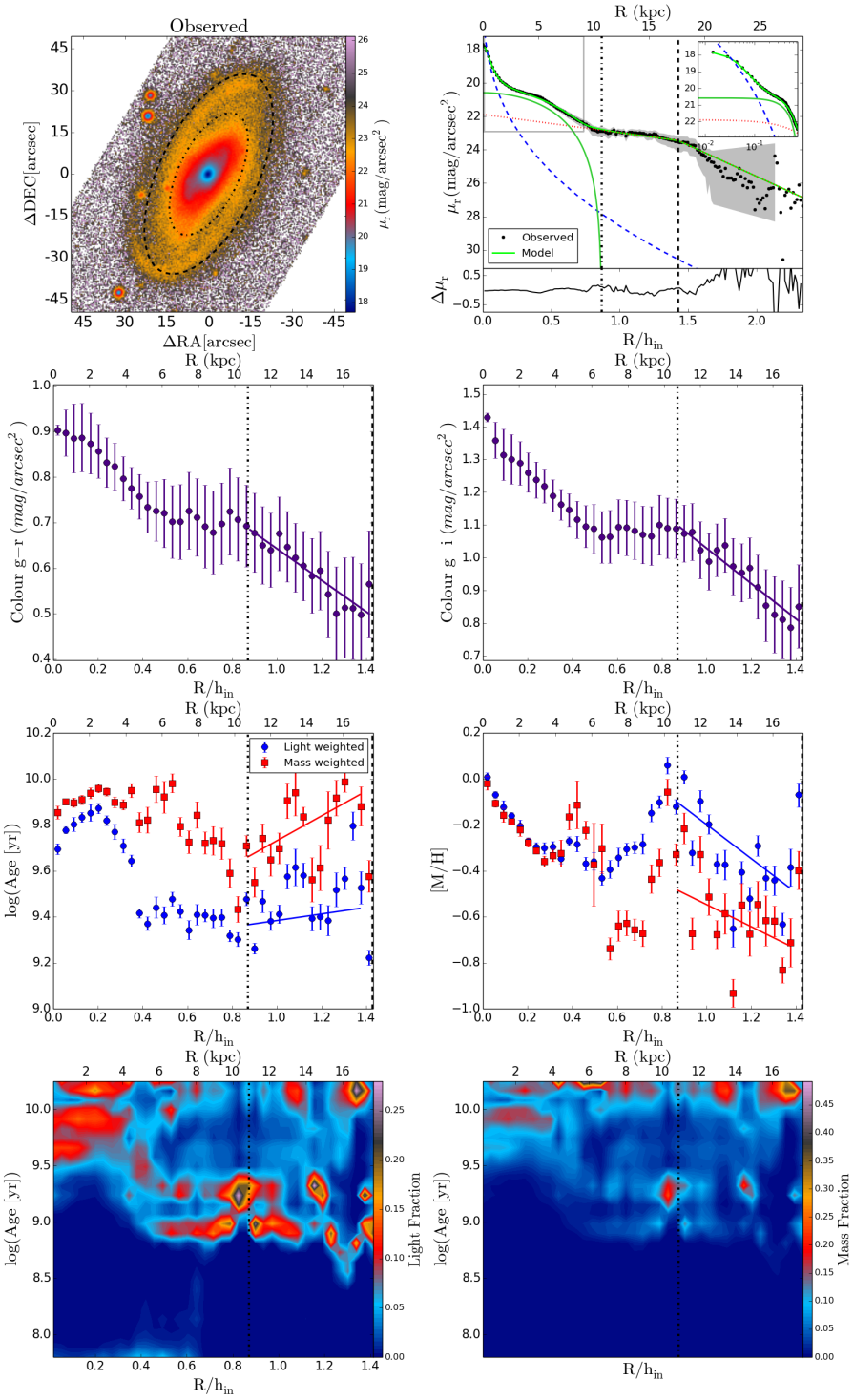

Figure B.85: UGC12185.

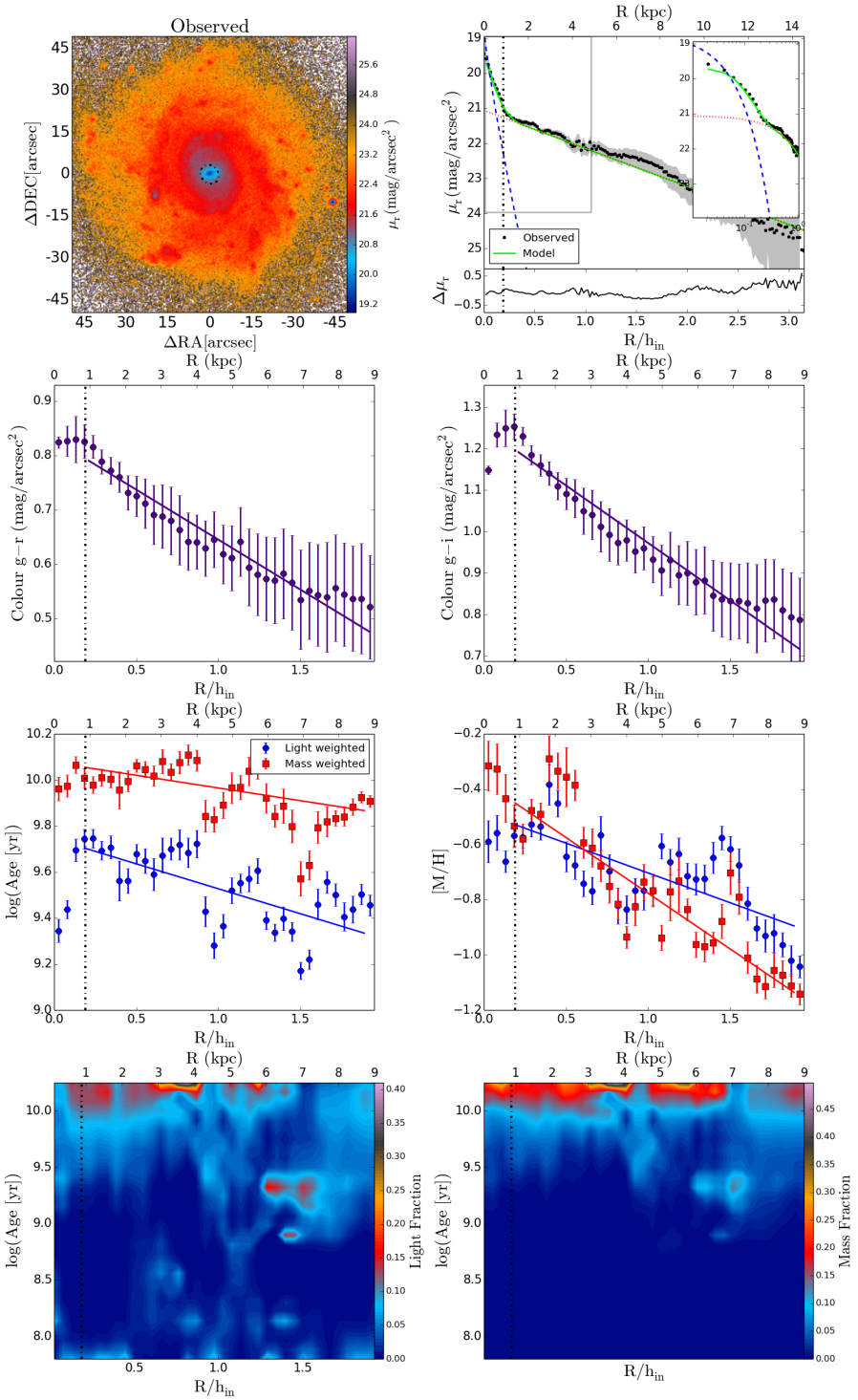

Figure B.86: UGC12224.

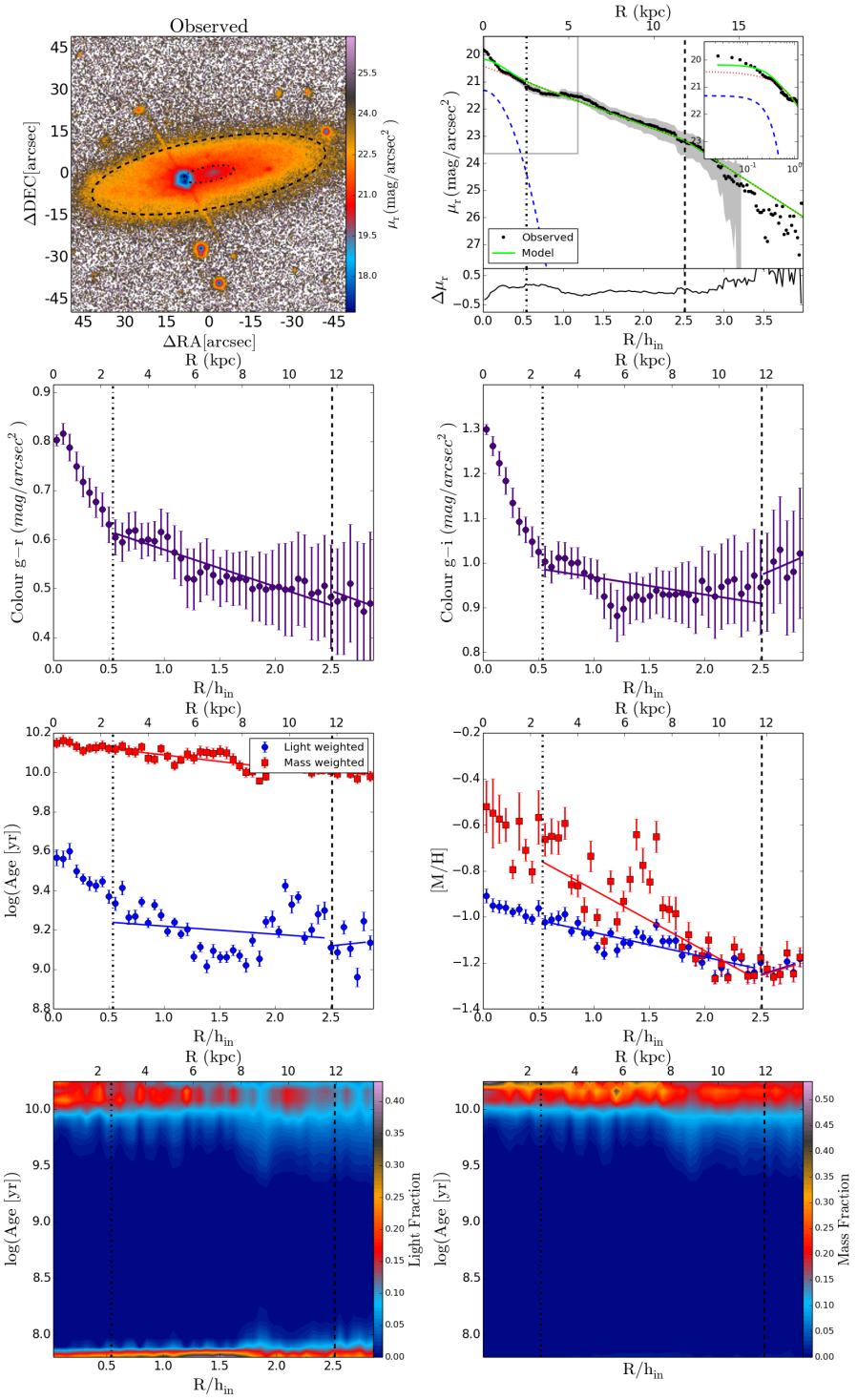

Figure B.87: UGC12653.

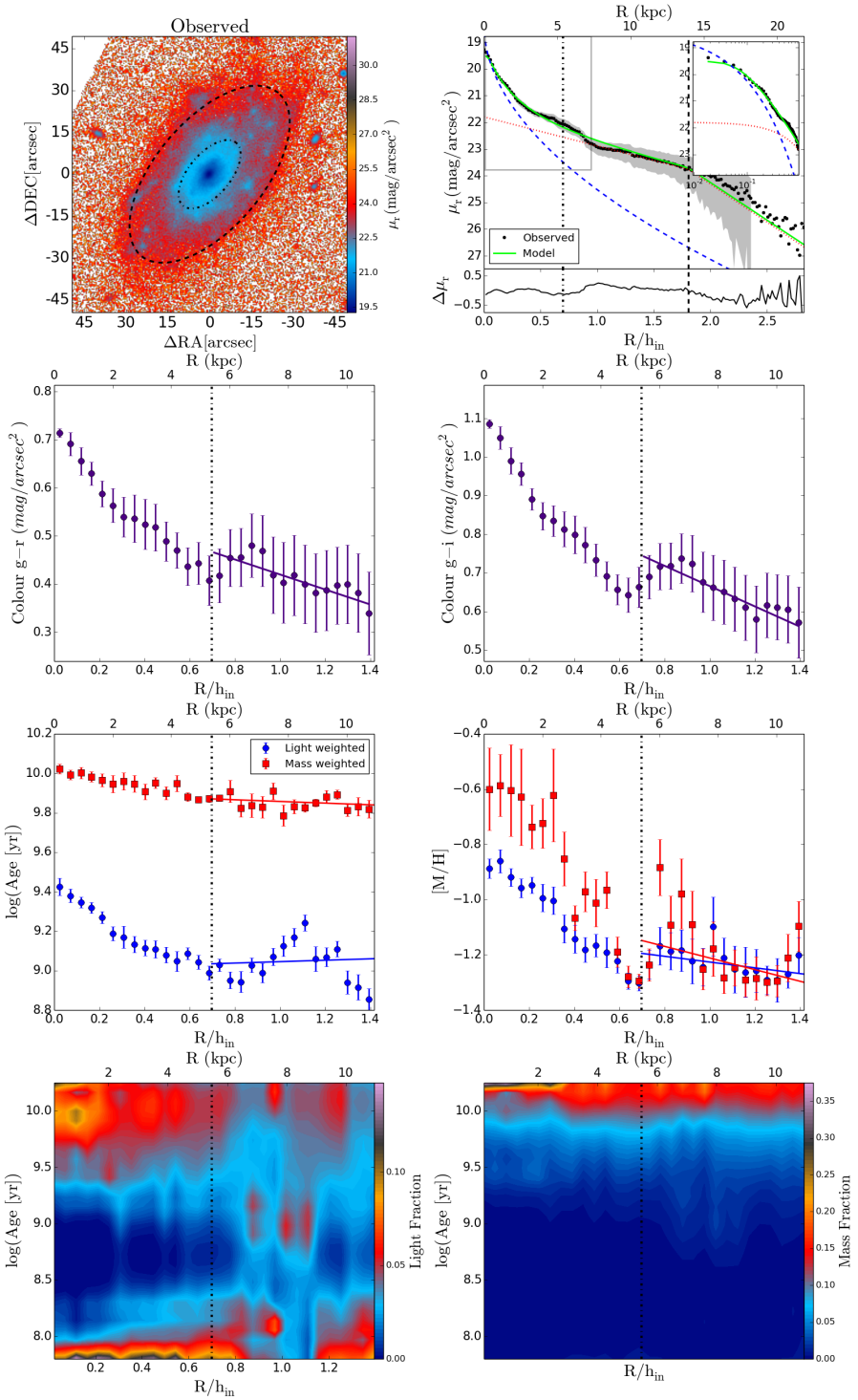

Figure B.88: UGC12816.

Appendix C

Recovered star formation histories for the STECKMAP tests, the LMC case

We include in this appendix the recovered SFH in the tests described in Sect. 3.2.1. We show the stellar content for the 24 tests in a similar way as in Fig. 3.7. As already outlined in the main body of this thesis, we note the consistency between different tests except in some extreme cases.

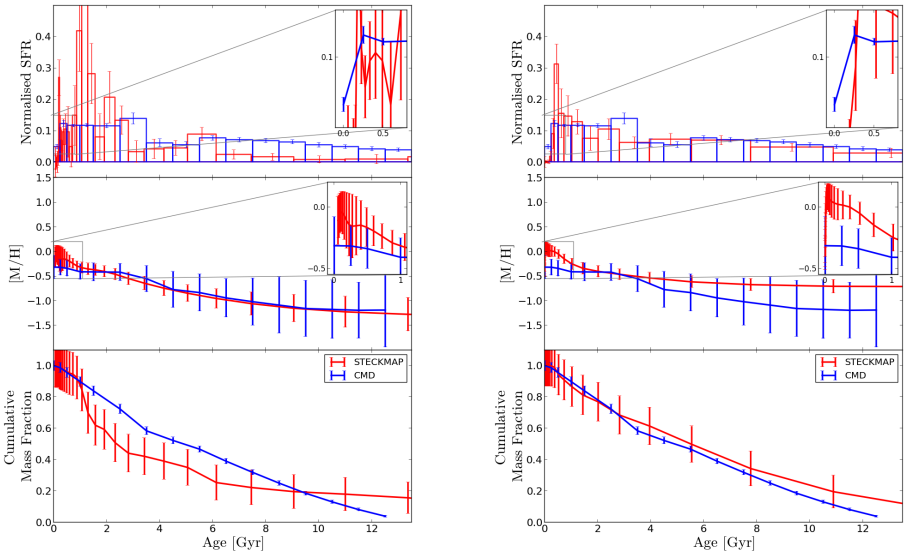

Figure C.1: Left: test 1; Right: test 2.

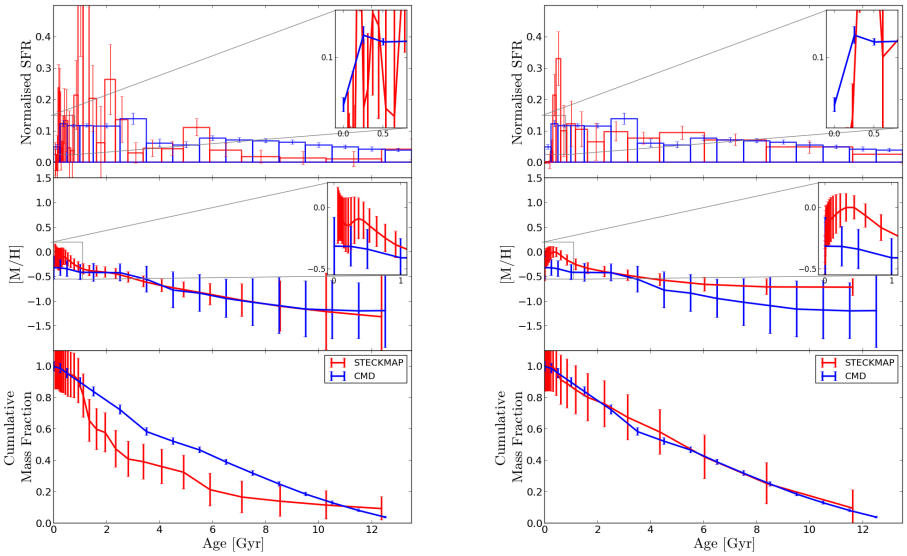

Figure C.2: Left: test 3; Right: test 4.

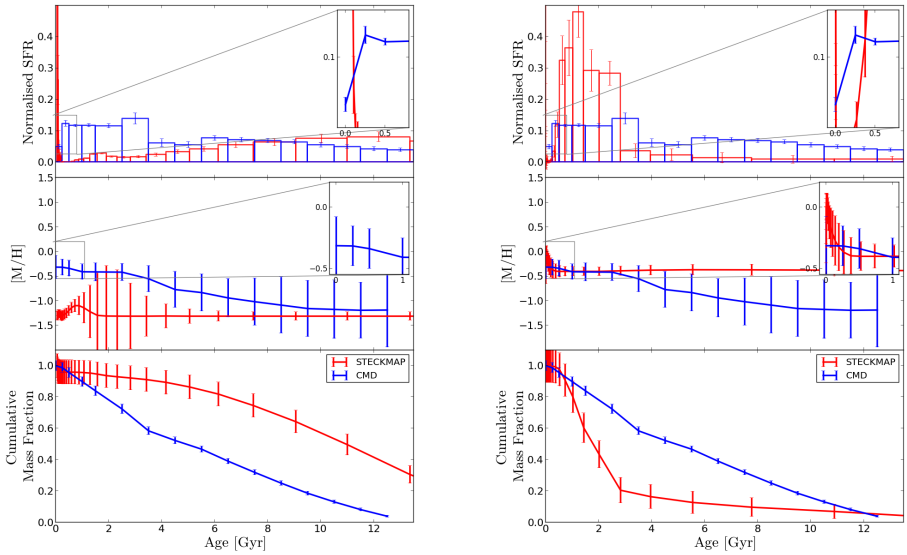

Figure C.3: Left: test 5; Right: test 6.

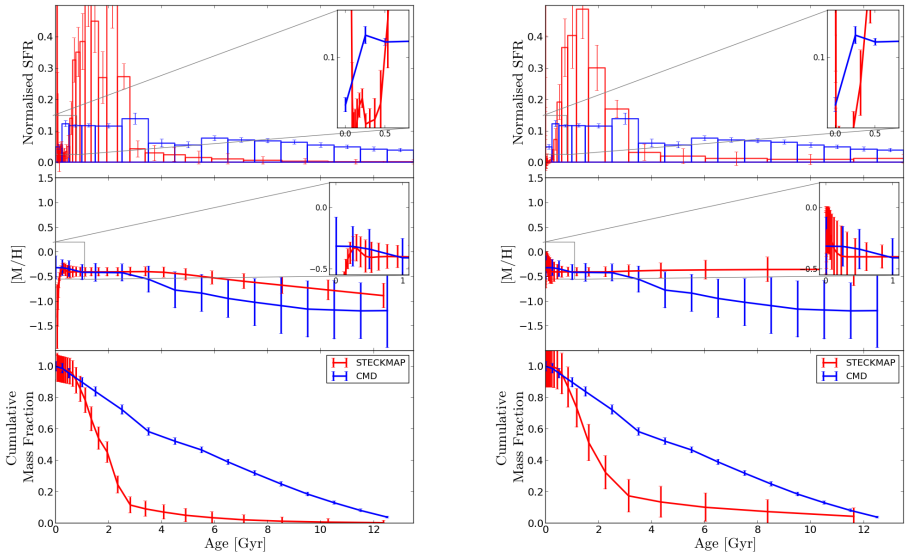

Figure C.4: Left: test 7; Right: test 8.

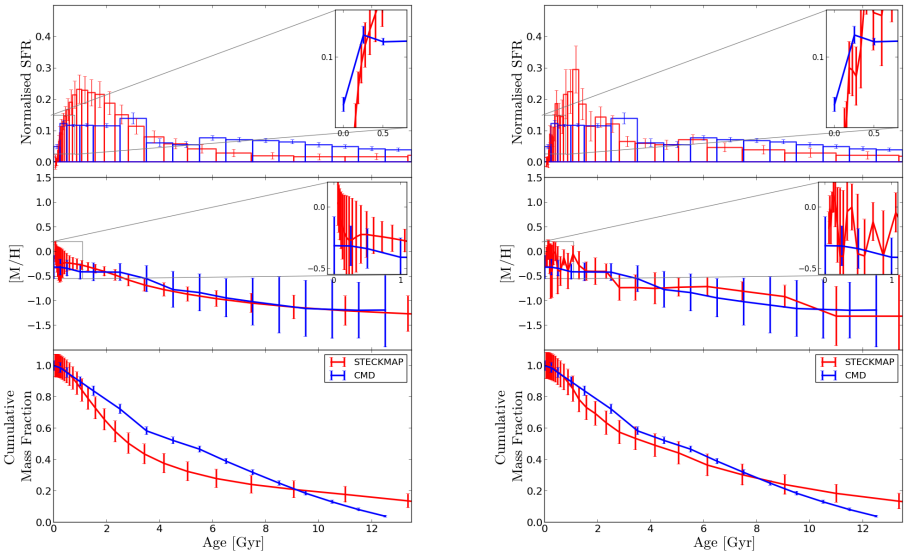

Figure C.5: Left: test 9; Right: test 10.

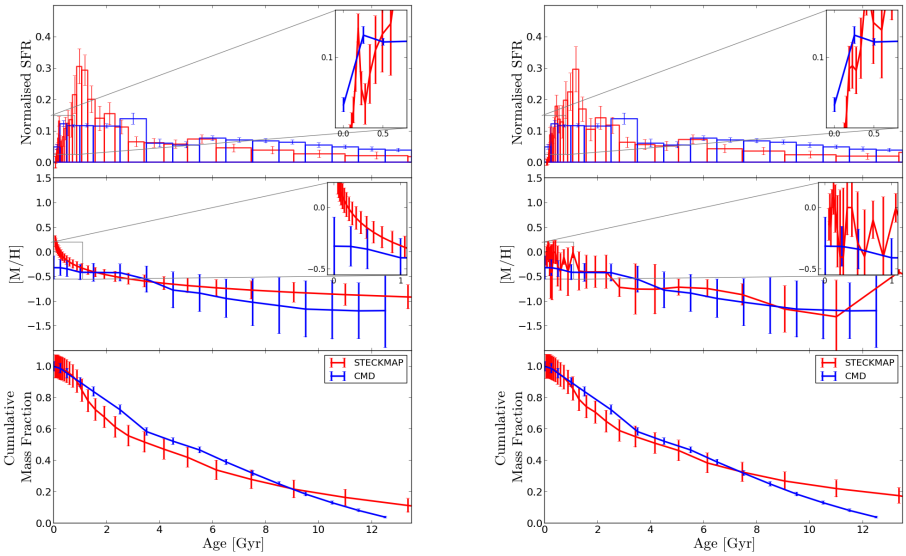

Figure C.6: Left: test 11; Right: test 12.

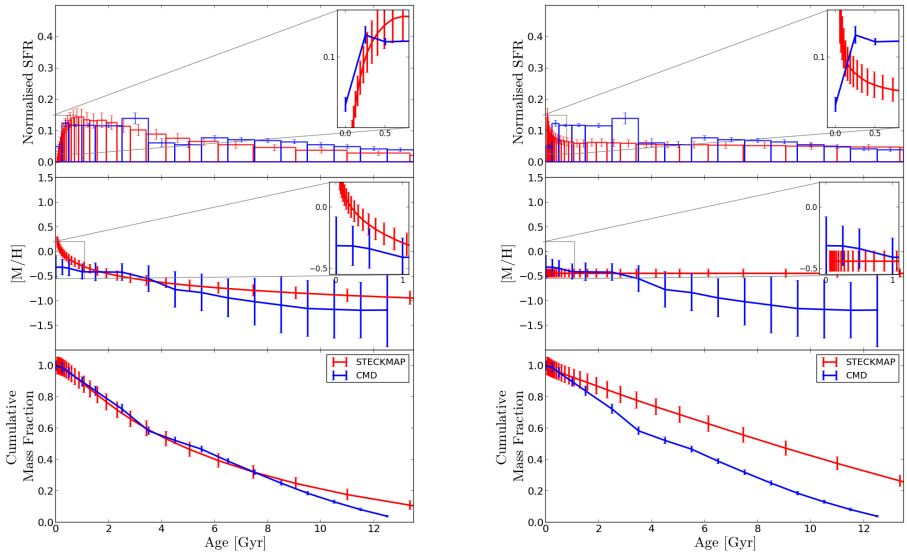

Figure C.7: Left: test 13; Right: test 14.

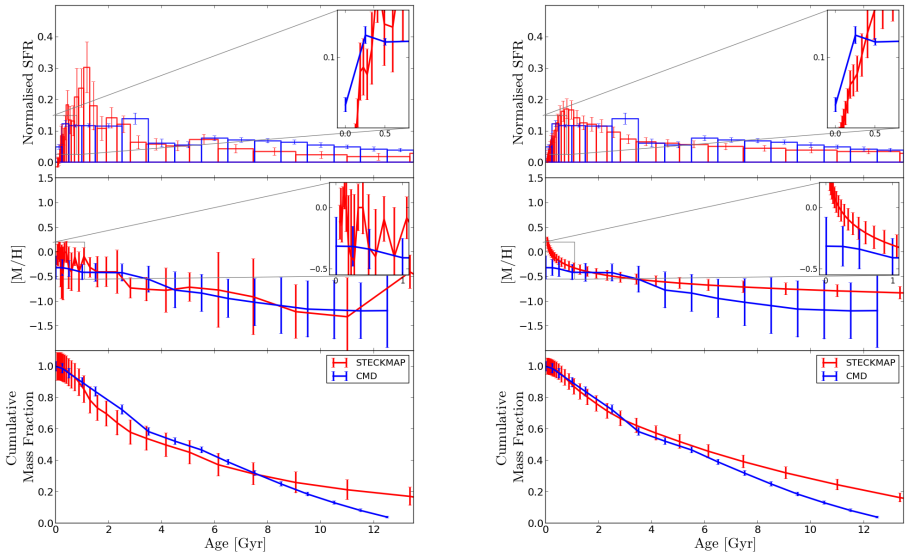

Figure C.8: Left: test 15; Right: test 16.

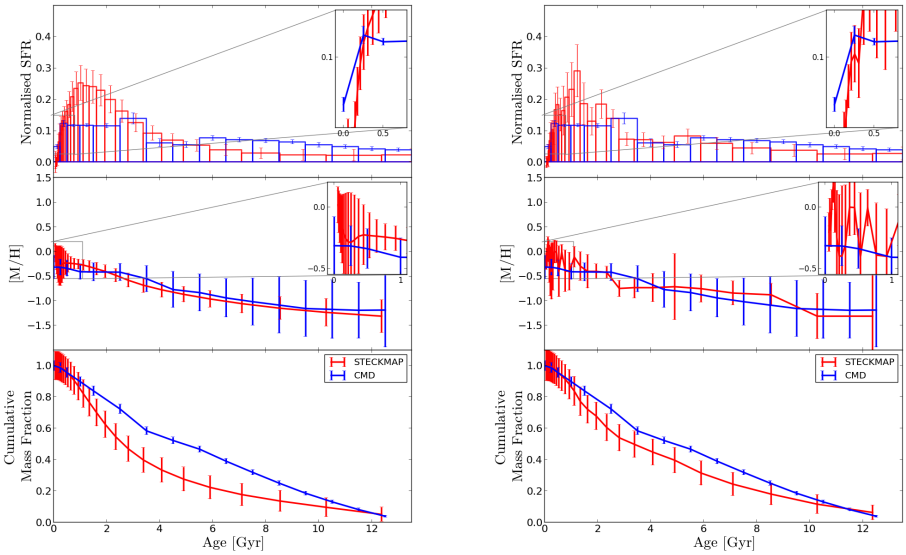

Figure C.9: Left: test 17; Right: test 18.

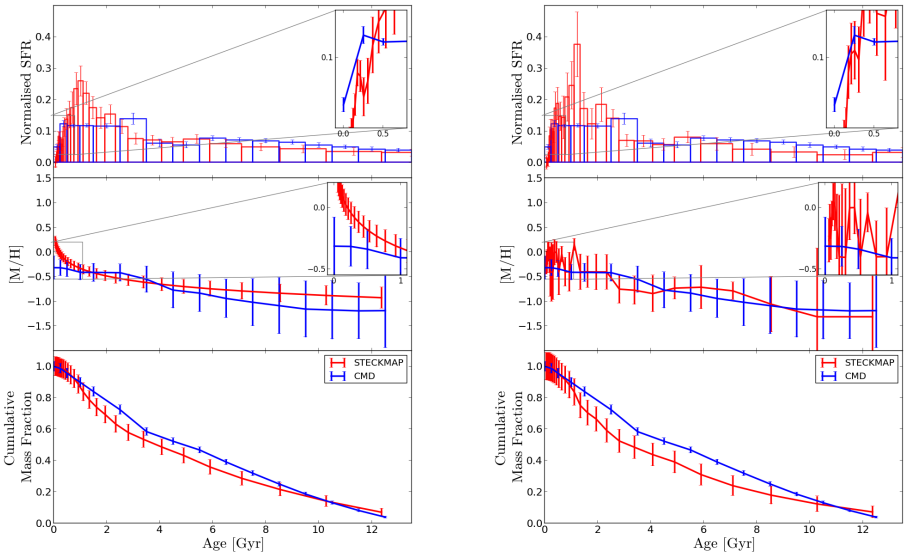

Figure C.10: Left: test 19; Right: test 20.

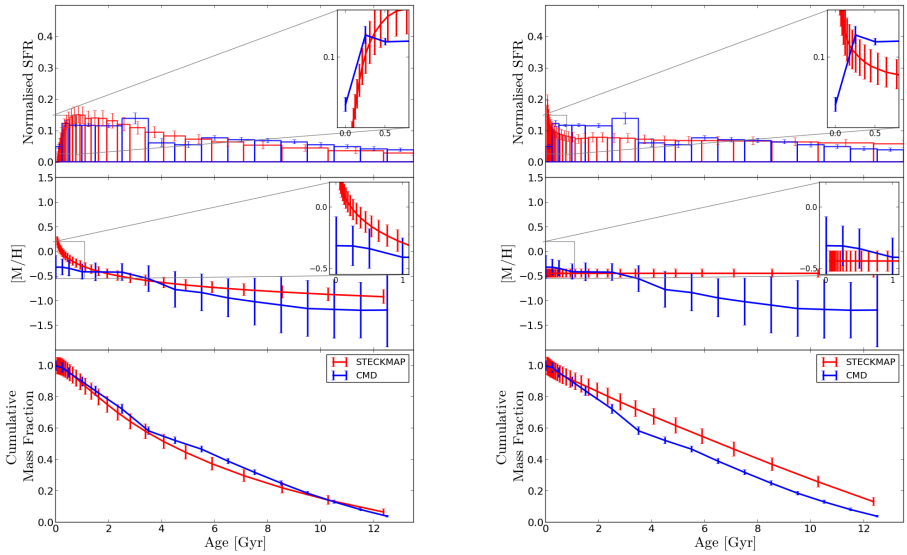

Figure C.11: Left: test 21; Right: test 22.

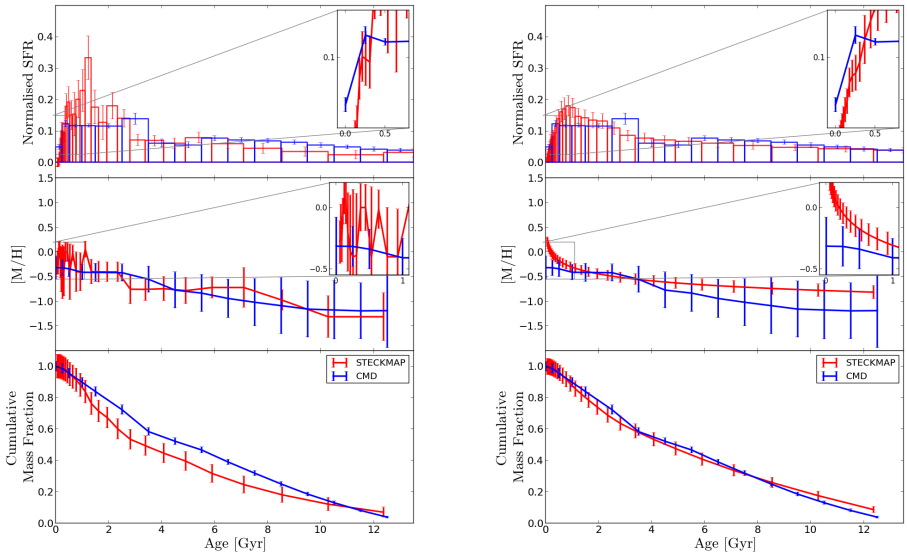

Figure C.12: Left: test 23; Right: test 24.

Appendix D

Characterisation of the RaDES galaxies

In this appendix we show all the plots and information we have gathered from the RaDES simulations to draw the conclusions discussed in Chapter 5. In that chapter we include just a selection of plots while the entire set can be found in this appendix.

Along with many other figures (already explained in Chapter 5 and below), we show here the light distribution of the RaDES sample, derived from one-dimensional SB profiles of the mock images presented in Few et al. (2012); these images were produced using SUNRISE (Jonsson 2006). SUNRISE uses the stellar and gaseous distributions, as well as SEDs for each stellar particle, drawn from the *Starburst99* stellar population models (Leitherer et al. 1999), in order to generate the bandpass-dependent mock images. One-dimensional profiles are then fitted with the function presented in Erwin et al. (2008, equations 5 and 6) with a broken exponential profile implemented. This way, we can distinguish between galaxies with exponential, up-bending, or down-bending profiles, as well as characterise the light distribution of the inner and outer discs. Table D.1 summarises the light distribution information for the 19 simulated galaxies.

The characteristics of the mock images generated by SUNRISE hampers the use of GASP2D (see Sect 2.3) to analyse the SB profiles of the RaDES galaxies. Consequently, a 1D approach as the one outlined in Sect. 2.3.1 is followed. Thus, the differences that we find between these structural parameters (1D) and those from the SDSS data of the sample of CALIFA galaxies studied along this thesis (2D) can be ascribed to the different methods used and the fact that these simulated galaxies are mainly Sb-Sc (see Sect. 2.3.1).

Name	SB type	h_{in} (kpc)			h_{out} (kpc)			R_{break} (kpc)		
		g	r	i	g	r	i	g	r	i
(1)	(2)	(3)	(4)	(5)	(6)	(7)	(8)	(9)	(10)	(11)
Apollo	II	2.68	2.34	2.19	1.24	1.39	1.44	5.14	4.96	4.94
Artemis	III	0.60	0.79	0.78	5.56	5.87	5.97	4.27	5.30	5.30
Atlas	II	5.08	4.39	3.43	2.31	2.47	2.53	7.63	7.43	7.91
Ben	II	5.88	5.28	5.03	3.15	3.36	3.36	12.33	12.18	12.42
Castor	II	10.06	5.70	5.32	0.95	0.96	0.96	5.37	5.35	5.32
Daphne	III	1.23	1.26	1.27	3.76	3.84	3.81	10.05	10.08	10.08
Eos	III	2.96	2.95	2.91	8.38	8.55	8.37	19.32	18.32	17.84
Helios	III	1.92	1.93	2.01	7.73	7.76	7.82	11.54	11.49	11.74
Hyperion	II	4.54	4.31	4.24	2.51	2.77	2.78	14.94	14.97	15.15
Krios	III	2.63	2.62	2.63	8.51	8.45	8.33	16.82	16.11	15.85
Leia	III	3.65	3.81	3.90	7.37	7.48	7.58	20.95	21.21	21.62
Leto	III	0.95	0.99	1.00	4.11	4.07	3.99	6.65	6.59	6.51
Luke	I	5.84	5.78	5.77	–	–	–	–	–	–
Oceanus	II	8.19	8.08	7.93	5.17	4.18	4.39	21.19	23.17	23.21
Pollux	III	1.20	1.25	1.22	4.33	4.03	3.93	8.80	8.61	8.41
Selene	II	5.74	5.68	5.36	1.73	2.01	1.98	12.75	11.98	12.13
Tethys	II	5.23	4.43	4.20	1.97	2.12	2.16	9.92	9.82	9.85
Tyndareus	III	1.34	1.33	1.33	3.67	3.39	3.22	7.69	7.12	6.89
Zeus	I	0.90	0.92	0.92	–	–	–	–	–	–

Table D.1: Main disc properties from the light distribution in the g, r and i SDSS bands for the RaDES galaxies. (1) Galaxy name; (2) surface Brightness type according to the Pohlen & Trujillo (2006) classification; (3)-(5) inner disc scale-length in kpc (g, r and i SDSS bands); (6)-(8) outer disc scale-length in kpc (g, r and i SDSS bands); (9)-(11) break radius in kpc (g, r and i SDSS bands).

For each of the RaDES galaxies we show one page displaying 7 different panels. The reader can find a brief description of all those panels below:

General information: radial distances are normalised to the inner disc scale-length (h_{in}). Dashed black vertical lines indicate the position of the break radius (R_{break}). Dashed cyan vertical lines indicate the time at which the last merge event (t_{jump}) took place. Dashed blue vertical lines indicate the position of the minimum in age (t_{min}). Vertical coloured arrows are located at the beginning and the end of the four regions defined in Table 5.2: blue, region 1; green, region 2; red, region 3; black, region 4.

First row (left): schematic representation of the satellite orbits for each of the RaDES galaxies. On the y-axis we plot the three-dimensional distance (R_{3D}) from the satellite centre to the host galaxy centre. On the x-axis we plot the lookback time (13.5 Gyr being the beginning of the simulation). Each point represents one satellite at a given snapshot with points corresponding to the same satellite at different timesteps linked by a solid grey line. In some cases, the halo tracking between snapshots fails leading to missing connecting lines. We colour-code the points according to $\log_{10}(M_{sat}/M_{host})$ as an indicator of the magnitude of the mergers (the size of each point is also proportional to that value). We have applied a cut in $\log_{10}(M_{sat}/M_{host})$ to clean the plot of the least massive satellites; satellites with (M_{sat}/M_{host}) below 0.005 when they merge with the host galaxy are ruled out in the plots. The dashed red line represents the time evolution of

the host galaxy virial radius.

First row (right): surface brightness profile in SDSS r-band for each of the RaDES galaxies. Black solid line: *observed* SB profile using the SUNRISE (Jonsson 2006) mock images; those images can be seen in Few et al. (2012). Green solid line: *model* SB profile after applying a 1D fitting procedure as the one outlined in Sect. 2.3.1 to the observed light distribution (black solid line).

Second row (left): stellar disc age radial profile. The age values are computed by applying a M-W average to all disc particles within 0.5 kpc-wide radial bins. The errors correspond to the M-W standard deviation of the ages of all the disc particles within those bins.

Second row (right): stellar disc metallicity radial profile. The metallicity values are computed by applying a M-W average to all disc particles within 0.5 kpc-wide radial bins. The errors correspond to the M-W standard deviation of the metallicities of all the disc particles within those bins.

Third row (left): stellar disc total velocity dispersion radial profile. The total velocity dispersion values are computed by applying a M-W average to all disc particles within 0.5 kpc-wide radial bins. The errors correspond to the M-W standard deviation of the total velocity dispersion values of all the disc particles within those bins.

Third row (right): radial velocity dispersion vs. age (AVR) for each of the RaDES galaxies. Solid lines represent the AVR for disc particles in each of the analysed regions: blue, region 1; green, region 2; red, region 3; black, region 4.

Fourth row: age-metallicity relation for the disc stars in each of the RaDES galaxies, colour-coded according to their current radial positions (see text, Table 5.2, and Fig. 5.4 for more information). Blue crosses represent stars currently located in region 1. Green asterisks represent stars currently in region 2. Red dots represent stars currently in region 3. Black triangles represent stars currently in region 4.

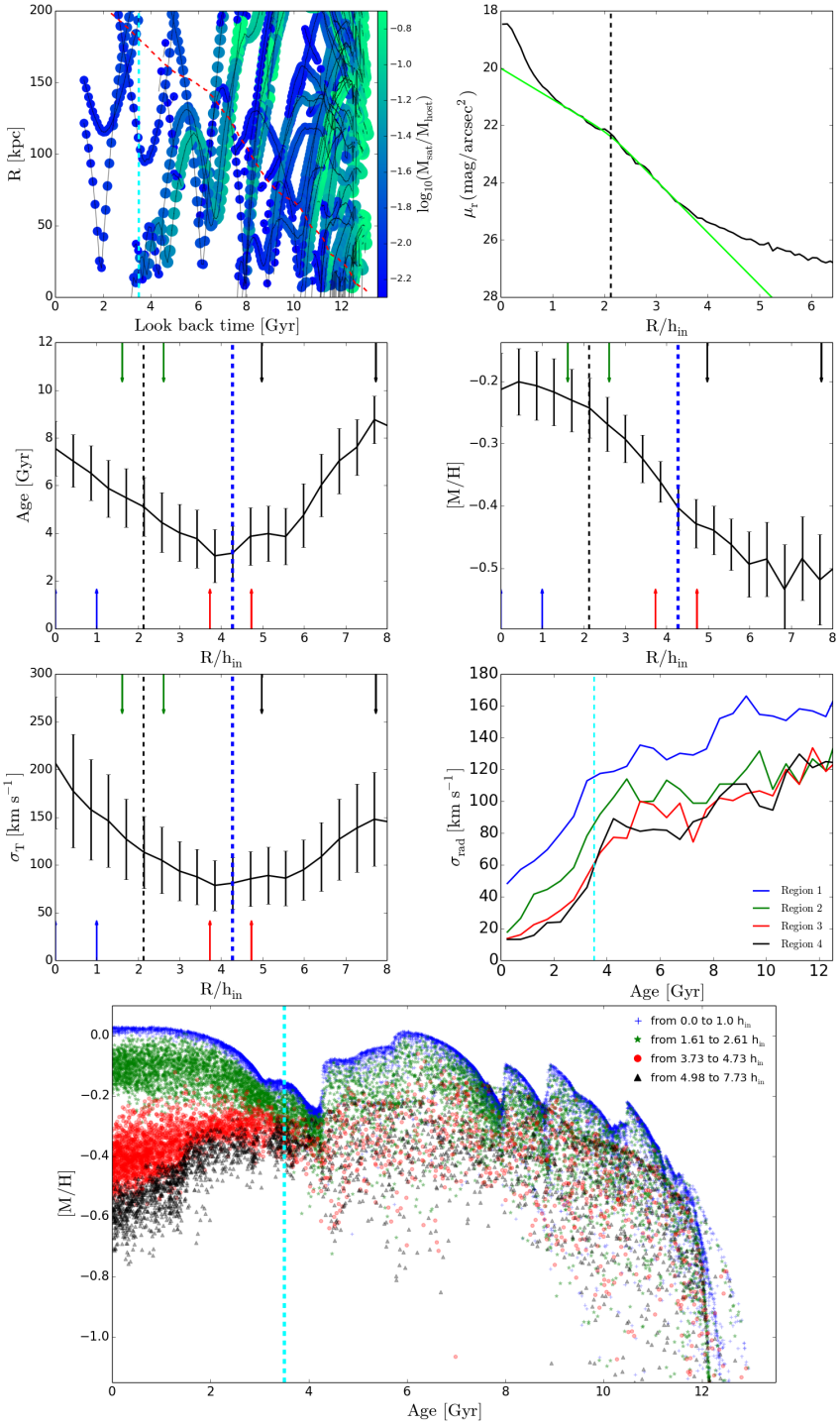

Figure D.1: Apollo.

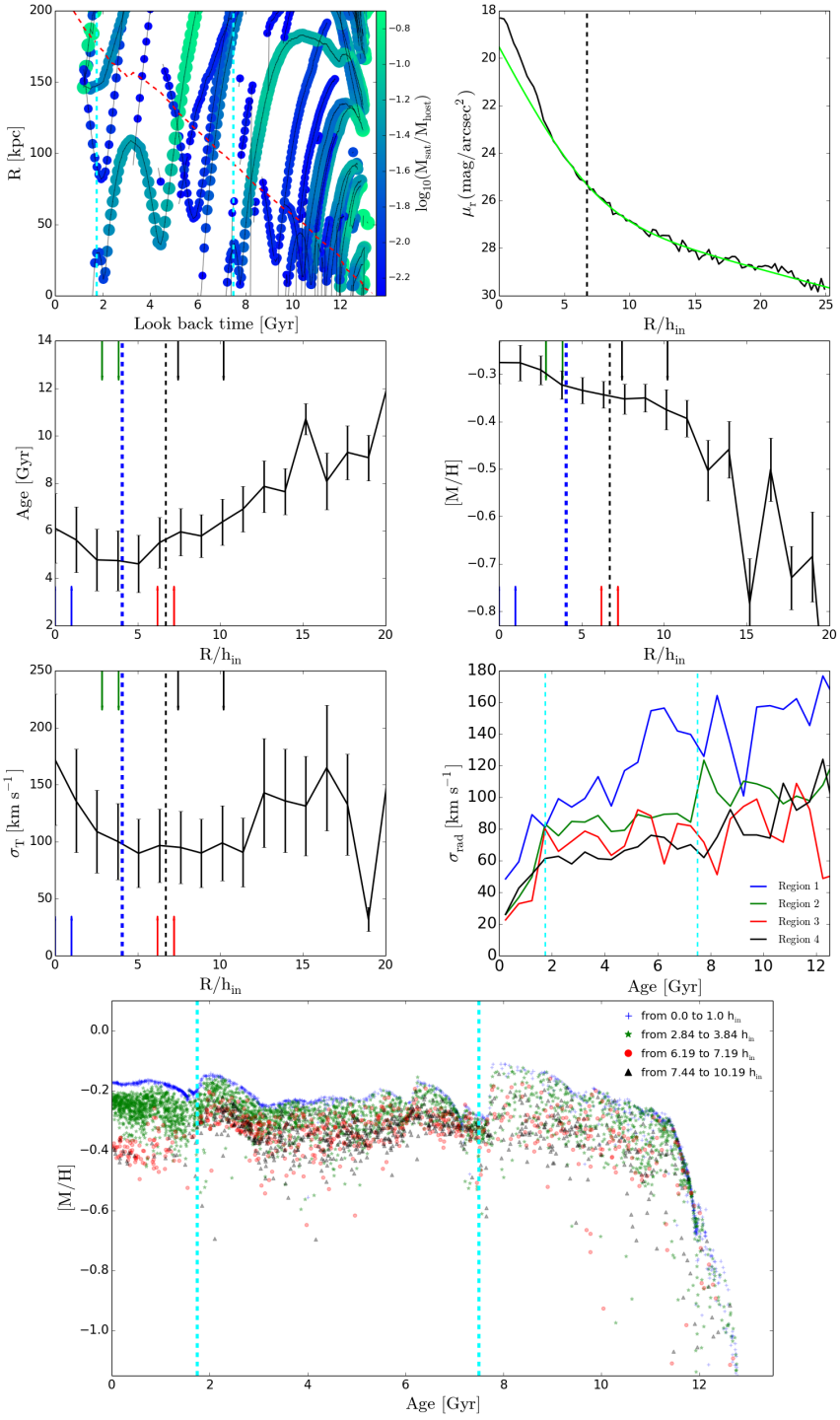

Figure D.2: Artemis.

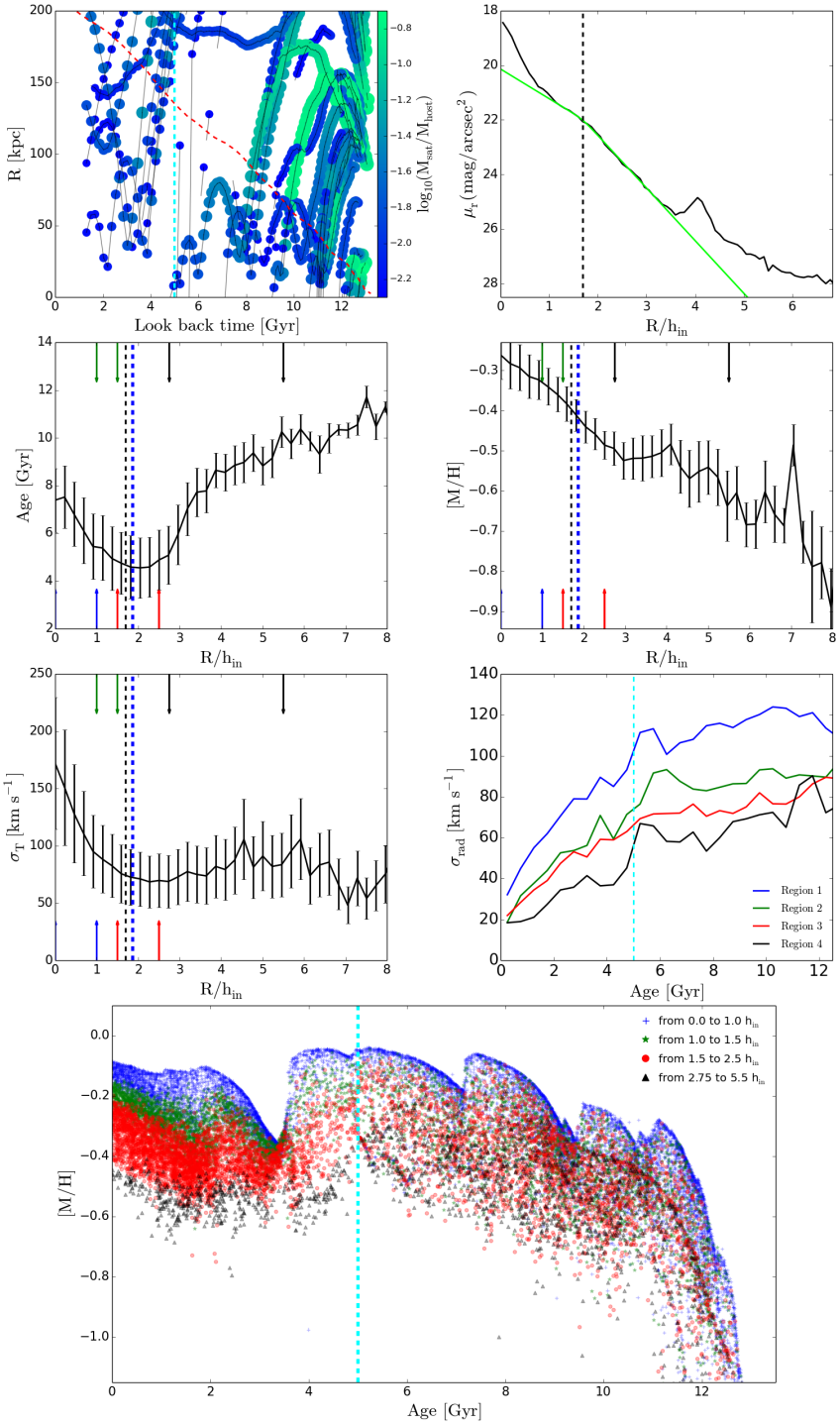

Figure D.3: Atlas.

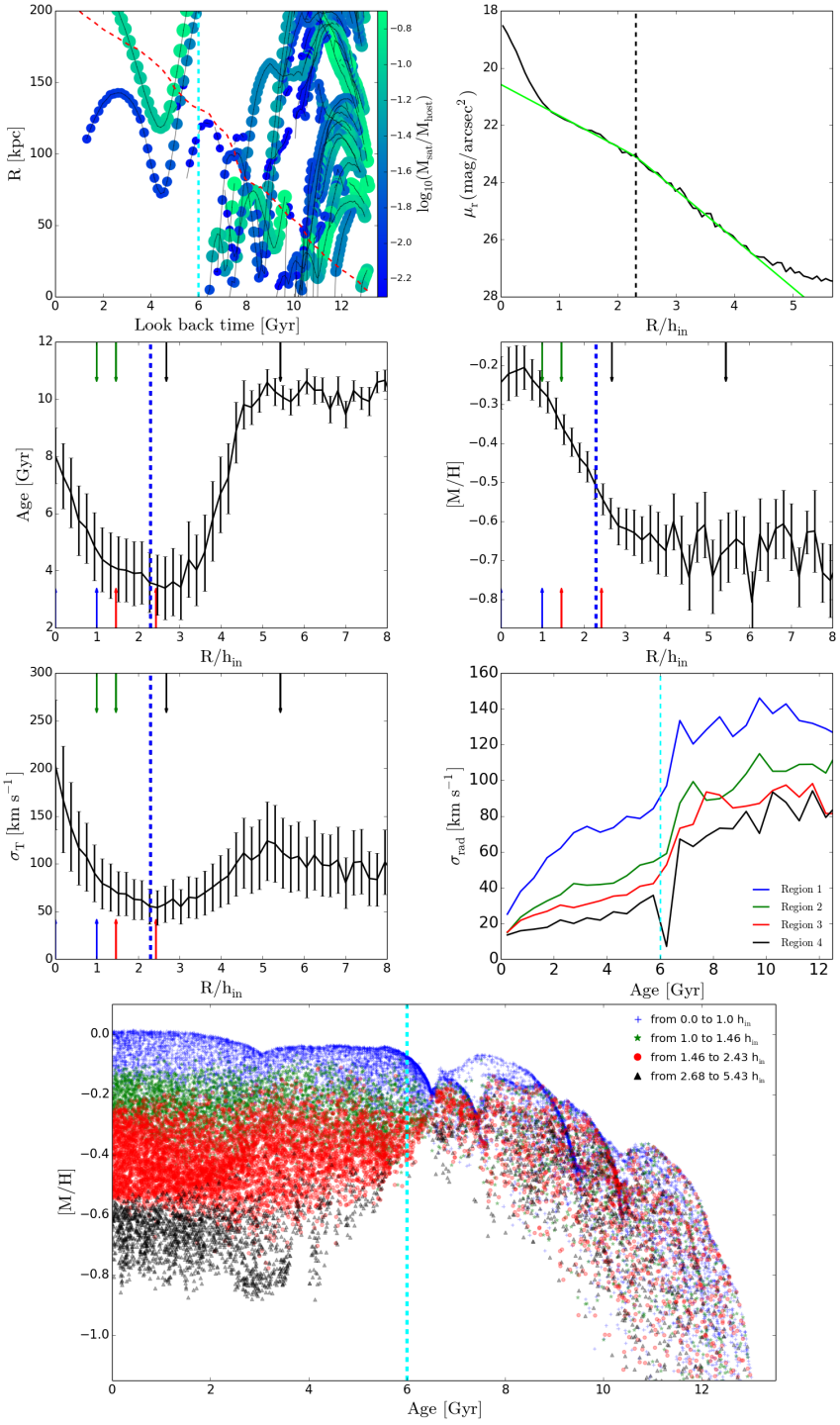

Figure D.4: Ben.

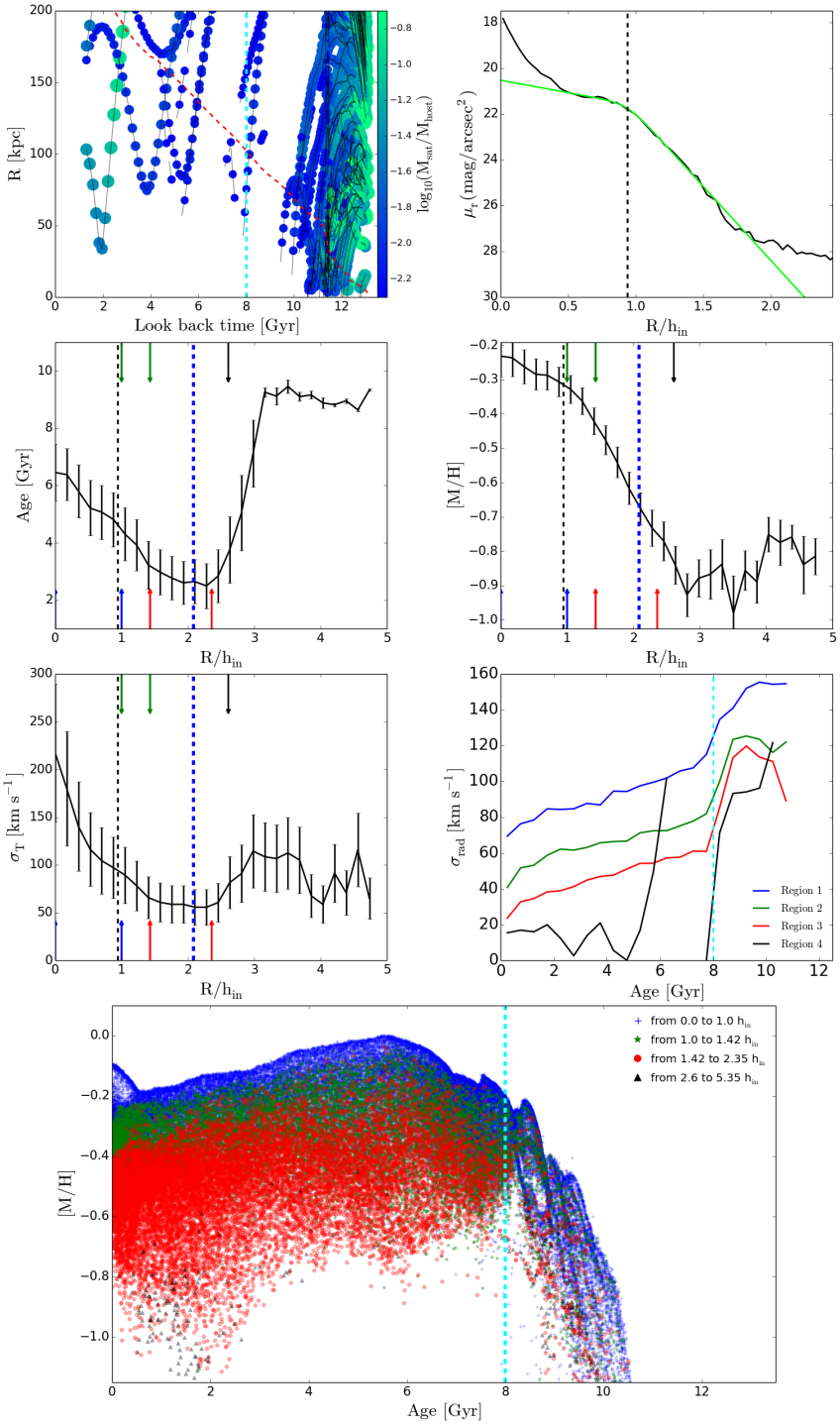

Figure D.5: Castor.

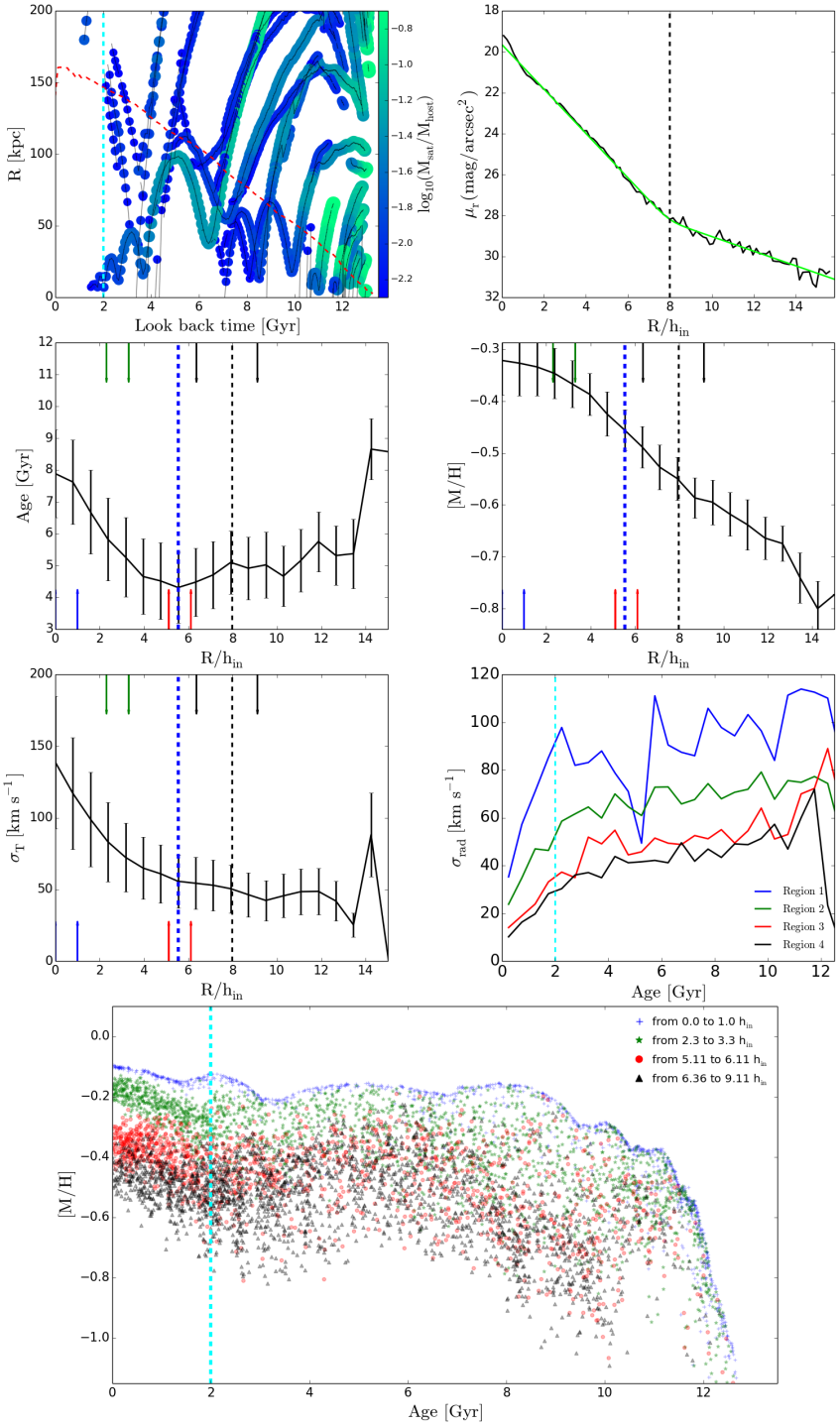

Figure D.6: Daphne.

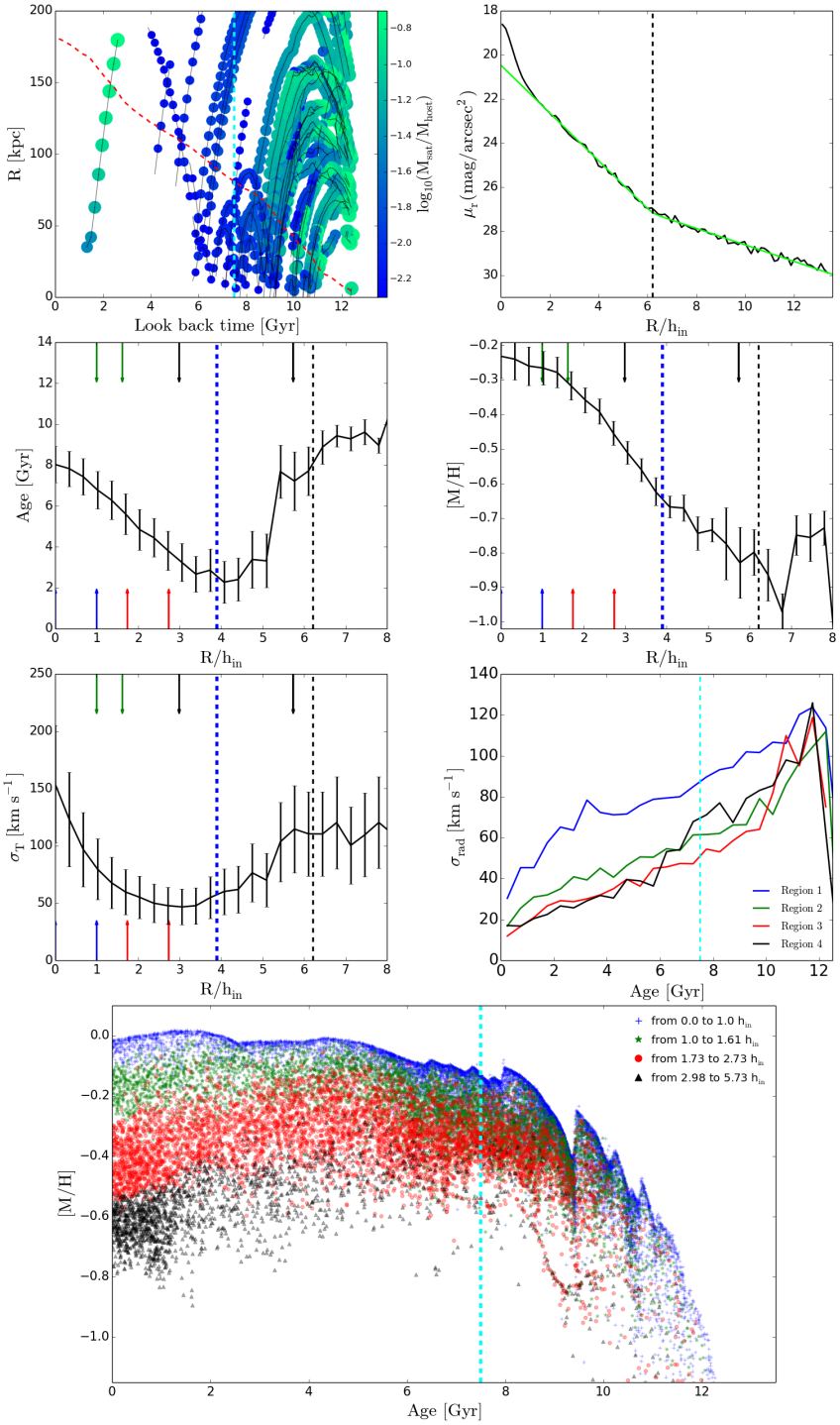

Figure D.7: Eos.

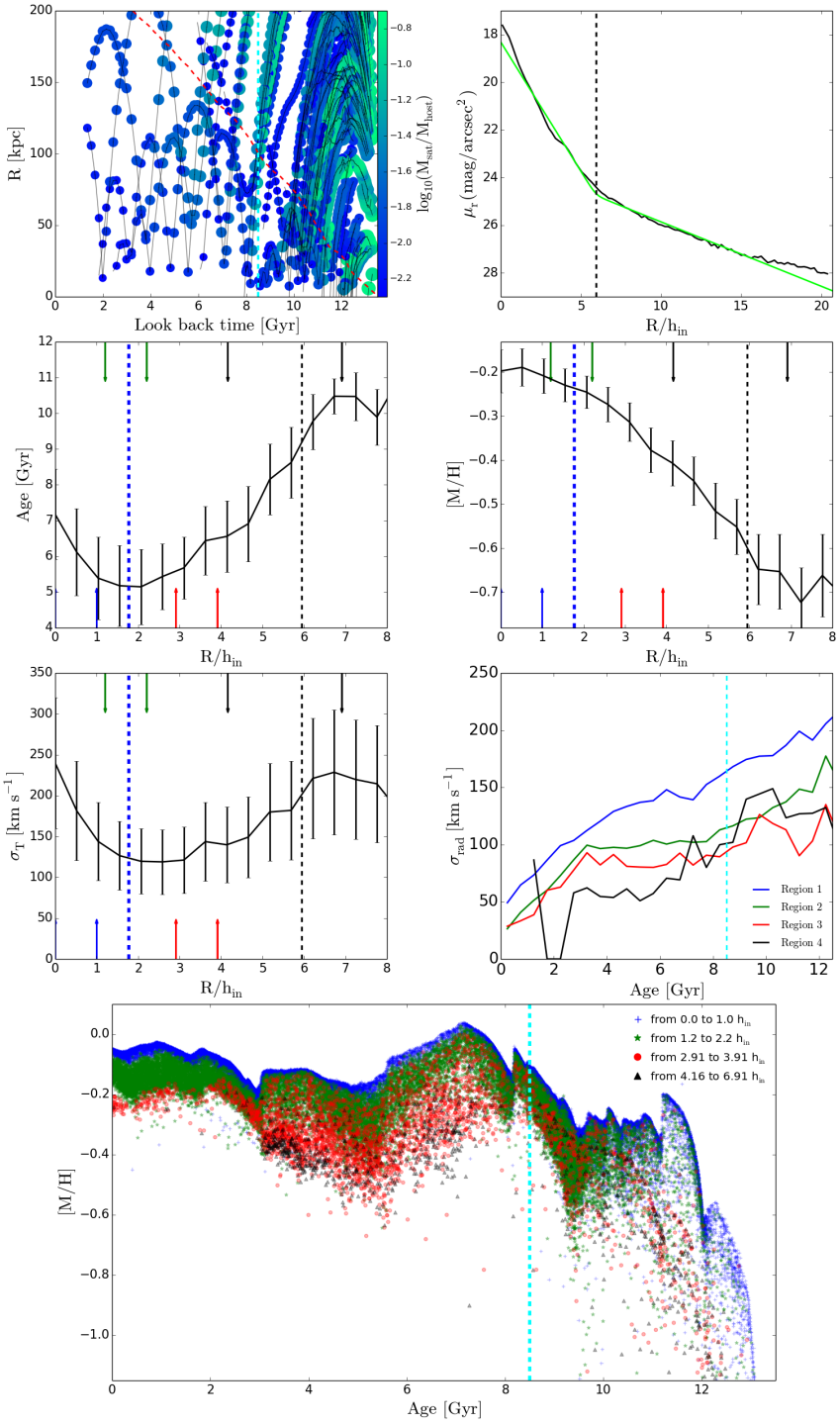

Figure D.8: Helios.

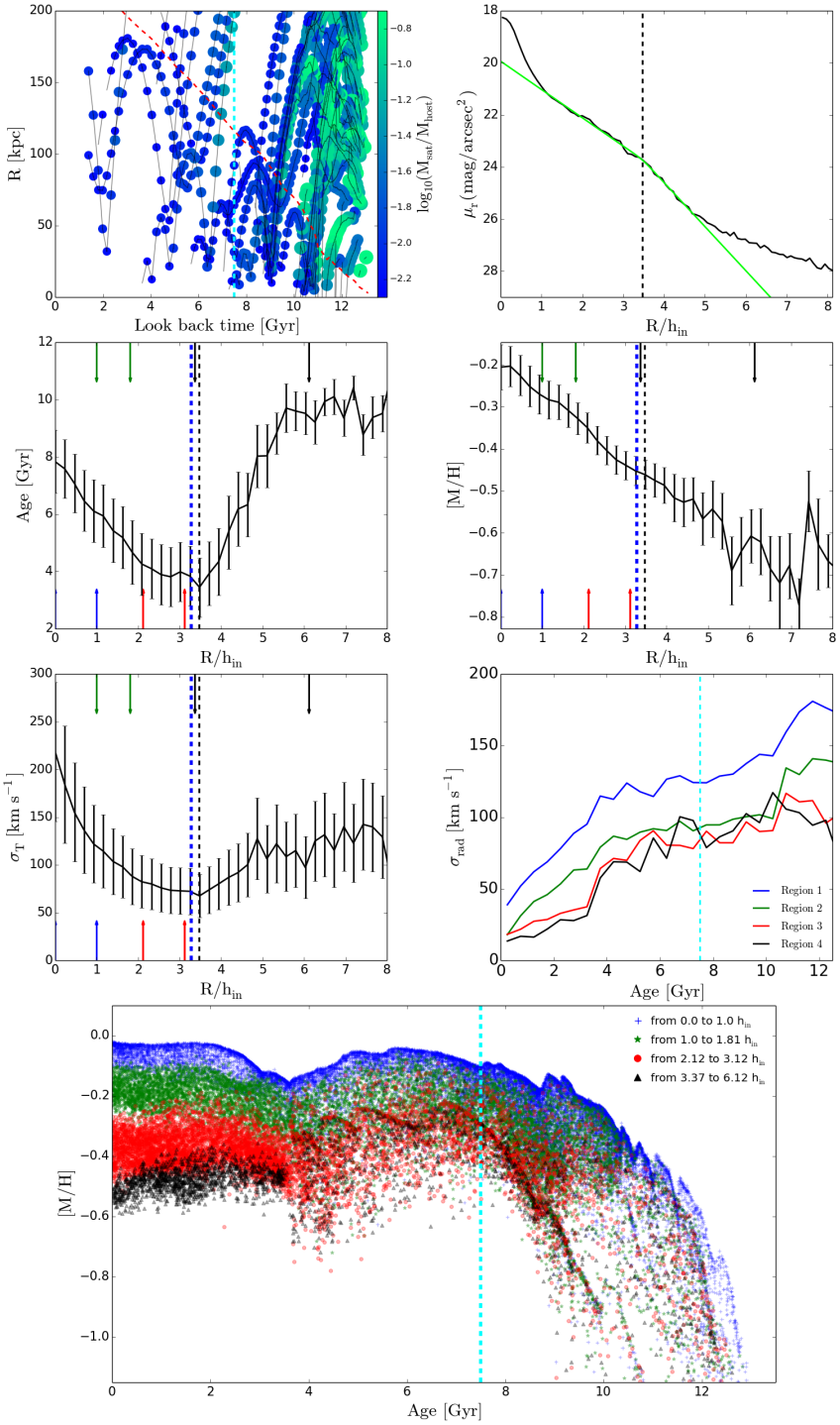

Figure D.9: Hyperion.

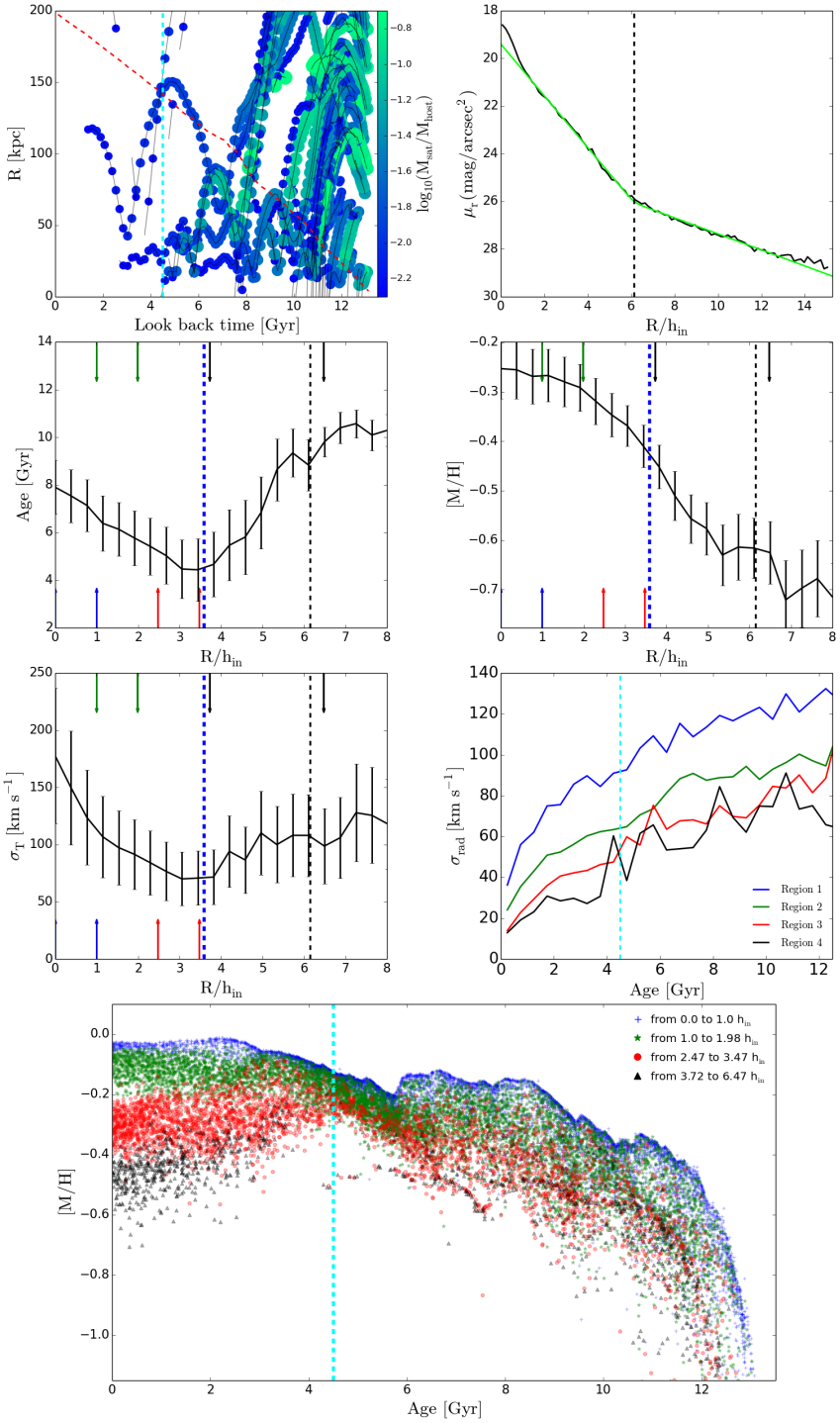

Figure D.10: Krios.

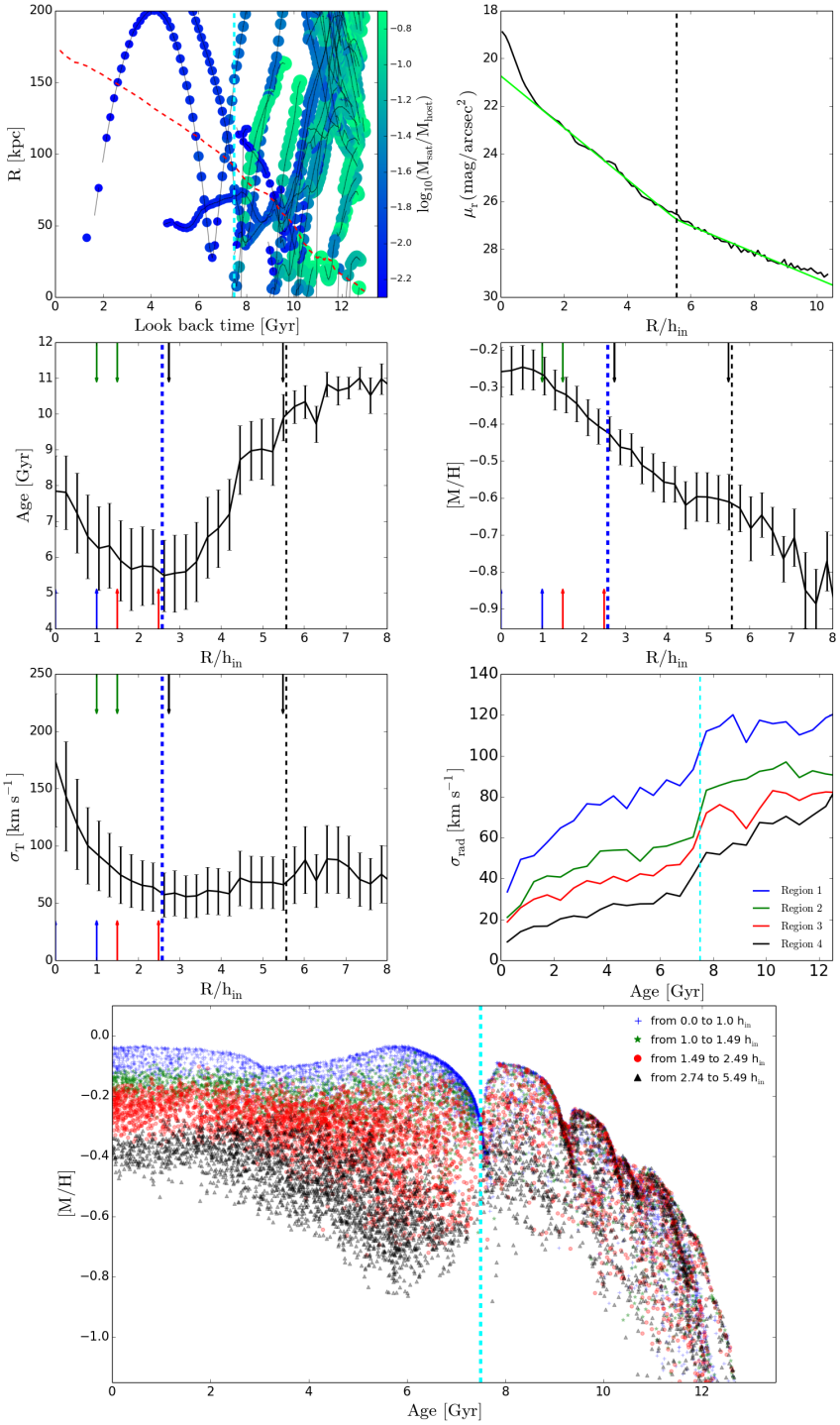

Figure D.11: Leia.

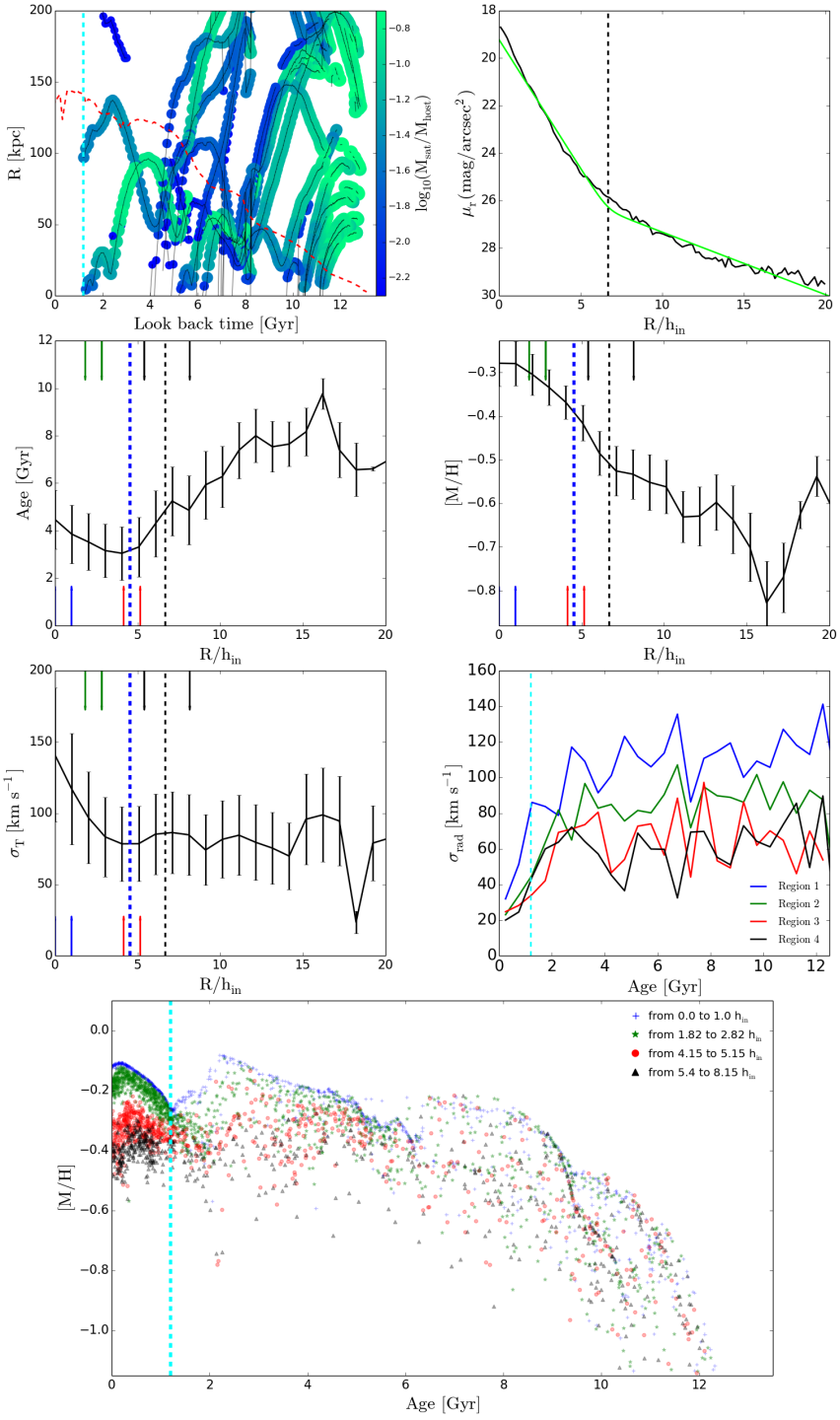

Figure D.12: Leto.

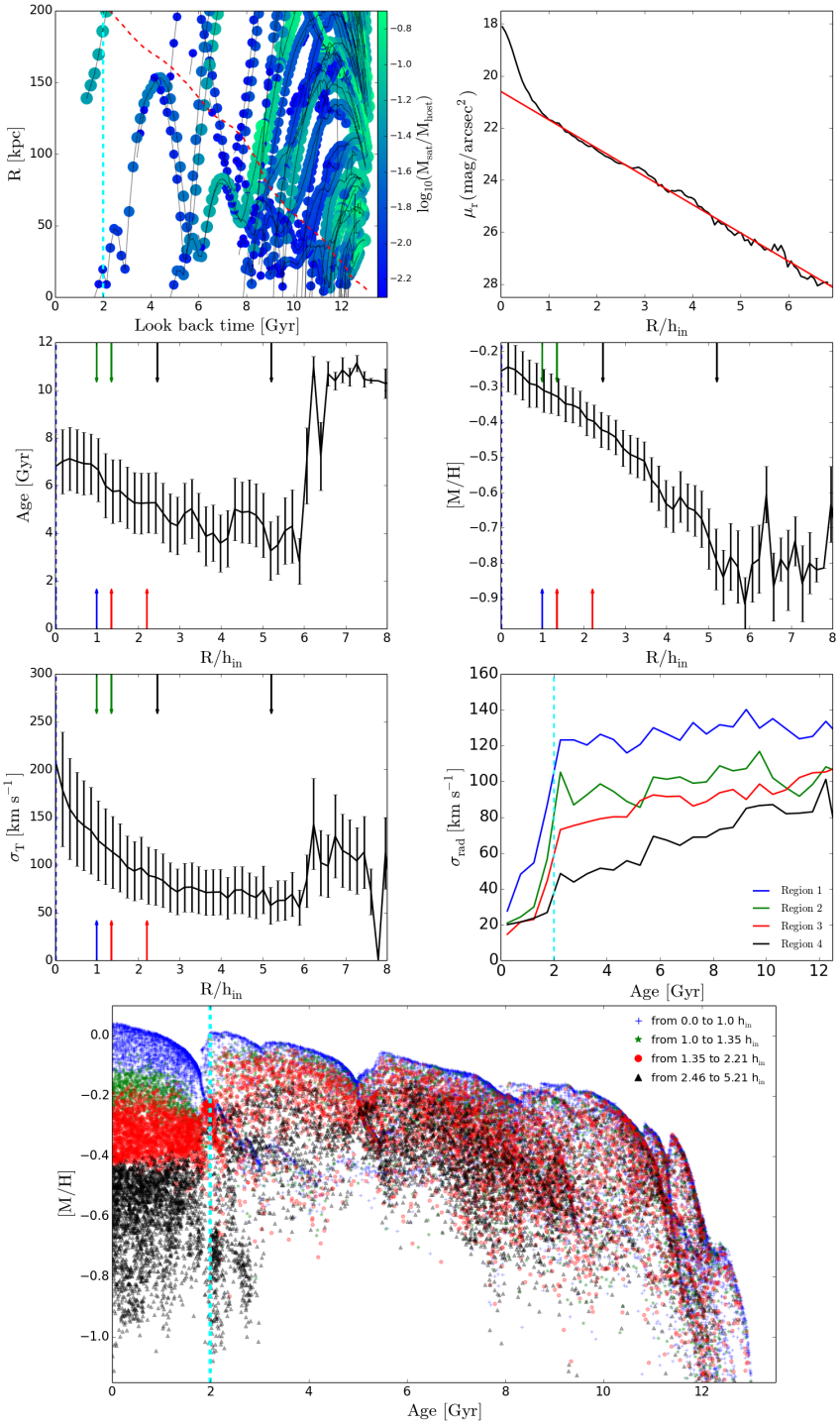

Figure D.13: Luke.

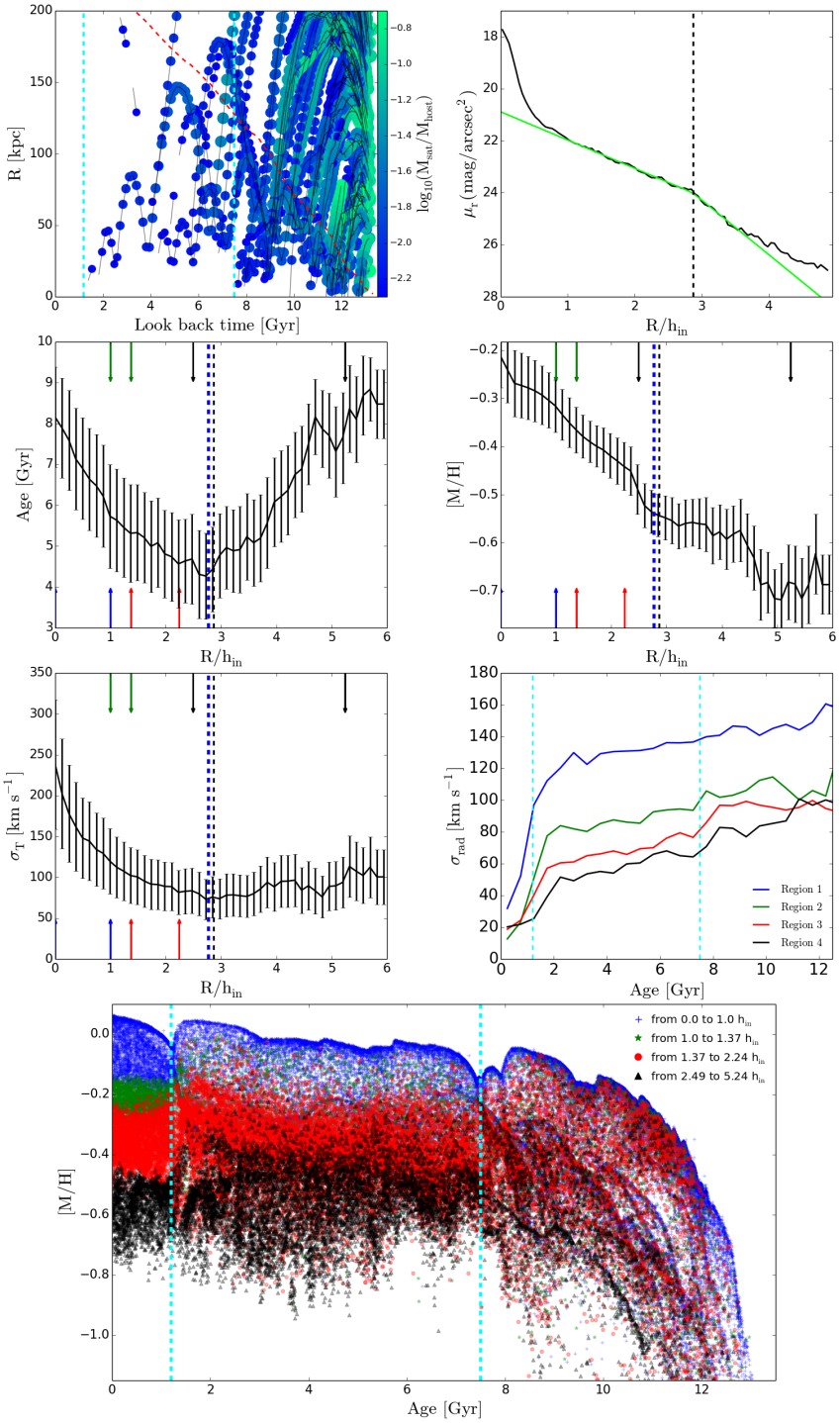

Figure D.14: Oceanus.

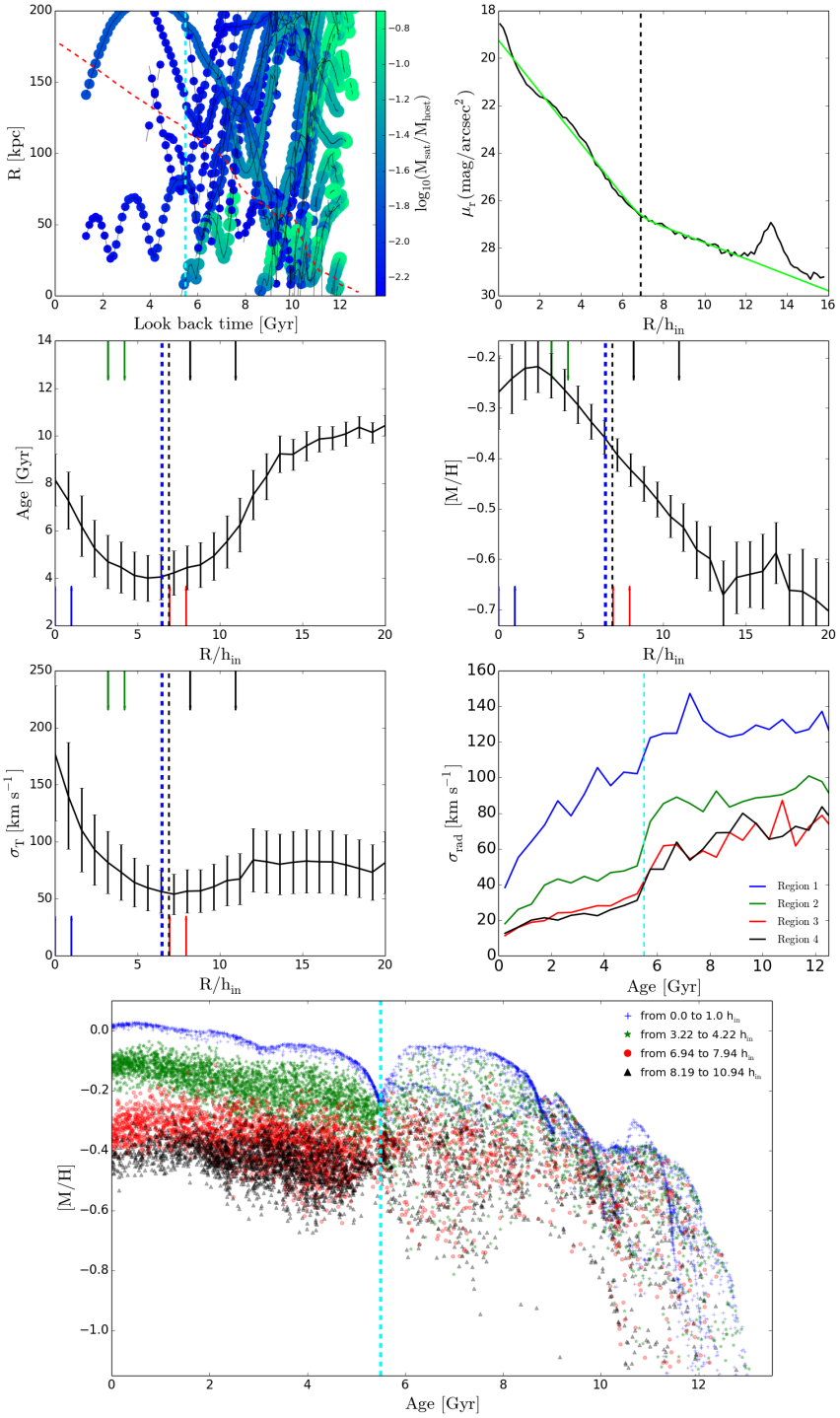

Figure D.15: Pollux.

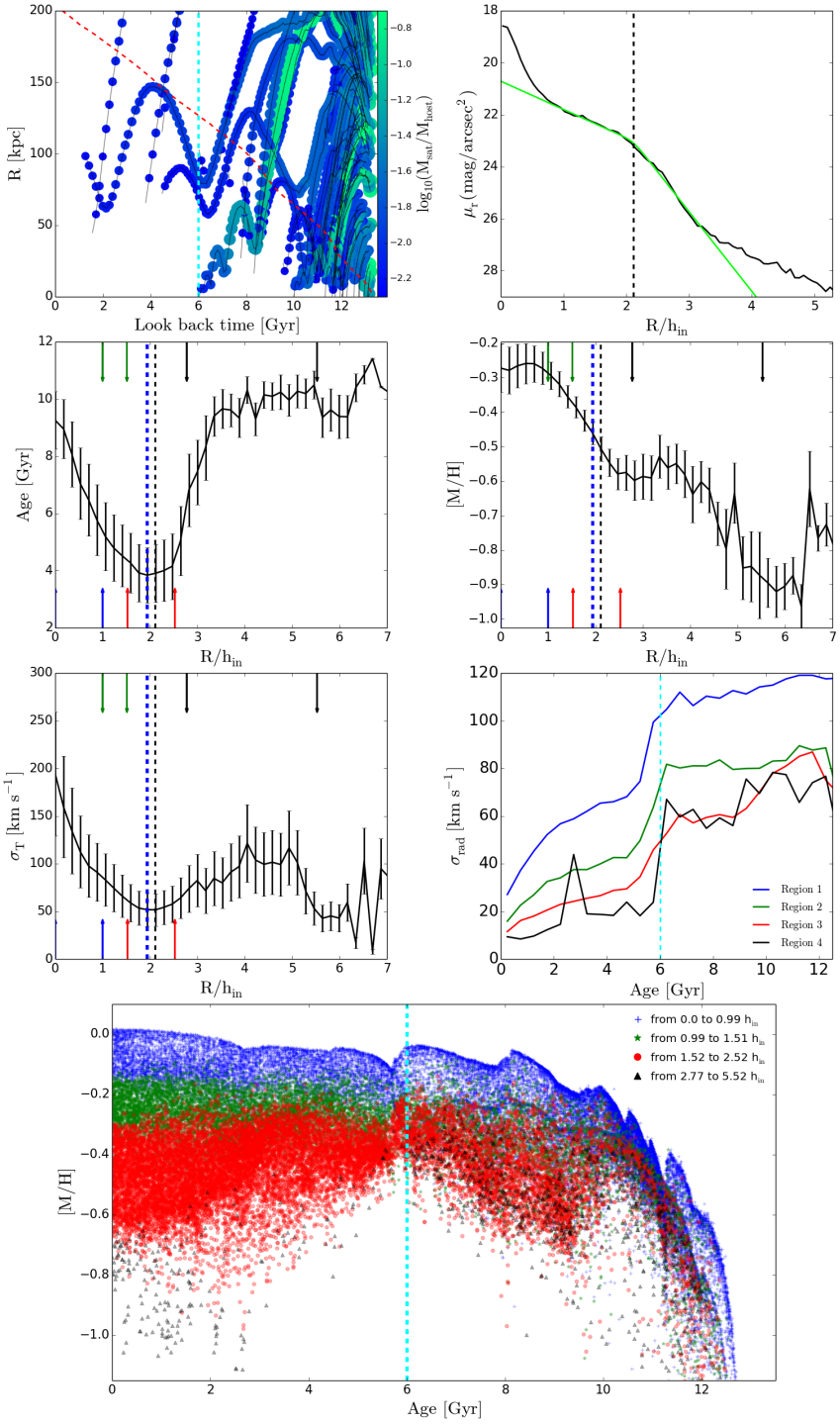

Figure D.16: Selene.

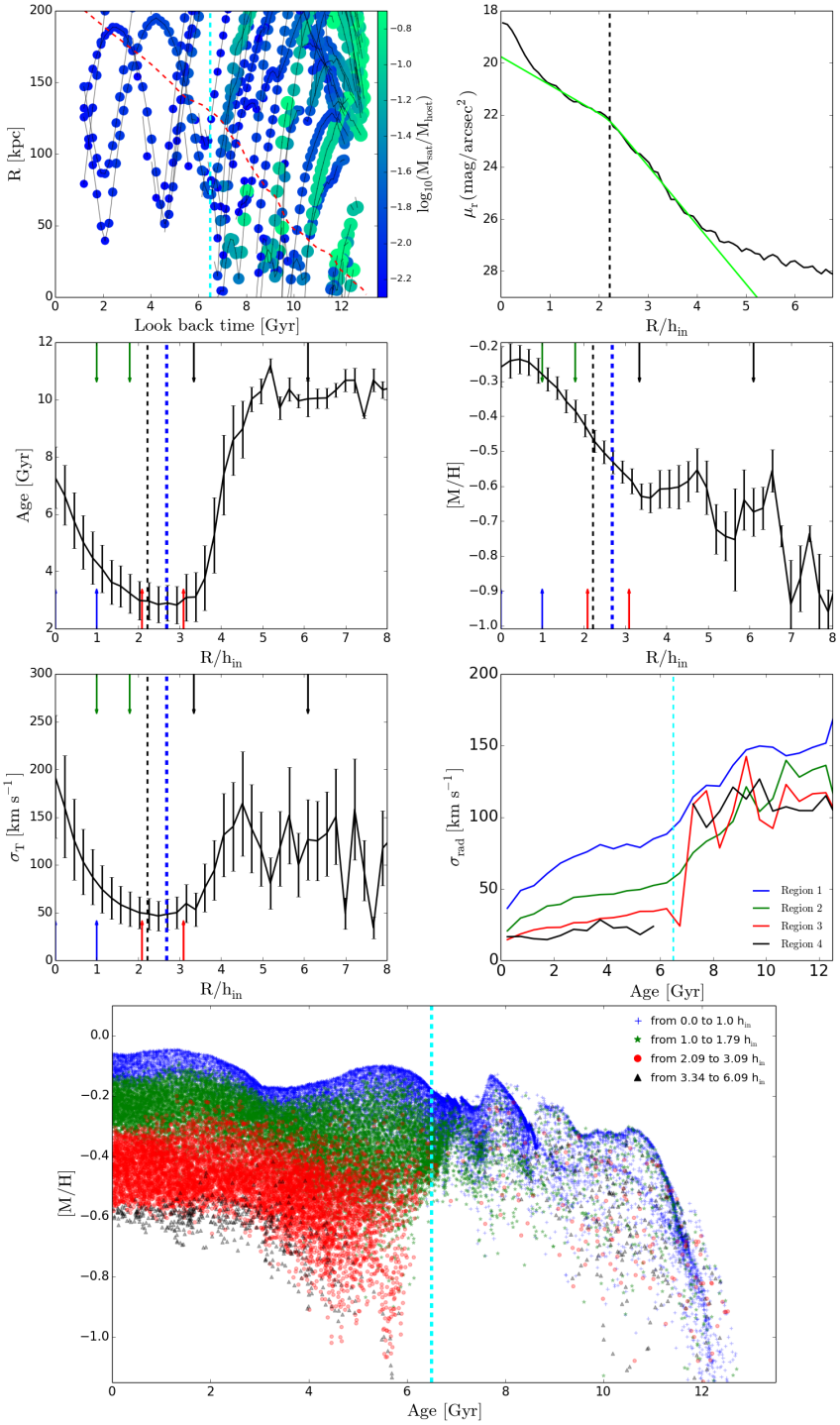

Figure D.17: Tethys.

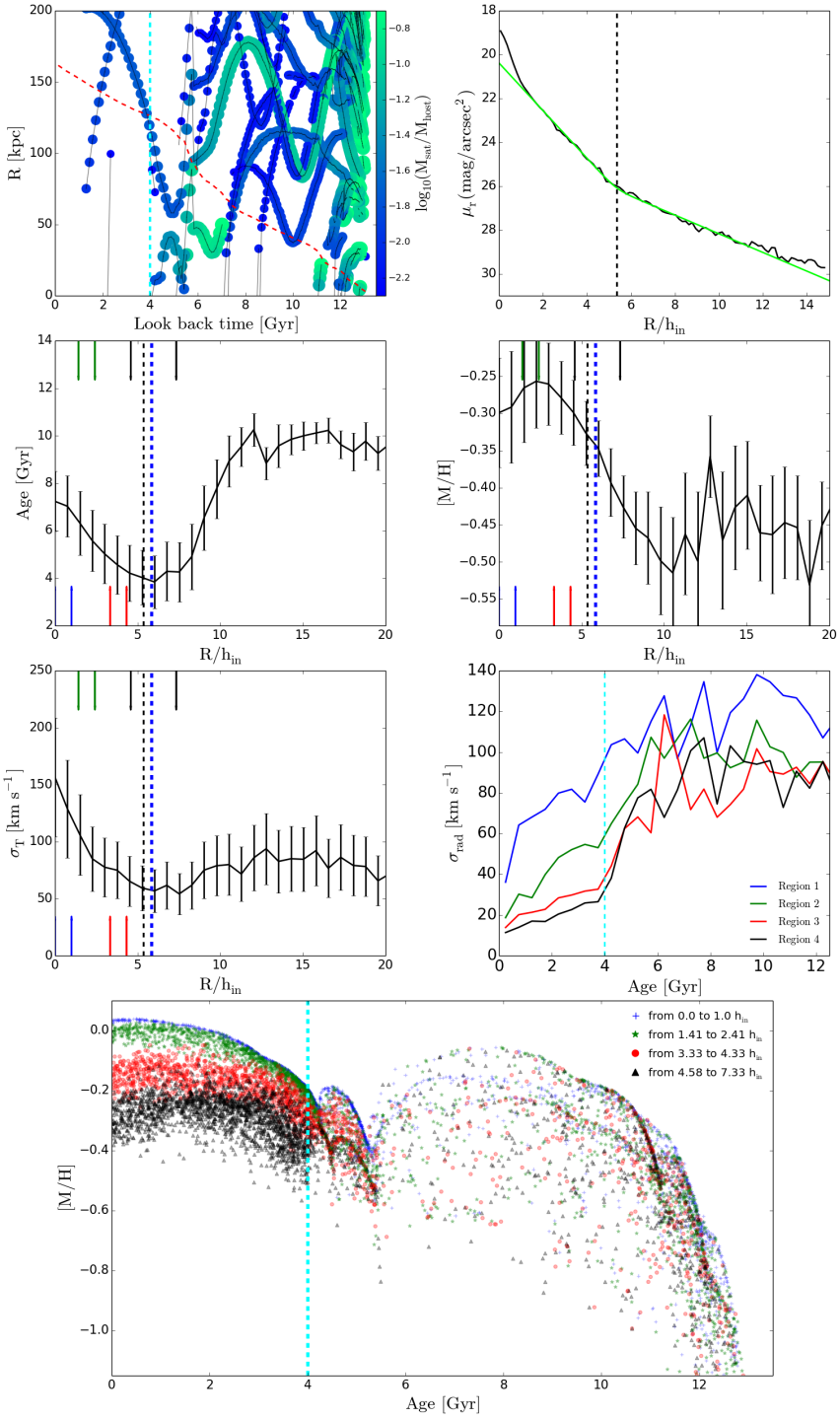

Figure D.18: Tyndareus.

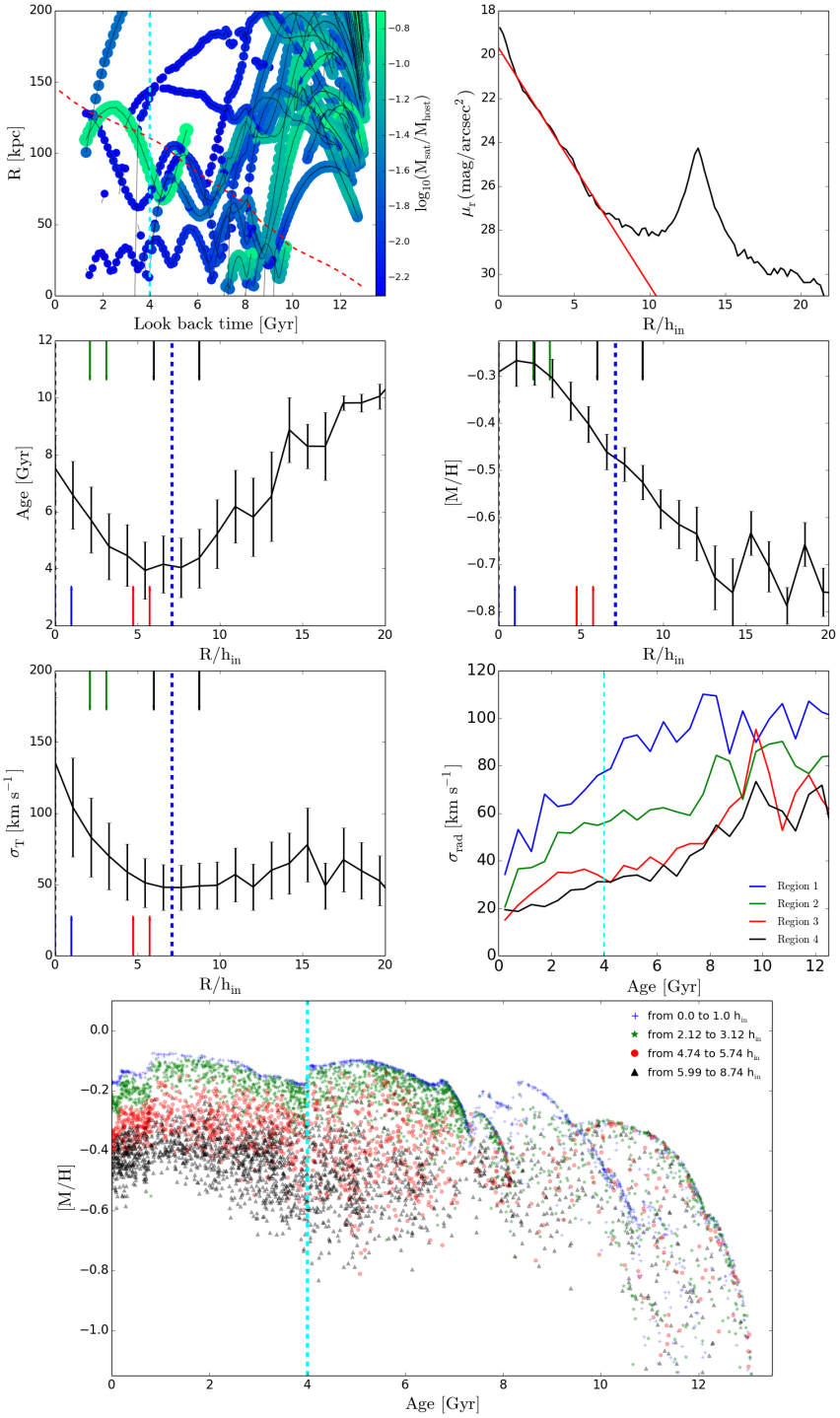

Figure D.19: Zeus.

List of Acronyms

$\mathbf{a_{bar}}$ bar length. 34

ACS Advanced Camera for Surveys. 112

AD Anderson-Darling. 108

AMR Age-Metallicity relation. 50

AURA Association of Universities for Research in Astronomy. 32

AVR Age-Velocity dispersion Relation. 134

CALIFA Calar Alto Legacy Integral Field Area. 22

CMD Colour Magnitude Diagram. 12

e ellipticity. 34

ESO European Southern Observatory. 13

FWHM Full Width at Half Maximum. 28

GANDALF Gas AND Absorption Line Fitting. 49

GASP2D GAlaxy Surface Photometry 2 Dimensional Decomposition. 34

GSS Giant Stellar Stream. 155

$\mathbf{h_{in}}$ inner disc scale-length. 34

$\mathbf{h_{out}}$ outer disc scale-length. 34

HR Hertszprung-Russell. 12

HST Hubble Space Telescope. 21

IAC Instituto de Astrofísica de Canarias. 56

IFS Integral Field Spectroscopy. 16

IFU Integral Field Unit. 27

IMF Initial Mass Function. 12

ISM Interstellar Medium. 12

KS Kolmogorov-Smirnov. 108

L-W light-weighted. 52

LMC Large Magellanic Cloud. 47

LOSVD Line-of-Sight Velocity Distribution. 48

M-W mass-weighted. 52

MC Monte Carlo. 53

MDF Metallicity Distribution Function. 138

MILES Medium resolution INT Library of Empirical Spectra. 49

MS Main Sequence. 14

oMSTO oldest Main-Sequence Turnoff. 14

PA position angle. 34

PMAS Potsdam Multi-Aperture Spectrograph. 25

PPak PMAS fiber Package. 25

pPXF "penalised pixel fitting". 30

PSF Point Spread Function. 34

R_{break} break radius. 17

RaDES Ramses Disc Environment Study. 22

RGB Red Giant Branch. 14

S/N Signal to Noise ratio. 16

SAD Stellar Age Distribution. 50

SB Surface Brightness. 17

SDSS Sloan Digital Sky Survey. 22

SED Spectral Energy Distribution. 12

SExtractor Source Extractor. 32

SFH Star Formation History. 12

SFR Star Formation Rate. 56

SGB Subgiant Branch. 63

SN SuperNova. 121

SPH Smooth Particle Hydrodynamics. 19

SSP Stellar Populations. 71

SSP Single Stellar Population. 15

STECKMAP STEllar Content and Kinematics via Maximum A Posteriori likelihood. 50

ULySS Université de Lyon Spectroscopic analysis Software. 56

WCS World Coordinate Systems. 47

WFPC2 Wide Field and Planetary Camera 2. 57

List of Figures

List of Tables

Index

Bibliography

Abadi, M. G., Navarro, J. F., Steinmetz, M., & Eke, V. R. 2003, ApJ, 597, 21

Abazajian, K. N., Adelman-McCarthy, J. K., Agüeros, M. A., et al. 2009, ApJS, 182, 543

Aguerri, J. A. L., Méndez-Abreu, J., & Corsini, E. M. 2009, A&A, 495, 491

Ahn, C. P., Alexandroff, R., Allende Prieto, C., et al. 2014, ApJS, 211, 17

Alloin, D., Andrillat, Y., & Souffrin, S. 1971, A&A, 10, 401

Alloin, D., Gallart, C., Fleurence, E., et al. 2002, Ap&SS, 281, 109

Aparicio, A. & Gallart, C. 2004, AJ, 128, 1465

Aparicio, A. & Hidalgo, S. L. 2009, AJ, 138, 558

Astropy Collaboration, Robitaille, T. P., Tollerud, E. J., et al. 2013, A&A, 558, A33

Athanassoula, E. 2005, MNRAS, 358, 1477

Athanassoula, E., Morin, S., Wozniak, H., et al. 1990, MNRAS, 245, 130

Athanassoula, E., Romero-Gómez, M., Bosma, A., & Masdemont, J. J. 2009a, MNRAS, 400, 1706

Athanassoula, E., Romero-Gómez, M., Bosma, A., & Masdemont, J. J. 2010, MNRAS, 407, 1433

Athanassoula, E., Romero-Gómez, M., & Masdemont, J. J. 2009b, MNRAS, 394, 67

Aubert, D., Pichon, C., & Colombi, S. 2004, MNRAS, 352, 376

Aumer, M. & Binney, J. J. 2009, MNRAS, 397, 1286

Azzollini, R., Trujillo, I., & Beckman, J. E. 2008, ApJ, 684, 1026

Bacon, R., Accardo, M., Adjali, L., et al. 2010, in Society of Photo-Optical Instrumentation Engineers (SPIE) Conference Series, Vol. 7735, Society of Photo-Optical Instrumentation Engineers (SPIE) Conference Series, 8

Bakos, J., Trujillo, I., & Pohlen, M. 2008, ApJ, 683, L103

Barber, C., Courteau, S., Roediger, J. C., & Schiavon, R. P. 2014, MNRAS, 440, 2953

Barker, M. K., Ferguson, A. M. N., Cole, A. A., et al. 2011, MNRAS, 410, 504

Barrera-Ballesteros, J. K., Falcón-Barroso, J., García-Lorenzo, B., et al. 2014, A&A, 568, A70

Barrera-Ballesteros, J. K., García-Lorenzo, B., Falcón-Barroso, J., et al. 2015, A&A, 582, A21

Battaner, E., Florido, E., & Jiménez-Vicente, J. 2002, A&A, 388, 213

Beasley, M. A., Hoyle, F., & Sharples, R. M. 2002, MNRAS, 336, 168

Beasley, M. A., San Roman, I., Gallart, C., Sarajedini, A., & Aparicio, A. 2015, MNRAS, 451, 3400

Bell, E. F. & de Jong, R. S. 2000, MNRAS, 312, 497

Bell, E. F. & de Jong, R. S. 2001, ApJ, 550, 212

Bergemann, M., Ruchti, G. R., Serenelli, A., et al. 2014, A&A, 565, A89

Bernard, E. J., Ferguson, A. M. N., Barker, M. K., et al. 2012, MNRAS, 420, 2625

Bernard, E. J., Ferguson, A. M. N., Richardson, J. C., et al. 2015, MNRAS, 446, 2789

Bershady, M. A., Verheijen, M. A. W., Swaters, R. A., et al. 2010, ApJ, 716, 198

Bertin, E. & Arnouts, S. 1996, A&AS, 117, 393

Bica, E. 1988, A&A, 195, 76

Bica, E. & Alloin, D. 1986a, A&A, 162, 21

Bica, E. & Alloin, D. 1986b, A&AS, 66, 171

Bica, E. & Alloin, D. 1987, A&AS, 70, 281

Bica, E., Alloin, D., & Schmitt, H. R. 1994, A&A, 283, 805

Bica, E., Arimoto, N., & Alloin, D. 1988, A&A, 202, 8

Binney, J., Dehnen, W., & Bertelli, G. 2000, MNRAS, 318, 658

Bird, J. C., Kazantzidis, S., & Weinberg, D. H. 2012, MNRAS, 420, 913

Blanc, G. A., Weinzirl, T., Song, M., et al. 2013, AJ, 145, 138

Bland-Hawthorn, J., Vlajić, M., Freeman, K. C., & Draine, B. T. 2005, ApJ, 629, 239

Bressan, A., Marigo, P., Girardi, L., et al. 2012, MNRAS, 427, 127

Brook, C. B., Kawata, D., Gibson, B. K., & Freeman, K. C. 2004, ApJ, 612, 894

Brook, C. B., Stinson, G., Gibson, B. K., Wadsley, J., & Quinn, T. 2012, MNRAS, 424, 1275

Brooks, A. M., Solomon, A. R., Governato, F., et al. 2011, ApJ, 728, 51

Bruzual, G. & Charlot, S. 2003, MNRAS, 344, 1000 (BC03)

Buzzoni, B., Delabre, B., Dekker, H., et al. 1984, The Messenger, 38, 9

Calura, F., Gibson, B. K., Michel-Dansac, L., et al. 2012, MNRAS, 427, 1401

Caon, N., Capaccioli, M., & D'Onofrio, M. 1993, MNRAS, 265, 1013

Cappellari, M. & Copin, Y. 2003, MNRAS, 342, 345

Cappellari, M. & Emsellem, E. 2004, PASP, 116, 138

Cappellari, M., Emsellem, E., Krajnović, D., et al. 2011, MNRAS, 413, 813

Carlberg, R. G., Dawson, P. C., Hsu, T., & Vandenberg, D. A. 1985, ApJ, 294, 674

Carrera, R., Gallart, C., Hardy, E., Aparicio, A., & Zinn, R. 2008, AJ, 135, 836

Catinella, B., Schiminovich, D., Cortese, L., et al. 2013, MNRAS, 436, 34

Cenarro, A. J., Peletier, R. F., Sánchez-Blázquez, P., et al. 2007, MNRAS, 374, 664

Cid Fernandes, R., Gu, Q., Melnick, J., et al. 2004, MNRAS, 355, 273

Cid Fernandes, R., Mateus, A., Sodré, L., Stasińska, G., & Gomes, J. M. 2005, MNRAS, 358, 363

Cid Fernandes, R., Pérez, E., García Benito, R., et al. 2013, A&A, 557, A86

Cole, A. A., Skillman, E. D., Tolstoy, E., et al. 2007, ApJ, 659, L17

Conroy, C., Gunn, J. E., & White, M. 2009, ApJ, 699, 486

Croom, S. M., Lawrence, J. S., Bland-Hawthorn, J., et al. 2012, MNRAS, 421, 872

de Boer, T. J. L., Tolstoy, E., Hill, V., et al. 2012, A&A, 544, A73

de Grijs, R. & Anders, P. 2006, MNRAS, 366, 295

de Grijs, R., Kregel, M., & Wesson, K. H. 2001, MNRAS, 324, 1074

de Jong, R. S. 1996, A&A, 313, 377

de Jong, R. S., Bellido-Tirado, O., Chiappini, C., et al. 2012, in Society of Photo-Optical Instrumentation Engineers (SPIE) Conference Series, Vol. 8446, Society of Photo-Optical Instrumentation Engineers (SPIE) Conference Series

de Vaucouleurs, G. 1958, ApJ, 128, 465

de Vaucouleurs, G. & de Vaucouleurs, A. 1959, PASP, 71, 83

de Vaucouleurs, G., de Vaucouleurs, A., Corwin, Jr., H. G., et al. 1991, Third Reference Catalogue of Bright Galaxies. Volume I: Explanations and references. Volume II: Data for galaxies between 0^h and 12^h. Volume III: Data for galaxies between 12^h and 24^h.

Debattista, V. P., Mayer, L., Carollo, C. M., et al. 2006, ApJ, 645, 209

Dekel, A. & Birnboim, Y. 2006, MNRAS, 368, 2

den Brok, M., Peletier, R. F., Valentijn, E. A., et al. 2011, MNRAS, 414, 3052

Dirsch, B., Richtler, T., Gieren, W. P., & Hilker, M. 2000, A&A, 360, 133

Dolphin, A. E. 2002, MNRAS, 332, 91

Donzelli, C. J. & Pastoriza, M. G. 2000, AJ, 120, 189

Dressler, A. 1980, ApJ, 236, 351

Edvardsson, B., Andersen, J., Gustafsson, B., et al. 1993, A&A, 275, 101

Elmegreen, B. G. & Hunter, D. A. 2006, ApJ, 636, 712

Erwin, P. 2015, ApJ, 799, 226

Erwin, P., Beckman, J. E., & Pohlen, M. 2005, ApJ, 626, L81

Erwin, P., Pohlen, M., & Beckman, J. E. 2008, AJ, 135, 20 (E08)

Faber, S. M., Friel, E. D., Burstein, D., & Gaskell, C. M. 1985, ApJS, 57, 711

Falcón-Barroso, J., Bacon, R., Bureau, M., et al. 2006, MNRAS, 369, 529

Feltzing, S., Holmberg, J., & Hurley, J. R. 2001, A&A, 377, 911

Fenner, Y. & Gibson, B. K. 2003, PASA, 20, 189

Ferguson, H. C. 1994, in European Southern Observatory Conference and Workshop Proceedings, Vol. 49, European Southern Observatory Conference and Workshop Proceedings, ed. G. Meylan & P. Prugniel, 475

Ferrers, N. M. 1877, Quart. J. Pure and Appl. Math, 14, 1

Few, C. G., Courty, S., Gibson, B. K., Michel-Dansac, L., & Calura, F. 2014, MNRAS, 444, 3845

Few, C. G., Gibson, B. K., Courty, S., et al. 2012, A&A, 547, A63

Florido, E., Battaner, E., Guijarro, A., Garzón, F., & Castillo-Morales, A. 2006, A&A, 455, 467

Florido, E., Battaner, E., Guijarro, A., Garzón, F., & Jiménez-Vicente, J. 2001, A&A, 378, 82

Florido, E., Battaner, E., Zurita, A., & Guijarro, A. 2007, A&A, 472, L39

Freeman, K. C. 1970, ApJ, 160, 811

Gallart, C., Freedman, W. L., Aparicio, A., Bertelli, G., & Chiosi, C. 1999, AJ, 118, 2245

Gallart, C., Stetson, P. B., Meschin, I. P., Pont, F., & Hardy, E. 2008, ApJ, 682, L89

Gallart, C., Zoccali, M., & Aparicio, A. 2005, ARA&A, 43, 387

Ganda, K., Peletier, R. F., Balcells, M., & Falcón-Barroso, J. 2009, MNRAS, 395, 1669

García-Benito, R. & Pérez-Montero, E. 2012, MNRAS, 423, 406

García-Benito, R., Zibetti, S., Sánchez, S. F., et al. 2015, A&A, 576, A135

García-Lorenzo, B., Márquez, I., Barrera-Ballesteros, J. K., et al. 2015, A&A, 573, A59

Gerhard, O. E. 1993, MNRAS, 265, 213

Gibson, B. K., Madgwick, D. S., Jones, L. A., Da Costa, G. S., & Norris, J. E. 1999, AJ, 118, 1268

Gibson, B. K., Pilkington, K., Brook, C. B., Stinson, G. S., & Bailin, J. 2013, A&A, 554, A47

Gil de Paz, A., Madore, B. F., Boissier, S., et al. 2005, ApJ, 627, L29

Gil de Paz, A., Madore, B. F., Boissier, S., et al. 2007, ApJ, 661, 115

Girardi, L., Bressan, A., Bertelli, G., & Chiosi, C. 2000a, A&AS, 141, 371

Girardi, L., Bressan, A., Bertelli, G., & Chiosi, C. 2000b, A&AS, 141, 371

González Delgado, R. M., Cerviño, M., Martins, L. P., Leitherer, C., & Hauschildt, P. H. 2005, MNRAS, 357, 945 (GD05)

González Delgado, R. M. & Cid Fernandes, R. 2010, MNRAS, 403, 797

González Delgado, R. M., García-Benito, R., Pérez, E., et al. 2015, A&A, 581, A103

González Delgado, R. M., Pérez, E., Cid Fernandes, R., et al. 2014, A&A, 562, A47

Gordon, K. D., Clayton, G. C., Misselt, K. A., Landolt, A. U., & Wolff, M. J. 2003, ApJ, 594, 279

Gorgas, J., Faber, S. M., Burstein, D., et al. 1993, ApJS, 86, 153

Governato, F., Mayer, L., Wadsley, J., et al. 2004, ApJ, 607, 688

Governato, F., Willman, B., Mayer, L., et al. 2007, MNRAS, 374, 1479

Grocholski, A. J., Cole, A. A., Sarajedini, A., Geisler, D., & Smith, V. V. 2006, AJ, 132, 1630

Gutiérrez, L., Erwin, P., Aladro, R., & Beckman, J. E. 2011, AJ, 142, 145 (G11)

Halle, A., Di Matteo, P., Haywood, M., & Combes, F. 2015, A&A, 578, A58

Haywood, M., Di Matteo, P., Lehnert, M. D., Katz, D., & Gómez, A. 2013, A&A, 560, A109

Hearnshaw, J. B. 1972, MmRAS, 77, 55

Heavens, A. F., Jimenez, R., & Lahav, O. 2000, MNRAS, 317, 965

Herpich, J., Stinson, G. S., Dutton, A. A., et al. 2015a, MNRAS, 448, L99

Herpich, J., Stinson, G. S., Rix, H.-W., Martig, M., & Dutton, A. A. 2015b, ArXiv e-prints [[arXiv]1511.04442]

Hidalgo, S. L., Aparicio, A., Martínez-Delgado, D., & Gallart, C. 2009, ApJ, 705, 704

Hidalgo, S. L., Aparicio, A., Skillman, E., et al. 2011, ApJ, 730, 14

Hidalgo, S. L., Monelli, M., Aparicio, A., et al. 2013, ApJ, 778, 103

Hill, G. J., MacQueen, P. J., Smith, M. P., et al. 2008, in Society of Photo-Optical Instrumentation Engineers (SPIE) Conference Series, Vol. 7014, Society of Photo-Optical Instrumentation Engineers (SPIE) Conference Series, 70

Hinshaw, G., Larson, D., Komatsu, E., et al. 2013, ApJS, 208, 19

Holmberg, J., Nordström, B., & Andersen, J. 2009, A&A, 501, 941

Holtzman, J. A., Afonso, C., & Dolphin, A. 2006, ApJS, 166, 534

House, E. L., Brook, C. B., Gibson, B. K., et al. 2011, MNRAS, 415, 2652

Hummels, C. B. & Bryan, G. L. 2012, ApJ, 749, 140

Hunter, J. D. 2007, Computing In Science & Engineering, 9, 90

Husemann, B., Jahnke, K., Sánchez, S. F., et al. 2013, A&A, 549, A87

Jansen, R. A., Fabricant, D., Franx, M., & Caldwell, N. 2000, ApJS, 126, 331

Jester, S., Schneider, D. P., Richards, G. T., et al. 2005, AJ, 130, 873

Jonsson, P. 2006, MNRAS, 372, 2

Kalirai, J. S., Anderson, J., Dotter, A., et al. 2013, ApJ, 763, 110

Katz, N. & Gunn, J. E. 1991, ApJ, 377, 365

Katz, N., Hernquist, L., & Weinberg, D. H. 1992, ApJ, 399, L109

Kauffmann, G., Heckman, T. M., White, S. D. M., et al. 2003, MNRAS, 341, 33

Kazantzidis, S., Bullock, J. S., Zentner, A. R., Kravtsov, A. V., & Moustakas, L. A. 2008, ApJ, 688, 254

Kelz, A., Verheijen, M. A. W., Roth, M. M., et al. 2006, PASP, 118, 129

Kennicutt, Jr., R. C. 1989, ApJ, 344, 685

Kereš, D., Katz, N., Weinberg, D. H., & Davé, R. 2005, MNRAS, 363, 2

Kewley, L. J., Geller, M. J., & Barton, E. J. 2006, AJ, 131, 2004

Koleva, M., Cenarro, A. J., de La Rosa, I., Sanchez-Blazquez, P., & Vazdekis, A. 2011, in EAS Publications Series, Vol. 48, EAS Publications Series, ed. M. Koleva, P. Prugniel, & I. Vauglin, 87–89

Koleva, M., Prugniel, P., Bouchard, A., & Wu, Y. 2009, A&A, 501, 1269

Koleva, M., Prugniel, P., Ocvirk, P., Le Borgne, D., & Soubiran, C. 2008, MNRAS, 385, 1998

Kordopatis, G., Gilmore, G., Steinmetz, M., et al. 2013, AJ, 146, 134

Kregel, M., van der Kruit, P. C., & de Grijs, R. 2002, MNRAS, 334, 646

Kroupa, P. 2001, MNRAS, 322, 231

Kuntschner, H., Emsellem, E., Bacon, R., et al. 2010, MNRAS, 408, 97

Lacey, C. & Cole, S. 1993, MNRAS, 262, 627

Laine, J., Laurikainen, E., Salo, H., et al. 2014, MNRAS, 441, 1992

Lambas, D. G., Tissera, P. B., Alonso, M. S., & Coldwell, G. 2003, MNRAS, 346, 1189

Laurikainen, E., Salo, H., & Buta, R. 2005, MNRAS, 362, 1319

Law, D. R. & MaNGA Team. 2014, in American Astronomical Society Meeting Abstracts, Vol. 223, American Astronomical Society Meeting Abstracts #223, 254.31

Le Borgne, J.-F., Bruzual, G., Pelló, R., et al. 2003, A&A, 402, 433

Lee, H.-c. & Worthey, G. 2005, ApJS, 160, 176

Leitherer, C., Schaerer, D., Goldader, J. D., et al. 1999, ApJS, 123, 3

MacArthur, L. A., Courteau, S., Bell, E., & Holtzman, J. A. 2004, ApJS, 152, 175

MacArthur, L. A., González, J. J., & Courteau, S. 2009, MNRAS, 395, 28

Macciò, A. V., Stinson, G., Brook, C. B., et al. 2012, ApJ, 744, L9

Majewski, S. R., Nidever, D. L., Muñoz, R. R., et al. 2009, in IAU Symposium, Vol. 256, IAU Symposium, ed. J. T. Van Loon & J. M. Oliveira, 51–56

Majewski, S. R., Wilson, J. C., Hearty, F., Schiavon, R. R., & Skrutskie, M. F. 2010, in IAU Symposium, Vol. 265, IAU Symposium, ed. K. Cunha, M. Spite, & B. Barbuy, 480–481

Makarov, D., Prugniel, P., Terekhova, N., Courtois, H., & Vauglin, I. 2014, A&A, 570, A13

Makarova, L., Koleva, M., Makarov, D., & Prugniel, P. 2010, MNRAS, 406, 1152

Marigo, P., Girardi, L., Bressan, A., et al. 2008, A&A, 482, 883

Marinacci, F., Pakmor, R., & Springel, V. 2014, MNRAS, 437, 1750

Marino, R. A., Gil de Paz, A., Sánchez, S. F., et al. 2016, A&A, 585, A47

Markwardt, C. B. 2009, in Astronomical Society of the Pacific Conference Series, Vol. 411, Astronomical Data Analysis Software and Systems XVIII, ed. D. A. Bohlender, D. Durand, & P. Dowler, 251

Márquez, I., Masegosa, J., Moles, M., et al. 2002, A&A, 393, 389

Martig, M., Minchev, I., & Flynn, C. 2014, MNRAS, 443, 2452

Martín-Navarro, I., Bakos, J., Trujillo, I., et al. 2012, MNRAS, 427, 1102

Martínez-Serrano, F. J., Serna, A., Doménech-Moral, M., & Domínguez-Tenreiro, R. 2009, ApJ, 705, L133

Martins, L. P., Riffel, R., Rodríguez-Ardila, A., Gruenwald, R., & de Souza, R. 2010, MNRAS, 406, 2185

Martins, L. P., Rodríguez-Ardila, A., Diniz, S., Riffel, R., & de Souza, R. 2013, MNRAS, 435, 2861

Matteucci, F. & Gibson, B. K. 1995, A&A, 304, 11

McConnachie, A. W., Irwin, M. J., Ferguson, A. M. N., et al. 2005, MNRAS, 356, 979

McConnachie, A. W., Irwin, M. J., Ibata, R. A., et al. 2009, Nature, 461, 66

Mehlert, D., Thomas, D., Saglia, R. P., Bender, R., & Wegner, G. 2003, A&A, 407, 423

Méndez-Abreu, J., Aguerri, J. A. L., Corsini, E. M., & Simonneau, E. 2008, A&A, 478, 353

Méndez-Abreu, J., Debattista, V. P., Corsini, E. M., & Aguerri, J. A. L. 2014, A&A, 572, A25

Meschin, I., Gallart, C., Aparicio, A., et al. 2014, MNRAS, 438, 1067

Michel-Dansac, L., Lambas, D. G., Alonso, M. S., & Tissera, P. 2008, MNRAS, 386, L82

Minchev, I., Chiappini, C., & Martig, M. 2013, A&A, 558, A9

Minchev, I., Chiappini, C., & Martig, M. 2014, A&A, 572, A92

Minchev, I. & Famaey, B. 2010, ApJ, 722, 112

Minchev, I., Famaey, B., Combes, F., et al. 2011, A&A, 527, A147

Minchev, I., Famaey, B., Quillen, A. C., et al. 2012a, A&A, 548, A127

Minchev, I., Famaey, B., Quillen, A. C., et al. 2012b, A&A, 548, A126

Minchev, I., Martig, M., Streich, D., et al. 2015, ApJ, 804, L9

Monelli, M., Gallart, C., Hidalgo, S. L., et al. 2010a, ApJ, 722, 1864

Monelli, M., Gallart, C., Hidalgo, S. L., et al. 2010b, ApJ, 722, 1864

Monelli, M., Hidalgo, S. L., Stetson, P. B., et al. 2010c, ApJ, 720, 1225

Moré, J. J., Garbow, B. S., & Hillstrom, K. E. 1980, Argonne National Laboratory Report ANL-80-74 [[arXiv]0806.2988]

Muñoz-Mateos, J. C., Gil de Paz, A., Zamorano, J., et al. 2009, ApJ, 703, 1569

Muñoz-Mateos, J. C., Sheth, K., Gil de Paz, A., et al. 2013, ApJ, 771, 59

Navarro, J. F. & Benz, W. 1991, ApJ, 380, 320

Navarro, J. F. & White, S. D. M. 1994, MNRAS, 267, 401

Nidever, D. L., Bovy, J., Bird, J. C., et al. 2014, ApJ, 796, 38

Noël, N. E. D., Aparicio, A., Gallart, C., et al. 2009, ApJ, 705, 1260

Nordström, B., Mayor, M., Andersen, J., et al. 2004, A&A, 418, 989

Obreja, A., Brook, C. B., Stinson, G., et al. 2014, MNRAS, 442, 1794

Ocvirk, P. 2010, ApJ, 709, 88

Ocvirk, P., Pichon, C., Lançon, A., & Thiébaut, E. 2006a, MNRAS, 365, 74

Ocvirk, P., Pichon, C., Lançon, A., & Thiébaut, E. 2006b, MNRAS, 365, 46

Oh, K., Sarzi, M., Schawinski, K., & Yi, S. K. 2011, ApJS, 195, 13

Olszewski, E. W., Schommer, R. A., Suntzeff, N. B., & Harris, H. C. 1991, AJ, 101, 515

Pagel, B. E. J. & Tautvaisiene, G. 1998, MNRAS, 299, 535

Patterson, F. S. 1940, Harvard College Observatory Bulletin, 914, 9

Paturel, G., Petit, C., Prugniel, P., et al. 2003, A&A, 412, 45

Peacock, M. B., Zepf, S. E., Maccarone, T. J., et al. 2014, ApJ, 784, 162

Peletier, R. F. 1989, PhD thesis, , University of Groningen, The Netherlands, (1989)

Peletier, R. F. 2013, Stellar Populations, ed. J. Falcón-Barroso & J. H. Knapen, 353

Peletier, R. F. & Balcells, M. 1996, AJ, 111, 2238

Peletier, R. F., Falcón-Barroso, J., Bacon, R., et al. 2007, MNRAS, 379, 445

Peletier, R. F., Kutdemir, E., van der Wolk, G., et al. 2012, MNRAS, 419, 2031

Pérez, E., Cid Fernandes, R., González Delgado, R. M., et al. 2013, ApJ, 764, L1

Pérez, I. 2004, A&A, 427, L17

Pérez, I. & Sánchez-Blázquez, P. 2011, A&A, 529, A64+

Pérez, I., Sánchez-Blázquez, P., & Zurita, A. 2009, A&A, 495, 775

Perryman, M. A. C., de Boer, K. S., Gilmore, G., et al. 2001, A&A, 369, 339

Pickles, A. J. 1985, ApJ, 296, 340

Pietrinferni, A., Cassisi, S., Salaris, M., & Castelli, F. 2004, ApJ, 612, 168

Pietrinferni, A., Cassisi, S., Salaris, M., & Hidalgo, S. 2013, A&A, 558, A46

Pilkington, K., Few, C. G., Gibson, B. K., et al. 2012a, A&A, 540, A56

Pilkington, K., Gibson, B. K., Brook, C. B., et al. 2012b, MNRAS, 425, 969

Pohlen, M. & Trujillo, I. 2006, A&A, 454, 759 (PT06)

Powell, A. L. T. 1972, MNRAS, 155, 483

Prantzos, N. & Aubert, O. 1995, A&A, 302, 69

Proctor, R. N., Sansom, A. E., & Reid, I. N. 2000, MNRAS, 311, 37

Prugniel, P. & Soubiran, C. 2001, A&A, 369, 1048

Prugniel, P., Soubiran, C., Koleva, M., & Le Borgne, D. 2007, ArXiv Astrophysics e-prints [astro-ph/0703658]

Quillen, A. C., Minchev, I., Bland-Hawthorn, J., & Haywood, M. 2009, MNRAS, 397, 1599

Quinn, P. J., Hernquist, L., & Fullagar, D. P. 1993, ApJ, 403, 74

Radburn-Smith, D. J., Roškar, R., Debattista, V. P., et al. 2012, ApJ, 753, 138

Rahimi, A., Kawata, D., Brook, C. B., & Gibson, B. K. 2010, MNRAS, 401, 1826

Reichardt, C., Jimenez, R., & Heavens, A. F. 2001, MNRAS, 327, 849

Riffel, R., Pastoriza, M. G., Rodríguez-Ardila, A., & Bonatto, C. 2009, MNRAS, 400, 273

Robertson, B., Yoshida, N., Springel, V., & Hernquist, L. 2004, ApJ, 606, 32

Roediger, J. C., Courteau, S., Sánchez-Blázquez, P., & McDonald, M. 2012, ApJ, 758, 41

Romano, D., Chiappini, C., Matteucci, F., & Tosi, M. 2005, A&A, 430, 491

Rosales-Ortega, F. F., Kennicutt, R. C., Sánchez, S. F., et al. 2010, MNRAS, 405, 735

Rose, J. A. 1984, AJ, 89, 1238

Roth, M. M., Kelz, A., Fechner, T., et al. 2005, PASP, 117, 620

Roškar, R., Debattista, V. P., Quinn, T. R., Stinson, G. S., & Wadsley, J. 2008a, ApJ, 684, L79

Roškar, R., Debattista, V. P., Quinn, T. R., & Wadsley, J. 2012, MNRAS, 426, 2089

Roškar, R., Debattista, V. P., Stinson, G. S., et al. 2008b, ApJ, 675, L65

Ruiz-Lara, T., Few, C. G., Gibson, B. K., et al. 2015a, ArXiv e-prints [[arXiv]1512.00625]

Ruiz-Lara, T., Pérez, I., Florido, E., et al. 2016, MNRAS, 456, L35

Ruiz-Lara, T., Pérez, I., Gallart, C., et al. 2015b, A&A, 583, A60

Saha, A., Olszewski, E. W., Brondel, B., et al. 2010, AJ, 140, 1719

Salpeter, E. E. 1955, ApJ, 121, 161

Sánchez, S. F., Kennicutt, R. C., Gil de Paz, A., et al. 2012a, A&A, 538, A8

Sánchez, S. F., Rosales-Ortega, F. F., Iglesias-Páramo, J., et al. 2014, A&A, 563, A49

Sánchez, S. F., Rosales-Ortega, F. F., Marino, R. A., et al. 2012b, A&A, 546, A2

Sánchez-Blázquez, P., Courty, S., Gibson, B. K., & Brook, C. B. 2009, MNRAS, 398, 591

Sánchez-Blázquez, P., Gorgas, J., & Cardiel, N. 2006a, A&A, 457, 823

Sánchez-Blázquez, P., Ocvirk, P., Gibson, B. K., Pérez, I., & Peletier, R. F. 2011, MNRAS, 415, 709

Sánchez-Blázquez, P., Peletier, R. F., Jiménez-Vicente, J., et al. 2006b, MNRAS, 371, 703

Sánchez-Blázquez, P., Rosales-Ortega, F. F., Méndez-Abreu, J., et al. 2014, A&A, 570, A6

Sánchez-Menguiano, L., Sánchez, S. F., Pérez, I., et al. 2016, ArXiv e-prints [[arXiv]1601.01542]

Santos, Jr., J. F. C., Clariá, J. J., Ahumada, A. V., et al. 2006, A&A, 448, 1023

Sarzi, M., Falcón-Barroso, J., Davies, R. L., et al. 2006, MNRAS, 366, 1151

Scannapieco, C., White, S. D. M., Springel, V., & Tissera, P. B. 2009, MNRAS, 396, 696

Schaye, J. 2004, ApJ, 609, 667

Schiavon, R. P. 2007, ApJS, 171, 146

Schmitt, H. R., Bica, E., & Pastoriza, M. G. 1996, MNRAS, 278, 965

Schönrich, R. & Binney, J. 2009, MNRAS, 396, 203

Seabroke, G. M. & Gilmore, G. 2007, MNRAS, 380, 1348

Searle, L., Sargent, W. L. W., & Bagnuolo, W. G. 1973, ApJ, 179, 427

Seidel, M. K., Cacho, R., Ruiz-Lara, T., et al. 2015, MNRAS, 446, 2837

Sellwood, J. A. & Binney, J. J. 2002, MNRAS, 336, 785

Sérsic, J. L. 1968, Atlas de galaxias australes

Siebert, A., Williams, M. E. K., Siviero, A., et al. 2011, AJ, 141, 187

Singh, R., van de Ven, G., Jahnke, K., et al. 2013, A&A, 558, A43

Skillman, E. D. & Gallart, C. 2002, in Astronomical Society of the Pacific Conference Series, Vol. 274, Observed HR Diagrams and Stellar Evolution, ed. T. Lejeune & J. Fernandes, 535

Skillman, E. D., Hidalgo, S. L., Weisz, D. R., et al. 2014, ApJ, 786, 44

Smecker-Hane, T. A., Cole, A. A., Gallagher, III, J. S., & Stetson, P. B. 2002, ApJ, 566, 239

Snaith, O. N., Haywood, M., Di Matteo, P., et al. 2014, ApJ, 781, L31

Soubiran, C., Bienaymé, O., Mishenina, T. V., & Kovtyukh, V. V. 2008, A&A, 480, 91

Spinrad, H. 1962, ApJ, 135, 715

Steinmetz, M. & Muller, E. 1995, MNRAS, 276, 549

Steinmetz, M. & Navarro, J. F. 2002, New A, 7, 155

Steinmetz, M., Zwitter, T., Siebert, A., et al. 2006, AJ, 132, 1645

Stinson, G. S., Bailin, J., Couchman, H., et al. 2010, MNRAS, 408, 812

Stinson, G. S., Brook, C., Prochaska, J. X., et al. 2012, MNRAS, 425, 1270

Storchi-Bergmann, T., Riffel, R. A., Riffel, R., et al. 2012, ApJ, 755, 87

Teyssier, R. 2002, A&A, 385, 337

Thilker, D. A., Bianchi, L., Meurer, G., et al. 2007, ApJS, 173, 538

Tinsley, B. M. & Gunn, J. E. 1976, ApJ, 203, 52

Tojeiro, R., Heavens, A. F., Jimenez, R., & Panter, B. 2007, MNRAS, 381, 1252

Trujillo, I., Aguerri, J. A. L., Cepa, J., & Gutiérrez, C. M. 2001, MNRAS, 328, 977

Trujillo, I. & Pohlen, M. 2005, ApJ, 630, L17

Twarog, B. A. 1980, ApJ, 242, 242

Tweed, D., Devriendt, J., Blaizot, J., Colombi, S., & Slyz, A. 2009, A&A, 506, 647

Valdes, F., Gupta, R., Rose, J. A., Singh, H. P., & Bell, D. J. 2004, ApJS, 152, 251

van den Bosch, F. C. 2001, MNRAS, 327, 1334

van der Kruit, P. C. 1979, A&AS, 38, 15

van der Kruit, P. C. 1987, A&A, 173, 59

van der Marel, R. P. & Franx, M. 1993, ApJ, 407, 525

Vazdekis, A., Casuso, E., Peletier, R. F., & Beckman, J. E. 1996, ApJS, 106, 307

Vazdekis, A., Sánchez-Blázquez, P., Falcón-Barroso, J., et al. 2010, MNRAS, 404, 1639 (V10)

Vera-Ciro, C., D'Onghia, E., Navarro, J., & Abadi, M. 2014, ApJ, 794, 173

Villalobos, Á. & Helmi, A. 2008, MNRAS, 391, 1806

Villalobos, Á. & Helmi, A. 2009, MNRAS, 399, 166

Walcher, C. J., Wisotzki, L., Bekeraité, S., et al. 2014, A&A, 569, A1

Walker, A. P., Gibson, B. K., Pilkington, K., et al. 2014, MNRAS, 441, 525

Weidner, C., Ferreras, I., Vazdekis, A., & La Barbera, F. 2013a, MNRAS, 435, 2274

Weidner, C., Kroupa, P., Pflamm-Altenburg, J., & Vazdekis, A. 2013b, MNRAS, 436, 3309

White, S. D. M. & Rees, M. J. 1978, MNRAS, 183, 341

Wielen, R. 1977, A&A, 60, 263

Williams, B. F., Dalcanton, J. J., Dolphin, A. E., Holtzman, J., & Sarajedini, A. 2009, ApJ, 695, L15

Worthey, G. 1994, ApJS, 95, 107

Worthey, G. & Ottaviani, D. L. 1997, ApJS, 111, 377

Yanny, B., Rockosi, C., Newberg, H. J., et al. 2009, AJ, 137, 4377

Yoachim, P., Roškar, R., & Debattista, V. P. 2010, ApJ, 716, L4

Yoachim, P., Roškar, R., & Debattista, V. P. 2012, ApJ, 752, 97

York, D. G., Adelman, J., Anderson, Jr., J. E., et al. 2000, AJ, 120, 1579

Younger, J. D., Cox, T. J., Seth, A. C., & Hernquist, L. 2007, ApJ, 670, 269

Zhang, H.-X., Hunter, D. A., Elmegreen, B. G., Gao, Y., & Schruba, A. 2012, AJ, 143, 47

Zheng, Z., Thilker, D. A., Heckman, T. M., et al. 2015, ApJ, 800, 120

Zwitter, T., Siebert, A., Munari, U., et al. 2008, AJ, 136, 421